

VIRTUAL

Proceedings of the
19th Annual Symposium
Imaging Network Ontario
March 23 – 24, 2021

Table of Contents

ImNO 2021 Co-Chairs	4
Welcome Letter	5
Imaging Network Ontario (ImNO) Code of Conduct	6
Sponsoring Consortia	7
Development of Novel Therapies for Bone and Joint Diseases	7
Heart Failure: Prevention through Early Detection Using New Imaging Methods	7
Ontario Institute for Cancer Research Imaging Program	7
Image-Guided Device Interventions for Cardiovascular Disease	8
Next-Generation Innovations in Ultrasonics (N-Genius)	8
Keynote Speakers	9
Muyinatu Bell	9
Charu Chandrasekera	10
Panels	11
Academic Alumni Panel	11
COVID-19 Panel	11
Industry Alumni Panel	12
Scientific and Organizing Committees	13
Scientific Committee	13
Student Sub-committee	13
Organizing Committee	13
Abstract Reviewers	13
Oral and Pitch Judges	13
Program	14
Oral & Pitch Abstracts	23
Session 1: Image-Guided Devices	24
Session 2: Lung & Cellular Imaging	30
Session 3: Imaging for Musculoskeletal Analysis	36
Session 4: Image-Guided Surgery	42
Session 5: Device, Hardware, System Development I	52

Session 6: Machine Learning for Cancer Applications	62
Session 7: Image Processing	72
Session 8: Device, Hardware, System Development II	81
Session 9: Contrast Agents I	90
Session 10: Musculoskeletal Imaging	98
Session 11: Deep Learning	106
Session 12: Contrast Agents II	114
Session 13: Cancer Imaging I	121
Session 14: Deep Learning for Segmentation	127
Session 15: Animal Model & Image Processing	133
Session 16: Machine Learning I	139
Session 17: Neuro Imaging I	145
Session 18: Computation Modeling	153
Session 19: COVID-19 & Brain Related Injuries	162
Session 20: Molecular Imaging	168
Session 21: Machine Learning II	174
Session 22: Machine Learning III	180
Session 23: MR Imaging	186
Session 24: Cancer Imaging II	194
Session 25: Machine Learning IV	202
Session 26: MRI Contrast & Devices	208
Session 27: Neuro Imaging II	214
Authors Index	220

ImNO 2021 Co-Chairs



[Pascal Fallavollita](#)

University of Ottawa



[Miranda Kirby](#)

Ryerson University

Welcome Letter

March 9, 2021

Dear ImNO 2021 Attendees:

Welcome to the Imaging Network Ontario (ImNO) 2021 Symposium. This year marks our 19th annual and second virtual meeting.

The ImNO Symposium is a two-day event that brings together best-in-class physicians, technologists, researchers, healthcare professionals and trainees. The emphasis is on compelling, cross-functional, and inter-disciplinary themes. The symposium focuses on the opportunities, challenges, and best practices of leveraging modern healthcare imaging to make it more equitable for all patients. Unique this year is engaging our past and present trainees in alumni panels that focus on both academic and industry career pathways. We also include a facilitated panel discussion focusing on COVID-19, and the current and future role of imaging in disease management.

The Symposium is a joint effort between a group of interdisciplinary consortia focused on accelerating medical imaging innovation in Ontario, and across Canada. This year, we would like to thank the following groups for supporting our symposium:

- Development of Novel Therapies for Bone and Joint Diseases
- Heart Failure: Prevention through Early Detection Using New Imaging Methods
- Image-Guided Device Interventions for Cardiovascular Disease
- Ontario Institute for Cancer Research Imaging Program

Since its inception in 2003, the annual ImNO meeting has invited presentations from world-class scientists and welcomed proffered presentations from Ontario and across the country. For the 2021 meeting, abstracts were reviewed by an average of 3 reviewers and 169 were accepted. The Symposium Co-Chairs and the Scientific Committee assembled the program of 2 keynote speakers, 3 panels, 60 oral presentations and 109 pitch presentations.

In closing, we would like to acknowledge the significant contributions made by the members of the Scientific and Organizing Committees. Together they have worked very hard to bring us a diverse program. We hope you enjoy this year's slate of short talks, pitch presentations, panels and keynotes.

Sincerely,

Miranda Kirby and Pascal Fallavollita

Chairs, Scientific Committee, 2021 ImNO Symposium

Imaging Network Ontario (ImNO) Code of Conduct

All attendees, speakers, sponsors and volunteers at ImNO are required to agree with the following code of conduct. Organisers will enforce this code throughout the event. We expect cooperation from all participants to help ensure a safe environment for everybody.

Need Help?

If you are being harassed, notice that someone else is being harassed, or have any other concerns, speak to ImNO staff or send an email to ombudsperson@ImNO.ca or chair@ImNO.ca.

Overview

Imaging Network Ontario is committed to providing a harassment-free conference experience for everyone, regardless of gender, gender identity and expression, age, sexual orientation, disability, physical appearance, body size, race, ethnicity, religion (or lack thereof), or technology choices. We do not tolerate harassment of conference participants in any form. Use of sexualised language and imagery that does not convey a scientific message is not appropriate. We expect participants and sponsors to follow these rules for the duration of the conference in any conference venue, including talks, workshops, parties, Twitter and other online media. Conference participants violating these rules may be sanctioned or expelled from the conference without a refund at the discretion of the conference organisers.

Details

All attendees, speakers, sponsors and volunteers at ImNO are subject to the anti-harassment policy.

Harassment includes offensive verbal comments related to gender, gender identity and expression, age, sexual orientation, disability, physical appearance, body size, race, ethnicity, religion, technology choices, sexual images in public spaces, deliberate intimidation, stalking, following, harassing photography or recording, sustained disruption of talks or other events, inappropriate physical contact, and unwelcome sexual attention. Use of images, activities, uniforms/costumes or other materials that create a sexualised environment will not be tolerated.

Anyone asked to stop any harassing behavior is expected to comply immediately.

If anyone engages in harassing behavior, the conference organisers may take any action they deem appropriate, including warning the offender or expulsion from the conference **with no refund**.

If you are being harassed, notice that someone else is being harassed, or have any other concerns, please contact a member of conference staff immediately. Conference staff can be identified as they'll be wearing clearly marked badges saying "ImNO staff". You can also send an email to the ImNO ombudsperson, Dr. Maria Drangova, at ombudsperson@ImNO.ca or the ImNO 2020 Chairs, Drs. Miranda Kirby and Pascal Fallavollita, at chair@ImNO.ca.

Conference staff will be happy to help participants contact hotel/venue security or local law enforcement, provide escorts, or otherwise assist those experiencing harassment to feel safe for the duration of the conference. We value your attendance.

We expect everyone to follow these rules for the duration of the conference within and outside conference venues, including but not limited to conference-related talks, workshops, and social events involving ImNO attendees, and in all conference related communications, including social media.

Sponsoring Consortia

The Annual Meeting of Imaging Network Ontario (ImNO) promotes Canada's role as a leader in medical imaging innovation by cultivating synergy among consortia and partnerships between Ontario and other Canadian imaging entities.

The following consortia and programs supported the 2021 ImNO Symposium financially.

Development of Novel Therapies for Bone and Joint Diseases

Lead Researcher: Dr. David Holdsworth

Ontario Research Fund

Musculoskeletal disorders are the most common cause of severe long-term pain and physical disability, affecting hundreds of millions of people around the world. The economic burden is high; joint diseases cost the Ontario economy more than \$2 billion per year. To reduce this disease burden, this Ontario Research Fund Research Excellence program focuses on the "Development of Novel Therapies for Bone and Joint Diseases," including improved diagnostic imaging techniques and new approaches for image-guided therapy. A multidisciplinary team of imaging scientists, biomedical engineers, physical therapists, and orthopaedic surgeons work together on key research projects, including the development of new ways to post-process 3D MRI and CT data to guide surgery, dynamic imaging of moving joints (under load), and image-based design of "patient-specific" orthopaedic components.

Heart Failure: Prevention through Early Detection Using New Imaging Methods

Lead Researcher: Dr. Frank Prato

Ontario Research Fund

Consortium partners: Lawson Health Research Institute, Sunnybrook Research Institute and University of Ottawa Heart Institute. Ten percent of Ontarians over 60 have heart failure. One quarter will die within one year of diagnosis and almost all in ten years. Our LHRI/SRI/UOHI consortium is developing combined PET and MRI imaging methods for early diagnosis when treatment is still possible. The imaging methods developed are being commercialized and will benefit Ontario by improving the health of its citizens and creating new jobs.

Ontario Institute for Cancer Research Imaging Program

Directors: Dr. Aaron Fenster and Dr. Martin Yaffe

Ontario Institute for Cancer Research

The OICR Imaging Program accelerates the translation of research into the development of new imaging innovations for earlier cancer detection, diagnosis and treatment through four major projects: probe development and commercialization, medical imaging instrumentation and software, pathology validation, and imaging for clinical trials. The Imaging Program facilitates improved screening and treatment options for cancer patients by streamlining advances in medical imaging through the complex pipeline from discovery to clinical translation and ultimately to clinical use.

Image-Guided Device Interventions for Cardiovascular Disease

Lead Researcher: Dr. Graham Wright

Ontario Research Fund

With advances in early identification and management of risk factors, combined with effective response to acute events, cardiovascular diseases have evolved from an acute killer to a chronic disease challenge. In recent years, there have been major advances in less invasive treatments. For minimally invasive device therapeutics, imaging and tracking technologies, along with the development of image-modality compatible tools, have unique roles in planning and guiding interventions, as well as monitoring functional results. In electrophysiology, imaging will guide positioning of pacing devices, identify ablation targets, and direct therapy through fusion of device representations with maps of myocardial structure and function. Similar advances facilitate planning and guidance of both percutaneous and minimally invasive valve repair/replacement and catheter-based revascularization of chronic total occlusions. Researchers at Sunnybrook and Robarts Research Institutes, working with local, national, and multinational diagnostic imaging and interventional device companies, are advancing the state-of-the-art in image acquisition and analysis with ultrasound, MRI, x-ray, and CT methods, including the design of visualization platforms and associated communication and control interfaces for interventional guidance, facilitating fusion and manipulation of prior and real-time imaging and device information. The ultimate goal is more effective utilization of imaging to improve outcomes for those suffering from chronic ischemia, complex arrhythmias, and heart failure related to structural heart diseases.

Next-Generation Innovations in Ultrasonics (N-Genius)

Director: Dr. Alfred Yu NSERC Collaborative Research Training and Experience (CREATE) Program

Ultrasound is well regarded for its broad application potential in both diagnostics and therapeutics. The N-GENIUS Program, hosted at the University of Waterloo, will aim to pioneer next-generation solutions for ultrasound imaging and therapy to address unmet clinical needs and, in turn, boost Canada's reputation as one of the global leaders in biomedical ultrasonics. N-GENIUS will also strive to cultivate a new generation of ultrasound R&D talent who will significantly contribute to Canada's ultrasound industry and scientific community.



Keynote Speakers

Tuesday, March 23 at 8:40

Listening to the Sound of Light to Guide Surgeries

[Muyinatu Bell](#), PhD, Assistant Professor, Johns Hopkins University

Muyinatu Bell is an Assistant Professor of Electrical and Computer Engineering, Biomedical Engineering, and Computer Science at Johns Hopkins University, where she founded and directs the Photoacoustic and Ultrasonic Systems Engineering (PULSE) Lab. Dr. Bell earned a BS. degree in Mechanical Engineering (biomedical engineering minor) from Massachusetts Institute of Technology (2006), received a PhD degree in Biomedical Engineering from Duke University (2012), conducted research abroad as a Whitaker International Fellow at the Institute of Cancer Research and Royal Marsden Hospital in the United Kingdom (2009-2010), and completed a postdoctoral fellowship with the Engineering Research Center for Computer-Integrated Surgical Systems and Technology at Johns Hopkins University (2016). She is Associate Editor-in-Chief of IEEE Transactions on Ultrasonics, Ferroelectrics, and Frequency Control (T-UFFC), Associate Editor of IEEE Transactions on Medical Imaging, and holds patents for short-lag spatial coherence beamforming and photoacoustic-guided surgery. Dr. Bell is a recipient of multiple awards and honors, including MIT Technology Review's Innovator Under 35 Award (2016), the NSF CAREER Award (2018), the NIH Trailblazer Award (2018), the Alfred P. Sloan Research Fellowship (2019), the ORAU Ralph E. Powe Jr. Faculty Enhancement Award (2019), and Maryland's Outstanding Young Engineer Award (2019). She most recently received the inaugural IEEE UFFC Star Ambassador Lectureship Award (2020) from her IEEE society and the SPIE Early Career Achievement Award (2021).



Dr. Charu Chandrasekera is the Founder and Executive Director of the Canadian Centre for Alternatives to Animal Methods (CCAAM) and its subsidiary, the Canadian Centre for the Validation of Alternative Methods (CaCVAM) – the internationally recognized Canadian counterpart to the global network of centers for alternative methods. She obtained her PhD in Biochemistry and Molecular Biology from the Faculty of Medicine, University of Calgary and has over two decades of experience in cardiovascular and diabetes research. In the CCAAM/CaCVAM research laboratory located at the University of Windsor, Dr. Chandrasekera uses a wide range of technologies, including 3D-bioprinting, organ-on-chip, and *in silico* modelling to create *Disease-in-a-Dish* and *Toxicity-on-a-Chip* – to reduce and replace animals in disease modelling and drug/chemical safety testing. Dr. Chandrasekera is an internationally recognized scientist – well versed in national and international regulatory testing frameworks, science policy, and bioethics – with an expansive network of national and international academic, industry, government, and non-profit stakeholders. She represents Canada, alongside Health Canada, on the International Cooperation on Alternatives Test Methods (ICATM consortium of global Centers for the Validation of Alternative Methods) and sits on US and EU government advisory committees on alternative test methods. The overarching vision of her Centres is to promote the replacement of animals in Canadian biomedical research, education, and regulatory testing through 21st century science, innovation, and ethics.



Panels

Tuesday, March 23 at 12:30

Academic Alumni Panel



[Sarah Mattonen](#), PhD
Western University



[Dafna Sussman](#), PhD
Ryerson University



[Eran Ukwatta](#), PhD
University of Guelph



[Yiwen Xu](#), PhD
University Health
Network

Wednesday, March 24 at 8:40

COVID-19 Panel



[Matthias Friedrich](#), MD
McGill University Health
Centre



[Simon Graham](#), PhD,
P.Eng
Sunnybrook Research
Institute



[Grace Parraga](#), PhD
Robarts Research
Institute



[Aaron So](#), PhD
Lawson Health Research
Institute

Wednesday, March 24 at 12:00

Industry Alumni Panel



Daniel Gelman, PhD

[Aufero Medical](#)



Eli Gibson, PhD

[Siemens Healthineers](#)



Zahra Hosseini, PhD

[Siemens Healthineers](#)



Cynthia Stewart, MBA

[GE Healthcare Canada](#)

Scientific and Organizing Committees

Chairs: Miranda Kirby and Pascal Fallavollita

Scientific Committee

Corey Baron	David Holdsworth	Frank Prato	Eran Ukwatta
Robert deKemp	Sarah Mattonen	Timothy Scholl	Graham Wright
Maria Drangova	Charles McKenzie	Adam Shuhendler	Martin Yaffe
Gabor Fichtinger	Tamie Poepping	Rebecca Thornhill	Alfred Yu
Ali Khan			

ImNO Student Sub-committee

Nova Alam	Colton Barr	Emilie Brun	Kesavi Kanagasabai
Sarah Aubert	Layale Bazzi	Rohini Gaikar	

Organizing Committee

Carol Richardson	Jean Rookwood	Kitty Wong
------------------	---------------	------------

Abstract Reviewers

Natasha Alves-Kotzev	Matthew Holden	Elka Miller	Jesse Tanguay
Corey Baron	David W Holdsworth	Michael Noseworthy	Ali Tavallaei
Stephen Breen	Amoon Jamzad	Alexei Ouriadov	Matthew Teeter
Greg Cron	Michael Jurkiewicz	Terry Peters	Jonathan Thiessen
Robert DeKemp	Ali Khan	Tamie Poepping	Rebecca Thornhill
Savita Dhanvantari	Miranda Kirby	Jessica Rodgers	Eranga Ukwatta
Mamadou Diop	Emily Lalone	Giles Santyr	Tamas Ungi
Maria Drangova	M. Louis Lauzon	Tim Scholl	Cari Whyne
Pascal Fallavollita	Ting-Yim Lee	Michael Seed	Graham Wright
Aaron Fenster	Daniel Lorusso	Adam Shuhendler	Yiming Xiao
Gabor Fichtinger	Chris Macgowan	Navneet Singh	Billy Yiu
Nilesh Ghugre	Sarah Mattonen	John Sled	Alfred Yu
Donna Goldhawk	Charles McKenzie	Kathleen Surry	
Michael Hardisty			

Oral and Pitch Judges

Coordinator: Corey Baron

Faranak Akbarifar	Nilesh Ghugre	Amir Manbachi	Kathleen Surry
Nova Alam	Donna Goldhawk	Sarah Mattonen	Dafna Sussman
Natasha Alves-Kotzev	Maged Goubran	Charles McKenzie	Ali Tavallaei
Corey Baron	Matt Gwilliam	Farah Mushtaha	Edward Taylor
Layale Bazzi	Miriam Hewlett	Nathan Orlando	Eranga Ukwatta
Elvis Chen	Eno Hysi	Alexei Ouriadov	Tamas Ungi
Spencer Christiansen	Amin Jafarisojahrood	Claire Park	Gabriel Varela-Mattatall
Jaryd Christie	Amoon Jamzad	Terry Peters	TianDuo Wang
Salma Dammak	Lueder A. Kahrs	Tamie Poepping	Jill Weyers
Jordan DeKraker	April Khademi	Mihaela Pop	Graham Wright
Maria Drangova	Andras Lasso	Naila Rahman	Kevin Wyszatko
Paul Dubovan	Ting-Yim Lee	Jessica Rodgers	Dan Xiao
Aaron Fenster	Daniel Lorusso	Tales Santini	Billy Yiu
Paula Foster	Chris Macgowan	Timothy Scholl	Brandon Zanette
Stewart Gaede			

Program

Tuesday, March 23, 2021

08:30	Opening Remarks Miranda Kirby and Pascal Fallavollita, ImNO 2021 Scientific Committee Chairs		Zoom Meeting Room 1
08:40	Keynote Session Chairs: Pascal Fallavollita, Miranda Kirby Listening to the Sound of Light to Guide Surgeries Muyinatu Bell, Johns Hopkins University		Zoom Meeting Room 1
09:25	Break		
09:30	Oral Sessions 1 - 3		
	Zoom Meeting Room 1	Zoom Meeting Room 2	Zoom Meeting Room 3
	Oral 1 Image-Guided Devices	Oral 2 Lung & Cellular Imaging	Oral 3 Imaging for Musculoskeletal Analysis
	Chairs: Stewart Gaede, Amoon Jamzad	Chairs: Daniel Lorusso, Donna Goldhawk	Chairs: Elvis Chen, Eno Hysi
09:30	1-1 Translation of an ultrasound-guided needle placement system to Mauritania Julia Wiercigroch, Queen's University	2-1 Variable Temporal Resolution Cartesian Sampling for Cell Tracking MRI Mark Armstrong, University of Windsor	3-1 Detecting treatment failure in rheumatoid arthritis with near-infrared light: in silico investigation within simulated disease states Seva Ioussoufovitch, Western University
09:45	1-2 Feasibility of fusing three-dimensional transabdominal and transrectal ultrasound images to visualize intracavitary gynaecological brachytherapy applicators Jessica R Rodgers, Robarts Research Institute	2-2 Computed Tomography Airways and Vessels: Bridging the Gap in COPD Huma Asghar, Ryerson University	3-2 Effect of body mass on cementless implant fixation for total knee replacement Jordan Broberg, Western University
10:00	1-3 Development of an open-source prostate biopsy training system Catherine O Wu, Queen's University	2-3 CT Emphysema and Small Airway Disease Clusters and Progression of Chronic Obstructive Pulmonary Disease Sarah Kadhim, Ryerson University	3-3 Reliability and concurrent validity of 3D ultrasound for quantifying knee cartilage volume Sam Papernick, Western University
10:15	1-4 Margin expansion study for mpMRI-defined prostatic lesions in the setting of focally boosted high-dose rate prostate brachytherapy Christopher W Smith, Western University	2-4 Progressive changes in glutamate concentration in early stages of schizophrenia - A longitudinal 7-Tesla MRS study Peter Jeon, Western University	3-4 In-vivo porcine tendon release using high-intensity focused ultrasound ablation William Chu Kwan, The Hospital for Sick Children
10:30	1-5 Feasibility and clinical utility of three-dimensional ultrasound in oral cavity cancers Jacob Wihlidal, Western University	2-5 Magnetic particle imaging quantifies the dilution of intracellular iron labels by proliferating breast cancer cells in vitro Maryam A Berih, Western University	3-5 In vivo porcine tendon release using high-intensity focused ultrasound long-pulse histotripsy followed by thermal ablation Imogen K den Otter Moore, The Hospital for Sick Children
10:45	Break		

Tuesday, March 23, 2021

10:55	Pitch Sessions 4 - 6		
	Zoom Meeting Room 1	Zoom Meeting Room 2	Zoom Meeting Room 3
	Pitch 4	Pitch 5	Pitch 6
	Image Guided Surgery	Device, Hardware, System Development I	Machine Learning for Cancer Applications
	Chairs: Nathan Orlando, Tamas Ungi	Chairs: Ali Tavallaei, TianDuo Wang	Chairs: Faranak Akbarifar, Sarah Mattonen
10:55	4-1 Validating 3D shape estimation using the Basel Face Model towards planning craniofacial reconstruction Zachary Fishman, University of Toronto - Sunnybrook Research Institute	5-1 Validation of a Retrospective Eddy Current Correction Algorithm for Advanced Diffusion MRI Paul I Dubovan, Western University	6-1 The Impact of the Variation of CT Scanner on the Prediction of Human papillomavirus (HPV) Association of Oropharyngeal Cancer (OPC) using Radiomic Models Reza Reiazi, Princess Margaret Cancer Research Center
11:00	4-2 Augmented Reality Relaxed Skin Tension Lines for Face Surgery - Initial Results on a Mobile Device Wenzhangzhi Guo, University of Toronto	5-2 A simple, realistic walled phantom for intravascular and intracardiac applications Hareem Nisar, Western University	6-2 Effects of Feature Type and Selection on Machine Learning Classifier Accuracy for Predicting Brain Metastasis Response to Stereotactic Radiosurgery David A DeVries, Western University
11:05	4-3 Preclinical Evaluation of a Bedside Image-Guidance System for External Ventricular Drainage Adam Hopfgartner, Sunnybrook Research Institute	5-3 Toward high-resolution PEM and US-guided core-needle biopsy Claire K Park, Western University	6-3 Impact of Radiomic Biopsies on Feature Extraction in Positron Emission Tomography (PET) Imaging for Non-Small Cell Lung Cancer Lauren M Zelko, Western University
11:10	4-4 Miniature C-Arm Simulator Using Wireless Accelerometer Based Tracking Daniel Allen, Robarts Research Institute	5-4 Evaluating the feasibility of resting-state fMRI at low-field MR scanner by investigating the relationship between temporal signal to noise ratio and resting-state networks Arjama Halder, Western University	6-4 Quantitative Imaging Derived Metrics for Prostate Cancer Therapy Induced Sarcopenia Kelly J Fullerton, Sunnybrook Research Institute
11:15	4-5 Optimization of MRI thermometry for controlled hyperthermia-mediated drug delivery in a murine model of pediatric sarcoma Suzanne Wong, The Hospital for Sick Children	5-5 Theoretical Comparison of the Detective Quantum Efficiency of Halide Lead Perovskite, Cesium Iodide and Selenium X-Ray Imaging Detectors Michael Belli, Ryerson University	6-5 Detection and localization of transition and peripheral zone prostate cancers on apparent diffusion coefficient (ADC) map MR images using U-Net ensemble Timothy Wong, University of Guelph
11:20	4-6 Quantifying Tissue Optical Properties using Structured Illumination for Oral Cancer Surgery Murtuza V Rajkotwala, University Health Network	5-6 B1+ Field Homogeneity and Signal Generation of a Koch Fractal RF Coil for Sodium MRI Cameron Nowikow, McMaster University	6-6 Validation of a CT based radiomics signature in oropharyngeal cancer: assessing sources of variation Philipp Guevorguian, Western University
11:25	4-7 A platform for robot-assisted intraoperative imaging in breast conserving surgery Laura P Connolly, Queen's University	5-7 Impact of Volumetric 4D-CT Motion Artifact Reduction on Ventilation Imaging Heather M Young, Western University	6-7 A CT-based radiomics model for predicting gastrostomy tube insertion in oropharyngeal cancer Tricia Chinnery, Western University
11:30	4-8 Transrectal diffuse optical tomography system to monitor photothermal therapy of localized prostate cancer Ivan Kosik, University Health Network	5-8 TITAN: A Hyperion Imaging System Data Analysis Software Sindhura Thirumal, Queen's University	6-8 Platform-Independent Management of Histopathologic Annotations in Cancer Research: Application in High-Dimensional Metabolomic Image Analysis Amoon Jamzad, Queen's University
11:35	4-9 Improving central line needle insertions using in situ vascular reconstructions Leah Groves, Robarts Research Institute	5-9 Evaluating Back-to-Back and Day-to-Day Reproducibility of Cortical GABA Measurements with MEGA-PRESS Using 32-channel Head Coil Sonja Elsaid, Centre for Addiction and Mental Health/University of Toronto	6-9 Automated Contouring of Breast Tumors using Machine Learning Josh H Ehrlich, Queen's University
11:40	Break		

Tuesday, March 23, 2021

11:45	Pitch Sessions 7 - 9		
	Zoom Meeting Room 1	Zoom Meeting Room 2	Zoom Meeting Room 3
	Pitch 7 Image Processing	Pitch 8 Device, Hardware, System Development II	Pitch 9 Contrast Agents I
	Chairs: Layale Bazzi, Lueder A. Kahrs	Chairs: Natasha Alves-Kotzev, Tales Santini	Chairs: Amin Jafarisojahrood, Timothy Scholl
11:45	7-1 Microscopic Fractional Anisotropy Imaging in the Human Brain: An Optimized Kurtosis Approach vs. the Gamma Model Nico J J Arezza, Western University	8-1 Theoretical Comparison of Energy-Resolved and Digital-Subtraction Angiography Sarah Aubert, Ryerson University	9-1 Longitudinal Observation of the Emphysema Progression in Alpha-1 Antitrypsin Deficiency Using 3He/129Xe MRI Elise Woodward, Western University
11:50	7-2 Sub-second and Dynamic Computed Tomography Development at the Canadian Light Source Xiao Fan Ding, University of Saskatchewan	8-2 Field profile analysis of a 2D spiral array for high-volume-rate 3D ultrasound imaging Rebekah Maffett, University of Waterloo	9-2 Effect of low dose daily aspirin on cerebral blood flow and kidney function in hypertensive rats Greg Cron, The Ottawa Hospital Research Institute
11:55	7-3 Reliability Assessment of Cerebrospinal Fluid Suppressed Microscopic Fractional Anisotropy Mohammad Omer, Western University	8-3 Inhomogeneity and ramping effects in delta relaxation enhanced magnetic resonance Matthew A McCready, Western University	9-3 A Remarkably Stable Manganese(III) Porphyrin as a Building Block for Bioconjugation Keith Tang, University of Toronto
12:00	7-4 A Systematic Study of the Effect of Scan Time on the Reproducibility of Cortical MEGA-PRESS GABA+ Measurements: Preliminary Data Peter Truong, Centre for Addiction and Mental Health	8-4 Network Parameter and Quality Factor Assessment of Fractal RF Coils for Sodium MRI Cameron Nowikow, McMaster University	9-4 Materials for Anthropomorphic MRI Phantoms Eunyoung Cho, Ryerson University
12:05	7-5 Automatic determination of the regularization weighting for low rank reconstructions Gabriel EM Varela-Mattatall, Centre for Functional and Metabolic Mapping	8-5 Evaluating Gradient Induced Main Magnet Coil Heating Diego F Martinez, Western University	9-5 Characterizing the chronic evolution of ablation lesion and edema using native T1 and 3D late gadolinium enhancement (LGE) after radiofrequency ablation therapy (RFA) in a swine model of ischemic VT Terenz R Escartin, Sunnybrook Research Institute
12:10	7-6 Measuring endogenous levels of GABA, GSH, and GLU in a human brain using MRI Kesavi Kanagasabai, Lawson Health Research Institute	8-6 Radiofrequency coils for single-sided portable magnetic resonance Doris Rusu, University of Windsor	9-6 A Bifurcating Microvessel Phantom to Assess Feature Resolvability in Sub-Diffraction Limit Contrast Ultrasound Imaging Hanyue Shangguan, University of Waterloo
12:15	7-7 Cost-effective micro-CT imaging of medical components fabricated with additive manufacturing Santiago F Cobos, Western University	8-7 DS- MT- Bound Solvent- And 4-Pool Glucoest Optimization Of Simultaneous Multiple Offset Saturation Pulse Via Genetic Algorithm Siddharth Sadanand, Ryerson University	9-7 Myocardial glucose suppression interferes with the detection of inflammatory cells with FDG-PET in a canine model of myocardial infarction Benjamin Wilk, Lawson Health Research Institute
12:20	7-8 In vivo molecular imaging of the mouse cholinergic projection system Kate M Onuska, Western University	8-8 Necessity of using Impulse-Sampled Notation and Fourier Transform rather than Discrete Fourier Transform for Determining Spectral Performance of Image Post Processing Ian Cunningham, Western University	
12:25	Break		
12:30	Academic Alumni Panel		
	Chairs: Layale Bazzi, Alfred Yu Sarah Mattonen, Western University Dafna Sussman, Ryerson University Eran Ukwatta, University of Guelph Yiwen Xu, University Health Network		
13:30	Break		

Tuesday, March 23, 2021

13:35	Pitch Sessions 10 - 12		
	Zoom Meeting Room 1	Zoom Meeting Room 2	Zoom Meeting Room 3
	Pitch 10 Musculoskeletal Imaging	Pitch 11 Deep Learning	Pitch 12 Contrast Agents II
	Chairs: Corey Baron, Nathan Orlando	Chairs: Nova Alam, Dafna Sussman	Chairs: Edward Taylor, Kevin Wyszatko
13:35	10-1 The Effect of Volar Scapholunate Tears on Carpal Kinematics Sydney M Robinson, Western University	11-1 A Deep 2D-UNet Ensemble for the Segmentation of Microstructural White Matter Damage in mTBI Patients using Diffusion Tensor Imaging Brian C McCrindle, McMaster University	12-1 Endobronchial Ultrasound and Drug-Loaded Microbubbles for In Vivo Targeted Lung Cancer Therapy Sean F McGrath, University of Toronto
13:40	10-2 Enhanced uCT imaging enables high resolution 3D visualization of microdamage in rat vertebrae Allison Tolgyesi, University of Toronto	11-2 Aliasing Removal in Color Flow Imaging using Deep Learning Hassan Nahas, University of Waterloo	12-2 Carbon-11 labelling of ALK2 inhibitors and PET neuroimaging in rodents Emily Murrell, Centre for Addiction and Mental Health
13:45	10-3 Examination of Radiocarpal vs Midcarpal Contribution to Flexion Motion of the Wrist Elizabeth Norman, Western University	11-3 Automatic Deep Learning-Based Segmentation of Neonatal Cerebral Ventricles from 3D Ultrasound Images Zachary Szentimrey, University of Guelph	12-3 Mapping vitamin B6 by CEST-MRI Emilie MSP Brun, University of Ottawa
13:50	10-4 Four-Dimensional Computed Tomography Scans Allow Dynamic Visualization and Measurement of Scapulothoracic Joint Kinematics Baraa Daher, Western University	11-4 Detection of COVID-19 from Chest X-ray Images using Transfer Learning Jenita Manokaran, University of Guelph	12-4 Feasibility Study of Simultaneous Hyperpolarized 129Xe MRI and [15O]water PET Measurements Ramanpreet K Sembhi, Western University
13:55	10-5 Validation of new 3-Dimensional Ultrasound Device for determining Synovial Tissue Volume in the Hands and Wrists Carla du Toit, Western University	11-5 Tissue Classification of Mass Spectrometry iKnife Data Using Graph Convolutional Networks Faranak Akbarifar, Queen's University	12-5 The Feasibility of Hyperpolarized 129Xe MRI for lung damage in COVID-19 Survivors using a Key-Hole Method Tuneesh K Ranota, Western University
14:00	10-6 Anatomical Measurement of Kangaroo Cervical (C3-C7) Vertebral Endplates Using Micro-CT Joseph U. Umoh, Robarts Research Institute	11-6 Deep learning model for motion correction of MRI images using small training sets Ivailo E Petrov, Robarts Research Institute	12-6 The Use of a Novel Sampling/Reconstruction Method for Non-Proton and Low Field MRI Samuel Perron, Western University
14:05	10-7 Effect of vitamin D and memantine supplementation on body composition in the APP/PS1 mouse model of Alzheimer's disease following chronic vitamin D deficiency Dana N Broberg, Western University	11-7 Deep Learning for Motion Correction using Multichannel MRI Data Miriam Hewlett, Western University	
14:10	Break		

Tuesday, March 23, 2021

14:15	Oral Sessions 13 - 15		
	Zoom Meeting Room 1	Zoom Meeting Room 2	Zoom Meeting Room 3
	Oral 13	Oral 14	Oral 15
	Cancer Imaging I	Deep Learning for Segmentation	Animal Model & Image processing
	Chairs: Aaron Fenster, Matt Gwilliam	Chairs: Jordan DeKraker, Graham Wright	Chairs: Amir Manbachi, Jessica Rodgers
14:15	13-1 Comparing the detection of breast cancer brain metastasis with magnetic particle imaging (MPI) to magnetic resonance imaging (MRI) Natasha Knier, Western University	14-1 Cross Attention Squeeze Excitation Network (CASE-Net) for Whole Body Fetal MRI Segmentation Justin Lo, Ryerson University	15-1 Microstructural Diffusion MRI in Mouse Models of Severe and Repetitive Mild Traumatic Brain Injury Naila M Rahman, Western University
14:30	13-2 In vivo evaluation of a cyclooxygenase-2 (COX-2) radiopharmaceutical, [¹¹ C]MC1, in human colorectal cancer xenograft mouse models Amanda Boyle, Centre for Addiction and Mental Health	14-2 DeepMV: Fully Automatic Ultrasound Segmentation for Patient Specific Mitral Valve Modelling Patrick Carnahan, Robarts Research Institute	15-2 CEST-MRI for Monitoring Effects of Cariporide on Intracellular Tumour pH in a Rat Glioma Model Maryam Mozaffari, Robarts Research Institute
14:45	13-3 Comparison of Dynamic Contrast Enhanced MRI Signal Analysis Methods to Assess Response to Single and Three-Fraction Stereotactic Ablative Radiotherapy for Early Stage Breast Cancer Allen Sun, Western University	14-3 Automatic whole cell segmentation for multiplexed images of ovarian cancer tissue sections Wenchao Han, University of Toronto	15-3 Spatial Dependence of CT Emphysema in COPD Quantified using Join Count Statistics Sukhraj Virdee, Ryerson University
15:00	13-4 Assessment of Locally Advanced Breast Cancer Response to Chemotherapy using Enhanced Ultrasound Elastography Niusa Kheirkhah, Western University	14-4 Renal Boundary and Tumour Segmentation in Multiparametric MRI using U-Net with Transfer Learning Anush Agarwal, University of Guelph	15-4 Fractal Dimensions of Airway Surfaces from Computed Tomography in Chronic Obstructive Pulmonary Disease Jason Todd Bartlett, Ryerson University
15:15	13-5 Molecular imaging reveals a high degree of cross-seeding of spontaneous metastases in a novel mouse model of synchronous bilateral breast cancer Shirley Liu, Robarts Research Institute	14-5 Automated myocardial segmentation of extracellular volume maps using a U-Net based convolutional neural network Nadia A Farrag, Carleton University	15-5 Contrast-Free Ultrasound Microvascular Imaging to Enhance Vascular Quantification in a Mouse Model of Peripheral Artery Disease Mahsa Bataghva, Western University
15:30	Break		

Tuesday, March 23, 2021

15:40	Pitch Sessions 16 - 18		
	Zoom Meeting Room 1	Zoom Meeting Room 2	Zoom Meeting Room 3
	Pitch 16 Machine Learning I	Pitch 17 Neuro Imaging I	Pitch 18 Computation Modeling
	Chairs: Jaryd Christie, Maged Goubran	Chairs: Corey Baron, Claire Park	Chairs: Miriam Hewlett, Dan Xiao
15:40	16-1 3D-DABTS: 3D Domain Adapted Breast Tissue Segmentation via Knowledge Distillation Mixup Grey C Kuling, University of Toronto	17-1 The trajectory of putative astroglial dysfunction in first episode schizophrenia - A longitudinal 7-Tesla MRS study Peter Jeon, Western University	18-1 Validation of a Monte-Carlo Model of a Photon-Counting X-ray Detector for Breast Imaging Applications James A Day, Ryerson University
15:45	16-2 Transfer Learning Approach for Automated Kidney Segmentation on MRI sequences Rohini P Gaikar, University of Guelph	17-2 Glutathione as a molecular marker of functional impairment in patients with at-risk mental state - 7-Tesla 1H-MRS study Peter Jeon, Western University	18-2 Highly Focussed Collimators for Increased Resolution of Hand-Held Gamma Probes Sydney Wilson, Western University
15:50	16-3 Surgical tool tracking with object detection for performance assessment in central venous catheterization Olivia O'Driscoll, Queen's University	17-3 Ultra-high field imaging of the human amygdala nuclei: manual segmentation to atlas development Sara M Pac, Western University	18-3 Determination of Lung Hyperelastic Parameters using 4D-CT and a Biomechanical Model Dayton Miranda, Western University
15:55	16-4 2D and 3D Labelling Methods for Facial Skin Tension Lines Bao Yi (Emily) Huang, University of Toronto	17-4 Reducing the Incidence of CT Perfusion Infarct Volume Overestimation in Acute Ischemic Stroke Kevin J Chung, Western University	18-4 Fatigue Analysis of Wireless Load Cells for Biomedical Applications William Anderson, Western University
16:00	16-5 Machine Learning to Detect Brain Lesions in Focal Epilepsy Andrea Perera-Ortega, Queen's University	17-5 Synthesis and PET imaging of the 4R-tau radiotracer [18F]CBD-2115 in rodents and non-human primate Anton Lindberg, Centre for Addiction and Mental Health	18-5 Ongoing Development of a Numerical Bloch Solver for Low-Field Pulse Sequence Modeling John Adams, Western University
16:05		17-6 Parcellation of the Piriform Cortex through Clustering of Laminar Features in the Unfolded 3D BigBrain: Correspondence with Diffusion Tractography, and Resting-state fMRI at 7T Nickolas K Christidis, Western University	18-6 Monte Carlo Simulation for Magnetic Resonance Diffusion Tristhal Parasram, University of Windsor
16:10		17-7 Brain network connectivity and neurodevelopmental outcomes in children with infantile hydrocephalus Ramina Adam, Western University	18-7 Exponential Analysis for 2D Magnetic Resonance Relaxation Spectrum using Neural Networks Tristhal Parasram, University of Windsor
16:15			18-8 Correlating Macro and Microstructure in the Hippocampus Bradley G Karat, Western University
16:20	Social Event in Gather Town		

Wednesday, March 24, 2021

08:30	Opening Remarks Miranda Kirby and Pascal Fallavollita, ImNO 2021 Scientific Committee Chairs		Zoom Meeting Room 1
08:40	COVID-19 Panel Chairs: Marat Slessarev, Sarah Svenningsen Matthias Friedrich, McGill University Health Centre Simon Graham, Sunnybrook Research Institute Grace Parraga, Robarts Research Institute Aaron So, Lawson Health Research Institute		Zoom Meeting Room 1
09:50	Break		
09:55	Oral Sessions 19 - 21		
	Zoom Meeting Room 1	Zoom Meeting Room 2	Zoom Meeting Room 3
	Oral 19 COVID-19 & Brain Related Injuries	Oral 20 Molecular Imaging	Oral 21 Machine Learning II
	Chairs: Kathleen Surry, Kevin Wyszatko	Chairs: Paul Dubovan, Jill Weyers	Chairs: Salma Dammak, April Khademi
09:55	19-1 Automated Registration of 3D Ultrasound Images of Preterm Neonates to Identify Intraventricular Hemorrhaging: Preliminary Findings using SPM-12 Nicholas K Belanger, University of Guelph	20-1 Magnetic Resonance Image Analysis of Mammalian Cells Expressing Essential Magnetosome Genes mamI and mamL Prushoth Vivekanantha, Western University	21-1 Central Line Tutor: using computer vision workflow recognition in a central venous catheterization training system Rebecca Hisey, Queen's University
10:10	19-2 The Severity of Spinal Cord Compression is Associated with Functional Plasticity in Degenerative Cervical Myelopathy Alicia Cronin, Western University	20-2 Toward a reporter gene for MRI: Essential proteins from magnetic bacteria interact in mammalian cells Qin Sun, Lawson Health Research Institute	21-2 Ultrasound Probe Pose Classification for Task Recognition in Central Venous Catheterization Colton A Barr, Queen's University
10:25	19-3 Correlating Concussion Symptoms and Brain Injury in Paediatric Concussion Ethan Danielli, McMaster University	20-3 Gadolinium-Free MRI Blood Pool Contrast Agents: Manganese(III) Porphyrins With Tunable Human Serum Albumin Binding Affinity Hanlin Liu, University of Toronto	21-3 Effect of dataset size and acquisition type on deep learning segmentation of the prostate in 3D ultrasound Nathan Orlando, Robarts Research Institute
10:40	19-4 NeuroCOVID19: Impact of the Virus on the Brain Simon J Graham, Sunnybrook Research Institute	20-4 Determination of cellular sensitivity for magnetic particle imaging Julia Gevaert, Western University	21-4 Effect of dataset size and acquisition type on deep learning segmentation of the prostate in 3D ultrasound Di Xiao, University of Waterloo
10:55	19-5 Long-term Effects of COVID-19 Illness in the Brain Assessed by 7T MRI Helma Heidari, Robarts research Institute	20-5 In vitro assessment of acoustically cavitated docetaxel-loaded nanobubbles on mouse breast cancer cells Patrick Dong Min Chang, University of Toronto	21-5 Classification of Spinal Curvature from 3D Spine CT Images using a Convolutional Neural Network Geoff Klein, University of Toronto
11:10	Break		

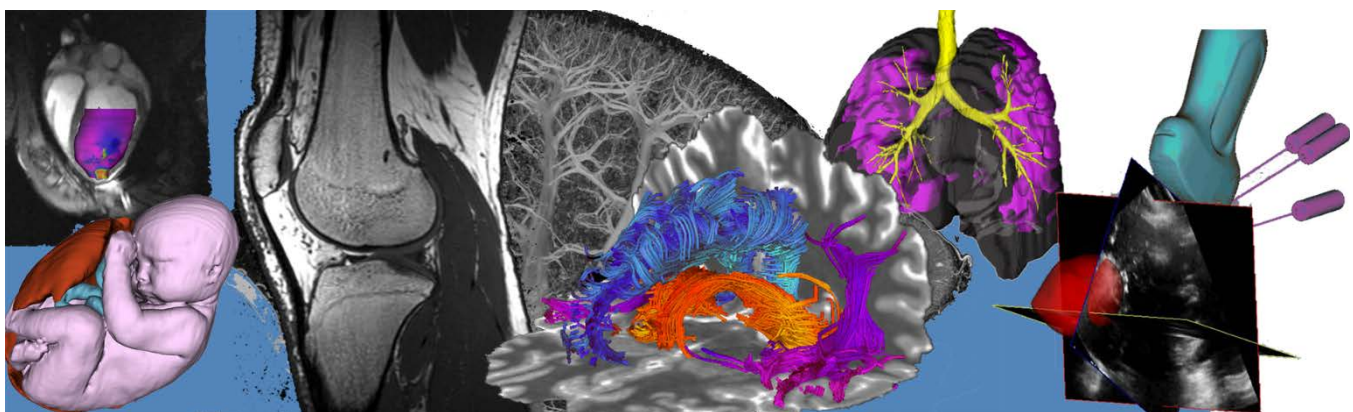
Wednesday, March 24, 2021

11:20	Pitch Sessions 22 - 24		
	Zoom Meeting Room 1	Zoom Meeting Room 2	Zoom Meeting Room 3
	Pitch 22 Machine Learning III	Pitch 23 MR Imaging	Pitch 24 Cancer Imaging II
	Chairs: Miriam Hewlett, Billy Yiu	Chairs: Mihaela Pop, Gabriel Varela-Mattatall	Chairs: Timothy Scholl, Naila Rahman
11:20	22-1 Domain Adaptation and Self-Supervised Learning for Surgical Margin Detection Alice ML Santilli, Queen's University	23-1 Loading Characteristics and Viability of Stem Cell-Derived Alveolar-Like Macrophages Tagged with Perfluoropolyether for 19F MRI of Chronic Lung Disease Janny Kim, The Hospital for Sick Children	24-1 Multi-Modality Imaging Assessment of the Heart and Lungs Before and After Stage III Non-Small Cell Lung Cancer Radiotherapy Oi Wai Chau, Western University
11:25	22-2 Investigating the Effects of Transfer Learning on Medical Ultrasound Models Calvin Zhu, McMaster University	23-2 Synthesis and Evaluation of [18F]meta-fluorobenzylguanidine For Cardiac Sympathetic Nerve Imaging Uzair S. Ismailani, University of Ottawa	24-2 Optimization of three-dimensional ultrasound acquisition parameters for diagnostic evaluation of thyroid nodules Viveka Sainani, Western University
11:30	22-3 Healthcare Utilization Prediction Using CT Images and End-to-End Deep Convolutional Neural Network Learning Pipeline Amir Moslemi, Ryerson University	23-3 Evaluation of gadolinium-loaded plaster as a potential means of characterizing antibiotic diffusion in MRI Gregory Hong, Robarts Research Institute	24-3 Longitudinal in-vivo quantification of tumour microvasculature and hypoxia via optical coherence tomography angiography in a pre-clinical model of radiation therapy Nader M Allam, University Health Network
11:35	22-4 Chronic Obstructive Pulmonary Disease and Asthma Differentiation by Dimension Reduction Based on Perturbation Theory for High Dimensional Quantitative CT Biomarkers Amir Moslemi, Ryerson University	23-4 pH-Weighted Chemical Exchange Saturation Transfer (CEST) MRI in the Spine Alicia Cronin, Western University	24-4 SPECT/CT Imaging [177Lu]Lu-DOTA-RW03, a Targeted Radioimmunotherapy against Cancer Stem Cell Marker CD133 Kevin Wyszatko, McMaster University
11:40	22-5 From pixels to cells: Development of biologically guided segmentation strategies for quantitative image analysis to interrogate single-cell data on multiplex immunostained tissue sections Trevor D McKee, STTARR Innovation Centre / University Health Network	23-5 Modelling Cellular Iron-handling in Inflammation: P19 Cells Secrete Biologically-active Hepsidin Rahil Prajapati, Western University	24-5 Comparison of ADC measurements from the MR-Linac and a diagnostic scanner in brain tumour patients Liam SP Lawrence, University of Toronto
11:45		23-6 Diffusion Tensor MRI Reveals Myocardial Fibre Architecture after Cell-Based Therapy in Myocardial Infarction Moses P Cook, University of Toronto	24-6 Response Assessment of Early-Stage Breast Tumours to Stereotactic Ablative Radiotherapy (SABR) using Fluorodeoxyglucose Positron Emission Tomography (FDG-PET) Zoe P Kerhoulas, Western University
11:50		23-7 Fetoplacental and Maternal Body Composition Effects of Life Long Western Diet Consumption at Mid-Gestation Guinea Pig Pregnancy Lindsay E Morris, Western University	24-7 Derivation of Monoclonal Antibodies Targeting GvpA, the major structural protein of Gas Vesicles: A New Set of Tool for Detecting and Imaging Gas Vesicles Ann Fernando, University of Toronto
11:55	Break		
12:00	Industry Alumni Panel Chair: Raphael Ronen Daniel Gelman, Aufero Medical Eli Gibson, Siemens Healthineers Zahra Hosseini, Siemens Healthineers Cynthia Stewart, GE Healthcare Canada		
13:00	Break		

Wednesday, March 24, 2021

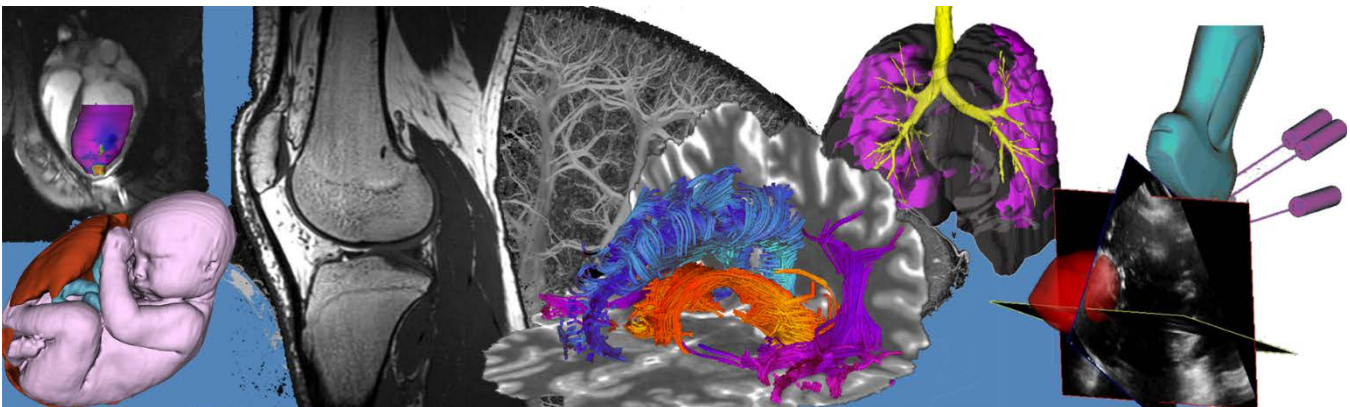
13:05	Oral Sessions 25 - 27		
	Zoom Meeting Room 1	Zoom Meeting Room 2	Zoom Meeting Room 3
	Oral 25 Machine Learning IV	Oral 26 MRI contrast & devices	Oral 27 Neuro Imaging II
	Chairs: Jordan DeKraker, Eranga Ukwatta	Chairs: Nilesh Ghugre, Matt Gwilliam	Chairs: Ting-Yim Lee, Naila Rahman
13:05	25-1 Prediction of stroke thrombus RBC content from multiparametric MRI using machine learning Emily Qin, Western University	26-1 Validation of a mechatronics-assisted needle delivery system for MRI-guided prostate focal laser ablation Eric Knoll, Western University	27-1 Characterization of the Cold Head Artifact Present in Simultaneous Studies of Functional Magnetic Resonance Imaging and Electroencephalography Alejandro Amador, McMaster University
13:20	25-2 A Multiple Instance Learning Framework for MRI-based Multifocal Cancer Outcome Prediction Jianan Chen, University of Toronto	26-2 An Exploration of Myocardial Blood Flow, Blood Volume, and Oxygen Consumption at Varying Levels of Hyperemic Stress Reveals Blood Flow as the Dominant Influence on T2 Relaxation Time Jill Weyers, Sunnybrook Research Institute	27-2 Two multi-echo SPGR acquisitions for the simultaneous generation of SWI, qT1 and other parametric maps: preliminary data Vishaal Sumra, University of Toronto
13:35	25-3 A multi-modality radiomics-based model for predicting recurrence in non-small cell lung cancer Jaryd R Christie, Western University	26-3 Development of a Human-Based Dual PET/MR Reporter Gene System for In Vivo Cell Tracking Nourhan Shalaby, Western University	27-3 Cross validation of 3AM Diffusion MRI phantoms using microscopy, synchrotron micro computed-tomography, and simulation Farah N Mushtaha, Robarts Research Institute
13:50	25-4 Radiomics for head and neck cancer prognostication: results from the RADCURE machine learning challenge Michal Kazmierski, University of Toronto	26-4 Magnetic Field Mapping in High Susceptibility Region using Pure Phase Encoding MRI Layale Bazzi, University of Windsor	27-4 Optimized oscillating gradients for frequency dependent in vivo diffusion kurtosis measurement Kevin B Borsos, Western University
14:05	25-5 Radiomics Analysis to Predict Chronic Obstructive Pulmonary Disease Presence in Computed Tomography Imaging using Machine Learning Ryan Au, Ryerson University	26-5 An activatable reporter gene system to visualize cell-cell communication in cancer immunotherapies TianDuo Wang, Western University	27-5 Measuring Ischemic Volumes using Quantitative Multiphase CT Angiography Perfusion Maps Kevin J Chung, Western University
14:20	Break		
14:30	Keynote Session Chairs: David Holdsworth, Miranda Kirby Beyond Animal Testing: New Frontiers in Human-Centred Science Charu Chandrasekera, University of Windsor		
15:15	Awards and Closing Remarks		

Oral & Pitch Abstracts (in order of the talks)



Oral Presentation Abstract

Session 1: Image-Guided Devices



Translation of an ultrasound-guided needle placement system to Mauritania

Julia Wiercigroch¹, Tamas Ungi¹, Ahmedou Moulaye Idriss², Yahya Tfeil², Ron Kikinis³, Parvin Mousavi¹, Gabor Fichtinger¹

1. Laboratory for Percutaneous Surgery, School of Computing, Queen's University, Kingston, Canada
2. Faculty of Medicine, University of Nouakchott Al Aasriya, Mauritania
3. Harvard Medical School, Boston USA

INTRODUCTION: Point-of-care ultrasound image-guided therapy (POCUS IGT) has potential to transcend geographic and socioeconomic boundaries and help bring modern therapies to underserved communities and countries. Current commercial systems are not feasible to deploy in low-resource settings due to prohibitive costs of purchase, support, and operation. We present the development of a versatile POCUS IGT system, optimized for financial and operating conditions in Mauritania. CIVCO produces mechanical needle guide brackets that are not feasible for use in Mauritania as the associated software does not support low-cost ultrasound scanners and their single-use patient kit (including coupling gel, probe cover, elastic bands, sterile outer bracket, 10-piece guide sleeves) is too expensive. We aimed to create a system that is functionally similar to the popular CIVCO (www.civco.com) product, while supporting inexpensive ultrasound scanners through free open-source software and costs only a small fraction of the price.

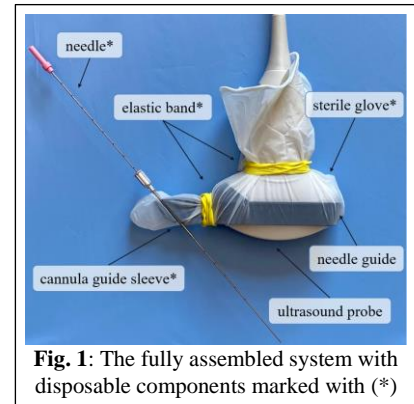


Fig. 1: The fully assembled system with disposable components marked with (*)

METHODS: A 3D-printed, plastic needle guide with 4 insertion channels was designed to securely attach around the Telemed L12 model (Telemed Ltd. Lithuania) using a CAD model from the PLUS toolkit ^[1] in Autodesk Fusion. The proposed sterile patient kit includes a surgical glove, elastic bands, pre-sterilized blunt cannulas, and coupling gel. The surgical glove wraps around the probe, coupling gel and guide, and is secured by elastic bands. The pre-sterilized 1-inch blunt cannula serves as a smooth guide sleeve for the needle. The guidance software was developed as an application over SlicerIGT (www.slicerigt.org) ^[2] and PLUS Toolkit (www.plustoolkit.org) ^[1] free open-source image-guided therapy development platforms. The software overlays the guide channels on the live ultrasound image, as shown in Fig. 2, right. The proposed device is shown in Fig. 1.

RESULTS: The system was demonstrated on a solid-gel phantom as shown in Fig 2, left. The hardware design and workflow are appropriate for abdominal interventions since all targets were accurately reached. Fig. 2 right shows the true position of the needle relative to the planned trajectory overlaid on the live ultrasound image. The needle accurately follows the planned trajectory and hits the center of the target. Compared to CIVCO, our system decreased the number of disposable pieces in the patient kit and replaced single-use custom components with ubiquitously available parts. The cost of supplying our system in 500 procedures would be ~\$500, compared to CIVCO's ~\$10,000, about \$1 per patient.

CONCLUSION: A POCUS IGT system was developed using free open-source guidance software that supports low-cost ultrasound scanners and low-cost consumables, ready to be shipped for prospective clinical trials at the National Center for Image-Guided Therapy in Mauritania. A successful launch of the POCUS IGT program may pave the way for paradigm shifting changes of the national healthcare in Mauritania and for providing a practical model for Western Africa.

REFERENCES

- [1] A. Lasso, T. Heffter, A. Rankin, C. Pinter, T. Ungi, and G. Fichtinger, "PLUS: Open-source toolkit for ultrasound-guided intervention systems," *IEEE Trans. Biomed. Eng.*, vol. 61, no. 10, pp. 2527–2537, Oct. 2014.
- [2] T. Ungi, A. Lasso, and G. Fichtinger, "Open-source platforms for navigated image-guided interventions," *Medical Image Analysis*, vol. 33. Elsevier B.V., pp. 181–186, 01-Oct-2016.

Feasibility of fusing three-dimensional transabdominal and transrectal ultrasound images to visualize intracavitary gynaecological brachytherapy applicators

Jessica R. Rodgers^{1,2}, Lucas C. Mendez³, Douglas A. Hoover⁴, Jeffrey Bax², David D'Souza³, Aaron Fenster^{1,2}
¹*School of Biomedical Engineering*, ²*Robarts Research Institute*, *Western University, London, Canada*; ³*Dept. of Radiation Oncology*, ⁴*Dept. of Medical Physics*, *London Health Sciences Centre, London, Canada*

Introduction: Brachytherapy is a type of radiotherapy that is often used during the treatment of gynaecological cancers to deliver high doses of radiation to tumours relative to the nearby healthy tissues. Commonly, the radiation source is positioned within the vagina and uterus using intracavitary applicators, to create conformal dose distributions. Tandem-and-ovoids and tandem-and-ring applicators are commonly used for this task and must be positioned appropriately to provide optimal treatment; however, the applicator components produce large shadowing artefacts (Figure 1(a) and (b)) in ultrasound (US) images, which inhibits the assessment of the applicator position, particularly in settings without easy access to intraoperative imaging.^{1,2} We propose the acquisition and fusion of three-dimensional (3D) transabdominal ultrasound (TAUS) and transrectal ultrasound (TRUS) images. We hypothesize that this will allow for the recovery of applicator and anatomical information that was previously obscured when using a single US perspective. The aim of this study was to evaluate the feasibility of the approach using a female pelvic phantom and to our knowledge, this is the first study investigating the fusion of these image types, particularly in the context of gynaecological brachytherapy.

Methods: An agar-based female pelvic phantom was designed to include key anatomical landmarks and a clinical tandem-and-ring applicator was embedded. TRUS and TAUS images of the phantom were acquired using mechanical 3D US systems developed in our laboratory. Two 3D TRUS images were acquired at two different positions to sufficiently capture the applicator in the image field-of-view, which were registered and merged based on the applicator position. This combined 3D TRUS image was then manually, rigidly registered to a 3D TAUS image that was acquired of the phantom, using the known applicator geometry to align the images, as other structures are non-rigid. The TRUS and TAUS images were fused and the combined image was rigidly registered to a magnetic resonance (MR) image of the phantom to validate the registration accuracy. To assess the associated localization error in each modality, each of the four fiducials were localized five times in both modalities with a minimum of 24 h between sessions.³

Results: Figure 1 shows a view of the fused 3D US image from the phantom. Comparing the positions of four spherical fiducials between the fused 3D US image and MR image resulted in a mean registration error of 1.37 ± 1.35 mm. The fiducial localization error³ was 0.58 mm for both the 3D US and MR images.

Conclusions: The ability to comprehensively visualize intracavitary brachytherapy applicators using US imaging, has the potential to improve their placement for gynaecological brachytherapy procedures, particularly in settings with limited resources. This work uses a phantom to demonstrate the feasibility of fusing 3D TAUS and TRUS images of these applicators to reduce the impact of shadowing when assessing the applicator placement, warranting future investigation in a patient study.

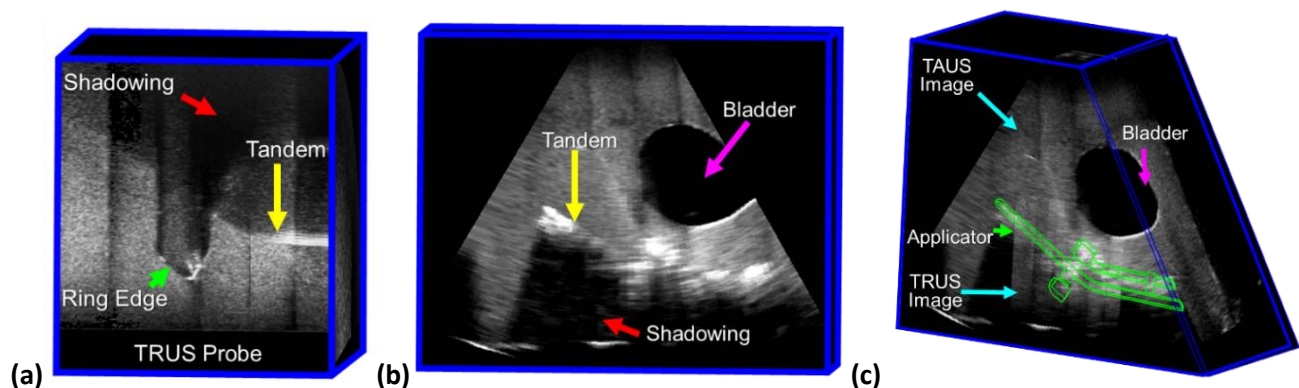


Figure 1: (a) Merged 3D TRUS image and (b) 3D TAUS image of the phantom containing a tandem-and-ring applicator, with key features indicated. (c) Fused 3D US image with outline of the applicator shown.

References: [1] Nesvacil et al. *Brachytherapy*. 2016. 15(6); [2] St-Amant et al. *Brachytherapy*. 2017. 16(4); [3] Fitzpatrick et al. *IEEE Trans. Med. Imaging*. 1998. 17(5).

Development of an open-source prostate biopsy imaging training system

Catherine O. Wu¹, B. Diao², T. Ungi¹, A. Sedghi¹, R. Kikinis³, P. Mousavi¹, G. Fichtinger¹

¹School of Computing, Queen's University, Kingston, Canada, ²Cheikh Anta Diop University, Dakar, Senegal,

³Harvard Brigham and Women's Hospital, Boston, USA

INTRODUCTION: Prostate cancer is the second most common malignancy diagnosed globally in males. In sub-Saharan Africa, unlike North America and Europe, screening for prostate cancer is not routine due to lack of resources and awareness, resulting in higher numbers of late-stage detection cases [1]. We have partnered with the international aid program, “Train the Trainers”, to develop a trans-rectal ultrasound (TRUS) guided prostate biopsy training system [2]. This system will be deployed in sub-Saharan countries to promote accessible instruction for prostate cancer diagnosis. In training the biopsy procedure, senior urologists recognize that the greatest challenge is the mental estimation of the prostate zones while using TRUS-guidance [3]. Thus, to produce a beneficial learning process and promote proper zonal sampling in the biopsy, our training system will teach users to identify zones on TRUS. This paper presents the implementation of a virtual, open source TRUS training simulator, highlighting the generation and evaluation of the critical training component of zonal anatomy overlaid on TRUS.

METHODS: For the simulator's dataset, we used anonymized patient TRUS volumes and prostate zone segmentations from separate sources. In 3D Slicer, an open-source platform, we overlaid the zonal segmentation onto TRUS [4]. This was performed by placing fiducials along the gland outline and the urethra of both the TRUS and the segmentation to drive a deformable fiducial registration. After generating 10 pairings of TRUS overlaid with zonal anatomy, we designed and implemented a virtual TRUS simulator in 3D Slicer (Fig. 1). The objective of the simulator is to train users to accurately identify prostate zones while manipulating a TRUS probe. To confirm the system's effectiveness in training and scoring users, we asked 7 expert urologists to first assess the quality of our zonal overlays as a component for TRUS training on a 5-point Likert scale. Then, we asked them to label the zones on plain TRUS volumes, allowing us to compare their interpretation to our overlay. The code for the simulator can be found at github.com/PerkLab/ProstateBiopsySim.

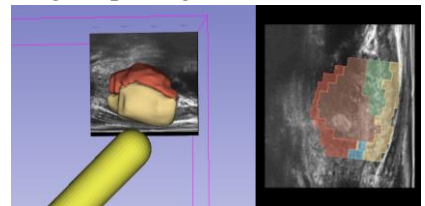


Fig. 1: Screen shot consisting of 3D view with movable TRUS probe (*left*) and corresponding 2D sagittal US slice with zonal overlay (*right*).

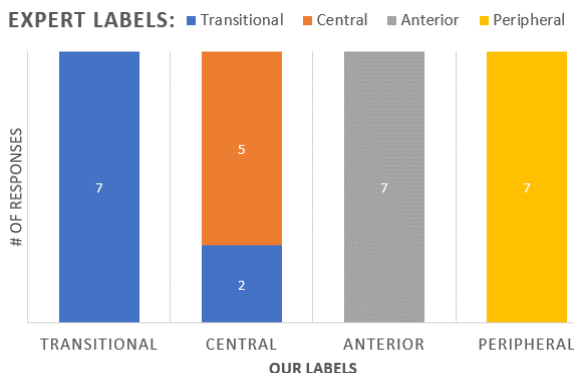


Fig. 2: Results from TRUS labelling questionnaire

RESULTS: When assessing the quality of the overlay, the experts, on average, rated the accuracy at 4 on a 5-point Likert scale. When viewing the TRUS, 7 out of 7 experts labelled the peripheral, anterior, and transitional zones in the regions we overlaid them, and 5 out of 7 labelled the central zone (CZ) in the region we overlaid it (Fig.2). This may be attributed to the challenge of identifying CZ borders or growth in TRUS.

CONCLUSION: We created the prototype of a TRUS biopsy imaging simulator in open-source software. A vital training component, zonal overlay, was generated using public image data and was validated by expert urologists for prostate zone identification, confirming the concept.

REFERENCES:

- [1] Jalloh M, et al. Prostate cancer in sub-Saharan Africa. *J. Nephrol. Urol.* 1, 15-20 (2013).
- [2] Ruiz-Alzola J, et al. Train the Trainers: medical technology for the sustainable development of Africa. *Proceedings of 2018 IEEE Global Humanitarian Technology Conference (GHTC)*. 2018; San Jose, CA, pp. 1-8.
- [3] Kelloff, GJ et al. Challenges in clinical prostate cancer: role of imaging. *AJR. American journal of roentgenology.* 192(9), 1455-70 (2009).
- [4] Fedorov A, et al. 3D Slicer as an image computing platform for the Quantitative Imaging Network. *Magn. Reason. Imaging* 30(9), 1323-1341 (2012).

Title: Margin expansion study for mpMRI-defined prostatic lesions in the setting of focally boosted high-dose rate prostate brachytherapy

C. W. Smith, BSc,^{1,2,3,8} T. Marcus, BSc,³ D. Hoover, PhD,^{2,3,8} K. Surry, PhD,^{2,3,8} D. D'Souza, MD,^{2,7,8} D. W. Cool, MD, PhD,^{2,4} Z. Kassam, MD,^{2,4} M. Bastian-Jordan, MD,⁹ J. A. Gomez, MD,⁵ M. Moussa, MBBCh⁵ J. Chin, MD,^{6,7} S. Pautler, MD,^{6,7} G. S. Bauman, MD^{3,7,8} and A. D. Ward, PhD^{1,2,3,7,8}

¹ Baines Imaging Research Laboratory, London, ON, Canada, ² Lawson Health Research Institute, London, ON, Canada, The following departments of Western University, London, ON, Canada: ³ Medical Biophysics, ⁴ Medical Imaging, ⁵ Pathology and Laboratory Medicine, ⁶ Surgery, and ⁷ Oncology, ⁸ London Regional Cancer Program, London, ON, Canada, ⁹ University of Queensland, Queensland, Australia

Introduction: Multiparametric magnetic resonance imaging (mpMRI) has demonstrated the ability to localize intraprostatic lesions however mpMRI may underestimate the true histopathologic extent of cancer necessitating the use of an expanded treatment margin when delivering focal therapies to the prostate.¹ Given the known dose heterogeneity due to the rapid dose fall off inherent in brachytherapy it was our goal to determine the necessary margins to deliver mpMRI lesion targeted intraprostatic high-dose rate brachytherapy (HDR-BT).

Methods: 10 prostatectomy patients had pathologist-annotated mid-gland histology sections registered to pre-procedural mpMRI scans, which were interpreted by four different observers. Simulated HDR-BT plans with real catheter placements were generated from this patient cohort by registering the mpMRI (T2W, dynamic contrast enhanced, and apparent diffusion coefficient) lesions and corresponding histology annotations to previously performed clinical HDR-BT treatment plans with a prescription dose of 15-Gy. Inverse treatment planning optimization was used to generate multiple plans that standardly targeted the entire gland equally, and additional plans were made with targeted doses of 20.25 Gy to the mpMRI lesions with 0 mm, 1 mm, and 2 mm margins added to the original lesions. The analysis compared the dose that would have been delivered to the corresponding histopathologically defined cancer within the different treatment planning techniques.

Results: mpMRI-targeted plans delivered a significantly higher D98 and D90 doses to the histologically defined cancer ($p < 0.0001$) in comparison to the non-targeted treatment plans. Additionally, it was found that plans with a 1 mm margin added to the mpMRI lesion delivered a significantly higher dose to the histologically defined cancer in comparison to the 0 mm margin targeted plans ($p = 0.019$), while there was no significant difference between the 1 mm and 2 mm margin plans.

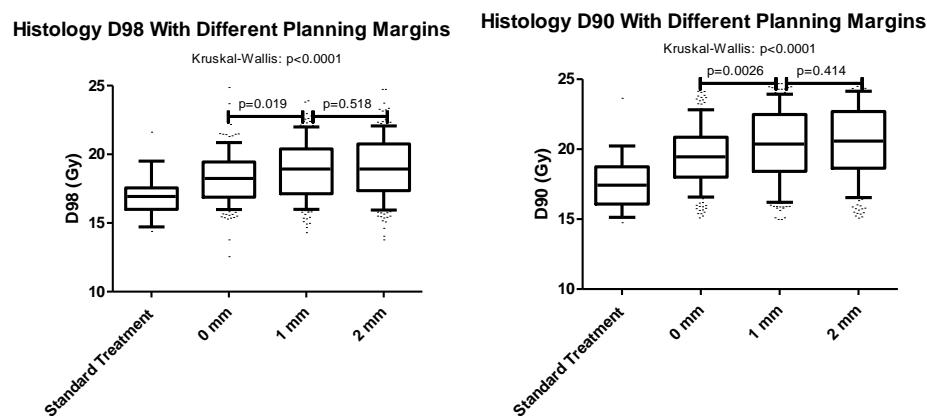


Figure 1. A box-whisker plot of the D98 (left) and D90 (right) dose delivered to histologic cancer depending on the different treatment planning method. The whiskers represent the 10th and 90th percentile values.

Conclusion: Adding a 1 mm margin to intraprostatic mpMRI lesions has shown the potential to further improve dose to histologically defined cancer in comparison to the original mpMRI lesion contours without violating dose constraints to organs at risk. No significant effect was observed by further expanding the lesions. Therefore, it is our recommendation to add at least a 1 mm margin to mpMRI-defined lesions when designing mpMRI-targeted prostatic HDR-BT treatment plans.

1. Gibson et al Int J Radiat Oncol Biol Phys 2016 Sep 1;96(1):188-96.

Feasibility and clinical utility of three-dimensional ultrasound in oral cavity cancers

Claire K. Park^{1,2*} and Jacob Wihlidal^{3*}, Adrian Mendez⁴, Aaron Fenster^{1,2}

¹Department of Medical Biophysics, ²Imaging Research Laboratories, Robarts Research Institute, ³Schulich Medicine, Schulich School of Medicine and Dentistry, ⁴Otolaryngology Head and Neck Surgery, London Health Sciences Center, London, Ontario, Canada *co-first authors

Introduction: Oral squamous cell carcinoma (OSCC) is the most common oral malignancy, representing approximately 90% of all malignant cancers originating in the oral cavity.¹ Imaging modalities such as computed tomography (CT), magnetic resonance imaging (MRI), and positron emission tomography (PET) are commonly used for the clinical exploration of OSCC extent, diagnosis, and staging, which are necessary for the management and prognosis of these cancers.² In consideration of the complexity of the oral cavity, imaging has an integral role in the classification of the primary tumour site and disease extent in relevant anatomy.² However, limitations including low sensitivity in small, superficial tumours, ionising radiation, and artifacts from metallic dental materials, can reduce its clinical utility.³ We propose three-dimensional ultrasound (3DUS) as an alternative imaging modality for oral cancer identification and tumour volume estimation. This work presents the novel utility of 3DUS for imaging oral cavity cancers with a clinical case study of OSCC in the oral floor, as compared to healthy control. We aim to demonstrate the potential clinical utility of 3DUS for anatomical identification and tumour volume quantification. We hypothesize that pre-operative 3DUS will provide a reliable and efficient method for tumour volume quantification with a percent error <10% from pre-operative CT and MRI images.

Methods: A handheld, mechanically motorized 3DUS device with in-house software was previously developed and validated.⁴ 3DUS images were acquired using an Aplio i800 US system (Canon Medical Systems, Otawara, Tochigi, Japan) and custom-fitted holders for 14L5 (10 MHz) and 11L3 (7 MHz) transducers. Acquisition protocol involved positioning the 3DUS scanner to the submandibular neck by a trained observer, while remaining midline. 3DUS acquisition was initiated manually with transducer placement perpendicular to the mandible and linearly translated over 5.0 cm posteriorly toward the hyoid. Scans were performed at a 4.0 cm depth-of-field to capture the entirety of the oral floor. 3DUS images of the patient and healthy control were obtained with 10 MHz and 7 MHz transducers, and anatomical structures were compared with expected literature findings. In the pathological case, the maximum solid tumour dimensions in anteroposterior (AP) and craniocaudal (CC) planes, and depth-of-invasion (DOI) were calculated and compared with the pre-operative CT and MRI measurements by quantifying the percent error in tumour volume estimation.

Results: In both healthy control and pathological states, full bilateral visualization was attained of the oral floor anatomy at 10 MHz and 7 MHz operating frequencies (Fig. 1A). While identification of anatomical structures was shown in healthy control with both transducers, tissue distortion secondary to tumour development in the pathologic case resulted in quality discrepancy, with decreased image quality at 7 MHz. The pre-operative CT images indicated tumour dimensions: 1.60×1.12 cm (AP/CC) and 0.44 cm DOI and pre-operative MRI images revealed a 1.45×1.90 cm (AP/CC) and 0.66 cm DOI. 3DUS with the 10 MHz transducer allowed for the approximation of tumour measurements at 1.44×1.37 cm (AP/CC) with a 0.49 cm DOI. The percent error in tumour dimension estimation was 6%, 9%, and 11% for AP, CC, and DOI between the pre-operative 3DUS and mean dimensions between CT and MRI images.

Conclusion: We demonstrated the clinical utility of 3DUS imaging in OSCC in the oral floor. 3DUS acquisition enabled the complete visualization of oral cavity anatomy, suitable for surgical resection and reconstruction planning. With the use of the 10 MHz transducer, complete tumour visualization was shown, which reasonably supplants the demand for pre-operative imaging of the primary site and tumour dimension estimation (<11% percent error) in comparison to pre-operative CT and MRI images. Future work will extend this assessment with improved tumour volume quantification, an increased number of patients, as well as anatomic and pathologic variations in presenting malignancy.

[1] AHNS (2016) [2] Mahajan A, et al. (2020) Oral Onco. 104658. [3] Perez M, et al. (2015) J. Cranio-Maxillo-Facial Surg. 43. [4] Papernick S, et al. (2020) Osteoarthritis and Cartilage Open. 100127.

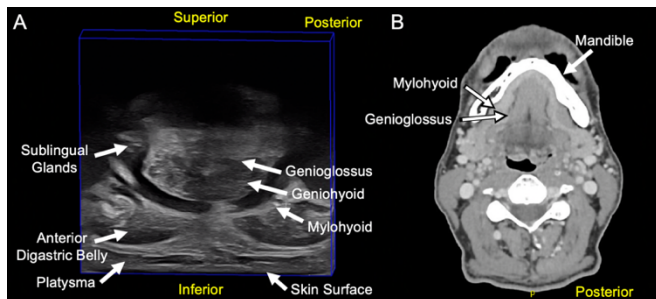
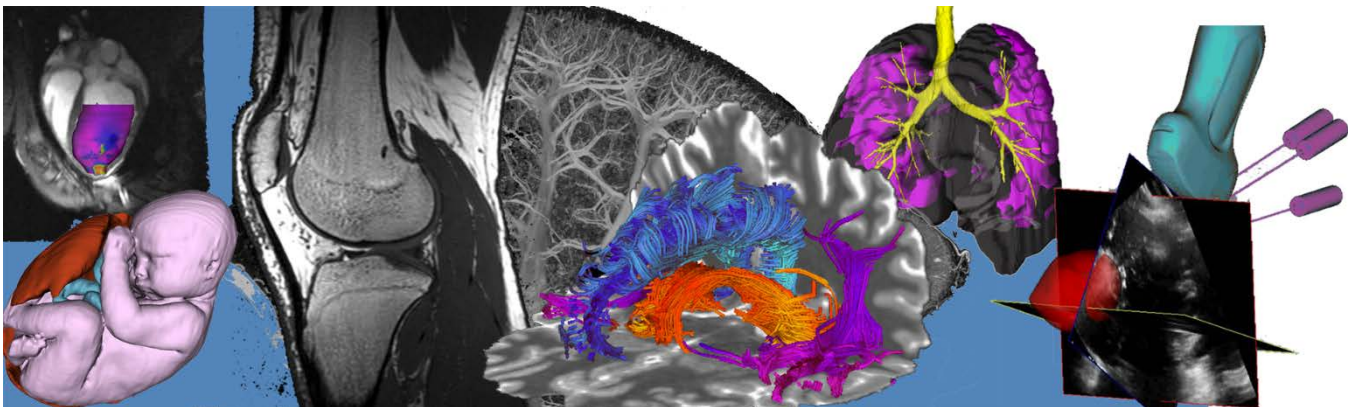


Figure 1. A. 3DUS (10 MHz) image illustrating the oral floor anatomy. **B.** Axial CT image of oral cavity anatomy in the pathological case.

Oral Presentation Abstract

Session 2: Lung & Cellular Imaging



Variable Temporal Resolution Cartesian Sampling for Cell Tracking MRI

Mark Armstrong¹, Cornelius Faber², Dan Xiao¹

¹Physics Department, University of Windsor, ON, Canada

²Institute for Clinical Radiology, University of Muenster, Muenster, Germany

Introduction: Magnetic Resonance Imaging (MRI) is a powerful imaging modality with excellent soft tissue contrast. Contrast agent can be used to “tag” individual cells. Time-lapse MRI to track the cell motion could provides insights in the studies of inflammatory diseases and metastasis of cancer. However, current methods cannot detect cells traveling faster than $1\mu\text{m/s}$ due to temporal blurring [1]. The temporal resolution can be improved by undersampling k-space. The optimal acceleration factor, however, can not be easily determined before the experiments. Strategies have been proposed for non-Cartesian flexible retrospective undersampling [2]. These methods require significant modification on the pulse sequence and may not be readily applicable for most users. We propose a Cartesian sampling scheme where undersampling ratio and temporal resolution can be chosen retrospectively.

Methods: The scheme is illustrated in Fig. 1. The central lines of k-space are acquired first. The high frequency lines are sampled in a sequence that has a relatively uniform coverage within any short time duration, with incoherent undersampling, as shown in Fig. 1c. This is achieved by dividing k-space into a number of bins, determined by the highest acceleration factor. One random phase encoding line is sample from each bin, generating one frame with the highest temporal resolution. No duplicate phase encoding lines are acquired until the full k-space are covered, except that the central $k=0$ line is acquired multiple times for motion and phase correction. A smaller undersampling ratio can be chosen in the reconstruction stage by grouping a larger number of phase encoding lines, as in Fig. 1b. A compressed sensing algorithm with dictionary learning regularization similar to [3] was used for image reconstruction.

Results and discussion: The method was applied to simulated cell tracking experiments, where cell speeds of $3.7\mu\text{m/s}$ and $9.4\mu\text{m/s}$ were considered. The fully sampled image had best overall quality, as shown in Fig. 2a. However, the high-velocity cells could not be identified due to significant temporal blurring. With higher acceleration factors, the image quality decreased, but the cell features were more discernible. It is possible to combine the cell features detected in the high temporal resolution images with the low temporal resolution high quality background mouse brain in the image processing stage.

Conclusion: We have presented a Cartesian sampling scheme for studying dynamic systems. Both the high temporal resolution images and fully sampled image are acquired. The undersampling ratio can be flexibly chosen retrospectively, providing a unique advantage when experimental conditions can not be predetermined.

References:

- [1] Masthoff et al, Sci Rep, 8:9563 (2018)
- [2] Feng et al, Magn Reson Med, 72 707 (2014)
- [3] Ravishankar et al, IEEE Trans Med Imaging, 30, 1028 (2011)

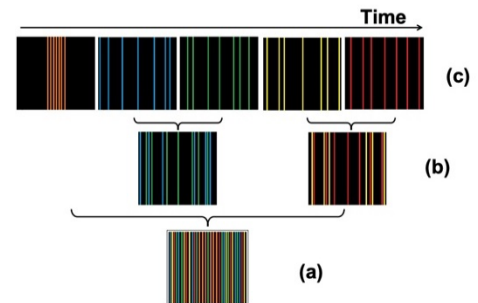


Figure 1. The cartesian sampling scheme illustration. A fully sampled k-space (a) can be retrospectively undersampled at different ratio such as (b) and (c).

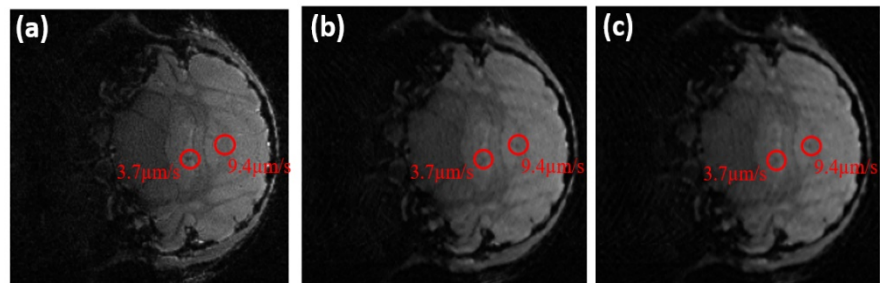


Figure 2. The reconstructed simulation images with different temporal resolutions, corresponding to the undersampling ratios in Fig 1. In the fully sampled image (a), the $3.7\mu\text{m/s}$ cell is significantly blurred and $9.4\mu\text{m/s}$ cell is not visible. (b) and (c) had acceleration factors of 2.3 and 4.7. Reduced temporal blurring led to more distinguishable cell features.

Computed Tomography Airways and Vessels: Bridging the Gap in COPD

Huma Asghar BSc¹, Wan C. Tan MD², James C. Hogg MD PhD² and Miranda Kirby PhD¹

Department of Physics, Ryerson University, Toronto, Canada; ²Center for Heart, Lung Innovation, University of British Columbia, Vancouver, Canada

Introduction: Chronic obstructive pulmonary disease (COPD) is characterized by irreversible airflow limitation and is one of the major causes of death worldwide^{1,2}. Several components of the lung are affected by COPD, and these disease-related changes can be quantified by computed tomography (CT) imaging. The impact of COPD on the parenchyma, known as emphysema, can be quantified as the percentage of low attenuation areas below -950 HU (LAA₉₅₀)³. In the airways, remodeling and destruction of the small airways leads to a reduction in their total number, and is quantified by segmenting the CT airways and measuring the total airway count (TAC)⁴. In the pulmonary vessels, inflammation also results in distal pruning of vessels that is quantified by segmenting the pulmonary vessel tree and measuring the total blood vessel volume (TVV)⁵. Studies have shown that CT LAA₉₅₀ measurements are significantly associated with both TAC and TVV measurements in COPD^{5,6}. However, to our knowledge, no studies have investigated the relationship between the disease in the airways and vessels in COPD. Therefore, our objective was to investigate the association between CT airway and vessel remodeling/loss in COPD. Because proximal vessel pruning may result in distal vessel dilation, CT TVV may not be a sensitive measure of pruning/vessel loss. Therefore, we first aimed to develop a total vessel count (TVC) measurement. We hypothesized that TVC would have a stronger association than TVV with established measures of vascular abnormalities. Further, we hypothesized that there would be a significant association between CT TAC and TVC measurements, independent of emphysema.

Methods: Participants from the CanCOLD study⁷ underwent CT imaging and spirometry for measurement of the forced expiratory volume in one second (FEV₁). Participants were categorized as never-smokers with normal lung function, smokers with normal lung function (at risk), mild COPD or moderate-severe COPD. CT images were analyzed using VIDA Diagnostics Inc. (Coralville, IA, USA) for airway and vessel segmentation, and for generating the LAA₉₅₀ measurement. The CT TAC⁴ and TVV⁵ measurement was generated as previously described. To generate the total vessel count from the pulmonary vessel tree segmentation, the following steps of morphological operations were performed: 1) Skeletonization of the segmented vessel structure to reduce the complexity and computation time; 2) Identification and removal of branch points in the skeletonized vessel structure to isolate individual segments of the vessel tree; 3) generation of the TVC based on the 3D connectivity of any two voxels connected by either faces, edges or corners. A one-way ANOVA was performed to test for significance between different disease severity groups for demographic variables. Pearson correlation was used to assess the correlation of TVC and TVV with diffusing capacity of lungs for carbon monoxide (DL_{CO}) and TAC. Multivariable linear regression model was used to determine the association between TAC and TVC, with adjustment for LAA₉₅₀. Age, sex, race, height, pack-years of smoking, center id, smoking status and LAA₉₅₀ were used as covariates in the multivariable model.

Results: CanCOLD participants included never smokers (n=256), ever smokers (n=357), mild (n=350) and moderate-severe (n=258) COPD. Participants with mild COPD were significantly older than never-smokers (p<0.05), however there were no other differences between the groups for age or BMI (p>0.05). DL_{CO} was positively correlated with TVC (r=0.24, p<0.0001), while there was no correlation between TVV and DL_{CO} (p>0.05). There was a significant positive correlation between CT TAC and TVC (r=0.30, p<0.0001), but TAC and TVV were not significantly correlated (p>0.05). In multivariable linear regression analysis, after adjustment for LAA₉₅₀ and other confounding variables, CT TAC remained significantly associated with TVC (p<0.0001).

Conclusion: We developed a novel method to quantify the remodeling and loss of pulmonary vessels in COPD and showed that there is a significant association between the loss of airways and vessels. Furthermore, the association between airway and vessel loss is independent of emphysema.

References: [1] Rabe K. F. et al., *American journal of respiratory and critical care medicine*, 2007; [2] Pauwels R. A. et al., *The Lancet*, 2004; [3] Müller, N.L., et al., *Chest*, 1988; [4] Kirby M. et al., *American journal of respiratory and critical care medicine*, 2018; [5] Estépar et al., *American journal of respiratory and critical care medicine*, 2013; [6] Diaz et al., *CHRONIC OBSTRUCTIVE PULMONARY DISEASE PHENOTYPES* (American Thoracic Society), 2010; [7] Bourbeau et al. *COPD: Journal of Chronic Obstructive Pulmonary Disease*, 2014.

CT Emphysema and Small Airway Disease Clusters and Progression of Chronic Obstructive Pulmonary Disease

Sarah Kadhim BSc¹, Wan C. Tan MD², James Hogg MD PhD², Jean Bourbeau³, and Miranda Kirby PhD¹

¹Department of physics, Ryerson University, Toronto, Canada; ²Centre for Heart, Lung Innovation, University of British Columbia, Vancouver, Canada; ³Montreal Chest Institute of the Royal Victoria Hospital, McGill University Health Centre, Montreal, QC, Canada

Introduction: Chronic obstructive pulmonary disease (COPD) is the 4th leading cause of mortality worldwide¹ and is characterized by irreversible airflow limitation measured using spirometry². While airflow limitation in COPD occurs due to disease in both the airways (i.e. small airway disease) and the parenchyma (i.e. emphysema), spirometry provides no information about the different underlying disease pathologies, nor the spatial or temporal pattern of progression of these distinct diseases. Parametric Response Mapping (PRM) is a clinically validated voxel-wise computed tomography (CT) image analysis technique that has been introduced to quantify emphysema (Emph) and small airway disease (fSAD) by registering images acquired at full-inspiration and full-expiration, and classifying each voxel based on established thresholds³. Although studies show fSAD and Emph progress in the lung over time⁴, it is unknown if the progression occurs by growth of spatially contiguous “clusters”. Therefore, the objective of this study is to quantify the longitudinal change in PRM fSAD (PRM_{fSAD}) and Emph (PRM_{Emph}) measurements using 3-D clustering method and to investigate the association with lung function changes in COPD.

Materials and Methods: Participants include smokers with normal lung function (At-Risk), mild COPD, and moderate-severe COPD from the Canadian Cohort of Obstructive Lung Disease (CanCOLD) study. Spirometry was performed at baseline (BL) and 3-year follow-up (FU) for measurement of the forced expiratory volume in 1sec (FEV₁) and forced vital capacity (FVC). CT was acquired at full inspiration and expiration at BL and 3-year at FU. The BL inspiration, FU expiration, and FU inspiration CT images were all spatially registered to the BL expiration CT images using a deformable image registration algorithm. A sponge model was applied to the FU images to account for any potential differences in lung volume between time points⁵. Using the spatially and temporally registered images, PRM_{Emph} and PRM_{fSAD} measurements were then generated from the inspiration and expiration images for each time point. Using the PRM_{Emph} and PRM_{fSAD} images, fSAD and Emph voxel clusters were defined as contiguous voxels with 6-way connectivity (i.e., voxels sharing a common surface). To quantify fSAD and Emph clusters, the slope “D” of the linear regression of the number of clusters vs. cluster size for BL and FU of PRM_{Emph} and PRM_{fSAD} images were quantified. Increased D indicates more large clusters; small D indicates many small clusters. Pearson correlation was used to test the association between the BL-FU change in FEV₁ and FEV₁/FVC with the change in PRM_{Emph} and PRM_{fSAD} measures.

Results: A total of 288 participants were included; n=134 At-Risk, n=72 mild COPD, and n=82 moderate-severe. There were no significant differences between BL and FU for At-Risk, mild COPD, and moderate-severe COPD for PRM_{Emph} (p>0.05) or PRM_{fSAD} (p>0.05). For PRM_{Emph}, there was a significant increase in D at FU compared to BL for the At-Risk (p=0.001) and moderate-severe COPD (p=0.02). For PRM_{fSAD}, there was a significant increase in D at FU compared to BL for the At-Risk (p<0.0001), mild (p<0.0001) and moderate-severe COPD (p<0.0001). Overall, the BL-FU change in FEV₁ was associated with the BL-FU change in D for PRM_{Emph} (r=0.33, p=0.004) and the change in FEV₁/FVC was associated with the BL-FU change in D for PRM_{fSAD} (r=0.32, p=0.002).

Conclusion: CT emphysema and small airway disease “clusters” significantly increase over time, and this change is associated with decreased lung function. Understanding the underlying disease pathologies responsible for disease progression could introduce possible targets for treatment in the future.

References: [1] Lozano, R. et al. The Lancet. 2012. [2] Devine J. F. American health & drug benefits. 2008. [3] Galbán, C. J. et al. Nature Medicine. 2012. [4] Wassim W.L. et al. Academic Radiology. 2018. [5] Staring, M. et al. Medical physics. 2014.

Progressive changes in glutamate concentration in early stages of schizophrenia: A longitudinal 7-Tesla MRS study

Peter Jeon^{1,2}, Roberto Limongi³, Sabrina Ford⁴, Michael Mackinley⁵, Kara Dempster⁶, Jean Théberge^{1,2,7,8}, Lena Palaniyappan^{1,3,4}

1. Department of Medical Biophysics, Western University, London, Canada 2. Lawson Health Research Institute, Imaging Division, London, Canada 3. Robarts Research Institute, Western University, London, Canada 4. Department of Psychiatry, Western University, London, Canada 5. Department of Neuroscience, Western University, London, Canada 6. Department of Psychiatry, Dalhousie University, Halifax, Canada 7. St. Joseph's Health Care, Diagnostic Imaging, London, Canada 8. Department of Medical Imaging, Western University, London, Canada

Background: Glutamatergic abnormalities are suspected in observed schizophrenia symptoms. Progressive reduction in glutamatergic transmission has been proposed as an important component of the illness trajectory of schizophrenia. Despite its popularity, to date, this notion has not been convincingly tested in patients in early stages schizophrenia.

Methods: In a longitudinal 7T magnetic resonance spectroscopy (1H-MRS), we quantified glutamate at the dorsal anterior cingulate cortex in 21 participants with a median lifetime antipsychotic exposure of less than 3 days and followed them up after 6 months of treatment. Healthy controls were also scanned at two time points. We studied time by group interaction on glutamate after adjusting for gender and age. Bayesian ANCOVA was also used to evaluate whether groups differed in effect of time on follow-up glutamate concentration measurements.

Results: While patients had significantly lower overall glutamate levels than healthy controls ($F(1,27) = 5.23$, $p = 0.03$), we did not observe a progressive change of glutamate concentration in patients ($F(1,18) = 0.47$, $p = 0.50$), and the group by time interaction was not significant ($F(1,27) = 0.86$, $p = 0.36$). On average, patients with early psychosis receiving treatment showed a 0.02 mM/year increase, while healthy controls showed a 0.06 mM/year reduction of MRS glutamate levels.

Conclusions: Bayesian analysis of our observations does not support early, post-onset glutamate loss in schizophrenia. Interestingly, it provides evidence in favour of a lack of progressive glutamate change in our schizophrenia sample – indicating that the glutamate level at the onset of illness was the best predictor of the levels 6 months after treatment. A more nuanced view of glutamatergic physiology, linked to early cortical maturation, may be required to understand glutamate-mediated dynamics in schizophrenia.

Magnetic particle imaging quantifies the dilution of intracellular iron labels by proliferating breast cancer cells *in vitro*

Maryam A. Berih^{1,2}, Olivia C. Sehl^{1,3}, Paula J. Foster^{1,3}

¹ Imaging Research Laboratories, Robarts Research Institute, Canada

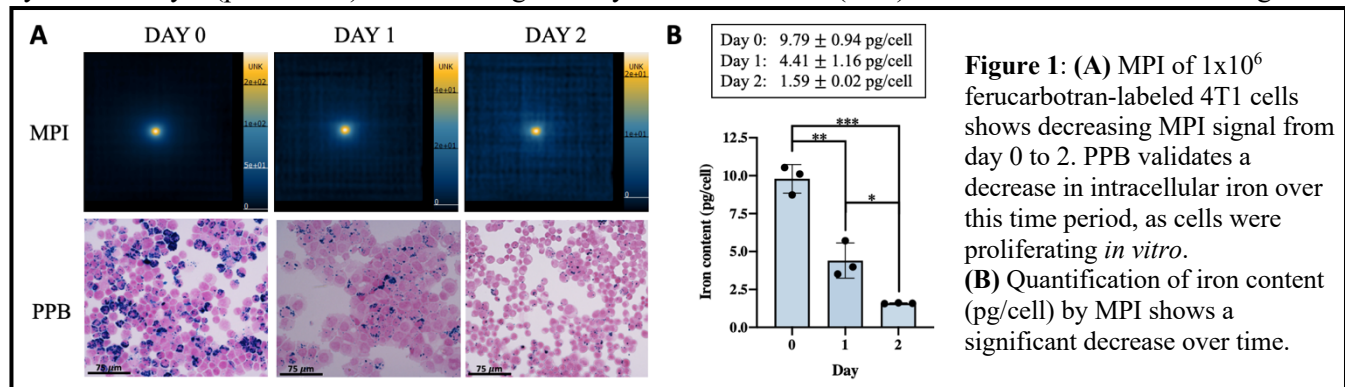
² Department of Physiology and Pharmacology, University of Western Ontario, Canada

³ Department of Medical Biophysics, University of Western Ontario, Canada

Introduction: Cell tracking with magnetic resonance imaging (MRI) has been used for many years to monitor the fate of cells *in vivo* after they have been labeled with superparamagnetic iron oxides (SPIOs). With MRI, SPIOs are indirectly detected owing to relaxation effects on protons, producing negative MRI contrast and unreliable quantification of cell number¹. In addition, SPIO-labeled cells are not easily visualized in tissues which appear dark in MRI (*i.e.* metastases in the air-filled lungs). Magnetic particle imaging (MPI) is an emerging imaging technique that directly detects SPIOs. MPI addresses the limitations of MRI based cell tracking by providing positive contrast and direct quantification. However, for imaging of proliferative cells the dilution of the SPIOs amongst cell progeny limits long-term tracking. Previous *in vitro* studies have demonstrated that cell division and metabolism of SPIO agents leads to loss of signal and cell detection within five to eight generations²⁻⁴. This is especially concerning for tracking rapidly dividing cells (cancer). **Our objective** is to characterize the dilution of SPIOs in a rapidly dividing breast cancer cell line *in vitro* using quantitative MPI and histological validation.

Methods: 4T1 murine breast cancer cells (doubling time = 14 hours) were labeled *in vitro* by co-incubation with ferucarbotran (Vivotrax, Magnetic Insight Inc.) and transfection agents, heparin and protamine sulfate⁵. 1×10^6 SPIO labeled 4T1 cells were collected after 24 hours (day 0), and the remaining cells were returned to culture. After 22 hours (day 1), 1×10^6 SPIO labeled cells were again collected, and this was repeated at 41 hours (day 2). Three cell samples were prepared from each day of cell collection. MPI images of cells were acquired on a MomentumTM MPI scanner (Magnetic Insight Inc.) in 2D using dual-channel 5.7 T/m gradients. Each day, a cytospin of 4T1 cells was performed to identify SPIOs intracellularly with Perl's Prussian blue (PPB) stain.

Results: The iron content in 4T1 cells (measured by MPI) decreased by 45% from day 0 to day 1 ($p = 0.0137$) and by 84% on day 2 ($p = 0.0001$). PPB staining visually showed less iron (blue) in cells over time. Refer to Figure 1.

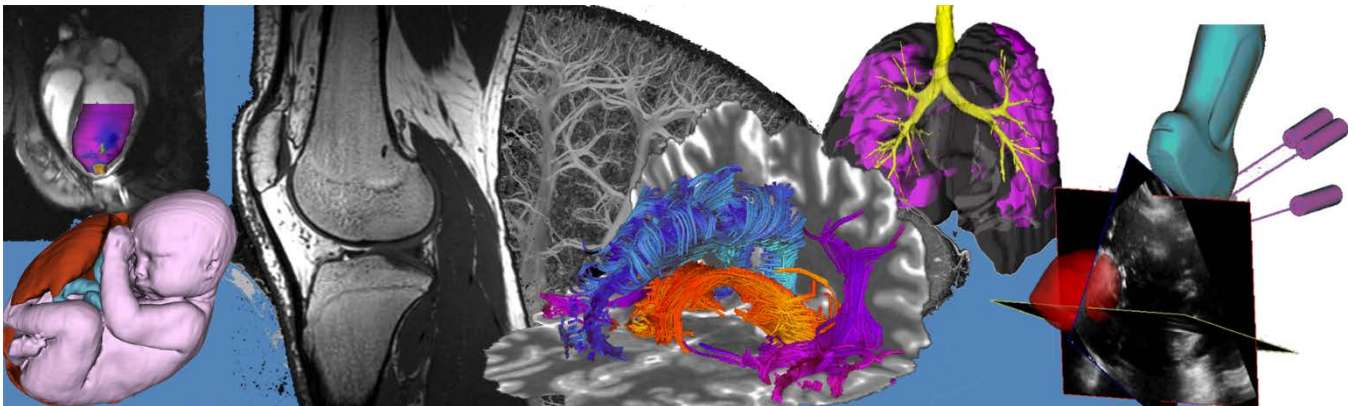


Conclusion: In this study we demonstrated a decline in MPI signal generated by SPIO labeled 4T1 cells during proliferation over time, owing to the reduction in intracellular iron content with cell division. MPI provides direct measurements of iron content per cell and this is the first time this phenomenon has been studied using MPI. Our measurements are in close agreement with a theoretical reduction of 66% in intracellular iron by day 1 and 87% by day 2, based on the doubling time of 4T1 cells *in vitro*. Cell tracking with MPI is in its infancy and this study contributes important knowledge for monitoring cells *in vivo*. We must consider that there are higher proliferation rates *in vitro* compared to *in vivo*, because of ideal culturing conditions, and there are other confounding factors occurring *in vivo* such as cell death, migration, and immune clearance. MPI is beneficial for studying SPIO-dilution because as cells proliferate *in vivo*, the MPI signal does not change as long as the cells and progeny remain in the same 1 mm region. This is different from MRI, where dilution of SPIOs between progeny reduces the ability to detect cells. In future work, we hope to study SPIO-dilution by cells *in vivo*, and other cell types, using MPI.

References: [1] Makela AV *et al. Sci. Rep.* 7, 1–9 (2017). [2] Arbab AS *et al. Radiology* (2003). [3] Foster PJ *et al. Neoplasia* 10, 207–216 (2008). [4] Economopoulos V *et al. Transl. Oncol.* 6, 347–354 (2013). [5] Thu MS *et al. Nat Med* 18, 463–467 (2012).

Oral Presentation Abstract

Session 3: Imaging for Musculoskeletal Analysis



Detecting treatment failure in rheumatoid arthritis with near-infrared light: in silico investigation within simulated disease states

Seva Ioussoufovitch^a and Mamadou Diop^{a,b,c}

^aWestern University, Faculty of Engineering, School of Biomedical Engineering, Collaborative Training Program in Musculoskeletal Health Research, Bone & Joint Institute, London, Canada

^bWestern University, Schulich School of Medicine & Dentistry, Medical Biophysics, London, Canada

^cLawson Health Research Institute, Imaging Program, London, Canada

Introduction: Rheumatoid arthritis (RA), a chronic autoimmune disease that affects about 1% of the population, is one of the most common types of inflammatory arthritis. While this disease can lead to significant reductions in patient productivity and quality of life, early treatment within 3 to 6 months of disease onset has been shown to substantially improve patient prognosis. Yet, even if a diagnosis can be quickly established, treatment failure—which is typically identified after a 3–6 month delay—still occurs in 30% of RA patients^{1,2} and puts patients at risk of irreversible joint damage. Near-infrared diffuse optical techniques are objective and non-invasive approaches which have previously been used to discriminate between healthy and inflamed joints;^{3,4} however, little investigation has been done into using these techniques to track gradual changes in disease progression over time. The objective of this study was to investigate the sensitivity of diffuse optical methods to RA disease progression. Specifically, we simulated time-resolved near-infrared light propagation through a realistic tissue distribution, manipulated this model to simulate different stages of disease, and investigated the resulting changes in the statistical moments (number of photons, mean time of flight, and variance) of the simulated data.

Methods: An MRI image of a healthy human finger was segmented using 3D Slicer^{5,6} into 5 tissue types: skin, subcutis, tendon, synovia, and bone. Transverse slices of the resulting segmentation were then linearly transformed in MATLAB 2020a to create several models which simulated different disease states with various degrees of synovial effusion. NIRFAST,^{7,8} an open source finite element method package, was used to generate a finite element mesh for each disease state and conduct time-resolved simulations at 800nm. Light sources and detectors were placed across the proximal interphalangeal (PIP) joint at similar surface locations in all four meshes; only data for transversely opposite pairs of sources and detectors (e.g., pair 1 and 5) was simulated. For each generated dataset, we calculated the statistical moments (number of photons, mean time of flight, and variance) and used each of these parameters separately to rank the expected disease severity of each mesh relative to each other mesh.

Results: Within each simulated state, we observed a substantial variation in the value of statistical moments depending on the source-detector (S-D) pair considered: averaged across all states, the coefficient of variation among S-D pairs was larger for number of photons (0.85 ± 0.09) than mean time-of-flight (0.19 ± 0.16) or variance (0.32 ± 0.25). When data was averaged across all S-D pairs, rankings of expected disease severity based on any of the statistical moments correctly matched actual disease severity; however, when examining only the data obtained from individual S-D pairs, ranking accuracy varied widely: on average, mean time-of-flight and variance had an equal ranking accuracy ($79 \pm 23\%$) which outperformed the ranking accuracy of number of photons ($58 \pm 24\%$).

Conclusions: On average, both mean time-of-flight and variance performed equally well and outperformed number of photons as a ranking criterion; however, none of the parameters were able to achieve perfect accuracy across all S-D pairs. Interestingly, increased joint swelling was found to occasionally result in higher light transmittance at certain S-D pairs. This is likely due to a light-guiding effect introduced by an increased volume of synovial fluid around the bone, and highlights the importance of obtaining measurements at multiple locations on the joint. Future work will test a larger set of models and the efficacy of more advanced approaches (e.g., combining parameters) for discriminating between different disease states.

References:

- [1] Goekoop-Ruiterman, Y. P., et al. *Arthritis and Rheumatism* **52**(11), 3381–3390 (2005).
- [2] Moreland, L. W., et al. *Arthritis and Rheumatology* **64**(9), 2824–2835 (2012).
- [3] Hielscher, A. H., et al. *IEEE Transactions on Medical Imaging* **30**(10), 1725–1736 (2011).
- [4] Lighter, D., et al. *Journal of Biomedical Optics* **24**(06), 1 (2019).
- [5] “3D Slicer,” <https://www.slicer.org/>, (2020).
- [6] Fedorov, A., et al. *Magnetic Resonance Imaging* **30**, 1323–1341 (2012).
- [7] Dehghani, H., et al. *Communications in Numerical Methods in Engineering* **25**, 711–732 (2009).
- [8] Jermyn, M., et al. *Journal of Biomedical Optics* **18**(8), 086007 (2013).

Effect of body mass on cementless implant fixation for total knee replacement

Jordan S. Broberg¹⁻³, M.F. Koff⁴, J.L. Howard⁵, B.A. Lanting⁵, H.G. Potter⁴, and M.G. Teeter^{1-3,5}

¹Department of Medical Biophysics, Schulich School of Medicine & Dentistry, Western University, London, Canada; ²Robarts Research Institute, London Canada; ³Lawson Health Research Institute, London, Canada; ⁴Department of Radiology and Imaging, Hospital for Special Surgery, New York, USA; ⁵Department of Surgery, Schulich School of Medicine & Dentistry, Western University, London, Canada

Introduction: Total knee replacement (TKR) is increasingly performed on obese patients, raising questions about the optimal implant fixation to bone. Traditionally, bone cement has been used for fixation; however, cemented implants have a greater risk of loosening in obese patients. Cementless fixation provides a potential solution, given the porous metal surface that allows bone ingrowth, creating a biological fixation mechanism that has the potential to provide improved long-term fixation in obese patients. However, further investigation is required to confirm if obese patients will benefit from cementless TKR fixation. Therefore, the objective is to use radiostereometric analysis (RSA) and modified magnetic resonance imaging (MRI) to study the bone ingrowth and fixation in cementless TKR, and to determine if there are differences with varying levels of obesity.

Methods: Thirty patients (equal male and female) with varying body mass indexes (BMI) will be recruited. Patients will undergo RSA and MRI in a supine position at a baseline exam one day after TKR surgery, then again at 2 weeks, 6 weeks, 3 months, and 6 months postoperatively. Standing weight-bearing RSA exams will be done at 2 weeks, 6 weeks, 3 months, and 6 months postoperatively. Supine RSA is used to measure implant migration at different locations of the tibial component (fictive points) relative to bone over time. Standing RSA exams are compared to their supine counterparts to determine inducible displacement, a measure of how much an implant migrates in weight-bearing conditions. MRI is performed using a 3T clinical scanner and the MAVRIC 3D multispectral imaging metal artifact suppression sequence. The bone-implant interface is determined to be normal, fibrous, fluid, or osteolytic. The percent contact of bone with the porous metal implant surface is also assessed. Implants are then scored as either loose or not loose.

Results: Two patients (Patient S01: male, age = 59 yrs, BMI = 34.5 kg/m²; Patient S02: female, age = 66 yrs, BMI = 32.8 kg/m²) have been recruited to date, with each having reached the 2 week timepoint. Figure 1 shows the amount of tibial component migration between Day 1 and 2 weeks at each fictive point. For Patient S01, the maximum migration at 2 weeks was 0.44 mm and occurred at the lateral point. For Patient S02, the maximum migration at 2 weeks was 0.80 mm and occurred at the anterolateral point. Figure 2 shows the amount of tibial inducible displacement at 2 weeks at each fictive point. For Patient S01, the maximum inducible displacement at 2 weeks was 0.61 mm and occurred at the posteromedial point. For Patient S02, the maximum inducible displacement at 2 weeks was 0.50 mm and occurred at the stem. MR images revealed no loose implant components at Day 1 or at 2 weeks and >66% contact of bone with the porous implant surfaces. Patient S01 had fibrous tissue in the posteromedial region of the femoral component at Day 1 and 2 weeks. Patient S02 had fibrous tissue in the lateral facet of the patella, and both the anteromedial and anterolateral regions of the tibial component. All other bone-implant interfaces were scored normal.

Conclusions: Early results from the study show a potential relationship between the amount of migration and the type of bone-implant interface, as a high amount of migration was seen at fictive points in regions where a fibrous membrane interface was located. Future work will be to investigate this relationship and the role body mass has on the migration and integrity of the bone-implant interface.

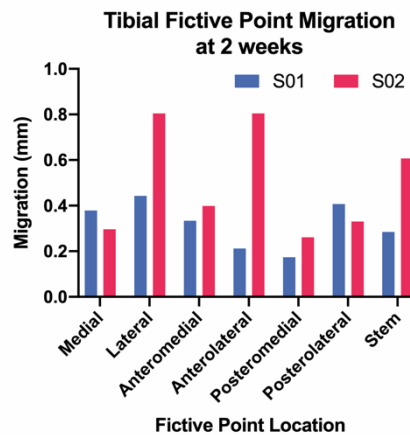


Figure 1. Bar graph depicting the amount of tibial component migration between Day 1 and 2 weeks postoperatively at each fictive point.

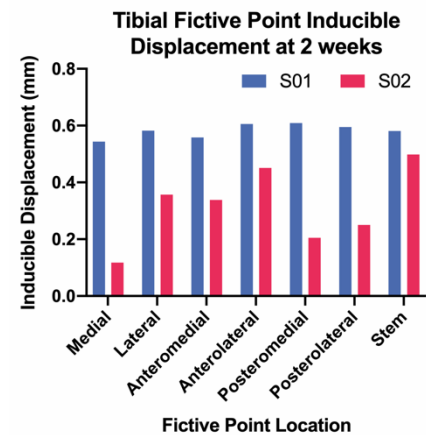


Figure 2. Bar graph depicting the amount of inducible displacement between Day 1 and 2 weeks postoperatively at each fictive point.

Reliability and concurrent validity of 3D ultrasound for quantifying knee cartilage volumeSam Papernick^{1,2}, Robert Dima³, Derek J Gillies^{1,2}, Tom Appleton^{3,4,5}, Aaron Fenster^{1,2,6}¹Department of Medical Biophysics, ²Robarts Research Institute, ³Department of Health and Rehabilitation Science, ⁴Department of Physiology and Pharmacology, ⁵Schulich School of Medicine and Dentistry,⁶Department of Biomedical Engineering; Western University, London, Ontario, Canada;

Introduction: Arthritis is the most prevalent chronic disease in Canada, affecting 21% of the population, with the most common form being osteoarthritis (OA). Cartilage degradation, a hallmark of knee OA (KOA), has motivated efforts to characterize disease severity through measuring loss of femoral articular cartilage (FAC). Clinical assessments and longitudinal monitoring of KOA are commonly performed by x-ray radiography and magnetic resonance imaging (MRI). However, x-ray imaging is not capable of assessing joint inflammation due a lack of soft-tissue contrast, and MRI is not feasible for point-of-care disease classification due to high manufacturing and operating costs, long acquisition times, and inaccessibility to many patients. There is currently a tremendous clinical need for an objective imaging-based tool that can overcome these limitations to assess KOA status, progression, and response to treatment at the patient's bedside. Conventional 2D ultrasound (US) imaging is an inexpensive, portable, and high-resolution imaging modality, but 2D US images are subject to detection bias and challenges with repeatedly measuring the same location over time with high accuracy. 2D US is also subject to operator dependencies and interpretations. We have developed a handheld mechanical 3D US device to monitor KOA-induced FAC degradation. The aim of this study is to assess the reliability and validity of our handheld 3D US device for measuring FAC volume in healthy volunteers compared to the current clinical standard of MRI.

Methods: Bilateral knee images of healthy volunteers ($n = 25$) were acquired using MRI and 3D US. MR images were acquired using a 3.0 Tesla MRI GE Healthcare scanner with an HD T/R Knee Array Coil (8 channels). The excitation flip angle was 5° with a repetition time (TR) of 30 ms and an echo time (TE) of 11.71 ms. The 3D US device features a motorized drive mechanism that acquires images by moving a 2D US transducer over a fixed distance while acquiring consecutive 2D images which are reconstructed into a 3D image. 3D US images were acquired using a Canon Aplio i800 US machine equipped with a 14L5 linear transducer with an operating frequency of 10.0 MHz (frequency range 3.8 MHz - 10.0 MHz). The trochlear FAC was manually segmented from MRI and 3D US by two raters after receiving training from a rheumatologist possessing extensive diagnostic musculoskeletal ultrasonography experience (Fig. 1). Five knees were randomly selected by each rater to conduct repeated segmentations during sessions separated by time. Intra- and inter-rater reliabilities were assessed using intraclass correlation coefficients (ICCs) calculated from FAC segmentation volumes.

Results: The mean age of the volunteers was 29.9 ± 14.5 and mean BMI was 23.4 ± 3.3 with 15 females and 10 males. Mean MRI segmentation volumes were $2.09 \pm 0.58 \text{ cm}^3$ and $1.86 \pm 0.48 \text{ cm}^3$ for each rater. MRI intra-rater ICCs were 0.97 [(0.79, 1.00), $p = 0.001$] and 0.90 [(0.25, 0.99), $p = 0.002$] for each rater with an inter-rater ICC of 0.83 [(0.48, 0.94), $p < 0.0001$]. Mean 3D US segmentation volumes were $2.29 \pm 0.72 \text{ cm}^3$ and $2.30 \pm 0.64 \text{ cm}^3$ for each rater. 3D US intra-rater ICCs were 1.00 [(0.98, 1.00), $p < 0.0001$] and 0.98 [(0.84, 1.00), $p = 0.0003$] for each rater with an inter-rater ICC of 0.96 [(0.90, 0.98), $p < 0.0001$].

Conclusions: We have demonstrated that 3D US FAC segmentations are associated with excellent intra- and inter-rater reliabilities ($\text{ICC} > 0.90$) and possess strong agreement with MRI FAC volume measurements. The development of a handheld 3D US device that is capable of imaging patients more rapidly than MRI while providing similar or greater volumetric measurement accuracy will improve the workflow of arthritis clinics and provide a more accessible alternative than MRI. Future work will assess the longitudinal construct validity of 3D US measurements in patients diagnosed with KOA to monitor the progression of FAC change and degradation.

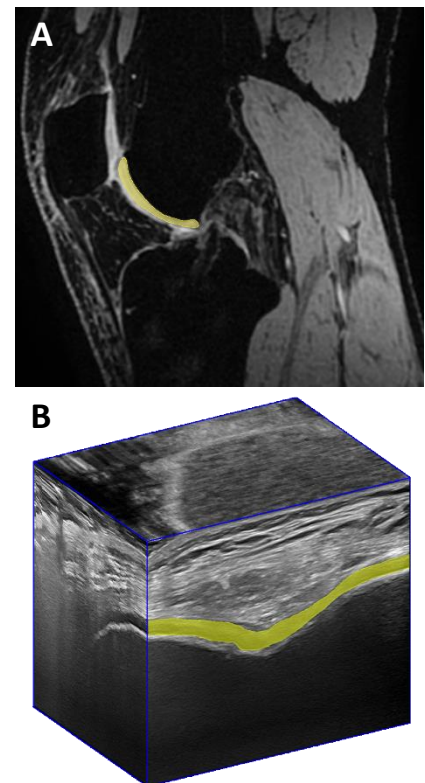


Figure 1: Manual segmentations of the trochlear FAC overlaid on MRI (A) and 3D US (B) images of a volunteer's healthy knee.

In vivo porcine tendon release using high-intensity focused ultrasound ablation

William Chu Kwan, Imogen den Otter Moore, Karolina Piorkowska, Adam C. Waspe, James M. Drake
The Hospital for Sick Children and University of Toronto, Toronto, ON, Canada

Introduction: Pediatric toe-walking and cerebral palsy are musculoskeletal conditions that present with musculotendinous contractures that are corrected with surgical resection of tendons. Given current trends towards non-invasive procedures, Magnetic Resonance-guided Focused Ultrasound Surgery (MRgFUS) is an ablation technique that has the potential to provide an incisionless non-invasive treatment for these conditions. This would translate into less exposure to anesthetics, less prophylactic antibiotic use, better pain management medication, reduced hospitalization time, and ability to perform conservative treatments with retreatments.

The hypothesis of this study demonstrates that tendon disruption increases as a function of the amount of energy delivered to the tendon of pigs *in vivo*. Additionally, we will examine the effect of heat spread during treatment by measuring the maximum temperature achieved and by calculating the area of thermal dose threshold above 240 EM during each treatment, as it could lead to undesired skin burns.

Methods: Pig Achilles tendons (n=14) were treated, each with two adjacent sonications of powers of either 20W and 40W for 30 seconds. Treatments were planned using the Achieva 3.0T Philips MRI using T1-weighted and T2-weighted MRI images. Ablation treatment was performed using a V1 Sonalleve (Profound Medical) and monitored using proton-resonance frequency (PRF) shift MR-thermometry during treatment and up to 5 minutes following sonication. Following MRgFUS, an area of hyperintensity in post-treatment T2-weighted images confirmed ablation on the tendon. Tendon disruption was confirmed both audibly during the ranging and later during necropsy. The temperature maps were analyzed to obtain the maximum temperature in the sonication point at the end of treatment. Maximum temperature and area of thermal dose were measured, and a t-test performed to determine statistical significance ($p < 0.05$) comparing ablation powers.

Results: Tendon disruptions occurred in 2 out of the 7 tendons treated with 20W ablation; disruption occurred in 7 out of the 7 treated with 40W ablation. The maximum temperature achieved immediately after sonication of 20W was of 58.93 °C (SD = 3.09), while the maximum temperature achieved immediately after sonication of 40W was of 67.58 °C (SD = 3.87). The area of thermal dose threshold above 240 EM for 20 W was of 19.71 mm² (SD = 9.97) while the area for 40W was of 51.04 mm² (SD = 24.84). A t-test indicated statistical significance between 20W and 40W for both maximum temperatures achieved and area of thermal dose above 240EM ($p = 0.001$).

Conclusions: Our results demonstrate that MRgFUS ablation is able to disrupt tendons in an animal model *in vivo*. The disruption was successful in all samples at a sonication power of 40W. Disruption was achieved in tendons with a higher temperature increase and a bigger area of thermal dose. The larger area of thermal dose adjacent to the skin leads to skin burns. Further work will include dose-response analysis of ablation power and tendon flexibility, and an examination into reducing the side effects of this treatment.

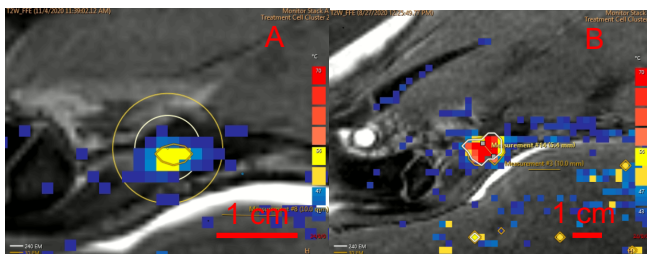


Figure 1: MRI images of the Achilles tendon in a pig with overlaying MR thermometry at 30 seconds of sonication. The temperature change (colour pixilation) and area of thermal dose threshold of 240 EM (uneven outline) for both 40W (A) and 20W (B) of ablation. The temperature scale on the right of each image associates a colour with temperature reached in the tissue blue <47°C, yellow <56°C and red >57°C.

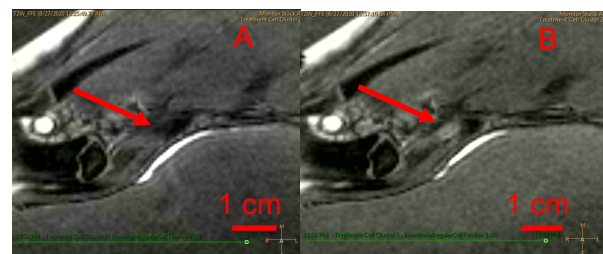


Figure 2: T2-weighted images for treatment of Achilles tendon (arrow) at 40W in the transverse plane. The pre-sonication image (A) and post-sonication image (B) show the change in area of hyperintensity (arrow), which corresponds to edema and successful delivery of FUS ablation onto the tendon.

In vivo porcine tendon release using high-intensity focused ultrasound long-pulse histotripsy followed by thermal ablation

Imogen den Otter Moore, William Chu Kwan, Karolina Piorkowska, Adam C. Waspe, James M. Drake
The Hospital for Sick Children and the University of Toronto, Toronto, ON, Canada

Introduction: Musculotendinous contracture is the shortening of connective tissue in skeletal muscles and tendons. Magnetic Resonance-guided Focused Ultrasound (MRgFUS) is a non-invasive treatment that has the potential to release tendons to improve range of motion in joints. The clinically-approved MRgFUS treatment is thermal ablation. A drawback of thermal ablation is thermal spread, which may cause undesired damage to adjacent structures. These treatments also occasionally produce skin burns. MRgFUS can also cause non-thermal bioeffects that generate microbubbles in tissue. At high negative pressures, these microbubbles can collapse leading to inertial cavitation that may cause tissue disruption. The goal of this study was to determine if long-pulse (boiling) histotripsy followed by mild thermal ablation exposure could non-invasively release musculoskeletal contractures while minimizing thermal spread around the focal point.

Methods: All animal procedures followed the Animal Care Committee protocols at the Hospital for Sick Children. Two pigs weighing 15-20 kg were ranged to obtain goniometric measurements of the ankles' baseline range of motion with the knee fixed in full extension. Each Achilles tendon (n=4) received two adjacent treatments. Treatments were planned using T2-weighted MRI images from an Achieva 3.0T MR system. Each treatment consisted of a long-pulse histotripsy sonication of 60 seconds with a peak negative pressure of 13.5 MP at 1.2MHz with a duty cycle of 1%, and a pulse duration of 0.01 seconds for 12000 pulses per burst. Histotripsy was immediately followed by thermal ablation at either 20W (n=2) or 30W (n=2) for 30 seconds. Proton-resonance frequency shift MR-thermometry (MRT) generated temperature maps during the treatment and for 5 minutes following the ablative sonication to measure tissue cool down. T2-weighted MRI images were also taken after each treatment. Following MRgFUS, the legs were ranged by an orthopaedic surgery resident. Tendon disruption was confirmed both audibly and tactilely during the ranging and later visually during necropsy. Post-treatment goniometry measurements determined any change in the range of motion of the Achilles tendons.

Results: A hyperintense region appeared on the post treatment T2 MRI, indicating tissue edema. This region showed tight containment around the planned sonication point. The maximum temperature in MRT during sonication was $45.14^{\circ}\text{C} \pm 0.91$ for an ablation power of 20W and $54.00^{\circ}\text{C} \pm 6.13$ for 30W. Tendon disruption was confirmed for 0% of the tendons that received 20W ablation and 100% of the tendons that received 30W ablation. Immediately following treatment no skin burns were visible. Goniometry measurements showed that 20W treatments increased range of motion by 6.5° while the change in angle for the 30W treatment was 26° . These results could imply that more range of motion is gained through higher thermal ablative power. Necropsy revealed that the treatment caused precise lesions at the target area with no visible effect on overlaying or adjacent tissue.

Conclusions: Our results demonstrate that MRgFUS long-pulse histotripsy followed by ablation is able to create precise tissue disruption in porcine tendons. Unlike ablation used on its own, this treatment modality has not caused any skin burns. This work demonstrates that MRgFUS long-pulse histotripsy followed by thermal ablation has great potential for the treatment of musculotendinous contractures. These sonication parameters will be further explored by performing additional *in vivo* experiments.

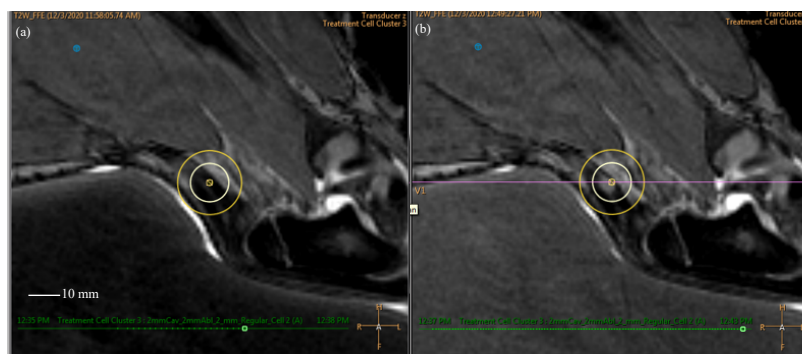
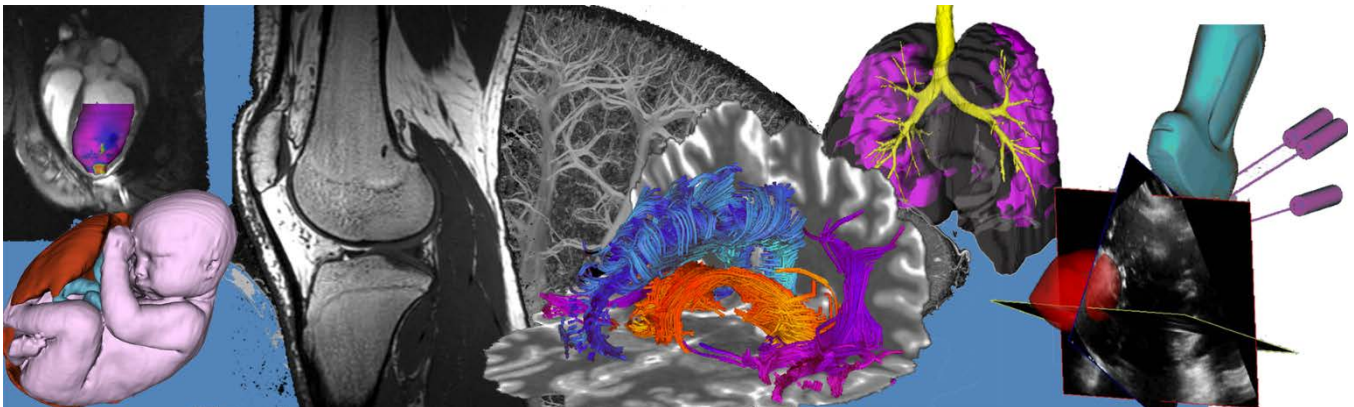


Figure 1: T2 weighted MRI images showing the sagittal plane of the tendon before the treatment (a) and after the histotripsy and ablation treatment (b). A hyperintense region in (b) indicates tissue edema. The small central yellow circle indicates the planned treatment point.

Pitch Presentation Abstracts

Session 4: Image-Guided Surgery



Validating 3D shape estimation using the Basel Face Model towards planning craniofacial reconstruction

Z. Fishman^{1,2}, Jerry Liu¹, Joshua Pope¹, J.A. Fialkov^{2,3,4}, C.M. Whyne^{1,2,3}

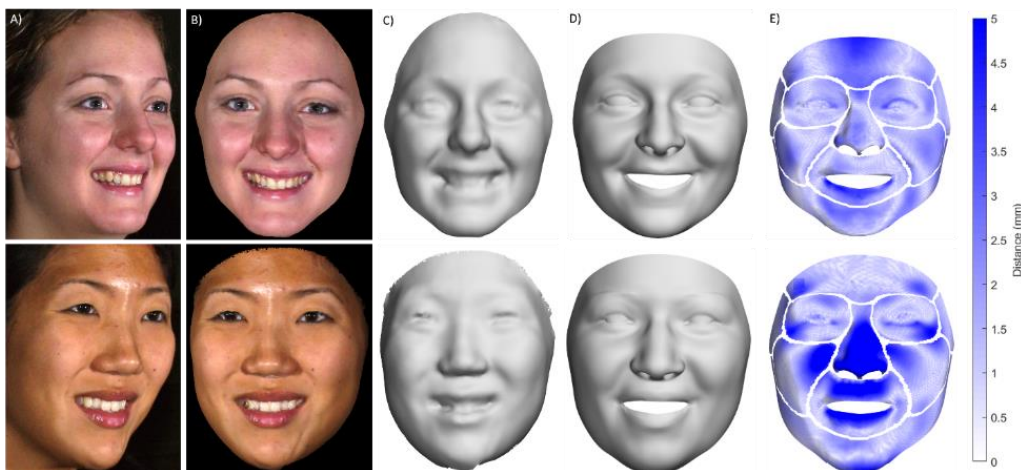
1. Orthopaedic Biomechanics Laboratory, Sunnybrook Research Institute, Toronto, ON;
2. Institute of Biomaterials and Biomedical Engineering, University of Toronto, Toronto, ON;
3. Department of Surgery, University of Toronto, Toronto, ON;
4. Division of Plastic Surgery, Sunnybrook Health Sciences Center, Toronto, ON

Introduction: Restoration of both mechanical function and pre-injury appearance are critical to the treatment of craniofacial trauma, tumor ablation and congenital deformities. As pre-trauma 3D imaging of the face rarely is available, critical shape information is often missing in cases of severe bilateral facial and nasal injuries, where the unaffected side of the face cannot be mirrored. Morphable models can be used to estimate 3D face shapes from 2D photographs but independent regional validation is required for the high accuracy needed in the craniofacial reconstructive surgical planning application.

Methods: 3D facial shapes were estimated using the Basel Face Model (BFM 2017) for 2D photos (front and side view) on 100 multi-racial subjects in the Binghamton University 3D Facial Expression database. This morphable model was fit using the “Scalismo” (scalable image analysis and shape modelling) software library. A 3D face can be morphed to a subject-specific 2D picture by projecting the 3D face to fit the 2D facial landmarks and matching the illumination and color textures. Shape accuracy was evaluated by comparing surface distances (per-vertex Euclidean) to the rigidly registered true 3D scan within defined facial regions. The true face shapes were captured by a calibrated stereo-photogrammetry technique (3DMD scanner). An accuracy of 2.5 mm was defined in this work as a clinically marginal error at the limits of facial perception. To evaluate the upper range of error for the 3D estimated face in the subject distribution, a measure of two standard deviations ($+2\sigma$) above the average is calculated.

Results: The average root-mean-square (RMS) distance error across all estimated facial regions was 2.68 ± 0.97 mm, for front view 2D photos processed with 10,000 iterations. The eyes, cheek, chin, forehead and mouth regions were within ~ 2.5 mm from the true 3D shape, which clinically represents error at the margins of perceivability. The nose and temple regions had lower accuracy (~ 3.1 mm) for all subjects. Significant differences were measured between noses depending on race (Caucasian: 2.4 mm, East-Asian: 4.8 mm) and sex (Male: 2.5 mm, Female: 3.6 mm), suggesting some model bias. Considering two standard deviations above the average, 95% of subjects has less than ~ 4.0 mm estimation error.

Conclusions: 3D face estimates using the BFM yielded clinically acceptable accuracy for the eyes, cheek, chin, forehead, mouth and Caucasian noses. These facial regions are capable for use in 3D planning and translational tool development to help guide craniofacial reconstruction.



Example subjects A) the $\frac{3}{4}$ side view 2D photo, B) front view 2D photo, and C) the 3D face shape surface. D) the 3D facial estimate and E) the per-vertex Euclidean distance error between of the estimate (0-5 mm).

Augmented Reality Relaxed Skin Tension Lines for Face Surgery - Initial Results on a Mobile DeviceWenzhangzhi Guo^{1,2}, Bao Yi (Emily) Huang^{1,2}, Joel C. Davies³, Vito Forte², Lueder A. Kahrs^{1,2}¹Department of Computer Science, University of Toronto, Ontario, Canada; ²Centre for Image Guided Innovation and Therapeutic Intervention, The Hospital of Sick Children, Toronto, Ontario, Canada;³Department of Otolaryngology, Medical University of South Carolina, Charleston, SC, USA

Introduction: Following resection of facial skin lesions, surgeons are challenged with determining the most optimal reconstructive options. The ideal wound closure is dependent on many factors including incision path, anisotropic skin tension, location with respect to anatomic subunits, and adjacent tissue types. Reconstructive surgeons have to rely on their training and experience to select the optimal flap design based on the patient's facial and skin characteristics, such as relaxed skin tension lines (RSTLs). Using RSTLs as guidance, the best cosmetic and functional outcome can be achieved since wound closure follows RSTLs [1]. Previous research has shown that Virtual Reality based approaches can be used to illustrate the different surgical flaps, but these methods are limited and used solely for educational purposes [2,3]. To our knowledge, there are no methods to assist facial reconstructive surgeons in flap selection and design using Augmented Reality (AR). As a first step towards achieving this goal, we present an iOS application that overlays RSTLs on a patient's face in real-time.

Methods: The image processing pipeline begins by taking an input image from the iOS device (either from the camera or photo album). Face tracking is performed on the image to retrieve 68 facial landmarks and pose. The face tracking utilizes a model trained with Supervised Descent Method (SDM) and the pose estimation is calculated with Linear Regression [4]. Based on the detected facial landmarks and poses, additional support points are calculated based on weighted averages of various detected landmarks: All support points on the forehead are extrapolated; as a further example, the interpolated support point in between two brows is the average of the two closest brow points (see Fig. 1). Lastly, RSTLs are drawn by fitting a spline through the landmarks and support points as an overlay on the input image and then displayed on the screen. Various sets of RSTLs are offered to head and neck surgeons from which they select the best fit visually. Afterwards they evaluate RSTLs on ten different faces and label the acceptable and unacceptable line segments on each image.

Results: The application can achieve real-time performance on modern iOS devices. On an iPhone XR, it takes 13.5 ± 2 ms to process a frame with a resolution of 1280×720 pixels. Out of the total run time, around 95% of the time is spent on face tracking and remainder is spent on visualization. On average, 80% of the visualized RSTLs are marked as acceptable by experts, where evaluations are done on front-facing and neutral expression faces.

Conclusions: We developed an initial prototype that can produce AR of RSTLs on a patient's face in real time. The visualization provided by this tool can aid head and neck surgeons in flap planning. It can also be used as an educational tool for medical students to familiarize themselves with RSTLs placement. A limitation of the app is the loss of tracking accuracy for non-frontal view images, which will be solved in future iterations. We will also further evaluate the accuracy of the application after more labels are collected with labelling tools [7].

References:

- [1] A. F. Borges and J. E. Alexander. Relaxed skin tension lines, z-plasties on scars, and fusiform excision of lesions. *British Journal of Plastic Surgery* 15: 242–254, 1962.
- [2] N. M. Mitchell, et al. A Real-Time Local Flaps Surgical Simulator Based on Advances in Computational Algorithms for Finite Element Models. *Plastic and Reconstructive Surgery* 137(2): 445e-452e, 2016.
- [3] R. M. Koch, et al. A framework for facial surgery simulation. *Proc. of 18th Spring Conference on Computer Graphics*, Budmerice, Slovakia, 2002 (pp. 33 - 42).
- [4] L. H. Vu. *HyperLandmark-iOS*. 2018, <https://github.com/elhoangvu/HyperLandmark-iOS>.
- [5] S. Gupta, et al. Anthropometric 3D Face Recognition. *International Journal of Computer Vision* 90(3): 331-349, 2010.
- [6] S. Gupta, et al. Texas 3D Face Recognition Database, URL: <https://live.ece.utexas.edu/research/texas3dfr/>.
- [7] Huang BY, et al. 2D and 3D Labeling Methods for Facial Skin Tension Lines. *IMNO* 2021.

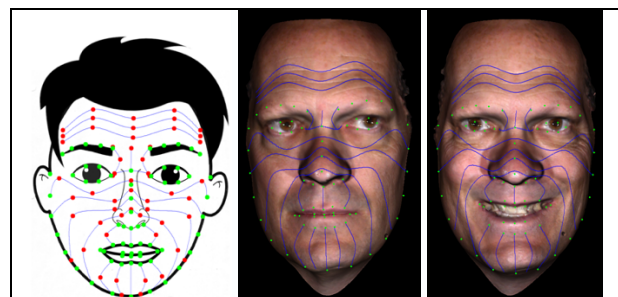


Fig. 1: Template and AR of RSTLs on two facial expressions from the Texas 3D Face Recognition Database [5,6]. In the template, green dots represent detected facial landmarks and red dots represent additional support points.

Preclinical Evaluation of a Bedside Image-Guidance System for External Ventricular DrainageAdam Hopfgartner¹, David Burns^{1,2}, Suganth Suppiah³, Allan Martin⁴, Michael Hardisty^{1,2,3}, Cari Whyne^{1,2,3}¹Holland Bone and Joint Program, Sunnybrook Research Institute, Toronto, Canada²Division of Orthopaedic Surgery, University of Toronto, Toronto, Canada³Department of Surgery, University of Toronto, Toronto, Canada⁴Department of Neurological Surgery, University of California, Davis, Sacramento, USA

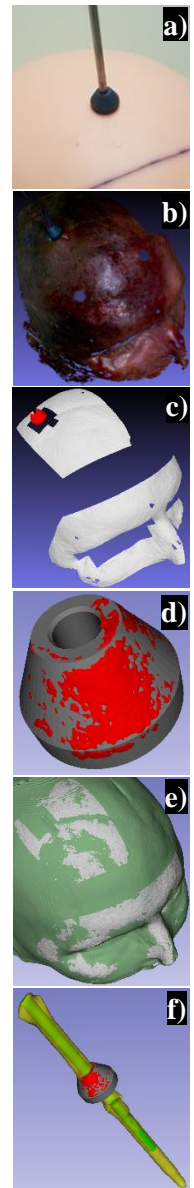
Introduction: External ventricular drainage (EVD) is a life-saving bedside procedure required to drain cerebrospinal fluid from the ventricular system in response to elevated intracranial pressure. The standard freehand EVD technique utilizes anatomical landmarks to insert an intracranial catheter into the frontal horn of the lateral ventricle. Non-navigated catheter placement results in malpositioning in up to 45% of initial EVD placements¹. Multiple placement attempts are associated with infection, haemorrhage, and EVD dysfunction^{1,2}. The aim of this study was to evaluate the accuracy of a novel structured-light-based, image-guidance system in its ability to visualize EVD position and trajectory in a preclinical cadaveric model.

Methods: Experimentation was performed on both sides of 3 cadaveric heads (n=6). After a pre-interventional computed tomography (CT) scan was acquired, for each location a guidewire (simulating the catheter) was inserted by a neurosurgical resident as in a clinical EVD procedure. A 3D-printed optical tracker (“Bullseye”) was placed over the guidewire on the surface of the scalp (a, Bullseye on a mannequin head) and an optical image of the Bullseye and experimental area was captured with a 3D structured-light scanner (b, Einscan, Shining 3D, China). A post-interventional CT image was taken to verify guidewire position and trajectory. A mesh model of the optical image was segmented to remove surfaces expected to be covered by hair or shadow in the clinic and to isolate features of interest (c). A mesh model of the Bullseye (d, grey) was associated with a co-linear mesh model representation of the intra-operative guidewire (1f, green). The Bullseye in the optical image was registered to the mesh model of the Bullseye (d), the optical image of the experimental area was registered to a mesh model of the head from the pre-interventional CT (e), and the post-interventional CT was registered to the pre-interventional CT (3D Slicer). The guidewire was segmented from the post-interventional CT (f, yellow) and fiducial markers were placed along the longitudinal axis of the guidewire. Angle error was calculated as the dot product of the segmented guidewire from the post-interventional CT (actual guidewire position) and the intra-operative guidewire model (predicted guidewire position). Offset error was calculated as the distance between central axes of the segmented guidewire and intra-operative guidewire model on the plane tangent to the surface of the head. The registration procedure was repeated with 6 distinct cranial regions (combinations of face, ear, and interventional region of interest (ROI)) captured with the optical imaging and analyzed to determine the effect of using different anatomy on registration accuracy.

Results: Optical imaging which included the face (eyebrow, cheek, nose) produced the most promising results. The lowest angle and offset errors between predicted and actual guidewire positions resulted from optical images that captured the face and ROI on the scalp surrounding the Bullseye and guidewire (mean $1.27 \pm 0.38^\circ$ and 0.33 ± 0.19 mm, range 0.67° to 1.71° and 0.10 to 0.56 mm, respectively). Inclusion of the ear in the registrations negatively impacted the results. Mean duration of the post-interventional optical imaging procedure was 128 ± 35 s (range 70-201 s).

Conclusions: This novel image-guidance system presents a precise, rapidly applicable, patient-specific alternative to freehand EVD positioning which may improve clinical accuracy. Use of facial features are key to improved accuracy in the registration. There is no clinical consensus on required angular accuracy of the EVD catheter however, the face + ROI angle error observed here was well within the appropriate range of $\pm 5^\circ$ as described by Abdoh et al². Future work will consider automation of the workflow and clinical implementation.

References: 1. Huyette DR, et al (2008) J Neurosurg 108(1):88–91. 2. Abdoh MG, et al (2012) Acta Neurochir 154:153-159.



Miniature C-Arm Simulator Using Wireless Accelerometer Based Tracking

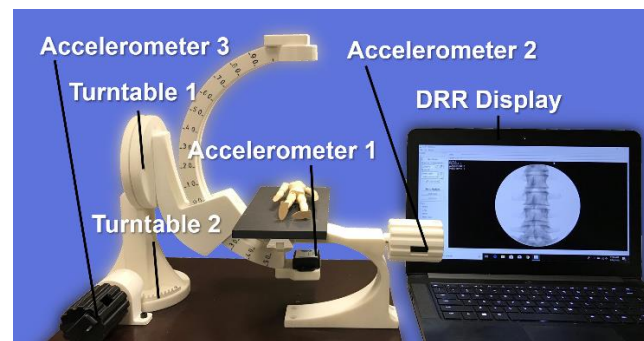
D.R.Allen, J.Moore, A. Joschko, C. Clarke, T.Peters, E.C.S.Chen

Robarts Research Institute, School of Biomedical Engineering, Western University

Purpose: The C-Arm has enabled minimally-invasive procedures to be performed under real-time image guidance. These procedures require extensive training on how to manipulate the C-Arm in order to produce the desired images. Standard training requires physical access to a C-Arm and exposes the trainee to prolonged radiation [1]. To provide a hands-on radiation-free means of training, we propose a miniature C-Arm simulator using wireless accelerometer-based tracking.

Methods: The C-Arm model was 3D-printed and fixed with wireless Bluetooth® Inertial Measurement Units (IMU's) to track the orientation of the C-Arm head (3 Degrees of Freedom (DoF)) and position of the table (1 DoF). The Digitally Reconstructed Radiographs (DRRs) were generated in real-time using a 1-dimensional transfer function and the tracked orientation of the C-Arm head. A user study was conducted in order to evaluate the efficacy of the simulator as a training tool. 20 medical residents (10 control, 10 experimental) were recruited. Both groups performed the same C-Arm placement evaluation task but the experimental group was given 5 minutes of training using the real-time DRR functionality of the system.

Figure 1: System overview



Results: Qualitative analysis shows that the system is capable of generating realistic real-time DRRs based on the tracked position of the C-Arm source. The results from the user study are shown in Table 1. Results from a 5-pt Likert scale questionnaire filled out by each participant indicated general positive feedback of the system with the mean score for each question being 4.0 or higher.

Table 1: User study results

Group	Angular Error (degrees)	Translational Error (mm)	Time (min)
Control	6.49 ± 10.88	16.64 ± 12.66	8.89
Experimental	5.43 ± 8.61	12.78 ± 8.03	9.59

Conclusions: We developed a C-Arm simulator system consisting of a miniature 3D-printed C-Arm, wireless Bluetooth® IMUs, and software capable of generating real-time DRRs. Results from a user study show promising potential for the use of our system as a C-Arm placement training tool. Future work includes incorporating an interface to simulate needle-guided interventions using web-cam-based needle tracking to provide low cost end-to-end training for interventional spinal procedures.

References: [1] Bott, O.J., Dresing, K., Wagner, M., Raab, B.W., Teistler, M.: Informatics in radiology use of a C-arm fluoroscopy simulator to support training in intraoperative radiography. *Radiographics* 31 (3) (2011)

Optimization of MRI thermometry for controlled hyperthermia-mediated drug delivery in a murine model of pediatric sarcoma

Suzanne Wong^{1,2}, Claire Wunker^{2,3}, Ben Keunen¹, Maryam Siddiqui⁴, Max Regenold², Karolina Piorkowska¹, Yael Babichev³, Warren Foltz^{2,5}, Christine Allen², Rebecca Gladdy^{2,3}, Samuel Pichardo⁴, Adam C. Waspe^{1,2}, James Drake^{1,2}

¹Hospital for Sick Children, ²University of Toronto, ³Mount Sinai Hospital, ⁴University of Calgary, ⁵University Health Network

Introduction. Sarcomas are the 2nd most common solid pediatric cancer and in advanced cases, 5-year survival rates are as low as 30%. A novel method for targeted drug delivery uses thermosensitive liposomes to encapsulate doxorubicin (TLD) and hyperthermia at 42°C to cause localized drug release. Magnetic resonance guided high intensity focused ultrasound (MRgHIFU) is an effective method of hyperthermia delivery as it is non-invasive, non-ionizing and provides high resolution imaging and real-time thermometry. Proteus is a custom hyperthermia software platform that receives MR thermometry information to modulate the amount of acoustic power the transducer delivers to maintain a steady temperature. Artifacts due to respiration and spontaneous motion are a substantial challenge in MR thermometry as they confound temperature measurement. Real-time motion compensation algorithms can reduce temperature uncertainty during treatment by adjusting for motion as it occurs, allowing Proteus to deliver more accurate powers for sonication. This study will demonstrate the need for a motion compensation algorithm, which will be implemented into Proteus for future real-time experiments.

Methods. Immune-competent mice (n=78) with hindlimb sarcomas received hyperthermia treatment using the small animal Bruker 7T MRI and IGT HIFU system. No motion compensation algorithm was used in these animals. A region of interest (ROI) for heating was selected and the temperature within the ROI was monitored with Proteus. Esophageal and rectal probes were used to monitor body core temperature to ensure no systemic heating occurred. After a 1.5min preheating cycle, TLD was injected into the mice. Hyperthermia treatments were set at a temperature of 41° for a 20-minute duration. Inclusion factors were tumour temperature greater than 39°C throughout the treatment, a temperature range of less than 6°C and a rectal temperature of less than 37°C.

Results. In the mice included (n=64), Proteus maintained an average ROI temperature of 40.5°C +/- 1.5°C. Experimental outliers (n=14) due to problems such as motion, bone and/or rectal heating, and far field heating had an average temperature of 40.7°C +/- 2.7°C. We mitigated some of these issues by moving the ROI farther from the femur or rectum and placing a gel pad underneath the mouse to absorb ultrasound energy and reduce reflections. With these strategies, we were able to demonstrate a reproducible treatment with small variation in temperature. However, motion still presents as a challenge during treatment. Motion artifacts can be mitigated by implementing motion compensation algorithms that employ prospective principal component analysis. Currently these algorithms are being integrated into Proteus and will be optimized to ensure precise temperature control.

Conclusions. The use of Proteus with a small animal MRgHIFU successfully controlled tumour temperatures for optimal drug delivery in a pre-clinical sarcoma model. Solutions for large temperature fluctuations were implemented and demonstrated to be successful, with exception of motion. Future work includes employing a motion compensation and temperature control algorithm to attempt to further reduce variation in temperature.

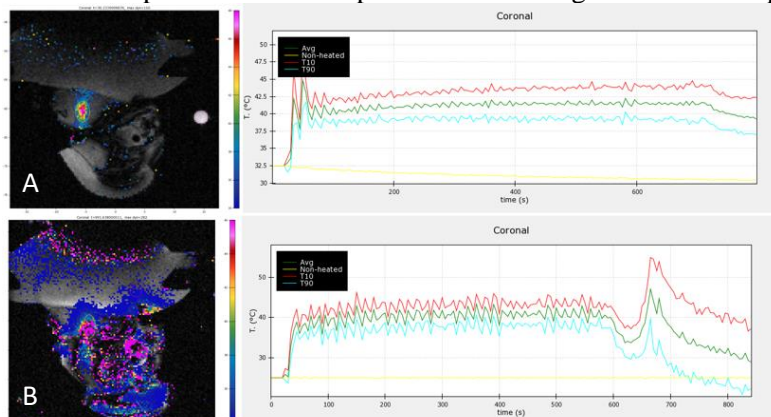


Figure 1: T1 weighted dynamic gradient echo image with temperature overlay and corresponding temperature chart. (A) Demonstrates a good treatment that would be included in our study; whereas (B) demonstrates motion artifacts caused by movement around the 650s time point and would be excluded from our study.

Quantifying Tissue Optical Properties using Structured Illumination for Oral Cancer Surgery

Murtuza Rajkotwala,¹ Ashley Gilbank,¹ Jacqueline Fleisig,¹ Axel Sahovaler,² Tommaso Gualtieri,² Brian C. Wilson,^{1,3,4} Jonathan C. Irish¹⁻³ and Michael J. Daly¹

¹TECHNA Institute, University Health Network, Toronto ON

²Department of Otolaryngology – Head & Neck Surgery, University of Toronto

³Ontario Cancer Institute, Princess Margaret Cancer Centre, Toronto ON

⁴Department of Medical Biophysics, University of Toronto

Introduction: Oral cancer is often associated with changes in tissue composition that can be revealed through measurements of tissue optical properties. Spatial frequency domain imaging (SFDI) is a non-contact approach to map optical absorption (μ_a) and scattering coefficients (μ'_s) based on the diffuse reflectance from tissue. We have assembled a prototype SFDI system for clinical applications in oral cancer surgery, but standard system calibration methods do not account for complex light interactions such as those found in the oral cavity. In this work, we combine SFDI with methods for surface profilometry and light mapping in order to compensate for the effects of surface topography and system geometry.

Methods: The stereovision structured illumination system is comprised of a 14-bit camera (PCO Pixelfly USB), a fiber-coupled projector (DLP LightCrafter 6500), and linear polarizers. Phase-shifted fringe patterns with multi-frequency phase unwrapping were used for surface profilometry. The resulting point clouds were reconstructed using a screened Poisson technique with Dirichlet boundary conditions to generate smooth, closed meshes. Light mapping onto meshes was based on radiometric calibration of the camera-projector pair and ray-triangle intersections. System accuracy was evaluated in tissue-simulating oral cavity phantoms and *ex vivo* tissue specimens placed at various positions relative to the imaging system.

Results: In agar tongue phantoms with realistic optical properties, phase shift profilometry recovered the surface topography to within <2 mm average accuracy. Light irradiance variations of up to 3-fold across the tissue surface were observed. Using standard “flat” calibration, μ_a and μ'_s varied by 35% and 8%, respectively, across phantom positions. In contrast, calibration with profile correction yielded μ_a and μ'_s variations of 12% and 4%. Limitations were found in regions with high curvature and shadows. Ongoing experiments are assessing fluorescence quantification after correcting for absorption and scattering.

Conclusions: Initial phantom studies demonstrate that light-mapping-enabled SFDI yields optical property images that are largely geometry-invariant, with additional studies warranted in more complex anatomical models. Further streamlining of the acquisition process and fabrication of a compact prototype will facilitate clinical studies to investigate if our system can accurately classify cancerous regions based on optical property variations, μ_a and μ'_s .

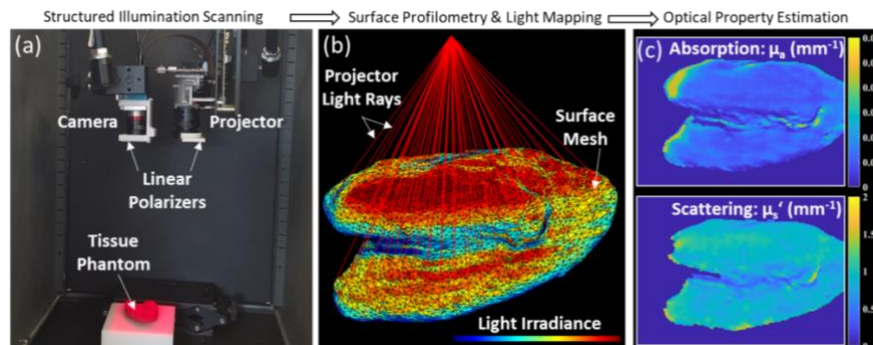


Figure. (a) Structured illumination system for surface profilometry and SFDI. (b) Light mapping algorithm using ray-triangle intersection between calibrated camera-projector system and mesh from surface profilometry. (c) Profile-corrected images of optical absorption (μ_a) and scattering (μ'_s) coefficients of agar tongue phantom.

A platform for robot-assisted intraoperative imaging in breast conserving surgery

Laura Connolly¹, Kyle Sunderland¹, Andras Lasso¹, Anton Deguet², Tamas Ungi¹, John F. Rudan¹,
Russell H. Taylor², Parvin Mousavi¹, Gabor Fichtinger¹

¹ Queen's University, Kingston Ontario; ² Johns Hopkins University, Baltimore, Maryland

INTRODUCTION: Breast conserving surgery is a procedure that involves removing a cancerous lesion from the breast while preserving the surrounding healthy tissue. The outcomes of these surgeries are more psychologically and cosmetically favourable when compared to treatment options like partial or full mastectomy where the entire breast is removed. A main shortcoming of these procedures is that precise tumor delineation is difficult whenever a tumor is irregularly shaped, non-palpable or if the surgeon has restricted visual access to the incision site. Recent advancements in optical, acoustic and biochemical imaging approaches such as spectroscopy, ultrasound and mass spectrometry, enable intraoperative tissue assessment as a potential solution to this problem [1]. With the assistance of machine learning, imaging data can be used to identify a cross section of tissue as either cancerous or healthy. However, effective use of these imaging tools is limited by the surgeon's ability to thoroughly scan the resection cavity by hand and retrace their motion to perform additional resection if necessary. Therefore, in this work we propose a robotic framework that can be used to deploy these imaging tools in breast cancer surgery. The system itself is unique when compared to existing surgical robotic devices that are designed for robust control and force feedback. As the breast itself poses practically no resistant force on the surgeon's tools, we made use of an inexpensive haptic manipulator and began the integration of this device with navigation technology.

METHODS: Our system consists of the Omni Bundle robot by Quanser, an electromagnetic tracking system, an imaging tool (spectrometer) and a mechanical retractor. The system is interfaced with the open-source medical imaging platform 3D Slicer (www.slicer.org) to enable real-time visualization of the robot and the surgeon's tools with respect to the breast, which is also electromagnetically tracked (Figure 1). A module was developed in 3D Slicer to display a 3D model of the robot as it moves, as well as models of the electromagnetically tracked surgical tool and retractor. In the experimental prototype, an optical spectrometer replaces the imaging tool, distinguishing variations in color inserts placed in a silicon breast phantom. To account for breast deformity, the EM sensor on the retractor is considered a moving reference to the breast.

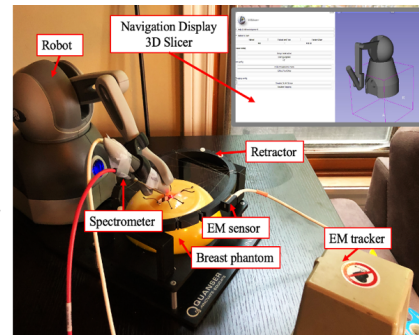
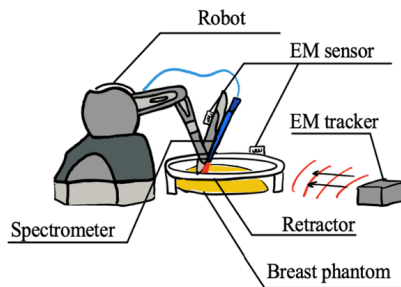


Figure 1: Hardware setup for the new platform.

RESULTS: We were successful in developing a proof-of-concept platform that enables cooperative robotic guidance of an imaging tool through a resection cavity, with real-time visual navigation and display. We evaluated the system based on the performance of the module in 3D Slicer.

CONCLUSIONS: This platform will serve as the basis for a navigation system that combines novel imaging tools and robotic assistance. Clinical implementation will likely improve the accuracy of breast conserving surgery and reduce the risk of incomplete resections. The system is also open-source and flexible so it can be translated to other institutions. Moreover, the proposed technology may also be extended to other areas of surgical oncology. Future work includes implementing more sophisticated control algorithms for the robot to fully scan the cavity.

ACKNOWLEDGEMENTS: Laura Connolly was supported by NSERC and CIHR. G. Fichtinger is supported as a Canada Research Chair. This work was funded, in part, by CANARIE's Research Software Program.

REFERENCES:

[1] A. Jamzad *et al.*, "Improved Resection Margins in Surgical Oncology Using Intraoperative Mass Spectrometry," in *Lecture Notes in Computer Science (including subseries Lecture Notes in Artificial Intelligence and Lecture Notes in Bioinformatics)*, Oct.2020, vol.12263 LNCS, pp. 44–53, doi: 10.1007/978-3-030-59716-0_5.

Transrectal diffuse optical tomography system to monitor photothermal therapy of localized prostate cancer

Ivan Kosik (University Health Network), **Robert Weersink** (Institute of Biomaterials and Biomedical Engineering, Radiation Oncology, University of Toronto), **Brian Wilson** (Medical Biophysics, University of Toronto)

Introduction: Nearly 1 in 9 men are diagnosed with PCa but low/intermediate-risk tumors often do not warrant the potential significant side effects of standard radical therapies (radiation, surgery). Conversely, PCa is the 3rd leading cause of cancer death in men, highlighting for a safe, effective and minimally-invasive treatment option. Our ongoing phase I/II clinical trials have shown that porphyrin-nanoparticle-enabled photothermal therapy (PTT) is effective in selectively destroying tumor tissue. However, the current use of indirect MRI thermometry to monitor and guide PTT treatments has resulted in ~30% of patients being under-treated. In addition, the cost and limited access to interventional MRI are significant impediments to routine clinical adoption. We have previously investigated transrectal diffuse optical tomography (DOT) for PTT treatment monitoring in preclinical models. However, the preclinical tests revealed a number of technical limitations that slowed data acquisition, preventing efficient operation in a demanding surgical environment. Here we report on system upgrades that aim to address these limitations. We *hypothesize* that these enhancements provide the necessary performance for our DOT system to function smoothly in a clinical environment, permitting time-efficient, and hence effective, PTT treatment monitoring evaluation.

Methods: System hardware was upgraded with new photomultiplier tube detector design and 3-wavelength laser multiplexing (670 nm, 750 nm and 808 nm). Software was enhanced with automatic detector-gain control, freeing the operator from tedious manual adjustments and as such, further improving the system clinical utility. Preliminary tests included 1% Intralipid™ liquid phantom, shown in Fig 1a, with absorption targets of Methylene Blue (MB⁺, 670 nm absorption peak) and NIR dye (ADS832WS, 832 nm peak) as well as a scattering target of 20% Intralipid™. To test system response for scattering and multispectral absorption, a transrectal probe was mounted on a linear translation stage permitting careful relative probe-target positioning.

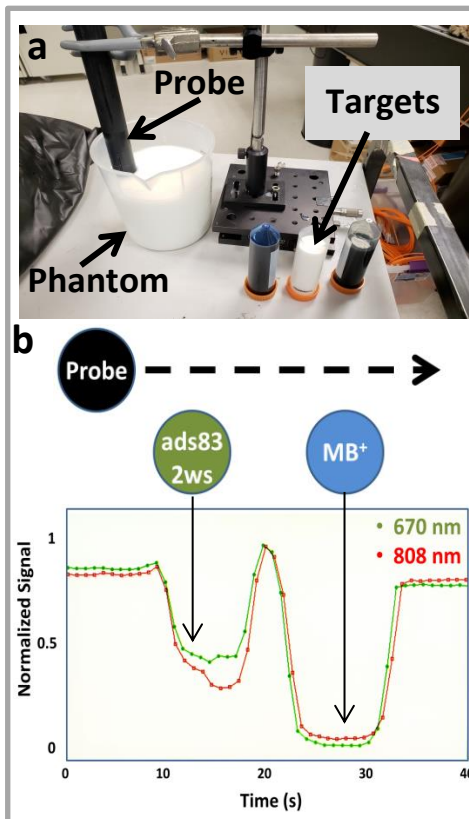


Figure 1(a) Photograph of transrectal probe immersed in liquid phantom along with the 3 targets. (b) Top view schematic showing probe, targets and track of probe (dashed arrow) as it is linearly translated over a 40 second time frame. The graph shows increased absorption (drop in signal) corresponding to the excitation wavelength and absorption peak of each laser and target, respectively.

Results: The hardware and software improvements facilitated a >50 fold increase in our detector gain adjustment rate. Furthermore, wavelength multiplexing allowed simultaneous probing at multiple wavelengths as shown in Fig 1b, where differential absorption of the targets is demonstrated. For clarity the figure shows signal from just one of 8 detector channels. As consistent with theory, the data shows that 670 nm light is more strongly absorbed by MB⁺ while 808 nm light is preferred by the NIR dye. In terms of sensitivity, an advantage of 3dB over previous detection system was observed, indicating potential of deeper imaging penetration.

Conclusions: We are in the process of beginning clinical testing of the refined instrument and believe that the new performance features will enable us to more efficiently gather clinical data both to evaluate clinical utility during PTT and inform towards potential future improvements.

Improving central line needle insertions using *in situ* vascular reconstructions

Leah A. Groves^{a,b}, Natalie Li^c, Blake VanBerlo^d, Natan Veinberg^d, Terry M. Peters^{a,b,c,d} and Elvis C. S. Chen^{a,b,c,d}

^aSchool of Biomedical Engineering, Western University, London, Canada

^bRobarts Research Institute, Western University, London, Canada

^cDepartment of Medical Biophysics, Western University, London, Canada

^dSchulich School of Medicine and Dentistry, Western University, London, Canada

Introduction: Millions of Central venous catheterizations (CVC) are performed annually, with the internal jugular vein (IJV) being the most common insertion site. Carotid Artery (CA) puncture is one of the most common and severe complications that can occur during CVC. In Canada, the standard of care is ultrasound (US)-guided CVC. However, CA puncture still occurs in upwards of 7.8% of ultrasound US-guided CVCs inserted at the IJV. One factor that contributes to the high complication rates under US-guidance is that the clinicians rely on 2D information to perform a 3D application. We hypothesize that providing clinicians with 3D visual information, including the anatomy and surgical tools, will improve the accuracy of CVC.

Methods: We developed a neck central line insertion guidance system that renders 3D ultrasound (US) surface reconstructions of the carotid artery (CA) and internal jugular vein (IJV), and tracked models of the needle and needle trajectory on a 2D monitor, as seen in Fig.1. The IJV is rendered as a semi-transparent wire-frame mesh providing an intuitive visual relationship between the position of the needle and the IJV. Twenty clinicians who are experts in CVC evaluated this system compared to US-only guidance on a phantom. Each participant underwent a training process with the 3D system and then performed a single experimental insertion. The time and accuracy of the two approaches were analyzed using insertion success, insertion time, and distance from the final needle tip position to the center of the vessel and to the vessel wall.

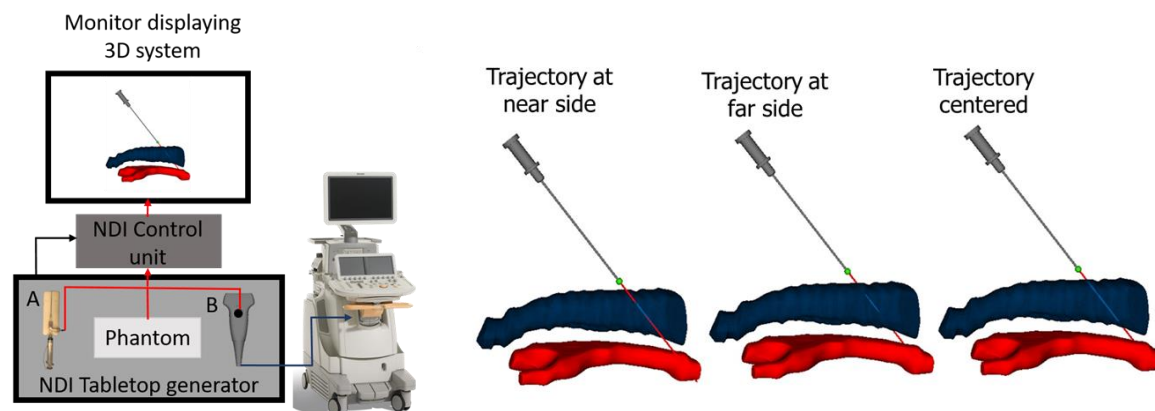


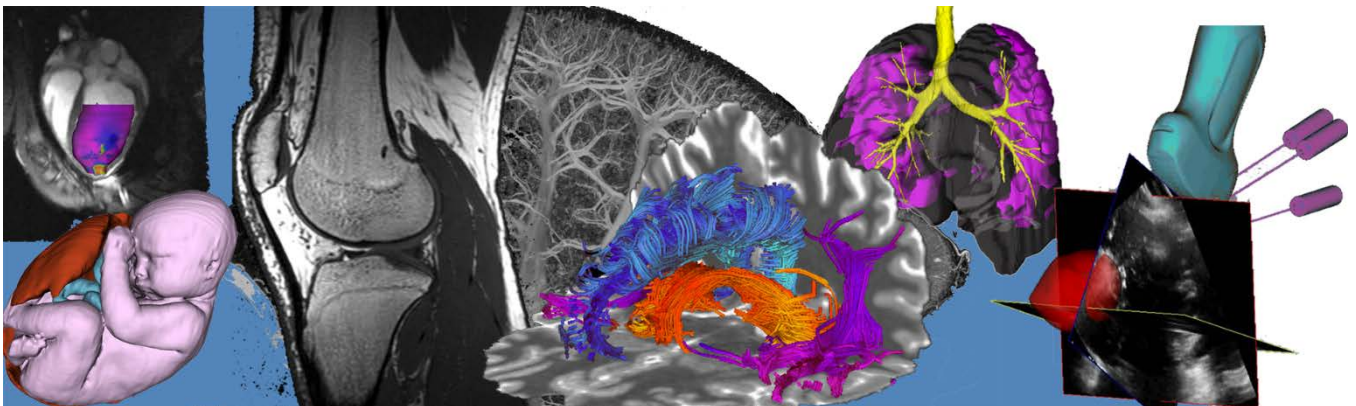
Fig 1. Experimental and system set-up and three visual representations of the visual information shown to the user for the 3D. For the US-only case the monitor displays the 2D US image.

Results: The 3D system had a 100% success rate compared to 70% for the US-only system. The average insertion times were 10.4 ± 5.5 seconds and 20.5 ± 9.8 , for the 3D and US-only systems respectively. The average distance from the center line of the US reconstructed IJV was 1.8 ± 0.9 mm under 3D guidance compared to 4.2 ± 2.9 mm for the US-only method. The average distance from the vessel wall of the US reconstructed IJV was 4.4 ± 1.6 mm under 3D guidance compared to 0.7 ± 4.3 mm for the US-only method.

Conclusions: Our system significantly improved needle insertion targeting accuracy compared to the US-only approach through a radiation-free surface reconstruction of the neck vascular structures. This work has the potential to provide a mobile 3D imaging and visualization system for needle-based vascular interventions.

Pitch Presentation Abstracts

Session 5: Device, Hardware, System Development I



Validation of a Retrospective Eddy Current Correction Algorithm for Advanced Diffusion MRI

Paul I. Dubovan^{1,2}, Jake J. Valsamis^{1,2}, and Corey A. Baron^{1,2}

¹ Department of Medical Biophysics, Schulich School of Medicine & Dentistry, Western University

² Centre for Functional and Metabolic Mapping, Robarts Research Institute, London, Ontario, Canada

Introduction: Diagnostic capabilities of diffusion magnetic resonance imaging (dMRI) are largely dependent on the gradients used to encode thermal motion of water molecules within biological tissue. Advancements in gradient hardware have the potential to broaden the clinical role of dMRI, however, image quality suffers from eddy currents induced by strong diffusion encoding gradients¹. A variety of correction techniques exist that aim to correct the effects of eddy currents, including the post-processing technique “eddy” offered by FSL. Corrections to data are made by accounting for eddy currents that are static in time². While generally effective for the traditional Pulsed Gradient Spin Echo (PGSE) diffusion sequence, this method does not necessarily apply to advanced forms of dMRI, such as microstructural sensitivity-enhanced Oscillating Gradient Spin Echo (OGSE)³, which exhibit complex time-varying eddy currents (abstract #130, ImNO 2020). The performance of an in-house algorithm which, contrary to existing approaches, includes a finite time-constant to model eddy current decay, was evaluated by correcting in-vivo PGSE and OGSE images and comparing correction quality with existing correction methods.

Methods: Opposite polarity diffusion gradients produce distortions that are equal in magnitude, but opposite in direction, as per the induced eddy currents⁴. Accordingly, the algorithm takes image pairs acquired with opposite polarity diffusion gradients and applies identical yet inverse corrections to the data until the mean squared error (MSE) in pixel intensity between corrected image pairs is minimized. Brain scans were performed on two healthy male subjects using a 7T MRI (Siemens). Diffusion MRI data was acquired using PGSE (0Hz) and cosine modulated trapezoidal OGSE (40Hz). The OGSE frequency was based on optimized diffusion dispersion sequence parameters determined by Arbabi et al⁵. The remaining parameters were 4 directions at $b = 750 \text{ s/mm}^2$, 3 averages per subject, echo time = 124 ms, field of view = $224 \times 224 \text{ mm}^2$, 2 mm isotropic resolution, axial view. The ground truth eddy current fields for each scan were also measured using a field monitoring system (Skopec) to validate the performance of the algorithm by comparing to a new gold standard correction tool. Images were corrected using FSL eddy, the algorithm’s time-constant (TCEDDY) and time-varying (TVEDDY) versions, and field monitoring (FM). Correction quality was assessed by comparing the pixel intensity MSE between pairs of images, after averaging MSE values over both subjects, the 4 directions, and 3 averages ($N = 24$).

Results: In the sample uncorrected OGSE brain image, diffusion gradient vector: [1,-1,1], (Fig. 1A), blurring is seen to extend past the edges of the frontal lobe, which is still apparent after correction with FSL eddy (B) and TCEDDY (C). This artifact is reduced significantly using the time-varying eddy current model (D), which is comparable to the field monitored correction (E). In Fig. 2, decreasing average MSE values are observed with increasing model complexity. Statistically significant changes in average MSE ($p < 0.01$) using paired t-tests were observed between subsequent correction techniques, excluding PGSE correction using TCEDDY and TVEDDY, showing that the improvements are more apparent for diffusion acquisitions that exhibit time-varying eddy currents such as OGSE.

Conclusions: This work presented a new method for correcting diffusion eddy currents that outperforms FSL Eddy for OGSE acquisitions. The capacity to correct distortions induced by advanced dMRI techniques without the substantial cost of a field monitoring system will promote the development and clinical application of dMRI.

References: ¹Setsonpop K et al. *Neuroimage* (2013). ²Andersson JLR et al. *Neuroimage* (2016). ³Baron C et al. *Magn Reson Med* (2014). ⁴Bodammer N et al. *Magn. Reson. Med* (2004). ⁵Arbabi A et al. *Magn Reson Med* (2019).

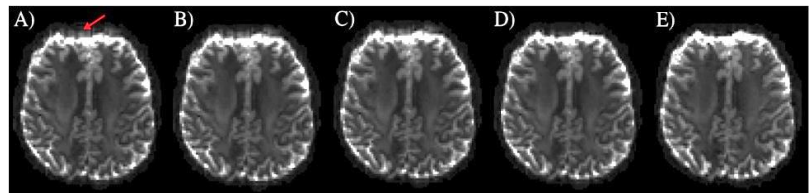


FIG. 1. Comparison between eddy current corrupted OGSE slice (A), slice corrected with FSL eddy (B), TCEDDY (C), TVEDDY (D), and with field monitoring (E). Red arrow indicating region of blurring.

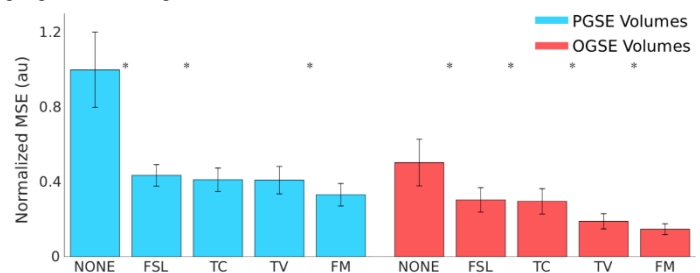


FIG. 2. Quantitative assessment of eddy current correction between FSL eddy (FSL), time-constant model (TC), time-varying model (TV), and field monitored correction (FM), for both PGSE and OGSE acquisitions.

A simple, realistic walled phantom for intravascular and intracardiac applications

Hareem Nisar¹, John Moore¹, Roberta Piazza², Efthymios Maneas³, Elvis C. S. Chen¹, Terry M. Peters¹

¹VASST Lab, Robarts Research Institute, Western University

²Department of Information Engineering, University of Pisa, Pisa, Italy

³Department of Medical Physics and Bioengineering, University College London, London, UK

Introduction: Ultrasound-compatible vascular phantoms are routinely used in clinical tool training, testing of intravascular devices, blood flow studies, and validation of algorithms for intravascular and intracardiac surgical systems. They are usually categorized as wall-only phantoms – with a prominent tube-like vessel layer but lack representation of surrounding tissue, and wall-less phantoms which are hollow on the inside and lack a vessel-layer. This work aims to develop a simple, anatomically and haptically realistic vascular phantom, compatible with intravascular and intracardiac ultrasound. The low-cost, dual-layered phantom bridges the gap between traditional wall-only and wall-less phantoms by showing both the vessel wall and surrounding tissue in ultrasound imaging.

Methods: Polyvinyl alcohol cryogel (PVA-c) incorporating a scattering agent was used to obtain vessel and tissue-mimicking materials. Our specific design targeted the inferior vena cava and renal bifurcations with the lumen diameters and bifurcation angles modelled in CAD software according to the average dimensions in humans (Fig.A). One core and two custom moulds were prepared using 3D printing. First the targeted vessel design was 3D printed as the core. Then a plastic mould was printed based on a slightly oversized version of the negative of the vessel. The core is secured inside the first mould and secured tightly. Vessel-mimicking material was injected via a sprue to fill the space between the core and the negative mould. The assembly was subjected to a few freeze-thaw cycles to obtain a solid, PVA-based vessel layer (Fig.B). Then a custom box is printed to hold the core along with vessel layer (Fig.C). Tissue-mimicking liquid was poured directly from the top and subjected to a freeze-thaw cycle, leading to the construction of one whole phantom with two layers. The layers attach to each other due to the cross-linking of the PVA polymer chains. Three phantoms were prepared by varying both the concentrations of scattering agent as well as the number of freeze-thaw cycles the vessel-layers were subjected to. Each phantom was evaluated qualitatively using intracardiac ultrasound imaging and compared against the targeted animal images (Fig.E). In animal images, the inner lumen is clear, but the outer layer of the vessel is fused with the surrounding tissue. Geometrical validation of the internal diameter and angles was provided by comparing CAD design to a CT scan of the phantom.

Results: From the three phantoms designed, the desired vascular phantom was constructed using 2.5% and 0.05% scattering agent concentration in the vessel and tissue-mimicking layers, respectively. Ultrasound image of that phantom (Fig.D) showed a tissue-to-vessel-layer pixel intensity ratio of 1:1.9, as compared to the ratio of 1:1.7 observed in the animal IVC image. Imaging of the three phantoms showed that increasing the number of freeze-thaw cycles did not significantly enhance the image contrast. Measurements of the designed phantom designed revealed a mean error of 1mm (5%), 0.9mm (7.5%), and 0.7mm (4.4%) for the IVC, left renal vein, and right renal vein, respectively. The left infra-renal angle was measured at 43.8° compared to the CAD designed value of 45° and the right infra-renal angle was 77.5° as compared to the CAD designed 78°.

Conclusion: The phantom is anatomically realistic with respect to the dimensions created, the presence of a bright vessel layer and a specular tissue layer, imaging quality and ultrasound reflection ratios. It also provides a smooth lumen surface for the ultrasound probe and catheter to maneuver. The phantom must be stored in carefully in full humidity to ensure it does not shrink over time. Since PVA-c is mostly water, there is only a fraction of difference in the speed of sound of the phantom and the human tissue.

The vascular phantom can enable the validation of intravascular and intracardiac image guidance systems.



Toward high-resolution PEM and US-guided core-needle biopsy

Claire K. Park^{1,2*}, Jeffrey Bax², Lori Gardi², Eric Knull³, Aaron Fenster^{1,2,3}

¹Department of Medical Biophysics, Western University, London, Ontario, Canada, ²Imaging Research Laboratories, Robarts Research Institute, London, Ontario, Canada, ³School of Biomedical Engineering, Faculty of Engineering, Western University, London, Ontario

Introduction: Definitive diagnosis of breast cancer still requires a suspicious lesion to be sampled, most commonly with an image-guided needle biopsy. Positron emission mammography (PEM) is a breast-dedicated functional imaging modality, which combines high-resolution imaging components and pre-eminent fluorodeoxyglucose (FDG) radiotracers to image changes in metabolic activity, a hallmark of cancer growth.¹ Although PEM shows potential to improve breast cancer detection, independent of breast tissue density, anatomical context and real-time needle visualization are not available. We have developed a mechatronic guidance system integrating US imaging and a core-needle biopsy (CNB) intervention with high-resolution PEM imaging. This work presents the proof-of-concept phantom testing the mechatronic guidance system and development of the visualization module to perform PEM-US-guided biopsy on simulated breast lesions.

Methods: A mechatronic guidance system was developed operate with the Radialis PEM system (Radialis Medical, Thunder Bay, Ontario, Canada) and any conventional US imaging system.² The system contains a user-operated manipulator and an end-effector biopsy device,³ with an integrated US transducer and CNB gun focused on a remote-center-of-motion (RCM). Registration of the mechatronic guidance system to a machined, simulated PEM detector plate, and therefore its PEM image coordinate space, was performed using a landmark-based method, as described in the methods of Park et al.² Breast phantoms were constructed with agar-based tissue-mimicking materials to simulate the US propagation speed-of-sound in soft-tissue, and scattering agent was added to simulate breast parenchymal tissue. Agar-based targets (6 mm in diameter and height) dyed red were embedded

with no added scattering agent to appear hypoechoic to the background. These targets were positioned in known three-dimensional positions, to simulate PEM localized breast lesions and corresponding to virtual targets in the software module for guidance. Real-time targeting was performed in three spatial dimensions, in-plane (x- and y-axis) and cross-plane (z-axis) directions (Fig. 1A). When positioned and the mechatronic guidance system was locked, the in-plane US image was used for targeting and the needle targeting error (NTE) was quantified as the shortest distance between the post-fire needle centerline and target location (Fig. 1B).

Results: We performed a proof-of-concept phantom study to evaluate the proposed workflow for PEM-US-guided biopsy to simulated breast lesions. All simulated breast lesions (N=8) were successfully sampled using our guidance approach, as identified in the core sample. Real-time guidance to the target breast lesions resulted in a three-dimensional positioning error of 0.89 ± 0.38 mm (N=8) with a 0.72 ± 0.31 mm in-plane and 0.34 ± 0.47 mm cross-plane component errors, relative to the PEM image coordinate space. Needle insertion was performed and the mean NTE (SD) was 0.90 ± 0.52 mm (N=8) with an upper 95% confidence interval of 1.26 mm.

Conclusions: Our proposed PEM-US-guided biopsy approach using our mechatronic guidance system and custom visualization modules shows an accurate method for guidance, positioning, and needle targeting to simulated breast lesions. Future work will perform an extensive analysis on the spatial distribution of error and integrate our developed system with the Radialis PEM system toward PEM-US-guided biopsy.

[1] BB Koolen, et al. (2012) J. Oncol. 438647 [2] CK Park, et al. (2020) SPIE Med. Imaging. 11315 doi: 10.1117/12.2549731 [3] CK Park, et al. (2019) Med. Phys. 46(6)296.

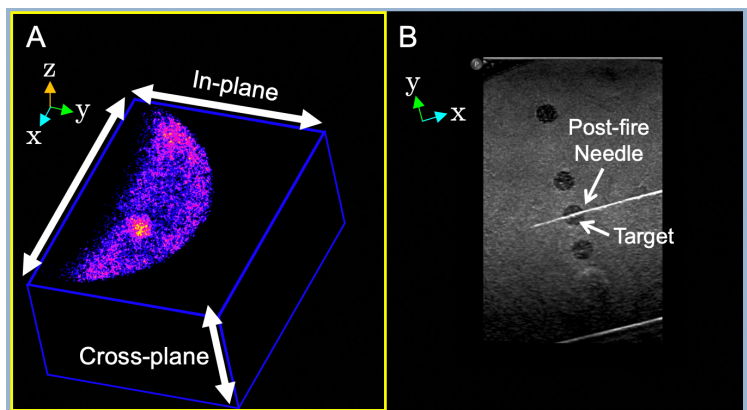


Figure 1: Adapted image of visualization module for image-guided breast biopsy. **A.** Simulated PEM phantom image (Radialis Medical, Thunder Bay, Ontario) in the PEM image coordinate space, illustrating in-plane and cross-plane directional components. **B.** In-plane US image for targeted needle biopsy (post-fire needle) of a simulated target breast lesion in an agar-based breast phantom.

Evaluating the feasibility of resting-state fMRI at low-field MR scanner by investigating the relationship between temporal signal to noise ratio and resting-state networks.

Arjama Halder^{1,2}, Demetrius Ribeiro de Paula³, WB Handler^{1,3}, Andrea Soddu³, BA Chronik^{1,2,3}

¹The xMR Labs, ²Medical Biophysics, ³Physics and Astronomy, Western University, Canada., ⁴Donders Institute, Radboud University, Netherlands

INTRODUCTION: Blood Oxygen Level Dependent (BOLD) functional magnetic resonance imaging (fMRI) studies have not been performed using low-field scanners due to low magnetic susceptibility contrast and inadequate gradient performance. However, with recent introduction of relatively easy to site and comparatively cheap low-field scanners equipped with high performance gradient coils, it is possible to re-evaluate the feasibility of low-field fMRI (1). This re-evaluation will be performed using a head-only 0.5T scanner which is equipped with an in-house built high performance gradient coil. The operation field strength of a scanner will have an impact on the signal to noise ratio (SNR) of the BOLD signal which will in turn determine the networks or regions that are activated during task-based or resting-state studies. Therefore, in this abstract we will investigate the relationship between the signal to noise ratio and the regions detected using a range of artificially created noisy resting-state functional data aimed to mimic behaviour seen at lower field strengths. **METHOD:** For the purpose of this abstract resting-state data were collected using a 3T scanner involving 4 healthy volunteers. SNR was determined independently for each voxel over the time course of the data and not based on the SNR from a single static image (2). The previously collected data was manipulated, by introducing additional Rician noise of varying scale parameters to the time series signal for each voxel. Both collected and modified data sets were passed on to GraphICA, a functional connectivity analysis platform developed by Brainet – Brain Imaging Solutions Inc., which performs independent component analysis (ICA) based on dual regression implemented in FSL. GraphICA uses a gradient-weighted Markov Random Field (gwMRF) parcellation technique (3) along with a mixture model approach (4) for thresholding. In GraphICA the resting-state networks from the original and modified range of data for each volunteer were compared statistically to a normative database of 570 cases with 206 females and 364 males. **RESULTS:** Figure 1. shows the number of found and missing regions identified within the Default Mode Network (DMN) over a range of tSNR respectively. Figure 2. shows the positive relationship between the correlation coefficient and tSNR for Auditory and DMN respectively. Figure 3. shows the Visual Occipital region for a specific healthy volunteer with 3a. referring to originally collected data with the average tSNR of 74.2 and 3b. referring to modified data with the average tSNR of 17.8.

DISCUSSION: Figure 1a. suggests an increase in the number of found regions within the DMN for each subject as tSNR increases. Figure 1b. suggests a decrease in the number of missing regions within the DMN for each subject as tSNR increases. The results from both these figures indicate that as field strength of the scanner is decreased, the number of found regions within a specific network decreases whereas, the number of missing regions within a specific network increases. Similar behaviours were observed for all other resting-state networks. Figure 3a. and 3b. show the visual occipital region detected from 2 different datasets implying that behaviour observed is mimicking the results from 2 different operation field strength. **CONCLUSION:** The overall behaviour shows that there is a positive correlation between the tSNR and regions detected. The tSNR on the other hand is dependent on the operational field strength of the scanner. This analysis will provide the lower limit on tSNR at which the network or regions of interest are still detectable, which will be used in future experimental studies with the 0.5T scanner. **REFERENCES:** 1. Wang, Y.et al. (2020). Transition-Band SSFP and EPI Functional MRI on a High-Performance 0.55 T Scanner. *ISMRM*. 2. Parrish, T. B. et al. (2000). Impact of Signal-to-Noise on Functional MRI. *MRM*. 3. Schaefer, A. at al. (2018). Local-Global Parcellation of the Human Cerebral Cortex from Intrinsic Functional Connectivity MRI. *Cerebral Cortex*. 4. Bielczyk, N. Z. et al. (2018). Thresholding functional connectomes by means of mixture modeling. *NeuroImage*.

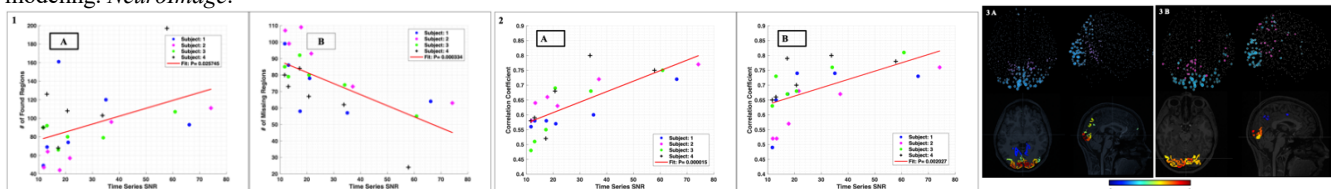


Fig 1. Shows the number of (a) found regions (b) missing regions within the DMN region for each subject as a function tSNR. **Fig 2.** Shows the correlation coefficient as a function of tSNR for (a) Auditory region and (b) DMN region for each subject. **Fig 3.** Shows the Visual Occipital regions' normalized Z values for a specific subject for (a) mean tSNR = 74.2 and (b) mean tSNR = 17.8 which causes the similarity index calculated between the normative database and volunteer's data to drop from 73% in (a) to 62% in (b) within a 95% confidence interval.

Theoretical Comparison of the Detective Quantum Efficiency of Halide Lead Perovskite, Cesium Iodide and Selenium X-Ray Imaging Detectors

Michael Belli and Jesse Tanguay
Ryerson University – Department of Physics

INTRODUCTION: Halide lead perovskites have been proposed for direct-conversion x-ray imaging because of their high stopping power, high charge mobility and high bulk resistivity. We modeled the detective quantum efficiency (DQE) of methylammonium lead iodide (MAPbI₃) detectors and compared with that of amorphous selenium (a-Se) and columnar cesium iodide (CsI) detectors for chest radiography, fluoroscopy and breast imaging.

METHODS: We used cascaded systems analysis (CSA), implemented in MATLAB, to model the DQE. Our model included detector quantum efficiency, x-ray fluorescence, fluorescence reabsorption, charge conversion, collection of secondary quanta (i.e. charges or optical photons), charge diffusion in MAPbI₃, optical blur in CsI, noise aliasing, and electronic noise; the electronic noise for each detector was calculated from published data. We validated our CSA models for CsI and a-Se by comparing with the experimental results of Zhao *et al.* (*Med. Phys.* vol. 31, pp. 2594-2605, 2004) and Zhao *et al.* (*Med. Phys.* vol. 24, pp. 1819-1833, 1997), respectively. Since MAPbI₃ is a novel technology and there are limited empirical studies of its imaging properties, we compared our model normalized noise power spectra (NNPS) of photoelectric interactions in Pb with the Monte Carlo results of Hajdok *et al.* (*Med. Phys.* vol. 33, pp. 3601-3620, 2006) The DQE of MAPbI₃ was compared to CsI for RQA-5, RQA-7 and RQA-9 x-ray spectra for 200 μm detector elements and a converter thickness of 500 μm . For RQA-5 and RQA-7 x-ray spectra, we considered fluoroscopic exposure ranges (0.1 - 10 μR); for the RQA-9 x-ray spectrum we considered chest radiography exposure ranges (i.e. 0.04 - 3 mR). MAPbI₃ was also compared to a-Se for a 28 kV tungsten spectrum filtered by 2 mm of aluminum, mammographic exposure ranges (0.6 – 250 mR), 75 μm elements and a 300- μm -thick converter.

RESULTS: For matched quantum efficiency, the theoretical DQE of MAPbI₃ for RQA-5 and RQA-7 spectra was greater than or equal to that of CsI for detector exposures greater than 1 μR , but was substantially worse than that of CsI at lower exposures (e.g. $\sim 40\%$ of that of CsI at 0.1 μR) due to the presence of electronic noise. For the RQA-9 spectrum, the theoretical DQE of MAPbI₃ was $\sim 25\%$ greater than that of CsI for chest radiography exposures (i.e. 0.04 – 3 mR). For mammography, the theoretical DQE of MAPbI₃ was $\sim 5\%$ greater than that of a-Se across all spatial frequencies for exposures ranging from 0.6 mR to 250 mR.

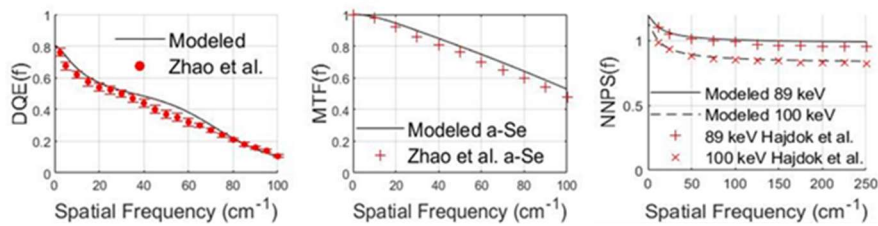


Figure 1. Comparison of our modeled DQE, MTF and NNPS to published data. **Left:** comparison our model DQE with the experimental DQE presented by Zhao *et al.* **Centre:** comparison of our MTF of a-Se with experimental work of Zhao *et al.* **Right:** comparison of our model photoelectric NNPS of lead with Monte Carlo NNPS presented by Hajdok *et al.*

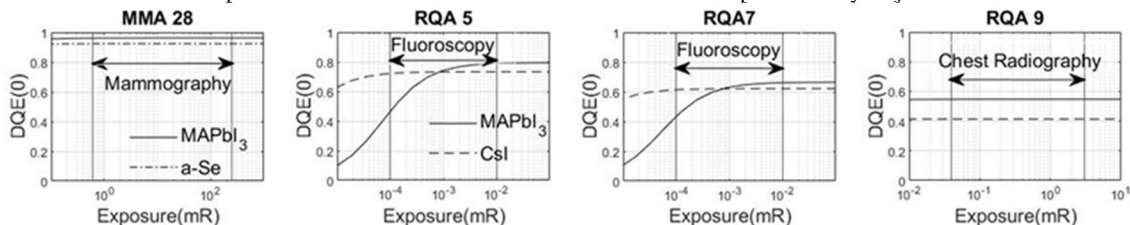


Figure 2. Modeled zero-frequency DQE vs. exposure for a-Se, CsI and MAPbI₃ for mammography, RQA-5, RQA-7 and RQA-9 spectra.

CONCLUSIONS: Our theoretical analysis suggests that halide lead perovskite x-ray detectors may provide dose efficiency that is superior to that of CsI-based x-ray detectors in chest radiography applications, but likely will not enable dose reduction in fluoroscopy. This latter effect is due to electronic noise, which remains relatively high in prototype halide lead perovskite detectors. Future work will focus on experimental validation of the DQE models presented here.

B₁⁺ Field Homogeneity and Signal Generation of a Koch Fractal RF Coil for Sodium MRI

Cameron Nowikow¹, Paul Polak¹, Norman Konyer², Natalia Nikolova³, and Michael D. Noseworthy^{1,2,3}

¹ School of Biomedical Engineering, McMaster University, Hamilton; ² Imaging Research Centre, St.

Joseph's Healthcare, Hamilton; ³ Electrical and Computer Engineering, McMaster University, Hamilton

Introduction

The biggest obstacle with ²³Na-MRI is the low signal-to-noise ratio (SNR) due to low inherent *in vivo* concentration, low gyromagnetic ratio and very short T₂'s.¹ These characteristics necessitate prolonged scans with low resolution. Improvements in pulse sequences and switching to higher magnetic field strengths are routes typically used to deal with these problems. However, very little has been done to assess the RF coil designs being used. To maximize image quality the B₁⁺ field needs to be as homogeneous as possible. Fractal antennas are a standard design in telecommunication systems for their compact nature^{2,3} and we hypothesize that there may also be some benefit in using a fractal geometry for MRI RF coils to produce a more homogeneous B₁⁺ field due to their configuration in space. Previous simulations and experiments pointed to a Koch fractal as a potential candidate.⁴⁻⁶ Thus, we explored ²³Na-MRI B₁⁺ field characteristics of a Koch snowflake fractal geometry RF surface coil. We compared the fractal design to that of a standard ²³Na surface coil of the same diameter.

Methods

Two different surface coils (Koch fractal and circular) were fabricated as copper etching on an FR4 substrate (**Figure 1**). Both coils were tuned and matched to 33.8MHz/50Ω, the Larmor frequency of sodium at 3T. MRI experiments were run for each coil using a GE 3T MR750 MRI and a saline phantom (0.9% w/v H₂O). The following sequences were acquired: (i) 2D B₁⁺ mapping through 4 slices (BSS method, TR=86ms, TE=25ms, 15cm FOV, 90° flip, 2kHz BS pulse, 120 NEX); and (ii) 3D radial sequence to assess SNR and image uniformity (7333 spokes, TR=23ms, 90° flip, 0.5ms hard pulse, 2 NEX, 15cm FOV).

Results

Mean field strength and standard deviation (in μT) from B₁⁺ maps for both coils are shown in **Table 1**. The

FIGURE 1

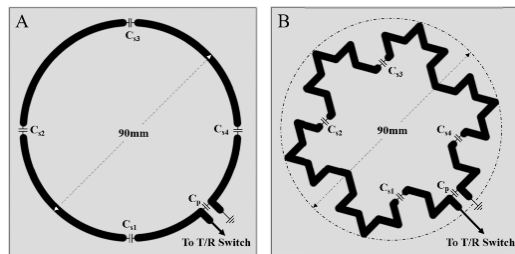


TABLE 1 B₁⁺ Field Homogeneities (mean ± std, in μT)

	Sagittal	Coronal (1)	Coronal (2)	Coronal (3)
Circular	26.91±10.99	33.37±7.15	25.96±9.30	29.73±12.19
Fractal	31.37±11.80	31.82±7.61	25.64±9.72	30.00±13.18

TABLE 2 SNR over 5 Signal Regions

Coil / ROI Radius (mm)	9.0	12.5	19.0	25.0	44.0
Circular	17.39	19.31	21.90	17.66	15.09
Fractal	15.46	17.87	21.45	15.30	11.43

coronal slices are ordered in terms of depth where (1) is the closest to the coil and (3) is the furthest from the coil. It should be noted that the final coronal slice was virtually just noise which is why it appears the field strength increased from (2) to (3) even though it is further away. It is noted that the circular coil consistently has the lower standard deviation which correlates to a more homogeneous field. **Table 2** shows the calculated SNR values for five signal ROIs selected using the 3D radial images. The first three ROIs are spherical in shape, and the last two are cylindrical in shape. The circular coil consistently had a higher SNR than the fractal coil.

Conclusions

It appears that a circular surface coil produces a more homogenous B₁⁺ field than that of a Koch snowflake

fractal surface coil. The higher SNR of the circular coil aligns with expectations that the coil with the more homogeneous B₁⁺ field would produce higher SNR images. While this result is opposite to our hypothesis, there are still potential benefits to fractal coils that need to be explored such as spectral field homogeneity over a wider bandwidth, which would be beneficial for imaging other nuclei with wide bandwidths such as ¹³C.

References

1. Madelin G, Regatte RR. Biomedical applications of sodium MRI in vivo: Biomedical Applications of Sodium MRI. *J Magn Reson Imaging*. 2013;38(3):511-529.
2. Gianvittorio JP, Rahmat-Samii Y. Fractal Antennas: A Novel Antenna Miniaturization Technique, and Applications. *IEEE Antenna's and Propagation Magazine*. 2002;44(1):20-36. doi:10.1109/74.997888
3. Cohen N. Fractal antenna applications in wireless telecommunications. In: *Professional Program Proceedings. Electronic Industries Forum of New England*. IEEE; 1997:43-49.
4. Ha S, Nalcioglu O, Roek WW, inventors; Fractal RF Coils for Magnetic Resonance Imaging. US Patent US 2015/0048828 A1. February 19, 2015.
5. Dona Lemus OM, Konyer NB, Noseworthy MD. Micro-strip Surface Coils Using Fractal Geometry for ¹²⁹Xe Lung Imaging Applications. In: *Proceedings of the Joint Annual Meeting of ISMRM-ESMRMB*, Paris, FR, 2018. Abstract No. 1713.
6. Nowikow CE, Konyer NB, Yazdanbakhsh P, Noseworthy MD. Koch Snowflake Fractal RF Surface Coils to Improve ²³Na-Magnetic Resonance Imaging at 3T. In: *Proceedings of the 36th Annual Scientific Meeting of ESMRMB*, Rotterdam, NL, 2019. Abstract No. A-1449.

Impact of Volumetric 4D-CT Motion Artifact Reduction on Ventilation Imaging

Heather M Young^{1,2,3}, Ting-Yim Lee^{2,3} and Stewart Gaede^{1,2}

¹Department of Physics and Engineering, London Regional Cancer Program, ²Department of Medical Biophysics, ³Robarts Research Institute, University of Western Ontario

Introduction: For patients with non-small cell lung cancer who receive radiation therapy, the dose delivered to healthy tissue surrounding the tumour is related to increased risk of radiation-induced toxicities. Clinical trials are currently underway to study the effects of using 4-dimensional computed tomography (4D-CT) ventilation imaging to identify high-functioning regions of the lung and minimize dose to these regions in particular. However, studies have shown that motion artifacts commonly found in 4D-CT images cause artifacts in the resulting ventilation images. In addition, previous work has shown that volumetric 4D-CT (v4D-CT) imaging reduces the presence of motion artifacts. The purpose of this study is to compare ventilation maps generated from clinical 4D-CT and volumetric 4D-CT (v4D-CT).

Methods: Four patients with non-small cell lung cancer received a clinical 4D-CT scan on a Philips Brilliance Big Bore CT scanner using the following parameters: helical mode, 0.5s/revolution, 120kV, 45-60mA, and 24mm axial field-of-view (aFOV). Patients were also imaged using a research protocol on a GE Revolution volumetric CT scanner using the following parameters: cine mode, 0.28s/revolution, 100kV, 100mA, and 160mm aFOV. The end-inhale and end-exhale phases were selected from each image set, and the lung volume was semi-automatically segmented in 3DSlicer to aid in registration. The images were non-rigidly registered in Elastix using a b-splines transformation and Mattes mutual information. Ventilation was calculated using an existing density-based method, and registration-based method. Finally, the v4D-CT and conventional 4D-CT ventilation maps were registered using Elastix and compared visually. The co-registered maps were then down-sampled and compared voxel-wise using Pearson correlation.

Results: Motion artifacts were visible in all clinical 4D-CT images, while none were visible in the v4D-CT images. For all patients, ventilation measured by clinical 4D-CT differed from v4D-CT in regions where motion artifacts were present. For two patients, motion artifacts led to mis-registration of the inhale and exhale phases, which resulted in visually obvious artifacts in the final ventilation image. For the entire ventilation image, voxel-wise analysis showed weak to moderate correlation between the v4D-CT and clinical 4D-CT images for each patient ($r=0.24-0.46$, $p<0.05$ for density-based ventilation, $r=0.23-0.43$, $p<0.05$ for registration-based ventilation).

Conclusions: Volumetric 4D-CT may eliminate motion artifacts which are often present in clinical 4D-CT and lead to invalid ventilation values in the affected region of the image. The accuracy of ventilation imaging may be increased with v4D-CT for prediction or assessment of radiation response, particularly when artifacts are near the treatment site.

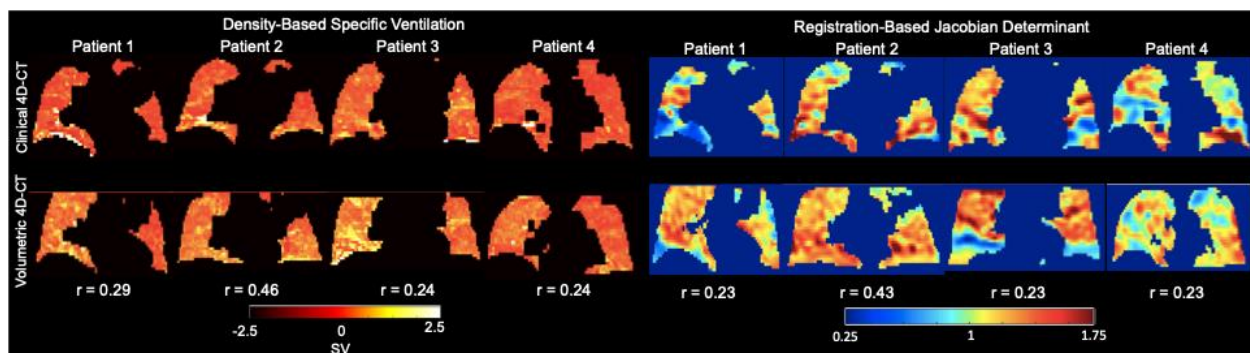


Figure 1. Density-based (left) and registration-based (right) ventilation maps generated from clinical 4D-CT (top row) and volumetric 4D-CT (bottom row) for 4 patients with non-small cell lung cancer. For each patient, the clinical 4D-CT and volumetric 4D-CT ventilation maps showed weak to moderate voxel-wise correlation.

TITAN: A Hyperion™ Imaging System Data Analysis Software

Sindhura Thirumal, Amoon Jamzad, Tiziana Cotechini, Charles Hindmarch, Charles Graham, Parvin Mousavi, Rob Siemens
Queen's University

Introduction: The Hyperion™ Imaging System is an imaging mass cytometry (IMC) technology that improves upon immunohistochemistry by quantifying up to 40 discrete signals with the use of metal-tagged antibodies rather than fluorophores [1]. The current methods of analysis for these data are provided by the manufacturer and are fairly preliminary, requiring the use of multiple independent software. We have developed a single platform to solve this issue via the open source 3D Slicer environment [2]. We present our software *TITAN* and demonstrate the ease of use, accuracy, and speed in comparison to the current software.

Method: Our software *TITAN* performs all analyses and visualization functions for the images generated by Hyperion without the need to change environments. *TITAN* allows the user to visualize up to seven channels at a time and performs auto-adjustments of the image, an improvement on the current software. Next, the nucleus of each cell can be located and segmented into individual cells, creating a cell mask. Unlike the current software, *TITAN* outputs the number of cells in each cell mask; crucial information for further analyses and interpretation. Finally, the resulting cell mask is used for various statistical analyses including heat maps and dimensionality

reduction plots for visualization of high-dimensional data (Fig 1). To assess the accuracy of the cell masks created by *TITAN*, we used a published breast cancer dataset that includes 749 nucleus channel images along with verified cell masks [3]. Since the masks were created using human annotation, we use them as a gold standard to compare both our *TITAN*-generated masks as well as masks generated by the current software. The metrics include Dice scores of the generated masks and the count of cells identified.

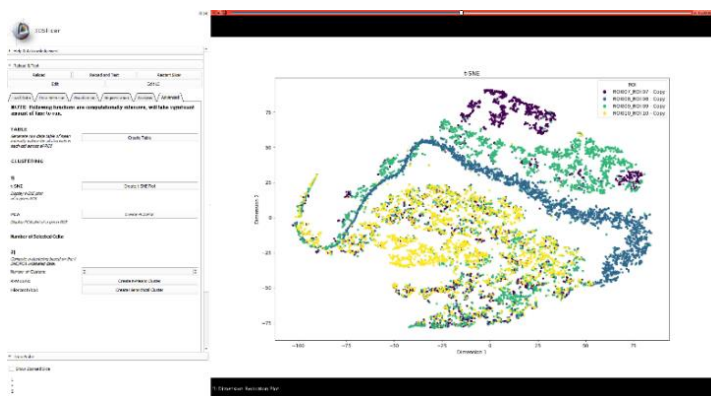


Fig 1. User interface of the Advanced Analysis tab of *TITAN*. Also shown are the tabs for Data Selection, Visualization, Segmentation, and Analysis. Plotted is a t-SNE of all data across multiple samples, where each colour represents a given sample.

Results: *TITAN*'s visualization functions work in a similar manner to the current software, though there is a distinct difference in speed. We observed that the sets of masks created from *TITAN* compared to the current software are similar in accuracy when compared to the gold standard set of cell masks. *TITAN* proves more accurate in the number of cells identified and both software result in a Dice score of 0.78 when compared to the gold standard. In addition, *TITAN* takes about 2 seconds to create masks for one sample while the current software takes 32 seconds for that same sample. Thus, *TITAN*'s segmentation is as accurate as the current software as well as more efficient. The analysis plots in *TITAN* mimic the ones in the current software, but with some added functionalities, including exportation of data and more user-friendly displays of the plots.

Conclusion: *TITAN* is an improvement on the current data analysis pipeline, which requires the use of various software tools to perform individual tasks and to exchange data results from one software to the next. It is able to perform all functions on mass cytometry data within one environment. As well, the platform is available via an open source environment, which will allow for deployment, collaboration and frequent updates to the software. We have shown that *TITAN* is comparable to the current methods and improves on it in various ways.

[1] Chang, Q., Ornatsky, O. I., Siddiqui, I., Loboda, A., Baranov, V. I., & Hedley, D. W. (2017). Imaging mass cytometry. *Cytometry part A*, 91(2), 160-169.

[2] Fedorov A., Beichel R., Kalpathy-Cramer J., Finet J., Fillion-Robin J-C., Pujol S., Bauer C., Jennings D., Fennessy F., Sonka M., Buatti J., Aylward S.R., Miller J.V., Pieper S., Kikinis R. 3D Slicer as an Image Computing Platform for the Quantitative Imaging Network. *Magnetic Resonance Imaging*. 2012 Nov;30(9):1323-41. PMID: 22770690.

[3] Jackson HW, Fischer JR, Zanotelli VRT, Ali HR, Mechera R, Soysal SD, Moch H, Muenst S, Varga Z, Weber WP, Bodenmiller B. The single-cell pathology landscape of breast cancer. *Nature*. 2020 Feb;578(7796):615-620. doi: 10.1038/s41586-019-1876-x. Epub 2020 Jan 20. PMID: 31959985.

Evaluating Back-to-Back and Day-to-Day Reproducibility of Cortical GABA Measurements with MEGA-PRESS Using 32-channel Head Coil

Sonja Elsaid^{1,2}, Peter Truong¹, Napapon Sailasuta¹, Bernard Le Foll^{1,2}, and Sofia Chavez^{1,2}

¹Brain Health Imaging Centre, Centre for Addiction and Mental Health (CAMH), Toronto, ON, Canada

²Institute of Medical Science, Faculty of Medicine, University of Toronto, Toronto, ON, Canada

Introduction: Imbalances in the inhibitory neurotransmitter γ -aminobutyric acid (GABA) and glutamate plus glutamine (Glx) cortical levels have been implicated in psychiatric disorders¹. The challenge with quantifying GABA is that concentrations are low, in the order of 1mM¹, and the peaks overlap with other metabolites in the spectrum^{1,2}. To overcome these technical challenges, the Meshcher-Garwood Point Resolved Spectroscopy (MEGA-PRESS)³ sequence, an edited proton magnetic resonance spectroscopy (¹H MRS) method, can be used. Currently, our 8-channel head coil protocol requires a scan time of 13 min per voxel, which is too long (>10 min) for patients with psychiatric symptoms.⁴ For this reason, we examine the 32-channel head coil (32-C HC), with a higher signal-to-noise ratio attainable in cortical brain regions, to see if we can obtain good back-to-back (B2B) and day-to-day (D2D), test-retest reproducibility of GABA and Glx in the dorsomedial prefrontal cortex /anterior cingulate cortex (dmPFC/ACC) using a MEGA-PRESS scan time of only 5:12 min.

Methods: Seventeen healthy volunteers (HV) (24.8±3.6 yrs. 10 males, age range 20 – 32 yrs) were scanned on a 3T, GE MR 750 scanner (General Electric Healthcare) with a 32-C HC (Nova Medical) as per institutional REB. Subjects were each scanned four times: two scans were conducted B2B in a single session, and another identical session was performed 1 to 3 days later at a similar time of day. The averages between day 1 and 2 B2B sessions were used in the D2D comparison. MEGA-PRESS parameters were: TE/TR = 68 ms/1500 ms, 192 averages, voxel size=4 cm (anterior-posterior) x 2 cm right-left x 3 cm superior-inferior = 24 cm³ in the dmPFC/ACC. From the difference spectra, GABA and Glx values were fitted and quantified using XsOs-NMR⁵. Gannet 3.0⁶ and SPM12 (www.fil.ion.ucl.ac.uk/spm) were used for voxel-to-T₁-weighted image registration. GABA and Glx values are reported in institutional units (I.U.) where the unsuppressed water signal is used as internal water concentration. The results were corrected for water relaxation and density in the tissue compartments⁷ using the fractions of cerebrospinal fluid/gray matter/white matter in the voxel resulting from tissue segmentation with FSL (FMRIB Software Library). The percentage of voxel overlaps for D2D was also determined with FSL. The reproducibility was assessed using Pearson's correlation coefficient *r*, its *p*-value, Intraclass correlation coefficient (ICC), and the coefficient of variation in percentage (CV%).

Results:

Neurotran.	B2B Day 1 Comparison (<i>r</i> / <i>p</i> -value/ICC/CV%)	B2B Day 2 Comparison (<i>r</i> / <i>p</i> -value/ICC/CV%)	D2D Comparison (<i>r</i> / <i>p</i> -value/ICC/CV%)
GABA	0.69/<0.01/0.81/6.23	0.58/<0.05/0.71/6.12	0.71/<0.001/0.83/5.69
Glx	0.77/<0.001/0.87/4.20	0.69/<0.001/0.81/8.08	0.83/<0.001/0.91/4.63

Voxel overlaps (79% - 95%) did not affect D2D reproducibility. Our results were comparable to two other studies that used longer scan times (20 min./388 ave/ CV= 5.3%⁸, and 13 min./218 ave./CV = 6 – 14%⁹).

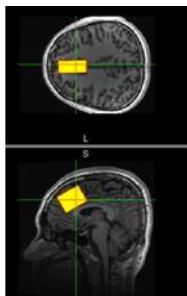


Fig. 1 Voxel Placement

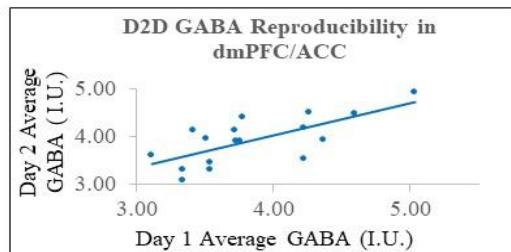


Fig. 2 Pearson's Correlation Plot for D2D GABA

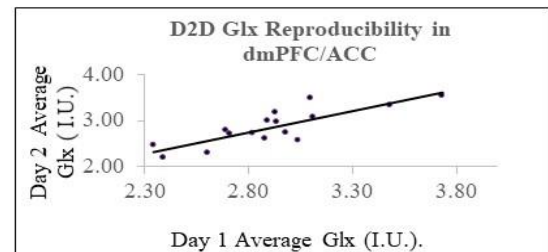


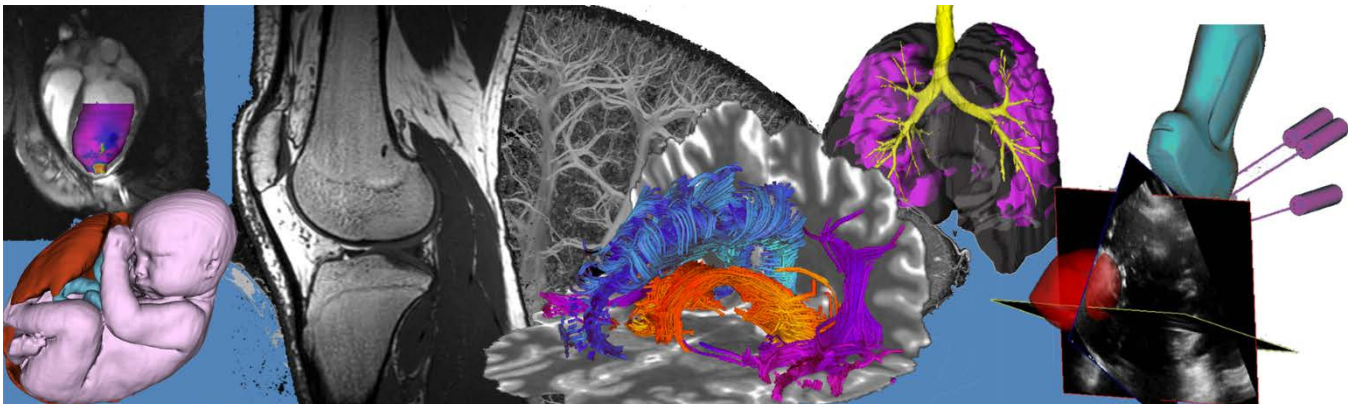
Fig. 3 Pearson's Correlation Plot for D2D Glx

Conclusion: The 32-C HC with 192 averages in the MEGA-PRESS provides a reliable tool for measuring GABA and Glx in the dmPFC/ACC with a scan time of only 5:12 min.

References: 1) Sanacora G et al. *Arch Gen Psych.* 2004.; 2) Li CT et al. *Front Psych.* 2018 3) Mescher M et al. *NMR Biomed.* 1998.4) Mullins PG et al., *NeuroImage* 2014 5) Shungu DC et al. *NMR Biomed.* 2016. 6) Edden RAE et al. *JMRI* 2014; 7) Gasparovic C et al. *MR in Med.* 2006 8) Geramita M et al. *NMR Biomed.* 2011 9) Brix MK et al. *JMRI.* 2017.

Pitch Presentation Abstracts

Session 6: Machine Learning for Cancer Applications



The Impact of the Variation of CT Scanner on the Prediction of Human Papillomavirus (HPV) Association of Oropharyngeal Cancer (OPC) using Radiomic Models

Reza Reiazi^{1,2,3}, Colin Arrowsmith¹, Mattea Welch^{1,2,3}, Farnoosh Abbas-Aghababazadeh¹, Christopher Eles¹, Aria Rezaie¹, Andrew J. Hope^{1,3}, Scott V. Bratman^{1,2,3}, Benjamin Haibe-Kains^{1,2,4,5,6}

1-Radiation Medicine Program, Princess Margaret Cancer Centre, University Health Network, 2-Department of Medical Biophysics, University of Toronto, 3-Department of Radiation Oncology, University of Toronto, 4-Ontario Institute for Cancer Research, 5-Department of Computer Science, University of Toronto, 6-Vector Institute

INTRODUCTION. Radiomics involves the use of high-dimensional quantitative imaging features for predictive purposes¹. However, studies showed that these radiomic features are sensitive to the variability of imaging parameters (e.g., scanner model). One of the major challenges in radiomics lies in improving the robustness of quantitative features against the variation in the imaging dataset in multi-center studies². In this study, we assessed the impact of scanner choice on the computed tomography (CT)-derived radiomic features to predict association of oropharyngeal cancer (OPC) with human papillomavirus (HPV).

METHOD. A total of 1,294 OPC patients with known HPV status were retrospectively included in this study. In this patient cohort, CT images were acquired with two different scanner types. HPV status was positive in 824 patients (641 Toshiba and 183 GE) and negative in 470 patients (385 Toshiba and 85 GE). We extract a total of 1,874 IBSI (International Biomarker Standard Initiation) compliant radiomic features from the primary gross tumor volume (pGTV) from each patient. Feature selection has been done by Maximum Relevance Minimum Redundancy Ensemble⁴ (mRMRe)³ technique. The dataset was subsequently stratified by CT scanner type (Toshiba scanner, GE scanner, and Mix) and splitted into train (adjusted for class imbalance) and test sets with the proportion of 75/25. Next, a random forest classifier was trained on the following configurations: (1) Toshiba-Toshiba, (2) GE-GE, (3) Toshiba-GE, (4) GE-Toshiba, (5) Mix-Mix, (6) Toshiba-Mix, (7) GE-Mix, (8) Mix-Toshiba and (9) Mix-GE.

RESULT. The highest and lowest mean AUC (area under the curve) values were 0.79 (p-value<0.001) and 0.70 (p-value<0.001) and obtained with Toshiba-Mix and Toshiba-GE respectively (Figure 1). For models trained on one scanner type, the highest and lowest result obtained when they were tested on Mix sample (i.e GE-Mix [0.75, p-value<0.001], Toshiba-Mix [0.79, p-value<0.001]) and other scanner types (i.e GE-Toshiba [0.73, p-value < 0.001], Toshiba-GE [0.70, p-value < 0.001]) respectively. We identified that there is bias in the results in favor of one scanner type (Toshiba). Models either trained or tested on the Toshiba scanner resulted in higher predictive value compared to other scanners in all the same configurations.

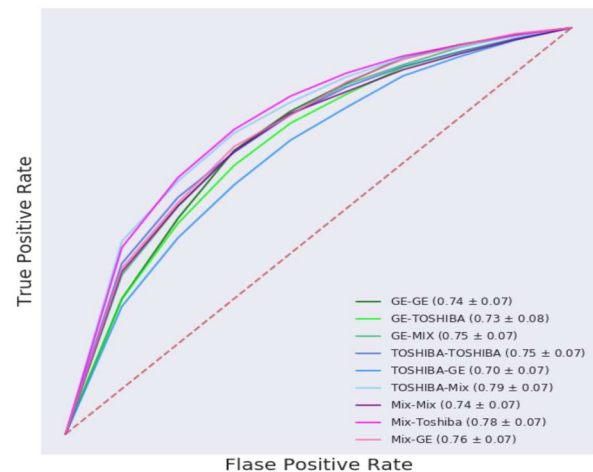


Figure 1: Receiver Operating Characteristic (ROC) curve of different configurations. The average AUC values are shown inside parentheses.

CONCLUSION. In this study, scanner type affects the prediction accuracy of the HPV status using hand-engineered radiomics features. The optimal prediction accuracy was achieved when the training set included only one specific type of scanner (i.e. Toshiba) which reflects a bias in radiomic features towards the scanner type. This result demonstrated the importance of imaging parameters, such as imaging scanners, for training radiomic-based classifiers. Future directions of this study are to evaluate how this finding will translate into clinical applications of radiomic models and potential solutions such as feature harmonization⁴ to remove this scanner dependency.

REFERENCES. [1] H.J.W.L. Aerts, Nat. Commun. 5, 4006 (2014), [2] D. Mackin, Invest. Radiol. 50(11), 757–765 (2015), [3] N. De Jay, Bioinformatics 29(18), 2365–2368 (2013), [4] R. Da-Ano, Sci. Rep. 10(1), 10248 (2020)

Effects of Feature Type and Selection on Machine Learning Classifier Accuracy for Predicting Brain Metastasis Response to Stereotactic Radiosurgery

D. DeVries^{1,2}, F. Lagerwaard³, J. Zindler^{4,5}, T. Yeung⁶, G. Rodrigues^{7,8}, G. Hajdok^{1,8}, A. Ward^{1,2}

¹Department of Medical Biophysics, Western University, London, Ontario; ²Gerald C. Baines Centre, London Regional Cancer Program, London, Ontario; ³Department of Radiation Oncology, Amsterdam UMC, VUMC Location, Amsterdam, The Netherlands; ⁴Department of Radiation Oncology, Haaglanden Medical Centre, Den Haag, The Netherlands; ⁵Holland Proton Therapy Centre, Delft, The Netherlands; ⁶Reflexion Medical, Hayward, California; ⁷Department of Oncology, Western University, London, Ontario; ⁸Department of Radiation Oncology, London Regional Cancer Program, London, Ontario

Introduction

Many types of cancers are known to spread, or metastasize, to the brain to form lesions called brain metastases (BMs). An established treatment for BMs is stereotactic radiosurgery (SRS). SRS delivers high doses of radiation in 1 to 3 sessions that are highly conformal to the BMs. To ensure accurate treatment, pre-treatment T1-weighted contrast-enhanced magnetic resonance imaging (MRI) is used for targeting. There is a need for tools to support clinician decision-making on how to prescribe SRS and optimize treatment planning. One such tool could be a machine learning classifier that predicts SRS treatment response for a BM, given pre-treatment clinical and MRI features. Previous research has shown links between BM MRI appearance and treatment outcomes [1], suggesting that such a classifier could be feasible. This study seeks to investigate the effect of the type of features and feature selection process on classifier accuracy when predicting SRS outcomes for BMs.

Methods

The study population consisted of 91 patients treated with SRS at Amsterdam UMC. Across the patients, 110 BMs were binarily classified for progression after treatment, according to an established protocol [1]. For each BM, 1281 features were gathered from three sets. Set F_C consisted of 11 clinical features, including data on the patient, primary cancer, and SRS parameters. Set F_{ROI} had 635 radiomic features that were extracted from the normalized pre-treatment MRI for the clinician defined BM region of interest (ROI). Set F_{EXP} had the same radiomic features extracted from a 5mm expansion around the BM ROI to capture possible features from BM mass effect or infiltrating disease. A leave-one-patient-out cross validation design was used with a support-vector machine classifier. Up to 10 features were selected using one of two feature selection algorithms: feature correlation filtering followed by forward feature selection (FFS) or minimum redundancy maximum relevance (MRMR) feature ranking [2]. For each algorithm, the set of features to select from was one of four combinations: F_C , F_{ROI} , $\{F_C, F_{ROI}\}$, and $\{F_C, F_{ROI}, F_{EXP}\}$ (having 11, 635, 646, and 1281 features, respectively). It was also investigated what the added benefit of MRI radiomic features would be to a set of selected optimal clinical features. For FFS, this was done by starting the feature selection for $\{F_C, F_{ROI}\}$ or $\{F_C, F_{ROI}, F_{EXP}\}$ from the optimal feature set from using FFS on F_C alone. For MRMR feature ranking, a similar process was done by ranking all the features in $\{F_C, F_{ROI}\}$ or $\{F_C, F_{ROI}, F_{EXP}\}$, and then setting the top-ranking features as the optimal feature set from the MRMR ranking on only F_C . These scenarios can be viewed as having two steps, with “Step 1” being the optimal selection of features from F_C , followed by the selection of additional features as “Step 2”.

Results

Shown to the right are the area under the receiver operating characteristic curve (AUC) values for each experiment at the optimal number of features. It was observed in the experiments with a single step of feature selection, that BM ROI features were preferred over BM ROI expansion features, while clinical features were ignored by FFS. The highest AUC achieved using only selected clinical features was 0.69, with a false positive rate (FPR) of 27% and a false negative rate (FNR) of 41%, while the highest AUC using only selected MRI radiomic features was 0.79 (FPR: 23%, FNR: 26%). The highest overall AUC was 0.82 (FPR: 23%, FNR: 17%), which was achieved by a combination of features from F_C , F_{ROI} , and F_{EXP} selected by the two-step MRMR feature selection process.

Conclusions

The results of this study reveal that between the FFS and MRMR feature selection algorithms, the MRMR algorithm offers higher AUCs for the two-step feature selection method, while similar performance was seen for single step feature selection. It was also found that clinical and MRI radiomic features independently offer predictive power of SRS treatment outcomes, with the radiomic features providing higher accuracy. A combination of clinical and MRI radiomic features produced the highest AUC, but interestingly this AUC was only achieved when the MRMR feature selection was constrained through the two-step process of first selecting clinical features. This suggests both the FFS and MRMR algorithms selected sub-optimal sets of features when unconstrained. Only the MRMR algorithm showed improvement when constrained, with the constrained FFS algorithm appearing to select a less optimal set of features compared to when it was unconstrained.

[1] Rodrigues, G., et al., *Oncologist*, 2013. [2] Ding, C., et al., *J. Bioinform. Comput. Biol.*, 2005.

Feature Set Combinations		AUC	
Step 1	Step 2	FFS	MRMR
F_C	-	0.69	0.67
F_{ROI}	-	0.79	0.77
$\{F_C, F_{ROI}\}$	-	0.79	0.79
$\{F_C, F_{ROI}, F_{EXP}\}$	-	0.79	0.79
F_C	$\{F_C, F_{ROI}\}$	0.74	0.78
F_C	$\{F_C, F_{ROI}, F_{EXP}\}$	0.74	0.82

Impact of Radiomic Biopsies on Feature Extraction in Positron Emission Tomography (PET) Imaging for Non-Small Cell Lung Cancer

Lauren M. Zelko¹, BSc, Sarah A. Mattonen^{1,2}, PhD

¹ Department of Medical Biophysics, ² Department of Oncology, Western University, London, ON, Canada

Introduction: Radiomics aims to extract quantitative information from medical images, which may provide information on disease prognosis and progression.¹ In patients with non-small cell lung cancer (NSCLC), 18-F-fluorodeoxyglucose (FDG) PET uptake in the bone marrow has been shown to provide prognostic information.² Mattonen et al. identified radiomic features in the bone marrow in an integrated machine learning model that are predictive of recurrence in patients with NSCLC.³ Typically, manual segmentations of the vertebral bodies are needed to calculate bone marrow radiomic features, but they can be time-consuming and variable. The use of “radiomic biopsies” to sample the full volume of interest would be useful, as they would require less time and wouldn’t require a complete and accurate segmentation. Therefore, our study aimed to investigate if radiomic biopsies can exhibit similar features to the manual segmentations and predict outcomes with similar accuracies.

Methods: We analyzed 134 patients from The Cancer Imaging Archive (TCIA) with NSCLC.⁴ MATLAB (Mathworks, Natick, MA) was used to manipulate original manual segmentations of the lumbar vertebrae (L3-L5) in order to simulate radiomic biopsies in the bone marrow. The original segmentations were eroded by 5mm, 7mm, and 9mm. The largest inscribed spheres were also created within the boundaries of the original segmentations as shown in Figure 1. The radiomic biopsies and original segmentations were processed through the MATLAB based Quantitative Image Feature Engine (QIFE), to extract first-order and second-order texture features. The intraclass correlation coefficients (ICC) were calculated for each feature to determine those that are most stable ($ICC > 0.8$) across different segmentations. To investigate the predictive ability of the radiomic biopsy texture features, we created a Cox model to predict recurrence and compared the results to a model with features from the original segmentations.³

Results: We extracted 156 features from each segmentation and these features were directly compared in each radiomic biopsy. A summary of the ICC results for each biopsy are found in Table 1. The 5mm erosion and the three inscribed spheres had 116 and 103 features respectively that were stable. Therefore, we focused our Cox regression model on these two regions due to their relative stability and potential utility in the clinic. Mattonen et. al. developed a Cox model which included stage and two bone marrow features as significant univariate predictors of recurrence (C-index = 0.78).³ Our 5mm Cox model had only one significant bone marrow feature (C-index = 0.78) and the three spheres model had none (C-index = 0.77).

Conclusions: When the volume of the radiomic biopsies decreased the number of features deemed stable also decreased. Our Cox model only defined one of same features from the original study as statistically significant in the prediction of recurrence. This indicates some instability in the extracted radiomic features, however overall performance of the model was not impacted. This suggest radiomic biopsies could potentially eliminate the need for complete and accurate manual segmentations, however further validation of this approach is needed. Similarly, automated methods to define the radiomic biopsies should also be investigated.

References:

1. Gillies, RJ et. al. Radiology 278:563–577 (2016)
2. Lee, JW et al. Clin Lung Cancer 18:198–206 (2017)
3. Mattonen, SA et al. Radiology 293:451–459 (2019)
4. Bakr, S et. al. Scientific Data, 5 (2018)

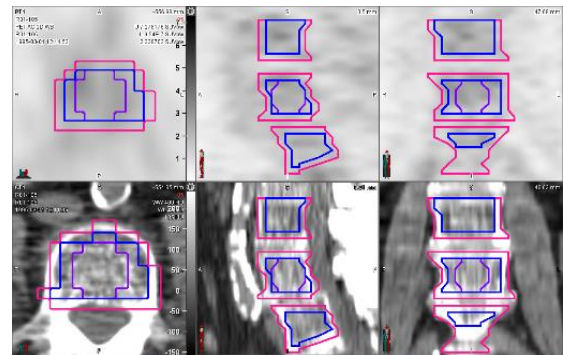


Figure 1: The original segmentation (pink), 5mm erosion (blue), and the largest inscribed sphere (violet). The top row is the PET image, and the second row is the CT images.

Table 1: Number of features that were deemed stable ($ICC > 0.8$)

Segmentation	All Features (n=156)	First Order Features (n=12)	Texture Features (n=144)
5mm Erosion	116	12	104
7mm Erosion	93	10	83
9mm Erosion	54	7	47
3 Spheres	103	9	94
2 Spheres	76	8	68
1 Sphere	37	5	32

Quantitative Imaging Derived Metrics for Prostate Cancer Therapy Induced Sarcopenia

Kelly Fullerton^{1,2}, Geoff Klein¹, Urban Emmenegger^{3,4}, Joel Finkelstein^{1,5}, Frank Lyons^{6,7}, Cari Whyne^{1,2,5}, Michael Hardisty^{1,2,5}

¹Physical Sciences Platform, Sunnybrook Research Institute ²Holland Bone & Joint Program, ³Biological Sciences Platform, Sunnybrook Research Institute, ⁴Odette Cancer Center, Sunnybrook Health Science Center, ⁵Department of Surgery, University of Toronto, ⁶Department of Orthopaedic Surgery, Mater University Hospital, Dublin, Ireland, ⁷School of Medicine, University College, Dublin, Ireland

INTRODUCTION: Highly prevalent in cancer patients, sarcopenia is a generalized and progressive loss of skeletal muscle mass, which is strongly correlated with surgical complications and mortality. Existing methods of quantifying sarcopenia involve labour intensive manual segmentation of 2D computed tomography (CT) slices or semi-automated methods prone to inaccuracy. The goal of this work is to develop a reliable tool for rapid, sensitive 3D quantification of sarcopenia, applying results to improve prostate cancer care.

METHODS: This pilot retrospective study proposes a deep learning algorithm, specifically a 3D U-Net convolutional neural network (CNN) for segmenting the psoas muscle between the L2/L3 and L4/L5 intervertebral discs in routine CTs. The dataset used to develop the algorithm was taken from 32 prostate cancer patients with initial and 1-year follow-up imaging ($n_{\text{training}}=26$, $n_{\text{validation}}=6$). Segmentation masks were created during an initial study using a semi-automated approach (atlas-based fiducial registration and deformation registration) with manual corrections to establish ground truth. Volumes were cropped to the area of interest and resampled to voxel sizes of $1.15 \times 1.15 \times 2.50 \text{ mm}^3$. They were also padded to $128 \times 128 \times 64$ voxels. Volume intensities were normalized. The algorithm was designed with intensity augmentation for improved reliability, and the network was trained for 300 epochs with a batch size of 6. Binary thresholding (0.5 cut-off) was used on the predicted 3D segmentation and evaluated against their manually contoured scans using a dice similarity coefficient (DSC) and compared to the existing manual 2D based assessment.

RESULTS: The model yielded a DSC of 89% in the validation set, with a training loss of 0.0116 and a validation loss of 0.0276. It took an average of 0.175s to segment the psoas muscle on a Nvidia Titan RTX GPU and Intel 9900X CPU. We found a strong correlation with the established manual 2D method ($R^2=0.93$, $p<0.001$). Temporal progression from initial to 1-year scans had a mean decrease of 7.5% and ranged from a 3% increase to a 32% decrease in the psoas muscle.

CONCLUSIONS: Rapid automated psoas segmentation enables future study of large datasets to understand sarcopenia progression using routine prostate cancer CTs. The developed deep learning approach was found to yield fast, accurate 3D quantification of sarcopenia, with potential for greater sensitivity to small muscle changes found than with 2D analyses. Future work will improve algorithm performance by implementing a framework that exploits the serial nature of the scan to improve sensitivity. Integration of this method into a clinical tool will allow accurate and robust quantitative sarcopenia assessments that could direct research into optimizing individual patient treatment models, decrease complications and mortality rates and improved overall patient outcomes.

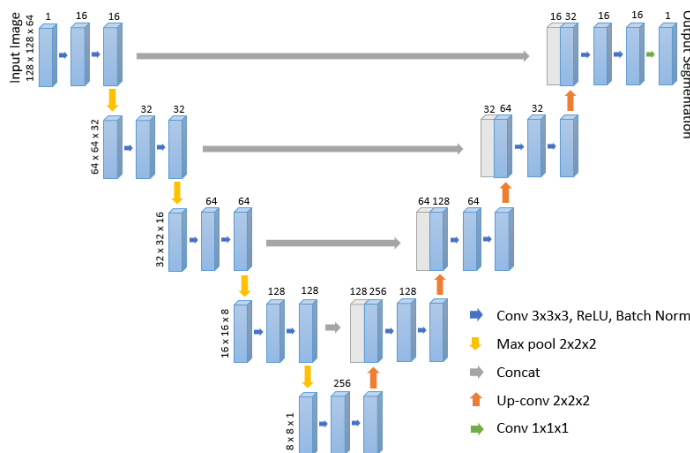


Figure 1: 3D U-Net Architecture (implemented in PyTorch). Each blue box represents a multi-channel feature map. White boxes represent copied feature maps. The number of channels is listed on the top of the box, whereas the x-y-z pixel dimension is shown to the side. The arrows demonstrate the different operations that take place in the CNN.

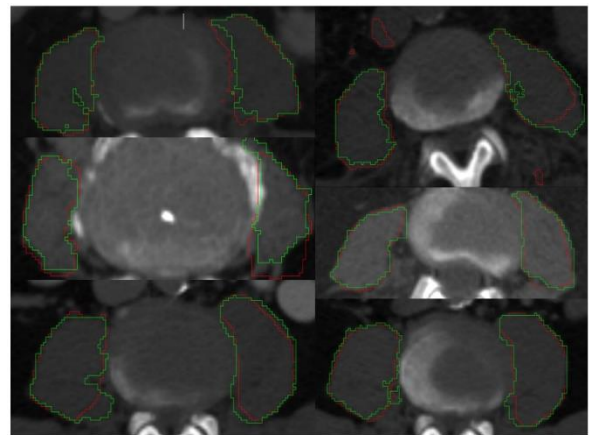


Figure 2: Segmentation masks overlaid onto an abdominal axial slice of the cropped original CT image for the 6 validation cases. The manual segmentation masks created for training are in green, and the masks predicted by the network are in red.

Detection and localization of transition and peripheral zone prostate cancers on apparent diffusion coefficient (ADC) map MR images using U-Net ensemble

Timothy Wong¹, Nicola Schieda², Eranga Ukwatta¹

¹School of Engineering, University of Guelph, Guelph, ON, ²Department of Medical Imaging, The Ottawa Hospital, Ottawa, ON

Introduction: Prostate magnetic resonance imaging (MRI) is increasingly being used in at risk men for prostate cancer (PCa) detection to plan biopsy and optimize PCa diagnosis. Despite the use of PI-RADS (Prostate Imaging – Reporting and Data System) as a standardized method to localize and score suspicion of PCa on MR images, this method has been reported to have low to moderate interobserver agreement which is particularly low in the transition zone (TZ). Also, though accuracy of MRI for detecting PCa is moderate-to-high overall, accuracy in the TZ is at best moderate. We propose the use of a deep convolutional network as an automated method of PCa detection by segmentation, to be used by radiologists as a diagnostic aid.

Methods: The dataset is comprised of 391 patients using only the apparent diffusion coefficient (ADC) map MR sequence because PCa is easily distinguishable on ADC by its hypointensity. Voxel-wise manual segmentations of the prostate gland and tumour were performed by a team of four genitourinary radiologists, with MRI-radical prostatectomy maps and targeted biopsy delineating the location of tumors. 103 patients were classified as patients with TZ tumour, 245 with peripheral zone (PZ) tumour, and 93 without tumour.

For fully automatic tumour detection, a single 2D U-Net is first used to segment the prostate in ADC map MR images. The prostate segmentation is then provided as a second channel alongside the ADC map to an ensemble of three 2D U-Net models trained to detect and localize prostate tumours. Hyperparameter configurations of the tumour detection ensemble were chosen as the three best performing combinations validated by 5-fold cross-validation. The Dice loss was used as the loss function during training. The entire validation set was used to select the model iteration with the lowest loss for prostate segmentation, and evaluated on only TZ tumours of the validation set for tumour detection.

Results: The proposed method was trained on the training set over 100 epochs and evaluated on the test set consisting of 133 patient images. The performance of the prostate segmentation model was evaluated by the Dice score, with results shown in Table 1. The tumour detection ensemble was trained with the manual segmentations as input. Performance on the test set using both manual and automatically generated segmentations was analyzed. The method was evaluated on its ability to detect tumours in MR images, using the precision and recall metrics on the tumour volume. A true positive was defined as non-zero overlap between the predicted and ground truth segmentation of a tumour. Table 2 shows precision and recall scores of the ensemble with automatic and manual segmentations, and Figure 1 shows an example tumour detection by the proposed method.

Table 1: Dice Score for Prostate Segmentation by Transverse Slice Region

Region	Mean Dice \pm Std.
Whole Gland	0.8049 \pm 0.0799
Base	0.7738 \pm 0.1303
Midgland	0.8766 \pm 0.0898
Apex	0.7110 \pm 0.1590

Table 2: Precision/Recall of Model for Tumour Detection using Automatic and Manual Prostate Segmentations

Model	Precision (all)	Recall (all)	Recall (TZ)	Recall (PZ)
Automatic	0.7182	0.6371	0.7436	0.5882
Manual	0.6769	0.7097	0.7949	0.6706

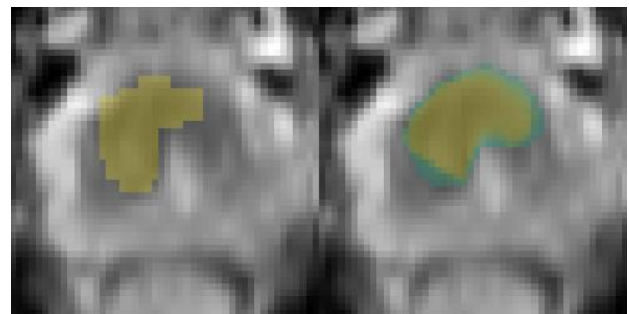


Figure 1: (Left) Ground Truth Tumour Segmentation, (Right) Predicted Tumour Segmentation

Conclusion: We presented a fully automated method to detect and localize tumours in both the TZ and PZ of the prostate in ADC map MR images, with precision and recall of 0.64 and 0.64, which utilized an automatically generated prostate segmentation with a mean Dice score of 0.80. There is opportunity to further improve tumour detection to reduce the performance gap between manual and automatic prostate segmentations.

Validation of a CT based radiomics signature in oropharyngeal cancer: assessing sources of variationPhilipp Guevorguian¹, Tricia Chinnery¹, Pencilla Lang², Anthony Nichols³, Sarah Mattonen^{1,2}¹Department of Medical Biophysics, ²Department of Oncology, ³Department of Otolaryngology, Western University, London, ON

Introduction: Oropharyngeal cancer (OPC) is one of the most prevalent head and neck cancers with 171 estimated deaths in 2017 in Canada alone¹. Patients are treated with surgery, immunotherapy or radiation therapy and chemotherapy treatments. CT scans are used for diagnosis and acquire prognostic information that allows for personalization of the patient's treatment. Radiomics is a novel high-throughput approach that allows for quantitative analysis of such imaging data which can then be leveraged for prognostic applications. However, the lack of validated models in the field has been a barrier to the translation of radiomic research to the clinic. Validation is very important in that it proves that a given radiomic model is sufficiently robust to provide utility in the context of a larger patient population, rather than a specific cohort at a single institution. Aerts et al. published a seminal paper in the field proposing a radiomic signature derived from a lung cancer dataset that demonstrated prognostic abilities similar to tumour staging in a second lung cancer dataset, as well as an independent head and neck cancer cohort². This model has since been externally validated several times, showing promise as a candidate for clinical implementation. One such study by Welch et al. demonstrated that a modified model accurately predicted overall survival in OPC patients³. Therefore, we hypothesize that we can validate this radiomic signature in an independent local cohort of OPC patients.

Methods: The radiomics signature in the derivation study that we seek to validate is comprised of four features derived from the primary gross tumour volume (GTVp). These features are energy, compactness, gray-level run length matrix (GLRLM) non-uniformity and HLH (high-low-high) -wavelet transformed GLRLM non-uniformity². These features were extracted from planning CT images of 224 OPC patients treated with chemoradiation at the London Regional Cancer Program. Extraction was conducted via Pyradiomics, an open-source software package developed by the research group that proposed the radiomics signature, in order to maintain consistency between feature calculations, with no additional data augmentation or preprocessing⁴. The signature presented in the original paper was a Cox proportional hazards model with weights associated with each feature value². The linear predictor of this model is symbolized as the prognostic index (PI) and is defined as the weighted sum of each feature in every patient. To assess the fit of the original model in the validation data, we estimated the regression coefficient on the PI exactly as reported for the derivation dataset, as well as by Welch et al. in their 2018 study. Signature performance was evaluated by conducting a likelihood-ratio test that the calibration slope is equal to 1 in the validation cohort.

Results: Feature extraction from the dataset yielded (mean \pm SD) compactness values of 0.018 ± 0.004 , energy values of $4.907e9 \pm 1.106e10$, GLRLM non-uniformity of $1.027e3 \pm 1.068e3$ and HLH-wavelet GLRLM non-uniformity of $2.295e3 \pm 2.666e3$. The regression coefficient on the PI from the Aerts study was found to be -0.367 (SE=0.2707). The coefficient for the Welch signature was found to be 0.0595 (SE= 0.321). For both models, the coefficient was below 1 and was found to be significantly different from 1 ($p < 0.05$), indicating that the discriminative value of these models was not preserved in the validation dataset.

Conclusions: The results suggest that the radiomic signature proposed by Aerts et al. and Welch et al. were not validated in the London cohort of OPC patients. Potential sources of variation that could explain this result include different feature extraction settings, regression algorithms and binary mask extraction procedures. A similar signature involving imaging data normalization such as isotropic voxel transformations, or a deep learning approach incorporating domain transformations, transfer learning, etc., might prove to be more robust. Further analysis would verify the reproducibility of feature calculations, address differences between patient populations and ameliorate the effects of dental artifacts.

References: [1] Statistics Canada. Table: 13-10-0111-01. [2] Aerts, H. J., *et al.*, Nat Commun, 5 (2014). [3] Welch, M.L., *et al.*, Radiother Oncol, 130 (2019). [4] van Griethuysen, J.J.M., *et al.*, Cancer Res, 77 (2017).

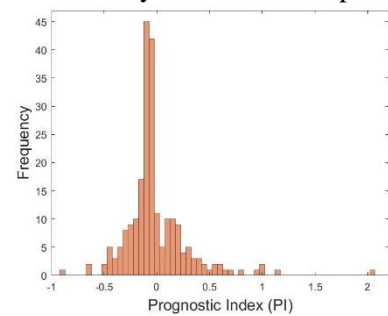


Fig 1. Distribution of prognostic indices derived from Aerts et al. signature

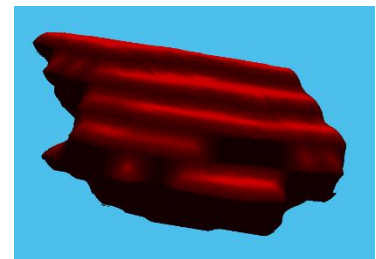


Fig 2. Primary gross tumour volume segmentation in OPC patient

A CT-based radiomics model for predicting gastrostomy tube insertion in oropharyngeal cancerTricia Chinnery¹, Pencilla Lang², Anthony Nichols³, Sarah Mattonen^{1,2}¹Departments of Medical Biophysics, ²Oncology, ³Otolaryngology, Western University, London, ON

Introduction: Oropharyngeal cancer (OPC) is the fastest-rising incident cancer in Canada, due to the rapidly increasing rates of oral infection with the human papillomavirus [1]. Nearly all patients with OPC treated with chemoradiation suffer treatment-related toxicities such as xerostomia (dry mouth) and dysphagia (trouble swallowing). Consequently, to combat nutritional deficiencies, approximately 25% of patients will require a gastrostomy tube (G-tube), an invasive procedure requiring hospital admission [2]. This may cause treatment delays or the need to forgo chemotherapy due to unanticipated hospital admissions and general deconditioning of patients, all potentially impacting the success of treatment. Currently, there are no clinical prognostic factors to determine which patients will require a G-tube during treatment [3]. Therefore, there remains an unmet clinical need for additional biomarkers to assist in identifying this patient population, who could benefit from prophylactic G-tube insertion prior to the start of their treatment. Radiomics aims to extract quantitative image features such as texture, which may not be visible to the human eye. These features can be used to develop predictive machine learning models and provide a more comprehensive view of diseases. We hypothesize that a radiomics-based machine learning model could predict a patient's need for a G-tube prior to treatment.

Methods: A dataset of patients (n=282) with OPC treated with chemoradiation at the London Regional Cancer Program was used for this study. A total of 90 patients (32%) required a G-tube during treatment. Primary tumour and nodal volumes were contoured on pre-treatment planning CT images as part of the routine radiation therapy workflow (Fig. 1). The Quantitative Image Feature Engine [4], was then used to compute radiomic image features from these volumes of interest. Volumetric, morphometric, and global features derived from the first-order histogram were extracted, along with second-order textural features. In this preliminary work, we developed and evaluated a machine learning model to predict the need for G-tube insertion. The dataset was split into independent training (n=197) and testing (n=85) datasets. Linear regularization with a least absolute shrinkage and selection operator (LASSO) penalty was applied to shrink non-significant features to zero and select the optimal radiomic features to predict G-tube insertion. A support vector machine, random forest classifier (RF), and K-nearest neighbour classifier were built using the selected radiomic features on the training dataset and performance was assessed in the testing dataset. Up-sampling was used to balance the classes, resulting in more meaningful performance metrics. A baseline model using only clinical features (Table 1) was also investigated and compared to radiomics.

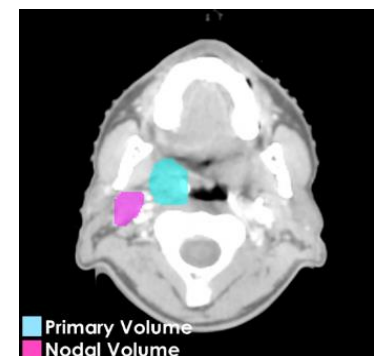
Results: Through the LASSO feature selection, fourteen predictive radiomic features were selected. This included three clinical, three texture, six shape, one size, and one intensity feature. The top performing classifier was the RF model, which resulted in a testing accuracy of 87%, a sensitivity of 86%, and a specificity of 89%. This was in comparison to an accuracy of 70%, a sensitivity of 77%, and a specificity of 61% achieved from a baseline model comprised of clinical features alone.

Conclusions: In this preliminary study, radiomics demonstrated a good accuracy to predict G-tube insertion. Ongoing work includes exploring different radiomic features and classification methods, as well as expanding our patient database. This will be the first study to use radiomics for the prediction of this supportive care intervention for OPC patients. Once refined and validated, this model has the potential to assist physicians in identifying patients that may benefit from prophylactic G-tube insertion, to ultimately improve outcomes and quality of life for OPC patients.

References: [1] S. Habbous et al., CMAJ, 189(32), 2017. [2] C. Friedes et al., Cureus, 12(4), 2020. [3] J. P. Reddy et al., IJROBP, 105(1), 2019. [4] S. Echegaray et al., J. Digit. Imaging, 31(4), 2018.

Table 1: Patient Demographics (n=282)

Mean Age	61±10 years
Sex (Male)	241 (85%)
Tumour Stage	
I	47 (17%)
II	123 (44%)
III	46 (16%)
IV	66 (23%)
Smoking Status	
Current Smoker	112 (40%)
Not a Smoker	79 (28%)
Past Smoker	91 (32%)
Tumour Subsite	
Tonsil	139 (49%)
Base of Tongue	124 (44%)
Other	19 (7%)

**Figure 1:** Tumour volumes contoured on pre-treatment CT.

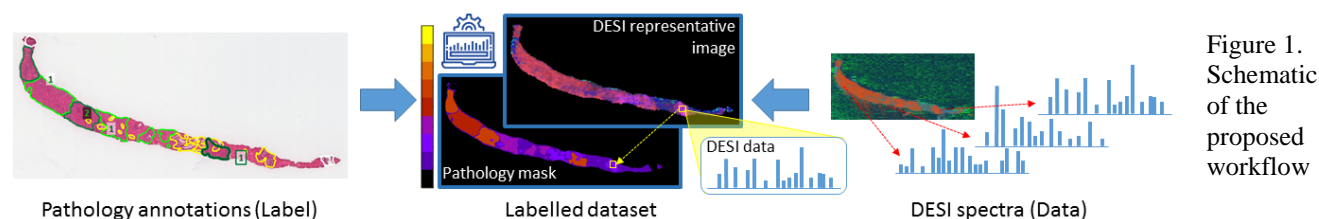
Platform-Independent Management of Histopathologic Annotations in Cancer Research: Application in High-Dimensional Metabolomic Image Analysis

Amoon Jamzad¹, Tamara Jamaspishvili², Rachael Iseman², Martin Kaufmann³,
David M. Berman², and Parvin Mousavi¹

¹*School of Computing, Queen's University,* ²*Department of Pathology & Molecular Medicine, Queen's University,* ³*Department of Surgery, Queen's University. Kingston, Canada*

INTRODUCTION: Histopathologic examination of tissues serves as the gold standard for diagnosis and prognosis in cancer research. Digital annotation of scanned histopathological slides, usually done through various digital imaging platforms, are used as “labels” in deep learning-powered studies to model biological and clinical features in data. However, extracting and mapping these annotations to high dimensional data remains challenging. Traditionally, image processing techniques have been applied to a single-layer snapshot of all annotations overlaid on the tissue to extract the labels. It limits the number of differentiable annotation colors that particularly needed for heterogeneous tissues like prostate [1], and also ignores the extra comment that pathologist may add to the platform during annotation. The spatial resolution of annotation is also limited by the area of the extracted region. We present a workflow for handling histopathologic annotations for deep learning oriented cancer studies, which is compatible with standard annotation platforms, and addresses the challenges mentioned above. We test the method in the application of prostate cancer grading using desorption electrospray ionization [2] mass spectrometry imaging (DESI).

METHODS: Thirty eight needle biopsy cores from 19 patients were sampled after radical prostatectomies, sectioned, and fixed on microscopic slides. The grading annotation was proposed based on the spatial distribution of cancer cells. The total of 9 classes of stroma, benign tissue, low grade cancer (Gleason pattern 3), high grade cancer (Gleason patterns 4 and 5), mixed low grade (low>high), mixed high grade (high>low), prostatic intraepithelial neoplasia, intra-ductal carcinoma, and artifact was considered. The spatial coordinates of the annotation boundaries were exported from the platform, post-processed, and combined into a multi-layer label image containing all 9 pathological classes. The metabolomic profiles of the biopsy cores were then collected and analyzed by DESI. The spectral dimensions for each pixel reduced to three principle components to generate an image representation of the tissue. The label images were then spatially registered to these corresponding DESI tissue images and the transformation information was used for final dataset generation (Figure 1). The generated dataset were then used for prostate cancer grading in a deep architecture consists of convolutional and residual layers.



RESULTS: The dataset was validated through qualitative assessment and quantitative analysis. Using slide-based unsupervised analysis of principle components of spectra for tissue regions, a high spatial correlation was observed between the representative ion images, and the corresponding histopathology label images. When the dataset was used for supervised training in a pixel-based manner, high accuracies in training (94%) and test (82%) sets were achieved. The achieved performance proves the validity of proposed workflow.

CONCLUSION: The proposed digitized pathology annotation protocol and dataset generation workflow is compatible with AI-oriented cancer research. Our method is capable of handling large numbers of pathological classes and data from high dimensional imaging platforms including, but not limited to DESI.

REFERENCES:

- [1] Morse N, Jamaspishvili T, Simon D. et al. Reliable identification of prostate cancer using mass spectrometry metabolomic imaging in needle core biopsies. *Lab Invest* 2019;99:1561–1571
- [2] Takats Z, Wiseman JM, Gologan B, Cooks RG. Mass spectrometry sampling under ambient conditions with desorption electrospray ionization. *Science* 2004;306:471–3

Automated Contouring of Breast Tumors using Machine Learning

J. Ehrlich¹, J. Gerolami¹, V. Wu¹, Z. Hu¹, P. Nasute Fauerbach², D. Jabs³, C. J. Engel⁴, J. Rudan⁴, S. Merchant⁴, R. Walker⁴, T. Ungi¹, P. Mousavi¹, and G. Fichtinger¹
 Queen's University, ¹School of Computing; ²Department of Pathology and Molecular Medicine; ³Department of Diagnostic Radiology; ⁴Department of Surgery

Introduction: Breast cancer is the second most common surgically treated cancer in women. The favoured procedure for this condition is *breast-conserving surgery*, which maximizes remaining healthy breast tissue after surgery.¹ The narrowest possible healthy tissue margin around the tumor is enough to maximize the chance of survival, as outlined in the joint statement by the Society of Surgical Oncology and American Society for Radio Oncology. However, in current clinical practice, 20-30% of patients need revision surgery, because some cancer is left behind after the first surgery due to excision margins containing cancer. A cancer-free margin is difficult to achieve because tumors are not directly visible, palpable, and the breast deforms during surgery making evaluation of the tumor difficult. A surgical navigation system for lumpectomy that generates a spatial location of the tumor in real time for surgeons will solve this problem. Previously, our lab (J. Gerolami and V. Wu) built a U-Net to automatically segment breast tumors, a key first step in building the surgical navigation system. In this paper, our goal is to improve the AUROC of the previous model. This project also seeks an additional focus of clinical relevance to evaluate our model because the statistical results do not always correlate with accurate characterization of the tumor. Therefore, we hope to improve the relevance of our work for our clinical colleagues.

Methods: The data was collected from 27 non-palpable lumpectomy patient cases totaling 6312 ultrasound B-mode images in the coronal, sagittal, and axial planes. The images were then segmented using 3D Slicer's extension Single Slice Segmentation (<https://github.com/SlicerIGT/aigt>) and checked by a radiologist to ensure accurate characterization of the tumor. Images were then split into 5 separate leave-4-out validation sets for evaluation. The "Old Model" architecture represents the previous U-Net architecture used in our lab with 7 contracting and 7 expanding layers. To improve the previous model, modifications were done incrementally resulting in an additional nine model architectures. This was to improve the interpretability of our model and determine effective components within each architecture. Example of modifications include: **1)** modifying the number feature maps of each down sampling layer (NF) from 12, 22, 32, 42, 52, 62, 72 to 8, 16, 32, 128, 256, 512, 1024, respectively; **2)** adding max pooling layers (MP) after each contracting convolutional layer (kernel size 2x2 and 4x4); **3)** increasing the number of convolutional layers; **4)** and finally overall architectural modifications such as utilizing attention networks.

Model	AUROC
Old Model	0.81
NF	0.90
MP	0.88
New Architectures	0.88

Figure 1: AUROC Results

Results: Based solely off 4 statistical metrics (e.g., AUROC - calculated by plotting the false positive against true positive rate for each predicted threshold and ground truth segmentation), the best model was NF. However, after visual

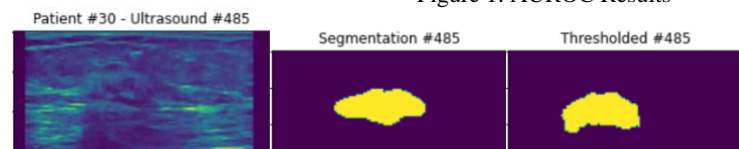


Figure 2: Segmentation vs Threshold of Ultrasound Tumor

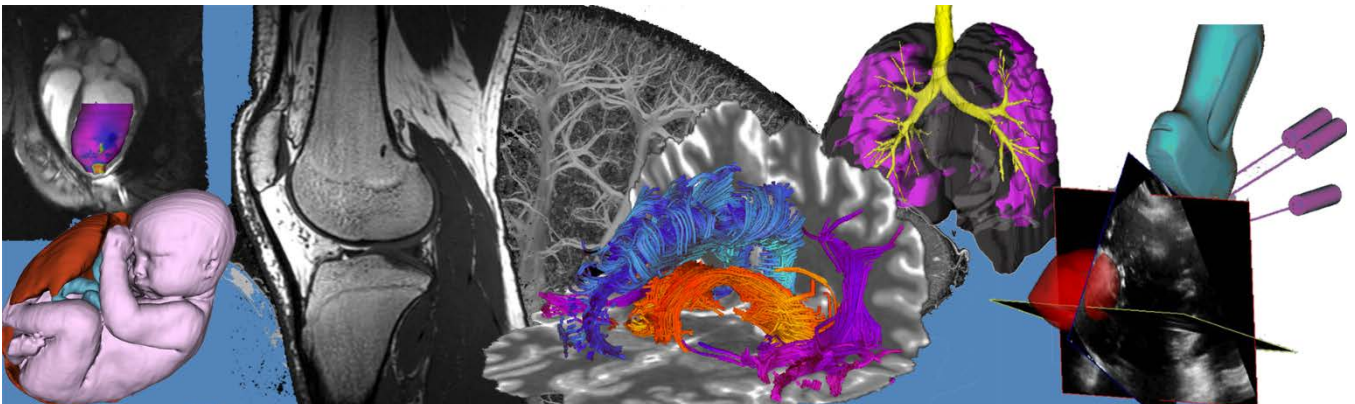
inspection of 80 images for each model, the new architectures (e.g., attention model) characterized more challenging aspects of the tumor with higher clinical relevance and accuracy. This was because it contoured regions of the tumor that were previously uncaptured by pre-existing models.

Conclusions: These results demonstrate an improvement upon previous automated breast tumor contouring in ultrasound images. With more accurate characterization of breast tumors, we get closer to the final goal of providing the surgeons with an automated surgical navigation system for lumpectomy.²

1. How Common is Breast Cancer? *American Cancer Society*. 2021.
2. Lund S, et al. Controlling virtual views in navigated breast conserving surgery. *SPIE Medical Imaging*. 2019

Pitch Presentation Abstracts

Session 7: Image Processing



Microscopic Fractional Anisotropy Imaging in the Human Brain: An Optimized Kurtosis Approach vs. the Gamma Model

Nico J. J. Arezza,^{1,2} Desmond H. Y. Tse,² and Corey A. Baron^{1,2}

¹Department of Medical Biophysics, Schulich School of Medicine and Dentistry, Western University, London, ON, Canada,

²Centre for Functional and Metabolic Mapping, Robarts Research Institute, Western University, London, ON, Canada

Introduction: Water diffusion anisotropy in the human brain can be used to depict neuron microstructure, and reduced anisotropy has been observed in neurological disorders. Microscopic fractional anisotropy (μ FA) imaging is a promising MRI technique because it can estimate diffusion anisotropy independent of neuron fiber orientation, giving it high specificity to tissue irregularities. However, most implementations of μ FA have had poor resolution, long scan times, or long computation times. Here, we demonstrated a rapidly-computable technique for μ FA brain imaging and compared it to the computationally-intensive gamma model [1].

Methods: Four healthy volunteers (2 males, mean age 28.0 ± 6.6 years) were imaged at 3T in a 4.5-minute diffusion MRI scan. The parameters were TE/TR = 94/4500 ms, 2 mm isotropic resolution, FOV = 220x220 mm², and 48 slices. The diffusion encoding scheme contained 3, 3, 6, and 6 linear-encoded directions and 6, 6, 10, and 16 spherical-tensor-encoded averages at $b = 100, 700, 1000, 1400$, and 2000 s/mm², respectively. Brain maps of μ FA were generated for each volunteer using the gamma model described by Szczepankiewicz et al [1] (μ FA_{gamma}) and using an approach based on the diffusion kurtosis model [2] (μ FA_{kurt}). White matter voxel values were compared between the two methods using scatter plots and Bland-Altman plots to assess the correlation and bias.

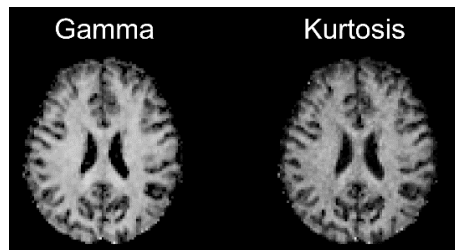


Figure 1: Sample μ FA images from one volunteer, estimated using the gamma model (left) and the kurtosis approach (right).

Conclusions: Qualitatively, the kurtosis approach produced μ FA maps with similar contrast and image quality to the gamma model despite a sixty-fold decrease in computation time; thus, this technique may be more suitable for clinical adoption. Despite strong correlation between the techniques, a bias was observed that likely resulted from different assumptions used in the models to estimate mean diffusivity (MD), an intermediate step in μ FA estimation. The kurtosis approach estimates the MD using a second order cumulant fit of the diffusion MRI signal, whereas the gamma model uses only up to the first order. Further investigation into this bias is the subject of future work.

References: [1] F. Szczepankiewicz et al. *Neuroimage* 2015. [2] N. Arezza et al. *medRxiv* 2020.

Acknowledgements: Canada First Research Excellence Fund to BrainsCAN, Ontario Graduate Scholarships, NSERC

Results: The μ FA_{gamma} brain maps each required ~120 mins to compute on our system, compared to only ~2 mins for the μ FA_{kurt} maps. Voxel-wise comparisons between the two approaches in white matter showed a strong correlation ($\rho=0.97$), but a moderate bias (-0.11) was observed in μ FA_{kurt} relative to μ FA_{gamma} (Fig. 2).

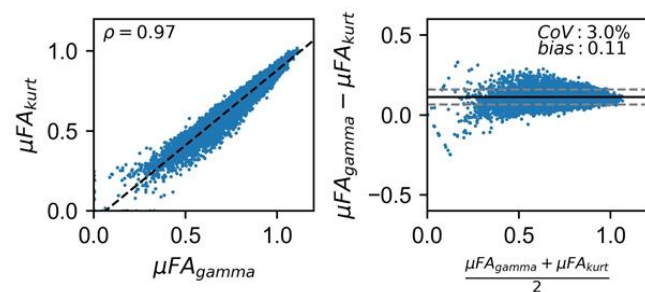


Figure 2: Scatter plot (left) and Bland-Altman plot (right) comparing the two μ FA techniques. Each blue dot represents one white matter voxel. The dashed black line depicts the best fit line and the solid black line depicts the mean bias.

Sub-second and Dynamic Computed Tomography Development at the Canadian Light Source

Xiao Fan Ding¹, Chen Li³, Lifeng Zhang³, Ning Zhu^{1,2,3}

¹ Department of Biomedical Engineering, University of Saskatchewan, SK, Canada, ² Canadian Light Source Inc., SK, Canada,

³ Department of Chemical and Biological Engineering, University of Saskatchewan, SK, Canada

Introduction: Dynamic CT is an emerging technique of uninterrupted acquisition of radiographic projections of a sample as it forms, deforms, or interacts to external conditions¹. However, a basic principle for correct tomographic reconstruction is that the sample remain unchanged during CT acquisition to avoid motion artefacts. To capture dynamic processes, either the sample stability is controlled above the limitations of the capture device, or tomographic data needs to be acquired faster^{1,2}. The former is used in dynamic CT joint studies through precisely controlled joint movements at clinical scanners³. The Canadian Light Source (CLS) uses the latter approach as the high flux is several orders of magnitude greater than laboratory X-ray sources and well suited for sub-second acquisitions^{1,4}. The greater temporal resolution allows for tomographic reconstruction of an evolving sample and the changing internal structures can be captured and visualized¹. Dedicated micro-CT systems are also capable of dynamic CT with scans on the order of 2 CTs/min⁵. Computational and mechanical constraints limit dynamic CT studies to small samples for short periods of time. Research applications have been in material sciences and preliminary studies in small animals and medical implant design^{1,3,6}. In this abstract, dynamic CT was used to visualize the wet granulation process of pharmaceutical powders once in contact with water.

Methods: This study was performed at the 05B1-1 beamline at the CLS with a photon flux density of 10^{12} photons/mm²/s in a filtered white beam. Projections of 2000×664 px at 5.3 µm/px were captured by a Hamamatsu AA-40 beam monitor with a 200 µm thick LuAG scintillator coupled to a PCO.DIMAX HS4 camera. With a 50 cm sample-to-detector distance, each individual scan consisted of 500 projections over 180° in 0.5 s. The wet granulation experiment consisted of a micropipette of deionized water, controlled by a syringe pump, held 2.5 cm above the powder bed. On a motorized rotation stage, cylindrical vessels containing the powders were positioned 26 m away from the light source. Two pharmaceutical powders, lactose monohydrate (LMH) and microcrystalline cellulose (MCC), were scanned for 20 and 13 s respectively once the water droplet contacted the powder bed. With a 1 ms temporal resolution, individual moments of the granulation process were reconstructed through selections of 500 consecutive projections. This allowed for characteristics such as the consolidation of the granule shape and the subsequent growth of pores to be visualized in animations with 1 ms interval between frames.

Results: In a single slice, the granule consolidated its shape for LMH (Fig 1 c) and less so for MCC (Fig 1 d) while both became more porous over the elapsed scan time. Focused on a sample area consisting of only solid granule, the total pore area in the sample was plotted over the scan time (Fig 1 e). Both granules grew during wetting however the MCC granule spread farther outward. Both samples shrank as pores formed (Fig 1 f).

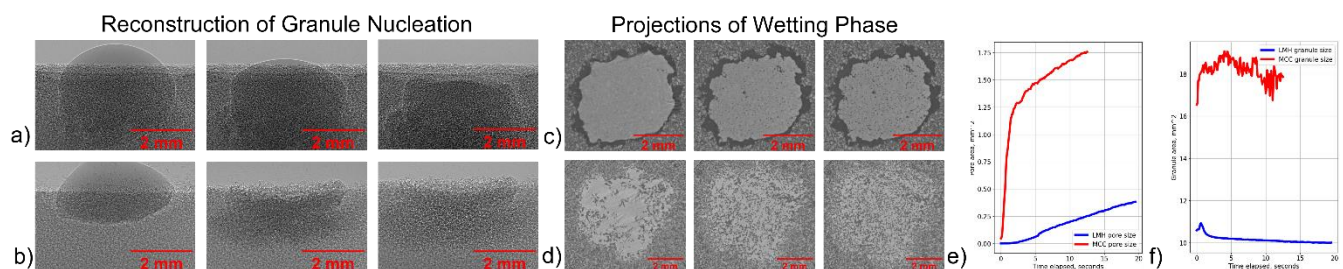


Fig 1: The early, middle, and late stages of wetting and nucleation are shown for LMH (a, c) and MCC (b, d). Sample pore area and granule area over the elapsed scan time for LMH in blue and MCC in red (e, f).

Conclusions: This abstract aimed to illustrate the dynamic CT capabilities at the CLS. The high-flux X-rays and high-speed camera can acquire a full tomographic dataset in 0.5 s. The dynamics of wet granulation were reconstructed with a temporal resolution of 1 ms. There were significant motion artefacts during the wetting due to droplet motion. The subsequent nucleation was better visualized with analysis on the granule shape and porosity. Faster data acquisition at the CLS is feasible for 0.5 ms resolution which may mitigate the persistence of motion artefacts during wetting.

¹ Dewackele et al (2020). *J. Microsc.*, ² Mokso et al (2011). *AIP Conf. Proc.*, ³ Kuczynski et al (2020). *Alberta BME Conference*, ⁴ Patterson et al (2016). *J. Mater. Sci.*, ⁵ Manuel et al (2014). *Nucl. Instrum. Methods Phys. Res., B*, ⁶ Fardin et al (2018). *Eur. Respir. J.*

Reliability Assessment of Cerebrospinal Fluid Suppressed Microscopic Fractional Anisotropy

Mohammad Omer, Naila Rahman, Nico J. J. Arezza, and Corey A. Baron

Robarts Research Institute, Western University

Introduction: Abnormal water diffusion anisotropy has been shown to be an indirect measure of neuron damage, and has been observed in disorders such as Alzheimer's¹ and Parkinson's² disease. Microscopic fractional anisotropy (μ FA) is a normalized measure of the anisotropy of water diffusion within and around cells. However, cerebrospinal fluid (CSF) partial volume effects can overwhelm the tissue signal and have deleterious effects on diffusion MRI³. This is expected to artificially decrease μ FA in voxels containing CSF. Accordingly, using a simple method to reduce CSF partial volume effects, we compared a CSF-suppressed method of calculating μ FA to the standard method of calculating μ FA.

Methods: 4 healthy volunteers (2 females, mean age 28.0 ± 6.6 years) were imaged at 3T in a 4.5-minute diffusion MRI scan with TE/TR = 94/4500 ms. The scan consisted of 3, 3, 6, and 6 linear-encoded directions and 6, 6, 10, and 16 spherical-tensor-encoded averages at $b = 100, 700, 1000, 1400$, and 2000 s/mm^2 , respectively. The coverage was a $220 \times 220 \text{ mm}^2$ field of view (FOV) with 2 mm isotropic resolution over 48 slices. Two μ FA volumes were generated for each volunteer using the method described by Arezza et al⁴: the standard μ FA volume was estimated by using a kurtosis fit to estimate the mean diffusivity (MD), while the CSF-suppressed μ FA volume was estimated using a linear fit of signal decay between the b-values of 1400 and 2000 s/mm^2 to estimate MD.

Results: Standard and CSF-suppressed maps from a healthy brain (Fig. 1) indicate that CSF-suppression may be more sensitive to structures in close proximity to the ventricles, like the thalamus and fornix, as both structures appear larger in the CSF-suppressed map. Fig. 2 shows a significant increase ($p < 0.01$) in μ FA between CSF-suppression and standard methods in the thalamus, fornix, and white matter. The largest percent increases seen in CSF-suppressed μ FA positively correlate with the volume of CSF in each region (data not shown).

Conclusions: These preliminary results reveal the potential of using CSF-suppression to calculate μ FA. More specifically, it was shown to significantly reduce CSF partial volume effects in structures such as the fornix and thalamus, where CSF is more prevalent, but has also shown to affect WM regions where CSF partial volumes are negligible. The increase in μ FA in CSF-free white matter regions may represent a bias that is introduced by our approach. Future work will explore models that do not create a bias in CSF-free regions.

References: [1] Englund, E. et al., *J. Neurol* (2004). [2] Ikenouchi, Y. et al., *Neuroradiology* February (2020). [3] Baron, C. A., & Beaulieu, C., *Magn Reson Med* April (2014). [4] Arezza, N. et al., *medRxiv* November (2020).

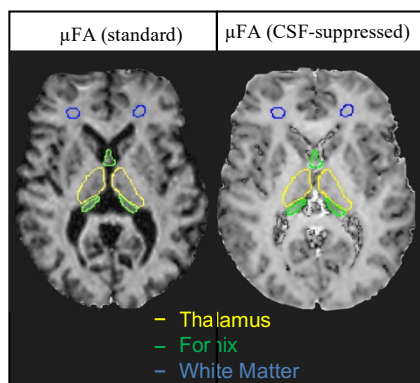


Fig 1. μ FA standard and μ FA CSF-suppressed maps from a healthy human

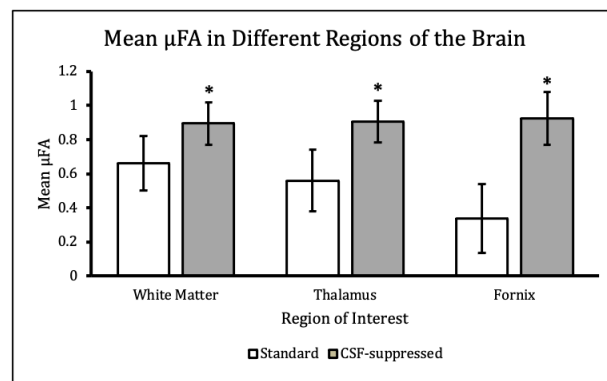


Fig 2. Mean μ FA from standard and CSF-suppressed methods in WM, thalamus and fornix

A Systematic Study of the Effect of Scan Time on the Reproducibility of Cortical MEGA-PRESS GABA+ Measurements: Preliminary Data

Peter Truong¹ and Sofia Chavez^{1,2}

¹Brain Health Imaging Centre – MRI, Centre for Addiction and Mental Health, Toronto, ON, Canada

²Department of Psychiatry, University of Toronto, Toronto, ON, Canada

Introduction

Magnetic Resonance Spectroscopy (MRS) scan optimization is essential in acquiring quality data in minimal scan time. Longer scans are used to increase signal-to-noise ratio (SNR) in a predictable fashion, by averaging out the random noise in the spectrum while maintaining the desired metabolite signal. Acquisitions such as MEGA-PRESS¹, have added complexity due to the introduction of editing pulses and spectral differencing and fitting. These effects may not act like random noise and thus the benefit of longer scan times on the reproducibility of results is less predictable. Given that long scans are not ideal due to subject motion, the benefit needs to be assessed. Here, we present a systematic study of the effect of number of averages (i.e., scan time) on the reproducibility of the GABA measurement and aim to determine an optimal minimal scan time with suitable reproducibility. We focused on two cortical regions-of-interest (ROI), the anterior cingulate cortex (ACC) and left dorsolateral prefrontal cortex (Lt-DLPFC).

Methods: Four healthy volunteers were scanned using a MEGA-PRESS sequence with editing for GABA¹ on a 3T GE MR750 (GE Healthcare) using a 32-channel head coil (Nova Medical) as per institutional REB. Two back-to-back GABA+ scans were acquired in each ROI: 4 cm (AP) × 2 cm (RL) × 3 cm (SI) in the ACC; and 3 cm (AP) × 2 cm (RL) × 3 cm (SI) in the Lt-DLPFC. MRS scan parameters are: TE/TR = 68/1500 ms; spectral width = 5000 Hz; number of points per spectra = 4096; NEX = 8; total averages acquired (#AVE) = 576; scan time = 14:48 (min:sec). Only data with autoprescan linewidths <10Hz are presented. Data were separated into different blocks of averages to mimic reduced scan time: #AVE= 64, 96, 128, 160, 192, 256, 288, 320, 488, and 512. This resulted in 9 spectra with #AVE=64, 6 spectra with #AVE=96 etc. until 1 spectrum was created for each of #AVE=320, 488, 512 and 572. The GABA peaks of the difference spectra were fit using XsOs-NMR² that includes frequency aligning and coil combining. GABA values are quoted relative to unsuppressed water. Due to the repeat scan, a standard deviation (STD) and average of GABA values could be computed at each value of #AVE so the coefficient of variation (CV% = STD*100%/AVE) was used as a reproducibility metric. CV% plotted against #AVE for each ROI gave similar plots across subjects so data were combined per ROI.

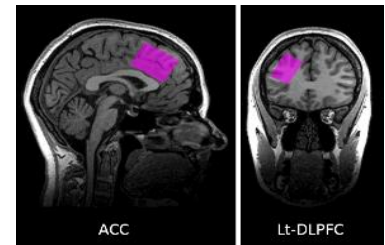


Figure 1-MRS voxel placement in the ACC (left) and Lt-DLPFC (right).

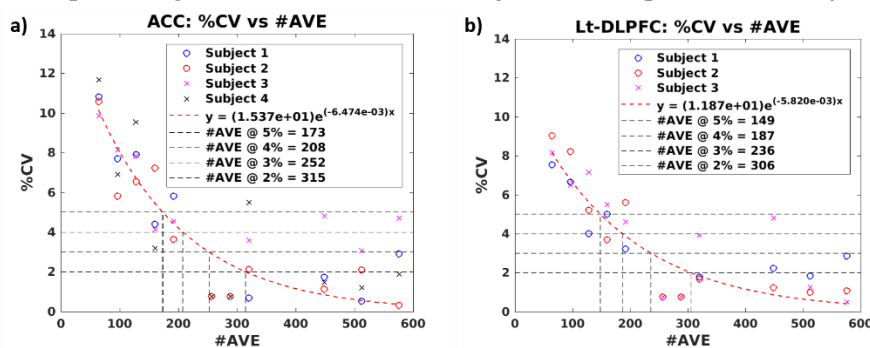


Figure 2-Plots of CV% vs Number of Averages in ACC (a) and Lt-DLPFC (b), combined for all subjects. Subject 4's Lt-DLPFC was omitted from (b) due to head shift during their scan.

each 1% gain in CV% comes at a gradual cost of more #AVE with a rather large increase in #AVE (i.e., scan time) required to go from CV%=3% to CV%=2% in both ROI.

Discussion The cases with larger CV% at #AVE>300 could be attributed to motion as seen by small sudden frequency changes for those later data frames. Based on the large increase in #AVE to go from STD=3% to STD=2% and the increased likelihood of motion for #AVE>300, we propose that #AVE=256 be used for maximum gain in reproducibility while minimizing scan time to 6:24 (min:sec).

References 1. Mullins P.G., et al. Neuroimage 2014. 2. Shungu D.C., et al. NMR in Biomedicine 2016

Results Subjects had linewidths <10 Hz in both regions. A head shift was observed during Subject 4's Lt-DLPFC scan, so that data was omitted. Plots of CV% vs #AVE are shown in (Fig. 2). The data were empirically fit using an exponential function and values for #AVE were determined for each of CV%=5%,4%,3% and 2%. It is clear from the plots that

Automatic determination of the regularization weighting for low rank reconstructions

Gabriel Varela-Mattatall^{1,2}, Corey A Baron^{1,2}, Ravi S Menon^{1,2}

¹ Centre for Functional and Metabolic Mapping (CFMM), Robarts Research Institute, Western University, London, Canada

² Department of Medical Biophysics, Schulich School of Medicine and Dentistry, Western University, London, Canada

Introduction: Low rank reconstruction [1] simultaneously reconstructs several images that share common information through the dataset. A low rank reconstruction,

$$\hat{X} = \operatorname{argmin}_X \|AX - Y\|_2^2 + \lambda \|X\|_{*}, \quad (1)$$

can be described as the combination between a data consistency term and a regularization term. The data consistency (left term of Eq. (1)) makes that the set of reconstructions, X , resemble the acquired data, Y , after the net operator, A . The regularizer (right term of Eq. (1)) promotes low rank and sparsity from X using the nuclear norm (only some singular values are activated across the dataset). One of the problems in using Eq. (1), is the determination of the regularization weighting, λ . An incorrect λ can easily generate diminished noise cancellation, emergence of artifacts, smoothing and loss of structural information. Although there are strategies to determine λ [2,3], the state of the art lacks an automatic, non-iterative, fast, and prospective approach to select the regularization weighting. In this work we present our attempts to develop such approach with those ideal traits. Our method is built under the assumption that singular values can be classified as noise- and signal-based and the regularization weighting is the boundary between these two groups. This is our interpretation from the application of the Marchenko-Pastur distribution to the singular values of a dataset corrupted with Gaussian noise [4,5].

Methods: We implemented Eq. (1) as a proximal descent algorithm [6,7,8,9]. We retrospectively applied different variable-density under-sampling patterns, with an under-sampling factor of 4x, to a diffusion MRI dataset (#images = 512) from the human connectome project [10] and to a functional MRI dataset (#images = 200) acquired with a 7T system at Western University.

Results: Figures 1 and 2 show the comparison between our reconstructions and their respective references.

Conclusions: First attempts show feasible a prospective and automatic procedure for low rank reconstructions. Future work will analyze the effect of noise and under-sampling in the determination of the regularization weighting, and the effect of these reconstructions to the estimation of quantitative biomarkers.

References: [1] Haldar, J et al. 2014. IEEE Trans Med Imaging [2] Otazo, R et al. 2015. MRM [3] Schloegl, M et al. 2017. MRM [4] Veraart, J et al. 2016. MRM [5] Does, M et al. 2018. MRM [6] Combettes, et al 2011. Springer [7] Parikh, N et al. 2014. Found Trends Opt [8] Cai, JF et al. 2008. Arxiv [9] Beck, A et al. 2009. SIAM J on Imaging Sciences [10] Fan, Q et al. 2016. NeuroImage.

Acknowledgements: Authors wish to acknowledge funding from CIHR Grant FRN 148453 to RSM and BrainsCAN-the Canada First Research Excellence Fund award to Western University. Also, thanks to Geoff Ngo for providing the functional dataset used in this study.

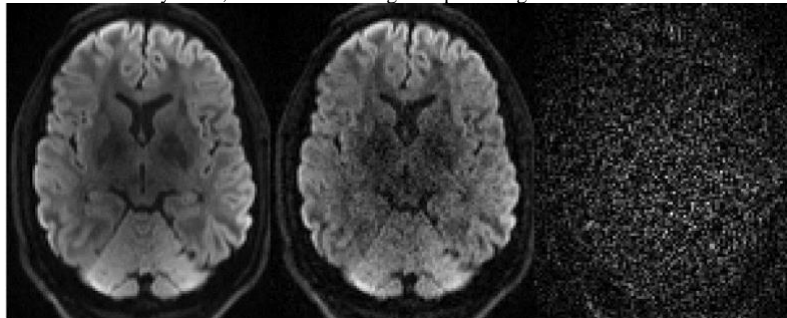


Figure 1. Qualitative comparison from diffusion MRI dataset. **Left:** reconstruction (\hat{x}); **Middle:** fully sampled image (x); **Right:** $5 \times |\hat{x} - x|$.

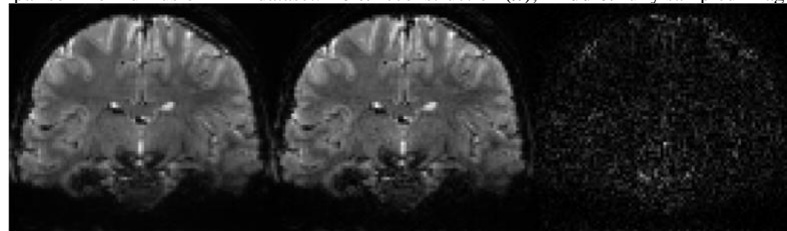


Figure 2. Qualitative comparison from functional MRI dataset. **Left:** reconstruction (\hat{x}); **Middle:** fully sampled image (x); **Right:** $5 \times |\hat{x} - x|$.

Measuring endogenous levels of GABA, GSH, and GLU in a human brain using MRIKanagasabai, K¹; Palaniyappan, L^{1,2,3}; Théberge, J^{1,2}

1. Medical Biophysics, Schulich School of Medicine and Dentistry, London, Ontario, Canada
2. Lawson Imaging, Lawson Health Research Institute, London, Ontario, Canada
3. Robarts Research Institute, London, Ontario, Canada

Introduction: Schizophrenia is a complex psychiatric illness where abnormal concentrations of neurotransmitters within the synaptic cleft lead to abnormal neurotransmission. Abnormal neurotransmission could be affecting the balance and role of a network of neurotransmitters such as gamma-aminobutyric acid (GABA) and glutathione (GSH), and glutamate (GLU) [1]. Magnetic Resonance Imaging (MRI), a non-invasive in-vivo imaging modality, can quantify the chemical composition of voxel in a human brain to study the abnormal neurotransmission in schizophrenia. Many MRI pulse sequences have been successful at detecting GLU, GABA, and GSH independently but none have been successful at providing high-quality measurements of all three simultaneously. This is due to their extremely low in-vivo concentrations, strongly coupled spins in their spectral signature, and interference of neighboring signals [2]. Therefore, there is an unmet need to implement an effective technique to quantify all three neurotransmitters accurately and simultaneously to understand the pathophysiology of schizophrenia. One promising technique involves the use of an advanced MRI pulse sequence known as Delays Alternating Nutation Tailored Excitation Point RESolved Spectroscopy (DANTE-PRESS). DANTE-PRESS uses a narrow-band radiofrequency pulse to selectively isolate the signal of a molecule of interest in the human brain spectrum [3]. In addition to this highly selective pulse sequence, the use of a higher field strength scanner will increase the sensitivity of all three neurotransmitters [2]. DANTE-PRESS at 7 Tesla could be used to quantify endogenous levels of GLU, GABA, and GSH in brain regions relevant to schizophrenia. The objective is to develop, test and validate DANTE-PRESS at 7 Tesla to target GLU, GABA and GSH in a human brain.

Methods: To complete this, DANTE-PRESS will be programmed within the software environment of the 7 Tesla MRI scanner at Robarts Research Institute at Western University. Phantom studies will be conducted to obtain data on water solutions of GABA, GSH and GLU at in-vivo and double in-vivo concentrations. This is to validate the technique and its ability to measure concentrations. Next, the pulse sequence will be tested in the anterior cingulate cortex and the temporal lobe in ten healthy volunteers to demonstrate feasibility and estimate test-retest reliability. The method will then be included in an ongoing longitudinal study of schizophrenia to explore its usefulness in early identification of patients that experience poor treatment outcome

Anticipated results: Many pulse sequences can quantify GABA, GLU and GSH in the anterior cingulate cortex independently with coefficient of variances of 3%, 3% and 24% respectively [4][5]. It is anticipated that DANTE-PRESS will be able to quantify high-quality measurements of GABA, GSH, and GLU at 7 Tesla with coefficient of variance below these values.

Conclusion: Due to variations in neuronal activations, patients with schizophrenia experience variability in their response to standard treatments [1]. It is crucial to develop a method that can obtain high-reliability measurements of GABA. This will provide in vivo human evidence to test GABA'S role in models of schizophrenia involving the simultaneous action of excitation or inhibition imbalance. Understanding GABA's role would enable psychiatrists and pharmaceutical companies to develop medication tailored towards patients who are predicted to not respond to standard treatment. This could reduce the distress associated with multiple unsuccessful treatment trials.

Bibliography

1. Balu DT. The NMDA Receptor and Schizophrenia: From Pathophysiology to Treatment. *Advances of Pharmacology* 2016; 76: 351-382.
2. Marsman A et al. GABA and Glutamate in Schizophrenia: A 7 T ¹H-MRS study. *NeuroImage: Clinical* 2014; 398-407
3. Li L, Miller KL, Jezzard P. DANTE-prepared pulse trains: A novel approach to motion-sensitized and motion-suppressed quantitative magnetic resonance imaging. *Magnetic Resonance in Medicine* 2012; 68, 1423-1438
4. Li Y et al. Reliable and reproducible GABA measurements using automated spectral prescription at ultra-high field. *Frontiers Humans of Neuorscience*; 2017
5. An L et al. Signal enhancement of glutamine and glutathione by single-step spectral editing. *Journal of Magentic Resonance*; 316

Cost-effective micro-CT imaging of medical components fabricated with additive manufacturing

Santiago F Cobos,^{1,4} Steven Pollmann,⁴ and David W Holdsworth,^{1,2,3,4}

¹Department of Medical Biophysics, ²Robarts Research Institute, ³Department of Surgery, ⁴Bone and Joint Institute, Western University, London, Ontario, Canada

Introduction: Patient-specific components fabricated using additive manufacturing (AM) have the potential to improve clinical outcomes in a variety of medical interventions. However, the versatility of AM introduces stability and repeatability concerns that are considered potential roadblocks for more routine use of bio-medical AM systems. A solution could include the use of cost-effective micro-CT imaging to perform 3D non-destructive testing (NDT) of the fabricated medical component. Unfortunately, current micro-CT NDT techniques require expensive infrastructure and equipment, which translates into prohibitively expensive scans. Here we describe our initial design and geometric calibration of a dedicated micro-CT prototype that could be used for NDT of AM-fabricated components. Our design aims to reduce the limitations of industrial micro-CT systems by optimizing image acquisition hardware and improving reconstruction software.

Methods: The image acquisition hardware is comprised of a scintillating screen (Lanex regular, Carestream Health) lens-coupled to a dSLR camera (Nikon D800)¹. The screen is configured in a tilted position with relation to the object, to increase light capturing efficiency at a lens aperture of $f/1.4$. A grid of shadow casting dots spaced a known distance was used to calculate the parameters of a nonlinear least-squares fit to correct the image distortion caused by the camera's lens and the tilted screen.² This image calibration was tested using a green LED light-source instead of an x-ray unit. (This was done due to reduced research capacity caused by the COVID-19 pandemic). The fully operating system will be equipped with a 50 μm focal spot x-ray unit capable of producing 500 uA at 80 kVp (Sourceblock SR-80-500). This energy was selected based on the low attenuation of Titanium and the high porosity characteristic of components used in bio-medical applications. All the components, including a precision turntable with $<5 \mu\text{m}$ run-out, were mounted in a light-tight frame made of 20x20 mm aluminum extrusion profiles. Geometric calibration of the system, as well as its mechanical stability, was tested using synthetic CT-sinograms generated by tracking the shadow cast by a wire-phantom at 9° increments.

Results: The use of a commercial dSLR camera provided a cost-effective ($< 60,000$ CAD) way to acquire high-resolution images that were successfully corrected for lens and geometrical distortions. The synthetic CT-sinograms presented subpixel (i.e. < 1 pixel) deviations from the ideal trajectory. We believe that the full implementation of the current prototype will produce micro-CT reconstructions with enough resolution to be an effective tool for NDT of AM-fabricated components.

Conclusions: We have presented the initial design and geometric calibration of a dedicated micro-CT prototype that could be used for NDT of AM-fabricated medical components. Additionally, the simplicity of the system, makes it a strong candidate for other applications where portability is key; for example, in the case of space exploration or remote archaeological sites. Future work includes the implementation of reconstruction techniques to reduce scan time, remove beam-hardening artifacts and improve image noise, as well as the characterization of the system image quality using micro-CT QA phantoms.

References: 1. Kim, H. K., J. K. Ahn, and G. Cho (2005). Development of a lens-coupled CMOS detector for an X-ray inspection system. *Nucl. Instr. Meth. Phys. Res. A*, 545, pp. 210–216. 2. Heikkila, J., (2000). Geometric camera calibration using circular control points. *IEEE Transactions on Pattern Analysis and Machine Intelligence* 22 (10), pp. 1066–1077.

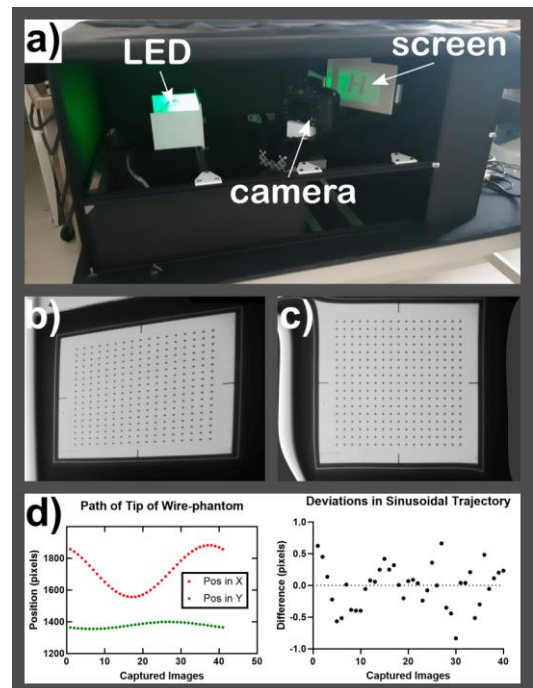


Fig. 1: a) current state of the cost-effective imaging system. b) Image of the circular dot pattern with no image correction. c) Image of circular dot pattern after lens and perspective correction. d) Results of the mechanical stability test for the system after image correction. Left – translation in the image plane of the tip of the wire-phantom. Right – residuals from ideal trajectory in pixels.

In vivo molecular imaging of the mouse cholinergic projection system

Authors and Affiliations: K. M. ONUSKA^{1,4,5,6,7}, H. R. C. SHANKS^{1,4,7}, M. FOX^{2,5,6}, J. HICKS^{2,5}, J. THIESSEN^{2,5,6,7}, V. F. PRADO^{3,4,6,7}, M. A. M. PRADO^{3,4,6,7}, T. W. SCHMITZ^{4,6,7}

¹Neurosci., ²Med. Biophysics, ³Anat. and Cell Biol., ⁴Physiol. and Pharmacol., Univ. of Western Ontario, ⁵Lawson Health Research Institute, ⁶Robarts Research Institute, ⁷Brain and Mind Institute, London, ON, Canada

Introduction: The cholinergic neurons of the basal forebrain (BF) are among the first cells to become damaged in Alzheimer's disease (AD). Structural magnetic resonance imaging (sMRI) studies have shown that this damage occurs prior to cortical degeneration and memory loss. Although sMRI is sensitive to early volumetric losses within the BF, it cannot specifically assay degeneration of distal BF cholinergic axons, which is thought to occur earlier than degeneration of the cell bodies within the BF. Positron emission tomography (PET) with the [¹⁸F] FEOBV radiotracer overcomes this problem. [¹⁸F] FEOBV binds to the vesicular acetylcholine transporter (VACHT), a protein found solely in cholinergic nerve terminals, thereby providing a cell-type specific measurement of the cholinergic projectome. However, the sensitivity and specificity of *in vivo* [¹⁸F] FEOBV-PET to the endogenous expression of VACHT is unknown. This has created a major obstacle for assessing the utility of [¹⁸F] FEOBV-PET as a biomarker for preclinical stages of AD. The goal of this study is therefore to calibrate the sensitivity and specificity of [¹⁸F] FEOBV-PET for measuring preclinical changes in the cholinergic cortical projectome.

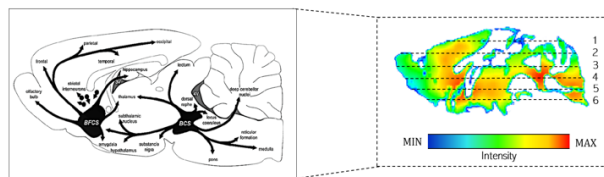
Methods: To do this, we used mouse lines in which endogenous VACHT expression is held under genetic control. We evaluated binding intensity patterns and uptake profiles of [¹⁸F] FEOBV in a wild type (WT, n=1) mouse and a knockdown (KD) mouse with 60% global reductions in VACHT expression (VACHT^{HOM} KD, n=1). **Results:** First, we demonstrated that [¹⁸F] FEOBV-PET binding patterns reflect the underlying anatomy of the mouse cholinergic projectome in both WT and VACHT^{HOM} KD mice (Results, *left*). Next, we observed that decreases in [¹⁸F] FEOBV uptake occur in regions that receive cholinergic input in the VACHT^{HOM} KD mouse when compared to the WT mouse, consistent with the 60% global reduction of VACHT present in this mouse. (Results, *right*).

Conclusions: Overall, these preliminary results support [¹⁸F] FEOBV-PET as a sensitive *in vivo* cell-type specific tool for measuring cholinergic integrity.

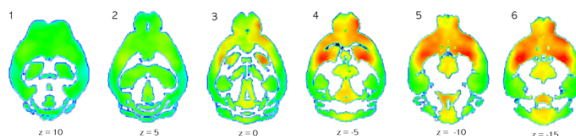
Results

[¹⁸F] FEOBV Binding Patterns in WT and VACHT^{HOM} KD Mice

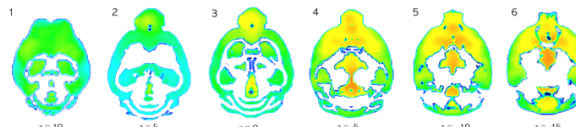
A Molecular Mapping of the Mouse Cholinergic Projectome with [¹⁸F] FEOBV



B [¹⁸F] FEOBV Binding Intensity Distribution in WT Mouse

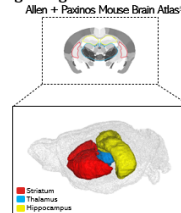


C [¹⁸F] FEOBV Binding Intensity Distribution in VACHT^{HOM} KD Mouse

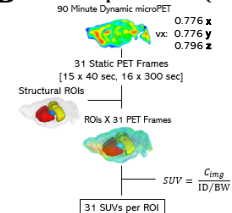


Dynamic uptake of [¹⁸F] FEOBV in WT and VACHT^{HOM} KD Mice

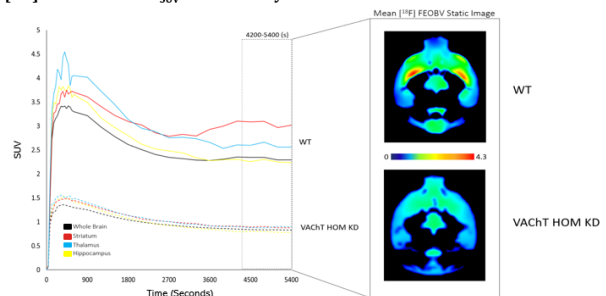
A Cholinergic Regions of Interest (ROI)



B Standard Uptake Values (SUV)

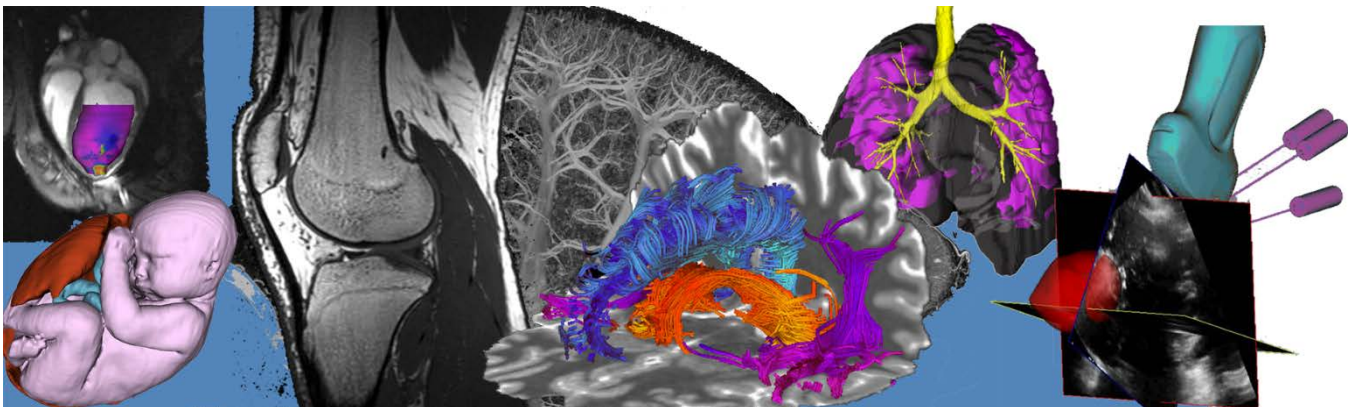


C [¹⁸F] FEOBV-PET ROI_{SUV} Time Activity Curves in WT and VACHT^{HOM} KD Mice



Pitch Presentation Abstracts

Session 8: Device, Hardware, System Development II



Theoretical Comparison of Energy-Resolved and Digital-Subtraction Angiography

Sarah Aubert, Michael Belli and Jesse Tanguay

Ryerson University

Introduction: Two-dimensional x-ray imaging of vasculature requires the administration of an iodine contrast agent and is used to verify diagnosis and guide vascular interventions. When imaging peripheral vasculature, digital subtraction angiography (DSA) is used to produce iodine-specific images, i.e. non-iodinated structures are suppressed from the images. However, DSA is not used to image coronary arteries because it is susceptible to motion artifacts. Dual-energy angiography acquires images at different average x-ray energies after iodine injection and can be used to image the coronary arteries since images are acquired in rapid succession, making this technique less susceptible to motion artifacts. However, dual-energy angiography can only suppress one material and therefore can not produce iodine specific images of coronary arteries. Energy-resolving x-ray detectors that estimate the energy distribution of x-ray photons may enable producing iodine-specific images of the coronary arteries from a single post-iodine injection patient exposure, yielding DSA-like images of the coronary arteries without the corresponding motion artifacts. Previous studies¹ showed that DSA, dual-energy angiography and energy-resolved angiography (ERA) are comparable in terms of iodine signal-to-noise ratio (SNR), but these studies did not account for the energy response of energy-resolving detectors, which is typically degraded by charge sharing due to diffusion of charge carriers and x-ray fluorescence. The purpose of this abstract is to compare the theoretical iodine pixel SNR and the zero-frequency SNR of ERA with that of DSA for matched patient entrance exposure using realistic models of the detector response of energy-resolving and energy-integrating detectors.

Methods: A numerical model was used to calculate the average image signal and image noise for ERA and DSA. Iodine-specific imaging was formulated as a basis material decomposition with three basis materials: iodine, bone, and water. Our ERA model used a validated energy response that accounts for the effects of charge sharing and characteristic emission in cadmium telluride energy-resolving x-ray detectors.² For DSA, we used cascaded-systems analysis to calculate the energy response for a columnar cesium iodide detector.³ We used the zero-frequency SNR per root of patient entrance exposure as a figure of merit in this study. Applied tube voltages and energy-bin thresholds were optimized by brute force. All calculations assumed a tungsten anode and an incident spectrum transmitted through 3.5 mm of aluminum, 20 g/cm² of water and 0.02 g/cm² of iodine. Calculations were performed for ideal and realistic detectors for 200 μm and 400 μm pixels.

Results: The optimal tube voltage was found to be 65 kV for DSA and 150 kV for ERA. Realistic detector response has a negligible effect on the zero-frequency SNR of DSA, but reduced the zero-frequency SNR of 3-bin, 3-material ERA by 60% and 40% for 200 μm and 400 μm pixels, respectively, yielding zero-frequency SNR values that are 30% to 40% of that of DSA. This degradation of image quality relative to DSA and to ideal detectors is a result of spectral overlap between energy bins, which is caused by charge sharing between neighbouring detector elements.

Conclusion: Energy-resolved angiography has the potential to provide zero-frequency SNR that is approximately 1/3 of that of DSA for the same patient entrance exposure. Energy-resolved angiography may therefore provide an alternative to DSA in situations where motion precludes the use of DSA, for example in cardiac imaging. Future work will focus on experimental validation using a cadmium telluride x-ray detector and a bench-top x-ray imaging system in our lab.

References:

- [1] J. Tanguay, H. K. Kim and I. A. Cunningham, "A theoretical comparison of x-ray angiographic image quality using energy-dependent and conventional subtraction methods," *Med. Phys.*, vol. 39, no. 1, 2011.
- [2] J. Tanguay and I. A. Cunningham, "Cascaded systems analysis of charge sharing in cadmium telluride photon-counting x-ray detectors," *Medical Physics*, vol. 45, no. 5, pp. 1926-1941, 2018.
- [3] S. Yun, J. Tanguay, H. K. Kim and I. A. Cunningham, "Cascaded-systems analyses and the detective quantum efficiency of single-Z x-ray detectors including photoelectric, coherent and incoherent interactions," *Medical Physics*, vol. 40, no. 4, 2013.

Field profile analysis of a 2D spiral array for high-volume-rate 3D ultrasound imaging

Rebekah Maffett¹, Enrico Boni², Alessandro Ramalli², Adrian J. Y. Chee¹, Alessandro S. Savoia³, Piero Tortoli², Alfred C. H. Yu¹, ¹Schlegel-UW Research Institute for Aging, University of Waterloo, Waterloo, Ontario, ²Department of Information Engineering, University of Florence, Florence, Italy, ³Department of Engineering, Roma Tre University, Rome, Italy.

Introduction

2D sparse array transducers coupled with unfocused transmissions are a potential solution to the inhibitive data-rates of high-volume-rate 3D ultrasound imaging with 2D matrix arrays. However, sparse arrays have thus far only been characterized with focused transmissions and little is known about how the element distribution impacts the formation of unfocused waves. Wavefronts with inhomogeneous intensity and phase properties would result in aberrations during receive beamforming reducing the image quality. This work presents a field profile analysis of unfocused transmissions from a density-tapered 256-element spiral capacitive micro-machined ultrasound transducer (CMUT) array. We focused specifically on characterizing the intensity and phase profiles of the emitted acoustic fields due to their high relevance to image quality.

Methods

The spiral array has 220 μ m-wide hexagonal CMUT elements distributed with a Blackman density-tapering over a 10mm diameter area [10.1109/ULTSYM.2018.8579867]. The array was connected to an ULA-OP 256 scanner and driven with 7.5MHz 3-cycle sinusoidal bursts. Acoustic pressure fields were acquired with an ONDA HGL-400 hydrophone and simulated using Field II. A total of five measurement planes were acquired (Fig A), three parallel to the array surface and two orthogonal. The measurement planes were sized to contain the entire beam width with 100 μ m steps. Two transmissions were considered: 1) plane wave and 2) diverging wave from a virtual point source 20mm behind the array.

Results

For 20mm scan depth, Figs B and C show the plane wave intensity and phase profile from the spiral array. Figs D and E show the same information for diverging waves. Both transmissions have fluctuations in the intensity map indicating some local variations in brightness should be expected in images. Plane waves had a near ideal phase profile (simulated mean absolute error (MAE) $\cong 0.002\lambda$). Diverging waves show a similarly promising phase except for the edge regions in experiment which were hindered by low intensities (simulated MAE $\cong 0.07\lambda$ with edges excluded). The other scan planes at 40 and 60mm showed similar performance.

Conclusions

This work indicates the feasibility of 2D sparse arrays for high-volume-rate ultrasound imaging with unfocused transmissions thereby laying the groundwork for future developments including 3D vector flow imaging.

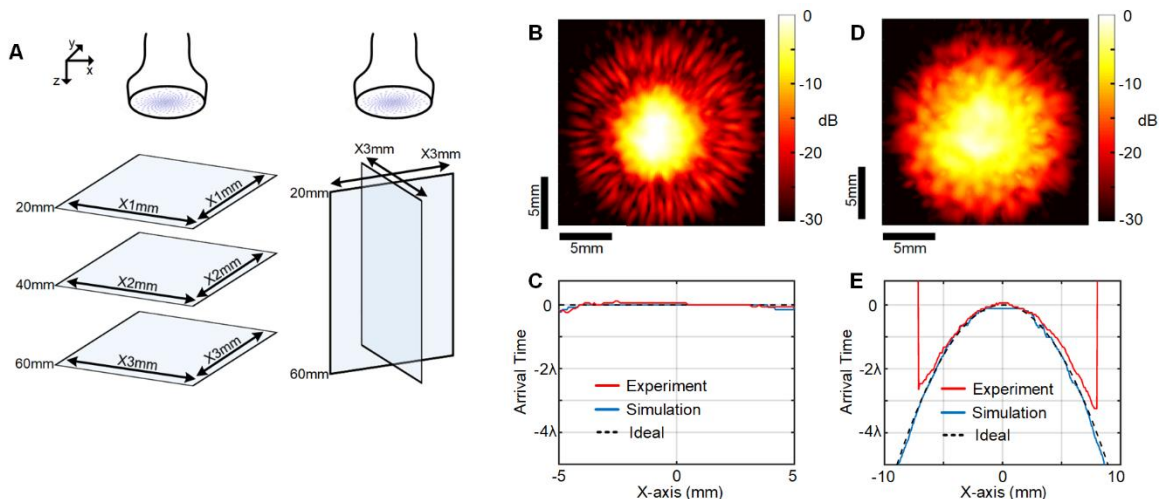


Figure: A) Measurement setup, B) measured peak amplitude and C) phase profiles for plane wave, and D-E) for diverging wave transmissions all at 7.5MHz and 20mm depth.

Inhomogeneity and ramping effects in delta relaxation enhanced magnetic resonance

Matthew A McCready¹, William B Handler¹, Blaine A Chronik¹

¹Department of Physics and Astronomy, Western University, London ON, Canada

INTRODUCTION: Delta relaxation enhanced magnetic resonance (DREMR) is a contrast-enhanced MRI method for quantitative molecular imaging. DREMR uses a B_0 insert magnet to shift the strength of the static field in a pulse preparation phase of the pulse sequence. Using contrast agents with longitudinal relaxivity (r_1) dispersion (field dependence), images taken at different field strengths can be subtracted, resulting in signal proportional to the concentration of these agents.¹ In development of the DREMR method and design of previous DREMR coils, it was assumed that field homogeneity is unimportant for the DREMR system, and effects of ramping periods were ignored. Here, we find that field inhomogeneities, and these ramping periods have significant effects on DREMR images and that the improved homogeneity design method we recently developed² can reduce these effects.

METHODS: To see inhomogeneity effects analytically, we use the original DREMR subtraction where the images differ in field by the given inhomogeneity. We apply this method in MATLAB to various concentration distributions of contrast agents using their r_1 dispersion data and fields given by DREMR coil designs. Ramping effects require a new set of Bloch equations, where longitudinal field strength varies in time, and therefore so does r_1 in the presence of contrast agent. We consider only the longitudinal magnetization as DREMR is unaffected by behavior of the transverse. This is solved numerically in MATLAB using ode45 for the ramping periods, and solved analytically using the assumptions that ramping field strength is linear in time, r_1 is linear with B_z , and overall ramping time is small, so we ignore terms of $O(\Delta t^2)$ or higher.

RESULTS: Inhomogeneities in field shift were found to result in signal from dispersion-free pixels, and artefacts in signal from contrast agents. These effects can be seen through (1) for dispersion-free signal where ΔB^* is the DREMR field with some inhomogeneity, and in Figure 1 where inhomogeneity artefacts can be seen in a simulated image. Using our new design method², we can improve homogeneity and minimize these effects as seen in Figure 2. Ramping effects were also found to result in non-zero signal from dispersion-free tissue, and a change in signal from contrast agents. These effects can be seen through (2) for dispersion-free signal where ξ is the DREMR coil slew rate, and Δt_2 the flat top duration of the DREMR pulse, and in Figure 3 where dispersion-free signal is plotted against slew rate.

$$(1) I_{sub0} \approx \frac{2B_0(\Delta B - \Delta B^*)}{B_0^2 - \Delta B^2} \quad (2) I_{sub0} \approx \frac{2M_0B_0}{T_1} \left(\frac{\Delta B^2}{B_0^2 - \Delta B^2} \right) \left(\frac{1}{\xi} \right) e^{-\Delta t_2/T_1}$$

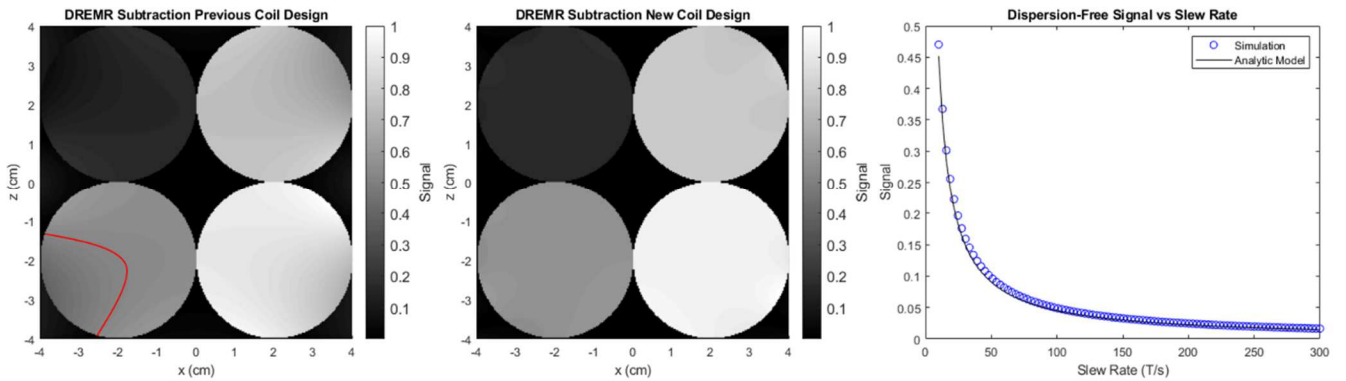


Fig 1 (LEFT). Simulated DREMR image of 4 cylinders of VivoTrax, in concentrations of 20, 80, 120, and 160 μM , using field of previously constructed coil. Banding (shown in red) occurs along field contour lines. Fig 2 (MID). Same simulation using field from new design method coil, banding is significantly reduced. Fig 3 (RIGHT). Simulated and analytic dispersion-free signal over slew rate, for same pulse parameters and signal scale as Figures 1 and 2.

CONCLUSIONS: Field inhomogeneities can lead to banding artefacts in DREMR images, and signal from dispersion-free regions. These effects can be minimized by using improved homogeneity coil designs. The ramping periods of DREMR pulses result in signal from dispersion-free regions and a change in signal from contrast agents, but these effects can be mitigated by using a high slew rate.

[1] Alford J, Rutt B, Scholl T, et al. MRM. 2009;61(4):796–802. [2] McCready M, Handler W, Chronik B, ISMRM. 2020;1258.

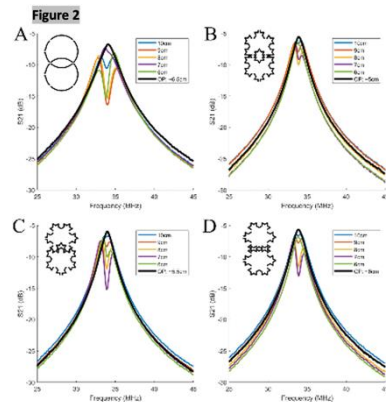
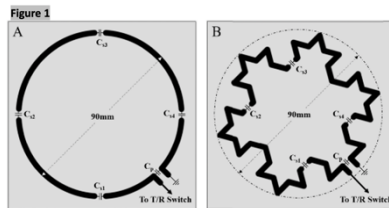
Network Parameter and Quality Factor Assessment of Fractal RF Coils for Sodium MRI

Cameron Nowikow¹, Norman Konyer², Natalia Nikolova³, and Michael D. Noseworthy^{1,2,3}

¹School of Biomedical Engineering, McMaster University, Hamilton; ²Imaging Research Centre, St. Joseph's Healthcare, Hamilton; ³Electrical and Computer Engineering, McMaster University, Hamilton

Introduction

Due to a low *in vivo* concentration, rapid T_2 relaxation and lower gyromagnetic ratio sodium MRI suffers from significantly lower SNR than typical proton-MRI scanning.¹ As such there have been many efforts focused on novel pulse sequences and higher field strengths in an effort to maximize signal. There has been minimal effort, for example, on the RF coils for both transmission and reception of the B_1 field. Coil geometry is important for performance and in efficiency of coupling to tissues and to each other (in phased arrays). There are a few parameters that are looked at when determining the intrinsic performance of an RF coil. The S_{11} parameter indicates quality of matching (to 50Ω), where for an optimal match there is less signal loss between the coil and the system. The quality factor (QF) is an inversely proportional measure of signal power loss between the coil and object being imaged, where the higher the QF, the less loss between the coil and the tissue. The S_{21} parameter shows the interaction between two coils in an array and how strong the mutual inductance between the two coils are, where the less interaction the better. In an attempt to improve signal generation in ^{23}Na -MR images we investigated basic RF metrics to determine whether fractal-based RF coil designs are better than routine circular designs. It has been documented that fractal antennas, when in arrays, tend to have a lower mutual inductance and interaction with each other which could lead to better signal for phased-array coils in ^{23}Na -MRI.^{2,3}



Load		Circular	Fractal
Unloaded	S_{11} (dB)	-2.50	-4.00
	Q_U	199	178
	Q_L	28.26	29.59
Phantom	S_{11} (dB)	31	43
	Q_U	6.48	4.14
	Q_L	4.62 ± 0.51	7.06 ± 0.68
Knee	S_{11} (dB)	111 ± 12	105 ± 9
	Q_U	1.82 ± 0.19	1.70 ± 0.15
	Q_L	78 ± 16	91 ± 14
Abdomen	S_{11} (dB)	-6.97 ± 1.56	-8.60 ± 1.71
	Q_U	2.65 ± 0.53	2.01 ± 0.33
	Q_L	108 ± 14	104 ± 9
Head	S_{11} (dB)	-4.76 ± 0.67	-7.18 ± 0.76
	Q_U	1.87 ± 0.25	1.73 ± 0.16
	Q_L	104 ± 9	104 ± 9

Methods

Two different surface coils (circular and Koch fractal) were fabricated as copper etching on an FR4 substrate (**Fig.1**). All S-parameter and QF measurements were performed using an Agilent 4395A network analyzer and S-parameter test kit. Both the circular and fractal surface coil were tuned and matched, while being loaded by a 0.9% w/v saline phantom, to 33.8MHz, the Larmor frequency of sodium at 3T. To explore how effective each geometry was at matching to various anatomical regions both single coils were loaded with different body regions in 11 subjects and S_{11} was measured. Coil QF was calculated as the ratio of unloaded to loaded Q ($QF = Q_U/Q_L$). Subsequently pairs of both circular and fractal coils were evaluated for effects on mutual inductance. The S_{21} of each coil pair were measured at distances (center to center) from 6-10cm of separation, as well as at the optimal separation for a single S_{21} peak.

Results and Discussion

The fractal coil showed better S_{11} with various anatomical loading, but Q measures were worse (**Table**). This was likely due to the apparent “self-loading” as the unloaded fractal coil had higher S_{11} (-4dB vs. -2.5dB). Based on S_{21} curves the fractal coil was less sensitive to separation distances compared to circular (less profound peak splitting) (**Fig.2**). Due to the different orientations that the fractal coil pair can be arranged there are multiple separation distances where the peak is not split and the mutual inductance effects are minimized (black curves in plots) as opposed to just one optimal distance for the circular coil.

Thus, the fractal coil is more robust than a circular coil when it comes to impedance matching when being exposed to a variety of loads and could be a viable alternative for phase array designs.

References

1. Madelin G, Regatte RR. Biomedical applications of sodium MRI in vivo: Biomedical Applications of Sodium MRI. *J Magn Reson Imaging*. 2013;38(3):511-529. doi:10.1002/jmri.24168
2. Gianvittorio JP, Rahmat-Samii Y. Fractal Antennas: A Novel Antenna Miniaturization Technique, and Applications. *IEEE Antenna's and Propagation Magazine*. 2002;44(1):20-36. doi:10.1109/74.997888
3. Ha S, Nalcioglu O, Roeck WW, inventors; Fractal RF Coils for Magnetic Resonance Imaging. US Patent US 2015/0048828 A1. February 19, 2015.

Evaluating Gradient Induced Main Magnet Coil Heating

Diego F. Martinez, Arjama Halder, William B. Handler, Blaine A. Chronik

The xMR Labs, Department of Physics and Astronomy, Western University, London ON, Canada

INTRODUCTION: Development of cryogen-free MR systems has provided the possibility for more accessible systems which using state of the art gradients could be used to provide high quality images comparable to higher field systems¹. These systems rely on a cold head to draw heat away from the superconducting coils, instead of the coils being directly immersed in the cryogen. Due to this, there is a higher variation in the possible temperatures of the coils, as the ability to regulate the temperature is somewhat limited by this heat sink process.

Earlier work has investigated both the effects on stability that are posed by nearby elements², and the general stability concerns from internal interactions³. In this study, we explore the effect that the operation of a gradient has on the main magnet, initially on the temperature of the coils with an eye towards analysing field shifts induced.

METHODS: The quench dynamics were investigated using series of 7 temperature probes which touch points throughout the coils of a cryogen-free superconducting magnet designed to operate at a maximum field of 0.5T at 101A. The temperature probe voltage outputs were exported with a NI DAQ system, using a LabVIEW program to collect data until the temperature was deemed to have settled to an equilibrium. Two gradient pulse sequences were tested using the x-axis gradient: a diffusion pulse made up of a single trapezoid with a rise time of 0.1ms and a duration of 100ms, as well as an EPI train with each trapezoid having duration 30ms. The maximum gradient amplitude was set by varying the voltage throughout the gradient coils, with trials at 3.5V and 7V. The analysis of the temperature shift was done using MATLAB and Python to optimize a fit using a simple $A(1-e^{-x})$ shape to model the behaviours of the main magnet coil temperature over the duration of the gradient operation. The model of the quench was used to test the predicted settling time (time until the temperature reached equilibrium).

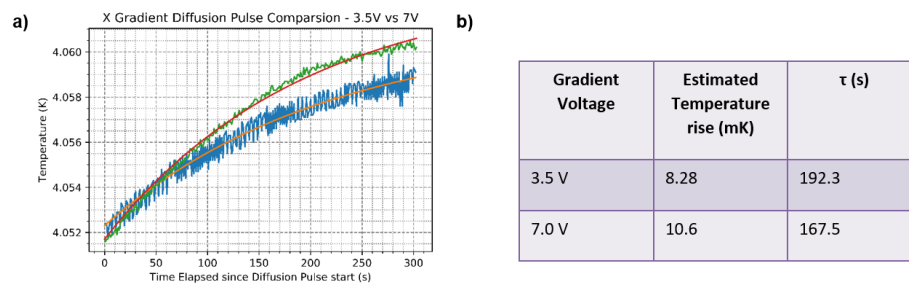


Figure 1: **a)** Set of Heating experiments comparing heating using different trapezoidal gradient strengths. **b)** Table analysing the fits, displaying the settling time constant for the heating.

RESULTS: The magnet temperature dynamics for a repeated diffusion gradient pulses are shown in **Figure 1a** with fits shown. In **Figure 1b**, the simple exponential fit parameters are described with the key term being the time constant which allows us to estimate the settling time until an equilibrium temperature is reached in the system.

DISCUSSION: In this preliminary study, **Figure 1b** is key in guiding our insight into the effects that the gradient has on the main magnet. The time constant until the equilibrium is reached being on the order of minutes should help to ensure that the appropriate amount of time is taken to fully see the effect that occurs in the magnet system. In a larger sense however, these results show that the estimated increase in temperature is only on the order of 10s of milli-Kelvin, which for the immediate concerns of reaching a critical temperature where the main magnet ceases to be superconducting is not a serious risk. It was always going to be unlikely to quench the magnet purely due to the gradient but ensuring this is still an important consideration in gradient design. The further concern to be investigated is the effect that these induced currents on the magnet have on the stability of the magnetic field, as there is a clear interaction effect found between the gradient pulse design and the main magnet coils.

CONCLUSION: In order to improve the design of gradients for cryogen free MR systems, the interaction between a common trapezoidal diffusion pulse run on an x axis gradient and the main magnet was investigated, with the resultant temperature change in the main magnet coils being quantified and guiding further study.

REFERENCES: [1] Campbell-Washburn, A. E., Ramasawmy, et al. (2019). Opportunities in interventional and diagnostic imaging by using high-performance low-field-strength MRI. *Radiology*, 293(2), 384-393. [2] Martinez, D. F et al. (2020) MRI Room Placement: The effect of an elevator operation on local magnetic environment. 2020 ISMRM Annual Conference Proceedings. [3] Kryukov, Eugeny, et al. (2020) On the magnetic field stability of cryogen-free magnets for magnetic resonance applications. *Solid State Nuclear Magnetic Resonance* 105 (2020): 101639.

Radiofrequency Coils for Single-Sided Portable Magnetic Resonance

Doris Rusu, Jean-Marc Beneteau, Jordyn Matthews, Dan Xiao

Department of Physics, University of Windsor, Windsor, ON, Canada.

Introduction: Magnetic resonance imaging (MRI) is an imaging modality that offers superior soft tissue contrast without ionizing radiation. However, the high cost of MRI limits its accessibility. A portable magnetic resonance device based on a permanent magnet is extremely cost-effective and could provide point-of-care diagnosis for near surface organs. However, the permanent magnet has a low magnetic field strength and severe field inhomogeneity which bring new challenges for quantitative measurements. In this work, radiofrequency (RF) coils are investigated in search for the optimal performance configuration.

Methods: A single-sided magnet based on the design of a three-magnet array [1] provides a static magnetic field with a homogenous volume of approximately 1 cm^3 centered 1cm from the surface, as shown in Fig. 1. The B_0 (0.1T) is parallel to the magnet surface. Three transceiver coil configurations were investigated: a surface loop coil, a D-loop coil and a meander line coil. The B_1 field of three RF coils were simulated using SIM4Life Lite. The coils were constructed and tuned to 4.4MHz. A Magritek Kea2 spectrometer was used to execute spin-echo experiments on a water phantom.

Results and discussion: The constructed coils, simulated B_1 fields, and spin echo signals are shown in Fig. 2. The meander line coil provided a B_1 field parallel to the surface and the other coils had a homogeneous B_1 in the center, perpendicular to the surface. From the spin-echo experiments with 128 signal averages, the signal-to-noise ratio values for the surface loop, D loop and meander line coil were 11.5, 8.2 and 4.8, respectively. The signal bandwidths varied between 50 and 100 kHz, due to the highly inhomogeneous static magnetic field. Only bulk signals have been acquired. Mechanical scanning is possible for spatial information. The inherent B_0 field distribution could be exploited for spatial encoding. Gradient and/or shimming coils will be incorporated in the future.

Conclusion: Three RF coils were constructed for a 0.1T single-sided magnet. The spin echo signals were acquired. The preliminary results indicate further optimization is required for this highly complex system. It will be beneficial to design an RF coil producing a B_1 field that matches the B_0 field distribution. The open MR system provides an affordable complement to the traditional high field MRI.

Reference: [1] Marble, JMR 186, 100-104 (2007).

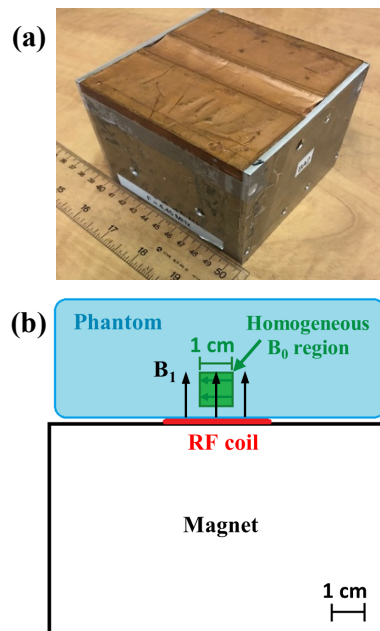


Fig 1. (a) The single-sided magnet and (b) a side-view schematic of the magnetic field configuration.

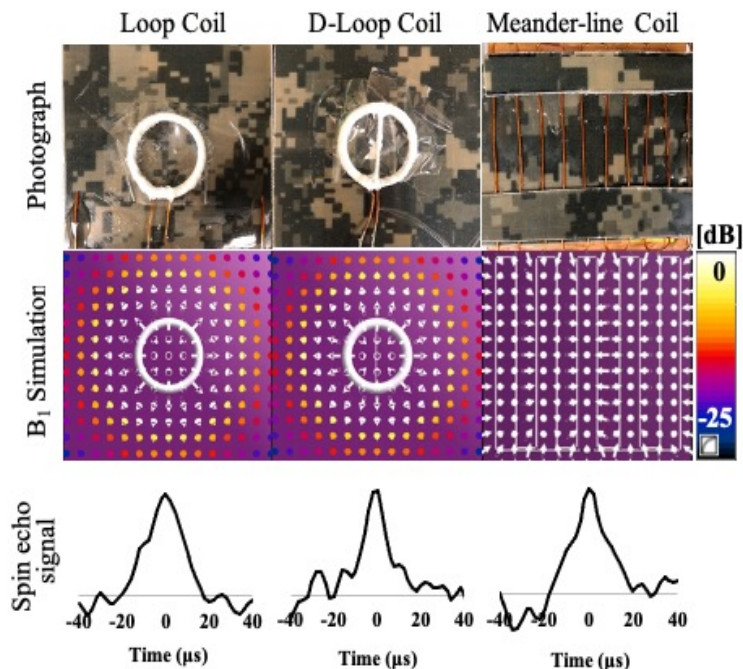


Fig 2. Design, simulation and performance comparisons of a loop coil, D-loop, and Meander-line Coil for a 0.1T permanent magnet.

DS- MT- BOUND SOLVENT- AND 4-POOL GLUCOCEST OPTIMIZATION OF SIMULTANEOUS MULTIPLE OFFSET SATURATION PULSE VIA GENETIC ALGORITHM

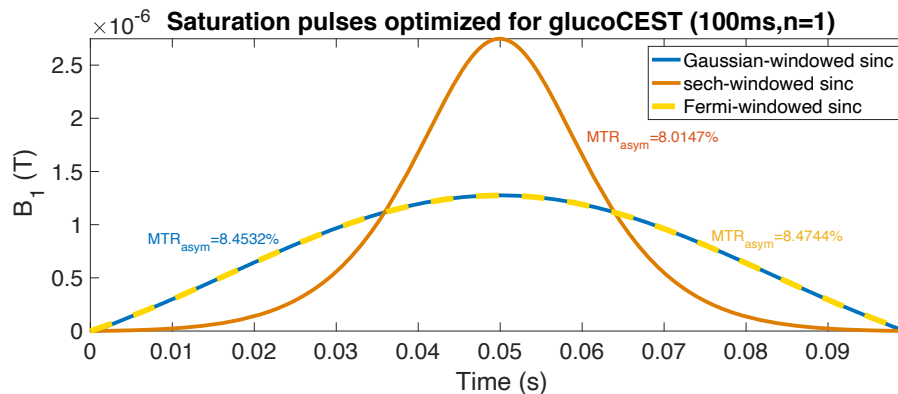
Sid Sadanand^{1,3}, Nicole Waddell^{1,3}, Greg Stanisz², Dafna Sussman^{1,3,4}

¹Departments of Biomedical Physics and of Biomedical Engineering, Ryerson University, ²Department of Medical Biophysics, University of Toronto & Sunnybrook Research Institute, ³Institute for Biomedical Engineering, Science and Technology (iBEST) at Ryerson University and St. Michael's Hospital, ⁴Department of Obstetrics and Gynecology, University of Toronto

INTRODUCTION: Glucose chemical exchange saturation transfer (glucoCEST) is a magnetic resonance (MR) imaging technique. It measures nuclear spin saturation transferred and accumulated through chemical exchange in the solvent, allowing for an amplification of the analyte signal through repeated (pulsed) or extended (continuous wave, CW) off-resonance saturation, forming a so-called Z-spectrum^[4]. The resultant increased signal allows for quantification of more dilute analytes and more rapid imaging^[8]. We propose to increase glucoCEST motion robustness by shortening acquisition duration through simultaneously saturating multiple glucose proton resonances in a single saturation pulse^{[1][2][5]}. We present an optimization algorithm for CW glucoCEST with multiple off-resonance saturation within a single pulse, considering CEST contrast confounds from direct saturation of water (DS), other magnetization transfer (MT) mechanisms, and bound solvent saturation^{[3][6][7][8]}. The resultant optimized saturation pulses facilitate rapid glucoCEST imaging that is both high in sensitivity and specific to analyte signal, mitigating confounding magnetization transfer mechanisms.

METHODS: Exchange rate, chemical shift, T_1 and T_2 of each proton pool were obtained from literature, alongside physiological glucose concentration of 4.0132mM. In a MATLAB script, equilibrium magnetization of each pool was then calculated. A differential equation solver was then used to model the time evolution of each pool's magnetization due to a hypothetical saturation pulse from these initial conditions using the rotating frame Bloch-McConnell equations. Additional pools in a neighbourhood of each glucose proton were generated and modelled similarly to reflect the confounding signal from glucose-bound solvent protons. The integral of the difference of these solutions with and without exchange to the solvent pool were the resultant CEST signal contributions from each pool. A genetic algorithm (GA) was used to optimize for the difference in CEST signal contribution from glucose protons to those of the confounding contributors by varying pulse apodization function shape parameters across 3 apodization function archetypes on a sinc pulse: supergaussian, Fermi, and pseudo-adiabatic sech. The GA was constrained to a parameter space determined by hardware and pulse sequence limits of available MRI scanners: CW 100ms pulse width, 8 μ T B_1 field, 2.89T B_0 field.

RESULTS:



The resultant optimized apodization functions are plotted above, alongside each pulse's glucoCEST signal (MTR_{asym}) as a percent attenuation of water signal without saturation. Gaussian and Fermi archetypes converged to similar solutions, marked by a dashed line. The optimization was constrained to a single ($n=1$) 100ms pulse.

CONCLUSIONS: A Fermi-apodized pulse resulted in both the highest CEST signal and the greatest specificity for glucose protons. These resulting optimized apodization functions are implemented in a CEST work-in-progress pulse sequence, and the simulated CEST effect and contrast will be verified on glucose phantoms of varying concentrations, with MT confounds.

REFERENCES: [1] Lee et al., JMR (2012) 215, 56–63. [2] Lee et al., Sci Rep (2013) 3(1), 1707. [3] Schmitt et al., MRM (2011) 65(6), 1620–1629. [4] Van Zijl et al., NeuroIm (2018) 168, 222–241. [5] Varma et al., JMR (2015) 260, 67–76. [6] Yoshimaru et al., JMR (2016) 263, 184–192. [7] Zaiß et al., NMR in Biomed (2015) 28(2), 217–230. [8] Zaiß et al., NMR in Biomed (2019) 32(9), e4113

Necessity of using Impulse-Sampled Notation and Fourier Transform rather than Discrete Fourier Transform for Determining Spectral Performance of Image Post Processing

A. Salsali (Western U), P. Picot (Robarts Research Inst), J. Tanguay (Ryerson U) and I.A. Cunningham
(presenter, Robarts Research Inst, Western U)

Introduction

Many detectors incorporate processing algorithms that are deeply embedded in the imaging chain and do not make unprocessed image data available as required for the presampling modulation transfer function (MTF) and detective quantum efficiency (DQE), which questions the value of these metrics. We describe a mathematical framework to determine the presampling frequency response of post-processing algorithms with implications for MTF and DQE calculations.

Methods

We show this can be achieved only if we express the digital image d_i (i denotes pixel) in an integrable form as a function of position, rather than simply a vector or matrix of discrete d_i values. We use the impulse-sampled notation in which an image is represented as $d^\dagger(x)$, a distributed array of uniformly-spaced δ functions scaled by d_i where $d^\dagger(x) = \sum_i d_i \delta(x - ix_s)$ having units mm^{-1} in one dimension.

Results

This enables the use of all Fourier transform properties, including the Wiener-Khinchin theorem to describe noise. Three-pixel binning, for example, corresponds to an offset-cosine MTF, $\text{MTF}_f(u) = \left| \frac{1}{3} + \frac{2}{3} \cos(2\pi x_s u) \right|$, rather than a sinc-shaped MTF as might otherwise be expected.

Conclusions

1. The impulse-sampled notation is necessary to enable the use of Fourier properties and theorems.
2. The MTF of discrete convolution is always unbounded, periodic with period $u = 1/x_s$, and is symmetric with respect to integer multiples of the sampling cut-off frequency $u_c = 1/2x_s$.
3. Sampling (digitizing an analog function) commutes with linear processing which provides a way of determining the presampling MTF from processed images.
4. The presampling MTF, including enhancement from post-processing, is correctly measured using the slanted-edge method when using processed images which necessarily contain aliasing artifacts, and the presampling MTF remains accessible to measurement even when unprocessed image data is not.

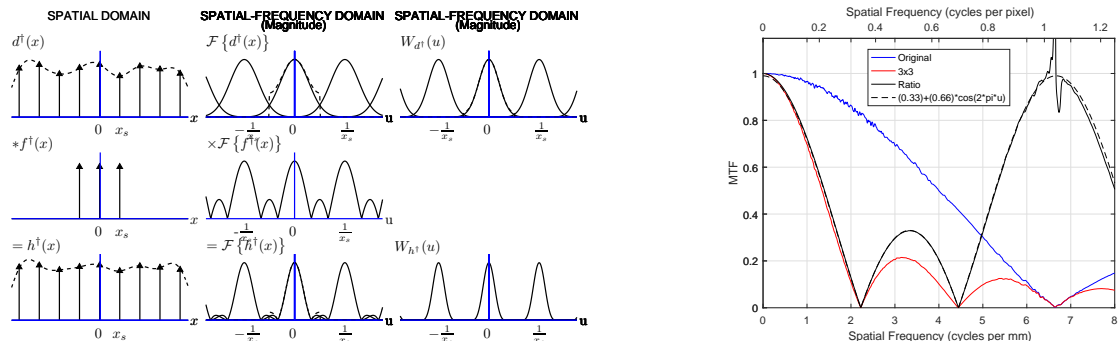
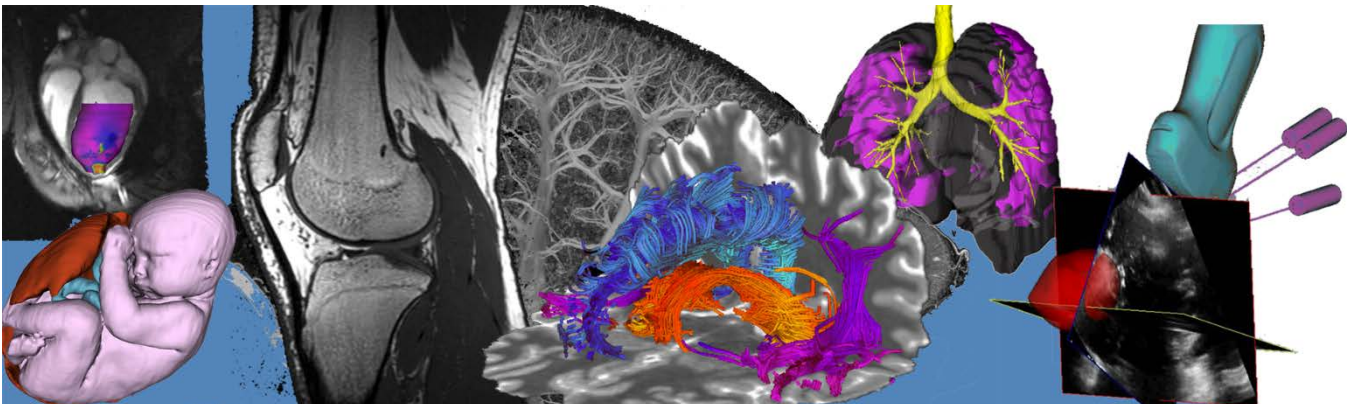


Figure 1. Left: Three-pixel binning is discrete convolution of d_i with $f_i = [\frac{1}{3} \frac{1}{3} \frac{1}{3}]$. Right: The corresponding MTF is an offset cosine curve (black), the Fourier transform of three δ functions, rather than a sinc function (red) as might be expected.

Pitch Presentation Abstracts

Session 9: Contrast Agents I



Longitudinal Observation of the Emphysema Progression in Alpha-1 Antitrypsin Deficiency Using $^3\text{He}/^{129}\text{Xe}$ MRI

Elise Woodward¹, Matt Fox^{1,2}, Tingting Wu¹, David G. McCormack⁵, Grace Parraga^{3,5}, Alexei Ouriadov^{1,2}

¹Department of Physics and Astronomy; ²Lawson Health Research Institute; ³Robarts Research Institute; ⁴Department of Medical Biophysics; ⁵Division of Respiriology, Department of Medicine, The University of Western Ontario, London, Canada.

RATIONALE: Hyperpolarized (HP) gas pulmonary MRI^{1,2} provides physiologically relevant biomarkers Apparent Diffusion Coefficient (ADC) and mean linear intercept estimate (L_m) of obstructive lung disease. However, the longitudinal observation of the emphysema progression using HP gas MRI-based ADC/ L_m can be problematic, as the disease progression can lead to increasing unventilated lung areas, which likely excludes the largest ADC/ L_m values.³ A solution is to combine static-ventilation (SV) and ADC/ L_m measurements; we have previously developed a lung morphometry method allowing us to acquire SV images and ADC/ L_m maps during a 16sec single breath-hold.^{4,5} We hypothesize that this morphometry method can overcome the above-mentioned shortcomings and provide an accurate assessment of the emphysema progression. For this work, we used the SV & ADC/ L_m data acquired using the traditional approach (^3He data, 2014) and our method (^{129}Xe data, 2018). A small group of patients was involved for 4 years of HP gas pulmonary studies focused on emphysema progression.

METHODS: 4 AATDs provided written informed consent to an ethics board approved protocol and underwent two visits, four years apart that included CT, spirometry, plethysmography, DLco and MRI including anatomical ^1H , $^3\text{He}/^{129}\text{Xe}$ diffusion-weighted (DW) & SV imaging. MRI was performed at 3.0T as previously described.³ 3D $^3\text{He}/^{129}\text{Xe}$ MRI-based ADC and lung morphometry maps were generated using the stretched-exponential-method⁴ which was extended and adapted for both $^3\text{He}/^{129}\text{Xe}$ to provide clinically-relevant biomarkers of emphysema.⁵ AATD=Alpha-one antitrypsin deficiency.

RESULTS: Figure 1 shows 5 representative SV slices obtained for the AATD-1 subject with ^3He (top-panel, 2014) and ^{129}Xe (bottom-panel, 2018). The global VDP/ADC/ L_m estimates for all subjects are summarized in Table 1. The global mean estimates obtained for four AATD subjects with ^3He (dark green, 2014) and ^{129}Xe (cyan, 2018). Only VDP^{He}/VDP^{Xe} & $L_m^{\text{He}}/L_m^{\text{Xe}}$ can be compared directly.

DISCUSSION: We showed that the emphysema progression over the 4-year term can be quantified by using MRI-based SV & ADC/ L_m . The estimates generated from the SV imaging shows lung health worsening over the study term and the emphysema biomarkers generated from the DW imaging suggest a slow disease progression. The increased number of the ventilation defects can be clearly seen on Figure 1. There were however, some significant decreases in ^{129}Xe L_m values ($p=.007$), which indicates an apparent lung health improvement. To avoid this analytical mistake, one should normalize the ADC/ L_m by the VDP and thus take into account the decrease in ventilated lung volume. The feasibility of such approach has been recently demonstrated using the ^3He SV & DW data.⁴ Our ^3He datasets were acquired using two separate breath-holds and different voxel-sizes between SV & DW data so, the slice resolution difference and slice mismatch make this task very difficult. Our ^{129}Xe datasets were acquired using a single breath-hold accelerated imaging approach allowing SV & ADC/ L_m mapping simultaneously^{4,5} so, there are no slice resolution difference and slice mismatch. For future work, we plan to normalize the ^{129}Xe ADC/ L_m estimates by ^{129}Xe VDP for an accurate assessment of the emphysema progression.

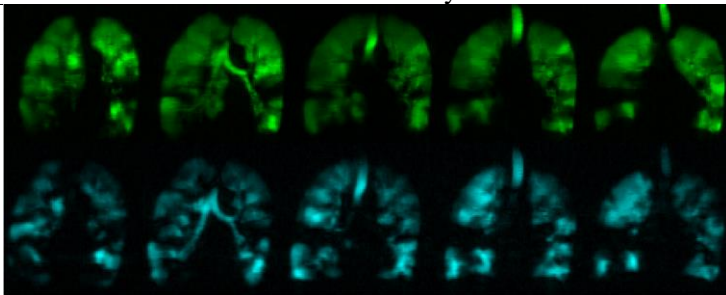


Table 1: ^{129}Xe MRI Parenchyma Measurements

	AATD-1	AATD-2	AATD-3	AATD-4
Global ADC (cm^2/s)	0.63 ± 0.11	0.53 ± 0.09	0.37 ± 0.10	0.43 ± 0.11
Global ADC (cm^2/s)	0.1 ± 0.02	0.08 ± 0.02	0.07 ± 0.03	0.07 ± 0.03
Global L_m (μm)	1000 ± 180	940 ± 115	690 ± 120	715 ± 130
Global L_m (μm)	870 ± 112	750 ± 111	640 ± 261	630 ± 159
Total VDP, %	15.0	7.0	7.5	26.0
Total VDP, %	9.4	7.0	3.0	24.0

AATD=Alpha-one antitrypsin deficiency; AATD-1= Ex-smoker AATD.

Figure 1. $^3\text{He}/^{129}\text{Xe}$ MRI SV Images obtained for AATD-1.

Table 1. $^3\text{He}/^{129}\text{Xe}$ MRI Parenchyma Measurements.

References

1. Mugler, J. P. et al *JMRI* **37**, (2013).
2. Driehuys, B. et al. *Radiol* **262**, (2012).
3. Kirby M et al. *Radiol* **265** (2012).
4. Westcott A et al *JMRI* **49** (2018).
5. Ouriadov A et al *MRM* **84** (2020).

Acknowledgments

A. Ouriadov was funded in part by the Alpha-1 Foundation.

Effect of low dose daily aspirin on cerebral blood flow and kidney function in hypertensive rats

Greg O. Cron^{1,2,3}, Rafael Glikstein^{1,3}, Jean-François Thibodeau¹, Anthony Carter¹, Chet E. Holterman¹, Alexey Gutsol¹, Lihua Zhu¹, Baptiste Lacoste¹, and Chris Kennedy^{1,2}

¹University of Ottawa, ²Ottawa Hospital Research Institute, ³The Ottawa Hospital

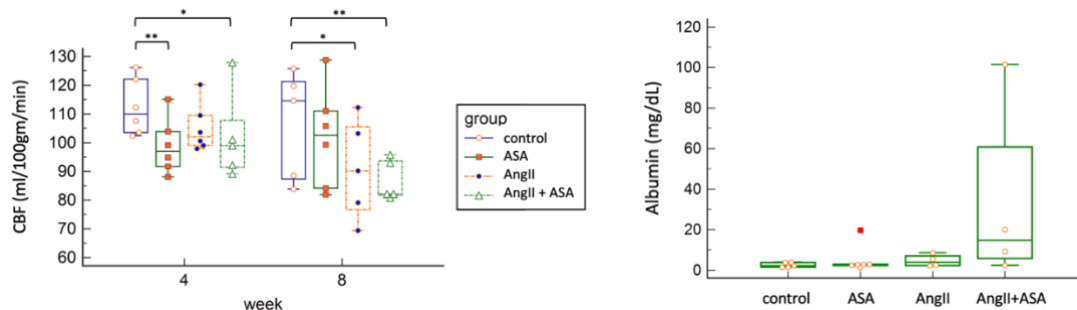
Introduction Patients taking low-dose aspirin to reduce the probability of future heart attack or stroke are usually well-informed about the risk of major bleeding. For hypertensive patients, however, nonsteroidal anti-inflammatory drugs (NSAIDs) such as aspirin may carry an additional risk of kidney injury. NSAIDs block vasoactive prostaglandin production, potentially blunting the reopening of hypertension-constricted renal vessels, thereby decreasing renal blood flow (1). We recently showed evidence of this in rodent models of hypertension (2-4). In this study, we hypothesized that hypertension would predispose rats to low-dose aspirin induced kidney and cerebrovascular injury, due to reduced blood flow.

Methods Four groups of animals were used: 1) control - wild-type male Sprague Dawley rats, n=6; 2) ASA - rats given low-dose acetylsalicylic acid (aspirin) at 1mg/kg/day, n=6; 3) AngII – rats given Angiotensin II at 200ng/kg/min to induce hypertension, n=6; 4) AngII+ASA – rats given the combination, n=7. The experiment was run for 8 weeks, with drugs delivered by osmotic minipumps, implanted subcutaneously at baseline. Whole-brain cerebral blood flow (CBF) was assessed *in vivo* using dynamic contrast-enhanced MRI at baseline, +4 and +8 weeks (5). Urinary albumin levels were measured by ELISA as a surrogate of kidney injury. At endpoint, cerebral and renal vascular injury were assessed by histology and immunohistochemistry for CD-31 and Caveolin-1.

Results Two rats from the AngII+ASA group died between weeks 0 and 4, leading to only n=5 at weeks 4 and 8 for that group. At +4 weeks, CBF for ASA and AngII+ASA were lower than controls (Dunnett's multiple comparisons test, P=0.003 and 0.04). At +8 weeks, CBF for AngII and AngII+ASA were lower than controls (P=0.03 and 0.004). Unique to the AngII+ASA group, we observed cerebral vascular remodeling of pial, intracerebral arteries/ arterioles as well as thickened arterial media, narrowed lumens and accumulation of PAS-positive material. Caveolin-1 was significantly enhanced in the endothelium and the media of the intracerebral arteries, arterioles and capillaries. Assessment of kidney injury revealed thickening of the arterial media with increased accumulation of PAS-positive material, rarefaction of smooth muscle cell (SMC) nuclei, accumulation of monocytes in the adventitia. Caveolin-1 was significantly enhanced while CD31 was reduced in glomeruli, interlobular and arcuate arteries. Albuminuria was highest for AngII+ASA, however due to high variance this was not statistically significant.

Conclusion Hypertensive rats who received low-dose daily aspirin appeared to have decreased CBF, however the data must be interpreted with caution, as statistical power was lacking. Of interest, rats given both AngII and ASA developed significant kidney and cerebrovascular injury, suggesting a possible deleterious effect of this drug combination on the vasculature.

References 1. Whelton A. Am J Ther. 2000 Mar;7(2):63-74. 2. Cron et al, Proc. ISMRM 23 (2015), abstract # 1575. 3. Thibodeau, Jean-Francois, et al. Antioxidants and Redox Signaling (2016). 4. Cron et al, Proc. ISMRM 26 (2018), abstract # 4598. 5. Livingston, Jessica M., et al. Neurobiology of Disease 137 (2020): 104756.



A Remarkably Stable Manganese(III) Porphyrin as a Building Block for Bioconjugation

Keith Tang^{1,2}, Xiao-an Zhang^{1,2,3*}

¹Department of Chemistry, University of Toronto. ²Department of Physical and Environmental Sciences, University of Toronto Scarborough. ³Department of Biological Sciences, University of Toronto Scarborough.

Introduction: Contrast agents (CAs) are routinely used in magnetic resonance imaging (MRI) to improve signal intensity and enhance tissue contrast. To date, gadolinium-based contrast agents (GBCAs) had dominated clinical applications, with small, non-specific, extracellular fluid agents being the most widely used. New advances in targeted MRI CAs with affinity for specific cellular biomarkers could dramatically expand the effectiveness of MRI applications for early disease detection. However, development is limited for two major reasons: 1) low MRI sensitivity prevents the detection of small number of targetable molecular disease biomarkers and 2) safety concerns over the in vivo stability of commercial GBCAs due to the release of dissociated toxic Gd^{3+} ions. To address the unmet need of more stable and safer MRI CAs with comparable or even higher sensitivity than that of commercial GBCAs, our group focuses on the use of manganese(III) porphyrin (MnP) complexes which have abnormally high r_1 at clinically relevant fields¹, as well as better biocompatibility than Gd .² Our studies on the stability of MnTCP (a small, polar, water soluble porphyrin) found them to be remarkably stable under a variety of stressed conditions including low pH and an excess of endogenous metal ions known to cause metal dissociation in GBCAs. In order to address the inherent low sensitivity of targeted MRI CAs, MnP complexes were synthesized with a functionalized bioconjugation handle that can be covalently attached to a polymeric backbone. This molecular design would enable linkage of the backbone to biomacromolecules (i.e. antibodies) with highly specific target recognition.

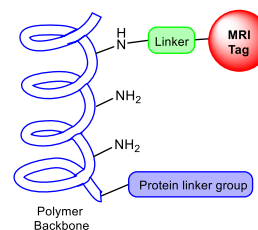


Figure 1: Molecular design of polymeric Mn(III)-porphyrin bioconjugates.

Methods: MnTCP and MnP-based MRI tags (Fig. 2) were synthesized using a 2+2 porphyrin synthesis with appropriate aldehyde precursor followed by metal insertion^{3,4} and characterized. For stability studies, MnTCP stock solutions were prepared in 25 mM citric acid buffer (pH 2, 3, 5, and 7) and was incubated with increasing concentrations of several divalent metal ions, including Ca, Cu, Mg, Fe and Zn at 25°C and 37°C. MnTCP solutions were prepared from the stock in 25 mM HEPES (pH 7.43) and measured over time using UV-Vis.

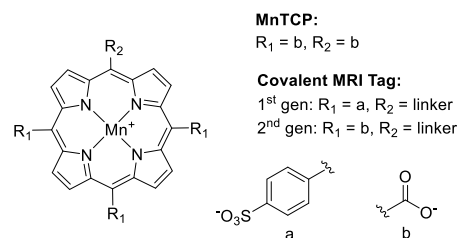


Figure 2: Structure of MnTCP and covalent MRI tag with bioconjugation handle for linking to polymeric backbone.

Results: *Stability:* There were no significant changes in the UV-vis absorption for MnTCP at pH 2-7 over the monitoring period up to 54 days, based on the absorbance ratio of 465 nm peak (for MnTCP) to 407 nm peak (for the free-base porphyrin). Increasing metal concentrations of Zn^{2+} , Ca^{2+} , Cu^{2+} , Fe^{2+} , and Mg^{2+} were investigated up to 10 times the MnTCP concentration and no change in the UV-vis absorption was observed at both 25 °C and 37 °C. Data suggests that MnTCP is thermodynamically stable and kinetically inert as no metal-free or trans-metallated porphyrin can be detected in solution. *Polymeric MRI CA:* The r_1 data of monomeric MnP and polymeric MnP bioconjugate demonstrated a considerable increase in r_1 upon linking with polymer across higher magnetic field strengths (1-3T). We then have synthesized and are currently working towards characterizing MnPs with improved water solubility and coupling efficiency towards the polymeric backbone.

Conclusion: MnTCP shows remarkable thermodynamic and kinetic stability under various stresses, making it a promising platform for targeted MRI. The design of a novel, covalent MRI tag linked to a polymeric backbone shows potential as a high relaxivity CA with specific epitope recognition once conjugated to a protein targeting moiety. Current work includes furthering improving solubility and coupling efficiency to achieve optimized covalent MRI tags for broad future applications.

References: ¹ *Magn. Reson. Med.* **1987**, 4 (3), 252–260. ² *Encyclopedia of Inorganic and Bioinorganic Chemistry*; Scott, R.A., Ed.; John Wiley & Sons, Ltd.: Chichester, UK, 2018; pp. 1–16. ³ *J. Med. Chem.* **2014**, 57, 516–520. ⁴ *Chem. Sci.* **2016**, 7 (7), 4308–4317.

Materials for Anthropomorphic MRI Phantoms

Eunyoung Cho^{1,2}, Mitchell Lee^{1,2}, Dafna Sussman¹⁻⁵

1. Department of Electrical, Computer, and Biomedical Engineering, Ryerson University, Toronto, ON, Canada
2. Institute for Biomedical Engineering, Science and Technology (iBEST), Ryerson University and St. Michael's Hospital, Toronto, ON, Canada
3. The Keenan Research Centre for Biomedical Science, St. Michael's Hospital, Toronto, ON, Canada
4. Department of Biomedical Physics, Ryerson University, Toronto, ON, Canada
5. Department of Obstetrics and Gynecology, University of Toronto, ON, Canada

Introduction: Magnetic Resonance Imaging (MRI) accuracy is often limited by motion and dielectric artifacts. Development of new MR sequences that avoid these artifacts pivots on extensive testing. Development of MRI phantoms that simulate tissue properties, anatomical structures, and gross body motion allows for rapid testing, along with reproducible data that will shorten the development time of such MR sequences. We identify materials that simulate the MR imaging and dielectric properties of the human muscle and brain tissues, which could be used for making anthropomorphic MRI phantoms of the human body.

Methods: Various experiments, including relaxometry and dielectric tests, were performed to determine the most appropriate tissue-mimicking material for simulating properties of the muscle, gray matter, and white matter tissues. In the relaxometry testing, Polyacrylic acid gels, and CAGN (Carrageenan+Agarose+Gadolinium +NaCl) gels, and silicone rubber were selected based on previously reported data from other studies and were measured by a 3.0-T scanner for T1 and T2 relaxation times. The dielectric constant (ϵ') and conductivity (σ) of CAGN gels and silicones were then evaluated to test whether they simulate the corresponding values of the tissue of interest.

Results: CAGN gels were found to simulate the relaxation times and dielectric properties of the muscle, gray matter, and white matter. The ability of CAGN gels to simulate high conductivities of the brain tissues will enable the resulting phantom to simulate the dielectric artifacts in MRI images due to field inhomogeneities at a high magnetic field strength. The silicone rubber was found to simulate the relaxation times of white matter and muscle, respectively. We determined that the structural and chemical stabilities of silicone rubber were more suitable to simulate muscle tissue than those of CAGN gels. Results are shown in Figure 1 and Table 1 below.

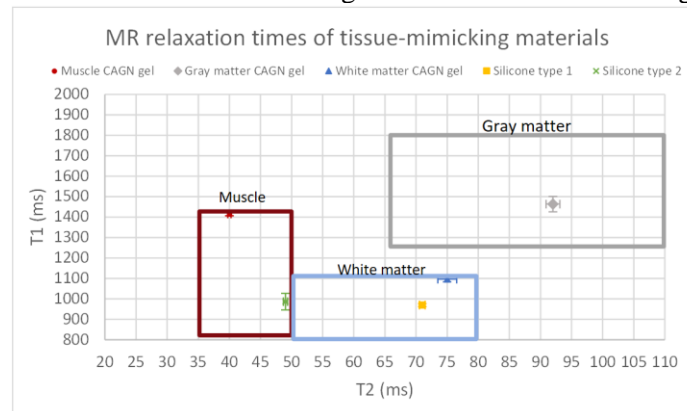


Figure 1. Relaxation times of tissue mimicking materials. The rectangular borders represent the T₁ and T₂ ranges of human tissues.

Targeted human tissues	Tissue-mimicking materials	Dielectric properties of human tissues		Dielectric properties of tissue-mimicking materials	
		ϵ' (F/m)	σ (S/m)	ϵ' (F/m)	σ (S/m)
Muscle	Muscle CAGN gel	64	0.717	82.02	0.713
	Silicone type 2			3.65	0.000267
Gray matter	Gray matter CAGN gel	74	0.585	83.39	0.582
White matter	White matter CAGN gel	53	0.344	79.75	0.345
	Silicone type 1			3.43	0.000226

Table 1. Dielectric properties of various human tissues and tissue-mimicking materials

Conclusions: We identified chemical formulations for tissue-mimicking materials that simulate the relaxation times and conductivities of muscle, gray matter, and white matter tissues. These could be used for making MRI phantoms the human body for MRI sequence optimization.

Characterizing the chronic evolution of ablation lesion and edema using native T1 and 3D late gadolinium enhancement (LGE) after radiofrequency ablation therapy (RFA) in a swine model of ischemic VT

Terenz Escartin^{1,3}, Philippa Krahn^{1,3}, Jen Barry¹, Melissa Larsen¹, Sheldon Singh^{1,2}, Graham Wright^{1,3}

¹ Sunnybrook Research Institute, Toronto, CA ² Dept. of Cardiology, University of Toronto, CA

³ Dept. of Medical Biophysics, University of Toronto, CA

BACKGROUND: Ischemic ventricular tachycardia (VT) is a life-threatening abnormally fast heart rate originating in the left ventricle (LV). Patients currently experience high recurrence rates¹ after standard catheter-based RFA therapy. VT recurrence may be related to resolving temporary electrical block due to ablation-induced edema which resorbs and results in reactivation of conduction channels (CCs). Non-contrast (Native) and late gadolinium enhancement (LGE) Magnetic Resonance Imaging (MRI) are emerging methods for guiding RFA therapy^{1,2,3,4,5,6}. Our goal is to characterize ablation lesion maturation, MVO and edema over a 30-day survival period in a swine model of ischemic VT.

METHODS: Myocardial infarction was created in N=2 swine via 100min occlusion-reperfusion. After 5 weeks, the pigs underwent CMR on a 3T GE scanner. We employed conventional native T₁ (TI = 750ms) and 3D LGE (1.4mm isotropic, TI = 300ms) imaging after a Gd-DTPA bolus (0.2mmol/kg). Pre-ablation 3D LGE images of the LV were segmented to identify the VT substrate (ADAS3D). Both pigs underwent conventional EP RFA therapy (CARTO3). Follow-up native T₁ (TI = 750ms-800ms) and 3D LGE (TI = 300ms) images were acquired on Day 0 (ablation day), D10 and D34 post-ablation. VT inducibility was performed after D34 (St. Jude EP-4 Stimulator). Anterior wall thickness was used to characterize edema (iTK-Snap).

RESULTS & DISCUSSION: Fig 1 shows the evolution of ablation lesion, MVO and edema. The ablation lesion is clearly visualized as a hyperintense signal in the anterior component of the LV where the ablation was prescribed on D0. This appears to subside by D34. The presence of edema is determined from the increased anterior wall thickness on D0 (10.6mm) compared to the pre-ablation image (4.1mm). Resorption of MVO and edema is clear by D10 and D34 with the wall thickness reducing to 6.3mm and 4.9mm respectively. The ablation lesion appears subendocardial and non-transmural. As such, VT was induced in both animals after D34 suggesting incomplete ablation of CCs.

CONCLUSION: We successfully demonstrated that native T₁ and 3D LGE at 1.4mm isotropic resolution characterizes the chronic evolution of ablation lesion, MVO and edema in a swine model of ischemic VT.

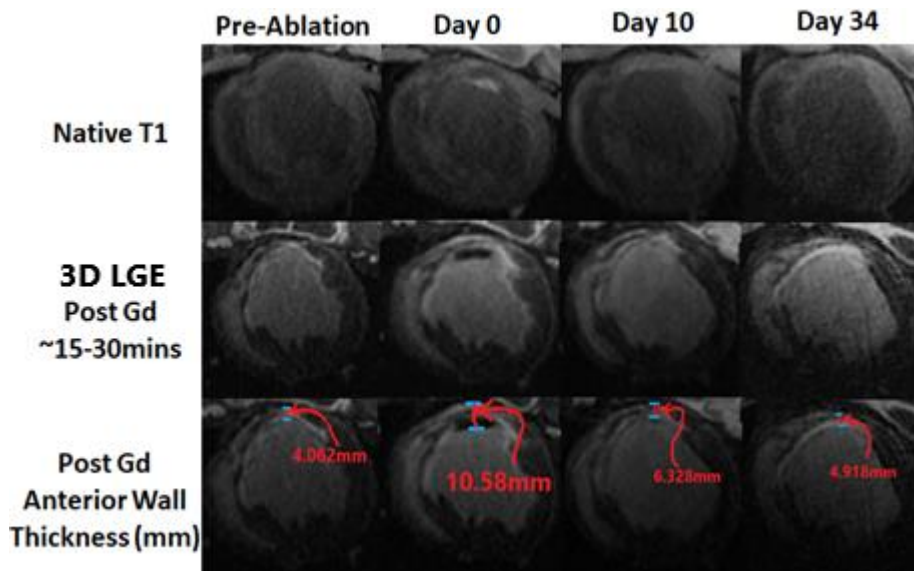


Figure 1. N=2 Yorkshire swine have recently completed the study timeline. Native T₁ (top row), 3D LGE (middle row), and 3D LGE with anterior wall thickness measurements (bottom row) of the LV across the study timeline in short-axis view. The evolution of ablation lesion as shown in the native T₁ appears as hyperintense signal in the anterior component of the LV and appears to have subsided by D34. The evolution of MVO and edema as shown in the 3D LGE images can be seen on the anterior side of the LV indicated by decreased wall thickness from D0 to D34.

REFERENCES

- [1] Soto-Iglesias D. et al. *JACC*, 4(6), 2020
- [2] Krahn P. et al. *JCMR* 20:20. 2018
- [3] Guttman, M. et al. *MR in Med.* 79.2 2018
- [4] Jauregui, B. et al. *JACC* 6.2 (2020): 207-218
- [5] Ghafoori, E. et al. *Circ Arr. Electro* 10.11 2017
- [6] Kholmovski, E. et al. *JCE* 29.11 1556-1562. 2018

A Bifurcating Microvessel Phantom to Assess Feature Resolvability in Sub-Diffraction Limit Contrast Ultrasound Imaging

Hanyue Shangguan¹, Billy Y. S. Yiu¹, Adrian J. Y. Chee¹, Alfred C. H. Yu¹, ¹Schlegel Research Institute for Aging, University of Waterloo, Waterloo, Canada

Introduction

The imaging resolution of medical ultrasound can be improved beyond the diffraction limit of ultrasound through Super-Resolution Imaging (SRI) techniques in leveraging the use of blood pooling contrast agents to visualize microvascular flow features. However, there is a lack of tools to assess the accuracy of resolved flow features, especially for microvessels at bifurcating junctions. Current strategies involve long-duration *in-vivo* acquisitions which does not allow for good understanding of interactions between flow rate, contrast concentration, and acquisition time. Conversely, an *in-vitro* tool provides informed assessment of SRI algorithms and parametric effects on feature resolvability. Here we propose the design of a two microvessel bifurcating phantom with vessel separability ranging from 50 μm to 1.3mm to validate the accuracy of microvessel feature cross-sections obtained using SRI.

Methods

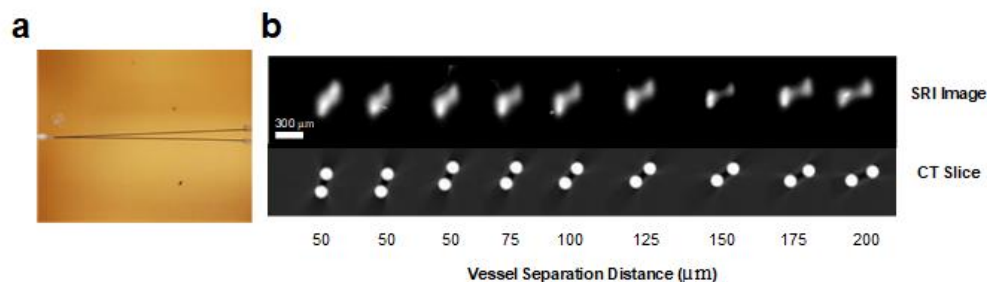
Bifurcating microvessels were created by mounting two 150 μm tungsten wires in a 3D printed box which positioned the wires in a Y-shape configuration (see Fig. A). Wires were twisted at the bifurcating face and tissue mimic was cast into the container. A micro-computed tomography (μCT) scan was taken with a 10 μm imaging resolution and slices analyzed using ImageJ to serve as the ground truth for vessel separability. After wire extraction, flow with contrast agent (concentration of 1.67×10^6 particles/ml) was fed into the lumen at a rate of 48 $\mu\text{l/s}$. Ultrasound imaging was performed on the short axis with unsteered plane wave transmissions (10 MHz; 3-cycle pulse) for 5s of acquisition with pulse repetition frequency of 1000 Hz. SRI processing was conducted using a contrast agent detection and deconvolution-based framework in MATLAB which visualizes the lumen by highlighting spatial positions that are most likely to contain detected contrast signals. Vessel separation was obtained as the distance between full-width half maximums of gaussians fit across the resolved channels for quantitative comparison with ImageJ measurements.

Results

Comparison of super-resolved lumens with μCT ground truth (Fig. B) demonstrate that the super-resolution algorithm assessed using our presented phantom is accurate in separating vessels up to 100-125 μm apart with the listed experimental conditions. The intensity of the right-side lumen was lower for all SR images and is apparent in the 150 μm SRI example, this was reflective of lower detected contrast signals within the right-side lumen due to slower flow relative to the left-side channel which was verified in experiment.

Conclusions

These results demonstrate the feasibility of the proposed phantom to assess feature separation of SRI under controlled *in-vitro* conditions facilitating future optimization in SRI experimental parameters.



Myocardial glucose suppression interferes with the detection of inflammatory cells with FDG-PET in a canine model of myocardial infarction

Authors: Wilk, B^{1,2}, Smailovic, H^{1,2}, Sullivan, R^{1,2}, Butler, J¹, Sykes, J¹, Kovacs, M¹, Wisenberg, G^{1,2,3}, Thiessen, JD^{1,2}, Prato, FS^{1,2}; 1: Western University, London, Ontario; 2: Lawson Health Research Institute, London, Ontario; 3: MyHealth Centre, Arva, Ontario

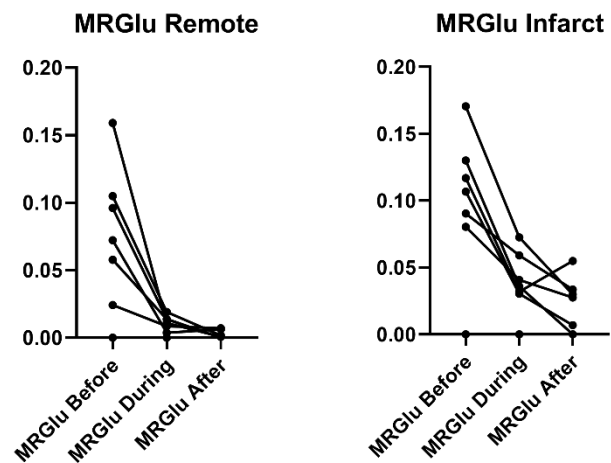
Introduction: Cardiovascular disease is the leading cause of death worldwide. Heart failure, specifically, is influenced to a major extent by dysregulation of inflammation which occurs after a myocardial infarction (MI)^[1]. MRI and extracellular volume (ECV) measurements have shown promise in detecting characteristics that can increase the risk of heart failure, including: infarct size, presence of hemorrhage and presence and size of an area of very low blood flow within the infarct called the region of microvascular obstruction (MO)^[2]. What is needed is an imaging method that can distinguish between pro-inflammatory (neutrophils and M1 macrophages) and anti-inflammatory (M2 macrophages) cells as dysregulation occurs when the pro-inflammatory phase is prolonged. It has been shown that FDG-PET can, in principle, distinguish between the pro- and anti-inflammatory cell types^[3]; however, post-MI there are some problems including uptake of FDG in resting healthy myocardium which has to be suppressed so that the uptake of glucose by inflammatory cells can be distinguished from uptake in healthy myocardium. Myocyte glucose uptake suppression in the canine model can be achieved through a combination of fasting, the injection of heparin and the lipid infusion. However, it is not known if this suppression of myocyte uptake of FDG may also affect the degree of uptake of FDG by the inflammatory cells (macrophages). Here we report on our investigation of this potential limitation. We have evaluated the use of a prolonged constant infusion of FDG and Gd-DTPA instead of a bolus injection to fully distribute to the area of MO. This prolonged constant infusion also allows us to show the effect of suppression on uptake of FDG of inflammatory cells within the region of infarction, through tracking of the metabolic activity before during and after the infusion of agents to nominally suppress myocardial glucose uptake.

Methods: Six canines were imaged with hybrid FDG PET and MRI using a Siemens Biograph mMR at baseline and 5 days post-MI when the pro-inflammatory response should be peaking. FDG and Gd-DTPA were infused for 150 minutes starting simultaneously with the dynamic PET acquisition. T1 maps were acquired every 10 minutes throughout the scan to calculate extracellular volume. Suppression was started at 40 minutes into the scan by heparin injection and a 50 min lipid infusion. Patlak modelling was done at three times during this constant infusion: 12-39 minutes (before suppression), 60 – 90 minutes (during suppression) and 120 – 150 minutes (after suppression). ECV was calculated at 40, 90 and 150 minutes.

Results: No significant difference is seen in ECV measurements before, during and after suppression, although ECV is approximately twice as high in the infarcted tissue than the remote tissue. The metabolic rate of glucose (MRGlu) is significantly lower during and after suppression, both in the infarcted and remote tissue, though the effect is larger in remote tissue (see figure).

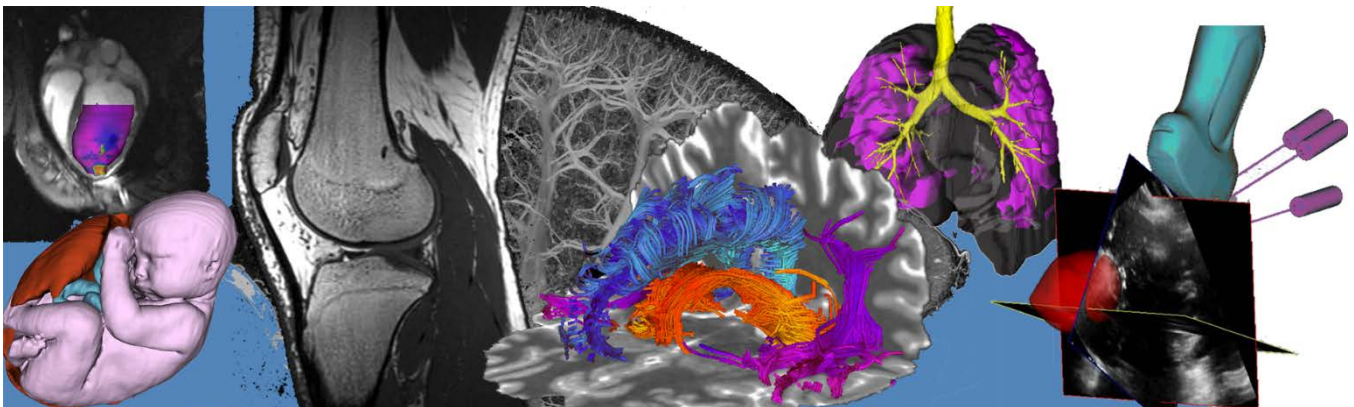
Conclusion: These results are the first to show an effect of heparin and intralipid on the metabolic rate of glucose activity in the infarcted tissue, suggesting either an effect of suppression on macrophages or alternatively, the presence of a significant volume of viable myocytes in the infarcted region. This potential effect of suppression on inflammatory cells highlights the need for tracers that are not only specific for the presence of inflammation but whose uptake is not confounded by the metabolic state present not only at the time of injection, but during the period of imaging.

[1] Frangogiannis, NG. (2014). *Nat Rev Cardiol.* 11(5): 255–265. [2] Kali A. (2016). *Circulation Cardiovasc Imaging.* 9(11): e004996. [3] Thackeray, J. (2017). SNMMI 2017. *J Nucl Med.* 58:302.



Pitch Presentation Abstracts

Session 10: Musculoskeletal Imaging



The Effect of Volar Scapholunate Tears on Carpal KinematicsSydney Robinson^{1,2}, Elizabeth Norman^{1,2}, Michael Rainbow^{3,4}, Emily Lalone^{1,2}, Nina Suh^{2,5}¹School of Biomedical Engineering, Western University, ²Roth McFarlane Hand and Upper Limb Centre,³Human Mobility Research Centre, Queen's University, ⁴Department of Mechanical and Materials Engineering, Queen's University, ⁵Schulich School of Medicine and Dentistry

Introduction: Scapholunate interosseous ligament (SLIL) tears are the most frequent ligamentous wrist injury and are known to lead to long-term degenerative arthritis. Radiographic assessment of scapholunate widening and clinical pain examination aid in the diagnosis of SLIL tears but early SLIL tears remain difficult to detect as clinical examinations rely heavily on clinician experience and standard radiographs typically identify late static SLIL instability. However, early dynamic instability detection is paramount to optimize surgical intervention for SLIL tears, yet dynamic instability is best visualized during motion which most current imaging modalities fail to capture. Four-dimensional computed tomography (4DCT) can capture abnormal bony movements and allows for quantification of carpal kinematics in real time. The purpose of this pilot study was to use 4DCT to evaluate the *in vivo* rotation of the scaphoid during radioulnar deviation and flexion-extension in healthy participants and patients with SLIL tears. Currently, reconstruction efforts focus predominantly on dorsal tears; however, understanding the dynamic effects of different tears on *in vivo* carpal motion may provide insight into whether it is important to repair isolated volar tears.

Methods: Six participants (n=3 uninjured; n=3 with SLIL tears – 1 volar, 1 dorsal, 1 combined) were recruited from a tertiary care academic centre, with approval from an institutional ethics board, and provided informed consent. The participants underwent unilateral imaging of the wrist using a 4DCT scanner while performing three cycles (8 s each) of radioulnar deviation (RUD) and flexion extension (FE). For RUD, the wrist began in radial deviation and moved to ulnar deviation in the first cycle, then reversed the motion. For FE, the wrist began in extension and moved to flexion in the first cycle, then reversed the motion. The first cycle was analyzed. The data was exported and models of the scaphoid, capitate and radius were made for every 10 degrees of motion: 20 degrees radial deviation to 20 degrees ulnar deviation (5 frames total); 50 degrees extension to 50 degrees flexion (11 frames total). The bones were registered (Python) and transformation matrices were used to calculate the helical axes (Matlab) relative to the radius in each position relative to neutral, thus measuring bone rotation in a radius-based coordinate system. The rotation data from the three healthy participants were averaged and used to create a healthy range.

Results: For the scaphoid in RUD: the volar tear was more flexed in UD; the combined tear was more extended in 20° UD; and the dorsal tear was more extended in 20° UD and 20° RD. As for FE, the scaphoid was more flexed in 10° extension and 10°-30° flexion for the volar tear; more extended in 20°-40° flexion for the combined tear; and more flexed in 20° F for the dorsal tear.

Conclusions: Previous studies have examined SLIL tears and determined that tears lead to scaphoid rotatory subluxation (abnormal scaphoid position relative to the lunate). Few studies have examined differences between types of SLIL tears or their impact on carpal kinematics. These preliminary results show that 4DCT may be used to detect subtle differences in scaphoid rotation indicative of an SLIL tear and may increase understanding of how SLIL tears affect carpal motion. These findings also show that volar tears may negatively impact carpal motion and may need to be repaired.

Enhanced μ CT imaging enables high resolution 3D visualization of microdamage in rat vertebraeAllison Tolgyesi^{1,3}, Normand Robert¹, Cari M. Whyne^{1,2,3}, Michael Hardisty^{1,2}¹Orthopaedic Biomechanics Laboratory, Sunnybrook Research Institute, Toronto, ON, Canada; ²Division of Orthopaedics, Department of Surgery, ³Biomedical Engineering, University of Toronto, Toronto, ON, Canada
allison.tolgyesi@mail.utoronto.ca

INTRODUCTION: While healthy bone balances damage and turnover, metastatic bone has disturbances in the homeostasis between bone forming and bone destroying cells. Consequently, an accumulation of microdamage can contribute to increased fracture risk. Experimentally, barium sulfate (BaSO_4) can be used to stain bone to visualize cracks and microdamage. However, prior investigations have not enhanced micro-computed tomography (μ CT) scanning protocols for delineation of damage. Backscatter electron imaging (BSE) provides a very high resolution, 2D image of biological samples and provides excellent contrast for identifying damaged regions of bone stained with BaSO_4 . Prior work has shown superior performance in visualization of damage with BSE for BaSO_4 stained specimens.¹ However, BSE only allows 2D assessment and is destructive, whereas μ CT can obtain high resolution, 3D images of vertebrae and is non-destructive. The objective of this study was to enhance μ CT imaging of whole rat vertebrae stained with BaSO_4 and compare the visualization of microdamage to BSE imaging.

METHODS: The first lumbar (L1) vertebrae from nine eight to nine week old athymic rats (Hsd:RH-Foxn1^{rnu}, Envigo, IN, USA) (three healthy, three inoculated with HeLa cancer cells, three inoculated with canine Ace-1 cancer cells) had previously underwent axial compressive loading of 50N for three hours and were stained with BaSO_4 . Institutional approval was obtained for this work and the ARRIVE guidelines were followed. Twelve slides (six healthy, three HeLa, three Ace-1) were prepared for BSE imaging and imaged with a μ CT scanner (μ CT 100 system, Scanco). The μ CT scan parameters were selected for high resolution scans with high contrast of the BaSO_4 . BSE images previously acquired for each slide were taken at $2\mu\text{m}/\text{pixel}$ resolution (SS BSE detector, FEI) using an ESEM (FEI/Philips XL30, FEI). Amira image analysis software (Amira 6.7.0, FEI) was used to manually align the μ CT and BSE images. 3D Slicer software (3D Slicer 4.8.1) was used to resample the μ CT image with reference to the BSE image. The μ CT and BSE images were used as the fixed and moving volumes, respectively, for affine registration. Amira was used to generate label fields of the BaSO_4 in the μ CT and BSE images using semi-automated segmentation with thresholding. Spatial correlation, $g(r)$, based on an “inflate algorithm”, was used to evaluate agreement between the labeled damage in the μ CT and BSE images on a voxelwise basis.¹ A spherical kernel with radius $r=0.02\text{mm}$ and a resolution of $128 \times 128 \times 128$ was used for the convolution of the μ CT label field to create the inflated region. The distance from each voxel considered as correlating is represented by r . A $g(r) > 1$ means voxels of labeled BaSO_4 in the two images were found nearer to each other than by chance.

RESULTS: By controlling the μ CT parameters, the contrast to noise ratio of the images were enhanced. The trabeculae were more clearly distinguished when the current was low. Reducing the current reduces the (proprietary) extent of the focal spot improving resolution. Current was reduced until there was no further noticeable increase in resolution at the fixed $4.9\mu\text{m}$ voxel spacing. Detector integration time and averaging were adjusted to compensate for the reduced x-ray fluence associated with low tube current to maintain signal to noise. The resulting enhanced scan parameters were 90kVp, $44\mu\text{A}$, 4W, 200ms integration time with 8 averaging with a $4.9\mu\text{m}$ voxel size. Each scan took 2.1 hours for a volume approximately $500\mu\text{m}$ in height. In comparison, bone sample preparation for BSE imaging requires three weeks. Spatial correlation ($g(r)=3.88-12.28$) was found between the enhanced μ CT scans and the corresponding BSE images. An examination of the enhanced μ CT images and the BSE images shows microdamage and microcracks that are obscured by noise in the original μ CT images (Figure 1).

CONCLUSION: Enhancement of μ CT scanning parameters allows for rapid high resolution 3D imaging able to quantify bone microdamage. This is important for understanding post-yield bone tissue mechanics and quantifying 3D microdamage in healthy and metastatically involved vertebrae and effects of cancer treatments on bone quality.

REFERENCES: 1. A. Atkins, et al., “Elevated Microdamage Spatially Correlates with Stress in Metastatic Vertebrae”, *Ann. Biomed. Eng.*, vol. 47, no. 4, pp. 980-989, 2019.

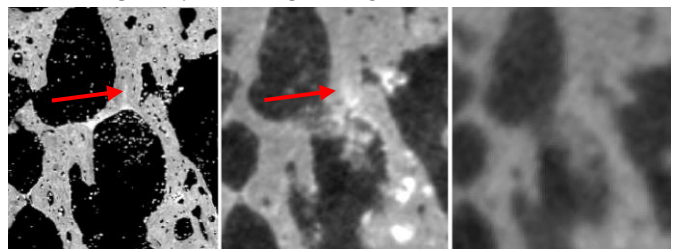


FIGURE 1: Zoomed in images of BaSO_4 labeled microdamage in BSE (left), enhanced μ CT (middle) and μ CT used in previous microdamage studies¹ (55kVp, $200\mu\text{A}$, $7.4\mu\text{m}$ resolution, 300ms integration time, no averaging) (right). BaSO_4 staining is obscured in the non-enhanced image.

Examination of Radiocarpal vs Midcarpal Contribution to Flexion Motion of the WristElizabeth Norman^{1,2}, Sydney Robinson^{1,2}, Nina Suh^{2,3}, Emily Lalone^{1,2}¹School of Biomedical Engineering, Western University, ²Roth McFarlane Hand and Upper Limb Centre,³Schulich School of Medicine and Dentistry

Introduction: The wrist is a complex condyloid synovial joint comprised of 8 carpal bones with a multitude of muscle attachments and interosseous ligaments. All of these components work synergistically to provide the wrist with its wide range of motion including: flexion, extension, radial/ulnar deviation, and circumduction. The aforementioned complexity of the wrist results in wrist injuries being common. To appropriately treat and diagnose these injuries, it is essential to have a thorough understanding of carpal kinematics. Many theories have been presented that describe the articulation of the carpal bones. One current theory is the row theory which postulates that the wrist moves in two rows: a proximal and distal row. However, a full understanding of the contributions of these rows is still unknown. The purpose of this study was to identify the contributions of these two aforementioned carpal rows, through the examination of the radiocarpal (RC) and midcarpal (MC) joints, to the flexion motion of the wrist using 4 dimensional computed tomography (4DCT).

Methods: Six young healthy patients with no prior history of wrist injury were recruited through our tertiary hand and upper limb clinic with approval from our institutional ethics board. Informed consent was obtained and all patients underwent unilateral imaging of the wrist from full wrist extension to full wrist flexion using a 4DCT scanner. The patients were instructed to completed one ‘pass’ of motion, extreme extension to extreme flexion, in 8 seconds. This data was then taken and three dimensional models of the radius, lunate, capitate, and third metacarpal were generated using Slicer 4.11.0. The models were made referencing the CT scans for 9 frames of interest, from 40 degrees of extension to neutral to 40 degrees of flexion in 10 degree increments. The neutral position was identified by the parallel alignment of the third metacarpal with the long axis of the radius. The bones were then registered (surface based registration) and the transformation matrices, obtained from the registration, were used in MATLAB to identify the helical axes and local coordinate system of each of the bones relative to the global coordinate system of the radius. The rotation of the lunate relative to the radius (radiolunate joint), identifies radiocarpal joint contribution and the rotation of the capitate relative to the lunate (capitolunate joint) identifies the midcarpal joint contribution. The respective radiocarpal and midcarpal contributions for each patient were identified and averaged to find the overall percent contributions of the aforementioned joints.

Results: In extreme wrist extension (40 degrees), the radiocarpal joint contributed more to wrist motion $25.37^\circ \pm 7.83^\circ$ as compared to the midcarpal joint $14.95^\circ \pm 8.28^\circ$. In percentages this equates to 63% RC compared to the midcarpal joint 37%. The radiocarpal joint continued to contribute more than the midcarpal joint throughout the flexion motion of the wrist up until 20 degrees of flexion. After flexing the wrist 20 degrees the contributions of the aforementioned joints equated; at 40 degrees of flexion they contributed almost equally RC: $20.08^\circ \pm 5.55^\circ$; MC $21.73^\circ \pm 5.60^\circ$ (RC 48%; MC 52%).

Conclusion: Previous studies have been conducted to examine the relative contributions to wrist motion; however, the results have been very controversial. With the use of 4DCT, this study was able to examine the *in vivo* kinematics of the carpal rows throughout the patient. These preliminary results show that in fact, the carpal rows have different contributions to the overall flexion motion of the wrist. This data collected may be used as a starting point to further examine the kinematics of the carpal rows during different motions of the wrist such as extension and radial/ulnar deviation. The results from this study, once completed, will provide novel insight into the kinematics of these bones and inform future surgical techniques and implant designs.

Four-Dimensional Computed Tomography Scans Allow Dynamic Visualization and Measurement of Scapulothoracic Joint Kinematics

Baraa Daher¹, George S. Athwal², Emily Lalone^{1,2}

¹Western University, London, ON, Canada, ²Roth McFarlane Hand and Upper Limb Center, St. Joseph's Health Care, London, ON, Canada

Introduction: The shoulder is the most mobile joint in the human body. Yet, measuring shoulder kinematics is challenging due to complex anatomy and functional complexity. The scapulothoracic joint of the shoulder describes the articulation of the concave anterior surface of the scapula as it slides over the convex surface of the thorax. Literature surrounding the characterization of this joint is limited and controversial. Some studies have considered this joint to be 'fictitious' or modelled it as 'fixed' in kinematic analysis. One of the many challenges faced when characterizing scapulothoracic motion is the difficulty in detecting/palpating anatomical landmarks and the limited use of static 3-dimensional (3D) imaging to measure complex motion. Therefore, the objective of this study is to use 4-dimensional computed tomography (4DCT) scanning to quantitatively evaluate scapular translation during dynamic internal rotation to the back.

Methods: A single healthy male with no previous history of shoulder injuries was recruited for this study and underwent dynamic 4DCT imaging of their shoulder joint while positioned lying on their side using a GE Revolution CT Scanner. The effective radiation dose from all scans for a male is 17.3 mSv. CT scans during the motion were performed for eight seconds (producing 25 frames of images). The participant started with the shoulder adducted and internally rotated with palm flat on their abdomen (i.e. first frame). The participant was then instructed to move their hand from their abdomen, around the thorax, to rest the dorsum of the hand on their back (i.e. last frame). This is called internal rotation to the back. Neutral CT frame obtained from the scan, along with the first and last frames of dynamic motion, were used to reconstruct 3D models of the scapula and spine. The neutral scapula surface was matched with the scapula of the two frames using a surface based registration algorithm (ICP). Landmarks were placed on the trigonum, superior angle and third thoracic (T3) vertebrae of the spine as shown in Figure 1. Translations of the trigonum relative to the neutral position of T3 (medial/lateral) and the superior angle relative to its neutral position (inferior/superior) were calculated using a MATLAB algorithm.

Results: Translation of the scapula was measured for first and last frame relative to the neutral frame. As shown in table 1, in the first frame, the trigonum moved 21mm laterally with respect to the T3, and the superior angle moved 19mm inferiorly with respect to its neutral position. In the last frame, the trigonum moved 19mm medially with respect to the T3, and the superior angle moved 17mm superiorly with respect to its neutral position.

Conclusion: The scapulothoracic joint is a mobile joint that contributes to the motion of the shoulder. Preliminary results suggest that the scapula translates with respect to the spine and glides across the thorax during shoulder motion and is not fixed. Figure 2 shows the neutral scapula (grey) and how the landmarks moved in the first and last kinematic frame (purple and blue). The technique of using 4DCT scans and a surface based registration algorithm can be used to better understand and measure the scapulothoracic joint kinematics in six degrees of freedom. Future work will develop a coordinate system and will model and measure joint translation and rotation over the full range of motion.

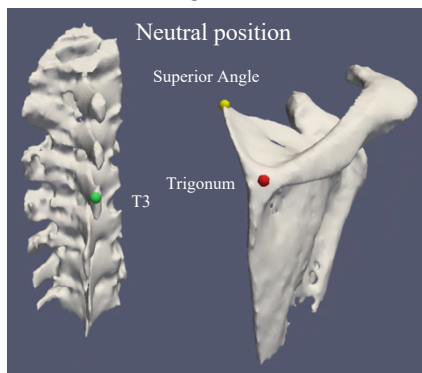


Figure 1: Landmarks used to quantify Scapular translation during active internal/external rotation

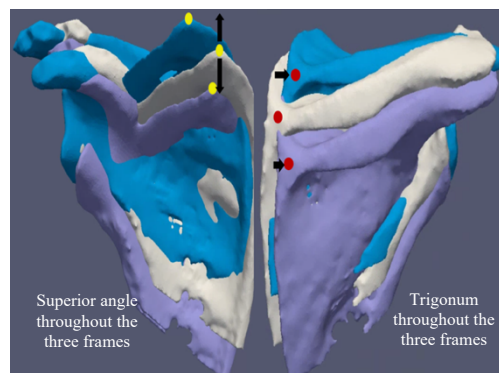


Figure 2: Scapular translation over the three frames

	Trigonum relative to spine	Superior angle relative to its neutral position
First frame	21 mm laterally	19 mm inferiorly
Last frame	19 mm medially	17 mm superiorly

Table1: Distances between spinal and scapular points

Validation of new 3-Dimensional Ultrasound Device for determining Synovial Tissue Volume in the Hands and Wrists

Carla du Toit^{1,3}, Dr. David Tessier³, Dr. Aaron Fenster^{2,3}, Dr. Emily Lalone^{1,4},

¹Department of Kinesiology, Western University, London, Ontario, Canada

²Department of Medical Biophysics, Western University, London, Ontario, Canada

³Center for Medical Imaging Technology, Robarts Research Institute, London, Ontario, Canada ⁴Department of Mechanical and Materials Engineering, Western University, London, Ontario, Canada

Introduction: The effect of chronic synovitis on the progression of osteoarthritis pathology is a relatively new but supported concept in the fields of rheumatology and hand surgery that has been linked to pain and disability in patients. Currently, the gold standard for diagnosing synovitis in the wrists and hands is a clinical examination and the use of 2D musculoskeletal ultrasound imaging. Major limitations associated with this method include: (1) its inability to provide accurate volumetric measurements which leads to high variability, (2) the need for operators to mentally transform 2D images to 3D impressions of the anatomy and (3) its reliance on transducer location and orientation for images limiting the ability to achieve certain views of an individual's anatomy [2]. These limitations can be overcome by using a 3D ultrasound system (3DUS) which can quantitatively measure tissue volumes and create 3D reconstructions. When compared to similar imaging modalities such as magnetic resonance imaging (MRI), 3DUS devices are able to acquire images at high frame rates and are more flexible in image orientation [3]. Previous studies examining the use of 3DUS to measure articular cartilage in the knee, found that 3DUS was able to provide a cartilage volume assessment with similar sensitivity to MRI in healthy volunteers [4]. The aim of this work is to develop a 3D ultrasound system for imaging the hand and wrist. This paper reports on the development, geometric, and volumetric validation for wrist/hand 3D ultrasound imaging.

Methods To establish the geometric validity of the 3DUS system, a multilayered monofilament grid phantom (12.2 x 12.2 x 3.1 cm) with string intersections spaced 10mm apart was scanned. An Aplio i800 US machine (Canon Medical Systems, Tustin, California, US) with a L12-5 linear transducer (8.5MHz center frequency) attached to a motor stage with a step size of 0.33mm was used. The volumetric validity of the system was determined using a simulated synovial tissue phantom with an embedded simulated synovial effusion (7cm³). The 3DUS images consisted voxel sizes of 0.114 x 0.114 x 0.333 mm³, with an average of 336 slices per image. These slices were manually segmented using 3D Slicer to construct a 3D segmentation of the phantom. The 3D volumes were compared to those found using magnetic resonance imaging (MRI) and the known volume of the agar phantom. Clinical feasibility will be determined by scanning two healthy volunteers and one distal radial fracture patient and comparing their synovial volumes to those acquired using MRI.

Results: The largest error and variance recorded from the geometric validation measurements was 0.0856±0.0087mm and was acquired from the reconstruction plane. The remaining linear measurement errors were all < 1%. The error between the mean phantom volume measurements and the known synovium phantom volume was 5.99% and 2.43% for the 3DUS device and MRI respectively. The percent difference in the volume measurements from the 3DUS device and MRI was 0.814%.

Conclusion: A mechatronic 3D ultrasound imaging system was developed for the wrist and hand. Successful geometric and volumetric validation demonstrates feasibility for implementation in a clinical setting. Current work evaluates system ability to accurately and quantitatively classify synovitis in first carpometacarpal joint and distal radial injury patients to investigate the relationship between chronic inflammation and the progression of osteoarthritis in patients.

Anatomical Measurement of Kangaroo Cervical (C3 - C7) Vertebral Endplates Using Micro-CTJoseph U. Umoh¹, Helium Mak², Wankei Wan², and David W. Holdsworth^{1,3}¹Preclinical Imaging Research Centre, Robarts Research Institute, ²Depts. of Chemical and Biochemical Engineering, ³Depts. of Medical Biophysics and Surgery, Western University, London, ON, Canada

Introduction: The endplates, between each vertebra and disc of the cervical spine, supply strength and stability that help keep the vertebrae from fracture as well as protect the disc. Accurate dimensions of the cervical vertebral endplate could help in the design of cervical disc prostheses which are often used in the treatment of cervical degenerative disease¹. Also, modelling of the cervical vertebrae using accurate data of the endplate can improve our understanding of the biomechanics of the cervical vertebra and susceptibility to injury. The kangaroo has recently been investigated as a model of human thoracic spine,² based on its pseudo-biped nature and relatively easy availability. The objective of this study is to create a database for the anatomical parameters of the kangaroo cervical (C3 - C7) vertebral endplates, using micro-computed tomography (micro-CT). These data could be used to explore the possibility of using the kangaroo as a model for human spine biomechanical experiments *in vitro*.

Methods: Five adult (*Macropus rufus*) kangaroo cervical spines were used in this study. Micro-CT imaging was used to acquire image data of the spines (Fig. 1). They were imaged on the same micro-CT scanner (GE Locus Ultra), with the same scan protocol (x-ray tube voltage 80 kV, tube current 55 mA, 1000 projections, exposure time 16 s) and the same reconstruction parameters (154 μ m 3D image voxels). Each of the cervical vertebrae was segmented and used to measure the endplate. We measured the anatomy of the cervical vertebral endplate using MicroView (an image-viewing and manipulation software). We first re-oriented the vertebrae body such that most portion of its anterior surface lay on a plane. On MicroView axes, the superior-inferior line was on the axial axis, the anterior-posterior line on the corona axis, and the line joining the two transverse processes on the sagittal axis. The two transverse foramina were two important landmarks in the endplate parameter-measurement procedure. The endplate superior width (EPSW) and the endplate inferior width (EPIW) were uniquely measured on the corona plane that passed through the two transverse foramina (Fig. 2). The endplate superior length (EPSL) was measured on the axial plane that cut through the endplate superior surface. The endplate superior depth (EPSD) was measured on the sagittal plane as the largest vertical distance between the superior flat surface of the plate and highest point on the plate. The endplate inferior depth (EPID) was defined as the distance on the sagittal plane where the plate began to curve inwards and the largest downward tip of the plate.

Results: Endplates were generally wider and longer at the superior surface than at the inferior (Fig. 3). It appeared that both EPSW and EPSL decrease from C4 towards C5 and also decrease from C7 towards C5 (Fig. 3). One-Way ANOVA showed that mean EPSL C3 - C7 was significantly different ($P < 0.05$, $R^2 = 0.43$) whereas EPSW was not. Data indicated that EPSD was larger than EPID for C4 - C7, indicating that the endplate at the superior surface was more concave than it was convex at the inferior surface.

Conclusions: Micro-CT data of the kangaroo cervical (C3 - C7) vertebrae were used to measure endplate superior width, length, and depth as well as endplate inferior width, length and depth. Endplate superior surface was concave (transversely) while the inferior surface was convex (laterally). Within this sample population, C5 (compared to C4 and C6) appeared to have a smaller superior length and width. Initial comparison with human cervical vertebral endplates in the literature appears to indicate that the shape of the kangaroo cervical vertebral endplates is similar to that in the human. Knowledge of the endplate geometric shape of the kangaroo cervical vertebrae will help to guide future *ex vivo* and *in vivo* studies of spine biomechanics, using the kangaroo model.

References: [1] Feng *et al.* *The Spine J.* 2017; 17: 269-276. [2] Balasubramanian *et al.* *Eur Spine J.* 2016; 25: 4140-4154.

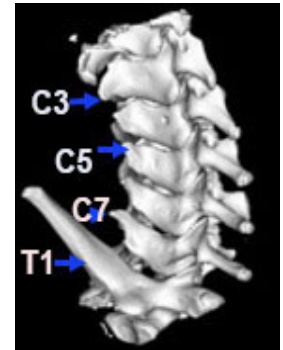


Figure 1: Micro-CT, isosurface-rendered image of a kangaroo cervical spine, showing C3 - C7, together with the reference T1.

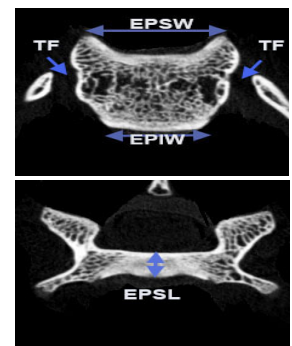


Figure 2: Anatomical structure of a cervical vertebra showing a plane that cuts through the centre of the transverse foramen (TR) where the EndPlate Superior Width (EPSW) and EndPlate Inferior Width (EPIW) were measured. EPSL is the EndPlate Superior Length.

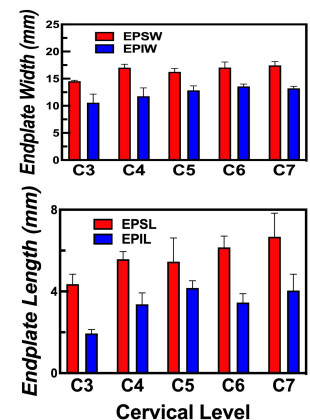


Figure 3: Estimates of the kangaroo EndPlate Superior Length (EPSL) and EndPlate Inferior Length (EPIW). Error bars are standard deviation.

Effect of vitamin D and memantine supplementation on body composition in the APP/PS1 mouse model of Alzheimer's disease following chronic vitamin D deficiency

Dana N. Broberg^{1,2*}, Dickson Wong^{1,2*}, Jagroop Doad¹, Joseph U. Umoh¹, Miranda Bellyou¹, Chris J. D. Norley¹, David Holdsworth^{1,2}, Manuel Montero-Odasso^{3,4,5}, Olivier Beauchet⁶, Cedric Annweiler⁷, Robert Bartha^{1,2} (*Co-first author)

¹Robarts Research Institute, London, ON, Canada; ²Department of Medical Biophysics, Western University, London, ON, Canada; ³Department of Medicine, Division of Geriatric Medicine, Parkwood Hospital, Western University, London, ON, Canada; ⁴Department of Epidemiology and Biostatistics, Western University, London, ON, Canada; ⁵Lawson Health Research Institute, London, ON, Canada; ⁶Department of Medicine, McGill University, Montreal, QC, Canada; ⁷Division of Geriatric Medicine, University Hospital of Angers, France

Introduction: Both vitamin D (vitD) deficiency [1] and changes in body composition [2] are frequently observed in Alzheimer's disease (AD). Combination treatment with memantine and vitD has been shown to protect cortical axons from beta-amyloid and glutamate toxicity in AD [3]. In addition to these central effects, vitD and memantine may act peripherally to alter metabolism. In this study, the effects of vitD deprivation and subsequent treatment with vitD and memantine on body composition (lean, adipose, and skeletal tissue) are assessed for the first time in a transgenic mouse model of AD.

Methods: 56 male APPswe/PS1dE9 mice were randomized into four groups. The first stayed on a control diet for the duration of the study (Control, n=14). The other three groups started on a vitD deficient diet at 6 months of age, with one of these groups remaining on this diet for the rest of the study (VitD-, n=14). In the final two groups, one had memantine added to their vitD-deprived diet (Mem & VitD-, n=14) while the other had both memantine and vitD added to their diet (Mem & VitD+, n=14) at month 9. Serum 25(OH)D levels were measured at months 6, 9, 12, and 15 to confirm lower levels of vitD in vitD-deprived mice. Micro-computed tomography scans were acquired at month 15 and segmented into lean, adipose, and skeletal tissue based on signal-intensity values (adipose: -380 to -31 HU; lean: -30 to 189 HU; skeletal: >190 HU).

Results: Serum 25(OH)D levels confirmed that the diet plans manipulated vitD levels as intended; mice on the vitD-deprived diet had lower levels of 25(OH)D whereas mice on the vitD enriched diet (Mem & VitD+) had higher levels of 25(OH)D relative to controls. No differences were observed in adipose or lean tissue between the four groups, however, there was a significant increase in skeletal tissue mass ($p < 0.05$) and volume ($p < 0.05$), and bone mineral content ($p < 0.01$) in the Mem & VitD- group relative to control mice. No differences were observed in any tissue type when total mass or volume of the mice were taken into account.

Conclusions: While vitD deprivation did not affect body composition in APPswe/PS1dE9 mice, memantine increased absolute skeletal tissue in mice that were vitD-deficient. However, memantine did not have this effect in mice that were vitD-enriched. We conclude that combination treatment of memantine and vitD enrichment had no negative effects on body composition in the APPswe/PS1dE9 mouse model. Future work should clarify whether vitD status impacts the effects of memantine on bone physiology in people with AD.

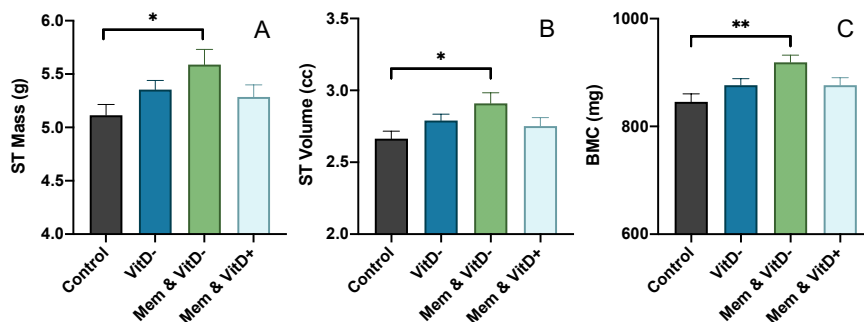
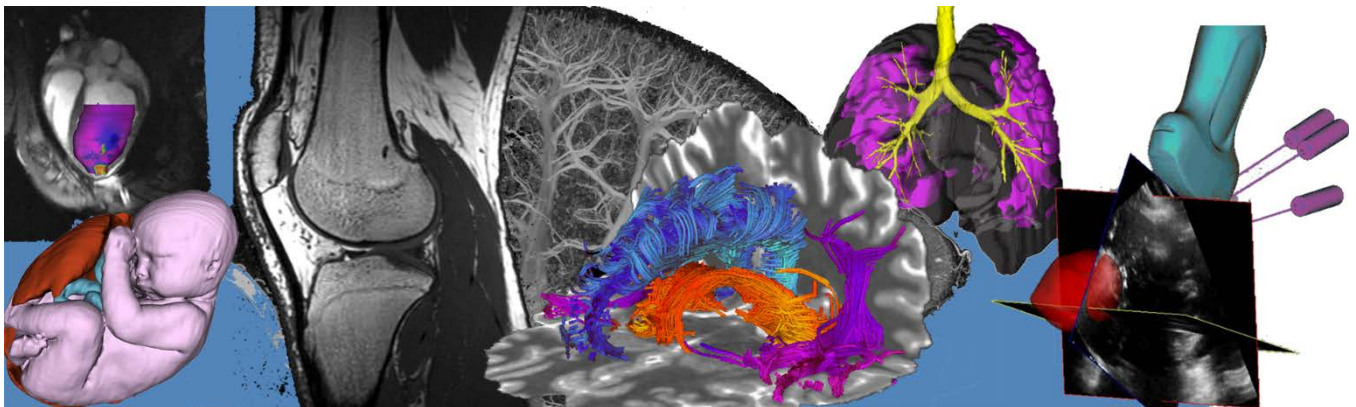


Figure 1. Absolute skeletal tissue: Micro-computed tomography was used to measure skeletal tissue mass (A) and volume (B), and bone mineral content (C) in 15-month-old APPswe/PS1dE9 mice. Data are expressed as mean \pm SEM. ST, skeletal tissue; BMC, bone mineral content; Mem, memantine; VitD+, vitamin D enriched; VitD-, vitamin D deficient. * $p < 0.05$; ** $p < 0.01$.

References: [1] Sohrabi HR, et al. (2015). *Front Aging Neurosci* 7:16; [2] Di Somma C, et al. (2017). *Int J Mol Sci* 18:2482; [3] Annweiler C, et al. (2012). *Neurobiol Aging* 35:331-5

Pitch Presentation Abstracts

Session 11: Deep Learning



A Deep 2D-UNet Ensemble for the Segmentation of Microstructural White Matter Damage in mTBI Patients using Diffusion Tensor Imaging

Brian McCrindle, B.Eng.^{1,2}, Nicholas Simard, MASC.^{1,2}, Thomas E. Doyle, PhD.^{1,3,4}, M.D. Noseworthy, PhD^{1,2,4}

¹ Electrical and Computer Engineering, McMaster University, Hamilton, ON, Canada.

² Imaging Research Center, St. Joseph's Healthcare, Hamilton, ON, Canada.

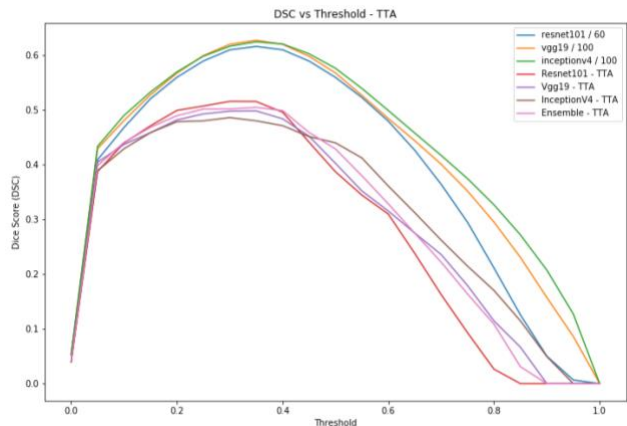
³ Vector Institute for Artificial Intelligence, 661 University Avenue, M5G 1M1, Toronto, Ontario, Canada.

⁴ School of Biomedical Engineering, McMaster University, Hamilton, ON, Canada.

Introduction: In North America alone, over 1.7 million people are affected by mild traumatic brain injury (mTBI) each year¹. Typically, victims are left with a vague diagnosis of their condition since there is no quantifiable way to clinically understand the patient's injury. The goal of this research was to develop a deep learning system capable of detecting and segmenting damaged white matter (WM) regions of an adult brain that has experienced an mTBI. We explore the implementation of a 2D-UNet, a framework designed specifically for biomedical segmentation tasks.

Methods: Ten patients (6 Male/4 Female, ages 22 to 66) who experienced an mTBI within 2 years of the study start date were recruited. Healthy control subjects (n = 88 per patient age, totaling 880 normal scans) were sourced from ADNI, HCI, ICMB, and PPMI databases. A deep 2D-UNet ensemble framework with various encoding backbones, random weight initialization, dropout probabilities of 0.4, and a weighted binary cross entropy loss function was implemented with PyTorch 1.5.0 and CUDA 10.1. A training/validation/test split of 60/15/25% was used to evaluate the performance of the system using only Fractional Anisotropy (FA) maps. Voxel-wise labelling of damaged regions were done through a novel Z-scoring technique using Tract-Based Spatial Statistics². Model predictions were ensembled using the method described in Lakshminarayanan et al.³. Performance curves were developed with and without test-time augmentation (TTA).

Results: The performance of all models with various thresholds is illustrated by the Dice score curves (Figure 1). Since the chosen threshold directly affects the precision and recall of the model, there is no one optimal threshold value. Further, the ensemble shows stability over the entire threshold range under TTA conditions (random scaling, affine transformations), indicating that its performance is robust to spurious performance drops that could be seen with a single model. Peak Dice scores with and without TTA were shown to average to 0.50 and 0.61, respectively. An expected performance drop during TTA was noted as this is a form of "out-of-distribution" (OOD) testing. These metrics are expected to improve as the patient sample size increases.



Conclusions:

This work shows the possibility of using an ensemble of deep 2D-UNet architectures to automatically segment damaged white matter regions within the brain. A platform such as this can provide clinicians with better healthcare solutions for their patients experiencing mTBI. Collaborations should be sought after to explore avenues for clinical implementation.

References:

- [1] M. Faul, L. Xu, M. Wald, Traumatic Brain Injury in the United States: Emergency Department Visits, Hospitalizations, and Deaths 2002-2006. U.S Centers for Disease Control (2010). https://www.cdc.gov/traumaticbraininjury/pdf/blue_book.pdf.
- [2] S.M. Smith, M. Jenkinson, H. Johansen-Berg, D. Rueckert, T.E. Nichols, C.E. Mackay, K.E. Watkins, O. Ciccarelli, M.Z. Cader, P.M. Matthews, and T.E.J. Behrens. Tract-based spatial statistics: Voxelwise analysis of multi-subject diffusion data. *NeuroImage*, 31:1487-1505, 2006.
- [3] B. Lakshminarayanan, A. Pritzel, C. Blundell, Simple and Scalable Predictive Uncertainty Estimation using Deep Ensembles, *Neural Inf. Process. Syst. (NIPS 2017)*. (2017). <https://doi.org/10.1007/BF00378152>.

Aliasing Removal in Color Flow Imaging using Deep Learning

Hassan Nahas¹, Takuro Ishii², Billy Y. S. Yiu¹, Jason Au³, Adrian J. Y. Chee¹ and Alfred C. H. Yu¹ ¹Schlegel

Research Institute for Aging, University of Waterloo, Waterloo, Canada

²Frontier Research Institute for Interdisciplinary Sciences, Tohoku University, Sendai, Japan

³Department of Kinesiology, University of Waterloo, Waterloo, Canada

Introduction

Ultrasound color flow imaging (CFI) is the go-to modality in clinics for visualizing *in vivo* flow dynamics, especially for monitoring and diagnosis of cardiovascular pathology. The modality, however, is setback by aliasing artifacts when flow is too fast and complex. Aliasing obscures the visualization of flow in tortuous or branching vasculature as fast flow is often rendered as a mosaic of colors. One solution for addressing these aliasing artifacts is to first segment them in the estimated flow map, and then rectify them to achieve a continuous flow profile. We hypothesize that deep neural networks can be used to consistently segment and correct the aliased regions, and in turn improve flow visualization.

Methods

We devised a framework for aliasing removal in CFI that consists of two algorithmic stages: 1) segmentation of aliased CFI pixels using the convolutional neural network, U-net (arXiv, 2015; 1505.04597); 2) adaptive correction of segmented regions by comparing the values on the interior of the segmented regions with exterior pixels (Med Image Anal, 2011;15:577-88). The neural network was trained with 525 CFI frames acquired from a spiral flow model (T-UFFC, 2017; 64:1840-8) and aliasing artifacts were manually segmented to serve as training references. The performance of our segmentation was evaluated on 350 systolic CFI frames from a 50% stenosed carotid bifurcation flow model. We finally applied the framework on an *in vivo* femoral bifurcation from a healthy volunteer for visual demonstration.

Results

The proposed framework succeeded in removing aliasing artifacts in CFI frames of the carotid bifurcation model and *in vivo* femoral bifurcation. In the carotid bifurcation model dataset, aliased pixel classification was achieved with mean accuracy, precision and recall greater than 99% with standard deviation under 0.1% in classifying aliased pixels compared with manual segmentation. After adaptive correction, error incidence rate in the carotid model was negligible (<1%). Fig. 1a shows the acquired femoral CFI at systole with an aliasing artifact observed in the deep femoral branch. The trained network identified the aliased region with high confidence (Fig. 1b) and upon aliasing removal, flow speed that is beyond the limitations of CFI could be estimated (Fig. 1c).

Conclusions

This framework holds promise as a new solution to resolve erroneous flow estimates due to aliasing in CFI. The segmentation achieved in this study may be used to improve the performance of aliasing removal techniques and should ultimately improve flow visualization of complex *in vivo* scenarios such as bifurcations.

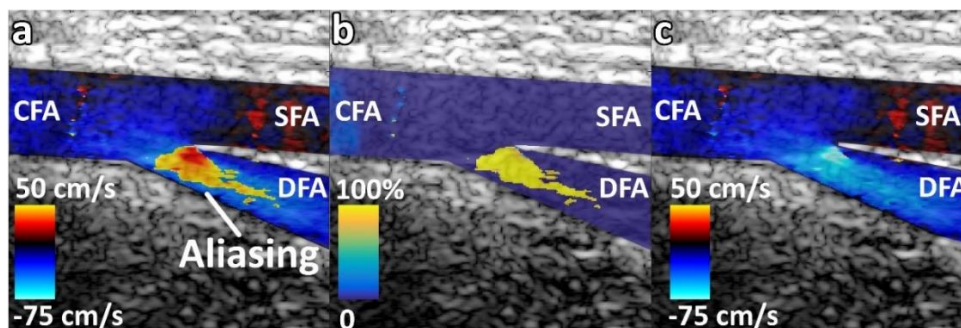


Fig. 1. Results of the framework on an *in vivo* femoral bifurcation, including the Common Femoral Artery (CFA), the Superficial Femoral Artery (SFA) and the Deep Femoral Artery (DFA). **a)** Original color flow imaging with aliasing artifacts in the lower branch. **b)** Aliasing segmentation confidence by U-net. **c)** Color flow image with the aliasing artifact removed by adaptive correction.

Automatic Deep Learning-Based Segmentation of Neonatal Cerebral Ventricles from 3D Ultrasound Images

Zachary Szentimrey¹, Sandrine de Ribaupierre^{2,3}, Aaron Fenster², Eranga Ukwatta¹

¹School of Engineering, University of Guelph, Guelph, Ontario, Canada; ²Robarts Imaging, University of Western Ontario, London, Ontario, Canada; ³Department of Clinical Neurological Sciences, University of Western Ontario, London Health Sciences Centre, London, Ontario, Canada

Introduction: Intraventricular hemorrhaging (IVH) affects 20-30% of very low birth weight infants (<1500g), which can lead to post-hemorrhagic ventricle dilation (PHVD) (the abnormal enlargement of the ventricles) and developmental delays. Monitoring the changes of the ventricles is critical because it can provide clinicians with more information for choosing the best treatment to prevent further neurological degradation. Most facilities routinely monitor PHVD using two dimensional ultrasound (2D US) measurements, which can be inaccurate and less sensitive to changes in ventricular size and shape compared to 3D US. The purpose of this research is to provide a fast, reliable, safe, and automated method of measuring neonatal cerebral ventricle size and shape using 3D US and deep learning methods. The current best non-deep learning-based automated method uses multi-phase geodesic level-sets (MGLS) with shape priors and an atlas but is very slow taking 54 min to segment one image with an average Dice Similarity Coefficient (DSC) of 0.77 ± 0.06 over 30 images.

Methods: The dataset consists of 87 3D images, which only includes images of both lateral ventricles and images with varying degrees of PHVD. The images were collected by a motorized 3D US system developed specifically for cranial imaging of neonates with the typical angular scan acquisition range between $60-72^\circ$ with 0.3° angular spacing and 25 frames/s with a motor gear ratio of 2100:1. Each image had a manual segmentation created by trained clinicians for use as a ground truth. The manual segmentations were performed on the sagittal view at 1 mm intervals using multi-planar reformatting software. The automated segmentation methods were implemented based on the U-Net model using supervised training. The basic U-Net model was tested as well as variants that include attention gates and more skip connection called Attention U-Net and U-Net++. Attention gates were included to focus on detailed aspects of the image such as the ventricle boundary and the inferior horns of the ventricles which are typically under segmented. Additionally, skip connections were tested based on research of endocardial ventricle segmentation using ultrasound that showed additional skip connections improved DSC. In addition, a deep learning shape prior based on an autoencoder was implemented for one test. In total, a 2D U-Net, 3D U-Net, 3D Attention U-Net, 3D U-Net++, 3D U-Net with Shape Prior and an ensemble of 3D Attention U-Net, 3D U-Net++, and 3D U-Net with Shape Prior were all tested and compared. The 2D U-Net extracted slices at random orthogonal views in the images and required post-processing to fuse predicted slices together. The data were split into train/validation/test with amounts 49/12/26 and each image was reduced in size to $128 \times 128 \times 128$ and evaluated as such. Data augmentation techniques were used which included reflecting the data about the symmetric plane to mitigate lack of data. The DSC between manual ground truth and predicted segmentations was used for evaluation.

Results: The mean and standard deviation of the DSC across all images was calculated as shown in Table 1. The automatic segmentation of each image was performed in approximately 1-2 seconds for the 3D models and 1-2.5 minutes for the 2D model. While variants of 3D U-Net yielded higher DSC than the vanilla U-Net, the ensemble model had the highest mean DSC with a sample segmentation from the ensemble model shown in Figure 1.

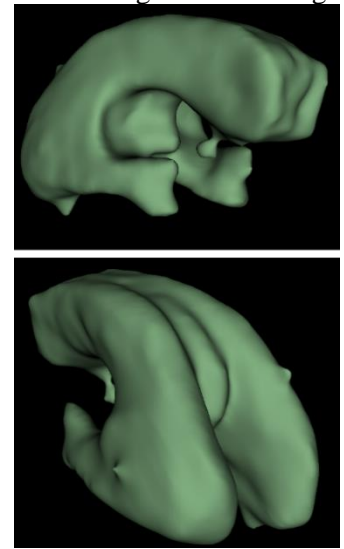


Figure 1: Example segmentation from the ensemble with DSC of 0.85

Table 1: DSC results for each model

Model	2D U-Net	3D U-Net	3D U-Net++	3D Attention U-Net	3D U-Net with Shape Prior	Ensemble
DSC	0.74 ± 0.07	0.76 ± 0.09	0.78 ± 0.08	0.77 ± 0.08	0.77 ± 0.09	0.79 ± 0.07

Conclusion: We implemented deep learning models to automatically segment neonatal lateral ventricle in 3D US images. It was found that the 3D models in general had higher DSC than that of the 2D model and were much faster at segmenting the images with the possibility of point of care implementation. When compared with the MGLS automatic segmentation method from previous work, the deep learning methods yielded higher DSC in a fraction of the time.

Detection of COVID-19 from Chest X-ray Images using Transfer Learning

Jenita Manokaran^a, Fatemeh Zabihollahy^b, Andrew Hamilton-Wright^c, Eranga Ukwatta^a,

^aUniversity of Guelph, School of Engineering; ^bThe Johns Hopkins University School of Medicine, Department of Radiation Oncology and Molecular Radiation Sciences; ^cUniversity of Guelph, School of Computer Science,
^{a, c}50 Stone Rd E, Guelph, ON, Canada N1G 2W1. ^b733 N Broadway, Baltimore, MD 21205.

Introduction: The novel coronavirus 2019 (SARS-CoV-2 or COVID-19), an infectious disease has been declared global pandemic by the World Health Organization on March 12, 2020. Polymerase Chain Reaction (PCR) is widely implemented as the key screening tool for COVID-19 detection. The enormous and calamitous effect of COVID-19 on the population worldwide has urged the need to develop an automated tool for COVID-19 diagnosis. Deep learning has been widely used in medical image classification task by implementing automatic feature extraction. The proposed method targets the application of deep learning technique that aids in developing a faster, accurate and reliable tool for the diagnosis of COVID-19 from Chest X-ray (CXR) images and can be used in complimentary with the PCR test.

Method: We developed a transfer learning-based approach using the state-of-art pre-trained deep learning models to classify the CXR images as COVID-19, pneumonia and normal. The most commonly used pre-trained models namely VGG16, VGG19, DenseNet121, DenseNet201, ResNet50, ResNet101, MobileNetv2 and Inceptionv3 are trained and tested to classify the CXR images into normal, pneumonia and COVID-19. We used the initial architecture and the pre-trained weights. The final classifier is replaced with the new network that includes global average, dropout, and a batch normalization layer. The feature extracted using the model is given to the fully connected layer developed using softmax activation for classification. The dataset used for training and testing the pre-trained models is a public dataset consisting of 8644 CXR images with 4000 normal, 644 COVID-19 and 4000 pneumonia images. The image sizes were down sampled to 299 X 299 for Inceptionv3 and to 224 X 224 for all other pre-trained models. The images were augmented only during training phase by performing rotation, zooming, and flipping horizontally to compensate for the lower number of COVID-19 cases. An 80-20 split was performed for training (10% for validation) and testing data on individual classes to maintain class imbalance. The training was performed using Adam optimizer with a learning rate of 0.0001 and a batch size of 32. The training was performed for 100 epochs for all the 8 models considered and the model check point was used to save the best model. The test dataset used for model evaluation comprises of a total of 1729 images with 129 COVID-19, 800 pneumonia and 800 normal CXR images.

Results:

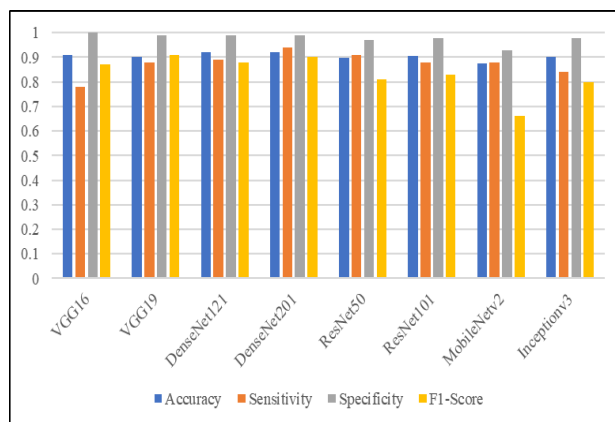


Figure 1 - Comparison results for 8 pretrained models

The evaluation results obtained for the pre-trained models are summarized in Figure 1. Since we are interested in detecting COVID-19 cases which is the minority class, and normal and pneumonia are majority classes in this dataset, the model performance cannot be judged based on the overall accuracy on the test dataset alone. Hence Accuracy, Sensitivity, Specificity, and F1-Score (provides balance between exactness and completeness of the model) that targets the minority class (COVID-19) are chosen as the metric for performance evaluation. *DenseNet201 and ResNet50 has the highest sensitivity rate of 94% and 91% and all the other models showed a sensitivity rate of 88%. VGG16 has the least sensitivity rate of 78%. Hence, DenseNet201 has achieved the best accuracy and sensitivity.

Conclusion:

DenseNet201 and 121 achieved the highest accuracy of 92% in terms of overall accuracy. Since our ultimate goal is to detect COVID-19, DenseNet201 outperformed all the other model with highest accuracy, sensitivity and F1-score, the important metrics to be considered when dealing with imbalanced dataset. The results obtained based on real world data representation with large training and testing set provides an insight on the effectiveness and robustness of the state of art pre-trained models in detecting COVID-19 from normal and pneumonia CXR images.

Tissue Classification of Mass Spectrometry iKnife Data Using Graph Convolutional Networks

F. Akbarifar, A. Jamzad, A. Santilli, M. Kauffman, N. Janssen, L. Connolly, K. Ren,
K. Vanderbeck, A. Wang, D. McKay, J. Rudan, G. Fichtinger, P. Mousavi
Queen's University, Kingston, ON, Canada

Introduction: The intelligent knife, iKnife, by Waters Corp. couples Rapid Evaporative Ionization Mass Spectrometry (REIMS) technology with conventional electrosurgical units. Mass spectrometry backend analyzes the chemical profile of the released smoke during cauterization in only a few seconds. It is hypothesized that these chemical profiles differ between neoplastic and healthy tissue. As previous studies show, Principal Component Analysis (PCA) followed by Linear Discriminant Analysis (LDA) and also an Autoencoder-based classifier can be used to successfully detect cancer from normal margins in Basal Cell Carcinoma (BCC) excision surgeries. Here, we propose to use a Graph Convolutional Network (GCN) to perform such classification. GCNs are powerful neural networks and their application has been extended to non-structural data. Hence, we also propose an approach to convert our non-structural data to graphs and test the feasibility of tissue classification using these graph structures and a GCN.

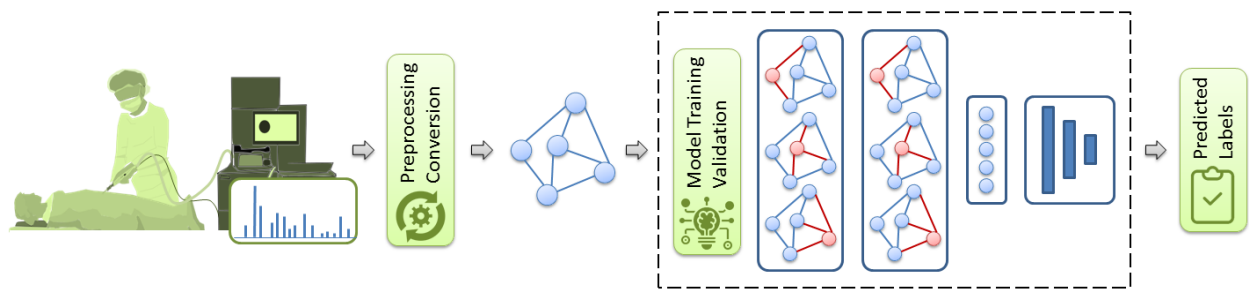


Figure 1. Proposed workflow: Labelled BCC spectra are preprocessed, converted to graph and used for training graph network.

Methods: Figure 1 depicts an overview of our workflow. The data was acquired from 42 specimens of 35 patients and contained 190 burn spectra (127 normal and 63 BCC). Preprocessing steps included background subtraction, normalization, lock mass correction, binning the intensity values, choosing 100-900 mass to charge ratio (m/z) range and reducing the number of peaks by max-pooling. Figure 2 illustrates our proposed method for graph conversion. In this approach, we consider different resolution levels of the signal created by down sampling. Edges are created between neighboring subbands in one level as well as between subbands in adjacent levels. Our model consists of 4 GCN layers followed by “mean” function as readout (to perform a graph classification task) and two fully connected layers to predictions. The implementation was based on the graph benchmarking framework proposed by Dwivedi et al [1]. We have stratified the data into training, validation and test sets, considering that the balance and separation of data must be consistent, and employed 4-fold cross validation.

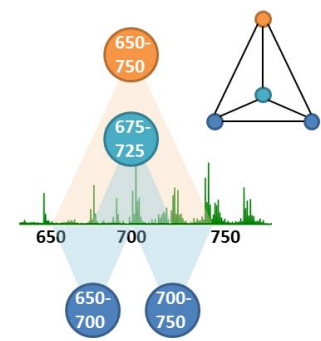


Figure 2. Two approaches for converting spectra to graphs.

Results: We achieved an average (standard deviation) accuracy of 97.30% (1.91%), sensitivity of 100.00% (0.00%), and specificity of 96.00% (2.83%) for BCC/normal classification on the test set without performing any data augmentation. These results outperform the PCA/LDA (p -value = 0.0043), but are comparable to the Autoencoder results of [2] achieved by increasing the number of spectra in each cross-validation fold to 1000.

Conclusion: Our results demonstrate the ability of a GCN network to reasonably classify BCC from normal iKnife burn profiles using our proposed graph structure.

References: [1] VP Dwivedi, arXiv preprint arXiv:2003.00982, 2020. [2] A Santilli, International Journal of Computer Assisted Radiology and Surgery 15, 887–896, 2020.

Deep learning model for motion correction of MRI images using small training setsIvailo E Petrov¹, Miriam Hewlett^{1,2}, Maria Drangova^{1,2}¹Robarts Research Institute, The University of Western Ontario, Canada²Department of Medical Biophysics, The University of Western Ontario, Canada

Introduction: Motion artefacts in the magnetic resonance imaging (MRI) lead to degradation of the image quality, manifesting as blurring, signal change, ringing, or ghosting artefacts, limiting their use for diagnoses or analysis using automated imaging techniques. Between 7.5 and 29.4% of the patients move during the scanning, 19.8% of which requiring at least one scan be repeated, causing financial and resource losses [1]. Recent publications show that using deep learning (DL) for motion correction can significantly improve the image quality. Most of the studies use some modifications of convolutional neural networks (CNN) [2] or generative adversarial networks (GAN) [3] and as large as possible training image sets. Our hypothesis is that similar results in motion correction can be achieved by using 2D training images, instead of 3D volumes, and a significantly smaller training set, allowing faster training and less computational demand.

Methods: A standard pix2pix cGAN was modified to correct motion artefacts simulated in MRI images. The generator and the discriminator had 15 layers each and were trained approximately for four hours on Google Colab Pro (27 GB RAM, 16 GB GPU). Several thousand images, collected from multiple locations and with multiple contrasts, from NYU fastMRI Dataset [4] were available for training. The network was trained and tested with 20 3D volumes from each contrast - FLAIR, T1 and T2 - with no image augmentation (total of 480 2D images for each test and train set). For each contrast in the training set there are images from only one location and field strength, while the test sets contained images from multiple locations with mix of field strengths. The model was trained with one contrast at a time, making use of transfer learning. Four error metrics were used to evaluate model performance compared to the ground truth results: mean absolute error (MAE), mean squared error (MSE), structural similarity index (SSIM), and peak signal-to-noise ratio (PSNR).

Results: Figure 1 shows consistently better results for the corrected images compared to their uncorrected counterparts for all three contrasts.

Motion correction for FLAIR images showed the largest percent improvement; this performance is comparable to models trained using thousands of 3D volumes. The improvement in T1 and T2 images was not as good.

Conclusions: These results confirmed the hypothesis that deep enough networks are capable of removing successfully the motion artefacts even when trained with small datasets. The curation and training of large datasets, from various locations using a variety of protocols, requires considerable amount of time and resources. Visually, the improvement in MAE and MSE comes mainly from removing of the motion artefacts around the skull and smoothing the image however SSIM has no significant improvement. The two most apparent types of motion artefacts influencing the images are ringing artefacts and blurring. Both types must be well-represented in the training dataset so that the model can learn to smooth ringing artifacts while maintaining (or reproducing in the case of blurring) the image features. In the case of FLAIR images, showing the largest improvement, this is the case. The T1 and T2 training images have more pronounced ringing artefacts, causing the DL model to favour smoothing of the image. Thus, image quality is improved but not to the same degree as that seen with FLAIR images. In future work, more attention should be paid to the motion artefacts present in the training images. This is especially the case when using small training sets, which are inherently more limited in the variety of motion artifacts present.

References: [1] Andre, et al. *J Am Coll Radiol*. 2015;**12**:689-695. [2] Pawar, et al. *Eur J Radiol*. 2020;**133**: 109384. [3] Johnson, et al. *Magn Reson Med*. 2019;**82**:901-910. [4] Knoll, et al. *Radiol Artif Intell*., 2020;**2**(1):e190007.

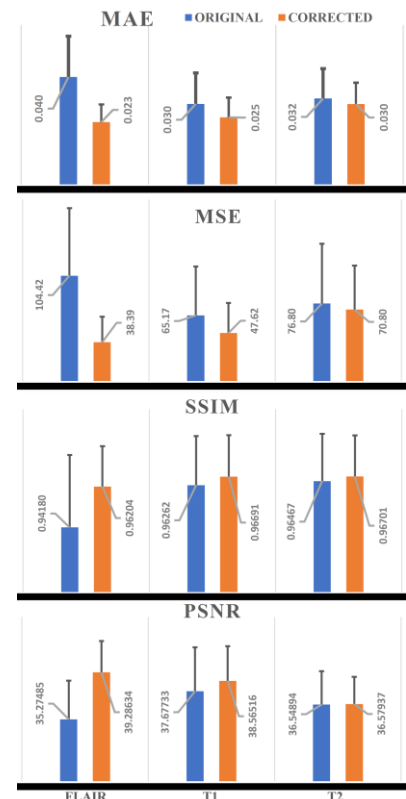


Figure 1. Comparison of MAE, MSE, SSIM and P-SNR (with standard deviations) of the original (uncorrected) and corrected images for FLAIR, T1 and T2.

Deep Learning for Motion Correction using Multichannel MRI Data

Miriam Hewlett,^{1,2} Ivailo E Petrov,¹ and Maria Drangova^{1,2}

¹Robarts Research Institute, The University of Western Ontario, Canada

²Department of Medical Biophysics, The University of Western Ontario, Canada

Introduction: Patient motion is a major source of artifacts in MRI, with as many as one in five MRI exams requiring that at least one scan be repeated due to motion artifacts [1]. While much research has been done on motion correction methods [2,3], motion still remains an issue due to limitations in clinical implementation or lack of generalizability to the variety of MRI sequences that exist. In the past few years, there have been several studies using convolutional neural networks (CNNs) for motion correction, with promising results. In this work we use a conditional generative adversarial network (cGAN) for motion correction using multichannel MRI data. We hypothesized that incorporating the channel data would improve network performance compared to that when correcting for motion in channel-combined images.

Methods: All networks were trained and evaluated on simulated motion artifacts in ~6000 brain images of the NYU fastMRI dataset [4]. These images were acquired at multiple centers with multiple contrasts, and contain images with a variety of neurological pathologies. Three cGANs were trained, each composed of a generator (3D CNN encoder-decoder) predicting motion free images from their motion corrupt counterparts and a discriminator (3D CNN classifier) identifying whether an image is the generated or target image (serving as an additional quality metric). The first cGAN was trained to correct for motion in the channel combined images. A second identical network was trained to correct for motion in the single channel images. A third, modified, network was trained to correct for motion on all channel data from a single image simultaneously (4D input; 3D image + channel dimension). To accommodate memory constraints imposed by the increased input size, the number of filters in each layer of this multichannel network was reduced.

Results: Motion correction with the single channel model provided a slight but significant improvement in both mean absolute error (MAE) and structural similarity index (SSIM, shown in Figure 1) between the corrected and ground truth images compared to the combined image model. The multichannel model provided significant improvement compared to the uncorrected (motion corrupt) images, but had relatively poor performance compared to the other approaches. This is likely a result of its limited modelling capacity, a consequence of reducing the number of convolutional filters in the network. Further optimization of memory usage during training would allow for a more complex multichannel model which could improve results.

Conclusions: Given that the networks were trained with large number of images acquired at a variety of sites, they will likely generalize well to brain MRIs of varying contrasts acquired at unseen centers. If multichannel data are available, correcting for motion prior to coil combination can provide a slight improvement in performance. This motion correction technique is relatively simple to apply in practice as it requires no modifications to image acquisition or additional hardware.

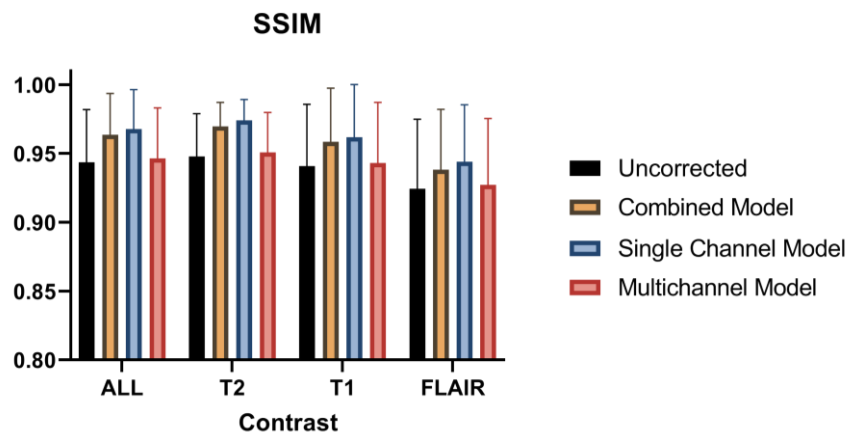
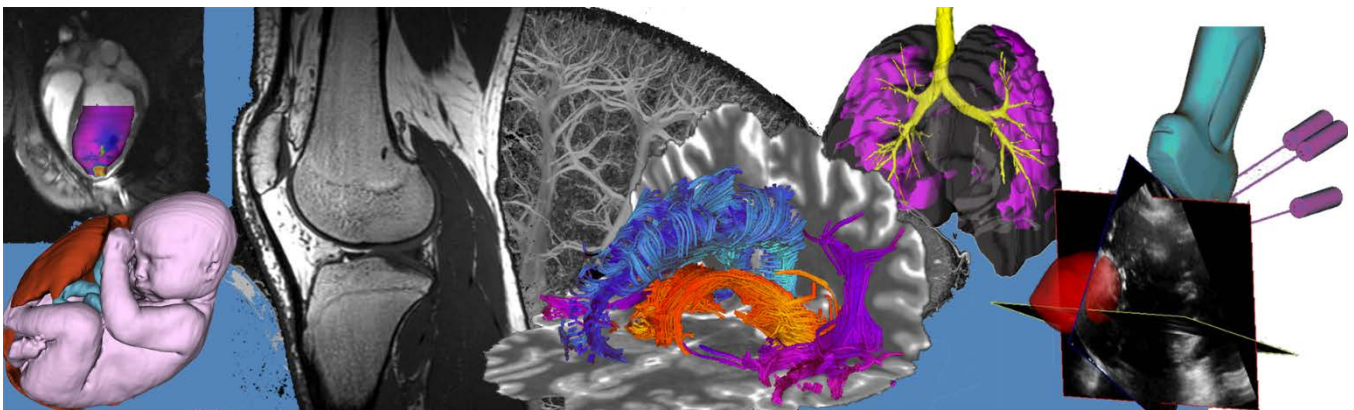


Figure 1. Structural similarity (SSIM) index comparing the ground truth images with uncorrected (motion corrupt) images, and those corrected with the combined, single-channel, and multichannel cGANs. All differences are significant ($p < 0.05$).

References: [1] Andre JB, et al. *J Am Coll Radiol*. 2015;**12**:689-695. [2] Frost R, et al. *Magn Res Med*. 2019;**82**:126-144. [3] Simegn GL, et al. *Magn Res Med*. 2019;**81**:2600-2613. [4] Zbontar J, et al. *arXiv*. 2019;1811.08839v2.

Pitch Presentation Abstracts

Session 12: Contrast Agents II



Endobronchial Ultrasound and Drug-Loaded Microbubbles for In Vivo Targeted Lung Cancer Therapy

Sean McGrath^{1*}, Masato Aragaki², Alexander Gregor², Yamato Motooka², Matthew Chen³, Samuel Penner³, Yu-Jack Shen³, Yiran Zou³, Yun Xiang⁴, Nicholas Bernards², Rimpei Kamegawa⁵, Kazuhiro Yasufuku² and Naomi Matsuura^{1,3,4}

¹*Institute of Biomaterials and Biomedical Engineering, University of Toronto*, ²*Division of Thoracic Surgery, Toronto General Hospital, University Health Network, Toronto*, ³*Department of Material Science and Engineering, University of Toronto*, ⁴*Department of Medical Imaging, University of Toronto*, ⁵*Department of Materials Engineering, University of Tokyo, Japan*

Introduction: Lung cancer is the leading cause of cancer-related death [1]. Endobronchial ultrasound (EBUS) is a clinical diagnostic tool developed for lung cancer staging [2], where a modified bronchoscope is introduced into the patient's airway and, using the integrated ultrasound probe, image-guided transbronchial biopsies of targets deep within the chest are obtained [3]. This study explores the use of EBUS as a technique for targeted lung cancer therapy via intravenously-injected, drug-loaded, acoustically-activated, microbubble agents. Under sufficient pressures, drug-loaded microbubble cavitation has been shown to physically damage tumour vasculature [4] as well as release loaded drugs for combined antivasular therapy and drug delivery. Although EBUS overcomes the limitations of standard clinical ultrasound systems, which cannot access the inner lung due to limited sound wave penetration of alveolar air, clinical EBUS systems emit lower power than non-EBUS therapeutic ultrasound systems. Additionally, microbubbles typically contain a hydrophobic perfluorocarbon core, limiting the loading of hydrophilic chemotherapeutic drugs. The aim of this study was to develop nanoparticles that can be loaded with high concentrations of hydrophilic drugs (such as the front-line chemotherapeutic cisplatin) and then be incorporated into microbubbles for activation by EBUS for therapy. This system would have the dual benefit of bringing antivasular therapy and targeted drug delivery to lung cancer care, improving possible outcomes.

Methods: Drug-loaded silica nanoparticles were synthesized [5]. To validate colocalization of the drug in the microbubbles, a hydrophilic fluorescent dye, fluorescein (Sigma Aldrich), was used as an optical surrogate for hydrophilic chemotherapeutics. Dynamic light scattering (DelsaMAX, Beckman Coulter, USA) was used to determine nanoparticle size. Nanoparticle-loaded microbubbles, composed of a decafluorobutane core (C4F10, Synquest labs) and a phospholipid shell (DPPA, DPPC, DPPE-PEG5k, Avanti Polar Lipids) were synthesized in-house. These were characterized for their stability and size distribution using a Coulter counter (Multisizer 4e, Beckman Coulter, USA). Fluorescein-loaded microbubbles were imaged using fluorescence microscopy to verify nanoparticle incorporation. Microbubbles were tested for their cavitation response to ultrasound (VIFU 2000, Alpinion) by flowing dilute microbubbles at 37°C through a 2% agar phantom. Murine AE17-OVA mesothelioma tumours were inoculated subcutaneously in the right flank of C57BL/6 mice (Taconic Bioscience, NY) as analogs for thoracic malignancy. A 150µL (~5x10⁸ microbubbles/mL) injection of microbubbles was followed by ultrasound (f=5MHz, MI~1.2) using EBUS (EU-ME2 PREMIER ultrasound processor with BF-UC180F EBUS bronchoscope, Olympus, Japan). Contrast-enhanced ultrasound (MI=0.06) with microbubbles was performed before and after the procedure to evaluate for changes in blood perfusion as a marker of vascular disruption (comparison through MATLAB, MathWorks).

Results: Drug-loaded nanoparticles with a mean size of 49.7±0.4nm (PDI=0.078±0.016) were successfully synthesized. Fluorescein nanoparticle-loaded bubbles were fluorescent, indicating the nanoparticles were successfully incorporated. Nanoparticle loaded microbubbles were acoustically active under ultrasound, and were able to be disrupted using the VIFU 2000 system. Non-loaded microbubbles were shown to reduce blood perfusion through thoracic malignancies in mouse tumor models.

Conclusion: This study developed a procedure for synthesizing and successfully incorporating hydrophilic drug-loaded nanoparticles into microbubbles. These microbubbles can be cavitated by current EBUS technology, enabling combined targeted drug delivery and antivasular therapy for the treatment of lung cancer.

References: [1] Cancer, www.who.int/news-room/fact-sheets/detail/cancer, [2] C. Kinsey et al, American journal of respiratory and critical care medicine, vol. 189, no. 6, pp. 640 – 649, 2014, [3] K. Czarnecka-Kujawa. and K. Yasufuku, Journal of Thoracic Disease, 9(Suppl 2), pp. S83-S97, 2017, [4] Y. Zhou, Journal of Therapeutic Ultrasound, vol. 3, no. 20, 2015, [5] R. Kamegawa et al, Nano Research, vol. 11, no. 10, pp. 5219 – 5239, 2018

Carbon-11 labelling of ALK2 inhibitors and PET neuroimaging in rodents

Emily Murrell¹, Junchao Tong¹, David Smil,² Methvin B. Isaac,² Iain D.G. Watson,² and Neil Vasdev¹

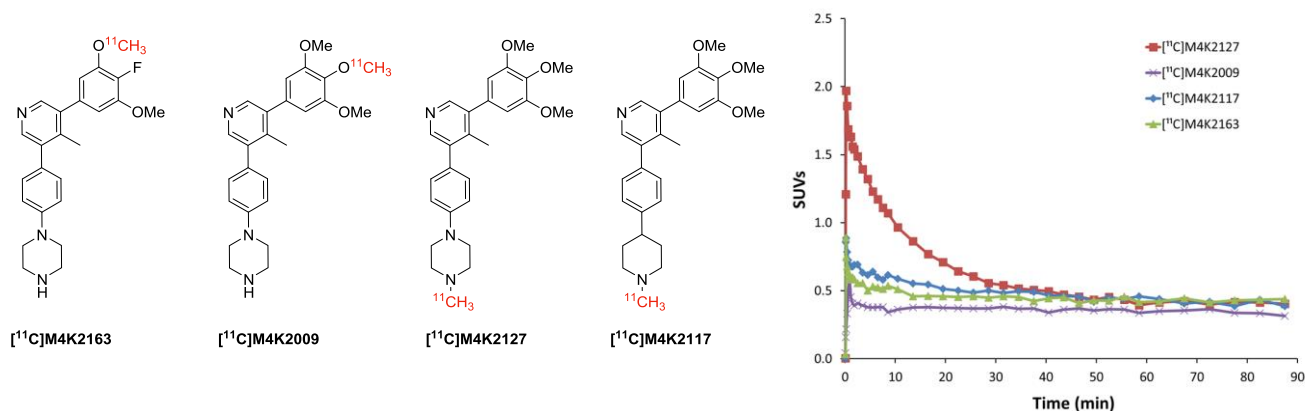
¹Azrieli Centre for Neuro-Radiochemistry, Brain Health Imaging Centre, Centre for Addiction and Mental Health & Department of Psychiatry, University of Toronto, Toronto, Ontario.; ²Drug Discovery Program, Ontario Institute for Cancer Research, Toronto, Ontario.

Introduction: Activin receptor-like kinase-2 (ALK2) is a kinase receptor encoded by the ACVR1 gene. Mutations in ACVR1 causing a gain-of-function in ALK2 signalling have been reported in approximately 25-30% of children with diffuse intrinsic pontine glioma (DIPG), a pediatric brainstem cancer with poor prognosis. M4K Pharma in collaboration with the OICR have developed a series of 3,5-diphenylpyridine ALK2-selective inhibitors for the treatment of DIPG (Smil D., et al. *J. Med. Chem.* **2020**, 63 (17), 10061-10085). Drug discovery of central nervous system (CNS) drugs can be facilitated by assessing blood-brain barrier (BBB) permeability through brain PET imaging with isotopically labelled drug candidates. The goal of the present study was to label four lead ALK2-selective inhibitors with carbon-11 (half-life = 20.4 min) and assess BBB permeability of these radiotracers by PET imaging in rodent models.

Methods: Four lead compounds identified by M4K Pharma were selected for radiolabelling. The compounds were radiolabelled via *N*- or *O*-methylation with ¹¹C-methyl iodide or ¹¹C-methyl triflate. Shake-flask logD values were experimentally determined with the radiolabelled compounds. Permeability of the radioligands into the brain was assessed through brain PET imaging in healthy Sprague-Dawley rats. Time-activity curves were constructed for the course of the scan for whole brain and for the pons as a region of interest.

Results: The ability of a radiotracer to cross the BBB is influenced by many characteristics (logD, pKa, efflux transporters). Prior to radiolabelling, CNS Multiparameter Optimization desirability scores were calculated for the lead compounds, giving scores of 4.34-5.04. All four compounds were successfully synthesized in radiochemical yields of 5-25% and isolated and formulated with >97% radiochemical purity. Molar activities ranged from 269-664 GBq/μmol. [¹¹C]M4K2117, [¹¹C]M4K2163 and [¹¹C]M4K2009 all had low brain uptake with SUVs less than 1 after first-pass. Fortunately, [¹¹C]M4K2127 showed high brain uptake, with a first-pass brain standardized uptake values (SUV) of 2, homogenous brain distribution including the pons, and moderate wash out from the brain over time.

Conclusions: We have synthesized four ¹¹C-isotopologues of drug candidates for DIPG through simple and robust radiochemical methods to allow for immediate visualization of BBB penetration in rodents through PET imaging. Of these four lead compounds, [¹¹C]M4K2127 is the radiotracer with the highest brain exposure and blocking studies are underway to confirm specific binding in brain regions.



Mapping vitamin B6 metabolism by CEST-MRI

Brun E¹, Suchý M^{1,2}, Calvert N^{1,2}, Kirby A^{1,2}, Truong Y^{1,2}, Pineault-Mason E^{1,2}, Shuhendler A^{1,2}

¹ Department of Chemistry and Biomolecular Sciences, University of Ottawa, Ottawa, Ontario, Canada; ² University of Ottawa Heart Institute, Ottawa, Ontario, Canada

Introduction: Chemical exchange saturation transfer (CEST) is an implementation of magnetic resonance imaging (MRI), mapping water signal suppression through the exchange of selectively spin saturated protons from contrast agent molecules. While several examples exist demonstrating the application of CEST contrast agents for mapping enzyme activity [1, 2], there are limited examples harnessing CEST-MRI for mapping endogenous metabolites [3, 4]. We previously introduced HydrazoCEST contrast agents based on 5-methoxy-aminoanthranilic acid, which can selectively map aliphatic aldehydes upon hydrazone formation [5]. Herein we introduce a second iteration of HydrazoCEST based on 2-hydrazinonicotinic acid (2-HYNIC) that shows selectivity for aromatic aldehydes, expanding our capacity to map endogenous metabolites. While endogenous aromatic aldehydes are limited in number, pyridoxal (Vit B₆) is of particular interest as imaging biomarker. Pyridoxal is critical for more than 120 metabolic reactions, and which is acquired exclusively from our diet. The phosphorylated form (pyridoxal 5'-phosphate) is the active form of the coenzyme and is the product of the balance of pyridoxal kinase and pyridoxal phosphatase activities [6]. Pyridoxal metabolism mapping may be valuable in lung cancer prognosis, where decreased pyridoxal kinase activity has been associated with drug resistance [7], and in neuropsychiatric disorders that have shown alterations in pyridoxal kinase activity with syndrome onset and progression [8]. Herein, we introduce and characterize 2-HYNIC as a next-generation implementation of HydrazoCEST and apply it to map pyridoxal metabolism in lung tumors.

Methods: Pyridoxal hydrochloride or pyridoxal phosphate hydrate were treated with 2-HYNIC acid trihydrochloride (Generation 2) or 5-methoxy-2-hydrazinobenzoic acid dihydrochloride (Generation 1). Z-spectra acquired on a 7T NMR were used to analyse the performance of both generations of HydrazoCEST compounds with aliphatic and aromatic aldehydes across a pH range of 6.0-12.0. *In vitro* Z-spectra were acquired on a 3T MRI in A549 and H460 lung cancer cells. Pyridoxal metabolism was evaluated by mass-targeted mass spectroscopy in order to corroborate *in vitro* imaging results.

Results: Through solution-based Z-spectral analysis, 2-HYNIC was shown to preferentially produce CEST-MRI contrast when bound to pyridoxal 5'-phosphate ($MTR_{\text{asym}}=28\%$) over pyridoxal ($MTR_{\text{asym}}=5\%$). Through Z-spectral and spectroscopic studies across pH, and with support from molecular modelling, we propose that the selectivity for the phosphorylated form derives from a planar conformation promoted by the 5'-phosphate, which promotes an intramolecular hydrogen bond necessary for adequate proton exchange. Through *in vitro* CEST-MRI, we were able to map the alteration in the balance of pyridoxal 5'-phosphate levels in lung cancer cell lines (Fig.1 left). The hydrazone of 2-HYNIC and pyridoxal 5'-phosphate was detected by mass spectroscopy, and whose magnitude corroborated imaging signal derived from CEST-MRI (Fig. 1 right).

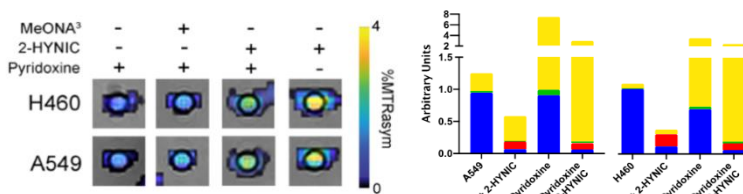


Figure 1. Mapping pyridoxal metabolism *in vitro*. Left: CEST-MRI of H460 and A549 cell pellets. Right: Mass spectroscopy of pyridoxal metabolism. Yellow: Pyridoxine, Blue: Pyridoxal phosphate, Green: Pyridoxal, Red: 2-HYNIC-pyridoxal 5'-phosphate hydrazone.

Conclusion: 2-HYNIC presents an opportunity to access pyridoxal metabolism as an imaging biomarker, which has not previously been possible.

Keywords: Chemical exchange saturation transfer, Magnetic resonance imaging, Pyridoxal 5'-phosphate, Lung cancer.

[1] Yoo B, Pagel LD., J Am Chem. Soc., **2006**;128: 14032-14033. [2] Yoo B et al., Magn Reson Med. **2014** Mar; 71(3): 1221-1230. [3] Wu B et al., EJNMMI Phys. dec **2016**;3(1):19. [4] van Zijl PCM, Yadav NN., Magn Reson Med. avr **2011**;65(4):927-48. [5] Trina Dang et al., Chem. Eur. J. 10.1002/chem.201801671. [6] Jun YW et al., Chem Commun (Camb). **2019** Dec 19;56(2):317-320. [7] Galluzzi L et al., Cell Reports 2, 257-269, August 30, **2012**. [8] Galluzzi L et al., Oncogene (**2013**) 32, 4995-5004

Feasibility Study of Simultaneous Hyperpolarized ^{129}Xe MRI and ^{15}O water PET Measurements

Ramanpreet K. Sembhi¹, Matthew S. Fox^{1,2}, Hacene Serrai¹, Kieffer J. Davieau^{1,3}, Adam Farag^{2,3}, Justin W. Hicks^{2,3}, Udunna Anazodo^{2,3}, Shawn N. Whitehead⁴, Jonathan D. Thiessen^{2,3} and Alexei V. Ouriadov^{1,2,5}

¹Department of Physics and Astronomy; ²Lawson Health Research Institute; ³Department of Medical Biophysics; ⁴Department of Anatomy and Cell Biology; ⁵School of Biomedical Engineering, Faculty of Engineering, The University of Western Ontario, London, Ontario, Canada

INTRODUCTION

Inhaled hyperpolarized (HP) ^{129}Xe magnetic resonance imaging (MRI) is a non-invasive imaging method, which is currently used to measure lung structure and function.^{1,2} This MRI approach provides a way to obtain simultaneous ventilation/perfusion (V/P) lung measurements. Due to various physical properties of the ^{129}Xe isotope, it can serve as a new probe for brain blood flow, grey and white matter mapping^{3,4} and functional measurements. ^{15}O -water positron emission tomography (PET) is the gold standard imaging method for determining cerebral perfusion.^{5,6} In this study, simultaneous ^{129}Xe -based MRI and ^{15}O water PET images were collected and compared.

METHODS

We used the ^{15}O water solution (30mL) contained in a 60mL plastic syringe to dissolve 30mL of the hyperpolarized ^{129}Xe gas. After dissolving, all leftover xenon gas was removed from the syringe. Hyperpolarized ^{129}Xe gas was obtained from a turn-key, spin-exchange polarizer system (Polarean 9820 ^{129}Xe polarizer). ^{129}Xe dissolved phase images were acquired in a 3T PET/MRI (Siemens Biograph mMR) scanner. ^{15}O water PET data were acquired simultaneously with ^{129}Xe MRI using the integrated PET system in the 3T PET/MRI.

RESULTS:

Figures 1a, b and 2a, b shows two consecutive 2D axial ^{129}Xe MRI images and two (2D and 3D) ^{15}O water PET images acquired simultaneously. ^{129}Xe /PET images indicate that the diameter of the phantom from both PET and MRI images are similar. Both ^{129}Xe images demonstrate a sufficient SNR level suggesting that 3D ^{129}Xe imaging is possible.

DISCUSSION AND CONCLUSIONS:

To our knowledge, for the first time ever, we have demonstrated that hyperpolarized ^{129}Xe dissolved in ^{15}O water can be used in multi-modal imaging. This demonstration will enable the next step, namely, *in-vivo* double tracer brain perfusion imaging. We plan to perform important validation work for ^{129}Xe -based brain perfusion techniques, directly and simultaneously with ^{15}O water PET using a small animal model. The comparison results show similarity between both imaging modalities and tracers, moving towards the next step in validating the Xenon imaging technique as a potential for brain perfusion measurement. The ability to use ^{129}Xe as a non-radioactive tracer, providing similar and complimentary information as ^{15}O PET may be a much more cost-effective alternative to PET for imaging stroke, brain cancer and other brain diseases and will significantly increase the number of the ^{129}Xe MRI clinical applications.

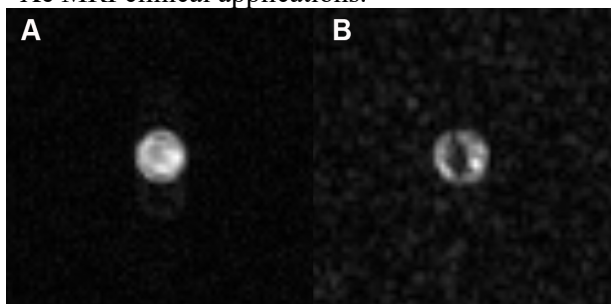


Figure 1. Two consecutive 2D axial ^{129}Xe MRI images. SNR of (a) is 80 and for (b) is 10.

References:

1. Kaushik, S. S. et al. MRM (2016).
2. Kaushik, S. S. et al. J Appl Physiol (2013).
3. Kershaw, J. et al. MRM (2007).
4. Wakai, A., et. al. ICS (2004).
5. Fan, A., et. al. JCBFM (2016).
6. Ssali, T., et. al. JNM (2018).

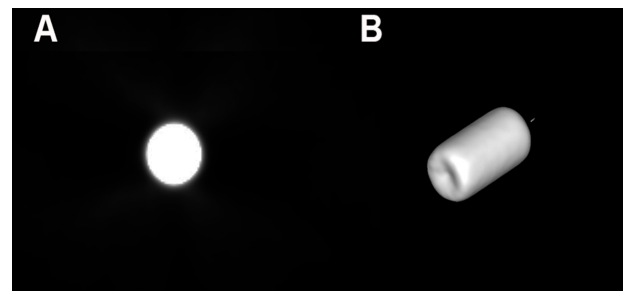


Figure 2. 2D axial (a) and 3D (b) ^{15}O water PET images

Acknowledgements

Research and financial supports received from BrainsCAN Accelerator Program. Thankful to Dr. Grace Parraga for providing us hyperpolarized ^{129}Xe gas.

The Feasibility of Hyperpolarized ^{129}Xe MRI for lung damage in COVID-19 Survivors using a Key-Hole Method.

Tuneesh K. Ranota¹, Hacene Serrai², David G. McCormack³, Grace Parraga^{1,3,4,5}, and Alexei Ouriadov^{1,2,6}

¹School of Biomedical Engineering, Faculty of Engineering; ²Department of Physics and Astronomy; ³Division of Respiriology, Department of Medicine; ⁴Robarts Research Institute;

⁵Department of Medical Biophysics, The University of Western Ontario, London, ON, Canada,

⁶Lawson Health Research Institute, London, ON, Canada

RATIONALE: The lungs cannot be visualized with proton MRI due to the low tissue density of the lungs. The use of hyperpolarized noble xenon-129 gas helps us overcome this difficulty and obtain lung structure and function, thus allowing investigation of pulmonary diseases.¹ To improve ^{129}Xe gas MRI performance, traditional COVID-19 survivors low resolution data acquired in a single breath-hold with an FGRE sequence were combined with acquired noisy data to generate high-resolution 3D static-ventilation images using the well-known key-hole method.² The SNR of the high-resolution 3D images was sufficient to precisely calculate the Ventilation-Defect-Percent (VDP), a sensitive indicator of lung ventilation abnormalities. Therefore, isotropic-voxel high-resolution 3D ^{129}Xe static-ventilation images obtained from processing traditional low-resolution data¹ using keyhole approach² could be used to measure VDP and increase our understanding on the effects of COVID-19 on the lungs.

METHODS: Three COVID-19 survivors provided written consent to an ethics board approved protocol and underwent spirometry and $^1\text{H}/^{129}\text{Xe}$ MRI scanning. ^{129}Xe imaging was performed at 3.0T (MR750, GEHC, WI) using specific ^{129}Xe RF coil.² Traditional coronal resolution xenon images, were acquired using a 3D FGRE sequence with acquisition parameters (TE/TR/initial-flip-angle=1.5ms/5.1ms/1.3°, variable-flip-angle, Bandwidth=16kHz, FOV=40x40x24cm³, voxel size=3x3x15mm³)³ All images were acquired in breath-hold (<16 second) after inspiration of 1.0L of gas ($^{129}\text{Xe}/^4\text{He}$ mixture, 30/70) from functional-residual-capacity. Pre-(baseline) and post-salbutamol data set acquired for each study subjects. Proton MRI was performed as previously described.¹ Image SNR³ and VDP⁴ values were calculated for five central slices for each coronal view. Extra four low-resolution images without xenon breath-hold were acquired to obtain the noise data sets. Using the key-hole technique², the four noisy data sets were combined with the single xenon signal data to obtain 3x3x3 mm³ isotropic high-resolution-images.

RESULTS: Figure 1 reports patient information and imaging results for the traditional and high-resolution images of the COVID-19 survivors. The calculated VDPs were lower for the high-resolution data compared to the traditional resolution data. The pre- and post-salbutamol values were similar except for Survivor 1, where the post-salbutamol value was twice as large. The calculated SNR values of the five isotropic-voxel images ranged between 26 and 29, and between 55 and 70 for isotropic-voxel and traditional data, respectively.

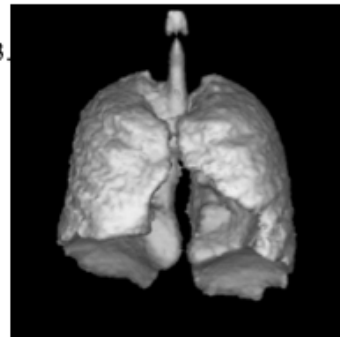
DISCUSSION: The sufficient SNR of the acquired traditional and 3D isotropic-voxel ^{129}Xe images allow for a precise VDP calculation, with mean values comparable to those obtained from asthma patients.⁵

CONCLUSIONS: In this proof-of-concept study, we demonstrated that 3D isotropic-voxel ^{129}Xe static-ventilation images can be acquired in a single breath-hold using the key-hole technique with sufficient SNR to analyze VDP, to assess lung damage in COVID-19 survivors.

Figure 1: High-resolution ^{129}Xe MRI results for COVID-19 survivors And 3D high-resolution isotropic static ventilation image for survivor 3.

	High-Res 1	High-Res 2	High-Res 3	Low-Res 1	Low-Res 2	Low-Res 3
Age	33F	57F	46F	33F	57F	46F
FEV ₁ %pred	95	117	97	95	117	97
VDP %	3	2.5	3	2.5	8	6
pre						
VDP %	8	4	2.5	7	9	5
post						
Voxel	3x3x	3x3x	3x3x	3x3x15	3x3x15	3x3x15
(mm ³)	3	3	3			
SNR _{coronal}	26	28	29	55	56	70
pre						

BMI=body mass index, FEV₁=forced expiratory volume in 1 second, VDP=ventilation defect percent, SNR=signal to noise ratio, calculated for baseline (pre-salbutamol) data only.



Acknowledgements
Thank you to the support from Western Research Catalyst Grant and the COVID-19 Rapid Research Fund.

References

1. Kirby M et al Radiol (2014).
2. Niedbalski P et al MRM (2019).
3. Ouriadov A et al MAGMA (2009).
4. Dominguez W et al MRM (2011).
5. Barker A et al ISMRM (2019).

The Use of a Novel Sampling/Reconstruction Method for Non-Proton and Low Field MRI

Samuel Perron¹, Matthew S. Fox^{1,2}, Hacene Serrai¹ and Alexei Ouriadov^{1,2,3}

¹Department of Physics and Astronomy, The University of Western Ontario, London Canada

²Lawson Health Research Institute, London, Canada

³School of Biomedical Engineering, The University of Western Ontario, London, Canada

Introduction: The MRI modality is generally a low sensitivity method¹ due to the nature of the MRI-signal formation governed by a very small number of the nuclear spins that contribute to the resulting signal. This low sensitivity can be overcome by very high concentrations of water content in body tissue and the high gyromagnetic ratio of ¹H. In cases of other nuclei with low gyromagnetic ratios (e.g., ¹³C/²³Na/¹²⁹Xe)²⁻⁴ or low field MRI⁵, image quality can presently be improved by using expensive MRI-hardware or expensive enriched isotopes. We propose a new method that does not require any extra signal averaging or hardware to improve the quality of MRI images. We will use a significant k-space under-sampling acquisition method where only a certain percentage of the k-space points will be acquired per image, corresponding to the acceleration factor (AF); it follows that one can acquire ten under-sampled images in the same time as one fully-sampled image. The MRI image SNR is directly proportional to the square root of the number of signal averages. Averaging each possible combination of images of the under-sampled set, a density decay curve can then be fitted and reconstructed using the Stretched-Exponential-Model (SEM) combined with Compressed Sensing (CS).^{6,7} We hypothesize that the SEM-equation can be adapted for fitting the SNR dependence of the MR-signal similar to fitting time/b-value dependences.^{8,9}

Methods: ¹H MR was performed on a resolution-phantom at 3.0T (MR750, GEHC, WI) using a clinical gradient coil set and commercial head RF coil. Nine 2D single-averaged fully-sampled k-spaces were acquired. Combinations of 2, 3, and 4 averages were carried out for each possible permutation, resulting in 14 k-spaces total (2 combinations for 4 averages, etc). Three Cartesian sampling schemes (FGRE, x-Centric¹⁰ and 8-sector FE Sectoral¹¹) were used. 14 fully-sampled k-spaces were retroactively under-sampled (AF=7/10/14) in SNR attenuation direction. It is assumed that the SNR attenuation reflects a decrease of the fluorinated-gas density in



Figure 1. Original fully-sampled ¹H resolution phantom image (right, SNR=6.5) and nine averages image (left, SNR=22).

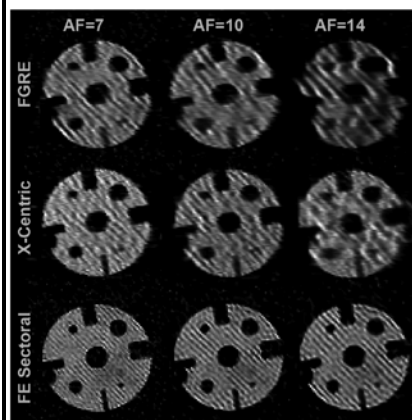


Figure 2. Representative ¹H resolution phantom images reconstructed from retroactively under-sampled k-spaces.

the lung after delivery of the O₂ wash-out breaths.¹² The signal intensity of the resulting images would be gradually attenuated with each new wash-out breath of O₂ (no real ¹⁹F lung data was acquired/presented). Thus, signal-intensity of the under-sampled k-spaces were fitted following the Abascal method.⁷

Results: The SNR of the 9 k-space averaged image and the original image was 22 and 6.5, respectively (Figure 1). Figure 2 shows the reconstructed images for three sampling-schemes and three AF. The SNR of the three sampling schemes is 20 for FGRE, 28 for x-Centric, and 25 for FE Sectoral.

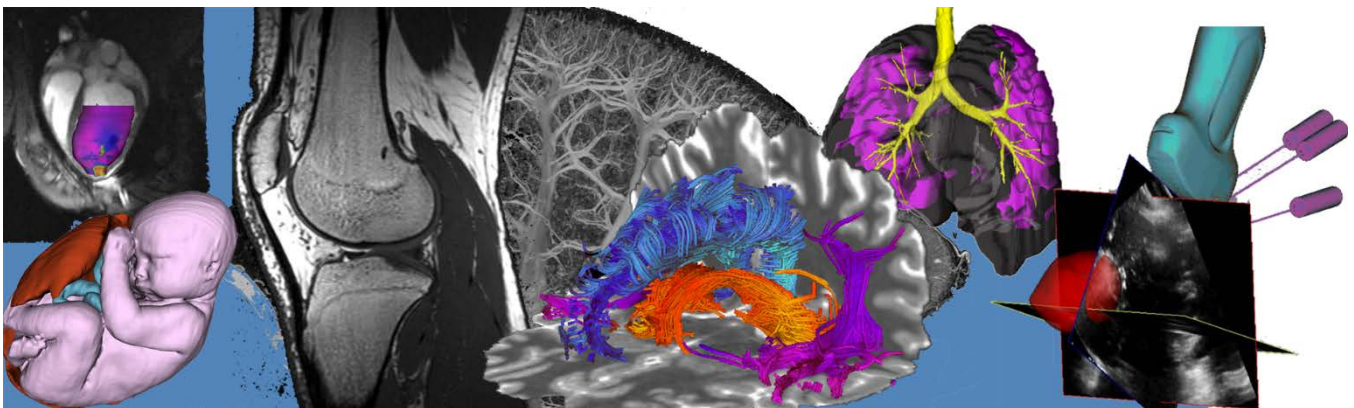
Conclusion: The improved SNR of the generated images for all three sampling schemes demonstrate that the SEM equation can be adapted for fitting the SNR attenuation dependence of the MR signal, similar to fitting the time/b-value dependences. Due to this technique not requiring extra hardware, the proposed method could be implemented in current MRI-systems and yield improved images. Due to the CS-based reconstruction, higher AF leads to more visible artefacting; this could be reduced by a DL-based correction after the fact.¹³⁻¹⁵

References:

1. Song, X.-x. et al. New J. Chem. (2014);
2. Thind, K. et al. MRM. (2013);
3. Fox, M. S. et al. Med Phys. (2014);
4. Farag, A. et al. JMRI. (2015);
5. Wawrzyn, K., et al. Proceedings of the 23th Annual Meeting of ISMRM. (2015);
6. Westcott, A. et al. JMR Imaging. (2019);
7. Abascal, J. et al. IEEE Trans Med Imaging. (2018);
8. Berberan-Santos, M. N., et al. Chemical Physics. (2005);
9. Parra-Robles, J. et al. ISMRM 21st Annual Meeting. (2013);
10. Ouriadov, A. V., et al. MRM (2017);
11. Khrapitchev, A. A. et al. JMR. (2006);
12. Ouriadov, A. V. et al. MRM. (2015);
13. Yang, Y., et al. IEEE Trans Pattern Anal Mach Intell. (2020);
14. Hammernik, K. et al. MRM. (2018);
15. Yang, G. et al. IEEE Trans Med Imaging. (2018).

Oral Presentation Abstract

Session 13: Cancer Imaging I



Comparing the detection of breast cancer brain metastasis with magnetic particle imaging (MPI) to MRINatasha N. Knier^{1,2} and Paula J. Foster^{1,2}¹Department of Medical Biophysics, Western University, London, ON, Canada²Imaging Laboratories, Robarts Research Institute, London, ON, Canada

Introduction: Magnetic particle imaging (MPI) is an emerging modality that sensitively detects the magnetization of superparamagnetic iron-oxide nanoparticles (SPIONs). Our lab has developed SPION based cellular magnetic resonance imaging (MRI) technology for many years to determine the fate of metastatic breast cancer cells to the brain.¹ MRI cell tracking with SPIONs has some limitations. First, quantification of iron-induced signal loss detected with MRI is challenging. Second, other regions of signal void in MR images lead to low specificity. MPI cell tracking has the potential to overcome these challenges. The MPI signal appears as a hot spot with no background, providing high specificity. The MPI signal is also proportional to iron content and directly quantifiable, providing the ability to measure iron mass and estimate cell number. Sensitivity and resolution in MPI depend heavily on the magnetic properties of the SPION tracer. Synomag-D™, a nanoflower particle, that has been shown to be superior to ferucarbotran, a commonly used MPI tracer, has been explored as a sensitive tracer for MPI. Currently, no studies exist that use this tracer to track cancer cells. Our aim was to utilize Synomag-D for quantitative MPI of iron-labeled breast cancer cells in the mouse brain and to compare to previous work where we used breast cancer cells labeled with micron sized iron particles (MPIO) and imaged by MRI.

Methods: Human brain metastatic breast cancer cells (231BR) were labeled with Synomag-D (MicroMod GmbH). Labeling efficiency was determined with a Perl's Prussian Blue (PPB) stain. NOD/SCID/IL2rg^{-/-} (NSG) mice (n=6) were injected with 2.5×10^5 cells intracardially (IC) using ultrasound guidance. MPI was performed on a MOMENTUM scanner (Magnetic Insight Inc., Alameda, CA, USA) on Day 0 (n=3) and Day 7 (n=6) to image the mouse brain. MPI data was compared to MRI obtained in a prior study using mice injected IC with 2.5×10^5 MPIO-labeled 231BR cells.

Results: 231BR cells were successfully labeled with Synomag-D with an efficiency of $98.0 \pm 0.40\%$ (Fig. 1A). A calibration line was generated from samples of Synomag-D to determine iron content for a given MPI signal based on imaging parameters. We determined there was a strong linear relationship between iron content and MPI signal (arbitrary units, A.U.) for Synomag-D ($R^2=0.96$, $p<0.0001$). The equation of the line was: $\text{MPI Signal} = 274.12 * (\text{Iron Content})$ (Fig. 1B).

Using this relationship, iron content could be determined for a given MPI signal. On the day of the injection, MPI signal was detected in the brain in 3/6 mice (Fig. 1C). The mean iron content measured for these brains was 0.08 ug. Strong MPI signal was also visible in the lung/liver region since cells injected IC are distributed throughout the body. We have shown that such strong MPI signal impedes detection and quantification in nearby regions with low signal.² Day 7 MPI revealed that lung/liver signal had diminished over time resulting in the ability to distinguish MPI signal in the brains of 5/6 mice at this timepoint. MPI signal in the brain on day 7 was lower, with mean iron content measuring 0.012 ug. This is expected, as a large proportion of arrested cancer cells are known to die and clear by day 7 in this model.³ In day 0 MRI, MPIO-labeled cells appear as discrete signal voids throughout the brain (Fig. 1D). Quantification of these images is challenging; voids can be counted, or the total signal void volume, or percentage of black pixels in the brain, can be calculated. However, this does not allow for the determination of cell number.

Conclusions: This is the first study to demonstrate that brain metastatic breast cancer cells can be labeled with Synomag-D, and subsequently, can be detected *in vivo* in the mouse brain with MPI. We calculated the iron content in each mouse brain using a calibration line which is used to relate MPI signal to known iron content in Synomag-D samples. This data indicated that we were detecting on average 16,000 cells in the mouse brain with a cell labeling of ~5 pg of iron/cell. Employing MPI for experimental cancer cell tracking will allow for the detection and quantification of the arrest, clearance, and retention of cancer cells *in vivo*.

References: 1. Heyn et al., *Magn Reson Med*. 2006. 2. Makela et al., *Mol Imaging Biol.*, 2020 3. Parkins et al., *Sci Rep.*, 2016

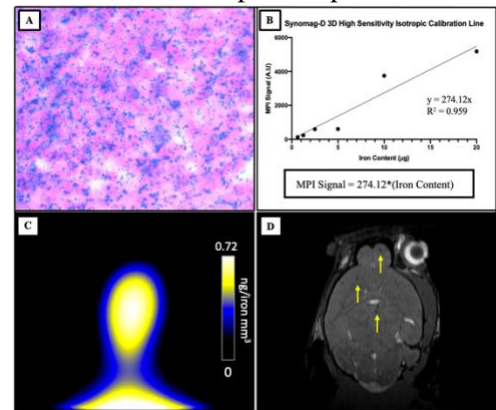


Figure 1: A) PPB showing cells labeled with Synomag-D. B) MPI calibration line to determine iron content for given MPI signal. C) Representative MPI of signal from mouse brain. D) Representative MRI with signal voids throughout brain (yellow arrows).

In vivo evaluation of a cyclooxygenase-2 (COX-2) radiopharmaceutical, [^{11}C]MC1, in human colorectal cancer xenograft mouse models.

Amanda J. Boyle¹, Junchao Tong¹, Sami S. Zoghbi², Victor W. Pike², Robert B. Innis², Neil Vasdev¹.

¹Azrieli Centre for Neuro-Radiochemistry, Brain Health Imaging Centre, Centre for Addiction and Mental Health, Toronto, ON, Canada, ²National Institute of Mental Health, Bethesda, MD, USA.

Introduction: The role of cyclooxygenase-2 (COX-2) as a putative biomarker for inflammation as well as cancer progression and prognosis is evident [1]. The radiopharmaceutical [^{11}C]MC1 has recently been translated for human use (ClinicalTrials.gov identifier: NCT04582916, NCT04396873) to explore the role of COX-2 in neurological diseases: major depressive disorder and dementia. Our laboratories have recently repurposed a COX-1 neuro-PET radiopharmaceutical for oncology [2]. The aim of the current study is to evaluate [^{11}C]MC1 as a PET radiopharmaceutical for the detection of COX-2 colorectal cancer in tumor xenograft mouse models.

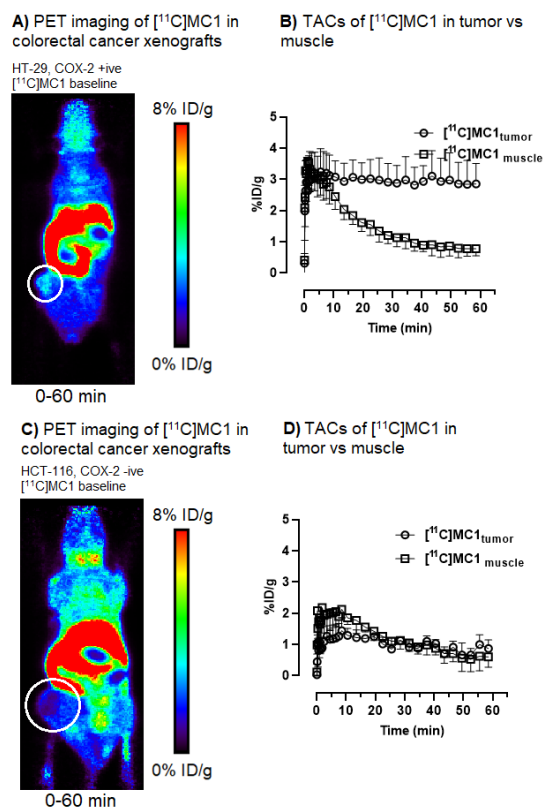


Fig. 1. Dynamic PET imaging of [^{11}C]MC1 in mice bearing **A)** HT-29 s.c. xenografts and **B)** associated TACs in tumor vs muscle, and in mice bearing **C)** HCT-116 s.c. xenografts with **D)** associated TACs in tumor vs muscle. White circles indicate the site of tumors.

Methods: Radiosynthesis of [^{11}C]MC1 was performed as previously described [3] and evaluated in human colorectal xenograft mouse models with HT-29 (COX-2 positive) and HCT-116 (COX-2 negative) cells inoculated subcutaneously (s.c.) on the right flank of ICRscid mice. Evaluation of [^{11}C]MC1 was performed by dynamic PET imaging, as well as biodistribution, and radiometabolite analysis of plasma and tumor homogenates. Cellular uptake and immunohistochemistry studies are underway.

Results: HT-29 xenografts were well visualized with [^{11}C]MC1 (0-60 min average image). Time-activity curves (TACs) show tumor radioactivity accumulation that quickly reached a plateau at 10-60 min with an average uptake of 3.07 ± 0.65 %ID/g (40-60 min, n=6). The signal in the tumor was significantly higher than femoral muscle tissue, 0.78 ± 0.25 %ID/g ($p=0.0002$) and was significantly reduced by pre-treatment with 33 mg/kg non-radiolabeled MC1 to 1.62 ± 0.29 %ID/g ($p=0.045$). The COX-2 negative HCT-116 xenografts had tumor radioactivity accumulation similar to that of femoral muscle tissue, 0.71 ± 0.27 %ID/g. *In vivo* PET imaging analyses were validated by biodistribution studies. Radiometabolite analysis revealed the parent compound, [^{11}C]MC1, to account for 91.2 ± 1.0 % of radioactivity in HT-29 tumor xenografts, versus 8.8 ± 5.8 % in cardiac blood plasma, at 40 min post-injection of the radiotracer.

Conclusions: [^{11}C]MC1 has a favorable radiobiological profile for studying the role of peripheral COX-2. Clinical translation of this radiopharmaceutical in oncology is planned.

References: [1] Cyclooxygenase-2 in cancer: A review. *J Cell Physiol.* 2019;234:5683-5699. [2] Boyle AJ, *et al.* *J Nucl Med.* 2020; ePub ahead of print. DOI: 10.2967/jnumed.120.249367. [3] Kim MJ, *et al.* *J Nucl Med.* 2018;59:1907-12.

Comparison of Dynamic Contrast Enhanced MRI Signal Analysis Methods to Assess Response to Single- and Three-Fraction Stereotactic Ablative Radiotherapy for Early Stage Breast Cancer

A. Sun¹, M. Mouawad⁵, H. Biernaski⁶, M. Brackstone^{4,5,6}, M. Lock^{4,5}, B. Yaremko^{4,5}, A. Kornecki^{3,6}, O. Shmuilovich^{3,6}, I. Ben Nachum^{3,6}, G. Muscedere^{3,6}, K. Lynn^{5,6}, F.S. Prato^{2,3}, R.T. Thompson^{2,3}, S. Gaede^{2,4,5,6}, N. Gelman^{2,3,6}, Depts. of ¹Electrical & Computer Engineering, ²Medical Biophysics, ³Medical Imaging, ⁴Oncology, Western University; ⁵London Health Sciences Centre; ⁶Lawson Health Research Institute, London, ON.

Introduction: Very few studies have investigated dynamic contrast enhanced magnetic resonance imaging (DCE-MRI) for assessing response to breast cancer radiation therapy (RT). Such studies could provide important insights for RT optimization and adaptation to individual patients. Previously our group showed that DCE-MRI can detect response of early stage breast cancers to stereotactic ablative radiotherapy (SABR)¹. For patients imaged prior to and approximately 2.5 weeks post single (21 Gy) or three-fraction (30 Gy total) SABR, we found a significant decrease in a perfusion related parameter (K^{trans} , rate of transfer of contrast agent from blood to extracellular-extravascular space). This parameter was obtained using the Tofts pharmacokinetic model² combined with a commonly applied population average function³ representing contrast enhancement in the blood (arterial input function (AIF)). The objectives of the present work were to (1) assess the robustness of our previous finding by utilizing a more recently reported AIF as well as using a simple empirical approach and (2) to compare the relative changes in K^{trans} between single and three-fraction groups using these different analyses.

Methods: The analysis was performed on DCE-MRI data that included pre- and post-SABR breast images for patients who received single-fraction SABR (N = 6) or three-fraction SABR (N = 7). Each image set included 1 pre-contrast and 28 post-contrast images with a time resolution of 18 to 20 s. Tumor segmentation and conversion of image signal versus time curves to contrast agent concentration versus time curves was performed previously¹.

For the present work, the parameter K^{trans} was extracted by fitting whole tumour concentration versus time curves to the Tofts model using two different AIFs. This included a commonly used AIF³ (AIF1) that we previously¹ applied (in voxel-wise analysis), as well as a more recently reported AIF⁴ (AIF2) that had been acquired with higher time resolution and had a different shape than AIF1. We applied a simple extrapolation to extend the tail of AIF2. In addition, an empirical parameter, representing the time at which the signal versus time curves peak, known as the time-to-peak (TTP), was extracted by fitting these curves with an empirical equation⁵. The Wilcoxon signed-rank test was used to assess significance of differences of K^{trans} changes between pre- and post-SABR. For each patient the relative (%) change between pre- and post-SABR were determined. These percent changes were compared between single- and three-fraction SABR groups using the Wilcoxon rank-sum test.

Results: Values of K^{trans} obtained with both AIFs decreased from pre- to post-SABR for all patients ($p = 0.031$ and 0.016 for single- and three-fraction, respectively). Values of TTP increased from pre- to post SABR for all patients ($p = 0.031$ and 0.016 for single- and three-fraction, respectively). Percent changes (Table 1) between pre- and post-SABR differed significantly between the single- and three-fraction groups for K^{trans} obtained with both AIFs ($p = 0.022$ and 0.035 for AIF1 and AIF2, respectively) and for TTP ($p = 0.014$).

SABR Dose	% Change in K^{trans} using AIF1	% Change in K^{trans} using AIF2	% Change in TTP
Single-fraction	-12.7 [-4.2, -33.8]	-11.8 [-2.9, -33.3]	30.6 [19.1, 58.2]
Three-fraction	-37.1 [-13.9, -57.9]	-36.7 [-11.8, -56.9]	66.7 [57.1, 312.9]

Table 1. Median and range of percent changes in parameters between pre- and post-SABR.

Conclusions: Similar pre- to post-SABR changes in K^{trans} were obtained with both AIFs, despite dissimilarities in the shapes of these AIFs. Pre- to post-SABR changes were also detected with TTP. These results provide confidence in the robustness of our previously reported finding. Importantly, three-fraction SABR led to stronger pre- to post-SABR changes in K^{trans} and TTP compared to single-fraction SABR. This may indicate larger changes in perfusion and/or vascular permeability with three-fraction versus single-fraction SABR in this context.

References: [1] Mouawad et. al. *Clin Transl Oncol* 2020; 21: 25-31. [2] Tofts et al. *J Magn Reson Imaging* 1999;10:223–32. [3] Parker et al. *Magn Reson Med* 2006; 56:993–1000. [4] Georgiou et al. *Magn Reson Med* 2019;81:1955–1963. [5] Gal et al. 29th *Proc. Annual International Conf of IEEE EMBS*, Lyon, Aug. 23-26, 2007.

Assessment of Locally Advanced Breast Cancer Response to Chemotherapy using Enhanced Ultrasound Elastography

Niusha Kheirkhah¹, Gregory J. Czarnota², Abbas Samani¹, Ali Sadeghi-Naini^{2,3}

¹School of Biomedical Engineering, Western University, London, ON, Canada

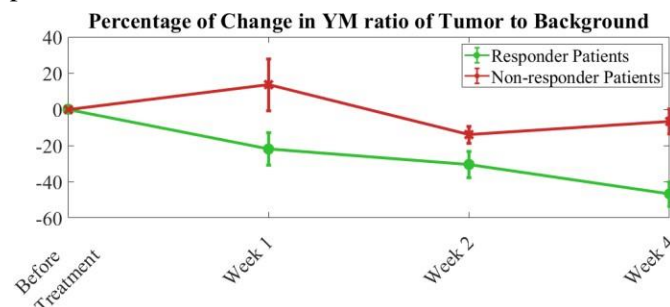
²Sunnybrook Health Sciences Centre, Toronto, ON, Canada

³Department of Electrical Engineering and Computer Science, York University, Toronto, ON, Canada

Introduction: Breast cancer is the most common type of non-dermal cancer and the second leading cause of cancer-related deaths in Canadian women in 2020. Among all breast cancer diagnoses, the incidence of locally advanced breast cancer (LABC) is estimated at 10% to 20%. In this type of breast cancer, the tumor is often larger than 5 cm and/or has grown into the muscles of the chest wall or the skin, making it inoperable. Current treatments for LABC include neoadjuvant chemotherapy (NAC), followed by surgery. The NAC is administered to shrink the tumor and detach it from the chest wall so that it becomes operable. While response to chemotherapy has demonstrated a strong correlation with overall treatment outcomes, unfortunately, 30% to 40% of patients respond poorly to chemotherapy. Therefore, identifying this group of non-responders as early as possible can have a remarkable impact on the overall patients' survival by facilitating early treatment adjustments or salvage therapies. It has been shown that there is a correlation between LABC response to NAC and tumor softening. Ultrasound (US) elastography is a non-invasive imaging technique developed for tissue stiffness mapping. This technique can potentially be used as a clinically viable tool to detect and characterize mechanical properties of breast cancer tumors, including stiffness changes over time. Noting that in responding patients, changes in tumor stiffness in response to chemotherapy occur significantly earlier than changes in tumor size, elastography can potentially be used effectively to determine the patient response ahead of time.

Methods: In US elastography, first the tissue is compressed using US probe. Using US radiofrequency (RF) data acquired at two compression states, the displacements and strains of the tissue can be estimated. We further improve this estimation using physics-based principles. The resulting displacement and strain data are then fed into an iterative reconstruction algorithm to generate a relative Young's modulus (YM) image of the breast tissue. In this work, the ultrasound data is acquired through an observational study of 18 patients diagnosed with LABC and underwent a full course of NAC followed by surgery. The patient responses to chemotherapy was determined based on standard clinical and histopathological assessment after surgery. Our method was applied to the US RF data of each patient before treatment, and at week 1, 2, and 4 weeks after the initiation of chemotherapy to generate relative YM images. YM ratio of the tumor to the surrounding tissues at each time was then calculated, and percentage changes in YM ratio of each tumor was estimated at weeks 1, 2 and 4 compared to pre-treatment ratio.

Results: The average percentage changes in YM ratio of tumors for 18 patients are shown in the figure below. The error bars indicate the standard deviation of this measurement. This plot shows that, in contrast to non-responders, responding patients demonstrated nearly 25% reduction in tumor stiffness at week 1 after the chemotherapy initiation. Furthermore, a consistent tumor softening is discerned in responding patients four weeks after the start of treatment, whereas minimal changes were observed in tumor stiffness of non-responders at week 4 compared to the pre-treatment.



Conclusion: Our preliminary results corroborate that change in YM ratio of tumor to background tissue can potentially be an effective biomarker for differentiating responding and non-responding patients to NAC as early as one week after NAC initiation. Further investigations with a larger dataset and statistical analysis are being conducted to consolidate this conclusion.

Molecular imaging reveals a high degree of cross-seeding of spontaneous metastases in a novel mouse model of synchronous bilateral breast cancer

Shirley Liu^{1,2}, Nivin N Nyström^{1,2}, John J Kelly¹, Amanda M Hamilton¹, Yanghao Fu^{1,2}, John A Ronald^{1,2}

¹Robarts Research Institute, The University of Western Ontario, London, ON, Canada

²Dept. of Medical Biophysics, The University of Western Ontario, London, ON, Canada

Introduction: Synchronous bilateral breast cancer (SBBC) patients present with cancer in both breasts at the time of diagnosis or within a short interval of 3-12 months. Compared to patients with unilateral breast cancer, SBBC patients have higher rates of distant metastasis and lower overall survival. It has been shown that worse prognosis is not due to increased tumor aggressiveness, but is owed to the combined effect of two tumors resulting in a higher chance of metastasis. However, a preclinical model of SBBC has not yet been described, which has led to a dearth in knowledge regarding the metastatic spread of cells from each primary tumor. Our objective was to establish an SBBC model by implanting human breast cancer cells expressing orthogonal imaging reporter gene systems into contralateral mammary fat pads of mice. *In vivo* dual bioluminescence imaging (BLI) was used to first visualize the formation of spontaneous lung metastases derived from each primary tumor over time, and subsequently the cellular makeup of each metastatic lesion was analyzed using *ex vivo* fluorescence microscopy.

Methods: MDA-MB-231 human breast cancer cells were engineered with lentiviral vectors to co-express the BLI reporter Antares2 and the fluorescence reporter zsGreen (zsG), or the BLI reporter Akaluc and the fluorescence reporter tdTomato (tdT). Female nod-scid-gamma mice received injections of zsG/Antares2 and tdT/Akaluc cells into contralateral fourth mammary fat pads (day 0; n=10). Antares2 and Akaluc dual-BLI was performed weekly for up to day 29 (n=3), 38 (n=4), or 42 (n=3) based on defined endpoints. Primary tumors and lungs were collected and fixed. The cell composition and distribution of micrometastases was analyzed using fluorescence microscopy and quantified by counting the number of micrometastases (>200 μm diameter) composed of only zsG-expressing cells, only tdT-expressing cells, or both zsG- and tdT-expressing cells.

Results: Signal from both Antares2 and Akaluc was first detected in the lungs on day 28, indicating metastasis from both primary tumors (Fig. 1A). By endpoint, nine of the 10 mice showed both Antares2 and Akaluc signal in the lungs. As expected, fluorescence microscopy of the lungs of mice showed both zsG- and tdT-expressing cancer cells (Fig. 1B). Mice sacrificed on day 38 showed the presence of small clusters of cells with a large percentage of micrometastases composed of cancer cells from both primary tumors (mean 37%; range 27% to 45%), while two mice sacrificed on day 42 showed percentages of 51% and 70%.

Discussion: Here we describe the first mouse model of SBBC and use it to study the fate of metastatic cells derived from each primary tumor. Dual-BLI showed the metastasis of both mammary fat pad tumors to the lungs in nine of 10 mice, which was confirmed with fluorescence microscopy at endpoint. While some micrometastases were composed of cells derived only from one primary tumor, a large percentage of metastases were composed of cells from both primary tumors. These results reveal a high degree of metastatic cross-seeding in this model, which may contribute to faster metastatic growth, intratumoral heterogeneity, and treatment resistance. Our work deepens our understanding of the mechanisms underlying poor outcomes of SBBC patients and may offer insight into optimal management of SBBC.

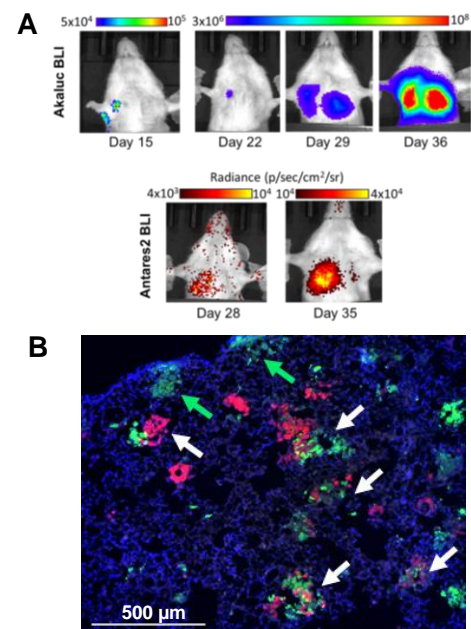
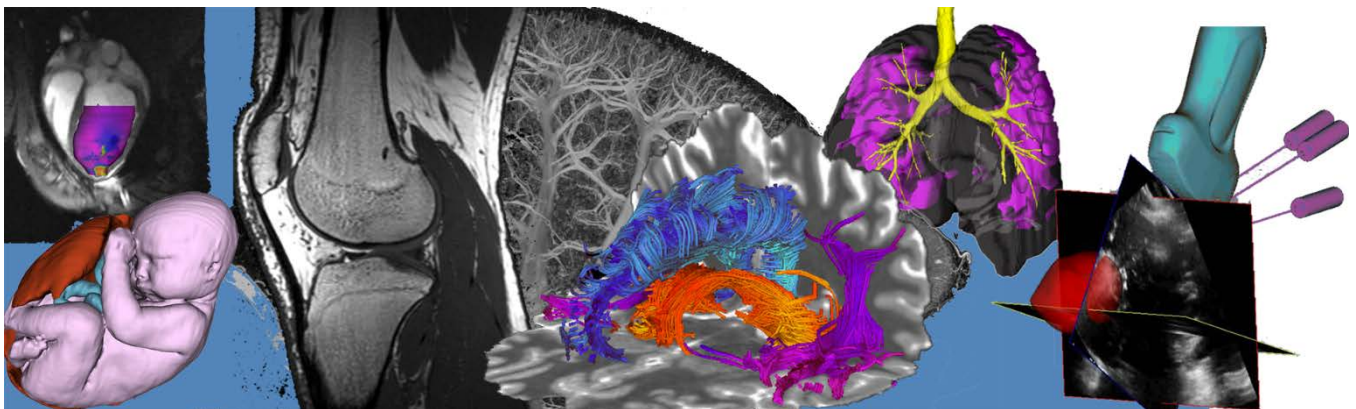


Fig. 1. A) Dual-BLI of lung metastasis, B) Fluorescence microscopy of lungs showing micrometastases composed of cells derived from both primary tumors (white arrows) or only the zsG/Antares2 tumor (green).

Oral Presentation Abstract

Session 14: Deep Learning for Segmentation



Cross Attention Squeeze Excitation Network (CASE-Net) for Whole Body Fetal MRI Segmentation

Justin Lo, MASc^{1,2}, Saiee Foustina Nithiyanantham, MASc¹, Jillian Cardinell, MASc^{1,2}, Dylan Young, BEng¹, Sherwin Cho, BEng², Matthias W. Wagner, M.D³, Roxana Azma, M.D³, Steven Miller M.D³, Mike Seed, M.D⁴, Birgit Ertl-Wagner, M.D³, Dafna Sussman, PhD^{1,2,5,6}

¹Electrical, Computer and Biomedical Engineering, Ryerson University, Toronto, Canada. ²Institute for Biomedical Engineering, Science and Technology (iBEST) at Ryerson University & St. Michael's Hospital, Toronto, Canada. ³Division of Neuroradiology, The Hospital for Sick Children, Toronto, Canada. ⁴Cardiology, The Hospital for Sick Children, Toronto, Canada. ⁵The Keenan Research Centre for Biomedical Science, St. Michael's Hospital. ⁶Department of Obstetrics and Gynecology, Faculty of Medicine, University of Toronto, Toronto, Canada.

Background: Segmentation of the fetus from 3D MRI provides radiologists with additional information about fetal development and serves as an important tool for advanced diagnostics. Automatic segmentation using machine learning can facilitate this process, making it more accurate and objective. The squeeze-and-excitation (SE) block adds adaptive weights to the channel-wise feature maps by modelling the interdependencies between these convolutional channels¹. Attention mechanisms provide greater emphasis on contextual information that will lead to higher segmentation performance². We propose a deep learning (DL) framework for 3D fetal MRI segmentation using a cross attention squeeze excitation network (CASE-Net) for research and clinical applications.

Methods: 34 T2-weighted coronal fetal MRI datasets were manually segmented by a collaborating radiologist. Attention gates were added after every deconvolution operation that becomes concatenated with the excited channels from the SE block from the encoding pathway. This is to place further emphasis on relevant features that are useful for whole fetal MRI segmentation. The implementation of these DL modules and hyper-parametric changes helped maximized segmentation performance.

Results: Our proposed CASE-Net achieved the highest testing segmentation score of 87.36%, surpassing other prominent architectures.

Conclusion: Attention networks and SE blocks, when used together, these mechanisms provide synergistic effects that result in superior segmentation performance. The dataset is a limitation in our model, but images are constantly being added. The proposed network is a useful approach for improving medical image segmentation.

Table 1: Aggregated Mean Testing Results

Model	Loss	DSC	Recall	Precision
CASE-Net	0.005	87.36	91.79	95.54
UNet	0.069	85.17	89.24	94.55
USE-Net	0.04	86.07	86.61	96.74
ATN-Net	0.131	82.27	88.69	96.51
LinkNet	0.096	82.72	80.39	95.87

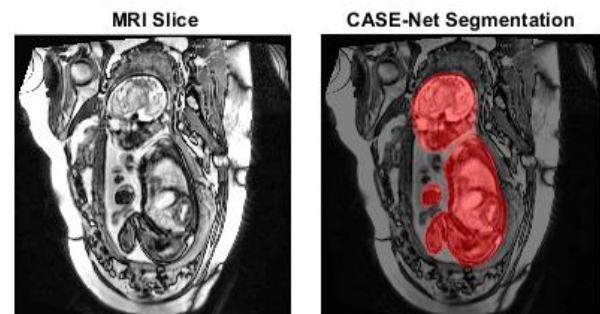


Figure 1: Predicted Segmentation Output

References: ¹ Hu J, Shen L, Albanie S, Sun G, Wu, E. (2018). CVPR, pp 7132-7141

² Cheng J, Shengwei T, Long Y, Hongchun L, Xiaoyi L. (2020). Artif Intell Med, 107, 101899

DeepMV: Fully Automatic Ultrasound Segmentation for Patient Specific Mitral Valve ModellingPatrick Carnahan^{1,2}, John Moore¹, Daniel Bainbridge³, Elvis C.S. Chen^{1,2,4}, and Terry M. Peters^{1,2,4}¹Imaging, Robarts Research Institute, London, CA,²School of Biomedical Engineering, ³Department of Anesthesiology, London Health Sciences Centre, ⁴Department of Medical Biophysics Western University, London, CA

Introduction: Recently, developments have been made towards modelling patient-specific deformable mitral valves from transesophageal echocardiography (TEE) [1]. Thus far, a major limitation in the workflow has been the manual process of segmentation and model profile definition. Completing a manual segmentation from 3D TEE can take upwards of two hours, and existing automated segmentations approaches have limitations in computation time and accuracy, with the state-of-the-art achieving a surface distance error of 0.7mm, while taking upwards of 3 hours of computation time [2]. Streamlining the process of segmenting the valve and generating a surface mold is important for the scalability and accuracy of patient-specific mitral valve modelling. We present a fully automatic, deep learning based mitral valve segmentation approach that can quickly and accurately extract the geometry of the mitral valve directly from TEE volumes.

Methods: Our segmentation technique is designed to be used on end-diastole images for use in creating molds for dynamic valve models. Our data set is composed of 40 diagnostic TEE volumes with corresponding segmentations from mitral valve surgery patients at University Hospital collected with ethics approval. We utilize 36 volumes for training and 4 for validation. Our proposed pipeline begins with preprocessing the images by resampling to 0.5mm isotropic spacing and normalizing the intensity values. Our model is based on the UNet architecture, utilizing 5 layers with 16, 32, 64, 128 and 256 channels respectively, and was trained in batches of 8 for 1000 epochs using batch normalization and the Novograd optimizer. Data-augmentation was not used as it resulted in decrease in validation accuracy. Evaluation of our proposed pipeline was performed against manual segmentations performed by a clinician as a gold-standard. The comparisons are made using the mean absolute surface distance (MASD) between the boundaries of the complete segmentations, as well as the 95% Hausdorff distances.

Results: Our preliminary results indicate that our proposed segmentation method achieves a MASD of 0.63 ± 0.11 mm and average 95% Hausdorff distance of 1.90 ± 0.57 . Additionally, we report a Dice score of 0.823. These results represent a major improvement over our prior work in which we reported a semi-automatic approach that achieve a surface distance of 1.45 ± 0.23 mm [3].

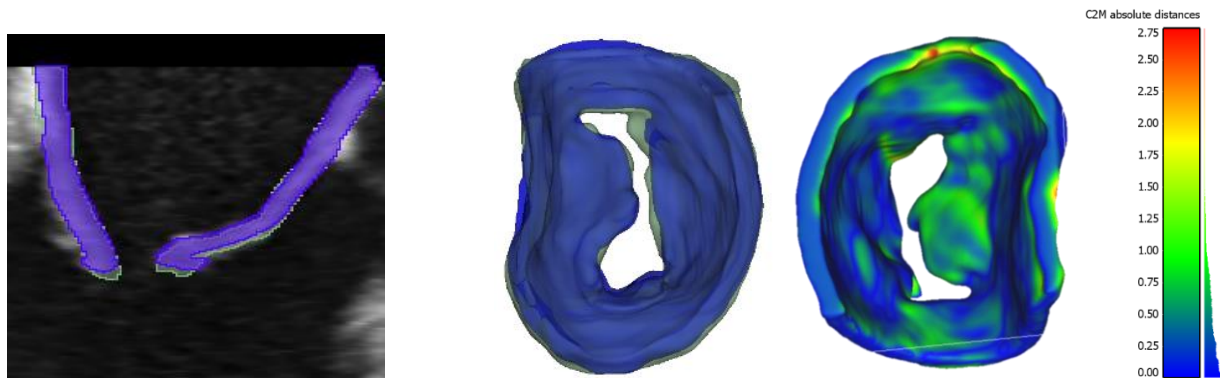


Figure 1. From left to right: Cross section of ground-truth (green) and automatic (blue) segmentations. 3D representation of ground-truth (green) and automatic (blue) segmentations. Surface distance heatmap comparison.

Conclusions: The resulting segmentations from our software successfully replicate the gold-standard segmentations with improved performance over existing state-of-the-art methods. Our method achieves a small improvement in MASD error to the state-of-the-art methods (0.6mm compared to 0.7mm), with a reduction in computation time from hours down to seconds. Surface error under 1mm in the segmentation stage does not significantly contribute to physical modelling error, and thus these results are sufficient for use in patient specific valve modelling without manual intervention. This segmentation method improves the workflow of the mitral valve modelling process by reducing the time required for completing an accurate mitral valve segmentation and providing more consistent results by removing user variability from the segmentation process.

References: [1] Ginty *et al.* J Cardiothorac Vasc Anesth (2018). [2] Pouch *et al.* Medical Image Analysis (2014) [3] Carnahan *et al.* FIMH (2018).

Automatic whole cell segmentation for multiplexed images of ovarian cancer tissue sectionsWenchao Han^{1,2}, Alison Cheung¹, Martin J. Yaffe^{1,2}, and Anne. L. Martel^{1,2}¹Biomarker Imaging Research Laboratory, Sunnybrook Research Institute; ²Department of Medical Biophysics, University of Toronto, Toronto, Ontario, Canada

Introduction: Immunofluorescence multiplexing is widely used for analyzing intratumoral heterogeneity, which could potentially impact diagnosis, treatment planning and subsequent response to treatment. Accurate and robust whole cell segmentation on the multiplexed immunofluorescent images are essential to support quantitative assessment. Recent deep learning methods have shown state of the art performance in various instance-level segmentation tasks (e.g. cell nuclei segmentation). However, these methods were not implemented for instance-level whole cell segmentation on multiplexed images, which is a challenging problem because signal intensities of the membrane marker vary depending on the cell type and orientation. Our objective is to develop and validate an automated system for instance-level whole cell segmentation on multiplexed images to support the downstream quantitative analysis.

Methods: To develop the core algorithm for whole cell instance segmentation, we trained a Mask-RCNN[1] model using two multiplexed immunofluorescent images of a 4',6-diamidino-2-phenylindole (DAPI, nucleus marker) stained image, and a Na⁺K⁺ATPase (MEM, membrane marker) stained image. The training includes two stages: 1) train a Mask-RCNN model using 42 regions of interests (ROIs) with size of 512×512 pixels (0.293μm/pixel) of an ovarian tissue section with labels generated using a semi-automatic method; 2) fine-tuning the trained model using two ROIs whose labels were generated by combining the annotations that were manually done by three different observers. We validated the system performance on six ROIs against the manual annotations from each of the three observers, and averaged the results. For each ROI, we computed object-level F1 score and Hausdorff distance for 1) the multi-observer performance, and 2) the system vs. observers' performance. Higher F1 score and shorter Hausdorff distance reflect better agreement. The overall performance was evaluated by averaging across all ROIs. To evaluate the overall performance of the system, we averaged the results across all the ROIs.

Results: The validation results are shown in Table 1. The average among observers F1 score is 0.76±0.03 with an average Hausdorff distance of 2.94±0.37 μm, while the average F1 score for algorithm vs. observers is 0.77±0.02 with a Hausdorff distance of 2.79±0.40 μm. Figure 1 shows the visual results for ROI6 as an example. This model is also deployed as a plug-in for use in Cellprofiler, a widely used cell analysis software.

Conclusion: In general, we developed and validated an automatic system for instance-level whole cell segmentation of multiplexed images with a performance that matches human observers. Our results should be interpreted with limitations as our samples used for training and testing are from the same tissue section, therefore, our future direction is to conduct a large-scale multi-center validation study.

Table 1: Quantitative results for the single cell segmentation			
	Validation method	F1 Score	Hausdorff distance (μm)
ROI1	Among observers	0.76	2.28
	Algorithm vs. observers	0.77	2.10
ROI2	Among observers	0.74	3.04
	Algorithm vs. observers	0.76	2.72
ROI3	Among observers	0.73	3.34
	Algorithm vs. observers	0.75	2.96
ROI4	Among observers	0.81	2.84
	Algorithm vs. observers	0.79	2.84
ROI5	Among observers	0.79	2.94
	Algorithm vs. observers	0.78	2.82
ROI6	Among observers	0.77	3.22
	Algorithm vs. observers	0.75	3.32
Avg. ± std. across all ROIs	Among observers	0.76±0.03	2.94±0.37
	Algorithm vs. observers	0.77±0.02	2.79±0.40

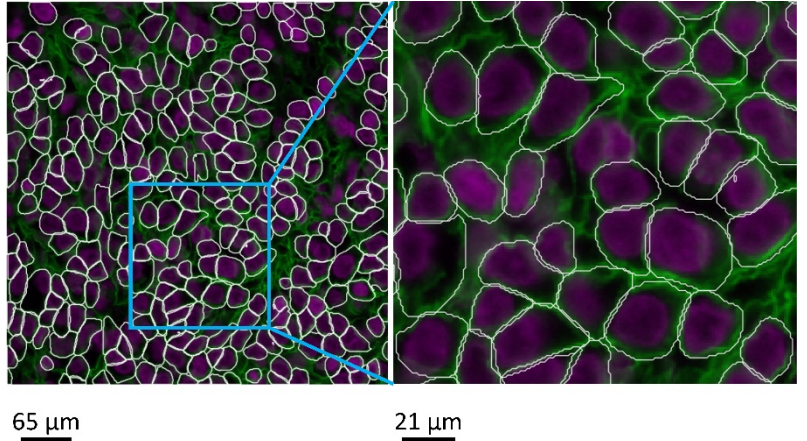


Figure 1: Cell segmentation overlay on a testing sample of synthesized color image. Purple represents DAPI stain. Green represents MEM stain. Yellow contours are system outputs for whole cell segmentation.

[1] He, Kaiming, et al. "Mask r-cnn." *Proceedings of the IEEE international conference on computer vision*. 2017.

Renal Boundary and Tumour Segmentation in Multiparametric MRI using U-Net with Transfer Learning

Anush Agarwal¹, Nicola Schieda², Mohamed Elfaal², Eranga Ukwatta¹

¹ School of Engineering, University of Guelph, Guelph, ON, Canada

² Department of Radiology, University of Ottawa, Ottawa, ON, Canada

Introduction: Although contrast enhanced computed tomography (CECT) is the clinical mainstay for renal mass evaluations, multiparametric MRI use is increasing due to a potential improved ability to differentiate benign from malignant renal masses and assess the aggressiveness of malignant tumours. U-Net models are effective at renal segmentation tasks in CECT [1]; however, their use in MRI is not well studied. In this work, U-Net models for kidney and renal tumour segmentation on MRI are developed in support of an autonomous renal lesion detection and classification algorithm. Asymmetric loss functions and transfer learning from CECT is also explored.

Methods: Our dataset consists of 79 contrast-enhanced nephrographic phase MRIs (NG-MRI) with a total of 156 renal masses. The volumetric data includes manual kidney segmentations and renal mass (Renal cell carcinoma, oncocytoma, fat-poor angiomyolipoma and benign cysts) segmentations, performed by a single fellowship-trained abdominal radiologist. We performed kidney segmentation on NG-MRIs using a U-Net model and measured performance against manual segmentations using 5-fold cross validation. The U-Net used has a depth of 4 encoder blocks and a kernel size of 3x3, resulting in 1,940,817 model parameters trained using a loss function that combines Dice loss with binary cross-entropy (BCE). A tumour segmentation model that operates within localized kidney boundaries is also developed and tested using the manual kidney segmentation boundaries as a localizer to establish an upper-bound on performance. Both segmentation models are pre-trained on a dataset of 299 volumetric CECT images containing a total of 680 renal masses with radiologist-provided kidney and renal mass segmentations from the same institution. Full network adaption transfer learning is then used to train the models on the NG-MRI dataset. In the case of tumour segmentation, an asymmetric loss function as described by [2] is combined with BCE loss to increase the recall score of results.

Results: Preliminary results are reported on the dataset of 79 NG-MRIs through 5-fold cross validation. The kidney segmentation algorithm reported a Dice Similarity Coefficient (DSC) of $91\% \pm 7\%$ (mean \pm SD). Applying transfer learning from CECT images resulted in a slight improvement to DSC at $92\% \pm 6\%$ (mean \pm SD). Using a model that combines transfer learning from CECT images and an asymmetric loss function, a precision and recall score of 54% and 58% respectively was found on the lesion segmentation task. In comparison, a U-Net model trained without transfer learning and with a BCE-Dice loss reported a precision and recall score of 46% and 41% respectively. Lesion segmentation performance was found to deteriorate for small and low contrast renal masses. As seen in Figure 1 below, the proposed models generally follow manual segmentation boundaries effectively.

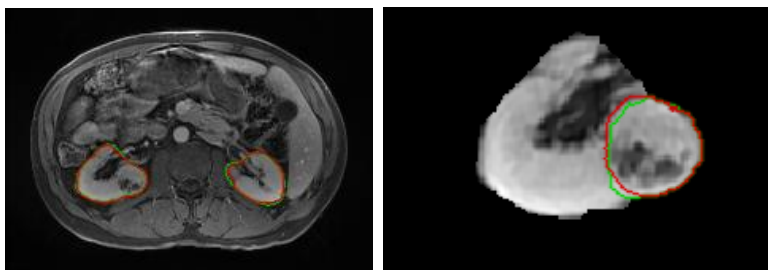


Figure 1. Example of results for the kidney segmentation task (left) and the tumour segmentation task (right) on an NG-MRI. Red represents the predicted segmentation and green represents the manual segmentation.

Conclusions: U-Net models are highly effective at kidney segmentation tasks in NG-MRI images. The proposed tumour segmentation algorithm using an asymmetric loss function and transfer learning from CECT images results in an improvement in the precision and recall of tumour segmentation on NG-MRI compared to a baseline U-Net.

References: [1] Z. Fatemeh, S. Nicola, K. Satheesh, and U. Eranga, “Ensemble U-net-based method for fully automated detection and segmentation of renal masses on computed tomography images,” *Med. Phys.*, pp. 1–13, 2020, doi: 10.1002/mp.14193. [2] S. R. Hashemi, S. S. M. Salehi, D. Erdogmus, S. P. Prabhu et al., “Asymmetric Loss Functions and Deep Densely Connected Networks for Highly Imbalanced Medical Image Segmentation: Application to Multiple Sclerosis Lesion Detection,” *IEEE Access*, vol. 7, pp. 1721–1735, 2019.

Automated myocardial segmentation of extracellular volume maps using a U-Net based convolutional neural network

Farrag, Nadia A.^a, White, James A.^b & Ukwatta, Eranga^{c, a}

^aDepartment of Systems & Computer Engineering, Carleton University, Ottawa, ON, K1S 5B6

^bDepartment of Cardiac Sciences, University of Calgary, Calgary, AB, Canada, T2N 1N4

^cSchool of Engineering, University of Guelph, Guelph, ON, Canada, N1G 2W1

Introduction: Myocardial fibrosis (MF) is a common feature of cardiac disease, characterized by excessive deposition of collagen (i.e., scar tissue) and expansion of the myocardial extracellular volume (ECV). This phenomenon contributes to cardiac dysfunction, promotes further cardiac disease and has implication in preceding cardiac morbidity and mortality. ECV mapping cardiac magnetic resonance (CMR) imaging has been proposed as a means for detection and quantification of diffuse myocardial fibrosis and may be particularly beneficial in the identification and quantification of diffuse fibrotic regions, which may be unremarkable on late gadolinium enhanced (LGE) CMR. ECV is expressed as a percentage (i.e., the fraction of tissue that is comprised of extracellular space) and has been shown to increase in diffuse and focal fibrotic regions. ECV can only be computed after the myocardial borders have been delineated in order to define an initial region-of-interest (ROI). This process is done manually by a trained expert, which is tedious and highly prone to operator error, introducing the possibility for erroneous ECV measurements. Therefore, an automated method for myocardial boundary delineation is ideal.

Methods: Seventy (70) patients with dilated (35) and ischemic cardiopathy (35) (DCM and ICM, respectively) underwent CMR imaging on a 3T Siemens (Skyra) imaging system at the Stephenson Cardiac Imaging Centre in Calgary, AB. A Siemens 3T magnet (Prisma/Skyra) system was used with a standardized CMR protocol, inclusive of short and long-axis CINE imaging using a SSFP pulse sequence. Short axis native (i.e. pre-contrast) and post-contrast T1-mapping was performed using the modified Look-Locker imaging (MOLLI) 5(3)3 technique at the basal, mid and apex positions of the left ventricle. Native and contrast-enhanced T1-maps were generated from raw MOLLI images obtained at varying inversion times (TIs) after applying a motion correction algorithm using cvi42 software (Circle Cardiovascular Imaging, Calgary, Canada), and ECV maps were then created using patient hematocrit data and native/post-contrast T1 values. A convolutional neural network based on the U-Net architecture was then used to segment native and post-contrast raw MOLLI images at each TI after dividing the dataset into training/testing subsets using five-fold cross validation. Resultant segmentations of each raw MOLLI image were then co-registered at every TI, yielding the final contours for the T1-maps. The motion-correction algorithm was then applied to the finalized native and post-contrast T1-map segmentations to align contours to the ECV maps. The proposed technique was evaluated against our alternative method, wherein we automatically segment myocardial borders in CINE images (using the same U-Net based CNN) and apply a non-rigid registration algorithm (MIND) to transform and propagate contours to ECV-maps directly.

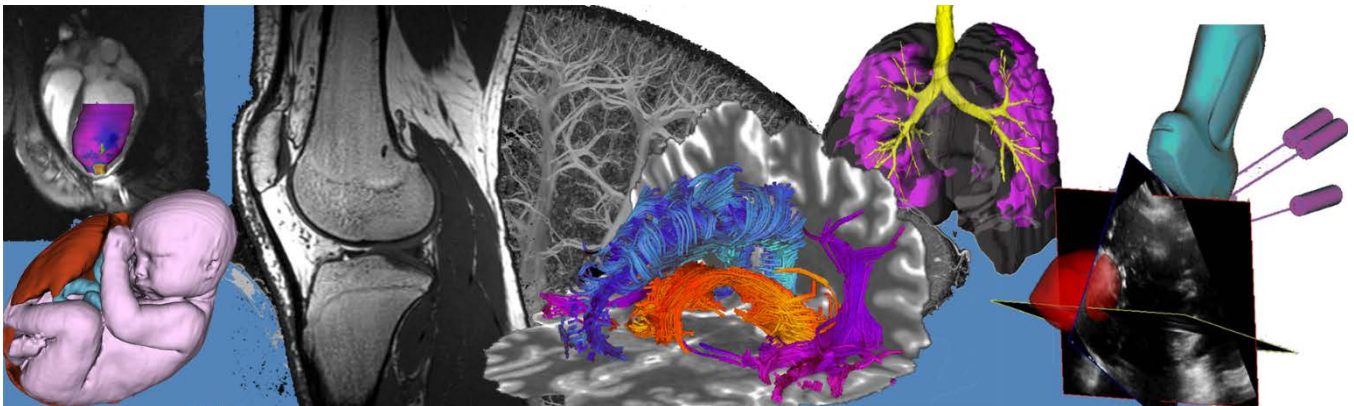
Results: Preliminary results based on the standard U-Net parameters yield DSC metrics of 79.8% in native T1-maps, 75.2% in post-contrast T1-maps, and 74.7% in ECV maps using our U-Net-based architecture and motion correction. Our comparative technique based on CINE-registration yields DSC of 83.4%, 75.4% and 77.9% in native, post-contrast and ECV maps, respectively.

Conclusions

In this study, we compare the efficiency of two methods for myocardial ECV segmentation; i.e., a U-Net-based CNN model combined with motion correction of raw MOLLI images, and an indirect segmentation method based on registration and propagation of contours derived from CINE images.

Oral Presentation Abstract

Session 15: Animal Model & Image Processing



Microstructural Diffusion MRI in Mouse Models of Severe and Repetitive Mild Traumatic Brain Injury

Naila Rahman, Kathy Xu, Nico J. J. Arezza, Kevin Borsos, Arthur Brown, Corey A. Baron
 Robarts Research Institute, Western University, London, ON, Canada

Introduction: Current neuroimaging techniques lack the sensitivity and specificity required to reliably detect signs of mild traumatic brain injury (mTBI) [1]. To enable the specificity required to track microstructure changes, two advanced quantitative diffusion MRI scans (“Microstructural dMRI”) sensitive to microstructure can be applied: 1. Structural disorder via oscillating gradient spin echo (OGSE) dMRI [2] and 2. Cell shape via microscopic anisotropy (μA) dMRI [3]. Here, we implement microstructural dMRI in mouse models of severe and repetitive mTBI to identify which model will be more relevant for an *in vivo* longitudinal study.

Methods: Each of a repetitive mild TBI (rm-TBI) and severe TBI (s-TBI) model were implemented (Fig. 1) on separate male C57Bl/6 mice. All mice were euthanized for histology after imaging. The goal of the single severe impact TBI (s-TBI) model was to match the stretch and strain in the rodent brain during TBI to that experienced by the human brain [4], whereas the rm-TBI model is more relevant for studying the possible long term neurodegenerative processes resulting from repetitive hits.

Imaging was performed at 9.4T with a 1 T/m gradient insert, in-plane resolution of 0.2 mm, 0.5 mm slice thickness, and a total scan time of 2 hours. The OGSE sequence was implemented with $b=800$ s/mm², TE=37ms, 10 directions and OGSE frequencies of 0, 50, 100, 145, and 190 Hz. The μA sequence was implemented using a single diffusion encoding (SDE) scheme [5] with linear and isotropic encodings at $b=2000$ s/mm² (30 directions) and $b=1000$ s/mm² (12 directions). Regions of interest included in the analysis were the corpus callosum, the hippocampus, and the prefrontal cortex (PFC), as defined by Carlen et al. [5].

Results: For all ROI's in both TBI models, the isotropic diffusion kurtosis (K_{iso}), calculated from the isotropic encodings in the μA protocol, decreased 48H post s-TBI, and increased 48H post rm-TBI and 1-wk post s-TBI (data not shown). For the OGSE protocol, linear regression of the non-zero frequencies revealed a lower slope post s-TBI (Fig. 2b and c), 28 % lower 48H post s-TBI and 38 % lower 1-wk post s-TBI. In contrast, no change in slope was found 48H post rm-TBI (Fig. 2a). Sample baseline images are shown in Fig. 3.

Conclusions: Changes in K_{iso} suggests the μA protocol is sensitive to cell size heterogeneity, which may result from the changing size of glial cells after TBI. A change in the MD (mean diffusivity) dependence on frequency post severe TBI suggests that OGSE dMRI is sensitive to structural disorder along the axon length, which may be due to a combination of edema and axon beading. In future studies, the developed microstructural dMRI protocol will be applied in a longitudinal study in a mouse-model of severe TBI during recovery, allowing us to investigate the interesting changes in the MD dependence on frequency post TBI.

References: [1] Giza, CC et al. 2014. *Neurosurgery*. [2] Baron, CA et al. 2015. *Magn. Reson. Med.* [3] Arezza, NJJ et al. 2020. *MedRxiv [Preprint]*. Available from: <https://doi.org/10.1101/2020.11.23.20237099>. [4] Duhaime, AC et al. 2012. *Neurosurgery*. [5] Carlen, M. 2017. *Science*.

Acknowledgements: New Frontiers in Research Fund, NSERC CGS-M

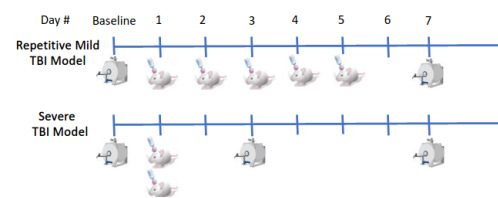


Figure 1. TBI models. The rm-TBI model consisted of 5 mild hits, with 24 hours separation between each hit. The s-TBI was a single hit. Scanning was done at baseline and 48H post TBI. Since differences in results may be a combination of the model and time post-TBI, a second mouse was scanned 1 week post s-TBI.

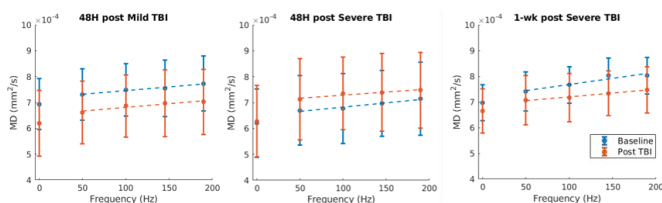


Figure 2. MD dependence on frequency in the PFC. The error bars represent the standard deviation in the ROI and the dotted lines are the linear regression curves fitted to the non-zero frequencies.

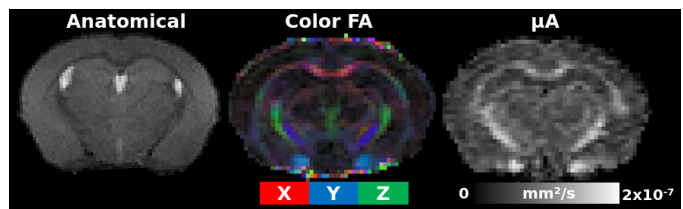


Figure 3. Anatomical, color FA (fractional anisotropy), and μA maps acquired from a healthy mouse brain. Note that the colors in the color FA map represent the primary direction of diffusion.

CEST-MRI for Monitoring Effects of Cariporide on Intracellular Tumour pH in a Rat Glioma ModelMaryam Mozaffari^{1,2}, Nivin Nystrom^{1,2}, Alex Li², Miranda Bellyou², Tim Scholl^{1,2}, Robert Bartha^{1,2}¹Department of Medical Biophysics, ²Robarts Research Institute, University of Western Ontario

Introduction: In biological systems, the difference between intracellular pH (pH_i) and extracellular pH produces a pH gradient across the cell membrane. The regulation of this pH gradient is dependent on the activity of several plasma membrane transporters that facilitate hydrogen ion efflux to maintain an alkaline pH_i in tumour cells. One of the main acid-base regulators in cells is the Na^+/H^+ exchanger isoform 1 (NHE1), which has been directly associated with pH regulation. One way to achieve tumour acidification as a therapeutic strategy is by blocking the NHE1 transporter. Cariporide is an anti-cancer agent that alters metabolism and pH_i by selectively inhibiting the NHE1 transporter.¹ Chemical exchange saturation transfer (CEST) MRI can be used to measure pH_i with high spatial and temporal resolution. CEST-MRI selectively excites exchangeable tissue protons and observes the transfer of magnetization to bulk tissue water. The rate of proton exchange is pH-dependent. Using a CEST technique called amine and amide concentration-independent detection (AACID) images can be pH-weighted.² We have shown that cariporide can selectively acidify U87MG gliomas in mice.³ The goal of this study is to monitor the change in tumour pH_i over time to determine whether cariporide can also selectively acidify rat C6 glioma following cariporide injection. We hypothesized that blockage of NHE1 by cariporide would produce selective intracellular tumour acidification detectable by AACID-CEST-MRI.

Methods: Approximately 10^6 C6 glioma cells were injected into the right frontal lobe of six 8-week-old male rats. To evaluate the effect of cariporide on tumour pH_i , rats received an intraperitoneal injection of cariporide (dose: 6mg/kg in 2ml) two weeks after tumour implantation. Animals received the drug inside a 9.4T MRI scanner to measure the change in pH_i following injection. CEST images were acquired for the slice of interest using a Fast-Spin-Echo pulse sequence to create CEST spectra for each pixel in the image and analyzed using custom software in MATLAB. AACID values are measured on a pixel-by-pixel basis to generate parametric maps. A paired t-test was used to measure changes in AACID value within the tumour and contralateral regions pre- and post-injections.

Results: Approximately five minutes after drug injection we started collecting CEST-MRI for three hours. For data analysis, we compare the first maximum change in AACID value post-injection with the pre-injection value. Figure 1.a-1.c show the AACID maps obtained for a representative experimental rat superimposed on an anatomical image, before and after injection of cariporide. Approximately 60 minutes after drug injection, the average AACID value in the tumour significantly increased ($p < 0.05$). The average AACID value in tumour post-injection was 5.4% higher compared to pre-injection corresponding to a 0.26 lower pH_i (Figure 1.d). The average AACID value in contralateral tissue also increased in a similar way.

Conclusion: In this work, we did not observe selective tumour acidification following injection as was observed in the mouse U87MG glioma model.³ The reason for this discrepancy is currently unknown but may be related to potential differences in tumour vasculature compared to the U87MG model that may limit the ability of cariporide to infiltrate the tumour.⁴ Future work includes increasing cariporide dose and modifying our quantification method to increase the temporal stability of the AACID measurement.

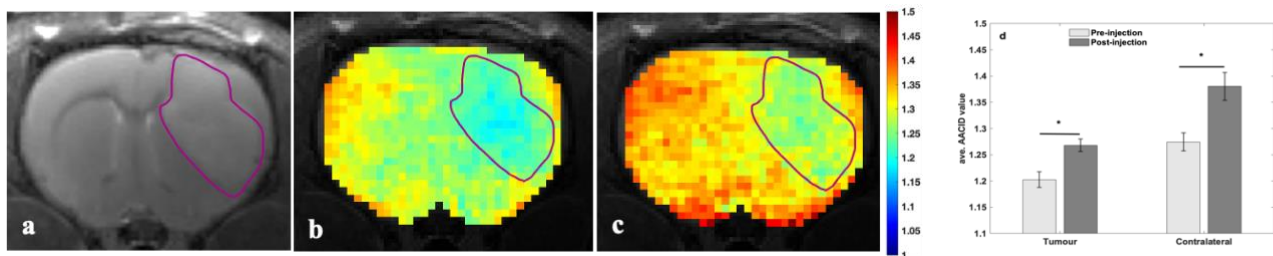


Fig. 1: a) Representative anatomical image (T2-weighted) and superimposed colour-coded AACID maps for b) baseline and c) 60 minutes after injection of cariporide at day 14 post-implantation of the tumour. The tumour region is highlighted by the purple line. The average AACID value in tumour regions pre- and post-injection of cariporide was 1.22 ± 0.02 and 1.27 ± 0.020 , respectively. d) The average AACID values in tumour and contralateral regions pre- and post-injection of cariporide ($N=6$). Error bars represent the standard error of the mean.

References: [1] J Transl Med 2013; 11(282):1-17, [2] J Cerebral Blood Flow & Metabolism 2014, 34:690-8, [3] Int J Clin Oncol 2018, 23:812-819, [4] J Magn Reson Imaging. 2010; 32(2):267-75.

Spatial Dependence of CT Emphysema in COPD Quantified using Join Count Statistics

S. Virdee BSc,¹ W.C. Tan MD,² J.C. Hogg MD, PhD,² J. Bourbeau MD,³ J.A. Leipsic MD,² C.J. Hague MD,² and M. Kirby PhD^{1,2}

¹*Department of Physics, Ryerson University;* ²*Center for Heart Lung Innovation, St. Paul's Hospital;* ³*McGill University Health Centre, McGill University*

Introduction: Chronic obstructive pulmonary disease (COPD) is a lung disease characterized by the destruction of lung tissue, known as emphysema. Computed tomography (CT) imaging allows emphysema to be quantified. There are several CT emphysema biomarkers, such as the low attenuation area below -950 HU (LAA₉₅₀) and the low attenuation cluster (LAC), which quantify the overall extent of emphysema, and whether emphysema is clustered (i.e., connected emphysema voxels)¹, respectively. However, LAC and other established CT-metrics fail to recognize the spatial disposition of voxels making up the emphysema cluster. In other words, while established CT-metrics quantify the volume of emphysema, the compactness of the cluster is not taken into account. We propose a Geostatistical method known as Join Count Statistics (JCS)². JCS determines the degree of clustering or dispersion among spatially adjacent objects. Our objective is to develop a modified Join Count Statistics method to quantify the spatial disposition of CT emphysema voxel clusters in COPD. We hypothesize that the CT emphysema spatial disposition will significantly distinguish patients based on disease severity and correlate with lung function and radiologist emphysema scores better than the established CT emphysema measures.

Methods: Spirometry and CT images from the multi-center CanCOLD study were obtained and approved by each Institutional Research Ethical Board³. Spirometry measurements included the forced expiratory volume in 1 second (FEV₁), forced vital capacity (FVC), FEV₁/FVC and the forced expiratory flow at mid-expiratory phase (FEF_{25-75%}). Plethysmography measurements included the residual volume/total lung capacity (RV/TLC) and diffusion capacity for carbon monoxide (DL_{CO}). All participants were categorized as according to the Global initiative for Obstructive Lung Disease: current or ex-smokers with normal lung function (at risk), mild COPD and moderate/severe COPD¹. CT measurements included the LAA₉₅₀, LAC and the lowest 15th percentile point for a CT lung density histogram (HU_{15%}). For radiologist assessment, the lungs were divided into 6 zones, and each zone was scored on a 5-point scale (0-4) based on the extent of emphysema and the summation was taken as the emphysema score. Emphysema prevalence was the summation of emphysema score of ≥ 1 . To generate the JCS, the CT images were first converted to binary maps, and voxels were identified as either “emphysema” or “other”. A “join” between two voxels counted as a single count if both voxels had an identical value and were neighboring via a connection of either their 6 faces, 12 edges or 8 corners. In addition, the Join Count was then normalized by dividing the Join Count of emphysema voxels by the total number of Join Counts within the lung (NJC). An analysis of variance (ANOVA) was used to determine differences between groups. Ridge regression was used to determine the relationship between the NJC measurements with measures of lung function and radiologist scores of emphysema prevalence, adjusting for age, sex, BMI and CT model.

Preliminary Results: A total of 1294 participants from the CanCOLD cohort were analyzed: n = 277 were never-smokers, n = 306 were at risk, n = 427 had mild COPD, and n = 284 moderate/severe COPD. NJC, LAA₉₅₀, HU_{15%} and LAC measurements were significantly greater in severe COPD than never-smokers (p<0.001) and at risk (p<0.001), however only NJC was significantly different between mild and severe COPD (p<0.001). In a multivariable ridge regression analysis that included all CT emphysema measurements, the NJC had the greatest relative contribution to lung function for FEV₁ (stand. β = -5.89, p<0.001), FEV₁/FVC (stand. β = -164.71, p<0.0001) FEF_{25-75%} (stand. β = -14.74, p<0.0001), DL_{CO} (stand. β = -39.27, p<0.0001) and RV/TLC (stand. β = 0.68, p<0.0001). Similarly, the NJC measurement had the greatest association with visual emphysema score (stand. β = 29.27, p<0.0001). However, HU_{15%} had the greatest association with emphysema prevalence (stand. β = 3.55, p<0.001).

Conclusions: In conclusion, CT NJC distinguished COPD participants based on disease severity and distinguished between the COPD severity groups better than conventional CT measurements. CT NJC also had greater relative influence on lung function measurements and radiologist's visual emphysema scores than established CT measurements that do not take into account spatial disposition. The increased sensitivity of NJC may indicate that COPD severity is not only dependent on the number of low attenuating voxels or the size of the clusters, but also on the spatial arrangement of such voxels.

References: 1. Mishima, M, *et al.* *PNAS* 1999; 96:8829-8834; 2. Cliff, A/D, *et al.* Spatial Autocorrelation. *Pion* 1973; 3. Bourbeau J, *et al.* *COPD* 2012; 11:125-132

Fractal Dimensions of Airway Surfaces from Computed Tomography in Chronic Obstructive Pulmonary Disease

Jason Bartlett (MSc Candidate)⁵, James C. Hogg (MD, PhD)⁶, Jean Bourbeau^{7,8},
Wan C. Tan (MD)⁶ and Miranda Kirby (PhD)⁵

Introduction: Chronic Obstructive Pulmonary Disease (COPD) is an under-diagnosed condition which accounts for 5% of all deaths worldwide¹. Histology has shown that in COPD afflicted patients, as the severity of COPD progresses both the outer and inner surfaces of the small airways undergo significant changes in their overall order and structure². Although airways can be studied *in vivo* by performing airway segmentation from computed tomography (CT) images, existing airway measurements, such as airway wall thickness and wall area percentage, do not directly measure these changes in surface topology. Fractal dimensional analysis has previously been applied to measure changes in natural and machined surface topologies, where the fractal dimensional value (FD) is a non-integer number associated with an objects overall structural complexity³. Our objective is to develop a FD measurement that can quantify changes in surface structure in COPD using CT imaging. More specifically, we hypothesize that CT FD measurements generated from airway tree segmentations will be able to distinguish between different COPD severity groups and will be significantly correlated with lung function.

Method: A total of 1324 subjects were selected from The Canadian Cohort Obstructive Lung Disease (CanCOLD)⁴ to be used for airway surface Fractal Analysis. Subjects were grouped based on disease severity according to the Global Initiative for Chronic Obstructive Lung Disease (GOLD) guidelines. For each subject, full-inspiration CT images were acquired, then segmented, labelled, and analyzed, using VIDA software (VIDA Diagnostics Inc.). The 3D reconstruction of the airway tree was generated, and an airway segment was defined as the segment between branch points. Each airway segment was made of multiple slices, defined by 72 points separated by 5° arcs. Segments were unrolled by finding the distance from each of the 72 points to the center of the slice. Surface reconstructions were generated for every airway segment whose inner diameter was >2.5 mm and >1 slice (Figure 1). Outer (blue) and Inner (red) surfaces were constructed by projecting the results into a 3D volume, where; x=slice point, y=slice #, z=distance from center. A Combined (purple) surface was generated by subtracting the Inner from the Outer surface volumes. Surface segment FD values were generated using the 3D box counting method, then grouped and extracted for the whole lung. Spirometry lung function measurements used were forced expiratory volume in one second (FEV₁) and the ratio of FEV₁ over forced vital capacity (FEV₁/FVC).

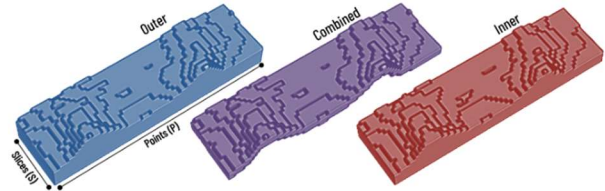


Figure 1. Reconstructed Right Main Bronchi Airway Segment

Results: Of the 1324 CanCOLD subjects evaluated, n=279 had no COPD, n=405 were At Risk, n=366 had mild COPD (GOLD I), n=274 had moderate to severe COPD (GOLD II+). There were significantly increased whole lung FD measurements for the GOLD I group compared to no COPD/At Risk groups, for Outer ($p<.001/p=.01$) and Inner ($p<.001/p<.001$) surfaces; for combined surfaces, the GOLD I group was significantly different than the no COPD group ($p<.001$). There were significantly increased FD measurements for the GOLD II+ group compared to the no COPD/At Risk groups for Outer ($p<.001/p<.001$), Inner ($p<.001/p<.001$) and Combined ($p<.001/p=.005$) surfaces. Finally, FEV₁ was weakly positively correlated with the Outer/Combined surface types [$r=.222/r=.192$, $p<.001$], and all surface types (Inner/Outer/Combined) were weakly negatively correlated FEV₁/FVC [$r=-.208/r=-.271/r=-.175$, $p<.001$].

Conclusion: We demonstrated FD measurements reflect abnormal surface topology/surface roughness in COPD and are related to airflow limitation. Taken together, these results indicate that CT airway topology is a novel imaging biomarker. We believe that such a biomarker could be potentially useful in identifying pre- and post-treatment differences related to inflammation of the airway tree surfaces. Future studies will investigate if there are any significant differences in FD between never- and ever-smokers with COPD and examine the impact of image acquisition parameters (e.g. slice thickness, CT scanner models, display field of view) on FD measurements.

References:

- ¹ World Health Organization, "Projections of Mortality and Causes of Death, 2016 to 2060."
- ² Baraldo, Turato, and Saetta, "Pathophysiology of the Small Airways in Chronic Obstructive Pulmonary Disease."
- ³ Ai et al., "Box-Counting Methods to Directly Estimate the Fractal Dimension of a Rock Surface."
- ⁴ Bourbeau et al., "Canadian Cohort Obstructive Lung Disease (CanCOLD)..."

Author Affiliations:

- ⁵ Department of Physics, Ryerson University, Toronto, ON, Canada; ⁶ UBC Centre for Heart Lung Innovation, St. Paul's Hospital, Vancouver, BC, Canada; ⁷ Montreal Chest Institute of the Royal Victoria Hospital, McGill University Health Centre, Montreal, QC, Canada; ⁸ Respiratory Epidemiology and Clinical Research Unit, Research Institute of McGill University Health Centre, Montreal, QC, Canada.

Contrast-Free Ultrasound Microvascular Imaging to Enhance Vascular Quantification in a Mouse Model of Peripheral Artery Disease

Mahsa Bataghva^{1,2}, Fiona Serak¹, Christopher Leclerc^{1,2}, David Hess^{2,3}, Lauren Flynn^{4,5}, James C. Lacefield^{1,2,6,7}

¹School of Biomedical Engineering, ²Robarts Research Institute, Departments of ³Physiology and Pharmacology, ⁴Chemical & Biochemical Engineering, ⁵Anatomy and Cell Biology, ⁶Medical Biophysics, and ⁷Electrical and Computer Engineering, Western University, London, Ontario, Canada

Background and Motivation: Ultrasonic power Doppler imaging is used to visualize blood flow in the interior of tissues without injected contrast media. However, microvessel detection is difficult due to the existence of non-stationary echoes (“clutter”) from tissue. Singular value decomposition (SVD) clutter filtering, which decomposes the signal into a set of mutually orthogonal and statistically independent eigen components, is recognized as an effective method to improve microvessel detection in contrast-free ultrasound. In standard SVD filters, the threshold separating blood and clutter is defined by the decay rate of the singular value curve and clutter is removed by zeroing low-rank singular values. However, that approach discards any blood signal power present in the low-rank eigenvectors. In previous work, we showed that the Gavish-Donoho method [1] for optimal shrinkage (i.e., re-weighting) of low-rank singular values significantly enhanced intratumor microvascular visualization and quantification [2]. In this study, we investigate the performance of optimal shrinkage clutter filtering for microvascular detection in mouse model of peripheral artery disease, which provides a more challenging vessel detection task due to the presence of higher power tissue clutter echoes.

Methods: Ultrasound images of mice hindlimb, which underwent femoral artery ligation, were acquired using a VisualSonics Vevo 2100 ultrasound system with a 40 MHz linear array. B-mode frames were extracted from power Doppler IQ data. Spatiotemporal SVD-based clutter filtering was applied to long-ensemble data sets (100 B-mode frames). Optimal shrinkage clutter filtering was employed to estimate singular values for the tissue signals, using formulae derived via mathematical optimization [1], that theoretically minimize the mean squared error between the true and estimated tissue signals. Subtraction of the estimated tissue singular values from the singular values of the original dataset, “shrinks” the low-rank singular values to non-zero magnitudes while leaving the higher rank singular values unchanged. The resulting images were analyzed using morphological image processing to extract binary skeletons of the microvascular networks for quantitative analysis.

Results/Discussion: Figure 1 shows images of the same mouse hindlimb acquired using standard SVD clutter filtering (panel A) and optimal shrinkage SVD clutter filtering (panel B). Comparing the two images, the optimal-shrinkage-filtered image better reveals the dense branching network of intramuscular vessels in the region of interest. The average number of short ($< 50 \mu\text{m}$) vessels detected in $n = 10$ images with the standard SVD and optimal shrinkage SVD filters were 18 ± 6 (mean \pm standard deviation) and 48 ± 9 , respectively. The optimal shrinkage SVD images also depicted 20 ± 5 more vessel branching points per image than the standard SVD images. Therefore, the Gavish-Donoho optimal shrinkage method significantly improves detection of fine microvascular network morphology in contrast-free ultrasound images that include substantial clutter due to strong scattering from muscle fibers.

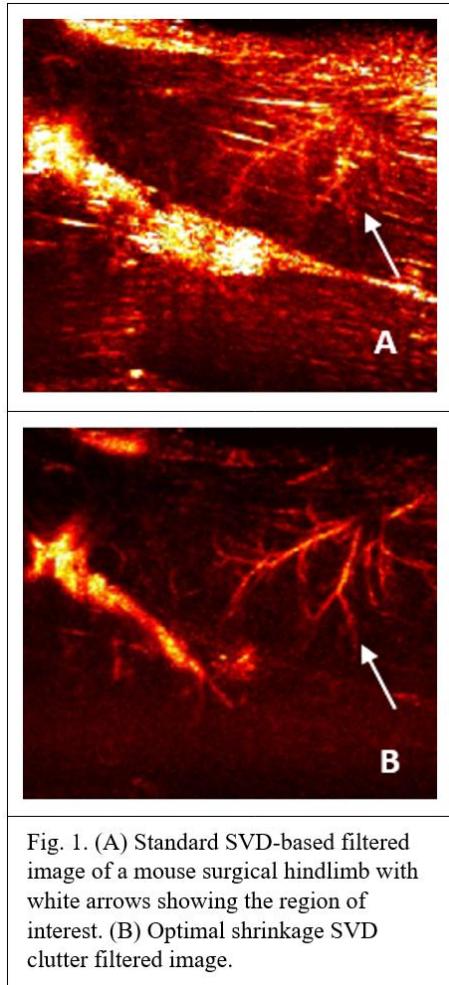


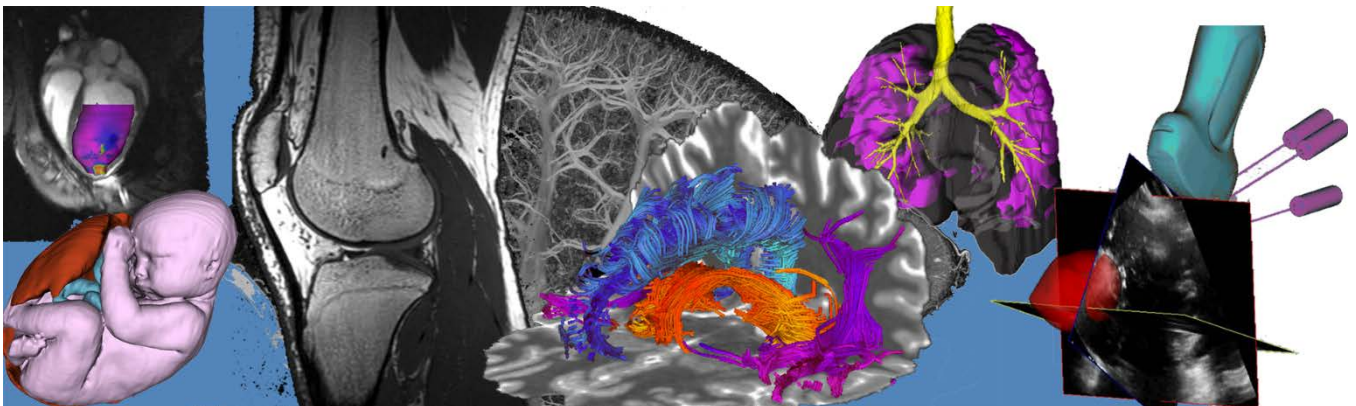
Fig. 1. (A) Standard SVD-based filtered image of a mouse surgical hindlimb with white arrows showing the region of interest. (B) Optimal shrinkage SVD clutter filtered image.

[1] M. Gavish and D.L. Donoho, “Optimal shrinkage of singular values,” *IEEE Trans. Inf. Theory*, vol. 63, pp. 2137-2152, 2017.

[2] M. Bataghva, D. Johnston, N. Power, *et al.*, “Contrast-free ultrasound microvascular imaging with optimal clutter shrinkage to enhance tumor vascular quantification,” *IEEE Ultrason. Symp. Proc.*, Paper 2392, 2020.

Pitch Presentation Abstracts

Session 16: Machine Learning I



3D-DABTS: 3D Domain Adapted Breast Tissue Segmentation via Knowledge Distillation MixupGrey Kuling^a, Belinda Curpen^b, and Anne L. Martel^{a,c}^aMedical Biophysics, University of Toronto, Toronto, ON, Canada^bDept of Medical Imaging, Sunnybrook Health Sciences Centre, Toronto, ON, Canada^cPhysical Sciences, Sunnybrook Research Institute, Toronto, ON, Canada

Introduction: Breast tissue segmentation (BTS) in MRI is an ongoing research topic that is vital to various applications, such as computer assisted diagnosis software, breast density quantification, and background parenchymal enhancement analysis[1]. A current challenge is domain adapted BTS (DABTS) in MRI as the imaging modality can obtain multiple soft tissue contrasts with varying acquisition techniques. For example, the segmentation task of identifying fat and fibroglandular tissue (FGT) between T1w images with and without fat suppression (FS, WOFS) is challenging due to the drastically different intensity level of fat tissue between the two acquisitions. Domain adaptation is the task of generalizing a trained model on one domain to be applicable in another. Domain adaptation has been attempted using knowledge distillation (KD)[2], where a neural network is optimized to give the same output as multiple teacher networks specialized in their own imaging domain. Unexplored is the use of Mixup[3] in conjunction with KD to improve model generalizability and ensure defenses against inputs that fool the network into an error. Mixup is a method of combining training images with a weighted sum to improve the model's linearity between them. This ultimately allows a neural network to make a better judgement on unseen test examples that could be in between the two training example. This project attempts to build a DABTS model of FS and WOFS T1w breast MR images using KD in combination with the Mixup technique to further generalize a DABTS model.

Method: A standard 3D UNet[4] architecture was trained in 4 different ways using 50 patients with T1w FS and WOFS images. FS and WOFS images were used as single channel inputs individually making training data a mixture of the two image domains. Data was preprocessed to have a volume dimension of (64, 128, 128) and a normalized voxel domain between (-1, 1). Training methods were: Classic training with the general dice similarity coefficient (DSC) and binary cross entropy, Mixup training, KD training, and KD Mixup training. Each model was then tested on 8 test patients in FS and WOFS MR images.

Results: The results are reported in Table 1. It can be seen that an improved performance with KD Mixup training can be achieved with an average DSC of 88% \pm 7% for fat tissue and 62% \pm 17% for FGT, where the aim is to improve FGT segmentation with a negligible decrease in fat tissue segmentation.

Conclusion: It can be seen from these preliminary results of this project that DABTS of FS and WOFS MR images is achievable via KD Mixup. It can be assumed that these results can be improved upon with a different image resolution and further investigation of Mixup and KD hyper parameters. Further developments will be to evaluate the performance on higher resolution data as the tissue delineation in the down sampled data is lost in resampling. A hyper-parameter grid search of KD Mixup parameters will also further fine tune the model to the DABTS task. Finally, other image domains acquired in breast MRI such as post dynamic contrast enhancement time points, signal enhancement maps and T2w images, will be introduced to the project to further adapt the model to all breast MR imaging domains. For a robust experiment, cross validation will also be introduced.

This project has shown that using KD Mixup to train a 3D UNet on 2 MR imaging domains can give a DABTS model. This model will further benefit automatic tissue analysis of breast MRI.

References:

- [1] Debelee, T. G., et al. (2020). Survey of deep learning in breast cancer image analysis. *Evolving Systems*, 11(1), 143-163.
- [2] Hinton, G., et al. (2015). Distilling the knowledge in a neural network. *arXiv preprint arXiv:1503.02531*.
- [3] Zhang, H., et al. (2017). mixup: Beyond empirical risk minimization. *arXiv preprint arXiv:1710.09412*.
- [4] Ronneberger, O., et al. (2015, October). U-net: Con... In *Int. Conf. on MICCAI* (pp. 234-241). Springer, Cham.

Training Method	Ave. DSC of Fat \pm STD	Ave. DSC of FGT \pm STD
Classic	90 \pm 4	55 \pm 19
Mixup	86 \pm 8	58 \pm 19
KD	93 \pm 2	60 \pm 19
KD Mixup	88\pm7	62\pm17

Table 1: Test results of the different training techniques on a test set of 8 test patients.

Transfer Learning Approach for Automated Kidney Segmentation on MRI sequences

Rohini Gaikar¹, Fatemeh Zabihollahy², Nicola Schieda³, Eranga Ukwatta¹

¹School of Engineering, University of Guelph, Guelph, Ontario, Canada; ²Department of Radiation Oncology and Molecular Radiation Sciences, The Johns Hopkins University School of Medicine, Baltimore, MD; ³Department of Radiology, The University of Ottawa, Ottawa, Ontario, Canada.

Introduction: Multiparametric MRI is increasingly being investigated for assessment of solid kidney masses in clinical practice due to its ability to provide unique insights into the nature of a kidney tumor with data suggesting an ability to differentiate between benign and malignant kidney masses and to predict aggressive malignant kidney tumors[1]. Despite promising results, automated assessment may improve upon subjective evaluation and reduce inter-observer variability. Precise segmentation of kidney and kidney tumors is important step for fully automated diagnosis to assist radiologists. In this study, we developed a transfer learning-based approach for segmenting kidneys on the T2-Weighted(T2W) and T1-In-Phase(T1IP) MRI pulse sequences which constitutes a renal mass MRI.

Methods: The data is acquired for 30 patients using heterogeneous MRI systems (Siemens, GE and Phillips) and magnetic field strengths 1.5T and 3T. The database consists of 3024 kidney masses that were segmented by a fellowship-trained abdominal radiologist on axial pulse sequences from a renal mass MRI in T2W and T1IP images, where the T1IP images are acquired using dual-echo GRE (2-Point Dixon) technique. Data is preprocessed by histogram equalization technique and augmented using elastic transformations to 14000 images for the deep learning model. We first developed fully automated 2D UNET-T2W model trained on T2W images for kidney segmentation. The weights of UNET-T2W used to train the T1IP sequence model UNET-TLIP using supervised transfer learning to delineate the kidney segmentation on T1IP images. We compared the performance of UNET-TLIP model with UNET-T1IP model which has same model architecture as UNET-T2W but trained on T1-IP data with random weight initialization. The developed algorithms are evaluated on unseen un-augmented test data using dice metric and volume difference between algorithm and manually computed volumes.

Results: The UNET-T2W model is evaluated on six T2W unseen test cases containing 236 images provided average dice score coefficient as 87.67%. The transfer learning approach, UNET-TLIP model has shown improvement in average dice score to 84.02% ($p < 0.05$) which outperformed the UNET-T1IP model giving average dice score of 75.29% on T1IP unseen test cases of 333 images. The average combined volume difference in both kidneys is reduced from 27.531ml to 3.187ml in UNET-TLIP model. The sample kidney segmentation results of UNET-TLIP is shown in Figure 1. The comparison results are summarized in Table 1. The segmentation results on unobserved test images are accurate that demonstrates the network has learned the kidney delineation task.

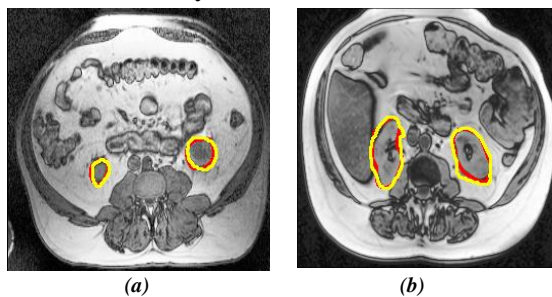


Fig 1: (a) and (b) showing sample Kidney segmentation in different slices by UNET-TLIP model where yellow line is ground truth and red line is predicted segmentation

Table 1: Comparison of Average dice score and Average combined volume difference in Both kidneys on trained models

Model	Average Dice Score (%) \pm Standard Deviation	Average and Standard Deviation of Combined Volume Difference in Left and Right Kidneys in ml
UNET-T2W (Trained on T2W)	87.67 \pm 0.04	6.70 \pm 10.72
UNET-T1IP (Without Pretraining)	75.29 \pm 0.12	27.53 \pm 78.66
UNET-TLIP (Transfer learning of UNET-T2W)	84.02 \pm 0.06	3.18 \pm 29.94

Conclusion: In this preliminary study, we demonstrated the supervised transfer learning approach for kidney segmentation in different MRI pulse sequences. The pretrained model of T2-Weighted sequence trains the network of T1-In-Phase sequence efficiently and improves the kidney segmentation results.

References:

- [1] N. K. Ramamurthy, B. Moosavi, M. D. F. McInnes, T. A. Flood, and N. Schieda, "Multiparametric MRI of solid renal masses: Pearls and pitfalls," *Clin. Radiol.*, vol. 70, no. 3, pp. 304–316, 2015, doi: 10.1016/j.crad.2014.10.006.

Surgical tool tracking with object detection for performance assessment in central venous catheterization

Olivia O'Driscoll¹, Rebecca Hisey¹, Daenis Camire², Jason Erb², Daniel Howes²,
Gabor Fichtinger¹, Tamas Ungi¹

¹Laboratory for Percutaneous Surgery, School of Computing, Queen's University, Kingston, Canada

²Department of Critical Care Medicine, Queen's University, Kingston, Canada

Introduction: Medical schools are adopting competency-based medical education, which requires continuous expert supervision to monitor trainee progress. Thus, they seek methods of objectively assessing trainee performance automatically, without expert supervision. Holden et al. revealed that each tool's path lengths are valuable trainee performance metrics in ultrasound-guided interventions, like central venous catheterization (CVC) [1]. We sought to develop a webcam-based approach for performance assessment to eliminate the need for costly systems and expert supervision. In this study, we evaluate the efficacy of using an object detection network for performance assessment in CVC. This project's code can be found here: <https://github.com/SlicerIGT/aigt>.

Methods: We used the object detection network Faster Region-Based Convolutional Neural Network (Faster R-CNN) to compute the usage time and two-dimensional (2D) path length of seven surgical tools used in central venous catheterization (CVC), as shown in Figure 1. The 2D path length is defined as the sum of Euclidean distances between the centers of sequential bounding boxes for a given tool. Usage time is defined as the number of frames in which a given tool appears divided by the frame rate. Mean average precision (mAP), defined as the area under the precision/recall curve, measured the network's ability to locate and recognize each tool.

To train the Faster R-CNN, we recorded four medical students each performing five CVC trials on a venous access phantom using a static recording setup. We used a leave-one-user out cross-validation scheme in which the network was trained four times, reserving all five recordings from a single trainee for testing. On each test set, we

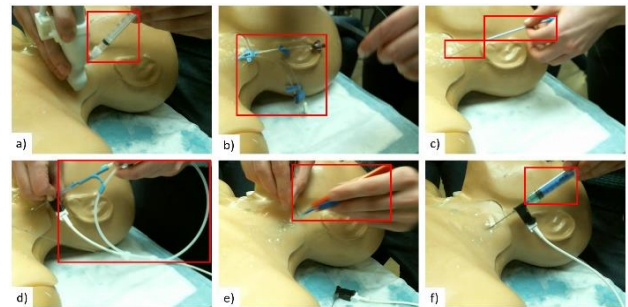


Figure 1. Class ground truth labels: a) anesthetic b) catheter c) dilator and guidewire d) guidewire casing e) scalpel f) syringe

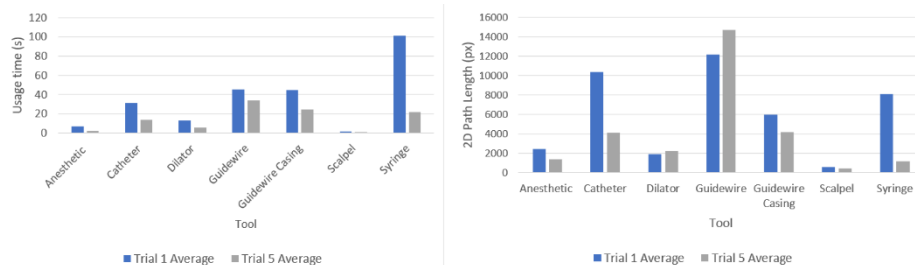


Figure 2. Comparisons of a) Tool usage times and b) 2D tool path lengths in trials 1 and 5

computed the 2D tool path lengths and usage times for each of the five trials. Comparing the percentage differences in these performance metrics across trials allowed us to evaluate Faster R-CNN's Effectiveness as a performance assessment method in CVC.

Results: The average tool usage

time reduction in the students' first and fifth procedural trials was 52%, and that of 2D path length was 29%, as shown in Figure 2. The neural network's mAP was 0.66, with tool-specific mAPs between 0.49 and 0.92.

Conclusions: Faster R-CNN recognized procedural tool accurately enough to compute metrics that demonstrated improvement with the trainee's skill level. Faster R-CNN is an effective skill-assessment method in CVC.

Acknowledgements: This work was funded in part by NIH/NIBIB and NIH/NIGMS (via grant 1R01EB021396-01A1), by CANARIE's Research Software Program, and is supported as a Collaborative Health Research Project (CHRP #127797) by the Natural Sciences and Engineering Research Council of Canada (NSERC) and the Canadian Institutes of Health Research (CIHR). R. Hisey is supported by the Queen Elizabeth II Graduate Scholarships in Science and Technology (QEII-GSST). G. Fichtinger is supported by a Canada Research Chair.

References:

[1] Holden, M., Xia, S., Lia, H., Keri, Z., Bell, C., Patterson, L., Ungi, T. and Fichtinger, G. "Machine learning methods for automated technical skills assessment with instructional feedback in ultrasound-guided interventions," International journal of computer assisted radiology and surgery, 1993-2003 (2019)

2D and 3D Labelling Methods for Facial Skin Tension Lines

Bao Yi (Emily) Huang^{1,2}, Wenzhangzhi Guo^{1,2}, Vito Forte², Joel C. Davies³, Lueder A. Kahrs^{1,2}

¹Department of Computer Science, University of Toronto, Ontario, Canada; ²Centre for Image Guided Innovation and Therapeutic Intervention, The Hospital of Sick Children, Toronto, Ontario, Canada;

³Department of Otolaryngology, Medical University of South Carolina, Charleston, SC, USA

Introduction: Facial relaxed skin tension lines (RSTLs) are important to reconstructive surgeons when designing surgical incisions that will optimize both cosmetic and functional outcome. Aligning surgical incisions with RSTLs minimizes wound contraction, distortion, and scarring [1]. We have been searching for 2D and 3D face databases and tools that are suitable for this labelling task in order to produce more accurate and reliable placement of RSTLs for Augmented Reality (AR) [2], Machine Learning (ML), and other automatic production methods.

Methods: The Texas 3D Face Recognition Database was selected, which includes over 1000 pairs of RGB and depth images of 3D face scans from over 100 subjects [3,4]. A custom implementation with the Visualization Toolkit (VTK) [5] was employed to reconstruct the textured mesh of each scan. The processing pipeline has two branches, one for 2D and one for 3D labelling method (see Fig. 1). Using pre-defined virtual camera poses of the rendered face mesh, automated 2D snapshots were captured from different perspectives. For a subset of samples from the Texas database, we generated over 2000 images from five standardized view angles and distances. These outputs will be labelled by head and neck surgeons using Labelbox (Labelbox, Inc., San Francisco, CA, USA). The experimental 3D branch uses further VTK methods to place support points interactively on the surface mesh and connects these points by line segments based on the shortest geodesic path.

Results: Fig. 2 shows RSTL labels of the same subject in the Texas database from two different virtual camera perspectives. For an initial set of RSTLs, the average labelling time was 6.5 minutes per image.

Conclusions: Methods for labelling facial skin tension lines were created and tested. Future work will compare the established 2D and experimental 3D labelling pipeline. Labels of different perspectives in the 2D branch can be overlaid and fused with the 3D rendering environment. As a result, an ideal user interface will be identified to label such facial RSTL on the basis of rendered face scans. AR- and ML-based methods will profit from the labelled data and learn the patterns of skin tension line placement.

References:

- [1] Borges AF. Relaxed Skin Tension Lines (RSTL) versus Other Skin Lines. *Plastic and Reconstructive Surgery* 73(1): 144-150, 1982.
- [2] Guo W, et al. Augmented Reality Relaxed Skin Tension Lines for Face Surgery - Initial Results on a Mobile Device. *IMNO 2021*
- [3] Gupta S, et al. Texas 3D Face Recognition Database, URL: <https://live.ece.utexas.edu/research/texas3dfr/>
- [4] Gupta S, et al. Anthropometric 3D Face Recognition. *International Journal of Computer Vision* 90(3): 331-349, 2010.
- [5] Schroeder W, et al. *The Visualization Toolkit* (4th ed.), Kitware, ISBN 978-1-930934-19-1, 2006.

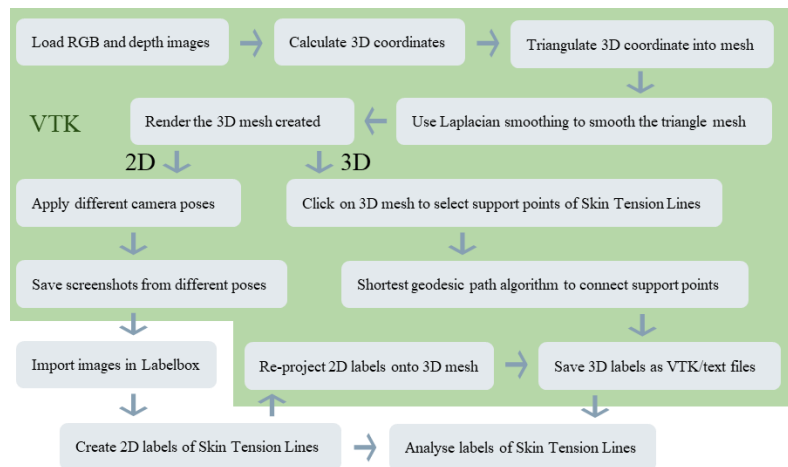


Fig. 1: Dataflow for 2D and 3D labelling process

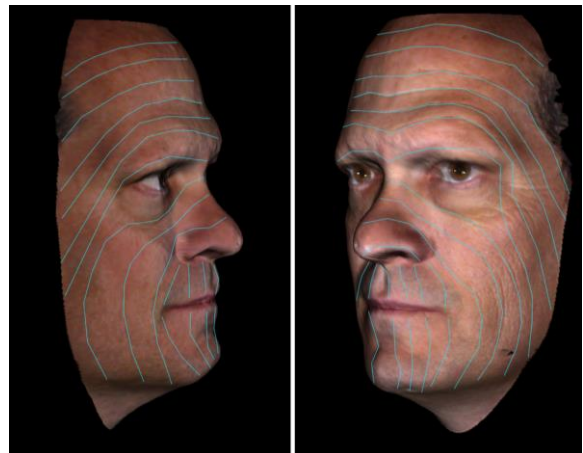


Fig. 2: A resulting set of RSTLs of the 2D labelling branch

Machine Learning to Detect Brain Lesions in Focal Epilepsy

Andrea Perera-Ortega¹, Alireza Sedghi¹, Jonah Isen¹, Sjoerd B. Vos^{2,3}, Parvin Mousavi¹, Gavin P Winston^{4,5}

¹Medical Informatics Laboratory, School of Computing, Queen's University, Kingston, Canada

²Centre for Medical Image Computing, University College London, United Kingdom

³Neuroradiological Academic Unit, Queen Square Institute of Neurology, University College London, London, U.K.

⁴Department of Medicine & Centre for Neuroscience Studies, Queen's University, Kingston, Canada

⁵Department of Clinical and Experimental Epilepsy, Queen Square Institute of Neurology, University College London, London, United Kingdom

INTRODUCTION: Identifying areas of abnormality on MRI brain scans with focal epilepsy is fundamental to the diagnosis and treatment of the condition. However, in about a third of patients with focal epilepsy, brain scans appear to be normal (MRI-negative) as human observers cannot detect any abnormality with current imaging technology. The lack of accurately identifiable lesions means that patients must undergo expensive and invasive testing in order to be considered for surgery. The objective of this work is to use machine learning in order to locate areas of abnormality on patients with focal epilepsy on a per-voxel basis by comparing them with healthy controls. As a proof-of-concept, the technique is first applied to patients with visible lesions providing a ground truth (MRI-positive), but future work will extend this to MRI-negative subjects. Recent approaches have used machine learning techniques to detect focal epilepsy lesions but with fewer MRI modalities and did not provide specific localization of abnormalities¹.

METHODS: The data consists of multi-modal brain MR images from 62 healthy control subjects and 38 MRI-positive (discrete) patients with focal epilepsy (with accompanying lesion masks). Epileptogenic lesion pathologies in the data set consist of focal cortical dysplasia, cavernoma, hippocampal sclerosis and various tumours. The five modalities used in this study were T1-weighted MRI data and diffusion-weighted MRI, which provided fractional anisotropy (FA) and mean diffusivity (MD) from Diffusion Tensor Imaging (DTI), as well as neurite density index (NDI) and orientation dispersion index (ODI) from Neurite Orientation Dispersion and Density Imaging (NODDI). A support vector machine (SVM) was utilized as a probabilistic classifier and trained with two classes of data over the five modalities. All of the images were pre-processed to undergo segmentation, smoothing, normalization and co-registration. Features were then extracted by calculating Z-score maps for all of the control and discrete patient images over each modality. The SVM was trained using stratified 5-fold cross-validation voxels. Probability maps for the individual test patients were generated for visualization purposes. Dice coefficient was used to quantify the similarity between the predicted areas of abnormality and the actual lesion.

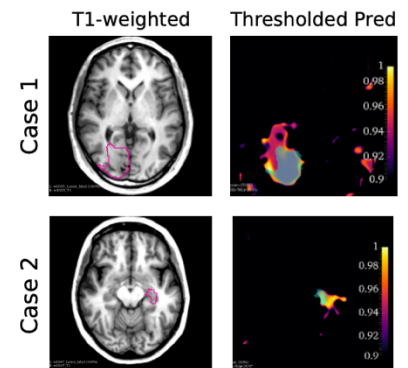


Figure 1. The original T1 scans of two MRI-positive patients compared with the thresholded SVM predictions on the right with the ground truth mask overlaid.

RESULTS: The proposed method achieved specificity of 83% and sensitivity of 91%. For 63% of the test patients, the Dice score increased significantly as the threshold value increased (Figure 1). This suggests that the model is classifying abnormal voxels with a high degree of confidence. Although the voxel-based analysis demonstrated good results in the classification, further analysis considering the neighboring voxels needs to be performed.

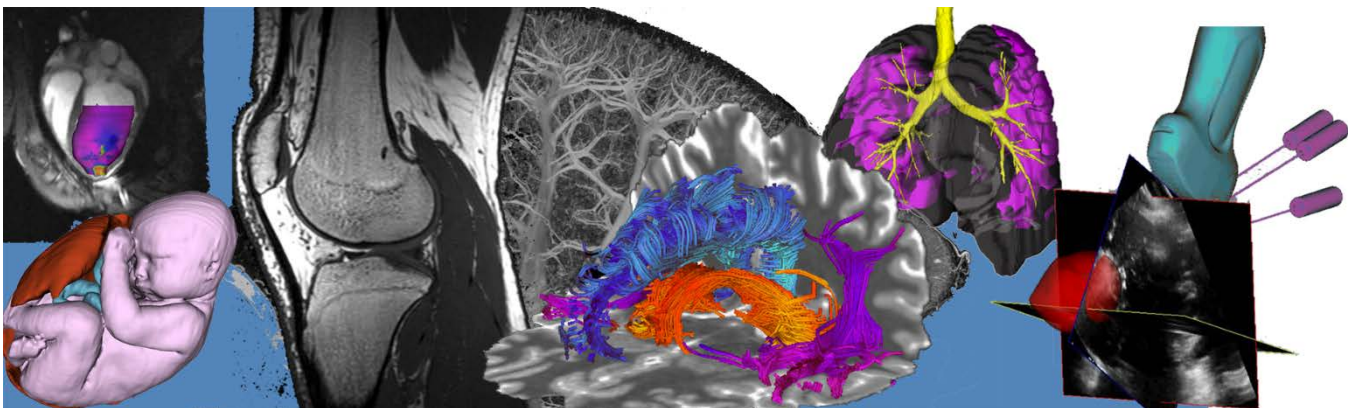
CONCLUSIONS: A novel approach in presenting localization using a machine learning method based on SVM to classify individual voxels as normal or abnormal in patients with focal epilepsy who have discrete lesions was demonstrated. The classifier was trained using voxel intensities of MRI images per each of the five modalities. Our model was able to achieve 83% specificity and 91% sensitivity in classification of voxel intensities from 18 control and 11 discrete group test patients.

REFERENCES

[1] Bennett, O. F., Kanber, B., et al., "Learning to see the invisible: A data-driven approach to finding the underlying patterns of abnormality in visually normal brain magnetic resonance images in patients with temporal lobe epilepsy," *Epilepsia* 60(12), 2499–2507 (2019).

Pitch Presentation Abstracts

Session 17: Neuro Imaging I



The trajectory of putative astroglial dysfunction in first episode schizophrenia: A longitudinal 7-Tesla MRS study

Peter Jeon^{1,2}, Michael Mackinley³, Jean Théberge^{1,2,4,5}, Lena Palaniyappan^{1,6,7}

1. Department of Medical Biophysics, Western University, London, Canada 2. Lawson Health Research Institute, Imaging Division, London, Canada 3. Department of Neuroscience, Western University, London, Canada 4. St. Joseph's Health Care, Diagnostic Imaging, London, Canada 5. Department of Medical Imaging, Western University, London, Canada 6. Robarts Research Institute, Western University, London, Canada 7. Department of Psychiatry, Western University, London, Canada

Background: Astroglial pathology has been long suspected in schizophrenia. Myo-inositol, a metabolic marker that is particularly abundant in astroglia, is reduced in the anterior cingulate cortex of patients with schizophrenia. This has been taken to indicate a deficit in astroglial activation and recruitment; though the status of this putative astroglial pathology in untreated first episode schizophrenia and its subsequent trajectory are unknown to date.

Methods: We employed 7T semi-LASER magnetic resonance spectroscopy (1H-MRS) and quantified myo-inositol spectra at the dorsal anterior cingulate cortex (TE=100ms; voxel size 2x2x2cm³; 32 spectra averages) in 31 participants; 21 patients with schizophrenia and a median lifetime antipsychotic exposure of less than 3 days, followed up after 6 months of treatment, and 10 healthy subjects scanned twice over the same time period. After using HSVD to remove any residual water peak, an in-house software was used for spectral fitting and quantification. No macromolecular contribution was assumed due to the long echo time employed. We studied time by group interaction on myo-inositol after adjusting for gender and age.

Results: There was a significant time by group interaction in myo-inositol concentration ($\eta^2 = 0.19$, $p = 0.02$), with patients showing a significant reduction at the baseline ($\eta^2 = 0.47$, $p < 0.001$) but not at the 6-months follow-up ($\eta^2 = 0.02$, $p = 0.44$). Older age and female gender were associated with lower levels at both time points ($\eta^2 = 0.14-0.36$, $p = 0.06-0.001$). On average, patients with early psychosis receiving treatment showed an 8.9% increase, while healthy controls showed an 8.2% decrease in MRS myo-inositol levels over the follow-up period.

Conclusions: We report a significant reduction in myo-inositol concentration in the anterior cingulate cortex in schizophrenia at an early, untreated state of acute illness that improves over time. This trajectory indicates that dynamic astroglial changes are likely to operate in the early stages of schizophrenia. MRS myo-inositol may be a critical marker of amelioration of active psychosis in early stages of schizophrenia.

Glutathione as a molecular marker of functional impairment in patients with at-risk mental state: 7-Tesla ¹H-MRS study

Peter Jeon^{1,2}, Roberto Limongi³, Sabrina D. Ford^{3,4}, Cassandra Branco⁴, Michael Mackinley^{3,5}, Maya Gupta⁶, Laura Powe⁴, Jean Théberge^{1,2,4,7,8}, Lena Palaniyappan^{1,2,3,4}

1. Department of Medical Biophysics, Western University, London, Canada 2. Lawson Health Research Institute, Imaging Division, London, Canada 3. Robarts Research Institute, Western University, London, Canada 4. Department of Psychiatry, Western University, London, Canada 5. Department of Neuroscience, Western University, London, Canada 6. Department of Psychology, Western University, London, Canada 7. St. Joseph's Health Care, Diagnostic Imaging, London, Canada 8. Department of Medical Imaging, Western University, London, Canada

Background: A substantial number of individuals with clinical high-risk (CHR) mental state do not transition to psychosis. However, regardless of future diagnostic trajectories, many of these individuals develop poor social and occupational functional outcomes. The levels of glutathione (GSH), a crucial cortical antioxidant, may track variations in functional outcomes in early psychosis and prodromal states.

Methods: Thirteen clinical high-risk and 30 healthy control volunteers were recruited for a 7-Tesla magnetic resonance spectroscopy scan with voxel positioned within the dorsal anterior cingulate cortex (ACC). Clinical assessment scores were collected to determine if any association was observable with glutathione levels.

Results: Bayesian Spearman test revealed a positive association between the Social and Occupational Functioning Assessment Scale (SOFAS) and the glutathione concentration in the clinical high-risk group (mode $\rho = 0.58$, posterior proportion [PP] = 0.98, Bayesian Factor in favour of H_1 over the null H_0 [BF_{10}] = 2.1) but not in the healthy control group (mode $\rho = 0.11$, PP = 0.44, $BF_{10} = 0.23$). After accounting for variations in SOFAS, CHR group had higher GSH levels than the healthy subjects (mode difference = -0.26, PP = 0.96; effect size -1.04, PP = 0.96).

Conclusions: This study is the first to use 7-Tesla magnetic resonance spectroscopy to test whether ACC glutathione levels related to social and occupational functioning in a clinically high-risk group and offers preliminary support for glutathione levels as a clinically actionable marker of prognosis in emerging adults presenting with risk features for various severe mental illnesses.

Ultra-high field imaging of the human amygdala nuclei: manual segmentation to atlas development

Sara M. Pac¹, Daniel J. Cao², Emma G. Duerden³, Ali R. Khan²

Neuroscience Graduate Program¹, Faculty of Medical Biophysics², and Faculty of Education³,
Western University, London, Ontario, Canada

Introduction

Manual segmentation by neuroanatomy experts is considered the gold standard when obtaining volumetric measurements of amygdalae structure. Yet the time required for the labour-intensive process of manual segmentation is prohibitive. Automated segmentation methods afford highly reproducible quantifications of larger more evident medial temporal lobe structures like the hippocampus but highly variable measurements of the small deeply embedded amygdala sub-nuclei at lower magnetic resonance imaging (MRI) scanner field strengths (Dewey et al., 2010; Morey et al., 2010). Saygin and colleagues (2017) developed a novel automated atlas of the human amygdala based upon high resolution *ex vivo* images obtained at 7 Tesla (T) MRI. However, their automated pipeline is prone to registration scaling errors when applied to *in vivo* datasets, inhibiting the accuracy of the atlas. Any speculations of volumetric amygdalae abnormalities in neurological or psychiatric disorders cannot progress until the precise labelling of the amygdala and its nuclei can be outlined with *in vivo* MRI. We are the first to collect ultra-high field 9.4T *ex vivo* MRI scans to visualize the amygdala nuclei at high resolution. Our objective is to develop a more accurate automated atlas of the human amygdala.

Methods

Ten post-mortem human brain specimens donated to University Hospital are scanned at the CFMM Robarts Research Institute, London, Ontario, Canada. The subjects did not pass away due to any neurological disorders and were an average of 73.5 years old at the time of death. The specimens are first scanned in their entirety in a 3D-printed container at 7T. Then specimens are dissected into medial temporal lobe portions containing the amygdala before they are scanned at 9.4T. The scanning sequences used for registration and segmentation are a T2-weighted SPACE MRI scan (TR = 4 msec; TE = 0.4 msec; flip angle = 120°) acquired with a 1 mm³ isotropic resolution at 7T, and a T2-weighted TurboRARE MRI scan (TE=30 msec; TR=30 msec; flip angle = 90°) acquired at 9.4T at 0.1x0.1x0.2mm³ resolution. ITK-SNAP (Yushkevich, 2006) is used to manually register the 9.4T scans onto their corresponding anatomical locations on the whole brain 7T images, which allows for more accurate registration when the atlas is later applied *in vivo*. The subnuclei of the amygdala are segmented using ITK-SNAP. SMP manually segmented all nuclei of the amygdala twice over the span of 3 months, and a Dice coefficient was calculated to determine the intra-rater reliability (Table 1). The Dice coefficient represents the number of overlapping voxels between two independently segmented cases divided by the union of those same voxels (Dice, 1945).

Results

Intra-rater reliability									
	Amygdala subnuclei								
	Lateral	Baso-lateral	Baso-medial	Central	Cortical	Medial	Anterior amygdala area	Paralaminar	Cortico-amygdaloid transition area
Dice coefficient	0.87	0.82	0.79	0.61	0.41	0.45	0.66	0.76	0.62

Table 1: The intra-rater reliability assessed using the Dice coefficient of nine amygdala subnuclei segmented at 9.4T. These Dice coefficient scores represent an average of six dissected and segmented *ex vivo* specimens.

Conclusions We outline the acquisition parameters obtained from a 9.4T scanner that have allowed for high resolution visualization of *ex vivo* human amygdala nuclei resulting in high intra-rater reliability. We describe steps for segmenting the nuclei and registering a small field of view MRI image onto its corresponding location on its whole brain counterpart. The next step towards creating an atlas of the amygdala is a multi-atlas segmentation with label fusion approach after all data has been collected. Ultimately this atlas can be applied to *in vivo* MRI datasets for better amygdalae nuclei anatomical localization even with noisy functional MRI.

Reducing the Incidence of CT Perfusion Infarct Volume Overestimation in Acute Ischemic Stroke

Kevin J. Chung,^a Bijoy K. Menon,^b Andrew M. Demchuk,^b Ting-Yim Lee^a

^aDepartment of Medical Biophysics, Robarts Research Institute, University of Western Ontario, London, ON;

^bDepartment of Clinical Neurosciences, Hotchkiss Brain Institute, University of Calgary, Calgary, AB

Introduction: CT perfusion-derived hemodynamic maps provide an efficient way to triage acute ischemic stroke patients for clot-removal therapy based on brain physiology. In clinical practice, brain infarction is often identified by tissue with cerebral blood flow (CBF) <30% of that in the contralateral hemisphere. However, this population-based threshold may overestimate infarction in patients who arrive promptly after stroke symptom onset (<180 minutes) and may falsely discourage treatment in those who may benefit. Previous studies have shown that infarction does not occur until cerebral blood volume (CBV) decreases in conjunction with CBF. We hypothesize that the incidence of infarct overestimation decreases using a CBF and CBV double threshold (CBF+CBV) compared to a CBF-only approach.

Methods: Fifty patients with acute ischemic stroke who were imaged within 180 minutes of stroke symptom onset were retrospectively obtained from a clinical database. Patients had admission CT perfusion and 24-hour follow-up imaging from which follow-up infarct volume (FIV) was measured. Infarct overestimation (“ghost core”) was defined as CT perfusion infarct minus FIV being greater than 10 ml. Two voxel-wise perfusion parameter thresholds for infarction were compared: (a) CBF<30% (current clinical standard) and (b) a fixed CBF and CBV threshold determined empirically from an independent dataset. A McNemar test compared the incidence of ghost core using CBF-only versus CBF+CBV thresholding. In a subgroup of patients who had early and successful treatment (within 90 minutes of imaging), volume agreement between FIV and CT perfusion infarct was assessed by Bland-Altman analysis. These patients are expected to have minimal infarct growth between baseline and follow-up (*i.e.* FIV nearly identical to CT perfusion infarct) as opposed to patients with late or unsuccessful treatment whose infarct is expected to grow between baseline and follow-up. A *P*-value less than 0.05 was considered statistically significant.

Results: Using only a CBF threshold, seven patients (14%) demonstrated ghost core compared to only one patient (2%) with CBF+CBV thresholding. In the single CBF+CBV ghost core case, infarct was predicted in the white matter, which inherently has lower CBV and is more prone to false positives with a fixed CBV threshold applied on both the grey and white matter. A McNemar test indicated a significant difference in the incidence of ghost core between CBF-only and CBF+CBV thresholding ($P=0.031$). Thirty-one patients had early and successful treatment. Mean difference (CT perfusion infarct minus FIV) was +0.1 (limits of agreement: -34.5 to 34.7) ml and -4.2 (-31.6 to 23.2) ml for CBF-only and CBF+CBV thresholding methods, respectively.

Conclusions: Including CBV with CBF thresholding reduced the incidence of CT perfusion ghost core compared to CBF-only thresholding. Narrower limits of agreement using CBF+CBV thresholding indicated better agreement to FIV compared to CBF-only thresholding and as expected the former showed minor infarct growth while the latter did not. CBV may account for homeostatic mechanisms such as autoregulation and collateral circulation that are not encompassed by a single CBF threshold. Future studies are warranted to determine the effect of CBF+CBV thresholding on treatment decision-making.

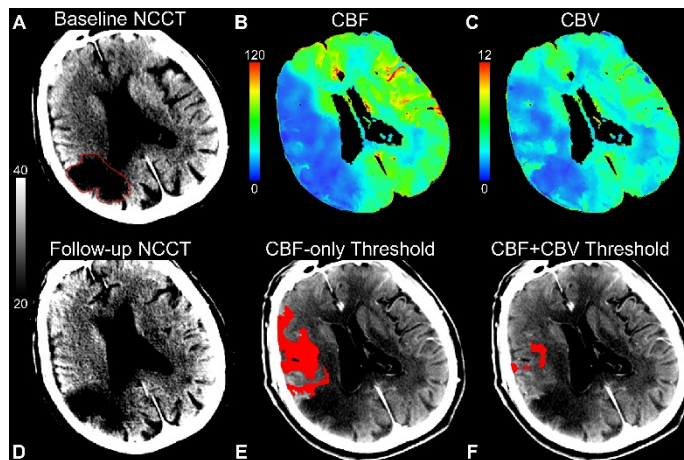


Figure. CBF-only and CBF+CBV thresholding to predict baseline infarction. (A) Baseline non-contrast CT (NCCT) showing a chronic infarct (red outline); (B) CBF and (C) CBV maps; (D) Twenty-four-hour follow-up NCCT showing no new acute infarction; (E) CBF-only threshold infarct; (F) CBF+CBV threshold infarct. Chronic infarction was excluded by thresholding dynamic CT perfusion images. The CBF-only threshold estimated an infarct volume of 44.3 ml (ghost core), while the CBF+CBV threshold estimated 9.8 ml (non-ghost core). False positives from CBF+CBV thresholding were primarily in the white matter, which inherently has lower CBV.

Synthesis and PET imaging of the 4R-tau radiotracer [^{18}F]CBD-2115 in rodents and non-human primate

Anton Lindberg,^a Ashley C. Knight,^{a,b} Daniel Sohn,^{c,d} Junchao Tong,^a April Radelet,^e N. Scott Mason,^e Samuel Svensson,^{c,f} Chester A. Mathis,^e and Neil Vasdev.^{a,b,*}

^a Azrieli Centre for Neuro-Radiochemistry, Brain Health Imaging Centre, Centre for Addiction and Mental Health, Toronto. ^b Department of Psychiatry/Institute of Medical Science, University of Toronto. ^c CBD solutions, Center for Molecular Medicine, Karolinska Hospital, Sweden. ^d Novandi Chemistry AB, Sweden. ^e Department of Radiology, University of Pittsburgh, USA. ^f Department of Physics, Chemistry and Biology, Linköping University, Sweden.

Introduction. Human tau protein tangles are a hallmark of many neurodegenerative diseases. Tauopathies are characterized by 3R- or 4R-tau isoforms, found in combination or separately. Recent progress has seen the development of [^{18}F]flortaucipir (FDA approved) and [^{18}F]MK-6240 among others as tau-PET imaging agents in multi-centre clinical trials of Alzheimer's Disease (AD) and related dementias. However, there are currently no high affinity PET radiotracers for imaging subtype-dominant 4R-tauopathies. In the present study we explore a novel 2-(6-(piperidin-1-yl)pyridin-3-yl)-1H-indole structural scaffold with high affinity for the 4R-isoform of tau protein. The lead compound, CBD-2115 ($IC_{50(4R\text{-tau})} = 5 \text{ nM}$, $\text{clogP} = 3.1$, $\text{efflux ratio} = 0.98$) was labelled with tritium, and with fluorine-18 (half-life = 109.7 min), for *in vitro* binding assays and autoradiography as well as *in vivo* PET imaging in rodents (mouse and rat) and non-human primate (NHP). **Methods.** CBD-2115 was identified from 148 synthesized compounds based on a novel structural scaffold, after screening for tau fibril affinity. Off-target interactions were evaluated in an affinity assay containing 93 central nervous system (CNS) targets (Eurofins). [^3H]CBD-2115 was synthesized and compared to [^3H]flortaucipir and [^3H]MK-6240. Scatchard assays were used to determine tau substructure affinity and selectivity in P301L mice and human brain tissues. [^{18}F]CBD-2115 was synthesized using a two-step radiofluorination method and translated for PET imaging studies in mouse, rat and NHP. **Results.** [^3H]CBD-2115 showed a decrease of specific binding by 40-60% in autoradiography experiments at baseline and blocking conditions with CBD-2115 using tissue from patients with corticobasal degeneration (CBD) and progressive supranuclear palsy (PSP). In Scatchard assays using P301L transgenic mice with confirmed 4R-tau aggregate expression, [^3H]CBD-2115 had a K_D value of 6.9 nM and B_{max} of 500 nM. Only one off-target interaction was discovered in selectivity assay for the melatonin binding site (MT3 (ML2)), which does not interfere with tau-rich regions in CNS. Comparison with [^3H]flortaucipir and [^3H]MK-6240, in Scatchard assays from human brain tissues, showed [^3H]CBD-2115 has the highest affinity (4.9 nM) for PSP specific 4R-tau deposits and similar affinity in AD tissues. [^{18}F]CBD-2115 was synthesized from the corresponding nitro precursor with radiochemical purity of 97% and molar activity (A_m) of $27.3 \pm 6.2 \text{ GBq}/\mu\text{mol}$ with radiochemical yields of $10.7 \pm 3.5\%$. Dynamic PET acquisitions using two healthy rats and three healthy mice showed a maximum of 0.5 standard uptake value (SUV) in whole rat brain and 0.65 SUV in mouse brain and decreased to below 0.1 SUV after 30 min in both species. PET measurement in NHP showed a maximum uptake in brain of 0.6 SUV followed by a decrease to below 0.2 SUV within 20 min. Arterial blood analysis showed 45% un-metabolized parent compound at 10 min with only one radio-metabolite. Poor brain uptake of [^{18}F]CBD-2115 is surprising given that the measured $\log D_{7.4}$ (2.99 ± 0.15) and CNS Multiple Parameter Optimization desirability score (4.65/6.00) is in the range of most brain penetrating compounds. However, the lower sub-score for hydrogen bond donors (0.167/1.00) is a parameter worthy of exploration for other analogues. **Conclusions.** [^{18}F]CBD-2115 is a first in class 4R-tau PET radiotracer. Despite promising characteristics *in vitro*, [^{18}F]CBD-2115 showed low overall brain uptake in PET measurements in three species. Future work will focus on exploring analogues of this compound with fewer hydrogen bond donors in attempt to achieve higher affinity and brain uptake.

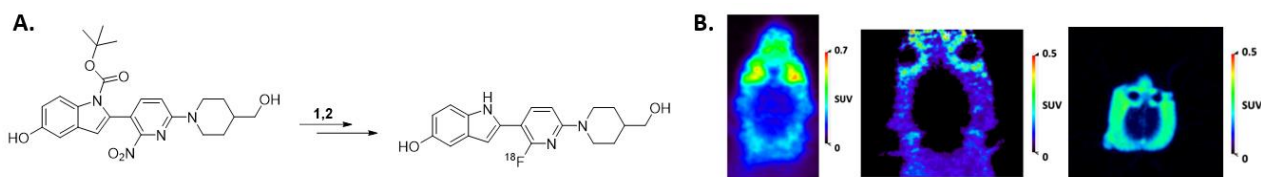


Figure 1. (A.) Radiosynthesis scheme for [^{18}F]CBD-2115. (B.) Summed PET images in mouse (left), rat (middle), and NHP (right).

Parcellation of the Piriform Cortex through Clustering of Laminar Features in the Unfolded 3D BigBrain: Correspondence with Diffusion Tractography, and Resting-state fMRI at 7T

Christidis, N.K.¹, Dekraker, J.¹, Xiao, Y.¹, Haast, R.¹, Köhler, S.², Steven, D.A.³, & Khan, A.R.^{1,2}.

Robarts Research Institute, Western University, London, Canada¹

The Brain and Mind Institute, Western University, London, Canada²

Departments of Clinical Neurological Sciences, Division of Neurosurgery, Western University, London Canada³

Introduction: Approximately 30% of patients undergoing surgical resection for temporal lobe epilepsy (TLE), the most common focal epilepsy, continue to have seizures postoperatively. In this cohort of patients, this suggests that the epileptic network extends beyond the typically resected structures into other critical regions that have yet to be discovered. The human piriform cortex is a three-layered allocortical structure with vast connectivity to the mesial-temporal structures (i.e. amygdala and hippocampus), that has been recently implicated in the epileptic network of the mesial temporal lobe, with resection of greater proportions of the piriform cortex being associated with a substantially improved seizure freedom outcomes. However, all previous in-vivo human anatomical studies have segmented the piriform cortex as a single structure, despite animal evidence demonstrating that the global piriform cortex is separable into subdivisions, which exhibit distinct structural and functional characteristics with differential susceptibility to epileptic activity. Thus, imaging techniques that allow quantification of local pathological changes within the human piriform are needed to truly unravel the role of the piriform cortex within the epileptic network. The current study aims to create a data-driven anatomical and functional parcellation of the human piriform cortex through imaging based on its: 1) intrinsic structural differences in histological laminar features, 2) intrinsic structural connectivity divisions, 3) intrinsic functional connectivity divisions.

Methods: Data-driven parcellations of the human piriform were individually generated based on: 1) Intrinsic structural-histology via clustering of unfolded laminar features in the Montreal Neurological Institute's 3D BigBrain (100 μ m); 2) Intrinsic structural-connectivity via clustering of diffusion MRI probabilistic tractography connectivity in the human connectome project's 7T diffusion data ($n = 178$); and 3) Intrinsic functional-connectivity via clustering of resting-state fMRI correlations in the human connectome project's 7T resting-state fMRI data ($n = 145$).

Results: Similar parcellations of the human piriform cortex were achieved through structural-histological features, structural-connectivity, and functional-connectivity. Through separate data-driven parcellations, the human piriform cortex could be separated into the following three subdivisions. Frontal piriform, exhibiting low neuronal density on histology, with strong connectivity to the insula and lateral temporal lobe; 2. Anterior-temporal-piriform, exhibiting high neuronal density on histology, with the strongest connectivity to the insula (i.e. 1.5 times greater than frontal piriform connectivity) and similarly strong connectivity to the lateral temporal lobe, and 3. Posterior-temporal-piriform, exhibiting high neuronal density on histology, with uniquely strong connectivity to the mesial temporal lobe (i.e. hippocampus).

Conclusions: Overall, these findings suggest that there are quantifiable imaging markers of the piriform cortex subdivisions that are reproducible across histology, structural-connectivity, and functional-connectivity, without requiring additional anatomical annotations. This level of anatomical detail permits quantification of subdivision specific pathological changes in the piriform cortex associated with epilepsy, which can aid in unraveling the role of the piriform cortex within the epileptic network and subsequently isolating the specific subdivisions of the piriform cortex responsible for improved seizure freedom outcomes following surgical resection of mesial temporal lobe epilepsy.

Brain network connectivity and neurodevelopmental outcomes in children with infantile hydrocephalus

Ramina Adam^{1,2}, Daamoon Ghahari¹, Roy Eagleson^{1,3}, Sandrine de Ribaupierre^{1,2,3}

¹Brain and Mind Institute, Western University; ²Clinical Neurological Sciences, Western University;

³Department of Electrical and Computer Engineering, Western University

Introduction: Infantile hydrocephalus is a condition in which there is an abnormal buildup of cerebrospinal fluid in the ventricles of the brain within the first few months of life. There are several causes of infantile hydrocephalus, including genetic abnormalities, complications of premature birth leading to bleeding in the brain, or an infection of the brain and spinal cord such as bacterial meningitis. The excess fluid increases the size of the ventricles (ventricle dilation) which then increases pressure on surrounding brain tissue. Compression of the developing brain increases the risk of secondary brain injury as well as cognitive and developmental disabilities. While previous research has focused on early behavioural outcomes (0-3 years of age), long-term outcomes at school-age have not been well studied. The main objectives of this study were to (1) investigate the effects of ventricle dilation on functional and structural brain networks in children with infantile hydrocephalus and (2) examine how these brain changes relate with cognitive and developmental outcomes.

Methods: Participants included 5 children with previous infantile hydrocephalus (6-10 years old) and 20 age-matched healthy controls. We collected resting-state functional MRI (TR=1000ms, TE=30ms, voxel size=2.5mm³) and diffusion-weighted imaging (30 directions, b-value=1000s/mm²) on a Siemens MAGNETOM Prisma Fit 3-Tesla MRI scanner. Executive function was evaluated using the Behaviour Rating Inventory for Executive Function which includes measures of behavioural, emotional, and cognitive regulation. Regions of interest for the functional and structural brain networks were defined using a 100-region brain parcellation (Schaefer et al., 2018, *Cereb Cortex*) grouped into large-scale cortical networks (Yeo et al., 2011, *J Neurophysiol*). Functional connectivity (FC) was defined as the temporal correlation of the blood-oxygen level-dependent signal between each pair of brain regions and structural connectivity (SC) was defined as the number of probabilistic streamlines connecting each pair of regions. Fractional anisotropy (FA) of anterior and posterior white matter was obtained from regions of interest shown in Figure 1.

Results: We found that children with infantile hydrocephalus showed decreased FC primarily between the frontoparietal control and default mode network ($p<0.05$; Fig. 2). Both FC and SC were decreased between right frontoparietal control and left visual network, left frontoparietal control and right dorsal attention network, and within the right dorsal attention network ($p<0.05$; Fig. 2). Notably, this decreased connectivity was mainly localized to the posterior brain. Indeed, we found that children with infantile hydrocephalus also had significantly decreased FA in posterior white matter compared to healthy controls ($p<0.001$). Interestingly, patients had increased FC and SC between the default mode and dorsal attention network, as well as increased FC between the left visual and left frontoparietal control and right default mode networks and increased SC of the right default mode and somatomotor networks ($p<0.05$; Fig. 2). Lastly, we found that greater whole-brain FC in patients correlated with worse executive function scores ($r=0.93$, $p=0.02$). There was no significant correlation between executive function and SC or FA in patients.

Conclusions: Our findings suggest that ventricle dilation during the first few months of life alters long-term functional and structural network connectivity. Increased FC in school-age children with previous infantile hydrocephalus suggests reduced functional segregation of large-scale brain networks, reflecting a deviation of typical brain development from a network perspective. Future studies will examine the relationship between ventricle volumes prior to shunt placement in infancy and brain network connectivity at school-age.

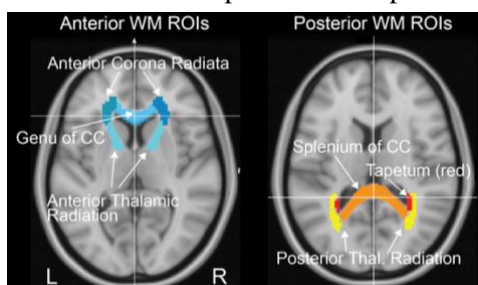


Figure 2. Regions of interest for FA analysis.

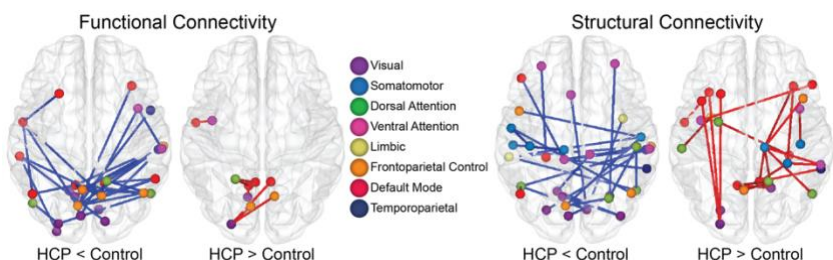
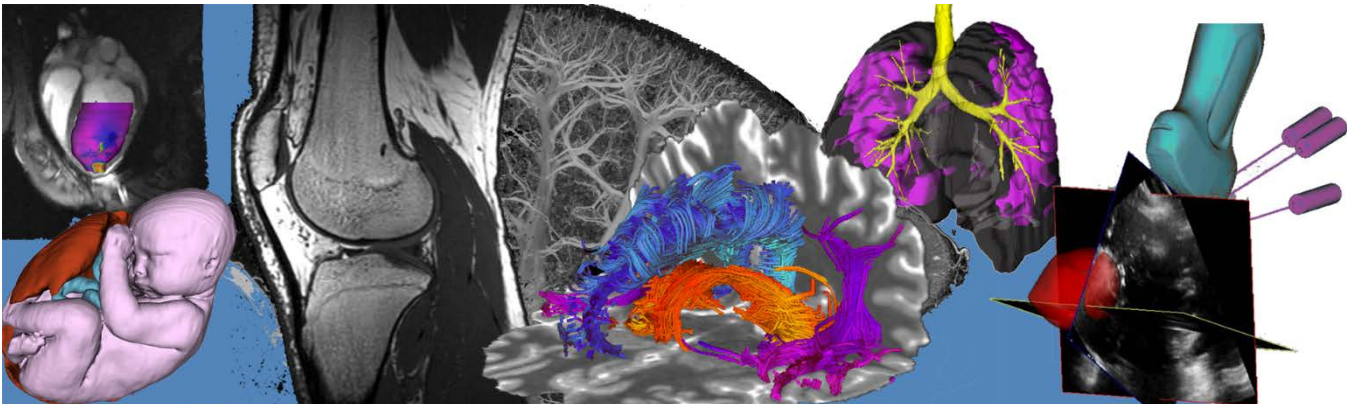


Figure 1. Significant FC and SC changes between HCP and controls.

Pitch Presentation Abstracts

Session 18: Computation Modeling



Validation of a Monte-Carlo Model of a Photon-Counting X-ray Detector for Breast Imaging Applications

James Day¹, Jesse Tanguay¹

¹ Ryerson University

Introduction

For women with dense breasts the sensitivity of standard mammography to cancer can be as low as 38%. The use of sensitive breast MRI machines is restricted due to cost and low availability. Dual energy contrast enhanced digital mammography (DE CEDM) presents an alternative to MRI. DE CEDM is performed with an iodine contrast agent combined with a high energy and a low energy x-ray image taken separately for each view. The low energy image is weighted and subtracted from the high energy image to suppress the fibrous tissue of the breast enhancing the iodine image; however, since these images are taken at different times the method is prone to motion blur. Since photon counting detectors can sort the energy responses from each photon this not only allows both the high and low energy images to be taken simultaneously but also the possibility of iodine specific imaging. Modeling of the imaging performance of photon-counting breast imaging can aid the identification of optimal designs and can enable comparing theoretical performance limits against those of conventional technologies. The goal of this work was to (1) develop a Monte-Carlo model of x-ray interaction-and-detection in cadmium telluride-based photon-counting x-ray detectors (2) and to validate our model by experiment.

Methods

The prototype detector used was an XCounter Thor which has a cadmium telluride layer 750um thick with a 100um pixel pitch. Comparisons were made using the Anti-coincidence mode, which sums up the total signal in a 3x3 square around the site of the first interaction. Simulations were performed in parts: first using Geant4 to account for high energy physics processes; and then a custom code to account for electronic noise and charge sharing. The charge sharing model was depth dependent, using a simplified version of the Hetch relation and diffusion equation to determine the intensity and standard deviation of the charge cloud for both electrons and holes. Comparisons were made using both Am241, 60 keV monoenergetic and an RQA3, 50 kVp poly-energetic, sources. Am241 spectra were matched using the width of the photopeak and the peak to valley ratio to set the values for the detector noise and charge cloud width. While keeping the same values for noise and charge cloud width, the RQA3 spectrum was then generated and compared to measured data. Comparisons were done using an average percent difference weighted to higher intensity regions of the spectra.

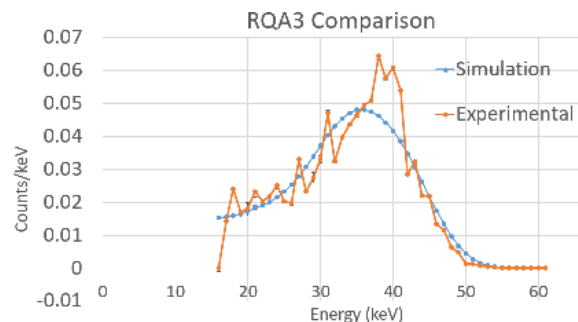
Results

Four measurements of Am241 were analyzed and matched to within a 1% difference by the simulated data. This yielded a charge cloud width of 37 um and a gaussian noise distribution with a standard deviation of 3.49 keV. The Am241 simulated and experimental spectra matched with an average difference of 2%; and an average of six measured RQA3 spectra were compared to the simulated result with an average difference of 9% due to a discrepancy in the peak values (see Figure).

Conclusion

Our Monte-Carlo model can simulate the energy response of photon-counting x-ray imaging detectors for breast imaging applications with reasonable accuracy. Future work will use the model described here to compare optimized photon-counting and conventional approaches for x-ray based breast imaging.

Keywords: Monte-Carlo, Photon counting, Mammography



Highly Focussed Collimators for Increased Resolution of Hand-Held Gamma Probes

Sydney L.M. Wilson¹, Steven Pollmann², Hristo N. Nikolov², Rob Stodilka^{3,6}, David W Holdsworth^{1,4,5}

¹School of Biomedical Engineering, ²Robarts Research Institute, ³Dept. of Medical Imaging, Schulich School of Medicine and Dentistry, ⁴Dept. of Surgery, ⁵Dept. of Medical Biophysics and Medical Imaging, University of Western Ontario, ⁶Dept. of Medical Imaging, Lawson Health Sciences Center, London ON

Introduction: Hand-held gamma probes are routinely used during radioguided surgery of breast cancer for tumour detection and localization of sentinel lymph nodes; however, these probes have a coarse resolution of 13 mm [1]. To increase the resolution of such devices while maintaining high sensitivity, our previous research focussed on the design of a highly focussed gamma collimator (FGC) with large geometric transmission efficiency that could accurately collect gamma photons from a point source 35 mm below the collimator face [2]. The objective of this study is to experimentally characterize the spatial resolution and sensitivity of the FGC and create a numerical model that could predict these trends for FGCs of differing parameters.

Methods: The FGC was manufactured using laser powder-bed fusion; the collimator was 3D printed in both a cobalt-chrome (CoCr) alloy (AM400, Renishaw plc) and tungsten alloy (AM125, Renishaw plc). To determine the spatial resolution of the FGCs, they were fitted to a hand-held Geiger counter (Ludlum 44-2) and placed over a precision xy-stage. A 33.3 kBq Americium-241 (Am-241) source (59.5 keV gamma rays, 35.9% emission probability), with 2 mm diameter, was placed in the center of the stage. The xy-stage was used to move the source and generate point spread functions for both FGCs; counts were collected for 100 s at each point, and then converted to traditional units of counts per minute (CPM).

GEANT4 Application for Tomographic Emission (GATE, OpenGATE Collaboration) was used to model the FGC, housing, lead shielding, scintillation crystal, and 2 mm diameter, 11.95 kBq source. The simulated source activity incorporates the emission probability of the experimental source. To determine the accuracy of the model, the CoCr and tungsten FGCs were simulated over an Am-241 source and CPM were recorded at each position. All photoelectric interactions with the crystal that deposited at least 20 keV were considered valid counts. Finally, the tungsten FGC was simulated over a 140 keV Technetium-99m (Tc-99m) source.

Results: The FGCs were successfully fabricated in CoCr and tungsten using 3D metal printing. Due to variations in the printing parameters, the CoCr and tungsten collimators had wall thicknesses of approximately 113 μm and 200 μm , respectively. The CoCr FGC had a full width at half maximum (FWHM) resolution of 6.57 mm and a sensitivity of 4.0 cps/kBq, whereas the tungsten FGC had a FWHM of 3.94 mm with a sensitivity of 2.9 cps/kBq. The simulated FWHM resolutions of the FGC over the Am-241 source were 4.15 mm and 3.55 mm for the CoCr and tungsten collimator, respectively. The differences in sensitivity in the model were consistent to the experimental data. Using the Tc-99m source in the simulation increased the tungsten collimator's FWHM slightly to 3.67 mm.

Conclusions: The results of this work demonstrate that the GATE model is an effective predictor of the behaviour of the FGC and could be used to optimize the FGC design. The model of the tungsten FGC had a 9.9% error in the FWHM resolution. The CoCr collimator model exhibited larger percent error, but consistently predicted poorer resolution and higher sensitivity of the CoCr collimator, in comparison to tungsten. From the data, it is clear that the higher attenuation properties of tungsten make it a superior material choice for the FGC as it can minimize septal penetration. The resolution of the tungsten collimator was at least three times better than existing gamma probes, even in the presence of Tc-99m; however, the collimator would benefit from an increase in detector area to improve sensitivity (> 5 cps/kBq). Overall, the high resolution of the FGC shows promise for detecting tumour margins to within a few millimeters to enhance the accuracy of margin resection during cancer surgery.

References: 1. E. N. Itikawa *et al.*, "Characterization of Resolution, Sensitivity, and Shielding of a Gamma-Probe for Sentinel Lymph Node Localization: An Experimental Study," *Nucl Med Commun*, 2017. 2. S. Wilson *et al.*, "Parametric Design of Focussed Collimator for Real-Time Intra-Operative Gamma Detection," in *18th Annual Symposium Imaging Network Ontario*, 2020.

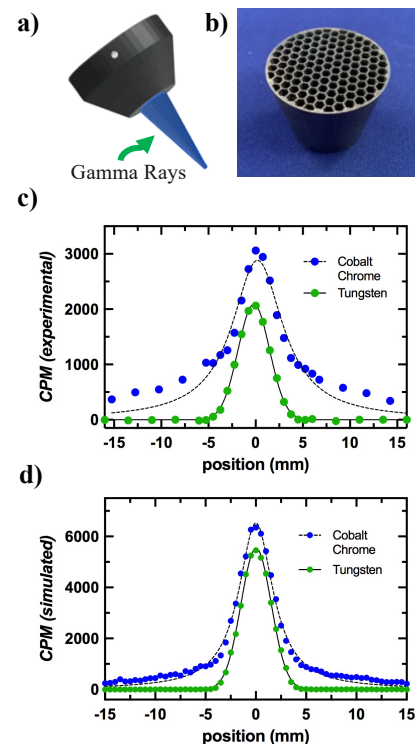


Fig. 1: (a) CAD model of FGC and housing. (b) Tungsten collimator. (c) Experimental point spread function with Am-241. (d) Simulated point spread function with Am-241.

Determination of Lung Hyperelastic Parameters using 4D-CT and a Biomechanical Model

Dayton Miranda¹, Parya Jafari², Sergio Dempsey¹, Abbas Samani^{1,3,4,5}

1. School of Biomedical Engineering, Western University, London, ON
2. Interaptix Augmented Reality
3. Department of Electrical and Computer Engineering, Western University, London, ON
4. Department of Medical Biophysics, Western University, London, ON
5. Imaging Research Laboratories, Robarts Research Institute, London, ON

INTRODUCTION: Lung cancer is the most prevalent cancer and causes the most cancer deaths worldwide. Over 60% of lung cancer patients are diagnosed in later stages when curative treatment is not possible. As such, timely detection and diagnosis of lung cancer is key to improving patient survival. Currently, Low-dose Computed Tomography (LDCT) is the gold-standard for initial lung cancer detection. A caveat with visual assessment of LDCT scans is that numerous benign lesions can present characteristics visually similar to lung cancer. These similarities could lead to misdiagnosis; hence, a biopsy is often needed to verify a diagnosis if ambiguity exists. To eliminate avoidable biopsies, additional imaging techniques have been used to complement LDCT for lung cancer diagnosis. Currently, integrated PET/CT reports the highest tumor sensitivity but is primarily restricted by its high cost due to the requirement of additional image acquisitions. To remove the need for an additional imaging research has pushed to develop techniques that derive additional information from CT data. A contender is lung elastography which uses 4D-CT scans which are more accessible and less costly. Elastography is a technique that provides information regarding the distribution of mechanical properties within a tissue and can be used to assess disease state. As cells become cancerous, the structure of the tissue extracellular matrix is affected and leads to an alteration in tissue mechanical properties. Therefore, a technique capable of detecting lung tissue mechanical properties would assist in the differentiation between lung cancer and benign lesions to reduce the need of avoidable biopsies. 4D-CT is also commonly used for pulmonary radiotherapy treatment planning which allows 4D-CT based lung elastography to be incorporated into the current staging and treatment methods for lung cancer without additional imaging or cost.

OBJECTIVE: To present a non-invasive, low-cost, 4D-CT based lung elastography technique that can be used in conjunction with conventional LDCT, for lung cancer diagnosis.

METHODS: The method relies on a patient-specific inverse finite element (FE) model of the lung solved using an optimization algorithm. The method relies on a pair of 4D-CT images one at end-exhale (EE) and end-inhale (EI). The FE model incorporates hyperelastic material parameters for all tissue and is deformed from (EE) to (EI) via a simulated diaphragm contraction and trans-pulmonary pressure. The tumor hyperelastic parameters and the parameters determining the trans-pulmonary pressure were estimated using a optimization technique where similarity between the experimental and simulated tumor and lung image data is maximized. The proposed technique was evaluated using an in-silico approach where the tumor hyperelastic properties were assigned. Following that evaluation, the methodology was applied to clinical 4D-CT data of two lung cancer patients.

RESULTS: Results from the in-silico study show that the elastography technique recovered known tumor hyperelastic stiffness (C_{tum}) and incompressibility (D_{tum}) parameters with 1.5% error and 4.3% error, respectively. Tumor hyperelastic properties from the clinical data are also reported in figure 1(*Initial Young's modulus and Poisson's ratio which corresponds to obtained C_{10} and D_{10}).

DISCUSSION/CONCLUSION: Results from this proof of concept study demonstrate the ability to recover in-vivo lung tissue hyperelastic parameters using 4D-CT data alone. Tumor stiffness parameters are similar to what's reported in the literature for pulmonary carcinoma. Improvements in this technique could lead to more accurate diagnosis and timely treatment of lung cancer.

Table 1: Tumor hyperelastic parameters from lung cancer patients, recovered using the proposed		
	Cases	
	Case 1	Case 2
C_{tum}	0.190 (1.04 kPa) *	0.147 (1.10 kPa) *
D_{tum}	1383 (0.37) *	1546 (0.39) *

Fatigue Analysis of Wireless Load Cells for Biomedical Applications

William D Anderson¹, Todor Ivanov², David W Holdsworth^{1,2,3,4}

¹School of Biomedical Engineering, ²Robarts Research Institute, ³Department of Medical Biophysics,

⁴Department of Surgery, Schulich School of Medicine and Dentistry, Western University, London, Canada

Introduction: Load data is a valuable outcome measure in many clinical and research studies, as well as in commercial weighing applications. Previously described advancements in automotive pressure sensor technology have enabled an alternative method of monitoring real-time load and strain data [1]. To be effective, the sensor package must be embedded within a deformable enclosure, which is designed to transduce compression and have a long fatigue life. Accurate prediction of fatigue failure of 3D printed structures can aid in improving the design of future components. The objective of this study is to determine if finite element analysis (FEA) and fatigue modelling are capable of predicting the experimental fatigue failure location of 3D printed load cells.

Methods: A deformable compression enclosure was created by generating a two-component rectangular structure with four internal cantilever beams. When under compression, load is evenly distributed to the unfixed end of each beam using a flat surfaced lid component. The two-component enclosure was imported into ABAQUS to determine the theoretical load capacity and the regions of high stresses for the enclosure when modelled in titanium alloy (Ti-6Al-4V) (Fig. 1a). Determining the load capacity of the load cell helps guide the test procedure for fatigue modelling. The structure was imported into the fatigue modelling software, Fe-Safe, to determine the number of compression cycles until specimen failure (Fig. 1b) and the location of fracture in the structure. Load cells were 3D printed using laser powder-bed fusion at ADEISS in Ti-6Al-4V and subjected to a cyclic compression fatigue test using an Instron (ElectroPuls E10000). Fatigue tests were performed at 10 Hz with a stress ratio of $R = 0.1$ until specimen failure or runout at 10^6 cycles. Using the results from the three described tests, an analysis was performed to determine if the experimental failure location of the 3D printed Ti-6Al-4V structures matches the location of highest stress, predicted by ABAQUS, and the failure location, as predicted by Fe-Safe. In addition, the difference between theoretical and experimental fatigue life can be observed.

Results: Theoretical fatigue analysis of the load cell was a good indicator of experimental fatigue performance as the 3D printed specimens failed less than 50k cycles before predicted failure. It was expected that the experimental specimens would fail before the theoretical specimens due to the reduced mechanical fatigue properties of 3D printed Ti-6Al-4V. The location of failure on the 3D printed specimens was at the fixed end of the shorter cantilever beams in the load cell. Similarly, the region of highest stress, as predicted by ABAQUS, and the location of failure, as predicted by Fe-Safe were both in the same location at the fixed end of the shorter cantilever beam.

Conclusion: The results of this study show that finite element analysis and fatigue modelling can be used to accurately predict the failure location of custom, 3D-printed, load cell enclosures. Prediction modelling can help improve the design of future iterations of the load cells, as modifications can be made to attempt to increase the fatigue life of the structure. Improving fatigue life greatly increases the number of applications in which the load cell can be feasible for use. In combination with our load sensor, a retasked tire pressure sensor [1], we have developed a range of wireless telemetric load cells with customizable load capacity and fatigue life. The load cells described in this study could be used to measure orthopaedic loads within joint replacements, vertebral replacements, and spinal fusion cages.

References: [1] Anderson, W.D.; Wilson, S.L.M.; Holdsworth, D.W. Development of a Wireless Telemetry Sensor Device to Measure Load and Deformation in Orthopaedic Applications. *Sensors* **2020**, *20*, 6772.

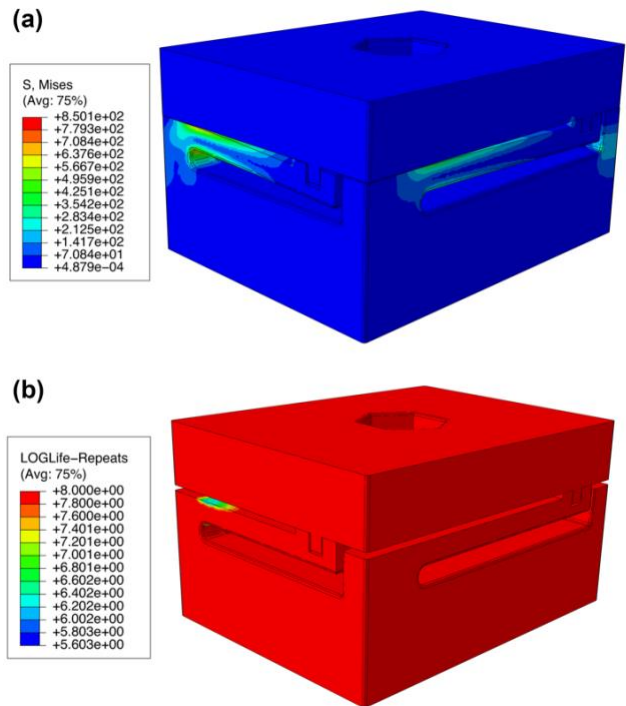


Fig. 1: (a) ABAQUS finite element compression analysis of two-component load cell spring body. (b) Results of fatigue modelling in Fe-Safe, indicating failure location.

Ongoing Development of a Numerical Bloch Solver for Low-Field Pulse Sequence Modeling

John Adams^{1,2}, William Handler^{1,2}, Blaine Chronik^{1,2}

¹ *Department of Physics and Astronomy, Western University, London, ON;* ² *xMR Labs, London, ON*

Introduction: Research interest in low-field (<1 Tesla) magnetic resonance imaging (MRI) has grown in recent years as a way to reduce the cost of MRI scans, and to make MR more accessible, by reducing or removing siting requirements for the magnet [1], [2]. However, as we change field strength we change how a sample's physical characteristics translate into MR image contrast through changing relaxation times [3], [4]. Furthermore, at low-field, changes in applied field due to the activation of modern high strength gradients can change relaxation times over the course of an MR sequence. This changes the contrast provided by existing techniques, and opens opportunities for novel, low-field specific contrasts.

To account for these effects while developing new MR hardware, we are developing a flexible MR pulse sequence modeling tool capable of modeling the results of an MR experiment. In contrast with many existing solvers, this tool is designed to simulate the system under the influence of arbitrary magnetic fields in order to allow novel hardware configurations and non-idealities to be included in the simulation. This presentation will discuss our development efforts to date, and our ongoing validation work for this tool.

Methods: Development of this simulation tool is being done in Python 3. A system of python classes are used to specify the magnetic fields being applied to a sample as time-dependent functions. Once defined, these field functions are used to solve the Bloch equations in the rotating reference frame for each voxel using SciPy's `solve_ivp()` function, itself using a Runge-Kutta 853 numerical integration method [5]. T_2^* relaxation is simulated by simulating each voxel in the sample multiple times with a small, randomly generated field offset calculated based on a tissue specific T_2^* value. With this structure, an end user can write a script calling different pulse sequence elements, which will output a simulated signal that can then be processed using existing signal analysis techniques to produce whatever images or other end data the user requires.

To validate the tool at this basic level, the tool was used to recreate a number of basic pulse sequences including a free-induction decay, a CPMG train, and a stimulated echo [3]. These sequences were then applied to a virtual sample with homogenous, user defined properties ($T_1 = 2$ s, $T_2 = 200$ ms, $T_2^* = 30$ ms). The resultant output was compared to the initial model used by the simulation for validation.

Results: A free induction decay was simulated to confirm that T_2^* was being appropriately modeled. After fitting the resultant curve we found a measured T_2^* value of 34 ± 1 ms. A CPMG sequence was simulated to confirm both that signal would be appropriately refocused into echoes with an appropriate RF pulse, and to validate T_2 relaxation timing. The following timing parameters were used; echo time (TE) = 0.1s, number of echoes = 6. The peaks of each echo were used to compute the T_2 relaxation time of the resultant signal which gave a result of 188 ± 5 ms. The simulated echo sequence was implemented with the parameters; TE1 = 50 ms, TE2 = 200 ms. With this, we expected and observed 4 echoes of varying amplitude; the primary stimulated echo at 50 ms after beginning signal acquisition, plus much smaller echoes at 150, 200, and 250 ms.

Conclusions: Our simulation tool in its current form is able to replicate the fundamental aspects of an MR pulse sequence. Future work will focus on applying this to imaging experiments, as well as adding features such as a field dependent relaxation times.

References:

- [1] A. Panther *et al.*, "A Dedicated Head-Only MRI Scanner for Point-of-Care Imaging," *Proc. Annu. Meet. Int. Soc. Magn. Reson. Med.*, 2019.
- [2] C. N. Wiens, C. T. Harris, A. T. Curtis, P. J. Beatty, and J. A. Stainsby, "Feasibility of Diffusion Tensor Imaging at 0.5T," *Proc. Annu. Meet. Int. Soc. Magn. Reson. Med.*, 2019.
- [3] D. G. Nishimura, *Principles of Magnetic Resonance Imaging*. Stanford: Stanford University, 2010.
- [4] R. A. DeGraaf, *in vivo NMR Spectroscopy*, 2nd ed. John Wiley & Sons, Ltd, 2007.
- [5] E. Hairer, S. P. Norsett, and G. Wanner, "Solving Ordinary Differential Equations I: Nonstiff Problems." 1993.

Monte Carlo Simulation for Magnetic Resonance Diffusion

Tristhal Parasram, Dan Xiao

Physics Department, University of Windsor, ON, Canada

Introduction: Quantitative analysis of molecular diffusion provides insights into the microscopic structure within an MRI image voxel. It has significance in the analysis of cell structures such as in the brain. For complex microscopic environment, it is difficult to analytically derive the diffusion signals. In this work, an open source Monte Carlo diffusion simulation has been developed that is fast and easy to use. It can be applied to any magnetic resonance pulse sequence with user defined microscopic environments and magnetic field distributions. The accuracy has been verified through the simulation of water restricted in an impermeable pore. The results agreed with the theoretical prediction for different pore sizes and diffusion times. The microscopic pore size could be determined using the simulated MR signals.

Methods: Python and NumPy were employed to develop the fully multithreaded diffusion simulation with Numba to provide C-like performance in Python. Python was chosen for its accessibility and flexibility. The algorithm is easy to modify, allowing custom pulse sequences, arbitrary magnetic field distributions and different microscopic environments. The motion and net displacement of the particles can be visualized during the simulation. The particles are propagated in time steps, undergoing Brownian motion in the user specified environment. The user specified pulse sequence is simulated with Bloch equations as the particles diffuse. The pulse sequence can include arbitrary waveforms of RF pulses, magnetic field gradient pulses, and inhomogeneous magnetic fields.

Results and Discussion: The simulation was applied to investigate the restricted diffusion of water in a 2D square pore. A pulsed gradient spin echo (PGSE) sequence with 8 different gradient amplitudes were simulated on water molecules trapped in the pore for 24 different diffusion times. The total simulation time was 9 minutes with 5000 particles, on an 8/16 core/thread system.

When the diffusion time was short relative to pore size, it is expected that the measured diffusion coefficient is a function of diffusion time and the surface-to-volume ratio [1]. With long diffusion times, the apparent diffusion coefficient approaches a constant value.

For a 200 μm pore, short diffusion times extended to 1s. The diffusion coefficients agreed with the theoretical values, as shown in Fig. 1. For a 40 μm pore, the short diffusion time regime ended at approximately 100 ms. The diffusion coefficient saturated to an asymptotic value at 1.2 s, which can be considered a long diffusion time for the small pore.

The dimensions of the microscopic pores can be determined based on these measurements.

Conclusion: We have developed a fast, easy to use algorithm for rapid diffusion simulation in different microscopic environments with inhomogeneous magnetic fields. The effectiveness of the simulation was demonstrated with a PGSE restricted diffusion measurement. Phantom experiments will be performed in the future. This tool could enable the development of new magnetic resonance diffusion pulse sequences and microstructural analysis.

Reference: [1] Mitra, PRB 47, 8565, 1993.

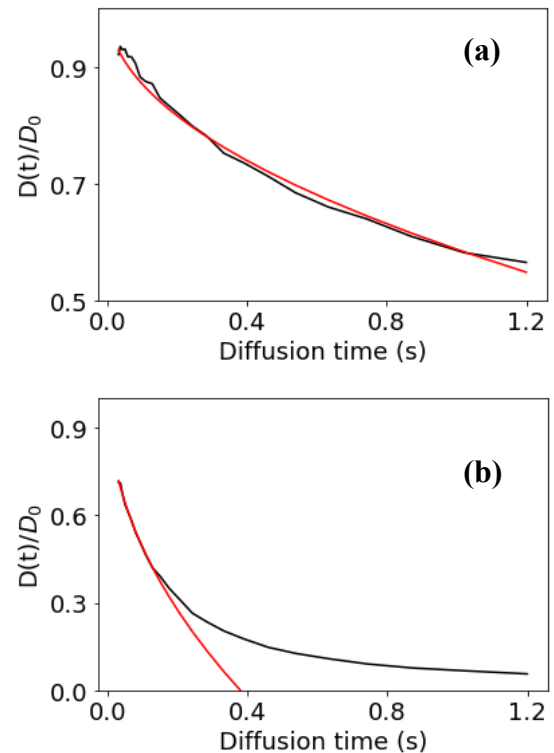


Figure 1. Normalized diffusion coefficients, in black, acquired with a PGSE sequence simulation as a function of diffusion time, for the pore size of (a) 200 μm and (b) 40 μm . The theoretical predictions for short diffusion times are shown in red.

Exponential Analysis for 2D Magnetic Resonance Relaxation Spectrum Using Neural Networks

Tristhal Parasram, Dan Xiao

Physics Department, University of Windsor, ON, Canada

Introduction: Quantitative analysis of magnetic resonance T_1 and T_2 relaxation times can reveal information on microscopic structure and composition, beyond the standard MRI image resolution. It is a powerful tool in the study of biological tissues such as brain and articular cartilage. A multicomponent model with continuous $T_1 - T_2$ spectra requires exponential analysis which is an inherently ill-posed problem. The traditional 2D inverse Laplace transform employs a nonnegative constraint and user defined regularization parameter for spectrum smoothness and requires phase correction [1]. Extending our previous work of using neural networks (NNs) for continuous T_2 spectrum analysis [2], neural networks have been developed to generate $T_1 - T_2$ correlation spectra.

Methods: Keras and NumPy were employed to create the networks, with a 2D array of decay signal values as input and $T_1 - T_2$ correlation spectrum as output. The network was trained on 64 000 simulated inversion prepared CPMG experiments. 128 equally spaced (echo spacing ES) CPMG signals were acquired (τ_2), with 32 inversion times (τ_1) logarithmically spaced from 0.1 ES to 128 ES. The signal equation is

$$s(\tau_1, \tau_2) = \int \int a(T_1, T_2) (1 - 2e^{-\frac{\tau_1}{T_1}}) e^{-\frac{\tau_2}{T_2}} dT_1 dT_2 + \epsilon,$$

where $a(T_1, T_2)$ is the spectrum to be solved, and ϵ is the Rician noise. The signal magnitude was considered to eliminate the phase correction step as negative signals were expected with the T_1 inversion. The loss function compared the mean squared error of the $T_1 - T_2$ correlation spectra with a factor to punish negative output spectrum values. The network consists of a fully connected feed-forward neural network sandwiched between convolutional layers. Three gaussian functions with random widths, positions and relative amplitudes on the logarithmic scale were combined to form the training spectra with one to three peaks. An example of the input signal is shown in Fig. 1a.

Results and Discussion: The peak positions and areas in the $T_1 - T_2$ correlation spectra were evaluated. Fig. 2 shows an example, corresponding to the signal in Fig. 1. The true $T_1 - T_2$ correlation spectrum had two peaks of equal magnitude, as in Fig. 1b. Without noise, the NN produced an accurate spectrum with -1% and 1% error in the area percentages for the top and bottom peak respectively, as shown in (a). In (b), the ILT result had area errors of -11% and -2%, with a spurious peak. The ILT peak shape deviated significantly from the true spectrum. The phase correction in ILT, based on the sign of the first data point in CPMG for the entire echo train, led to the large error. With a signal-to-noise ratio (SNR) of 200, the area errors were -1% and 1% for NN, and -10% and -8% for ILT, as shown in (c) and (d). The regularization parameter in ILT can be increased for broader spectrum peaks, but the area ratios remain unchanged. No manual parameter was required in the NN data processing.

Conclusion: We demonstrated the effectiveness of NNs for analyzing $T_1 - T_2$ correlation spectra with noise. The technique can be easily extended to other multi-dimensional correlation analysis such as $T_2 - \text{Diffusion}$ and $T_1 - T_2 - \text{Diffusion}$ correlation measurements.

Reference: [1] Song, JMR 154, 261, 2002 [2] Parasram, JMR Revised

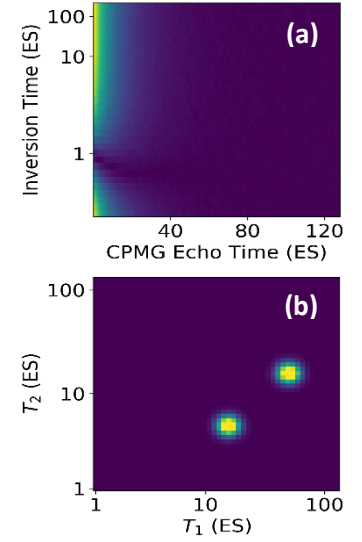


Figure 1. (a) The simulated inversion-CPMG signal with 200 SNR, which is typical for a bulk measurement. (b) is the corresponding true $T_1 - T_2$ correlation spectrum.

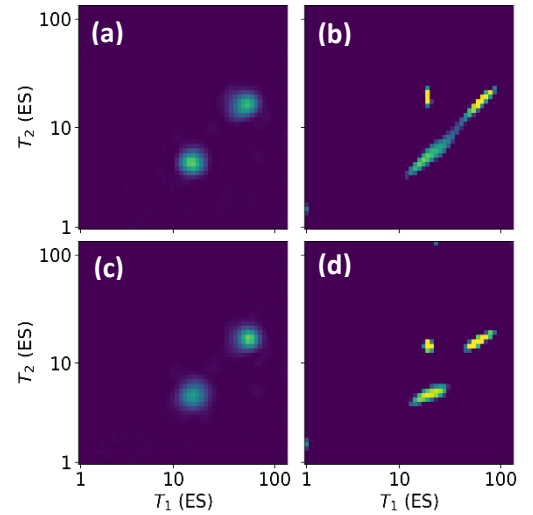


Figure 2. The $T_1 - T_2$ spectra, with two peaks at (T_1 64ES, T_2 20ES) and (T_1 16ES, T_2 5ES), produced by NN (1st column) and ILT (2nd column, regularization 0.01). There was no noise in (a) and (b) signals. (c) and (d) had 200 SNR. The true spectrum is shown in Fig. 1b.

Correlating Macro and Microstructure in the Hippocampus

Bradley Karat¹, Jordan DeKraker¹, Uzair Hussain², Ali Khan^{1,2}

¹Department of Neuroscience, Schulich School of Medicine and Dentistry, Western University, London, Ontario, Canada, ²Centre for Functional and Metabolic Mapping, Robarts Research Institute, Western University, London, Canada

Introduction- The hippocampus is vulnerable to certain neurological diseases, in which it is often one of the earliest aberrant structures¹. Microstructural characterization of intra-hippocampal pathways and neurites within these subfields has the potential to provide increasingly specific markers of hippocampal integrity. The hippocampus possesses an intrinsic coordinate system with defined axes along the anterior-posterior (AP), proximal-distal (PD), and inner-outer (IO) directions. Importantly, hippocampal microstructure is aligned with these macrostructural axes. Recent studies have proposed an approach to computationally unfold the hippocampus to define these macrostructural axes². The objective of this study is to investigate how the morphology of the hippocampus, namely the macrostructural gradients formed along the canonical axes, are related to local

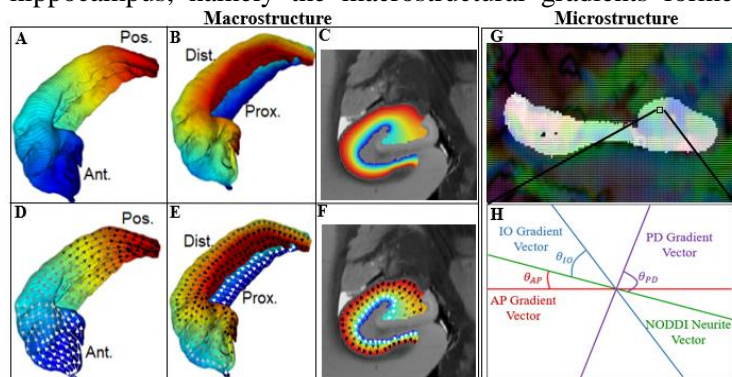


Figure 1. Hippocampal macrostructure and microstructure. (A-C) Laplacian potential fields in anterior-posterior, proximal-distal and inner-outer dimensions. (D-F) Gradient vectors from first derivation of potential field in (A-C). (G) NODDI neurite vectors on a hippocampal mask. (H) Square in (G) - zoom of a single voxel NODDI neurite vector. Red, purple, and blue lines depict gradient vectors at that voxel for anterior-posterior, proximal-distal, and inner-outer, respectively.

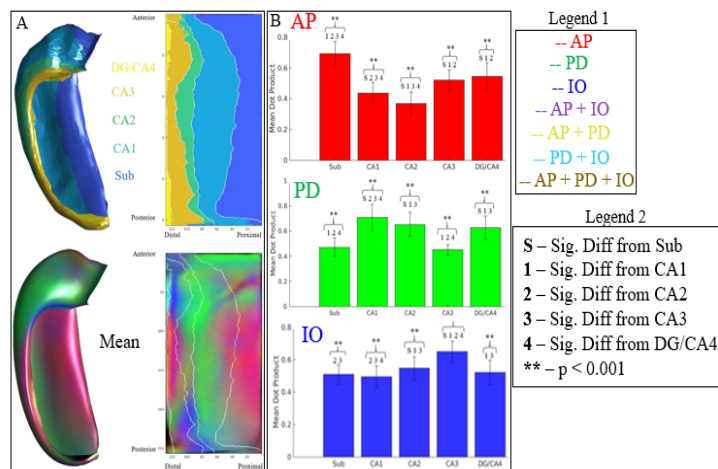


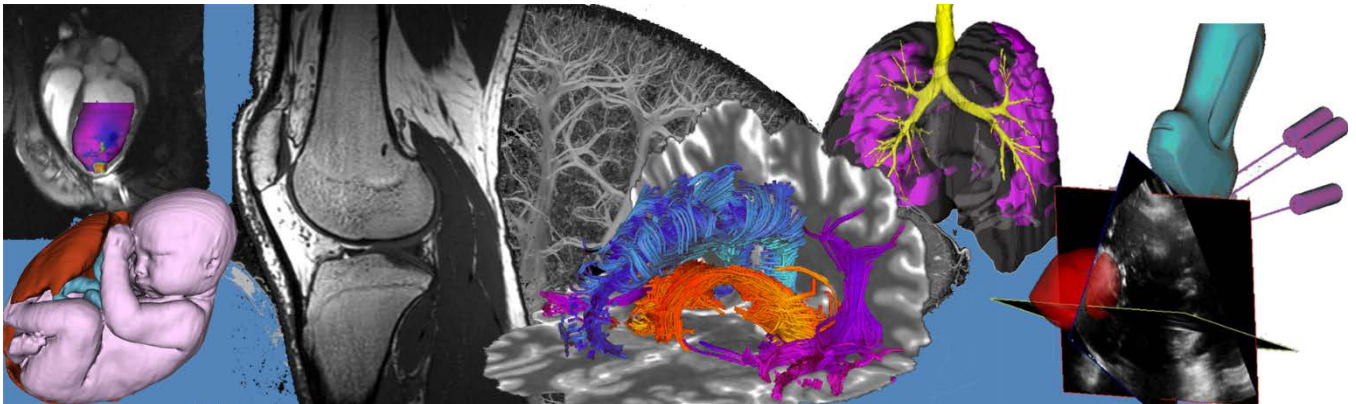
Figure 2. Mean dot product across gradient direction. (A) Top figure depicts subfield borders coloured by legend in the middle. Bottom depicts mean dot product by gradient direction across all hippocampi (N = 192) coloured according to legend 1. Colour mixing occurs when dot product values are similar in magnitude between gradient directions (addition in legend 1). Intensity of colour scales with increased dot product values. (B) Mean dot product within each gradient direction across each subfield. Error bars represent one standard deviation. One-way ANOVA and Tukey's post-hoc test revealed significant differences of mean dot product between subfields within gradient direction. Legend 2 depicts significant correlations.

Methods- The Human Connectome Project (HCP) 1200 dataset³ was used. Specifically, the Unrelated 100 subset was chosen. Unfolding of hippocampi was performed to generate the Laplacian potential field in the AP, PD, and IO directions² (fig. 1A-C). The first derivative of the potential field resulted in the gradient or local vector field along each dimension (fig. 1D-F). Neurite Orientation Dispersion and Density Imaging (NODDI)⁴ was applied on diffusion data. Specifically, the NODDI neurite vectors (“sticks”) (fig. 1G) were used. Fig. 1H shows the macrostructural vectors (AP, PD, and IO) and the NODDI neurite vector in a single voxel. The angle between each macro and NODDI vector was used to calculate dot products. **Results-** Fig. 2A presents these dot products averaged across all hippocampi (N = 192) plotted on an average hippocampal surface and in unfolded space². One-way ANOVA and post-hoc Tukey tests indicated significant differences within each gradient direction of mean dot product across the subfields (fig. 2B). **Conclusion-** Here we show that the macrostructural gradients appear to be systematically correlated to local microstructure measured using NODDI. This method may allow for the development of anatomical microstructure priors and potentially increase the accessibility of hippocampal integrity measures through pathway-specific markers. Future studies will examine these gradients in high-resolution ex-vivo data where fibre bundles will be more apparent.

References- 1. Moodley K, and Chan D. The Hippocampus in Neurodegenerative Disease. *Front Neurol Neurosci.* 2014;34:95-108. 2. DeKraker J, Ferko K, Lau J, Köhler S, and Khan A. Unfolding the hippocampus: An intrinsic coordinate system for subfield segmentations and quantitative mapping. *NeuroImage.* 2018;167:408-418. 3. Van Essen D, Smith S, Barch D, Behrens T, Yacoub E, and Ugurbil K. The WU-Minn Human Connectome Project: An overview. *NeuroImage.* 2013;80:62-79. 4. Zhang H, Schneider T, Wheeler-Kingshott C, and Alexander D. NODDI: Practical in vivo neurite orientation dispersion and density imaging of the human brain. *NeuroImage.* 2012;61:1000-1016.

Oral Presentation Abstract

Session 19: COVID-19 & Brain Related Injuries



Automated Registration of 3D Ultrasound Images of Preterm Neonates to Identify Intraventricular Hemorrhaging: Preliminary Findings using SPM-12

Belanger, Nicholas¹, Szentimrey, Zachary¹, De Ribaupierre, Sandrine², Fenster, Aaron², Ukwatta, Eranga^{1,3}

¹*School of Engineering, University of Guelph, Guelph, ON, Canada;* ²*Robart Research Institute, The University of Western Ontario, London, ON, Canada;* ³*Department of Systems & Computer Engineering, Carleton University, Ottawa, ON, Canada*

Introduction: Neonates weighing less than 1500 grams at birth have a 20 to 25% chance of developing intraventricular hemorrhaging (IVH) over the following months. Of those that develop a severe case of IVH have a 33 to 50% chance of developing post haemorrhagic ventricular dilation (PHVD). The infants who develop PHVD are at a high risk for needing invasive surgery to install a shunt in the brain or developing other neurological problems including cerebral palsy, epilepsy, cognitive impairment and behavioural problems. These severe consequences later in life for infants with PHVD make early diagnosis and treatment imperative. Currently, 2D ultrasound (US) is used to track the progression of PHVD by imaging the brain ventricles, but recent studies have shown that 3D US is more sensitive to changes in brain ventricles (Neonatal Neurology Foundation, 2016). A registration method to align the ventricles between longitudinal time points in 3D US scans will enable us to realize regions of localized changes to the volume attributing to both normal brain growth and abnormal swelling caused by IVH. The goal of this study is to develop and evaluate a fully automated algorithm for registration of brain ventricles in 3D US. This will be achieved by comparing the registration results of an image-based, surface-based and hybrid approach and determining the best model possible, however this study will focus on the image-based approach.

Methods: Time series 3D US images were acquired for 62 patients, of these patients, 10 patients with consistent data were chosen that had 6-12 times points for each patient. We aligned the images by an affine registration of the time-series 3D US images using the SPM-12 software (The Wellcome Centre for Human Neuroimaging, 2020). Two-pass registration was performed where initially all grouped images were first registered to the first image in the group and an averaged image was created from the registered images. In the second pass of affine registration, each time-point was registered to the averaged image. Since these are time series images comparison of registered results is performed by pairing consecutive images in time and calculating the target registration error (TRE) between the moving and fixed image at each landmark. For each 3D US image, 12 anatomical landmarks on the ventricle were manually chosen for algorithm evaluation. These landmarks include the three horns of the two ventricles, the midpoint of the thalamus, the foramen of Monro and the anterior and posterior limit of the septum. Fiducial localization error (FLE) was also determined by placing fiducial markers on five images, five separate times and confirming that landmarked points were consistent across all time points.

Results: Placing fiducial markers on five images, five separate times led to a FLE of 6.35 ± 4.92 mm. The baseline TRE of the 12 landmarks of the unregistered images was 102.96 ± 34.98 mm with the TRE of images registered using SPM-12 being 86.34 ± 33.40 mm. The average difference between registered and unregistered TREs was 16.64 ± 2.38 mm. These results show that while registration error improved using the SPM-12 method further refinements or other methods will need to be applied to this dataset.

Conclusion: Our preliminary findings suggest that an affine voxel property-based registration of 3D ultrasound images shows promise for aligning images to compare changes within the ventricles of neonates. Consistent landmarking of points found within each image showed that this landmarking method can be used for confirming results of various registration methods, however other methods should be explored to further quantify registration results.

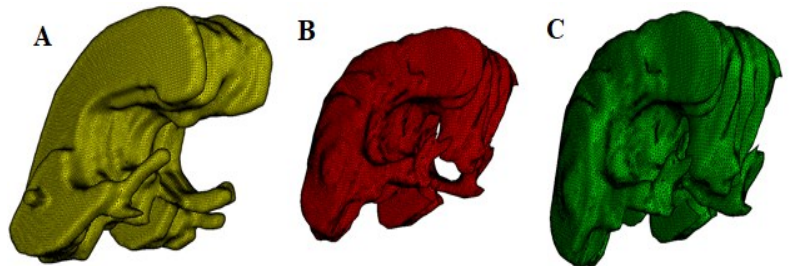


Fig. 1. Registration results with the target (a) and source (b) affine registration in SPM-12 to transform source (c)

The Severity of Spinal Cord Compression is Associated with Functional Plasticity in Degenerative Cervical Myelopathy

Alicia Cronin^{*1,2} Sarah Detombe³, Camille Duggal², Neil Duggal³ and Robert Bartha^{1,2}

¹Department of Medical Biophysics; ²Centre for Functional and Metabolic Mapping, Robarts Research Institute, The University of Western Ontario; and ³Department of Clinical Neurological Sciences, University Hospital, London Health Sciences Centre

Introduction: Degenerative cervical myelopathy (DCM) is one of the most common forms of spinal cord dysfunction, with the incidence and prevalence in North America estimated to be 41 and 605 per million, respectively.¹ It is a unique model of spinal cord injury that can result in compression of the spinal cord and lead to neurological dysfunction.² Surgical intervention can effectively prevent the progression of neurological decline and improve functional outcome, however, some patients continue to deteriorate and predicting surgical outcome has proven difficult. Predicting a patient's potential for functional recovery following surgical intervention remains elusive in part because the pathophysiological mechanisms of the disease are only partially understood. To improve the prognostic determinates of DCM, we must better understand the relationship between localized compression in the cord, neuronal damage, and cortical reorganization. We hypothesized that cortical reorganization would be greater in patients with more severe compression, indicating neurological injury in the spinal cord.

Methods: A 3.0 T Siemens Prisma Fit MRI scanner was used to acquire functional images of the brain in 23 DCM patients (14 men, mean age (\pm SD) 65 ± 14.5 years). Patients were instructed to perform a structured finger-tapping task to activate the motor cortex to assess the extent of cortical activation. Volume of activation (VOA) and % blood oxygen level-dependent (BOLD) signal were determined using region-of-interest analysis. T₂-weighted images of the spine were also acquired to quantify the severity of spinal cord compression. Total compression volume was found by using semi-automatic segmentation software³ and in-house MATLAB code, with segmentation shown in Figure 1A. To measure the reliability of the compression measurement, two raters performed repeated measurements of cord compression and the intraclass correlation (ICC) was used to determine intra- and inter-rater reliability.

Results: Measurements of the spinal cord volume were highly reproducible, with the reliability between the two raters characterized with an ICC of 0.977. The observed BOLD signal increase in the contralateral primary motor cortex was associated with spinal cord compression severity when patients tapped with their left hand ($r = 0.49$, $p = 0.02$) and right hand ($r = 0.56$, $p = 0.005$), as shown in Figure 1B. The VOA in the contralateral primary motor cortex also increased with compression severity when patients tapped with their left hand ($r = 0.55$, $p = 0.006$) and right hand ($r = 0.45$, $p = 0.03$).

Conclusion: DCM patients with severe spinal cord compression recruit larger regions of the motor cortex to perform finger-tapping tasks. This significant correlation is consistent with the presence of ischemia and hypoxia in the spine and it is reasonable to hypothesize that the observed cortical reorganization is a compensatory mechanism to neurological injury in the spinal cord. Future studies measuring hypoxia and/or ischemia at the site of compression may provide more insight into the mechanisms of the neurological injury and help us further understand the prognostic determinates of DCM patients.

References: [1] Nouri, A. *et al.* Spine 2015; [2] Toledano, M. & Bartleson, J. Neurol. Clin. 2013; [3] De Leener, B. *et al.* NeuroImage 2017.

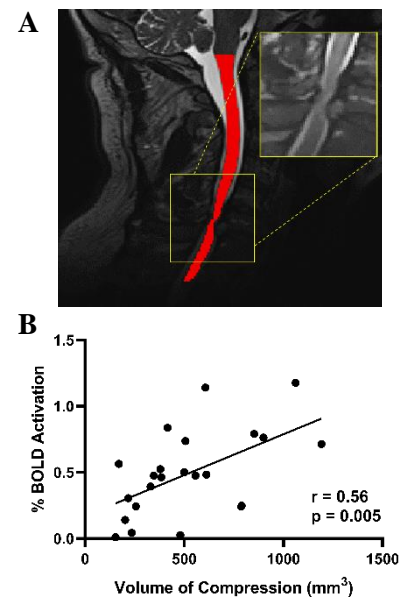


Figure 1:

A: Segmented cord shown in red with compression site displayed on inset.

B: % BOLD signal correlation when tapping with right hand.

Correlating Concussion Symptoms and Brain Injury in Paediatric Concussion

Ethan Danielli,^{1,2} David Stillo,^{1,2} Rachelle A Ho,^{3,7} Carol DeMatteo,^{3,8} Geoffrey B Hall,⁷ Nicholas A Bock,⁷ John F Connolly,^{2,4,7,8} Michael D Noseworthy^{1,2,5,6,8}

1. Imaging Research Centre, St. Joseph's Healthcare, Hamilton, ON, Canada; McMaster University, Hamilton, ON, Canada; 2. School of Biomedical Engineering, 3. School of Rehabilitation Sciences, 4. Department of Linguistics, 5. Department of Electrical and Computer Engineering, 6. Department of Radiology, 7. Department of Psychology, Neuroscience & Behaviour, 8. ARIEAL Research Centre

Introduction: A quantitative diagnostic tool is required to effectively understand concussion-related symptoms, brain damage and recovery. Diffusion tensor imaging (DTI) can accurately characterize changes in white matter (WM) integrity following a concussion by measuring voxel-wise water diffusion metrics such as Fractional anisotropy (FA), axial diffusivity (AD) and radial diffusivity (RD).¹ After sustaining a concussion, children are more likely to suffer from worsened symptoms and a longer recovery than adults.² However, the comparison of clinical demographic information against MRI data has often been overlooked in concussion-based MRI research. The purpose of this research was to determine if DTI metrics were correlated with clinical demographic information in paediatric concussion subjects. It was hypothesized that greater WM injury, measured by total injury burden, would correlate with worsened symptoms in younger subjects.

Methods: Paediatric concussion subjects (n=26, 9 male/17 female, mean age 14.22 ± 2.64) were recruited from the Emergency Department of the McMaster Children's Hospital following a recent concussion. Healthy age and sex matched control data (n=49) was downloaded from the *NIH MRI Study of Normal Brain Development*.³ For concussion subjects, demographic information was collected such as age at the time of injury, time between injury and MRI scan, and Post-Concussion Symptom Scale (PCSS)⁴ score. Concussion subjects were scanned using a 3T GE Discovery MR750 MRI system and a 32-channel head and neck coil (General Electric Healthcare, Milwaukee, WI). Patient-specific brain injuries were identified and quantified against the normative values of the entire healthy dataset using a statistical Z-scoring approach. Processing of all MRI data was performed using FSL,⁵ where subject-specific Z-scoring was determined using MATLAB (v. R2020b). The correlation of total injury burden with concussion symptoms and subject demographics was completed using multiple linear regression implemented in R (v.3.6.1) and RStudio (v.1.2.1335).

Results: Demographic features were significantly correlated with total injury burden, defined as the total number of brain ROIs with outlier Z-scores per DTI metric per subject, of FA (Adjusted R-squared: 0.5725, $p < 0.001$) and RD (Adjusted R-squared: 0.3295, $p = 0.013$) (**Table**). Significantly reduced FA was positively associated with age at injury ($p < 0.001$) and increased symptom severity indicated by PCSS score ($p = 0.038$). Further, significantly increased RD was correlated with age at injury ($p = 0.029$) and the interaction between time to scan and PCSS score ($p = 0.0078$). There were no significant correlations between AD and demographic data.

DTI Metric	Coefficient	Estimate	Std. Error	t value	Pr (> t)
FA	Intercept	27.474	3.985	6.894	8.20e-7 ***
	Age	-1.362	0.239	-5.691	1.20e-5 ***
	TTS	-0.0281	0.0271	-1.038	0.311
	PCSS	-0.0809	0.0365	-2.214	0.038 *
	TTS:PCSS	0.000876	0.000510	1.718	0.101
RD	Intercept	32.923	2.419	13.609	6.91e-12 ***
	Age	-0.341	0.145	-2.344	0.0290 *
	TTS	-0.0306	0.0164	-1.859	0.0771
	PCSS	-0.0446	0.0222	-2.011	0.0573
	TTS:PCSS	0.000911	0.000310	2.941	0.0078 **

Conclusions: Performing a personalized concussion assessment using DTI metrics successfully quantified total injury burden based on abnormalities of specific brain ROIs. The results supported the hypothesis that a loss of WM integrity would correlate with injury related demographic information. The results also confirmed that PCSS and DTI are effective diagnostic tools for paediatric concussion. The correlation statistics indicated that age influenced injury severity, as seen by increased injury burden in younger subjects, and that worsened concussion symptoms aligned with a greater injury burden. We hypothesized that these results occurred because paediatric brains are still undergoing development. Further research is required, but it is suggested that age must be considered for the diagnosis and treatment of concussions.

References: [1] Asken BM, et al., *Brain Imaging and Behav* 2018;12(2):585–612. [2] Zuckerman S, et al., *Surg Neurol Int* 2012;3(1):130. [3] Rivkin M, et al., <http://paediatricmri.nih.gov>. Accessed May 5, 2016. [4] Lovell MR, et al., *Appl Neuropsychol* 2006;13(3):166–174. [5] Jenkinson M, et al., *Neuroimage* 2012;62:782–790.

NEUROCOVID19: Impact of the Virus on the Brain

S. J. GRAHAM¹, J. J. CHEN⁵, A. GILBOA⁵, B. J. MACINTOSH², A. B. SEKULER⁵, S. E. BLACK², J. A. CHAD⁵, I. CHENG³, R. FOWLER⁴, F. GAO², M. GOUBRAN², C. HEYN², A. JEGATHEESAN¹, X. JI², B. LAM², M. MASELLIS², J. S. RABIN², E. ROUDAIA⁵

¹Physical Sciences Platform, ²Hurvitz Brain Sciences Program, ³Evaluative Clinical Sciences, Integrated Community Program, ⁴Evaluative Clinical Sciences, Trauma, Emergency & Critical Care, Sunnybrook Research Institute, Toronto, Ontario, Canada; ⁵Rotman Research Institute, Baycrest Centre, Toronto, Ontario, Canada

Introduction: The symptoms of coronavirus disease 2019 (COVID-19) are highly variable, ranging from minor to potentially life threatening - the latter requiring intensive critical care medical response at prevalence levels that can strain healthcare systems. Significant concern is also emerging over the potential for lingering symptoms in COVID-19 survivors. In particular, numerous cases of hospitalized COVID-19 patients with neurological symptoms are being reported, including deficits in sensation, cognition and consciousness, as well as vascular and inflammatory lesions observed by magnetic resonance imaging (MRI). Very little is known about how these brain effects persist or resolve - and the extent of the effects in the much larger population of COVID-19 survivors, who self-isolated while infectious. To fill this knowledge gap, we have created NEUROCOVID19: a multidisciplinary study involving neuroimaging scientists and academically-oriented clinicians, that aims to: 1. Test whether COVID-19 survivors have incident brain lesions compared to matched COVID-19 negative controls; 2. Evaluate neuroanatomy and neurophysiology, clinical, sensory, and behavioural findings when COVID-19 survivors are no longer infectious (at baseline) and at follow-up; 3. Test for multivariate relationships between these measurements across COVID-19 survivors, including associations with risk variables such as age and indices of cerebrovascular health.

Methods: The study involves recruitment of COVID-19 survivors in two groups: those that were hospitalized, and those that self-isolated; and a control group of participants that tested negative for COVID-19 and self-isolated consequent to cold or flu-like symptoms. NEUROCOVID19 measurements include comprehensive, state-of-the-art brain MRI at 3 Tesla, including acquisitions and associated metrics probing brain anatomy and physiological function, lung MRI, olfactory and behavioural (NIH toolbox) assessments, and electroencephalography. Baseline measurements are undertaken within 3 weeks after hospital discharge or leaving quarantine, with 3-month follow-up.

Results: Baseline data have been obtained from 23 cases and 11 controls at the time of abstract submission, ranging in age from 19 to 70 years (mean 42 years, 15 male). Across the groups of COVID-19 survivors (2 hospitalized, 17 self-isolated), the anatomical MRI data show multiple instances of a) signal hyperintensity in the olfactory bulb; b) areas of infarct, ischemia, and microbleeds; and c) areas of inflammation or other neuropathy. These findings were more pronounced in the hospitalized COVID-19 survivors, but were also well apparent in the self-isolated COVID-19 survivors. Findings were seen to a lesser extent in the control group as expected, due to effects such as healthy aging.

Conclusions: Our initial pilot data strongly support our hypothesis that coronavirus infection produces brain lesions in some COVID-19 survivors with and without hospitalization, over a broad age range. Recruitment and testing are ongoing, as well as continued analysis of all data measured in the study. Knowledge translation of our protocol and findings to radiology, neurology and COVID-19 recovery clinics will help to address on-going health needs of COVID-19 survivors, and will help to understand the mechanisms that underpin the heterogeneous brain symptoms.

Long-term Effects of COVID-19 Illness in the Brain Assessed by 7T MRI

Helma Heidari^{*}, BSc^{1,2}, Stephanie Handsor³, Koula Pantazopoulos⁴, Laurn Richardson⁴, Kristy Coleman⁴, Michael Silverman⁵, Erin Spicer³, Stephen Pasternak^{4,6}, Luciano Sposato⁶, Doug Fraser⁷, Anthony Tang⁸, Ravi Menon^{1,2}, Corey Baron^{1,2}, Michael Jurkiewicz⁹, Elizabeth Finger^{4,6}, Marko Mrkobrada³, Megan Devlin³, and Robert Bartha, PhD^{1,2}

¹Robarts Research Institute, ²Departments of Medical Biophysics; ³Internal Medicine, ⁵Infectious Diseases, ⁶Clinical Neurological Sciences, ⁷Paediatric Critical Care, ⁸Medicine, ⁹Medical Imaging, The University of Western Ontario, and ⁴Parkwood Institute.

Introduction: The novelty of the new corona virus (SARS-Cov2), which can cause severe acute respiratory syndrome in humans, has elicited a broad scientific response. Previous studies have provided evidence that the virus can also cause neurological effects.¹ These neurological effects vary from fever, headache, nausea, vomiting, loss of taste or smell to impaired consciousness, seizure and acute cerebrovascular disease. These symptoms may originate from cerebral tissue damage and may have long-term cognitive and neurological consequences even after respiratory recovery. However, it is currently unknown if cerebral tissue damage occurs as a direct effect of the virus in the brain, as a consequence of deoxygenation due to respiratory failure or from microbleeds initiated by the infection. We hypothesize that some COVID-19 patients with neurological symptoms will have long-term cognitive and neuropsychological dysfunction that may be associated with microbleeds in the brain, altered tissue pH suggestive of viral or ischemic injury, vascular damage, or alterations in tissue microstructure. Ultra-high field (7T) MRI provides unprecedented opportunities to increase image resolution and contrast sensitivity to sensitively detect subtle brain pathology. The objective of this study is to determine whether lingering neurological symptoms and cognitive dysfunction in patients recovered from acute COVID-19 respiratory illness are associated with changes in the brain identified on 7T MRI. In this work initial feasibility data are presented.

Methods: All images of the brain were acquired on a Siemens 7T MRI Plus scanner. Six patients have been recruited to-date for this ongoing study from the multidisciplinary COVID19 clinic (LUC3) in London. Included patients had neurological symptoms during their illness, were recovered for at least one month from their COVID-19 respiratory symptoms, and did not have acute psychosis, pre-existing dementia, or claustrophobia. Patients undergo cognitive testing over the phone at baseline and six months, and participate in one in-person session including 7T MRI and detailed cognitive testing using the repeatable battery for the assessment of neuropsychological status (RBANS). The 7T MRI protocol includes T₁-weighted MP2RAGE (700 μ m iso), FLAIR (800 μ m iso), 3D time of flight imaging (470 μ m iso), susceptibility weighted imaging to assess microbleeds (0.1x0.1x1.3 mm³), diffusion weighted imaging (including μ FA, 2 mm iso) and chemical exchange saturation transfer (CEST) imaging (3.3 mm iso) to produce pH-weighted MRI contrast using amine/amide concentration-independent detection (AACID).² Images are viewed by a neuroradiologist to detect microbleeds and other signal variations. Initial AACID-CEST MRI results are presented in this abstract.

Results: Four patients have completed imaging and neuropsychological testing. Two patients showed imaging changes indicative of atherosclerosis, and one patient showed signal changes in FLAIR. AACID maps were successfully acquired in all subjects (Figure 1). Amide proton CEST effect was observed at 3.50 ppm as expected. These preliminary results demonstrate the feasibility of obtaining pH weighted CEST brain maps in this cohort.

Conclusion: Feasibility has been demonstrated to acquire 7T MRI in patients following COVID-19 illness, including advanced susceptibility weighted, diffusion, and CEST imaging. Further recruitment is needed to begin testing for associations between neuropsychological scores and imaging findings.

References:[1] Li et al. J Med Virol 2020;[2] McVicar et al. J Cereb Blood Flow Metab 2014.

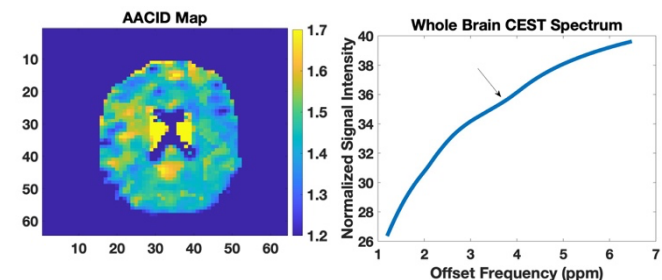
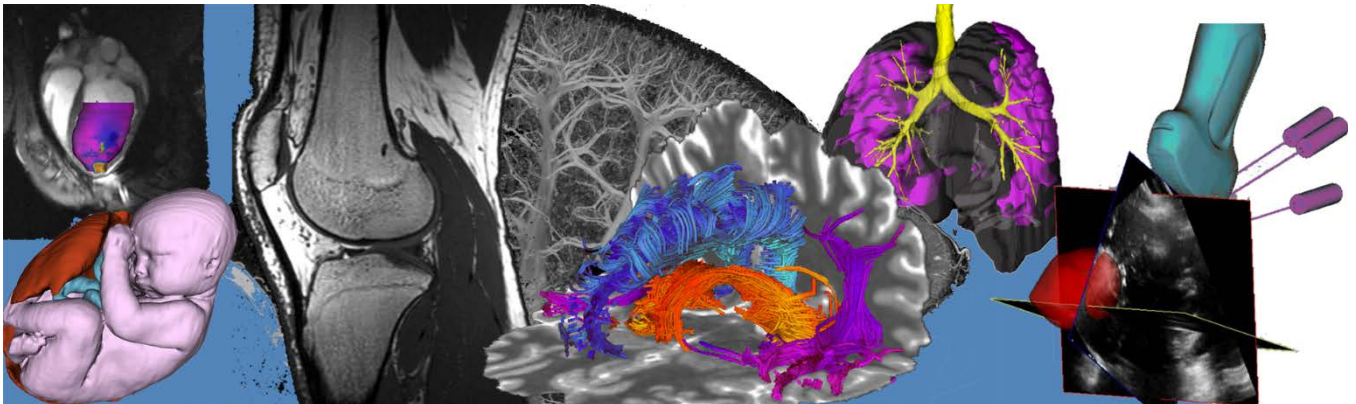


Figure 1: AACID map (left) and CEST spectrum (right) for one participant in the study (arrow identifies 3.5 ppm CEST peak).

Oral Presentation Abstract

Session 20: Molecular Imaging



Magnetic Resonance Image Analysis of Mammalian Cells Expressing Essential Magnetosome Genes *mamI* and *mamL*

P. Vivekanantha^{1,2}, Q. Sun^{1,3,4}, R.T. Thompson^{1,3}, F.S. Prato^{1,3,4}, D.E. Goldhawk^{1,3,4}

¹Imaging Program, Lawson Health Research Institute, ²Physiology & Pharmacology, ³Medical Biophysics and

⁴Collaborative Graduate Program in Molecular Imaging, Western University, London, Canada

Introduction: Magnetic resonance imaging (MRI) can be used to track cellular changes in pre-clinical models of disease with high spatial and temporal resolution [1]. However, enhancement of cellular contrast is required and may be achieved through manipulation of cellular iron [2]. Magnetotactic bacteria (MTB) possess genes that confer the ability to synthesize refined iron crystals within vesicles called magnetosomes [3]. Adapting magnetite-containing structures such as these in mammalian expression systems should enhance MR signal detection [4]. Within the complement of magnetosome genes, several are essential for its formation in MTB, including *mamI* and *mamL* [5]. To encode magnetosome-like nanoparticles in mammalian cells, we recently showed that MamI and MamL co-localize, suggesting a possible effect on the MR signal.

Hypothesis: Expression of essential magnetosome genes *mamI* and *mamL* in mammalian cells increases MR relaxation rates.

Methods: MTB genes *mamI* and *mamL* were previously cloned from *M. magneticum* sp. AMB-1 genomic DNA. Green (EGFP-MamI) and red (Tomato-MamL) fluorescent fusion proteins were expressed in the human MDA-MB-435 melanoma cell line, either alone or in combination, using antibiotic selection and fluorescence-activated cell sorting. Cells were cultured in the presence and absence of iron supplementation (250 μ M ferric nitrate/medium). At harvest, cells were either mounted in a gelatin phantom for MRI at 3 Tesla (3T, Biograph mMR) [6] or analyzed by inductively-coupled plasma mass spectrometry (Analytical Services, London). Total cellular iron content was normalized to amount of protein, quantified by the BCA assay [7]. A custom MATLAB-based program (The Viewer) was used to obtain relaxation rates. Analysis of Variance (ANOVA) and Dunnett's post-hoc tests were performed in SPSS.

Results: Total transverse relaxation rates ($R2^*$) of mammalian cells expressing MamI (Fig. 1) were no different than the parental control (measured in a prior study) [6]. However, in the presence of iron supplementation (+Fe), MamI-expressing cells showed a significant increase in transverse relaxivity. A similar increase was obtained from MamI+MamL co-expression (+Fe, black bar); although, this combination of magnetosome genes provided no additional increase in relaxivity. $R2$ followed the same pattern as $R2^*$. Longitudinal relaxivity ($R1$) in iron-supplemented cells expressing MamI or MamI+MamL was also greater than the parental control.

Conclusions: The essential magnetosome-associated membrane protein MamI increases MR relaxation rates in response to iron supplementation, even when expressed in a foreign cell environment. The mammalian cell model indicates a role for this bacterial membrane protein in iron-handling activity, as may be expected of an essential magnetosome protein. Iron supplemented co-expression of MamI+MamL, contributing no additional increase in transverse relaxivity, suggests that MamL may not have a direct role in iron-handling.

References: 1) Goldhawk *et al* (2017) in Design and Applications of Nanoparticles in Biomedical Imaging, p. 187; 2) Alizadeh *et al* (2020) Sci Rep 10, 3163; 3) Goldhawk *et al* (2012) Nanomed Nanobiotechnol 4, 378; 4) Brown *et al* (2014) in Magnetic Resonance Imaging: Physical Principles and Sequence Design, p. 113; 5) Sun *et al* (2020) in Imaging by Light and Electromagnetics in Medicine and Biology, p. 201; [6] Sengupta *et al* (2014) Front Microbiol 5, 29; [7] Smith *et al.* (1985) Anal. Biochem 150, 76

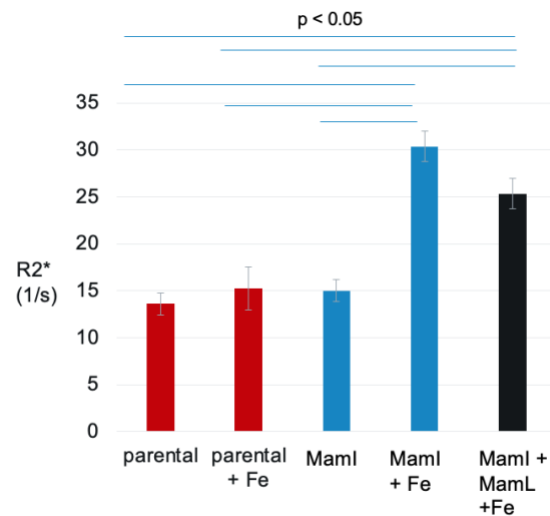


Fig. 1. Essential magnetosome genes increase transverse relaxation rates. Cells (parental, red; MamI-expressing, blue; MamI+MamL co-expressing, black) were cultured in the presence (+Fe) or absence of iron supplementation prior to mounting in a gelatin phantom for 3T MRI. Blue lines above the bar graph indicate significant differences in $R2^*$ ($p < 0.05$, $n = 4$).

Toward a reporter gene for MRI: Essential proteins from magnetic bacteria interact in mammalian cells.Q. Sun^{1,2,3}, C. Fradin⁴, R.T. Thompson^{1,2}, F.S. Prato^{1,2,3}, D.E. Goldhawk^{1,2,3}¹Imaging Program, Lawson Health Research Institute; ²Medical Biophysics & ³Molecular Imaging, Western University, London, Canada; ⁴Physics & Astronomy, McMaster University, Hamilton, Canada

Introduction: With its superb spatial and temporal resolution, magnetic resonance imaging (MRI) has great potential to track cellular activities that define early stages of disease [1]. To improve molecular imaging techniques, we are developing MRI reporter gene expression based on the magnetosome. In magnetotactic bacteria (MTB), magnetosome formation compartmentalizes iron biominerals in membrane-enclosed vesicles [2]. Biosynthesis of magnetosome-like nanoparticles in mammalian cells would provide an endogenous magnetic resonance (MR) contrast agent under genetic control [3]. This patented technology [4] would provide long-term molecular imaging for tracking cellular and molecular activities throughout the cell's life cycle.

Hypothesis: The interaction of MamI and MamL in mammalian cells demonstrates that essential magnetosome genes will initiate the formation of a rudimentary magnetosome-like nanoparticle in any cell type.

Methods: MTB genes *mamI* and *mamL* were cloned from *M. magneticum* sp. AMB-1 genomic DNA by PCR and inserted into fluorescent vectors (pEGFP and ptdTomato, respectively). GFP-MamI and Tomato-MamL were stably expressed in human MDA-MB-435 melanoma cells, alone and in combination. Cines of mobile elements detected in intact cells were captured with confocal microscopy (Nikon A1R Confocal Laser Microscope) and analyzed using the ImageJ Mosaic Particle Tracker 2D/3D plugin. Particles undergoing directed motion were defined as travelling along a trajectory with slope of the mean-squared displacement above $1.2 \mu\text{m}^2/\text{s}$, while particles undergoing Brownian motion had a slope between 0.7 to $1.1 \mu\text{m}^2/\text{s}$. Directed motion data is reported as apparent velocity and calculated with the equation $v \propto e^{y-\text{intercept}/2}$, while Brownian motion data is reported as apparent diffusion coefficient, as calculated by the software.

Results: Tomato-MamL displayed mobility whether expressed alone or in conjunction with GFP-MamI (Figure 1). In both cases, analysis of motility revealed both directed and Brownian motion. The apparent velocity of particles moving with directed motion in Tomato-MamL/GFP-MamI co-expressing cells was approximately 3-fold faster than in cells expressing Tomato-MamL alone (6.4 ± 2.2 vs $2.0 \pm 0.7 \mu\text{m}/\text{s}$; $p < 0.01$). The apparent diffusion coefficient of Tomato-MamL/GFP-MamI particles undergoing Brownian motion was over 70-fold larger than Tomato-MamL particles (0.03 ± 0.01 vs $2.2 \pm 1.6 \mu\text{m}^2/\text{s}$; $p < 0.05$).

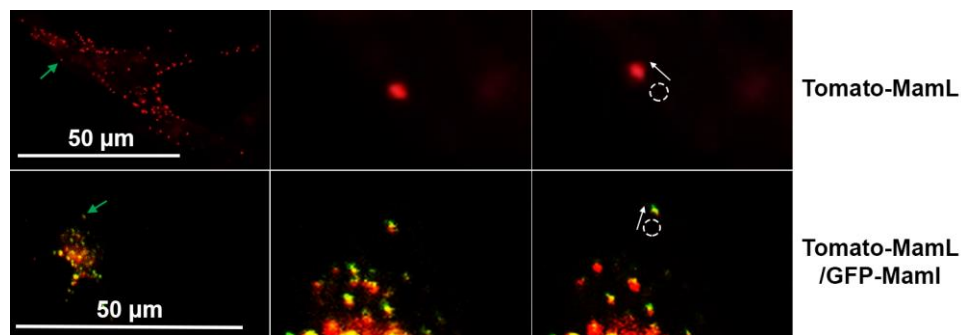


Figure 1. Cine snapshots reveal mammalian cells stably expressing Tomato-MamL (top row, red fluorescence) or Tomato-MamL/GFP-MamI (bottom row, yellow fluorescence). The leftmost panels show a full cell; green arrows indicate mobile particles. Middle and righthand panels show a zoomed in view of each, with the trajectory of movement (at right) indicated by a white arrow. Dotted circles represent initial particle position.

Conclusions: We have shown that GFP-MamI and Tomato-MamL co-localize, interact, and are mobile in a mammalian system. Analysis of particle directed motion reveals that Tomato-MamL travels at apparent velocities comparable to transport kinesins when singly-expressed and to myosin and axonemal dynein when co-expressed with GFP-MamI [5]. Analysis of Brownian motion reveals that Tomato-MamL particles may be more constrained than Tomato-MamL/GFP-MamI particles, resulting in very small apparent diffusion coefficients. These data provide additional evidence that MamI and MamL interact and may form the scaffold on which a magnetosome-like nanoparticle is built.

References: [1] Goldhawk *et al* (2017) In: Design and Applications of Nanoparticles in Biomedical Imaging, p. 187; [2] Uebe & Schuler (2016) Nat Rev Microbiol 14:621 [3] Sun *et al* (2020) In: Bioimaging: Imaging by Light and Electromagnetics in Medicine and Biology, p.201; [4] Goldhawk *et al* (2019) European Patent #3110952; [5] Howard, J (2001) Mechanics of Motor Proteins and the Cytoskeleton

Gadolinium-Free MRI Blood Pool Contrast Agents: Manganese(III) Porphyrins With Tunable Human Serum Albumin Binding Affinity

Hanlin Liu^{a,b} and Xiao-An Zhang^{a,b,c}

^aDepartment of Chemistry, University of Toronto. ^bDepartment of Physical and Environmental Sciences,

^cDepartment of Biological Sciences, University of Toronto Scarborough.

Keywords: MRI, Contrast Agents, Blood pool agents, Manganese, Porphyrin

Introduction: Classic MRI contrast agents (CAs) are mainly based on Gadolinium (Gd) complexes, which operate by the paramagnetic enhancement of NMR T_1 relaxation (r_1) of surrounding water protons.¹ In MR angiography (MRA), specialized CAs called blood pool agents (BPAs) can selectively enhance the blood stream. An optimal BPA must be (a) **efficient** (measured in T_1 or T_2 relaxation), (b) **safe** to use, and (c) selectively **retained in the vasculature**. Gd(III) complexes partially, but not optimally achieve the above by providing high T_1 relaxation in a stable complex; moreover, the chelate structure can be modified to bind to the serum protein human serum albumin (HSA) in the case of Ablavar® and MultiHance® for prolonged vasculature retention. However, the r_1 of Gd-based CAs decreases sharply as the magnetic field is increased to the current clinic field strengths of 1-3 T. The long circulation of BPAs also unavoidably increases the risk of the dissociation and accumulation of toxic Gd(III) ions in vivo, a mechanism known to lead to adverse effects such as nephrogenic systemic fibrosis (NSF) in patients with impeded renal clearance. To address these issues, our group previously developed MnP2,²⁻⁴ the first Manganese (III) porphyrin (MnP)-based BPA with high affinity for HSA. MnP2, however, exhibited a slight decrease in r_1 upon HSA binding (Fig. 1 left). Here we present the development of a series of smaller and polar MnPs with improved r_1 at 3T and tunable binding with HSA.

Methods: One dimeric and two monomeric MnP-based BPAs (Fig. 1 middle) were designed and synthesized via a dipyrromethane pathway. Products were characterized using ¹H-NMR, UV-Vis as well as mass spectroscopies where applicable, and their purities determined by HPLC. The field-dependent r_1 (NMRD) profiles were obtained with a fast field cycling NMR relaxometer (SMARTTracer™) coupled with a cryogen-free superconducting magnet (HTS-110), covering magnetic fields from 0 to 3 tesla. CA binding affinity to HSA was acquired through optical studies with UV, fluorescence and circular dichroism spectroscopies, or NMRD titration.

Results: All three MnPs have been successfully synthesized and fully characterized spectroscopically. The purity of all MnPs were confirmed by HPLC. All MnPs have moderate to high affinity for HSA, and unlike MnP2, exhibit increased r_1 enhancement upon HSA binding. This is in stark contrast to MnP2, which exhibits a small decrease in r_1 upon HSA binding. This was thought to be due to hydrophobic water coordination blockage, which was backed up by its high affinity to HSA ($K_d = 0.55$ μ M). New MnPs with smaller carboxylates were initially designed to address this issue; the replacement of the three benzyl groups was expected to decrease the interactions with the nonpolar protein. As a result, **1** exhibits a 400-fold decrease in affinity, now comparable to that of Ablavar, and maximal r_1 enhancement upon protein binding (Fig. 1 right). Future work will also involve **2**, which was designed to target the ibuprofen binding pocket, Sudlow's site II, as well as in vivo evaluation in animal models.

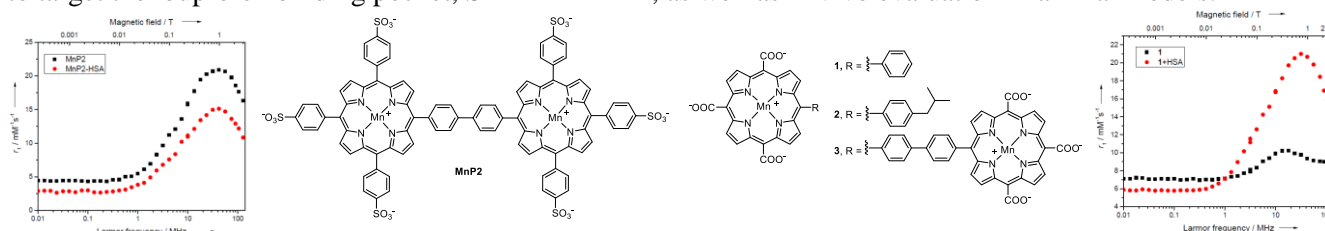


Figure 1. Left: NMRD profile of MnP2 with (red) and without (black) HSA. Middle: MnPs discussed in the above text. Right: NMRD profile of **1** with (red) and without (black) HSA.

Conclusions: We demonstrated the viability of MnPs as superior alternatives to the commonly used GBCAs. MnPs fulfill the requirements necessary for a BPA in that they exhibited high r_1 at high clinic fields, high stability from metal dissociation and tunable affinity for HSA. We also successfully demonstrated the role of polarity on r_1 and HSA binding, which offers insights on rational design to further optimize the r_1 and pharmacokinetics of the CAs.

References: ¹ *Encyclopedia of Inorganic and Bioinorganic Chemistry* **2018**, 1–16. ² *J. Med. Chem.* **2014**, 57, 516–520. ³ *J. Biol. Inorg. Chem.* **2014**, 19, 229–235. ⁴ *J. Magn. Reson. Imaging* **2014**, 40, 1474–1480.

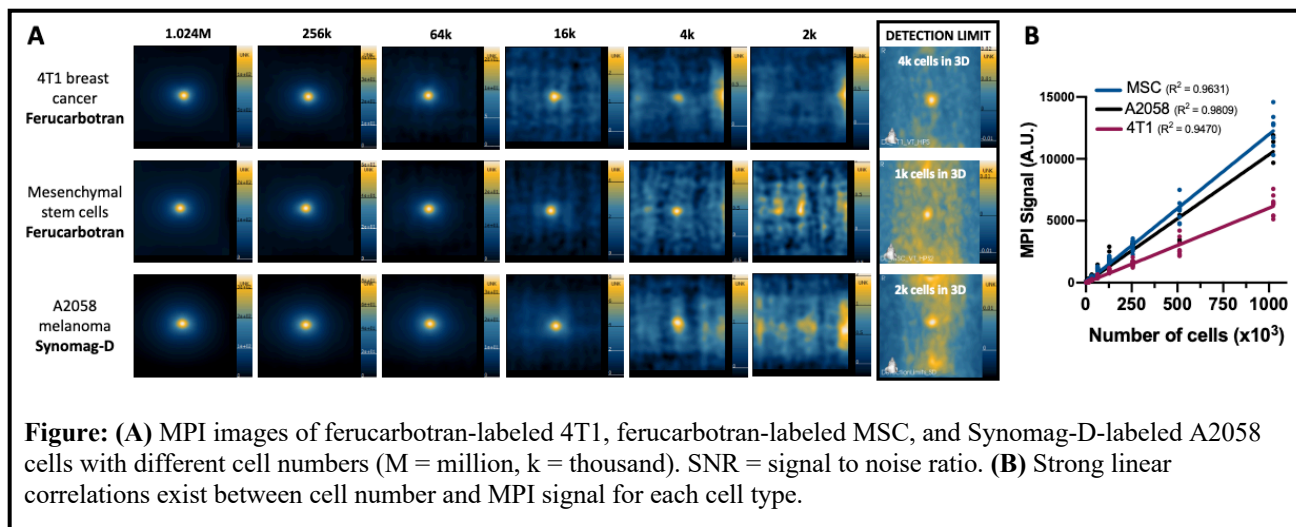
Determination of cellular sensitivity for magnetic particle imaging

Julia J. Gevaert*, Olivia C. Sehl*, Paula J. Foster *co-authorship

Robarts Research Institute, Department of Medical Biophysics, University of Western Ontario

Introduction: Magnetic Particle Imaging (MPI) is an emerging, non-invasive, and non-ionizing imaging technique capable of detecting cells labeled with superparamagnetic iron oxide nanoparticles (SPIOs). MPI signal varies linearly with iron content, allowing direct quantification, and with high sensitivity¹. MPI for cell tracking applications is in its infancy and requires SPIOs that have a high cellular labeling efficiency while preserving intracellular magnetic properties. Lowering cellular detection limits requires increased iron uptake in cells using optimized MPI tracers. Some cell types have an enhanced ability for taking up and storing SPIO², and therefore produce more MPI signal. Additionally, it has been shown that Synomag-D (an SPIO designed for MPI) produces more MPI signal than ferucarbotran (the current Gold Standard) per mass of iron content³. Cellular sensitivity for MPI has not been carefully studied and the cellular detection limit of MPI using these common SPIOs is unknown. **Our objective** is to comparatively analyze cellular sensitivity and detection limits for mesenchymal stem cells (MSC) and breast and melanoma cancer cell lines, using Synomag-D and ferucarbotran.

Methods: 4T1 breast cancer cells and MSCs were labeled by coincubation *in vitro* with ferucarbotran and A2058 melanoma cells were labeled with synomag-D, using transfection agents⁴. The next day, the following cell numbers were collected in triplicates: 1024k, 512k, 256k, 128k, 64k, 32k, 16k, 8k, 4k, 2k, 1k (k = thousand, $\times 10^3$) cells. MPI of these cells were acquired on the MomentumTM scanner (Magnetic Insight Inc.) using dual-channel 3.0 T/m gradients. Iron content per cell was determined by inductively coupled plasma mass spectrometry (ICP-MS).



Results: MPI signal was strongly correlated with cell number for each cell type. The slope of the linear regression for MSC with ferucarbotran (11.97) was higher than 4T1 cells with ferucarbotran (6.02) and A2058 cells with Synomag-D (10.34), indicating higher MPI sensitivity in MSC. The cell detection limit using projection imaging (3D) was 4k 4T1 cells, 1k MSCs, and 2k A2058 cells. ICP-MS measured enhanced labeling in MSCs (11.15 ± 2.18 pg/cell) and A2048 cells (12.68 ± 2.18 pg/cell) compared to 4T1 cells (5.38 ± 1.64 pg/cell) ($p < 0.001$).

Conclusion: Using the same SPIO (ferucarbotran), we have demonstrated that the cellular sensitivity (slope) and detection limits of MSCs was superior to 4T1 cells due to enhanced SPIO loading. Additionally, the use of MPI-tailored SPIOs (Synomag-D) increased cellular iron content and MPI sensitivity in A2058 melanoma cells compared to ferucarbotran-labeled 4T1 cancer cells. As few as 1000 cells were detected in this study. Tailored tracers, increased labeling efficiency, and advanced imaging parameters should be explored as methods to improve MPI cellular sensitivities. This is important knowledge for designing cell tracking experiments to anticipate the minimum number of cells that are required for detection *in vivo*.

References: [1] Zheng, B. *et al. Sci Rep* **5**, 1–9 (2015). [2] Mcfadden, C. *et al. Contrast Media Mol Imaging* (2011). [3] Bender, P. *et al. J. Phys. Chem. C* **122**, 3068–3077 (2018). [4] Thu, M.S. *et al. Nat Med* **18**, 463–467 (2012).

***In vitro* assessment of acoustically cavitated docetaxel-loaded nanobubbles on mouse breast cancer cells**Yiran Zou¹, Patrick Dong Min Chang^{*,2}, Yun Xiang^{2,3}, Yara Ensminger¹, Alex Wright⁵, Sharshi Bulner⁵, David Goertz^{4,5}, and Naomi Matsuura^{1,2,3}¹Department of Materials Science & Engineering, ²Institute of Biomedical Engineering, ³Department of Medical Imaging, and⁴Department of Medical Biophysics, University of Toronto, Ontario, Canada; ⁵Sunnybrook Research Institute, Toronto, Ontario, Canada

*Presenting author

Introduction. Breast cancer is the leading cause of cancer death for women worldwide [1]. Docetaxel (DTX; commercially known as Taxotere[®]) is part of the standard of care for breast cancer therapy but exhibits suboptimal pharmacokinetic profiles, leading to limited drug accumulation in cancerous tissues [2]. DTX has been shown to be loaded on phospholipid encapsulated microbubble (sizes ~1-8 μm) carriers through the association of DTX to lipids prior to bubble synthesis. The DTX can then be released locally to tumour sites via focused ultrasound (FUS) stimulated cavitation to mitigate systemic toxicity [3]. Recently, bubbles in the submicron range (i.e. nanobubbles; NB) have been proposed for ultrasound-triggered drug delivery owing to their enhanced drug loading capacities [4-6]. Although *in vitro* cytotoxicity of non-drug loaded nanobubbles have been examined in the literature, the acoustic response, DTX loading, and cytotoxicity of DTX-loaded nanobubbles (DTX-NB) pre- and post-exposure to FUS has not yet been investigated. In this study, the DTX loading and cytotoxicity of DTX-NB under various FUS exposures was assessed in comparison to Taxotere[®] using a custom-built sterile FUS chamber.

Methods. DTX was localized in a precursor oil-in-water droplet emulsion stabilized by phospholipids. After purification, droplets were lyophilized to form hollow lipid shells to form a bubble suspension via gas exchange and reconstitution. Size distribution was assessed by Coulter counting (Multisizer 4e, USA) and DTX loading was quantified by ultra-performance liquid chromatography coupled with a mass spectrometer system (Acquity H-Plus, Waters, USA). The *in vitro* cytotoxicity of Taxotere[®], plain NB, and DTX-NB with or without ultrasound exposure was assessed on EMT-6 cells using the MTT assay. Samples were cavitated using a 1 MHz FUS transducer (Valpy Fisher IL0112HP 1.5" diameter, 6" focal length) under peak negative pressures (from 0.25 to 1.36 MPa) and then incubated with cells. 3-sec contrast-enhanced ultrasound videos were taken before and after FUS exposure to monitor bubble cavitation using a clinical ultrasound scanner (EPIQ 7G, Philips, Netherlands).

Results. 104 ± 8 μg of DTX was loaded onto $\sim 10^{10}$ bubbles with a mode diameter of ~ 230 nm per ~ 0.4 μL of gas ($n > 6$). At a clinically viable gas volume of ~ 9 $\mu\text{L}/\text{kg}$, a DTX dosage of ~ 2.5 mg/kg can be achieved, comparable to FDA-approved clinical dosing of Taxotere[®]. As shown in **Fig. 1**, FUS cavitation resulted in the disruption of DTX-NB. No significant differences in cell viability were found between the culture media in chamber, plain NB, and plain NB exposed to 1.36 MPa FUS compared to the positive control ($p > 0.05$). This demonstrated the sterility of the chamber setup and biocompatibility of the phospholipids used in the NB formulation. Cells incubated with 20 nM of DTX-NB ($\text{IC}_{50} \sim 14$ nM) cavitated at all pressures exhibited significantly reduced cell viability ($p < 0.001$), with equivalent cytotoxicity compared to that of the Taxotere[®].

Conclusions. This study demonstrates acoustically responsive NBs can load high DTX concentrations equivalent to clinical dosages and that the DTX can be successfully released to exert significant *in vitro* cytotoxic effects on EMT-6 cells. Future work aims to examine the *in vivo* biodistribution and pharmacokinetic profile of DTX-NB in preclinical breast cancer animal models, and subsequent evaluation on animal survival.

References. [1] K. Tryfonidis et al., *Nat. Rev. Clin. Onc.*, vol. 12, no. 3, 2015. [2] L. Feng et al., *Cancer let.*, vol. 334, no. 2, 2013. [3] I. Lentacker et al., *Soft Matter*, vol. 5, no. 11, 2009. [4] T. Li et al., *Biomater. Sci.*, vol. 8, no. 5, 2020. [5] Z. Yu et al., *Int. J. Nanomed.*, vol.15, 2020. [6] P. Nittayacharn et al., *Front. Pharma.*, vol. 11, 2020.

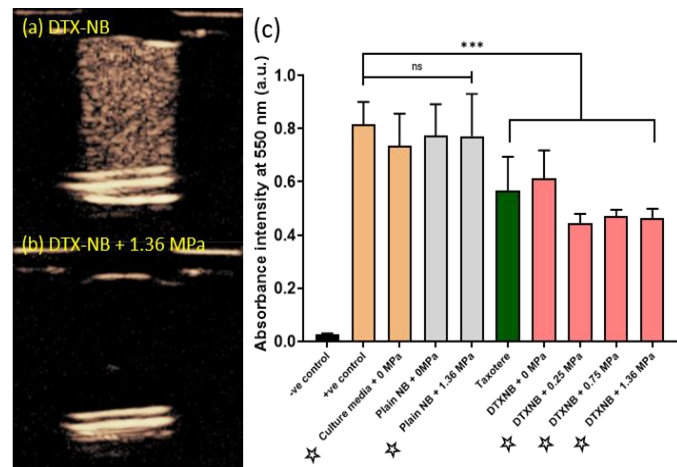
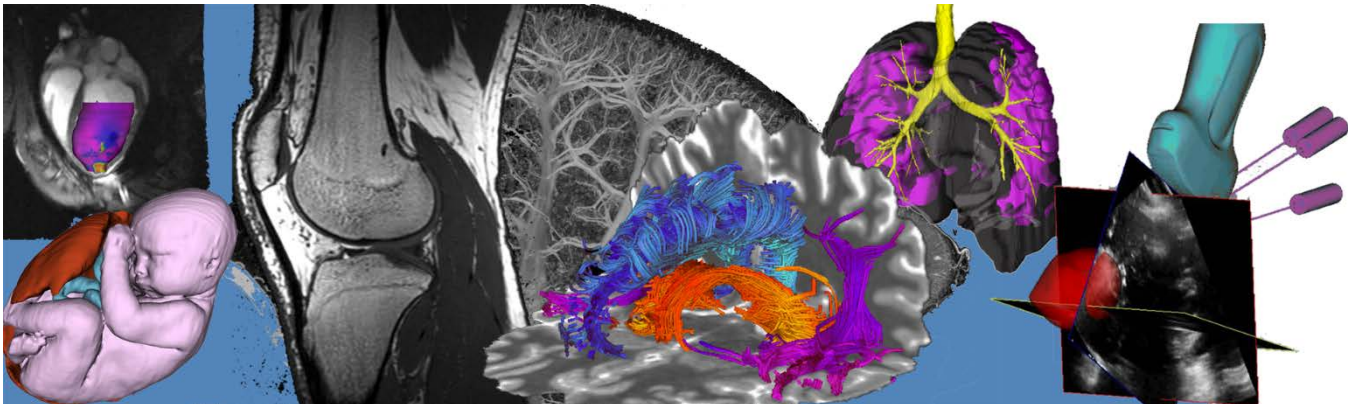


Figure 1. Contrast-enhanced ultrasound images of DTX-NB in sample chamber before FUS exposure (a), and after exposure to 1.36 MPa FUS, confirming shell material release via bubble disruption (b), with a column chart showing the peak absorbance of the MTT assay, demonstrating enhanced cytotoxicity of cavitated DTX-NB compared to Taxotere[®] (c). DTX concentration is 20 nM for all Taxotere[®] and DTX-NB groups. Data presented as mean \pm STD ($n \geq 6$) (***) $p < 0.001$. A star in the sample label indicates the chamber groups.

Oral Presentation Abstract

Session 21: Machine Learning II



Central Line Tutor: using computer vision workflow recognition in a central venous catheterization training system

Rebecca Hisey¹, Daenis Camire², Jason Erb², Daniel Howes², Gabor Fichtinger¹, Tamas Ungi¹

¹Laboratory for Percutaneous Surgery, School of Computing, Queen's University, Kingston, Canada

²Department of Critical Care Medicine, Queen's University, Kingston, Canada

Introduction: Feedback is an essential component for learning, yet many medical trainees report being dissatisfied at the amount of performance-based feedback they receive. The most commonly cited reason for this lack of feedback is that attending physicians simply do not have enough time. We present here a system for training central venous catheterization (CVC) that is capable of providing trainees with instruction and feedback without needing an expert observer to be present. The system, called Central Line Tutor, uses workflow recognition to provide trainees with prompts about upcoming tasks and visual cues about workflow errors. In this study, we evaluate the accuracy and time delay of our workflow recognition method, and evaluate the usability of the system.

Methods: The system is made up of a computer, webcam, central venous access phantom and an electromagnetic tracking system. We use workflow recognition to automatically update an interactive checklist that is displayed to the user, which provides prompts about upcoming tasks and notify users when errors are made. For the majority of tasks, our workflow recognition uses a combination of a convolutional neural network (CNN) and a form of recurrent neural network that uses long-short-term memory (LSTM) units. For tasks that involve the ultrasound probe and needle, we identify them based on their position and orientation which we obtain using an electromagnetic tracking system.

To evaluate our system, we collected videos of 4 medical students performing CVC using the Central Line Tutor system. Each student recorded five trials of the procedure. To train the networks, we divided these videos into individual frames that were labelled with the task that was being performed at that time. Both the CNN and the recurrent neural network were trained separately on this data, using a leave-one-trial-out cross validation scheme for a total of five folds. We evaluate our workflow recognition in two ways: the first is the average number of tasks that the system recognizes, and the second is by measuring the average transitional delay. The average transitional delay is defined as the average number of seconds between when the system recognizes the start of a task compared to a human reviewer. A negative transitional delay indicates that the system recognized the start of the task ahead of the human reviewer. Finally, to evaluate the usability of the system, each of the students was asked to complete a questionnaire about their experience using the system. Participants were asked to rate the usefulness of each of the instructional features of the system on a 5-point Likert scale.

Results: The system was able to recognize tasks in the workflow with 96% accuracy and with an average transitional delay of 0.25 ± 6.1 s. The average score on the participant survey was 4.6 out of 5 for the system overall (Fig 1). The participants found the interactive task list to be the most useful component of the system with an average score of 4.8 out of 5.

Conclusions: Overall the system performed well. It was able to reliably recognize tasks in the CVC workflow with minimal delay compared to a human reviewer. The participants were happy with the system and felt that it would improve CVC training without needing an expert observer.

Acknowledgements: This work was funded, in part, by NIH/NIBIB and NIH/NIGMS (via grant 1R01EB021396-01A1), by CANARIE's Research Software Program, and is supported as a Collaborative Health Research Project (CHRP #127797) by the Natural Sciences and Engineering Research Council of Canada (NSERC) and the Canadian Institutes of Health Research (CIHR). R. Hisey is supported by the QEII-GSST scholarship. G. Fichtinger is supported as a Canada Research Chair.

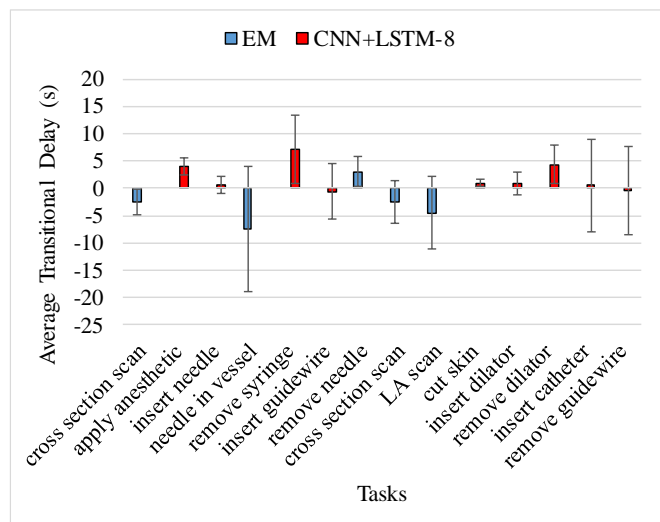


Figure 1. Average transitional delay between central line tutor and human reviewers

Ultrasound Probe Pose Classification for Task Recognition in Central Venous Catheterization

Colton Barr, Rebecca Hisey, Tamas Ungi, Gabor Fichtinger

Laboratory for Percutaneous Surgery, School of Computing, Queen's University, Kingston, Canada

INTRODUCTION: Due to the restricted time and availability of expert observers, medical trainees are often limited in the feedback they receive when practicing a new skill. Central Line Tutor is a training system for central venous catheterization (CVC) that aims to alleviate this problem by automatically providing instruction and feedback to students using computer vision-based task recognition [1]. As students practice CVC on a simulated patient, the system monitors their progression through the workflow using a combination of an RGB camera and electromagnetic (EM) tracker. While almost all tasks can be detected in RGB images based on the presence of a particular tool, distinguishing between different ultrasound tasks requires knowledge about the pose of the ultrasound probe. Using an EM tracker to extract ultrasound (US) probe pose, however, effectively doubles the overall cost of the system and reduces the feasibility of deploying Central Line Tutor for widespread use. In order to remove the need for EM tracking and substantially reduce the overall cost of the Central Line Tutor system, we propose the use of deep learning to classify US probe orientation in real-time from streamed US images.

METHODS: A classification architecture was created that combined a U-Net with a CNN-based classifier. Our dataset was generated by segmenting the carotid and jugular vessels in 20 tracked US sequences collected from 4 trainees. Each sequence yielded approximately 1100 US images for a total dataset of 22000 images. The images were also labelled with the corresponding US probe orientation relative to the major vessels of the neck. The probe poses were categorized as either “long-axis”, “cross-section” or “undefined”. Both the U-Net and subsequent pose classifier were tested using a leave-one-user-out scheme, where one trainee’s data was reserved for testing each round and the rest of the data was used for training and validation. For each fold, the U-Net and classifier were trained on the same dataset, followed by testing using the same test set. This ensured that both networks were tested on novel data in each fold. The U-Net performance was quantified using Intersection over Union (IoU), which measured the overlap between the human segmentations and network predictions, while classification performance was quantified using accuracy, precision and recall.

RESULTS: The mean testing set IoU score for U-Net cross-validation was 0.727 ± 0.045 . The mean classification performance on the testing set across 4 folds was an accuracy of 0.905 ± 0.036 , with a weighted mean precision of 0.913 ± 0.008 and weighted mean recall of 0.905 ± 0.038 across all 3 classes. Figure 1 illustrates two sets of US images captured with different probe poses, as well as the U-Net performance on these images.

CONCLUSIONS: The classification of US probe pose directly from US images can be achieved with a high level of accuracy using a combined U-Net and CNN classification model. This model’s performance demonstrates that US pose classification may be suitable for recognizing US tasks during central line insertion, and future work will be aimed at testing the network’s performance in real-time task recognition within Central Line Tutor. All code associated with this project is available at github.com/SlicerIGT/aigt.

ACKNOWLEDGEMENTS: C. Barr was supported by an NSERC CGS M award. R. Hisey is supported by the QEII-GSST award. G. Fichtinger is supported as a Canada Research Chair. Work funded, in part, by NIH/NIBIB and NIH/NIGMS (via grant 1R01EB021396-01A1 - Slicer+PLUS: Point-of-Care Ultrasound) and by CANARIE’s Research Software Program. This work also was financially supported as a Collaborative Health Research Project (CHRP #127797).

REFERENCES:

[1] Hisey, R., Ungi, T., Holden, M., Baum, Z., Keri, Z., McCallum, C., Howes, D. and Fichtinger, G. "Real-time workflow detection using webcam video for providing real-time feedback in central venous catheterization training," Proc. SPIE 10576, Medical Imaging 2018: Image-Guided Procedures, Robotic Interventions, and Modeling, 1057620 (2018)

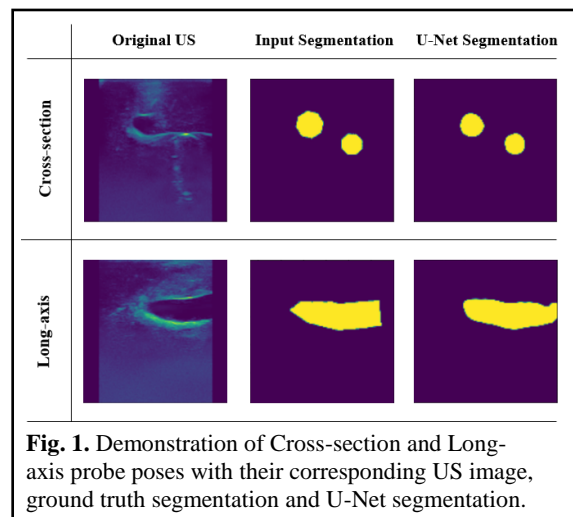


Fig. 1. Demonstration of Cross-section and Long-axis probe poses with their corresponding US image, ground truth segmentation and U-Net segmentation.

Effect of dataset size and acquisition type on deep learning segmentation of the prostate in 3D ultrasoundNathan Orlando^{1,2}, Derek J Gillies⁴, Igor Gyacskov², Cesare Romagnoli⁴, David D'Souza^{3,4}, Doug Hoover^{1,3,4}Aaron Fenster¹⁻³¹Department of Medical Biophysics, ²Robarts Research Institute, ³Department of Oncology, Western University;⁴London Health Sciences Centre; London, Ontario, Canada

Introduction: Three-dimensional (3D) transrectal ultrasound (TRUS) imaging is utilized in several minimally invasive procedures for diagnosing and treating prostate cancer. Manual prostate segmentation, necessary for target definition and image registration, is a time-consuming and difficult process. We have previously developed an algorithm capable of accurate 3D TRUS prostate segmentation in less than one second [Orlando and Gillies *et al.* 2020]. Our method involved deep learning prediction on 12 2D images sampled radially around the approximate centre of the prostate, followed by reconstruction into a 3D surface. Our algorithm was trained on a large and diverse dataset, a rarity in medical imaging, especially ultrasound. We hypothesize our radial approach will allow for more efficient training and thus similar performance when trained with less diverse and smaller datasets.

Methods: The training dataset consisted of 6773 2D images, sliced from a total of 206 3D images acquired in biopsy & brachytherapy procedures using two acquisition types (side fire (SF) & end fire (EF)) and several ultrasound machines. Our modified version of the popular U-Net architecture was once again used for deep learning prediction. A U-Net++ architecture was also implemented, as it is a state-of-the-art network that has been shown to perform well with small datasets [Zhou *et al.* 2020]. First, we split our dataset into EF and SF halves and trained a separate network for each image type. The EF dataset was then reduced in size from the full 2738 images to 1000, 500, 250, and 100 images, with networks trained for each. Manual contours provided the ground truth for training and testing, with the testing set consisting of 20 EF and 20 SF 3D TRUS images unseen during training.

Results: When trained only on EF images, the U-Net and U-Net++ performed with a mean \pm SD 3D dice similarity coefficient (DSC) of $89.2 \pm 4.8\%$ and $94.3 \pm 2.3\%$ when tested on EF images, and $80.7 \pm 6.5\%$ and $86.7 \pm 7.2\%$ when tested on SF images, a type the network had never seen. When trained only on SF images, the U-Net and U-Net++ had a 3D DSC of $86.9 \pm 5.2\%$ and $92.8 \pm 3.4\%$ when tested on SF images and $84.3 \pm 7.1\%$ and $81.5 \pm 7.6\%$ when tested on EF images. When trained on EF datasets of 1000, 500, 250, and 100 images, the U-Net++ performed with a 2D DSC of $93.4 \pm 2.8\%$, $93.4 \pm 2.7\%$, $92.8 \pm 2.6\%$, and $90.1 \pm 3.4\%$ when tested on EF images.

Fig 1: (Left) Mean \pm SD 3D DSC for our U-Net and U-Net++ trained only on end fire images and tested on both end fire and side fire images. (Right) Mean \pm SD 2D DSC for our U-Net++ trained on a reduced number of end fire images. Asterisk denotes a significant diff. ($p < .05$)

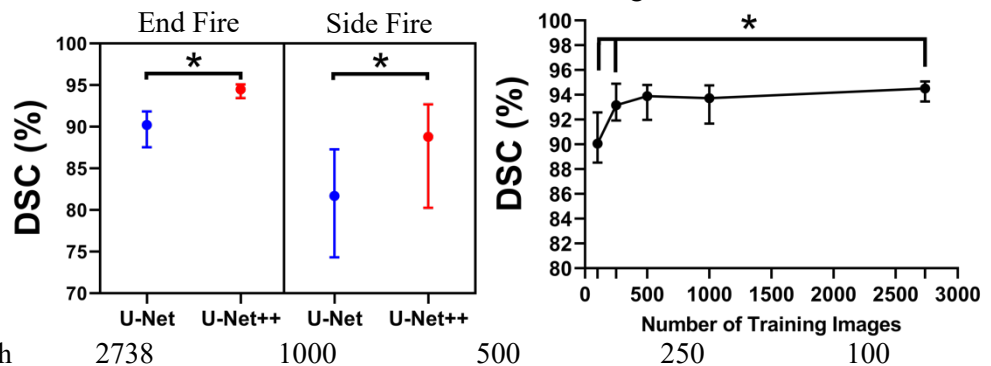


Fig 2: An example 2D slice from an end fire image, the ground truth mask, and the segmentation output of the U-Net++ trained with the full end fire dataset (2738 images) and 1000, 500, 250, and 100 image datasets, from left to right.

Conclusions: With a split dataset, the U-Net++ outperformed the modified U-Net, matching the performance of the modified U-Net trained on the full dataset when tested on the image type it was trained on. DSC $>80\%$ when tested on the image type the network had never seen demonstrated the generalizability of our method. U-Net++ performed well with smaller datasets, matching performance on the full EF dataset to within 1% DSC. This demonstrates the efficiency of our 2D radial deep learning plus 3D reconstruction segmentation approach in the realistic scenario of small clinical datasets, providing the potential for widespread use, even when data is scarce. Future work includes expanding these results to smaller SF and mixed datasets and assessing the impact of image quality on performance, with the end goal being successful translation to the clinic.

Preservation of Image Quality for Sparse Linear Ultrasound Probes via Supervised Deep Learning-based Inference

Di Xiao¹, Billy Y. S. Yiu¹, Adrian J. Y. Chee¹, Alfred C. H. Yu¹, ¹Schlegel Research Institute for Aging, University of Waterloo, Waterloo, Ontario

Introduction

Unfocused acoustic transmissions help enable the sub-millisecond time resolution of high-frame-rate ultrasound imaging. A critical bottleneck for real-time HiFRUS (High-FRame-rate UltraSound) is the data transfer from the probe to the imaging system (can be over 10GB/s). Sparse arrays with fewer transducer elements naturally reduce the data rate compared to full channel probes, but there is a trade-off in image quality (e.g. grating lobe artifacts). We hypothesize that the data from the sparse channels can be used in an inference scheme to artificially form full channel radiofrequency (RF) data; this inference scheme can be implemented via supervised deep learning. In this work, we propose using a trained convolutional neural network (CNN) to regenerate full channel data from received sparse array data without compromising image quality.

Methods

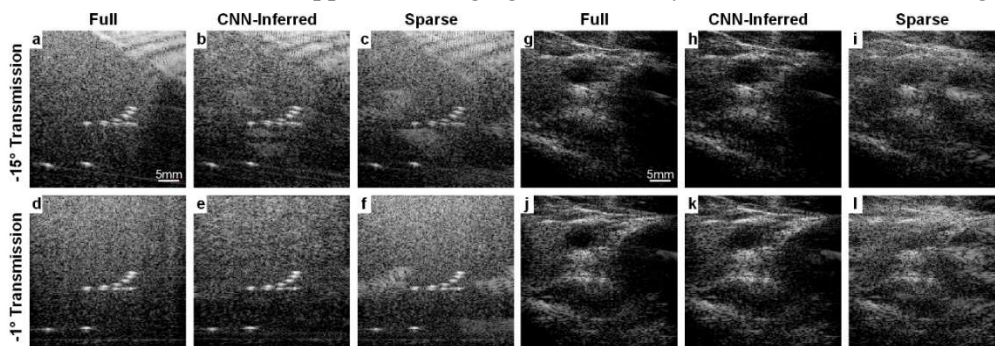
Drawing from image processing literature, we employ an encoder-decoder CNN architecture to perform inference. To train the CNN, over 60,000 instances of *in vivo* human carotid was collected via steered plane wave transmissions using a SonixTouch scanner (L14-5 array) with 15% of the collected data reserved for evaluation of the neural network. Each training example consisted of 128 channels sampled at 20MHz; the data was then split into the odd-numbered channels (training input) and the even-numbered channels (training output reference). Thus, our proposed framework is designed to artificially double the number of receiving elements. The trained network was then applied for separately acquired sparse array data *in vitro* and *in vivo*; images were then beamformed from the inferred full channel data to assess image quality.

Results

Images beamformed from CNN-inferred data resemble images beamformed from full channel data, while demonstrating significant improvement over images beamformed from sparse array data. The figure shows B-mode *in vitro* (Fig. a-f) and *in vivo* (Fig. g-l) images on a 40dB scale for two different steered plane wave transmissions. Spatial aliasing artifacts (Fig. f – left and right of point targets) were reduced *in vitro* using CNN-inferred data (Fig. b, e) compared to using only the sparse channel data (Fig. c, f) by around 10dB. The mean full-width half maximum of the line of point targets in Fig. e are within 0.02mm of those in Fig. d. For the *in vivo* scenario, the carotid lumen (top-center in Fig. g-l) has much higher contrast using CNN-inferred data (Fig. h, k) compared to only using the sparse channel data (Fig. i, l), also improving by around 10dB. In both the *in vitro* and *in vivo* images, the images beamformed from CNN-inferred data (Fig. b, e, h, k) show strong resemblance to images beamformed from full channel data (Fig. a, d, g, j) despite having only half the channel count. Evaluated for real-time performance on an RTX 2080, an inference rate of 4ms per 64 channels of RF data is achieved.

Conclusions

Our framework successfully regenerated full channel data from half channel ultrasound acquisitions on the order of milliseconds. Using a trained CNN, image quality was preserved both *in vitro* and *in vivo* compared to using only sparse channel data; artifacts were dramatically reduced, but not altogether eliminated. Because our framework is RF-to-RF, it can also be applied to imaging scenarios beyond B-mode such as imaging blood flow.



Classification of Spinal Curvature from 3D Spine CT Images using a Convolutional Neural NetworkGeoff Klein^{1,2}, Michael Hardistry^{1,4}, Isaac Carreno^{5,6}, Joel Finkelstein^{4,5,6}, Young Lee³, Arjun Sahgal^{1,3}, Cari Whyne^{1,4}, Anne Martel^{1,2}¹Physical Sciences, ⁵Division of Spine Surgery, ⁶Orthopaedic Surgery, Sunnybrook Research Institute; Department of ²Medical Biophysics, ³Radiation Oncology, ⁴Surgery, University of Toronto

Introduction: Approximately two-thirds of cancer patients develop bone metastases, with the spine being the most common location [1]. Vertebral metastases can lead to biomechanical instability, pain, and neurological compromise [1]. Stereotactic body radiation therapy (SBRT) delivers high-dose focal treatment to tumours; SBRT application to spinal metastases has been rapidly expanding because of its effectiveness for local tumour control. A significant side effect of SBRT is vertebral compression fracture, occurring in 10% to 40% of patients following SBRT. The broad goal of this work is to build automated, quantitative tools to aid clinical decision making related to mechanical stability and fracture risk in metastatically involved vertebrae. Spinal malalignment (scoliotic deformity characterised as abnormal lateral spinal curvature) is one measure that has been used in predicting vertebral fracture and progression following SBRT [2]. However, current evaluation of spinal malalignment, can be time consuming (requiring Cobb angle measurement) with significant inter-observer variation. As such, an automated algorithm to evaluate Cobb angle in 3D Computed Tomography (CT) scans was developed and applied to patients with spinal metastasis treated with SBRT.

Methods: A 3D U-Net [3] model [4] which determined a Gaussian heatmap for spine localization. Using the heatmap a spline curve was calculated and projected into the coronal plane. The gradient of the spline was determined and the Cobb angle is extracted from the spline [5]. To account for varying voxel spacing and the number of vertebrae in the field-of-view, we used the median angle from an axially sliding window.

Data: The VerSe 2019 dataset [6][7] was used to train the 3D U-Net to predict the Gaussian heatmaps of the spine. Vertebral body centroid ground truth labels were used to generate the Gaussian heatmaps. Scans were augmented for training by random resampling isotropic voxel spacing between 3.5- and 6-mm, as well as affine and deformation transformations, and finally cropped/padded to a 128 x 128 x 64 grid. An in-house dataset from diagnostic imaging (45 CT scans including spines with malalignment) was then used for parameter tuning to calculate Cobb angles from the predicted heatmaps. The method was then validated on an additional spine dataset collected for SBRT treatment planning (63 CT scans). The in-house data was a retrospective dataset of patients who underwent SBRT for spinal metastases where dosimetry calculations were done on the SBRT treatment planning images and diagnostic images were follow-ups after treatment. Scans in both showed a mix of malalignment in terms of existence and severity, surgical intervention (screws), metastases and vertebral fractures. Malalignment frequently extended beyond the field-of-view of the scan and pelvic involvement was common in the scans. Ground truth Cobb angles and scoliosis classification for the in-house datasets were conducted by a Spine Fellow. Ground truth and predicted angles above 10° were classified as scoliotic.

Results: The model was able to predict scoliosis with accuracy of 79.5% and 76.2% on the diagnostic imaging and SBRT planning datasets, respectively. The mean ground truth and predicted Cobb angles in the SBRT treatment planning were $8.8^\circ \pm 7.0^\circ$ (ranging from 0.8° to 28.0°) and $9.5^\circ \pm 7.5^\circ$ (ranging from 1.2° to 35.6°), respectively. The mean ground truth and predicted Cobb angles in the diagnostic imaging dataset were $8.5^\circ \pm 6.7^\circ$ (ranging from 0.2° to 28.6°) and $12.0^\circ \pm 12.6^\circ$ (ranging from 0.4° to 51.4°), respectively.

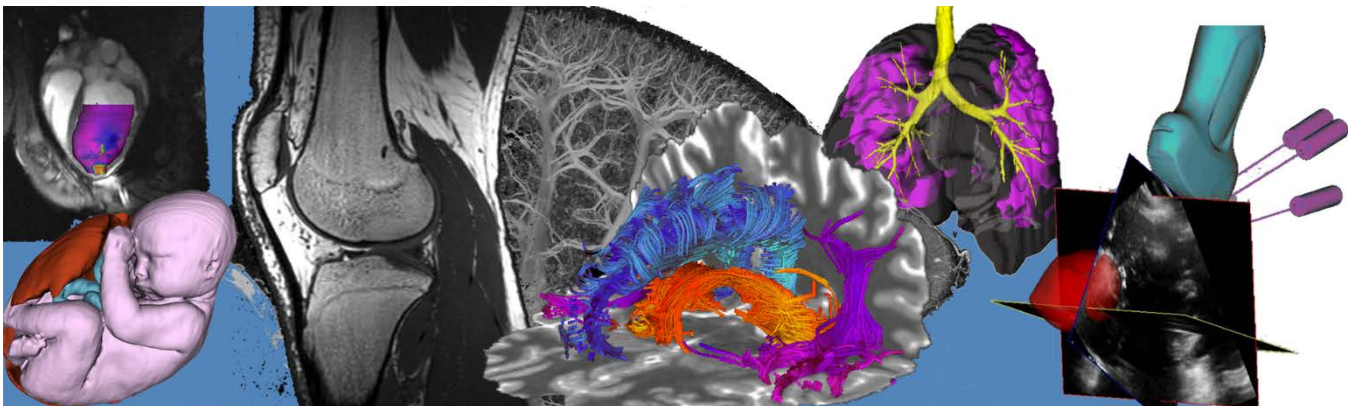
Conclusion: A fully automated model was constructed to predict scoliotic spinal curvature in 3D CT spine scans by evaluating the Cobb angle. Spinal curvature (scoliosis deformity) is contributing parameter for the SINS classification to determine instability. In its current form, spinal malalignment is a dichotomous variable, (present or absent), but what may be more useful is gradation of degree of deformity for outcome prediction. This algorithm can be used in clinical decision making to aid in spinal curvature classification and scoliosis severity assessment. Future work will focus on improving accuracy, expansion to kyphotic deformity, and combining with other image features related to fracture risk.

Acknowledgements: Varian Medical Systems, CIHR, and Feldberg Chair in Spinal Research at Sunnybrook.

References: [1] Maccauro, G. *et al. Int. J. Surg. Oncol.* **2011**, 107969 (2011). [2] M. V. R. Cunha *et al. Int. J. Radiat. Oncol.*, vol. 84, pp. e343–e349, Nov. 2012. [3] Ronneberger, O., P. Fischer & Brox, T. *MICCAI* **9351**, 234–241 (2015). [4] C. Payer *et al. Proc. 15th Int. Joint Conference on Comp. Vis.*, 2020. [5] F. Dubost *et al. Lecture Notes in Computer Science*, Oct. 2020, vol. 11963 LNCS. [6] M. T. Löffler *et al., Radiol. Artif. Intell.*, vol. 2, Jul. 2020. [7] A. Sekuboyina *et al., arXiv*. 2020.

Pitch Presentation Abstracts

Session 22: Machine Learning III



Domain Adaptation and Self-Supervised Learning for Surgical Margin Detection

A. Santilli¹, A. Jamzad¹, A. Sedghi¹, M. Kaufmann², K. Logan³, J. Wallis³, K. Ren³, N. Janssen¹, S. Merchant², J. Engel², D. McKay², S. Varma³, A. Wang³, G. Fichtinger¹, J. Rudan² and P. Mousavi¹

¹School of Computing, Queen's University, ²Department of Surgery, Queen's University, ³Department of Pathology, Queen's University

Introduction: Breast cancer is the most frequent cancer in women worldwide [1]. Breast conserving surgery (BCS) has become the standard treatment for early-stage breast cancer. The goal of BCS is to remove the complete tumor while leaving behind as much healthy tissue as possible. One of the main challenges of BCS is removing all of the cancerous tissue in the first surgery. If the tumor is not palpable, the surgeon may accidentally leave behind a portion of the tumor, resulting in a positive margin which demands repeat surgery. The current positive margin rate is around 35% [2]. The iKnife is a modality that was developed to address the challenges surrounding intraoperative margin detection through the real time analysis of tissue using rapid evaporative ionization mass spectrometry (REIMS). To achieve real-time feedback of tissue typing, we first need to develop a recognition model. One of the main difficulties faced when developing a real time tissue detection model with the iKnife is the collection and labelling of a training dataset. The destructive nature of the cautery tip during data collection and the sensitivities associated with affecting routine pathology assessment make acquisition of breast cancer burns intensive and time consuming. We propose a method of domain adaptation for classification. In our application, we use data from a more easily accessible tissue type, basal cell carcinoma (BCC), to train a model on the shared domain features of iKnife. We demonstrate the use of self-supervised domain adaptation for creating a generalizable and high performing classification model for breast cancer iKnife data. **Methods:** All burns were collected using the iKnife. *Breast Data:* We collected 144 burns (41 tumor and 103 normal) from 11 patients. The classification model was then trained using 4-fold cross validation. *BCC Data:* Fresh BCC specimens were obtained from patients treated at the out-patient skin clinic. We have a skin dataset of 320 BCC burns (129 tumor, 191 normal), taken over 6 clinic days from 51 patients. Figure 1 depicts the architecture used for our 2- part model. On the top, we display the curation and training of the relative patch algorithm [3]. This self-supervised method was trained using BCC data. Through the reassembly of the shuffled

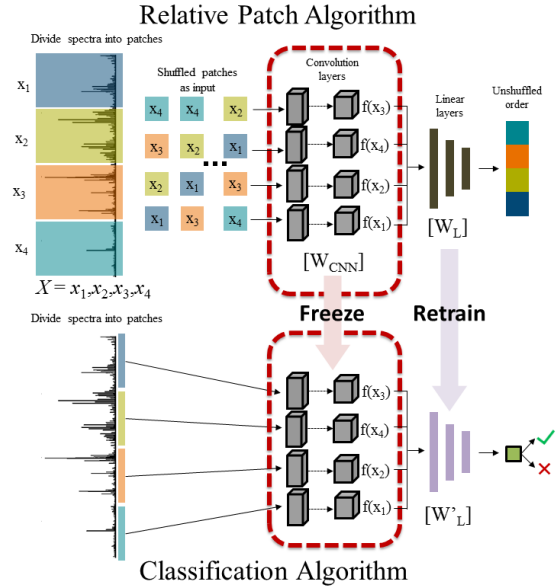


Fig 1: Overview of the network architecture and workflow

Table 1: Table shows the performance metrics of the classifier after training the paired self-supervised learning model with the given training and validation sets in the left most columns.

Self-supervised Training Set	Classification Performance on Breast Data			
	Accuracy	Sensitivity	Specificity	AUC (std)
Train: Skin Validation: Skin	92.27 (5.7)	89.17 (10.4)	95.75 (8.5)	90.63 (7.32)
Train: Skin Validation: Breast	92.68 (5.2)	88.45 (9.1)	96.37 (5.7)	92.74 (6.17)
Train: Skin + Breast Validation: Breast	89.31 (7.2)	65.75 (22.1)	98.25 (3.5)	82.12 (13.7)
Train: Breast Validation: Breast	88.56 (7.3)	78.33 (20.2)	91.71 (11.6)	85.42 (9.1)
Baseline Model no self-supervised training	90.74 (5.6)	71.20 (19.0)	98.25 (3.1)	84.83 (9.4)

influence of added data diversity in the form of a pretraining task to maximize classification performance. We show that having a limited number of breast data for training the cancer classification model, can be compensated by self-supervised learning on a set of unlabeled skin data.

References: [1] B.W. Stewart "World cancer report," 2014 [2] B.W. Maloney. (2018) doi: 10.1117/1.JBO.23.10.100901. [3] M. Noroozi and P. Favaro (2016), arXiv: 1603.09246

Investigating the Effects of Transfer learning on Medical Ultrasound Models

Authors: Calvin Zhu^{[1][3]}, Dr. T. E. Doyle^{[1][2][4]}, Dr. M. D. Noseworthy^{[1][2][3]}

[1] McMaster University School of Biomedical Engineering, [2] McMaster University Department of Electrical and Computer Engineering, [3] St. Joseph's Healthcare, Imaging Research Centre, [4] Faculty Affiliate, Vector Institute for Artificial Intelligence

Introduction: Ultrasound (US) is the most widely used medical imaging modality due to its low cost, portability, and use of non-ionizing radiation. However, US is heavily operator dependent and successful imaging requires trained expertise. Many are turning to deep learning (DL) models with transfer learning to assist US operators and support medical advisory systems; however, we have identified two primary issues with this approach.^[1] First, DL models are less successful when the training data is not fully representative of the problem.^[2] Second, the standard, generic training image datasets are incongruous with US imaging, which questions the validity of this method^[1]. This paper presents a methodology to address both issues by using US images for initial model training (increased congruence) and then employing transfer learning to other US imaging locations and equipment (improved representation). The goal of this paper is to investigate the use of pre-trained US models as a means to reduce the number of training images required for deployment compared to common methods.

Methods: A uniform gelatin phantom, with a 'mock tumour' was scanned using three different ultrasound machines (Siemens S3000, Clarius L15, and Ultrasonix SonixTouch) each with linear array transducers operating at 6MHz. Three dataset were generated for a total of 10,337 images: Set A (initial training, Siemens and Clarius) 6191 images, Set B (re-training, SonixTouch) 3184 images, and Set C (testing, SonixTouch) 962 images. Sample images are shown in Figure 1.

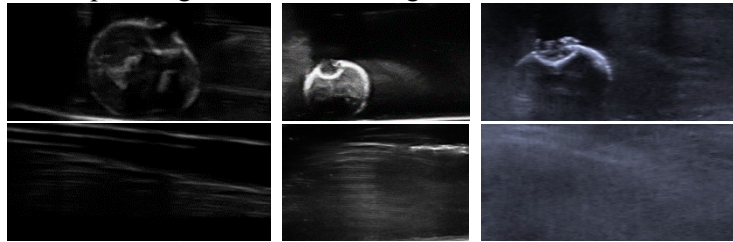


Figure 1: Sample Images. From left to right, Ultrasonix SonixTouch, Clarius L15, Siemens S3000.

Four DL models were trained in parallel using Xception and ResNet50 architectures to classify the presence of the 'mock tumour': M0, trained using Set A and Set B; M1, initialized with ImageNet weights and trained on Set B; M2, trained using only Set A; M3, initialized with Set A weights and trained on Set B with 1000 image increments. M0 and M1 present common methods. M2 in our opinion presents a likely clinical dataset. M3 presents our transfer learning approach. Accuracies are calculated based on number of correct classifications on a combined dataset consisting of images from Set C.

Results:

Model	Testing Accuracy
0 - No Transfer	99.68 %
1- ImageNet Transfer	100 %
2 - Ultrasound No Transfer	92.51 %
3 - Ultrasound With Transfer	98.36 %

Table 1: Xception Models

Model	Testing Accuracy
0 - No Transfer	94.69 %
1 - ImageNet Transfer	85.75 %
2 - Ultrasound No Transfer	45.84 %
3 - Ultrasound With Transfer	83.16 %

Table 2: ResNet50 Models

Conclusion: Models without transfer learning, but large amounts of varied data appear to have the best performance. In practice, it is not feasible to collect sufficient data from every ultrasound machine in use. This work shows the potential for transfer learning to produce similar results with significantly less data.

References:

- [1] Maithra Raghu, Chiyuan Zhang, Jon Kleinberg, and Samy Bengio. Transfusion: Understanding transfer learning for medical imaging. In H. Wallach, H. Larochelle, A. Beygelzimer, F. d'Alch'e-Buc, E. Fox, and R. Garnett, editors, Advances in Neural Information Processing Systems, volume 32, pages 3347–3357. Curran Associates, Inc., 2019.
- [2] Adarsh Subbaswamy and Suchi Saria. From development to deployment: dataset shift, causality, and shift-stable models in health AI. *Biostatistics*, 21(2):345–352, 11 2019

Healthcare Utilization Prediction Using CT Images and End-to-End Deep Convolutional Neural Network Learning Pipeline

Amir Moslemi MSc,¹ W C. Tan MD,² J. C. Hogg MD, PhD,² J. Bourbeau MD,³ and Miranda Kirby PhD^{1,2}

¹*Department of Physics, Ryerson University;* ²*Centre for Heart Lung Innovation, University of British Columbia, Vancouver;* ³*Montreal Chest Institute of the Royal Victoria Hospital, Canada.*

Introduction: Chronic obstructive pulmonary disease (COPD) is a debilitating and progressive lung disease. According to the Global Burden of Disease study¹, COPD was responsible for 3.2 million deaths in 2015, and both the number of deaths and prevalence of COPD are increasing. Further, hospitalization due to COPD is the 2nd leading cause of hospitalization in Canada, and the leading cause of repeat of hospitalization². Predicting COPD patients at an increased risk of hospitalization and other healthcare utilization is an important goal for COPD management. Although few studies have demonstrated computed tomography (CT) imaging can be used to predict hospitalizations in COPD³, these studies relied on engineered features, which may not capture all the relevant information in the image. Convolutional neural network (CNN) is a powerful tool that can be used for predictions based on large amounts of disparate data. Therefore, the objective of this study was to predict subsequent healthcare utilization in COPD using CNN.

Method: A total of 527 COPD participants from the Canadian Cohort of Obstructive Lung Disease (CanCOLD) study were evaluated and they had baseline CT images and healthcare utilization reported at follow-up: age=67±10 years, BMI= 28±5 kg/m², forced expiratory volume in 1s= 3.07±0.19 L. The mean time between the initial visit and follow-up was 2.28±0.23 years. Of these participants, 179 (35%) used healthcare services during the follow-up interval. In all participants, demographic information, spirometry and CT imaging was collected at the initial visit. A follow-up visit was performed and participants were asked for details related to healthcare utilization. Healthcare utilization was defined as any COPD hospitalization or emergency room visit in the 12 months prior to the follow-up visits. An end-to-end deep CNN pipeline was applied to the dataset for healthcare utilization prediction. The pipeline had two phases; data preparation and prediction. For data preparation, the lung was segmented by using V-Net and the lung was divided to patches of 32*32. For healthcare utilization prediction, three layers convolutions were used for feature extraction and all the features were fed into a fully connected neural network. The “relu” was used as the activation function for the hidden layer to avoid a vanishing gradient, and the “sigmoid” layer was used for binary classification. The loss function and optimizer were “cross-entropy” and “adam”, respectively. A fixed learning rate of 0.0001 was used and the model was trained for 100 epochs with a batch size of 128 using Keras with a Tensor Flow backend. To prevent overfitting in the fully connected layer, 20% dropout considered. Out of a total of 527 CT images, 3703 patches were generated; we considered 70% for training, 10% for validation and 20% for test data. The network was tested on patches.

Result: The classification results for test data were accuracy=75%, F1-score=71%, recall=70.6%, precision=70.5% and Matthews Correlation Coefficient (MCC)=0.50. Patching the images increased the number of the training set and therefore decreased the probability of overfitting. The lung was segmented as region of interest by V-Net and patches were generated from this region of interest that could be useful to acquire essential information for classification. The performance was increased by optimizing the parameters of the deep learning algorithm, including the number of epochs and batch size.

Conclusion: We presented a patch-based Convolutional Neural Network (CNN) model with a supervised decision to predict future healthcare utilization in COPD participants. This system can be used as an application to predict future hospitalization or can be used to identify high risk patients for more monitoring.

References:

[1] Mathers CD, et al. PLoS Med. 2006;3(11):e442; [2] Canadian Institute for Health Information, Health Indicators 2008; [3] A.Moslemi et al. 2020 European Respiratory Journal 56:2082

Chronic Obstructive Pulmonary Disease and Asthma Differentiation by Dimension Reduction Based on Perturbation Theory for High Dimensional Quantitative CT Biomarkers

Amir Moslemi MSc¹ and Miranda Kirby PhD^{1,2}

¹Department of Physics, Ryerson University; ²Centre for Heart Lung Innovation, University of British Columbia

Introduction: Chronic obstructive pulmonary disease (COPD) and asthma are leading causes of hospitalization in Canada.¹ There are considerable similarities between the symptoms in COPD and asthma patients, and misdiagnosis has been reported.² Importantly, COPD and asthma have different treatment recommendations, and therefore misdiagnosis can lead to inappropriate treatment, and poor patient outcomes. Differentiation of these two diseases is essential for proper patient management. Computed tomography (CT) imaging can quantify lung disease features, and a previous study has shown that there are structural differences in the airways and parenchyma features between COPD and asthma.³ However, this study investigated each CT feature independently, and therefore it is unknown whether CT can discriminate with high accuracy whether a patient has COPD or asthma. Therefore, the objective of this study was discriminate COPD and asthma using CT quantitative features and machine learning. We hypothesized that by undertaking a robust machine learning method in terms of feature selection and training, COPD and asthma can be discriminated by CT features.

Method: Asthma and COPD patients were recruited from Thoraxklinik at Heidelberg University Hospital (Heidelberg, Germany). A total 59 subjects were investigated; n=24 COPD and n=35 asthma. There was no significant difference between the COPD and asthma participants for age, BMI or lung function measured by the forced expiratory volume in 1s. CT images were acquired at full-inspiration and full-expiration. All quantitative CT measures were generated by VIDA (Coralville, IA, USA). A total of CT imaging features were investigated, including the CT features for the whole lung (WL) and in regions of interest (RUL=right upper lobe, RML=right middle lobe, RLL=right lower lobe, LUL=left upper lobe). Select CT parenchymal features investigated include: low attenuation areas of the lung below -950HU (LAA₉₅₀), and CT attenuation value at the 15th percentile (HU15). CT airway dimension features selected were the airway lumen inner perimeter (Pi). The full-inspiration and full-expiration CT images underwent deformable image registration, and each voxel was classified as normal (Norm), small airway disease (fSAD) or emphysema (Emph); two different classification approaches were utilized the parametric response map (PRM)⁴ and the disease probability map (DPM).⁵ Dimension Reduction Based on Perturbation Theory (DRPT) is an unsupervised technique for feature selection. This technique solves $Ax=b$ and $(A+E)\hat{x}=b$ by the normal equation technique to calculate x and \hat{x} and $\Delta x=x-\hat{x}$ (A =original feature matrix, E =perturbation matrix and b =target). $x=(A^T A)^{-1} A^T b$ and $\hat{x}=((A+E)^T (A+E))^{-1} (A+E)^T b$, where T is the transpose and so Δx shows the correlation of each feature with other features. K-means algorithm was applied to cluster the features that have similar Δx . The features were then ranked by measuring the entropy in each cluster.⁶ The top features were selected and SVM was used to discriminate COPD and asthma participants, as a binary classification problem. The data was divided into training and testing, and the average of 100 runs were reported.

Results: The features selected included: RML Pi, LUL Pi, RLL LAA₉₅₀, WL HU15, WL PRM_{Norm}, and WL DPM_{Norm}. Classification of asthma and COPD using these selected features yielded an accuracy=72%, precision=67%, recall=73%, F1-score=72% and AUC=73%. The top 5, top 6 and top 7 features were assessed and the top 6 features achieved the highest accuracy.

Conclusion: Quantitative CT imaging in combination with machine learning can discriminate COPD and asthma patients using only 6 CT features with moderate accuracy. The DRPT technique selected both airway and emphysema features as the top features for discriminating COPD and asthma. DRPT is an unsupervised technique, and can be categorized as filter-based feature selection, therefore it decreases the probability of overfitting for. Future studies will compare the proposed approach feature selection with other methods in feature selection.

References

- [1] Canadian Institute for Health Information, Health Indicators 2008. (Ottawa: CIHI, 2008) [2] Tinkelman, DG. *et. al. Journal of Asthma*, 43:75–80, 2006; [3] Choi, S. *et. al. BMJ Open Resp Res.* 9;4(1):e00252, 2017; [4] Galban CJ., *et. al. Nat Med.* 18:1711–1715, 2012; [5] Kirby, M. *et. al. Respiration* 94(4), 336–345, 2017; [6] Afshar, M. *et. al. Knowledge-based Systems.* 206:106370, 2020.

From pixels to cells: Development of biologically guided segmentation strategies for quantitative image analysis to interrogate single-cell data on multiplex immunostained tissue sections

Mark Zaidi^{1,2}, Veronica Cojocari¹, Trevor D. McKee^{1,3,4}

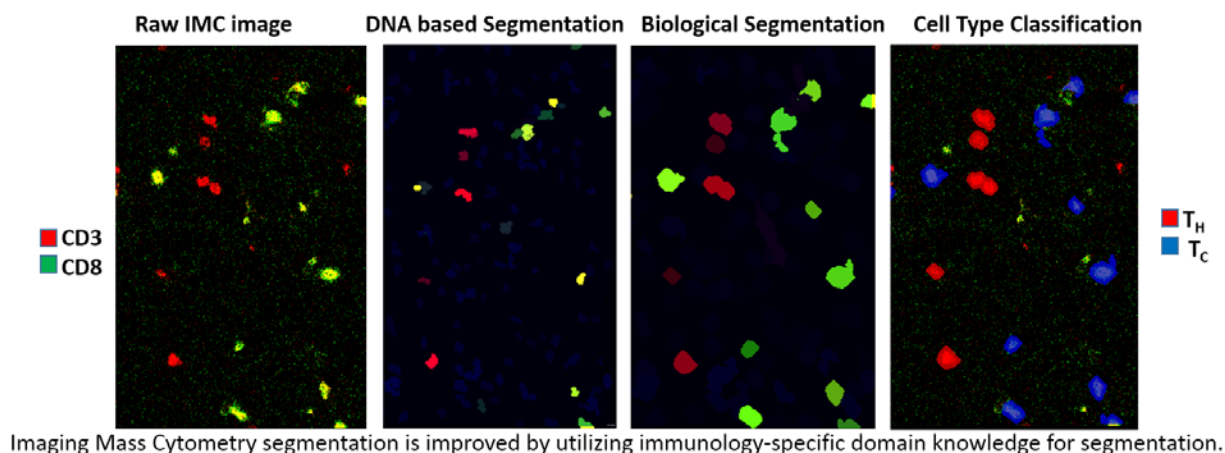
¹ Computational Pathology & Image Analysis Core, STTARR Innovation Centre, University Health Network, Toronto, Canada. ²Department of Medical Biophysics, University of Toronto, Toronto, Canada.

³Department of Laboratory Medicine and Pathobiology, University of Toronto, Toronto, Canada.

⁴Temerty Centre for AI Research and Education in Medicine, University of Toronto, Toronto, Canada.

Email: trevor.mckee@utoronto.ca

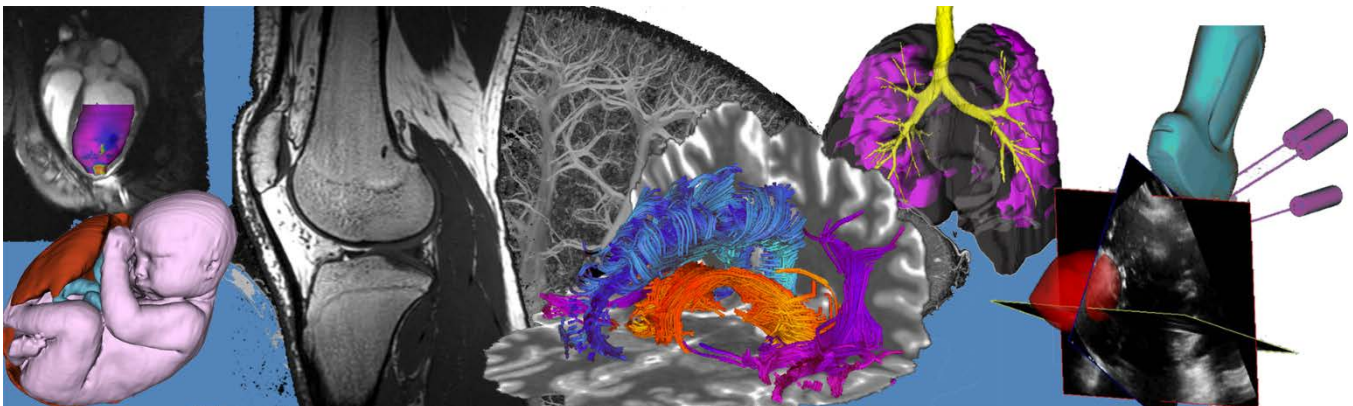
Background: The advent of highly multiplexed methods for antibody staining, including both imaging mass cytometry and multiplex fluorescence, allows for precise understanding of relationships between multiple protein biomarkers. These methods have advanced the capability to perform “tissue cytometry” – flow cytometry-like analysis on tissue sections. However, a major challenge for effective implementation of cytometric analysis on multiplex images remains the availability of robust segmentation algorithms to break the image into sub-regions representing single cells. **Methods:** Our core facility, working in close collaboration with several laboratories, have developed image segmentation pipelines for handling immune cell segmentation, that take into account the biological domain knowledge (i.e., which specific marker combinations are permissible on immune cells) to assist with cell segmentation. We apply cell type specific masks in a sequential fashion to guide the segmentation in such a way as to avoid the appearance of “biologically impossible” marker combinations. An example utilizing Tcytotoxic and Thelper markers to improve on segmentation that would otherwise just use nuclear localization is shown in figure 1 below. **Results & Conclusions:** Biologically-guided segmentation has successfully been applied to a number of tissues stained with multiplex imaging mass cytometry approaches. Validation against manual annotations reveal an improvement in the accuracy of segmentation over traditional image analysis methodologies. In one study, a random forest classifier was applied to differentiate immune cell populations, reaching an accuracy of 0.87, f1-score (macro) of 0.84, precision of 0.86 and recall of 0.88. Visualizations adopted from flow cytometric analysis including scatterplots allow for accurate image-based thresholds for cell identification; This modified strategy allows for a more thorough interrogation of the resulting dataset, assessing not only distinct cellular populations, but also spatial relationships between distinct populations, providing a robust methodology to assess immune cell subpopulations in a spatial context.



Imaging Mass Cytometry segmentation is improved by utilizing immunology-specific domain knowledge for segmentation.

Pitch Presentation Abstracts

Session 23: MR Imaging



Loading Characteristics and Viability of Stem Cell-Derived Alveolar-Like Macrophages Tagged with Perfluoropolyether for ^{19}F MRI of Chronic Lung Disease

Janny Kim^{1,2}, Michael Litvack¹, Daniel Li¹, Brandon Zanette¹, Martin Post^{1,2}, Giles Santyr^{1,2}

¹Translational Medicine Program, Peter Gilgan Center for Research and Learning, The Hospital for Sick Children, Toronto, ON, Canada. ²Department of Medical Biophysics, University of Toronto, Toronto, ON, Canada.

Introduction: In bronchopulmonary dysplasia (BPD) patients, altered innate immune activation and inflammatory signaling inhibit branching morphogenesis in lungs¹. Stem cell-derived alveolar-like macrophages (ALMs) have been shown to treat similar lung injury in animal models by promoting gas exchange and tissue repair². In order for ALMs to be used as therapeutics, a non-invasive imaging modality to guide treatment and monitor improvement is essential. Magnetic Resonance Imaging (MRI) is a non-invasive imaging technique, suitable for longitudinal monitoring of cells. In particular, hyperpolarized (HP) ^{129}Xe MRI in combination with superparamagnetic iron oxide nanoparticles (SPIONs) has been used to track ALMs in the airways of the rat lung regionally 1 hour post-instillation³. However, HP ^{129}Xe MRI requires expensive polarizing equipment and invasive mechanical ventilation to deliver the gas precluding longitudinal studies. Fluorine-19 (^{19}F) MRI of fluorinated compounds does not require mechanical ventilation and is a potential imaging technique to track ALMs non-invasively and longitudinally in the lungs. In preparation for longitudinal in vivo ^{19}F MRI, the loading and viability of perfluoropolyether-labeled ALMs were investigated to determine optimum conditions.

Methods: ALMs were produced and cultured following the protocols of Litvack et al² and Riberdy et al³. Perfluoropolyether (PFPE)-based agent, CS-ATM DM Green (CelSense Inc., Pittsburgh, PA), was used to investigate the effects of fluorinated compounds on ALMs. FITC fluorophores in PFPEs allow us to measure the fluorescence of PFPE-labeled cells. Various concentrations of PFPEs with different co-incubation times were tested using flow cytometry with a Beckman Coulter Gallios 10/3 flow cytometer and analyzed using Kaluza data analysis software (Beckman Coulter, Mississauga, Canada). ALMs were labeled with 0%, 1%, 2%, and 4% PFPEs, corresponding to 0, 1.2, 2.4, 4.8 mg perfluorocarbon emulsion/mL. Four-hour co-incubation timepoint was tested once initially as a starting point. More efficient co-incubation times, thirty minutes, one hour, and two hours, were then tested to determine the optimal loading conditions. Cells were stained using 7-AAD viability staining solution (Invitrogen) by incubating for 10 minutes in ice before running flow cytometry. The experiments were repeated three times.

Results: Flow cytometry results indicate that 4% PFPEs with two hours of co-incubation time is optimum for ALMs. The four-hour co-incubation time did not show much difference when compared to the two-hour co-incubation time as shown in Figure 1. Thus, the experiments afterwards were done with shorter co-incubation times. Figure 2 shows the shift in fluorescence in PFPE-labeled cells with different concentration compared to cells with 0% PFPEs (unlabeled control). 4% PFPEs show the greatest uptake by ALMs, since larger shift from the control indicates more cells with stronger fluorescence. The inset to Figure 2 represents the average loading of PFPEs from the three repeated experiments with two hours of co-incubation time. It is observed that the graph reaches a plateau between 2% and 4%, suggesting that increasing PFPE concentration beyond 4% provides minimal benefit. The average viability of 4% PFPE labeled cells was 94.33% (data not shown).

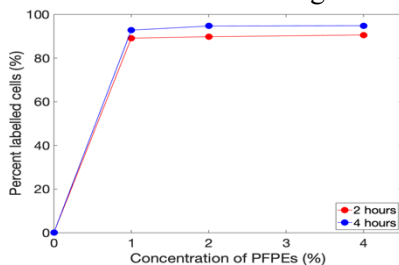


Figure 1: Loading of PFPEs at two hours and four hours of co-incubation

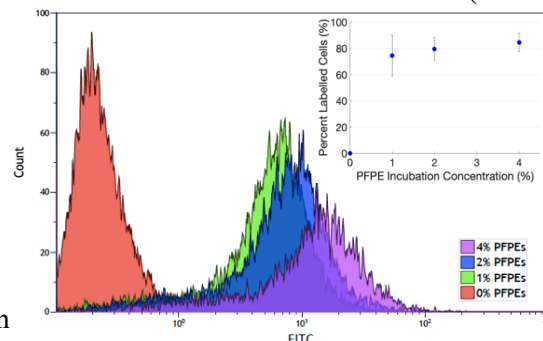


Figure 2: Histogram overlays of different PFPE concentrations. Inset: Average percentage of labeled cells as a function of PFPE concentrations. The error bars are standard deviations of three repeated experiments.

Conclusion: The optimum loading concentration of PFPEs in ALMs was 4% PFPEs with 2 hours of co-incubation. These conditions will be used in future studies to image cells using ^{19}F MRI both in vitro and in vivo in rat lungs. For longitudinal studies, loading and viability of PFPEs for longer periods of time (~2 weeks) will be investigated, taking into account cell differentiation. **References:** [1] Blackwell, T. S. et al. *J Immunol*, 2011. [2] Litvack M. et al. *Am J Respir Crit Care Med*. 2016. [3] Riberdy, V. et al, *Magnetic Resonance in Medicine*, 2019. The authors would like to thank NSERC and OGS for funding and support.

Synthesis and Evaluation of [^{18}F]meta-fluorobenzylguanidine For Cardiac Sympathetic Nerve Imaging

Uzair S. Ismailani^{1,2}, Ariel Buchler^{1,2}, Gedaliah Farber^{1,2}, Maxime Munch^{1,2}, Braeden Mair^{1,2}, Benjamin H. Rotstein, PhD^{1,2}

¹University of Ottawa, Ottawa, ON, Canada, ²University of Ottawa Heart Institute, Ottawa, ON, Canada.

Introduction: Downregulation or dysfunction of the cardiac norepinephrine transporter (NET) has been associated with the progression of heart failure (HF), ultimately resulting in left ventricular hypertrophy and the development of cardiac arrhythmias. Clinical trials report accurate prognosis of significant cardiac events using the single photon emission computer tomography (SPECT) imaging radiotracer iodine-123-metaiodobenzylguanidine ([^{123}I]MIBG) or the positron emission tomography (PET) imaging radiotracer [^{11}C]methoxyphenethylamine ([^{11}C]HED). However, due to semi-quantitative measures available with SPECT imaging, neither global downregulation of NET nor regional NET heterogeneity can be quantified. PET enables higher resolution imaging, and the ability to provide absolute quantification for sympathetic nerve density, as shown by [^{11}C]HED. Unfortunately, [^{11}C]HED exhibits high NET affinity, rendering this tracer insensitive to early changes in sympathetic nerve density. The objective of this study is to synthesize and evaluate the PET analog of [^{123}I]MIBG, [^{18}F]meta-fluorobenzylguanidine ([^{18}F]mFBG, fluorine-18 $t_{1/2}$ = 109.7 min) for sympathetic nerve imaging, as we hypothesize that this tracer will have i) slower and measurable uptake kinetics that represent NET density independent of blood flow; ii) reversible binding; 3) good metabolic stability.

Methods (n=4/grp): The evaluation of this tracer was performed in Sprague-Dawley rats. Ex vivo biodistribution (30-minute time point, analyzed using gamma counter) was performed to determine the baseline distribution of [^{18}F]mFBG in males and females (%ID/g). To establish NET selective radiotracer uptake into sympathetic neurons, two treatment groups were used: 1) pre-treatment with NET selective inhibitor desipramine (DMI, 1 mg/kg), followed by radiotracer injection after 10 minutes, 2) treatment cycle of 6-hydroxydopamine (6-OHDA), a drug known to cause destruction of sympathetic nerve terminals. PET imaging was performed on each treatment group. The NET-dependent reversibility of [^{18}F]mFBG was also investigated by PET (n=3/grp). Animals were dosed with the radiotracer, and DMI (1 mg/kg) was administered following peak myocardial uptake (10 min) to observe whether tracer washout occurred. Metabolic stability (percent intact tracer in protein free fractions) was determined in human serum (0-2 hours), male and female myocardia (30-minute time point), and plasma (n=2/group, 30-minute time point). Protein free fractions of all samples were acquired, and samples of filtered supernatant were injected onto an HPLC. Fractions were analyzed in a gamma counter to determine the percent intact tracer.

Results: [^{18}F]mFBG was routinely obtained from the automated synthesis module in 24% decay-corrected yield. Time-activity curves from initial PET scans revealed strong myocardial uptake that peaked after eight minutes, followed by an approximately linear washout rate over the next 50 minutes. Ex vivo biodistribution in males and females (%ID/g) revealed similar cardiac uptake of 3.45 ± 0.69 and 3.08 ± 0.59 . Differences in hepatic (0.54 ± 0.28 vs 0.90 ± 0.46), kidney (0.87 ± 0.05 vs 0.63 ± 0.09), blood (0.60 ± 0.03 vs 0.24 ± 0.08), and thyroid (1.29 ± 0.27 vs 1.77 ± 0.68) uptake was observed in males and females, respectively. DMI pre-treatment resulted in reduced uptake in the myocardium (3.45 ± 0.69 to 2.40 ± 0.23), spleen (0.99 ± 0.25 to 0.44 ± 0.11), and adrenal glands (1.59 ± 0.43 to 0.58 ± 0.37). In 6-OHDA treated rats, a 34% reduction in myocardial uptake (2.04 ± 0.07) was observed in comparison to those treated with vehicle (1.32 ± 0.27). PET studies indicate tracer reversibility is independent of the NET. The metabolic stability of [^{18}F]mFBG incubated in human serum was found to contain >96% of the parent tracer intact. The percent intact tracer in male and female myocardia was found to be $83 \pm 2.8\%$ and $86 \pm 7.7\%$, respectively. Plasma samples from males and females showed $21 \pm 2.1\%$ and $19 \pm 2.7\%$ of the parent tracer intact, respectively.

Conclusion: PET imaging and bio-distribution has displayed strong myocardial uptake of [^{18}F]mFBG in male and female rats, and tracer retention into sympathetic neurons via the NET has been observed to be a contributing mechanism to myocardial uptake. The tracer displays good metabolic stability in human serum, and in male and female myocardia, but is less stable in plasma. Altogether, [^{18}F]mFBG possesses favorable properties for imaging sympathetic nerves due to its slower myocardial uptake and rapid washout rate in comparison to currently available radiotracers. The utility of this tracer will be evaluated in higher species as significant uptake from extra-neural cardiomyocyte receptors is typically observed in rats.

Evaluation of gadolinium-loaded plaster as a potential means of characterizing antibiotic diffusion in MRI

Gregory Hong^{1,2,3}, Spencer Christiansen^{1,3}, Tina Khazaei^{1,2,3}, Santiago Cobos^{1,2,3}, Junmin Liu^{1,3}, Maria Drangova^{1,2,3}, David W Holdsworth^{1,2,3}

¹Robarts Research Institute, ²Western Bone and Joint Institute, ³Department of Medical Biophysics, Western University, London, Ontario, Canada

Introduction: The demand for hip and knee replacements continue to rise in Canada with a 17% increase in the number of arthroplasties performed over the past 5 years. Unfortunately, 9700 (7%) of these surgeries were for implant revisions. Infection is the most common reason for early revision (within 5 years of primary surgery) of both hip and knee replacements for arthritis.¹ The gold standard treatment of periprosthetic infection is to implant temporary antibiotic impregnated cement spacers in a 2-stage revision. This has the obvious downside of requiring two surgeries, with the associated cost and potentially problematic bone loss. We aim to address this concern with a 3D printed porous metal (titanium) scaffold with favorable mechanical properties that can be filled with antibiotics and deployed as a permanent cementless replacement for the failed solid implant. We have previously shown that artifact size and effective susceptibility are strongly correlated with porosity, resulting in reduced artifact around porous implants in MRI². Previous work in our lab quantified contrast agent diffusion in CT as a surrogate for antibiotic diffusion out of calcium sulfate³; We now look to similarly study the potential benefits of adding gadolinium contrast agent to calcium sulfate plaster for MRI based monitoring of antibiotic diffusion. This study aims to: 1) determine if the gadolinium diffusing out of the plaster provides signal enhancement and 2) quantify the concentration of the diffused gadolinium for use as a surrogate for tracking antibiotic elution

Methods: *Phantom design:* Cylindrical cores are made using calcium sulfate Plaster of Paris set in a mold with 17mm diameter and 40 mm height. The plaster is mixed with water containing a percentage of a gadolinium contrast agent (2.5-20%). The core is set in a custom 3D-printed plastic phantom that is filled with agar for the contrast agent to diffuse into. The agar filled container is placed in a holder that contains calibration vials (distilled water with varying amounts of Magnevist) and fiducial markers for registration.

Imaging: The phantom was scanned with a 3D multi-echo gradient echo sequence (32 channel head coil, 160x160x60 resolution, 160x160x60 mm FOV, TR = 47.7 ms, flip angle = 10, echo train length = 10). Scans were acquired at 1-hour, 5-hours, 9-hours, 3 days, and 7 days after setting the core in agar.

Analysis: Channel-by-channel images are reconstructed then combined and processed with the B0-NICE³ algorithm. Acquired images are aligned through iterative closest point registration of the marker centroids. The resulting quantitative maps were radially averaged around the central plaster core with line profiles spaced 10° apart across 5 contiguous slices.

Results: Magnitude images of plaster cores with gadolinium concentration >10% show visual signs of susceptibility artifact. Magnitude images (figure 1) clearly shows gadolinium diffusion through the agar volume over time through signal enhancement. Quantitative R2* measurements, which are proportional to Gd concentration, show small but significant (P<0.05) increases over time.

Conclusions: We have demonstrated that adding a gadolinium contrast agent to a calcium sulfate core improves signal in the surrounding volume. There is evidence that MRI is useful in quantifying the concentration of the diffused gadolinium. The addition of gadolinium contrast agent to antibiotic loaded calcium sulfate looks to be a promising surrogate for monitoring antibiotic elution with MRI.

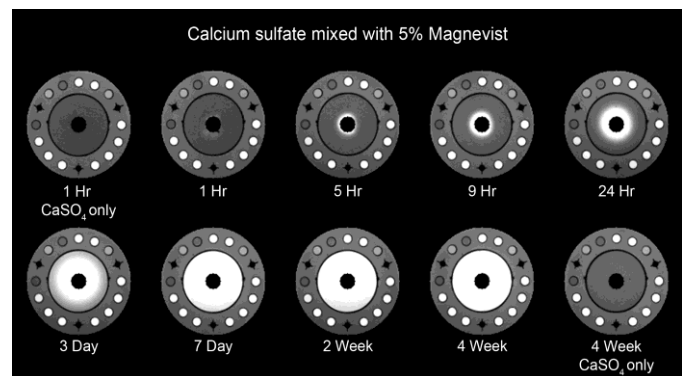


Figure 1: Magnitude images showing diffusion of Magnevist contrast agent out of calcium sulfate core

1. Canadian Institute for Health Information. Hip and Knee Replacements in Canada, 2017–2018: CJRR Annual Report. Ottawa, ON: CIHI; 2019.
2. Hong G. *et al.* MRI characterization of a novel porous 3D printed metal scaffold. In: Proceedings of the 2020 IMNO Symposium; 2020
3. Khazaei, T., "Characterization and Enhancement of Local Drug Delivery in Orthopaedic Infection" (2020). Electronic Thesis and Dissertation Repository. 6851 <https://ir.lib.uwo.ca/etd/6851>
4. Liu, J. *et al.*: Single multi-echo GRE acquisition with short and long echo spacing for simultaneous quantitative mapping of fat fraction, B0 inhomogeneity, and susceptibility. 2018 Neuroimage

pH-Weighted Chemical Exchange Saturation Transfer (CEST) MRI in the Spine

Alicia Cronin^{*1,2}, Patrick Liebig³, Sarah Detombe⁴, Neil Duggal⁴, and Robert Bartha^{1,2}

¹Department of Medical Biophysics; ²Centre for Functional and Metabolic Mapping, Robarts Research Institute, The University of Western Ontario; ³Siemens Healthineers, Erlangen Germany; and ⁴Department of Clinical Neurological Sciences, University Hospital, London Health Sciences Centre

Introduction: Degenerative cervical myelopathy (DCM) is a unique model of spinal cord injury that can result in spinal cord compression and neurological dysfunction.¹ Pathophysiological mechanisms, like ischemia and hypoxia in the spinal cord, could impact recovery after surgery but direct in-vivo evidence of such changes has been limited in humans. Chemical Exchange Saturation Transfer (CEST) is a relatively new MRI contrast method that produces image contrast based on the rate of exchange between protons in amine and amide groups within tissue and bulk water protons as an example. Since exchange rate is pH dependent, CEST images can be acquired with pH-weighting using a ratiometric method called amine/amide concentration-independent detection (AACID).² However, the spinal cord is in close proximity to the lungs. Consequently, CEST image acquisition is complicated by motion artefacts and magnetic susceptibility changes during data acquisition that cause signal fluctuations. Spinal cord CEST could have widespread applications in understanding disease processes, however a method to overcome these artefacts needs to be developed first. The objective of this study is to develop AACID CEST MRI on a 3.0 T Siemens system incorporating respiratory correction, with sufficient sensitivity and resolution to characterize the pH heterogeneity in the spine in DCM patients.

Methods: In collaboration with Siemens, a prototype CEST package was used on a 3.0 T Siemens Prisma Fit MRI scanner. The CEST sequence incorporates a single slice 2D gradient echo (GRE) readout and initial optimization was performed in the brain to avoid motion artefacts. CEST saturation was performed with 21 Gaussian shaped pulses ($B_1=1\ \mu\text{T}$, total saturation time of 1.9 s), applied at 91 offsets from -6.5 ppm to 6.5 ppm. Other relevant parameters include: TR/TE = 10.0/4.4 ms, voxel size = 1.5 mm x 1.5 mm, slice thickness = 5 mm, 2 averages. The respiratory cycle was monitored throughout CEST acquisition using the respiratory bellows to determine respiration volume per unit time (RVT), defined by dividing the range of the cycle magnitude by the mean respiration time between peaks.³ Non-saturated scans were interleaved throughout the acquisition to account for variation of intensity resulting from the global effect of respiration. A respiratory correction was applied by scaling the RVT using the global effect to regress signal variation due to breathing out of the data. Healthy subjects will be recruited to determine the reproducibility of the pH measurements in the cord using the proposed correction.

Results: Initial optimization of the AACID CEST imaging method was completed in the brain of a healthy subject. Currently, optimization is being performed in the spinal cord and the retrospective respiratory correction algorithm is being implemented in MATLAB. Figure 1 demonstrates a spinal cord CEST image and spectrum successfully acquired with interleaved non-saturated scans. The interleaved scans had a coefficient of variation of 1.28%.

Conclusion: The CEST sequence produced homogeneous AACID maps in the brain. The CEST sequence also produced high quality images in the spinal cord. The interleaving of the non-saturated scans demonstrates the expected global signal variation due to breathing. In the future, a respiratory correction will be implemented and tested on healthy subjects to determine the reproducibility of pH-weighted measurements. AACID CEST will then be performed on DCM patients to examine the heterogeneity of pH in the spinal cord near the site of compression.

References: [1] Toledano, M. & Bartleson, J. Neurol. Clin. 2013; [2] McVicar, N. et al. J. Cereb. Blood Flow & Metab. 2014; [3] By, S. et al. Magn. Reson. Med. 2018

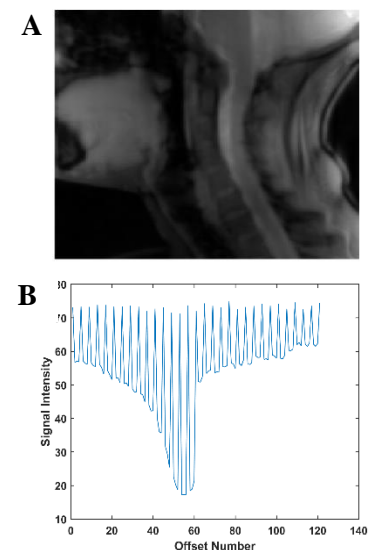


Figure 1:

A: Raw sagittal spinal cord CEST image.

B: Interleaved CEST spectrum of spinal cord

Modelling Cellular Iron-handling in Inflammation: P19 Cells Secrete Biologically-active HepcidinR. Prajapati¹, Q. Sun^{1,2,3}, F.S. Prato^{1,2,3} and D.E. Goldhawk^{1,2,3}¹Imaging Program, Lawson Health Research Institute, ²Medical Biophysics and ³Collaborative Graduate Program in Molecular Imaging, Western University, London, Ontario, Canada

INTRODUCTION: Magnetic resonance imaging (MRI) may provide a suitable non-invasive method to track cellular activity during inflammation [1]. This is due in part to the unique iron-handling abilities of monocytes [2] and their influence on magnetic resonance (MR) transverse relaxation rates. Pro-inflammatory cytokines that stimulate hepcidin secretion target the iron export (ferroportin, FPN) activity of monocytes and macrophages. These hepcidin-FPN interactions result in post-translational downregulation of the only known iron export protein in mammalian cells. Moreover, the selective endocrine activity of hepcidin may extend to paracrine/autocrine regulation within sites of inflammation [3]. Hepcidin-FPN interactions have been identified in P19 cells, which exhibit high iron import and export activities similar to alternatively-activated macrophages [1,4]. In addition to endocrine hepcidin regulation, the evidence suggests that P19 cells may also self-regulate FPN expression in an autocrine/paracrine fashion, presumably through hepcidin secretion [1]. To test this, FPN-expressing THP-1 monocytes were exposed to culture medium from P19 cells suspected of hepcidin secretion.

HYPOTHESIS: P19 cells secrete biologically-active hepcidin that degrades ferroportin in THP-1 monocytes.

METHODS: Mouse P19 embryonic carcinoma cells were cultured in α -MEM supplemented with 25 μ M ferric nitrate for 5-7 days [1]. To stimulate hepcidin secretion, iron supplement was removed and cells were further cultured in non-supplemented α -MEM for an additional 24 hours.

This stimulated medium, presumed to be enriched with hepcidin, was centrifuged at $1000 \times g$ for 2 min to remove any cells prior to diluting supernatants 1/2 with RPMI 1640 medium for culture with THP-1 monocytes. After 24 hours, THP-1 samples were harvested. Protein concentration was determined by the bicinchoninic acid (BCA) assay. THP-1 cells cultured in RPMI 1640 alone served as a control. Non-stimulated medium consisted of P19 cell supernatant not exposed to iron supplement. Relative changes in FPN and glyceraldehyde-3-phosphate dehydrogenase (GAPDH) protein levels were determined from western blots using primary rabbit antibodies to FPN and GAPDH, respectively. Images were captured using a Gel Doc XR+ Documentation System. Densitometry was performed using ImageLab software (Bio-Rad). Analysis of variance (ANOVA) and Tukey's honestly significant difference (HSD) test were performed with RStudio software.

RESULTS: Compared to both the control and non-stimulated condition, the level of FPN in monocytes decreased after treatment with stimulated medium (Fig. 1, $p < 0.01$). In these samples, evidence of lower molecular weight species revealed by FPN immunostaining (arrow, Fig. 1A) was consistent with post-translational degradation of FPN [5]. Using full-length FPN (~ 63 kDa) and densitometry, the ratio of FPN/GAPDH in THP-1 controls ($n = 4$) and non-stimulated THP-1 cultures ($n = 3$) was approximately 2-fold greater than the ratio obtained after treatment with stimulated media ($n = 7$, Fig. 1B).

CONCLUSIONS: Hepcidin activity is present in stimulated P19 cell medium, indicating the potential for autocrine/paracrine regulation of iron export activity in P19 cells. Given the influence of hepcidin on transverse relaxation rates [1], the possibility of autocrine/paracrine hepcidin activity in iron-exporting cell types [3,6], and the behaviour of monocytes during inflammation [3], hepcidin-FPN interactions may provide a suitable molecular imaging target for MR characterization of inflammation.

REFERENCES: [1] Alizadeh et al (2020) Sci Rep 10, 3163. [2] Coma et al (2010) Haematologica 95, 1814. [3] Theurl et al (2008) Blood 111, 2392. [4] Liu et al (2019) PLOS ONE 14, e0217842. [5] Goldhawk et al (2015) Magnetic Resonance Insights 8, 9. [6] Dassanayake (2019) MSc thesis.

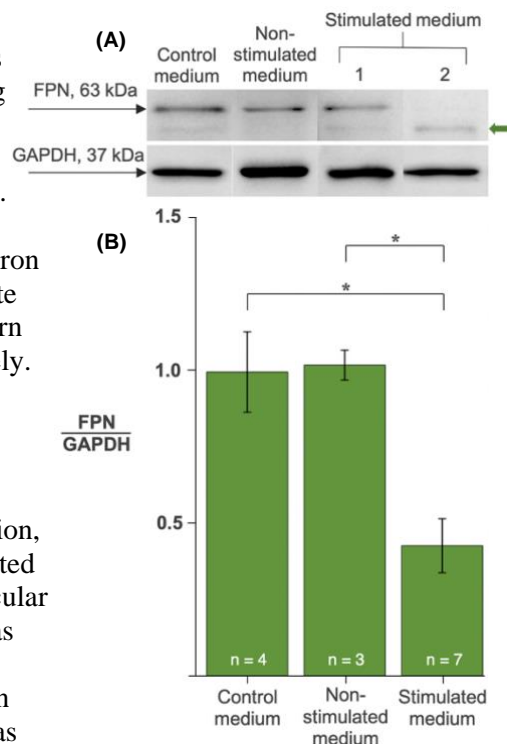


Fig. 1. Regulation of ferroportin levels in monocytes by secreted hepcidin activity. (A) FPN and GAPDH protein levels were determined from western blots. Each lane contains 20 μ g total cellular protein. (B) FPN levels are expressed as a ratio of FPN to GAPDH protein levels. Data is normalized to the control medium treatment. Values are the mean \pm SEM. *, $p < 0.01$.

Diffusion Tensor MRI Reveals Myocardial Fibre Architecture after Cell-Based Therapy in Myocardial Infarction

Moses Cook BSc¹; Wahiba Dhahri PhD^{2,4}; Graham A. Wright PhD^{1,3,5}; Michael A. Laflamme MD PhD^{2,4}; Nilesh R. Ghugre PhD^{1,3,5}

¹Department of Medical Biophysics, University of Toronto; ²McEwen Centre for Regenerative Medicine, University Health Network; ³Schulich Heart Research Program, Sunnybrook Research Institute; ⁴Toronto General Hospital Research Institute, University Health Network; ⁵Physical Sciences Platform, Sunnybrook Research Institute Toronto, ON, Canada

Introduction: Cardiac regenerative therapies using pluripotent stem cell-derived cardiomyocytes (PSC-CM) (the graft) have shown early promise in animal models of myocardial infarction (MI), however, in vivo response, therapeutic efficacy and the associated mechanisms of repair remain less understood. Magnetic Resonance Imaging (MRI) is non-invasive, is the gold standard measurement of cardiac function and tissue viability and offers advanced quantitative tissue characterization. Diffusion Tensor (DT) MRI has demonstrated the ability to quantify myocardial structure in other cardiac regenerative strategies. The objective of our study was to employ and optimize a 3D high-resolution DT-MRI protocol to localize and characterize structural changes in the infarct and cellular graft regions after PSC-CM transplantation in an ex vivo guinea pig model of MI.

Methods: Guinea pig hearts were cryoablated to induce infarction and infarct regions were injected either with PSC-CMs (n=4), vehicle (n=2), or healthy control (n=) on Week 2 post-MI. Hearts were harvested on Week 5 and perfusion fixed. Ex vivo MRI was performed on a 7T Bruker system. We utilized 3D DT-MRI (resolution 0.3x0.3x0.3 mm, b-value 700 s/mm², 30 diffusion directions) to quantify myocardial structure parameters such as fractional anisotropy (FA) and mean diffusivity (MD). Contrast enhancement (CE, resolution = 0.2x0.2x1 mm) was used to distinguish infarcted from healthy tissue via accumulation of gadolinium-DTPA (0.3ml/kg) injected prior to sacrifice. DT-MRI parameters were measured in infarct, graft and remote myocardial territories. Histological images were aligned to DT-MR images using local cardiac anatomical landmarks.

Results: PSC-CM engraftment was in agreement between CE-MRI and histology (Fig.1). Results are presented as mean \pm standard deviation. Cell therapy subjects demonstrated a higher level of FA within the engraftment (0.26 ± 0.0045) compared to the infarction (0.084 ± 0.0026 , $p < 0.0001$) (Fig. 2), and was similar to that of the healthy control (0.21 ± 0.064 , $p < 0.0001$). Likewise, MD of the graft region was not significantly different than that of the healthy control ($1016 \mu\text{m}^2\text{s}^{-1} \pm 148$ vs. $1009 \mu\text{m}^2\text{s}^{-1} \pm 207$ respectively, $p=0.41$) and was improved compared to infarct ($1770 \mu\text{m}^2\text{s}^{-1} \pm 208$, $p < 0.0002$). Overall, the DT-MRI measures within graft tissue were indicative of greater structural organization compared to the infarcted territory, similar to that in remote tissue, attributed to the presence of PSC-CM graft.

Conclusion: DT-MRI can help evaluate the degree of structural remodelling after MI and how host-graft structural integration can impact functional recovery. Future studies can incorporate in vivo MRI sequences to perform serial response to therapy.

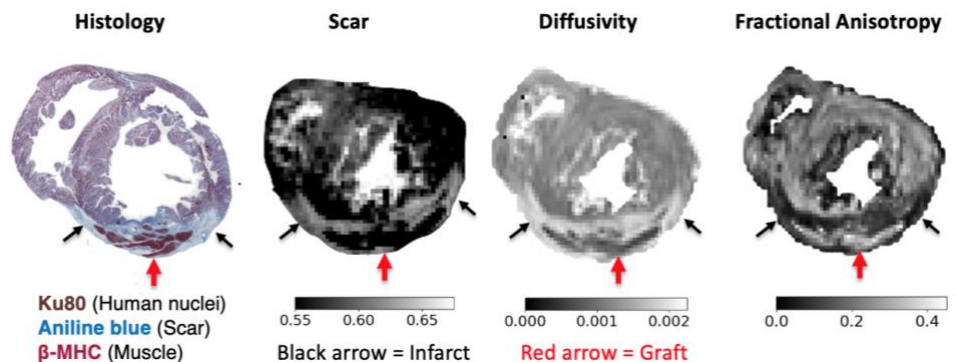


Figure 1: From left to right: Histological slice, CE-MR image, MD map and FA map showcasing graft adherence to anterior wall. Black arrows highlight infarction, red arrows highlight graft.

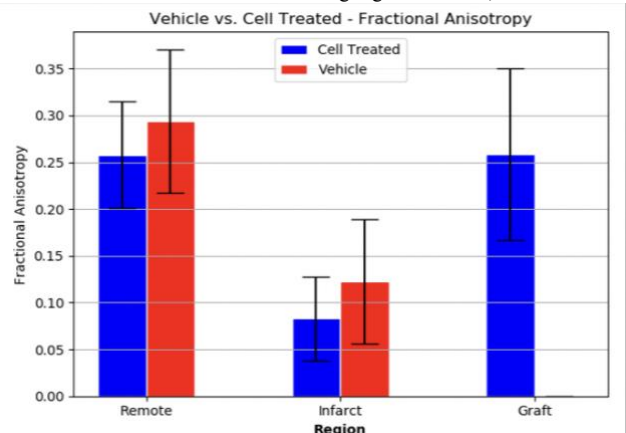


Figure 2: Fractional Anisotropy plot showcasing elevated FA within graft tissue

Fetoplacental and Maternal Body Composition Effects of Life Long Western Diet Consumption at Mid-Gestation Guinea Pig Pregnancy

Lindsay E. Morris¹, Flavien Delhaes², Lanette J. Friesen-Waldner¹, Trevor P. Wade¹, Lauren M. Smith¹, Mary-Ellen ET. Empey¹, Simran Sethi¹, Timothy RH. Regnault^{2,5,6}, Charles A. McKenzie^{1,6}

¹Medical Biophysics Western University, London, ON, Canada, ²Physiology and Pharmacology Western University, London, ON, Canada, ³Obstetrics and Gynaecology, Western University ⁶Division of Maternal, Fetal and Newborn Health, Children's Health Research Institute, London, ON, Canada

Introduction: The prevalence of energy-dense diets, such as the Western Diet¹ (WD), and sedentary lifestyles have increased dramatically over the last several decades.² The WD is predominantly composed of saturated fats and simple sugars.¹ WD consumption negatively impacts metabolic health, in association with altered body composition and liver steatosis.³ WD consumption is also associated with altered *in-utero* fetal metabolic programming and body composition,⁴ increasing the risk for later life metabolic disease.^{5,6} Previous research has focused on the effects of a maternal WD near-term,⁷ however, maternal metabolism changes throughout pregnancy. This current project focuses on identifying key markers using fetal and maternal imaging parameters at mid-term pregnancy. The project's objective was to investigate the effects of the life long WD on fetal and maternal body composition in a guinea pig pregnancy at mid-gestation.

Methods: Ten in-house-bred Dunkin-Hartley sows were randomly weaned onto either a WD (33% carbohydrates, 46% fat, 21% protein, n=6) or a control diet (CD, 60% carbohydrates, 18% fat, 22% protein, n=4). Following a first pregnancy, sows were mated at 259 ± 44 days. At ~38 days gestation (term ~ 68 days), each sow underwent an MRI exam.⁸ A total of 21 WD fetuses and 14 CD fetuses (litter size: 2-5 and 3-5, respectively) were imaged. T1-weighted and IDEAL water, fat, and proton density fat fraction (PDFF) images were acquired at 3T. Regions of interest (ROI) were thresholded and manually segmented in 3D Slicer around the whole body (WB), liver, subcutaneous adipose tissue (SAT), visceral adipose tissue (VAT), fetuses, and placentae on the T1-weighted and PDFF images to obtain the organ volumes and median PDFF values.⁹ SAT, VAT and total adipose tissue (TAT: SAT plus VAT) volumes were normalized to the WB volumes. The SAT/WB, VAT/WB and TAT/WB percentages, liver volumes and liver median PDFF values were compared between the two diets using an independent samples t-test in R. Placental and fetal volumes and PDFFs were analyzed using a linear mixed model (LMM), where the maternal sow was controlled for as a random variable.

Results: Maternal liver volume and median PDFF were significantly higher ($p < 0.05$) in WD than CD animals. The SAT/WB, VAT/WB and TAT/WB percentages were not significantly different ($p > 0.05$) between WD and CD groups. The elevation in the liver median PDFF was consistent with previous WD studies in near-term pregnancy sows.⁷ We observed differences in maternal liver composition but no differences between adipose tissue depots, highlighting a lean nonalcoholic fatty liver disease (NAFLD) phenotype, an observation that aligns with the concept that metabolically unhealthy individuals are not necessarily obese.³

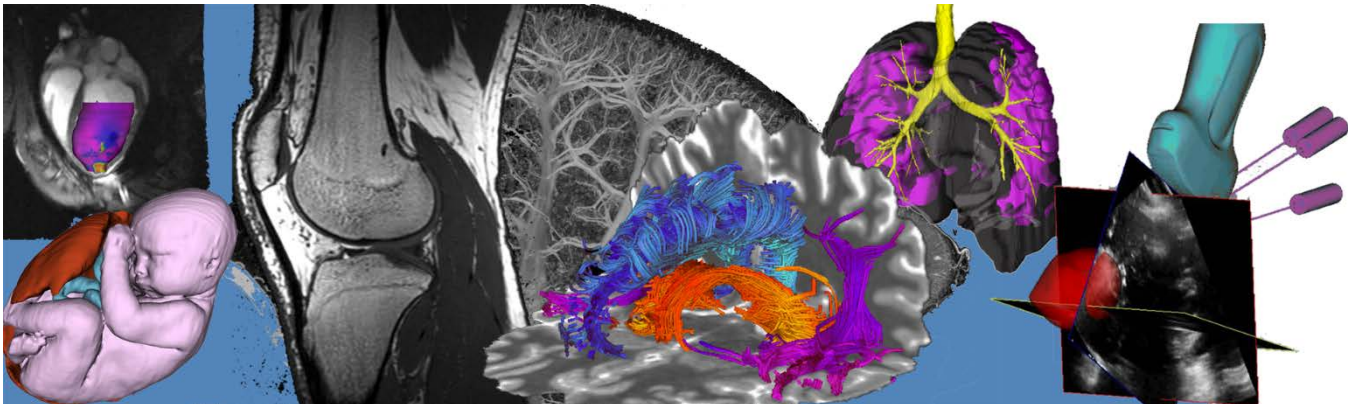
There were no significant differences ($p > 0.05$) between the maternal diets for fetal and placental volumes or median PDFFs. This outcome at mid-gestation suggests that a WD's potential impact is not observable at this stage in pregnancy. In contrast, differences have been reported in near-term WD exposed fetuses, displaying increased fetal volumes, and increased liver PDFFs.⁷ Increased TAT volume to fetal volume ratios, increased liver to fetal volume ratios, and decreased brain to fetal volume ratios were also observed.⁷

Conclusions: We analyzed the maternal, fetal and placental units separately to investigate how a lifelong WD affects body composition at mid-gestation. We conclude that the WD was associated with increased maternal liver lipid content, while observing no changes in SAT, VAT and TAT content. WD exposure did not alter the placental and fetal volumes relative to the CD at ~38 days gestation; long term effects may manifest after birth. A limitation of this study was the small sample size. Future work correlating the imaging data with collection measures will improve our understanding of the ontological effects of life long WD during pregnancy to help identify key fetal and maternal metabolic dysfunction biomarkers over pregnancy.

[1] Cordain, et al., *Am. J. Clin. Nutr.* 2005, [2] Hruby and Hu, *Pharmacoeconomics* 2015, [3] Osadnik, et al., *Nutr. J.* 2020, [4] Heerwagen, et al., *Am. J. Physiol. Regul. Integr. Comp. Physiol.* 2010, [5] Boney, et al. *Pediatrics* 2005, [6] Catalano, et al. *Am. J. Clin. Nutr.* 2009, [7] Sinclair, et al., *PLoS ONE* 2018, [8] Friesen-Waldner, et al., *J. Magn. Reson. Imaging* 2016, [9] Fedorov, et al. *Magn. Reson. Imaging* 2012.

Pitch Presentation Abstracts

Session 24: Cancer Imaging II



Multi-Modality Imaging Assessment of the Heart and Lungs Before and After Stage III Non-Small Cell Lung Cancer Radiotherapy

O Chau^{1,2}, H Young^{1,2,3}, K Burgers^{1,3}, T Lee^{1,3,4}, F Prato^{1,4}, G Wisenberg^{1,4}, S Gaede^{1,2,4}

(1) Western University, London, ON, CA, (2) London Regional Cancer Program, London, ON, CA, (3) Robarts Research Institute, London, ON, CA, (4) Lawson Health Research Institute, London, ON, CA

Introduction: Radiation therapy for non-small cell lung cancer is known to cause cardiac and lung toxicity in many patients. Multi-modality imaging can be used to assess the response of both the tumor and surrounding healthy tissue after radiation therapy. Imaging may also be used to develop patient-specific strategies for minimizing toxicity risk, such as ventilation-guided treatment.

Methods: Two Stage III non-small cell lung cancer (NSCLC) patients were imaged before and 6 weeks after radiotherapy; one with coronary artery stents (patient 1), and one with no previous cardiac history (patient 2). Both patients had primary tumors in the left upper lobe. The imaging protocol on the GE Revolution CT scanner consisted of two dynamic contrast-enhanced scans: rest and an adenosine-induced stress scan. ¹⁸F-FDG PET images were acquired on a Siemens 3T hybrid PET/MR scanner using a glucose suppression technique. Perfusion analysis of the heart and tumour was completed using CT-Perfusion5 software (GEHC). Myocardial perfusion reserve was calculated as the ratio of blood flow of stress/rest scans. End-inspiration and end-expiration images were non-rigidly registered using Elastix, and ventilation was calculated using an established density-based method. PET images were analyzed in MIM software. Myocardial mean standard uptake volume was compared using the standard six-segment model.

Results: A global increase in myocardial uptake and decrease in tumor uptake were observed with FDG-PET after treatment in both patients. In the dynamic contrast-enhanced CT perfusion imaging, myocardial perfusion reserve increased in some segments but decreased in others for patient 1, but decreased in all segments for patient 2. Tumor blood flow visually increased for both patients. CT specific ventilation in the treated lobe decreased after treatment for both patients.

Conclusions: Here we demonstrated the feasibility of collecting extensive functional imaging data with two imaging sessions before and after radiation therapy for NSCLC and showed that these methods are sensitive to changes 6 weeks after treatment and may suggest an acute inflammatory response. This protocol may be used to provide important patient-specific information for clinical decision making.

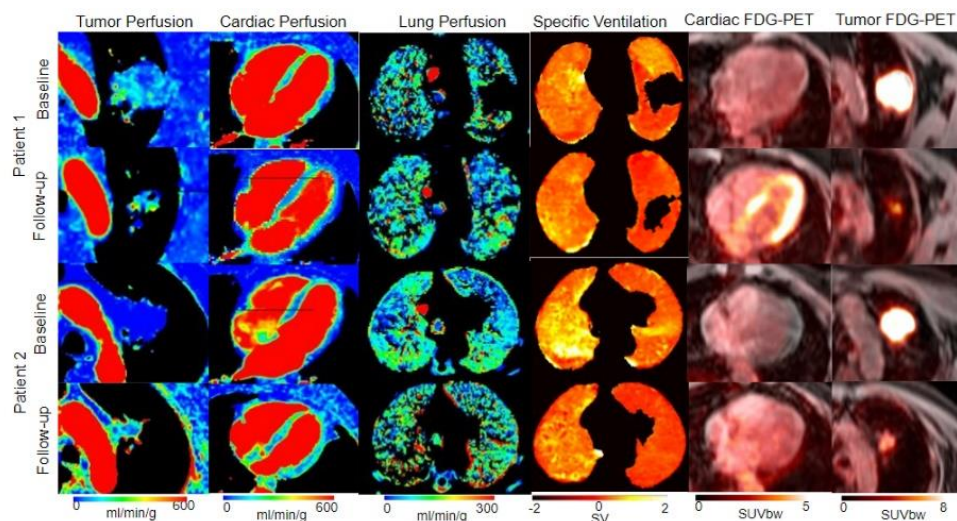


Figure 1. Representative slices from the multi-modality functional imaging acquired for patient 1 (top 2 lines) and patient 2 (bottom 2 lines). Tumor perfusion (column 1), cardiac perfusion (column 2), specific ventilation (column 3), cardiac FDG uptake (column 4) and tumor FDG uptake (column 5) are shown.

Optimization of Three-dimensional Ultrasound Acquisition Parameters for Diagnostic Evaluation of Thyroid Nodules

Viveka Sainani¹, Claire K. Park^{2,3}, Sam Papernick^{2,3}, David Tessier³, Kevin Barker³, Lori Gardi³, Aaron Fenster^{2,3}

¹Department of Medical Biophysics, Faculty of Sciences, ²Schulich School of Medicine and Dentistry, ³Imaging Research Laboratories Robarts Research Institute, Western University, London, Ontario, Canada

Introduction: The incidence of thyroid cancer is increasing due to overdiagnosis by widespread use of traditional screening techniques [1]. Thyroid nodules are currently diagnosed using imaging techniques such as ultrasound (US), computed tomography (CT), and magnetic resonance imaging (MRI). These modalities are limited as malignant nodules are often incorrectly diagnosed as benign. Improvements in accurate diagnostic ability will reduce this overdiagnosis but improvements in CT or MRI-based modalities may require the use of ionizing radiation and can be costly. Two-dimensional (2D) US is used for lesion detection with a high positive predictive value in thyroid cancer diagnosis [2]. However, limitations still exist for monitoring thyroid nodules due to difficulties with reproducing 2DUS images during each examination. Importantly, 2DUS is a widely used, portable, and inexpensive modality, and therefore it is possible to improve this accessible technique with three-dimensional (3D) US by acquiring and reconstructing multiple 2DUS images. 3DUS can enhance visibility and improve analysis with multiple view planes [3]. We developed a 3DUS imaging device with a motorized mechanically assisted mechanism to evaluate the utility of thyroid nodule identification and diagnosis. This work aims to optimize the 3DUS image acquisition parameters on the thyroid imaging device using a string phantom, and to assess the 3DUS volumetric measurement accuracy using a thyroid phantom with simulated nodules of known volumes.

Methods: The US transducer is held by a custom mechanically assisted system, designed for efficiency and comfort of use in the clinical environment (Figure 1A). Custom software was used to acquire the 2DUS images and reconstruct them into a 3DUS image. To optimize acquisition parameters, a tungsten filament phantom (10.0 mm distance between filaments) was imaged at different 2DUS acquisition rates based on a combination of 16-20 frames per second (fps) in increments of 2 fps and 1-8 frames per mm (fpm) in increments of 1fpm. In each image, the distance between filaments was measured and compared to the known 10.0 mm distance (Figure 1B). An additional error will be quantified for 3DUS images of an agar phantom with embedded nodules (0.45 cm³ volume) upon fabricating the phantom and manually segmenting volumes.

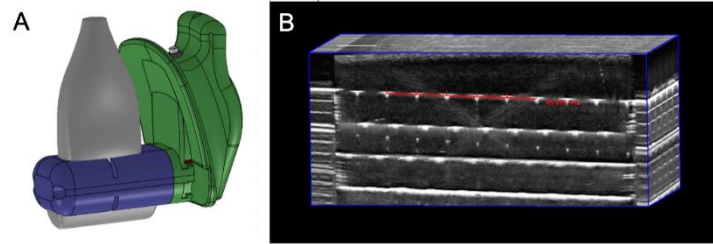


Figure 1. (A) Illustration of handheld mechanical 3DUS acquisition device (Adapted from: Papernick et al. 2020). (B) 3DUS string phantom image for optimization of acquisition parameters.

Results: The mean distances were $9.59 \pm 0.1\text{mm}$, $9.87 \pm 0.08\text{mm}$, $9.94 \pm 0.07\text{mm}$, $9.94 \pm 0.04\text{mm}$, $9.96 \pm 0.09\text{mm}$ and $9.97 \pm 0.04\text{mm}$ were associated with increasing frame rates 1 to 6 fps, respectively. The percent errors were 4.07%, 1.28%, 0.63%, 0.62%, 0.41% and 0.32% for increasing frame rates of 1 to 6 fps, respectively. The mean distances plateaued at 3 fpm, but the percent error at 5 fpm was preferable based on a 0.5% error threshold. One healthy volunteer was imaged using these optimized acquisition parameters to assess its clinical utility (Figure 2).

Conclusions: We found that using 5 fpm at 13 fps for 2DUS acquisition parameters can optimize 3DUS image acquisition to improve diagnostic confidence. Future work will focus on quantifying the volume through segmentation of healthy volunteer thyroid nodules. We expect to translate these methods to identify the optimal parameters for imaging thyroid nodules on phantoms and healthy volunteers. The impact of this work will improve diagnostic confidence in 3DUS nodule identification.

References: [1] Li, X., et al. *Lancet Oncol.* 20(2):193-201 (2019). [2] Li, WB., et al. 41(12):3096-3101 (2015). [3] Fenster, A., Downey, DB. *Annu Rev Biomed Eng.* 2:457-475 (2000).

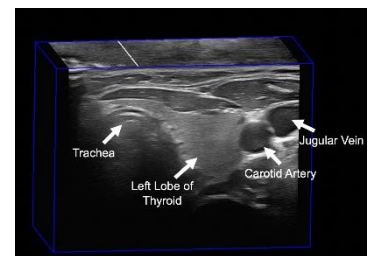


Figure 2. Healthy volunteer image using optimized parameters. Anatomy was identified by a trained operator.

Longitudinal *in-vivo* quantification of tumour microvasculature and hypoxia via optical coherence tomography angiography in a pre-clinical model of radiation therapy

Authors: Allam, N¹, Zabel, WJ¹, Jones, B¹, Demidov, V¹, Taylor, E^{1,2}, and Vitkin, IA^{1,2}.

¹Department of Medical Biophysics, University of Toronto, Toronto, ON M5G 1L7, Canada;

²Radiation Medicine Program, Princess Margaret Cancer Centre, 610 University Avenue, Toronto, Ontario, M5G 2M9, Canada.

Introduction: Stereotactic body radiotherapy (SBRT) shows potential for improved local tumour control of cancers such as pancreatic ductal adenocarcinoma (PDA). Unlike conventional radiotherapy, which delivers radiation in 2 Gy fractions, SBRT employs much higher doses per fraction (>5-10 Gy), enough to ablate small blood vessels. The impact of microvascular ablation by SBRT on response is still unknown and likely multi-factorial: while ablation reduces the supply of vital nutrients needed for tumour re-growth, the potential reduction of oxygen during treatment – a state known as hypoxia – is known to negatively impact response. *In order to understand the impact of SBRT on tumour response, it is crucial that a means of quantifying vascular properties and hypoxia longitudinally, throughout and after treatment, be developed.* Optical coherence tomography (OCT), a non-invasive volumetric imaging technique capable of resolving structures down to $\sim 10\mu\text{m}$, provides a way to do this. We hypothesize that *OCT can be used to accurately monitor changes in tumour microvasculature and hypoxia longitudinally in pre-clinical tumour models subjected to SBRT-like hypofractionated radiation regimes.*

Methods: A cohort of $n=22$ mice subcutaneously inoculated with a patient-derived PDA cell-line, BxPC-3, were irradiated at a range of single-fraction doses 10-30 Gy to simulate the effects of the first fraction of standard SBRT. OCT microangiography was performed prior- and post-irradiation over the course of 6-8 weeks. Towards the hypothesized quantification of hypoxia, the *avascular density* (AD) metric was developed measuring the proportion of tissue occupying “voids” in the 3D microvascular networks (taken here as $>150\mu\text{m}$ from the nearest blood vessel, a threshold related to the estimated oxygen diffusion-limit in tissue). Histological studies with CA9 staining for hypoxia at multiple tissue sections were also performed at selected time points to corroborate the OCT imaging trends of AD as they compare to true hypoxia.

Results: The time-course of the OCT-derived average avascular density per dose cohort is shown in *Figure 1*. The control tumours (unirradiated mice) steadily increase in vascularization (drop in AD), indicative of uninterrupted disease development. Conversely, the irradiated mice show an initial increase in AD, proportional to dose. This is consistent with the empirical threshold of 5-10 Gy for triggering vascular endothelial cell apoptosis reported in the literature. The following period of revascularization is expected given that single fraction irradiation is non-curative. This OCT-derived 3D microvascular metric showed positive correlation with CA9-hypoxia stains.

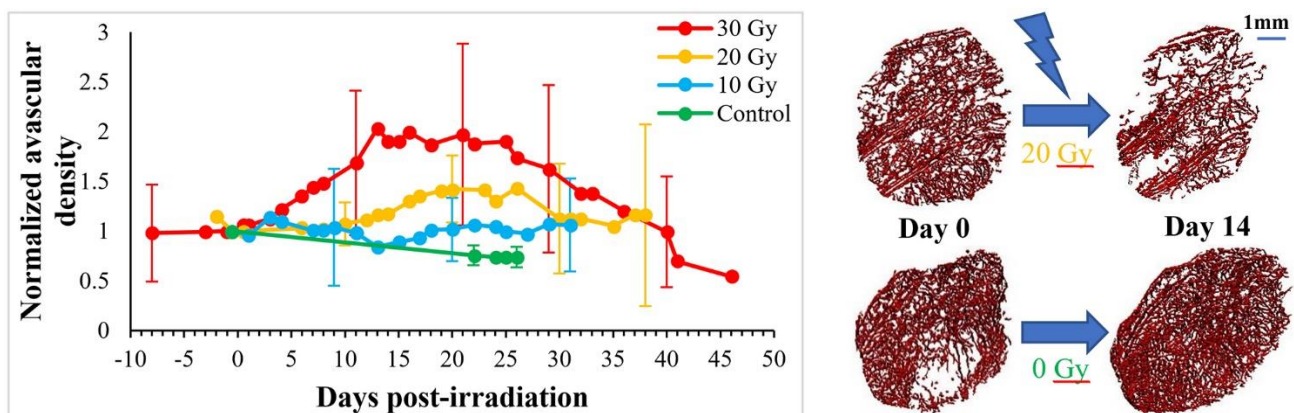


Figure 1. (Left) Differences are observed in OCT-derived microvascular voids (\sim tumour hypoxia levels) as a function of radiation dose over 6-8 weeks. (Right) 3D binarized OCT microvascular maps, before and after irradiation (un-irradiated control and 20Gy dose examples).

Conclusion: We demonstrate the utility of this novel methodology for accurate *in-vivo* quantification of hypoxia in pre-clinical tumour models. Next, we will investigate the temporal kinetics of additional vascular metrics in a full standard SBRT irradiation schedule with magnetic resonance imaging correlation for clinical translatability.

SPECT/CT Imaging [^{177}Lu]Lu-DOTA-RW03, a Targeted Radioimmunotherapy against Cancer Stem Cell Marker CD133

Kevin Wyszatko¹, Saman Sadeghi¹, Sheila Singh^{1,3}, John Valliant^{1,2}

1. Department of Chemistry & Chemical Biology, McMaster University; 2. Fusion Pharmaceuticals; 3. Stem Cell and Cancer Research Institute, McMaster University

Introduction: Cancer stem cells (CSCs) drive tumor growth and resist treatment to repopulate tumors following therapy. Eliminating this critical cell population promises improved treatment while inhibiting relapse.^{1,2} Precision molecular SPECT/PET imaging for CD133 can identify the aggressive and resilient tumors to improve treatment planning and identify tumors amenable to CD133 targeted therapy. Here, cancer stem cell targeted treatment of HT-29 tumor bearing mice with a Lu-177 labelled antibody ([^{177}Lu]Lu-DOTA-RW03) was evaluated by tumor volume measurements and tumor uptake was confirmed by SPECT over the first week of treatment.

Methods: HT-29 xenograft mice (n=5 per group) were injected with escalating [^{177}Lu]Lu-DOTA-RW03 doses (vehicle, 3.7, 9.25, 14.8 MBq) and measured by calipers until endpoint. Mice receiving [^{177}Lu]Lu-DOTA-RW03 were imaged by SPECT/CT using a Mediso NanoScan SPECT/CT/PET by STTARR (UHN, Toronto), with a Mediso APT62 (Mouse HSHR-WB - high-sensitivity, high resolution whole body) collimator/aperture (0.85 mm resolution), followed by anatomical imaging by CT scan (125 μm isotropic resolution, 50 kVp, Current: 980 uA, maximum FOV with 1:4 binning).

Results: Escalation dose therapy demonstrated that 14.8 MBq [^{177}Lu]Lu-DOTA-RW03 significantly decreases tumor growth rate. Increased tumor growth rate for mice treated with 3.7 MBq and control mice was unexpected and may be due caliper measurement conversion to tumor volume, where tumor height and width are measured but height is not measured (underestimates spheroid-shaped tumor volume). SPECT imaging ROI analysis demonstrates increasing tumor uptake (10% ID/cc after 168 h) for mice treated with 14.8 MBq, with a

maximum tumor-to-muscle ratio of 10:1 over the first week of treatment. Minimal bone uptake is observed and the therapy was well tolerated, attesting to the highly stable [^{177}Lu]Lu-DOTA complex.

Conclusions: [^{177}Lu]Lu-DOTA-RW03 targets the rare cancer stem cell population in HT-29 tumor xenografts for tumor treatment visualized by SPECT/CT. Development of PET imaging agents are underway for identifying target expression and as companion diagnostics for stratifying tumors amenable to targeted alpha therapy.

References

1. Singh, S. K. *et al.* Identification of human brain tumour initiating cells. *Nature* **432**, 396–401 (2004).
2. Aomatsu, N. *et al.* CD133 is a useful surrogate marker for predicting chemosensitivity to neoadjuvant chemotherapy in breast cancer. *PLoS One* **7**, e45865 (2012).

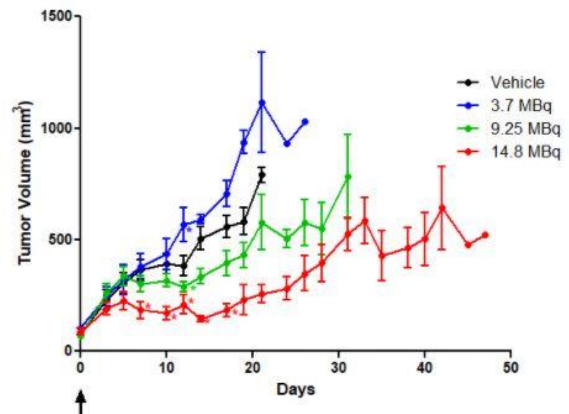


Figure 1. CD133 targeted [^{177}Lu]Lu-DOTA-RW03 reduces tumor growth rate in mice.

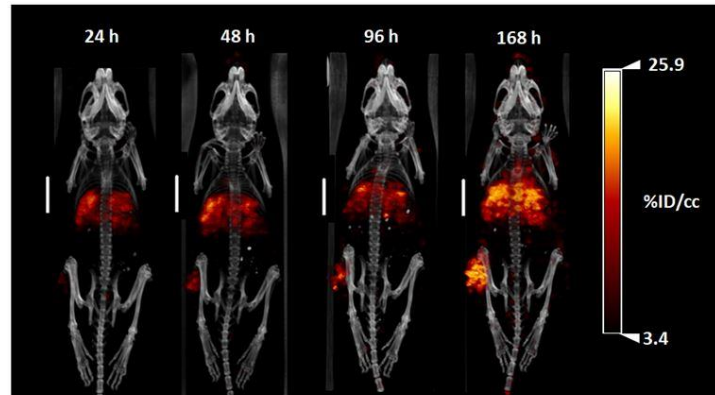


Figure 2. SPECT/CT visualizes [^{177}Lu]Lu-DOTA-RW03 tumor uptake over the first week of treatment.

Comparison of ADC measurements from the MR-Linac and a diagnostic scanner in brain tumour patients

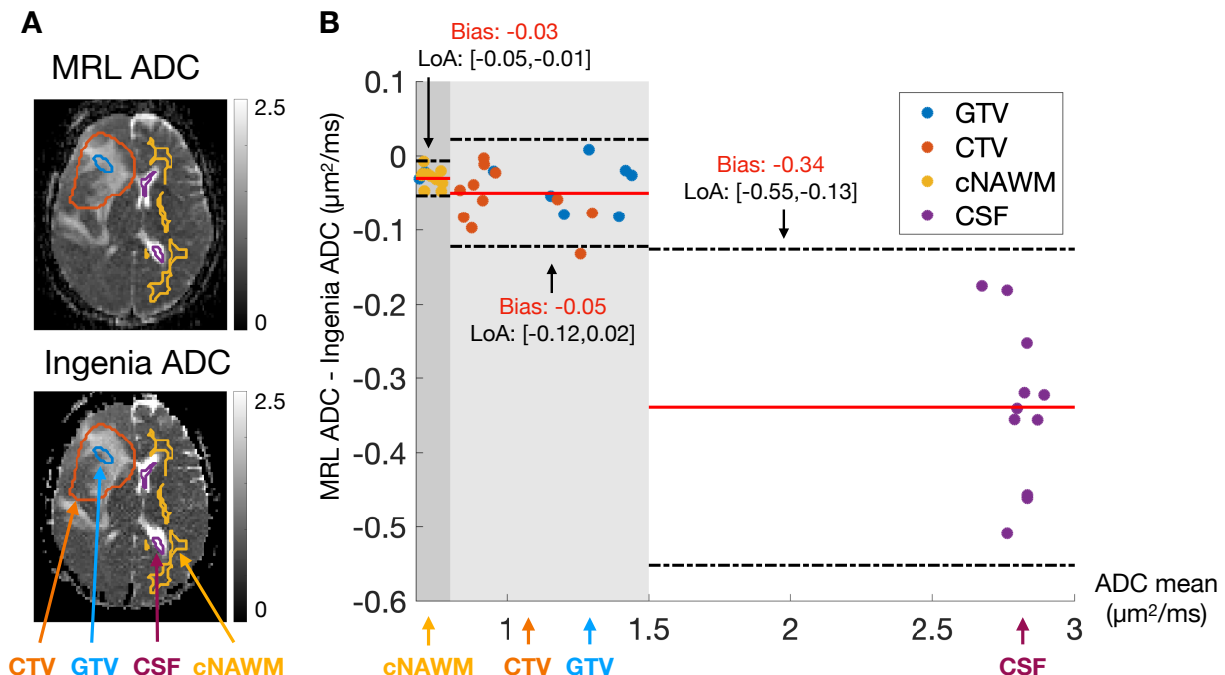
Liam S.P. Lawrence,^{ab} Rachel W. Chan,^a Brian Keller,^a James Stewart,^a Mark Ruschin,^a Brige Chugh,^a Mikki Campbell,^a Greg J. Stanisz,^{ab} Scott MacKenzie,^a Sten Myrehaug,^a Jay Detsky,^a Pejman J. Maralani,^a Chia-Lin Tseng,^a Greg J. Czarnota,^{ab} Arjun Sahgal,^a Angus Z. Lau^{ab}

a. Sunnybrook Health Sciences Centre, Toronto, ON b. Medical Biophysics, University of Toronto, Toronto, ON

Introduction: Combined MR scanner and linear accelerator (MR-Linac/MRL) devices allow daily monitoring of radiotherapy (RT) using potential imaging biomarkers, including apparent diffusion coefficient (ADC). Characterizing the technical performance of imaging biomarkers on the MR-Linac is an important step towards clinical application because the hardware modifications required to make the scanner and accelerator compatible have an unknown effect on *in vivo* scan quality. To evaluate ADC measurement accuracy, we compared patient scans from the MR-Linac and a diagnostic-quality 1.5 T MR scanner taken the same day.

Methods: Patients (N=7) with central nervous system tumours received 15-30 fractions of RT and concurrent daily imaging using a 1.5 T Elekta Unity MR-Linac (Elekta, Stockholm, Sweden). At fractions 10 and 20, the patients were imaged with a Philips Ingenia 1.5 T MRI immediately following treatment. A total of 11 paired scans were analyzed. Single-shot spin-echo EPI diffusion weighted-images (DWI) were acquired. (MRL: 8 ch posterior/anterior coil, TR/TE=4300ms/84ms, voxel size 2×2.2×5mm, FOV 240×240×155mm. Ingenia: 16 ch head coil, TR/TE=6894ms/74ms, voxel size 1.1×1.4×5mm, FOV 200×240×150mm.) Images were rigidly registered using FSL FLIRT. The median ADC was computed over the gross tumour and clinical target volumes (GTV and CTV), contralateral normal-appearing white matter (cNAWM), and cerebrospinal fluid (CSF). cNAWM was defined using FSL FAST and manual restriction to the contralateral side. CSF was defined using a region-growing algorithm in the ventricles. The GTV and CTV were registered using the planning CT. ADC maps were computed with a linear fit to the log-transformed signal versus b-value data (MRL: b=[100,200,400,800] s/mm², Ingenia: b=[200,400,600,800] s/mm²). The bias and limits of agreement (LoA) (the 95% confidence intervals) were computed using the ADC difference between the MR-Linac and the Ingenia for three ranges of ADC values ([0.68-0.8], [0.8-1.5], [1.5-3] $\mu\text{m}^2/\text{ms}$) and for the GTV/CTV differences.

Results: The confidence intervals for the ADC difference in the GTV ($-0.04 \pm 0.06 \mu\text{m}^2/\text{ms}$) and CTV ($-0.06 \pm 0.08 \mu\text{m}^2/\text{ms}$) encompassed zero, indicating agreement. Panel A of the figure below shows example ROIs overlaid on ADC maps. Panel B shows the median ADC comparison as a Bland-Altman plot. The background colours indicate the ADC ranges. Negative bias is increased at higher ADC values. Possible reasons for the bias include differing diffusion times, signal-to-noise ratios, and geometric distortions causing ROI shifts.



Conclusions: ADC measurements on a MR-Linac are accurate for normal-appearing tissue, as well as tumour and target volumes, but are biased at higher ADC values. Future work includes comparisons of the signal-to-noise ratio and the repeatability of ADC measurements.

Response Assessment of Early-Stage Breast Tumours to Stereotactic Ablative Radiotherapy (SABR) using Fluorodeoxyglucose-Positron Emission Tomography (FDG-PET)

Zoe Kerhoulas, Heather Biernaski, Muriel Brackstone, Michael Lock, Terry Thompson, Frank Prato, Neil Gelman, Stewart Gaede, Matthew Mouawad

Ontario Institute for Cancer Research Imaging Translation Program, Lawson Health Research Institute, London Health Sciences Centre, London, ON

Introduction: The current treatment standard for early-stage breast cancer is breast-conserving surgery followed by adjuvant radiotherapy, delivering whole-breast radiation in 30 fractions over 4-6 weeks. However, the prolonged treatment time can be a strain on elderly, immobile, or rural patients. To address this, researchers are investigating the efficacy of hypo-fractionated treatment regimens. The SIGNAL (Stereotactic Image-Guided Neoadjuvant Ablative radiation then Lumpectomy) trial was a clinical trial initiated to determine the safety and efficacy of neoadjuvant stereotactic ablative radiotherapy (SABR) for early-stage breast cancer patients.

Neoadjuvant treatment presents a unique opportunity to assess patient response to SABR using functional imaging techniques. We present quantitative results from FDG-PET scans performed on early-stage breast cancer patients before and three weeks after neoadjuvant (pre-operative) SABR. The objective was to quantify pre- to post-SABR changes in FDG uptake in both the tumour and surrounding tissue of a subset of patients from the SIGNAL trial. **Methods:** Pre- and post-SABR (21 Gy in 1 fraction or 30 Gy in 3 fractions) FDG-PET scans were obtained from a subset of 10 patients in the SIGNAL study. Using a 3T PET-MRI system, PET images were acquired in list mode beginning one hour after injection. Images were reconstructed at 5 minute intervals, the first of which was used for this analysis. Response to SABR in the tumour was quantified using changes in mean standardized uptake value (SUV) within the V50 uptake volume (defined as connected voxels with an $SUV \geq 50\%$ of the average maximum SUV), maximum SUV, and V50 uptake volume. To characterize changes in the tissue surrounding the tumour, an area-under-the-curve (AUC) analysis was applied. This involved using MATLAB to select a 20x20x20 pixel cube centered around the tumour maximum SUV, calculating the number of voxels in the cube with an SUV that lies above 1000 incrementing thresholds defining the tumour region, and taking the area under the curve (figure 1). Significance for each parameter was determined using a Wilcoxon signed-rank test for paired samples. **Results:** The percent change for each patient and parameter is shown in table 1. The median (range) percent changes in all parameters across patients were 1) mean tumour SUV = -20.8% (-51.1 – 78.2) and not significant (NS), 2) maximum tumour SUV = -19.8% (-50.3– 31.6) and NS, and 3) uptake volume (V50%) = 368.8% (91.8 – 1903.0) and significant ($p=0.00512$). The change in AUC was 32.5% (-14.7 – 138.0) and significant ($p=0.046$). **Conclusions:** We quantified changes in tumour and surrounding tissue response after SABR using FDG-PET in early-stage breast cancer patients. The decrease in SUV may indicate an immunological tumour response to therapy. The significant increase in AUC and V50 volume indicates an increase in surrounding tissue FDG tracer uptake and may show an inflammatory response, particularly macrophage activity. This study shows that FDG-PET may have potential to assess patient response to SABR. In future studies, we hope to correlate changes in SUV and AUC after SABR with changes in genomic markers of immune response from tissue biopsy acquired before and after SABR. We also hope to validate these findings by comparison to the current treatment standard.

Patient #	% Diff. (Mean SUV)	% Diff. (Max SUV)	% Diff. (V50 Volume)	% Diff. (AUC)
1	-20.52	-25.9	450.66	36.23
2	-21.3	-5.79	184.03	17.01
3	-2.83	-6.29	116.47	-14.66
4	-25.13	-20.65	488.40	87.80
5	-51.08	-45.44	1764.33	137.95
6	51.83	31.61	316.88	28.70
7	-24.55	-28.98	102.51	14.39
8	-50.64	-50.26	1903.02	108.40
9	36.02	15.85	459.83	65.08
10	78.24	-18.91	91.79	-0.91
Median	-20.8	-19.8	368.8	32.5

Table 1: Displays the percent change in the four parameters measured after SABR.

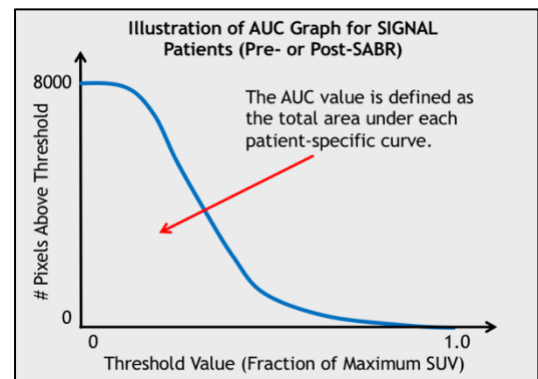


Figure 1: Displays an illustration of AUC curves generated for all 10 patients in the SIGNAL study subset.

Derivation of Monoclonal Antibodies Targeting GvpA, the major structural protein of Gas Vesicles: A New Set of Tools for Detecting and Imaging Gas Vesicles

Ann Fernando^{1,2} and Jean Gariépy*^{1,2,3}
¹ Department of ²Pharmaceutical Sciences, University of Toronto, Toronto, Ontario, Canada
³ Sunnybrook Research Institute, Toronto, Ontario, Canada
 Department of Medical Biophysics, University of Toronto, Toronto, Ontario, Canada

Introduction: Gas Vesicles (GVs) are proteinaceous nanoparticles that are expressed by certain microbes to aid in their flotation (Walsby 1994). GV's are a class of ultrasound contrast agent due to the presence of their air-filled core (Shapiro 2014). They are amenable to modification at the protein level to incorporate new ligands (Sremac and Stuart 2008, Balakrishnan et al. 2016) and therapeutic agents (Fernando and Gariépy 2020). Despite their capabilities, the study and application of GV's is limited by a lack of agents to detect or target them to disease sites. To address these issues, we have developed monoclonal antibodies (mAbs) targeting the dominant protein on *Halobacterium* sp. GV's, termed gvpA. Our aim is to develop bispecific single-chain variable fragments (scFv) derived from these antibodies in order to target GV's directly to tumor cells, by fusing the GV binding domain with clinically validated variable fragments such as MFE-23, a scFv that binds the human tumor antigen carcinoembryonic antigen. We expect that such targeted GV's bearing therapeutic payloads can deliver treatment at a sustained rate in order to augment efficacy and reduce off-target effects.

Methods: mAbs were created (Genscript) by injecting mice with a 26-residue synthetic peptide version of the C-terminal domain of gvpA (Strunk et al. 2011). Surface plasmon resonance (SPR) and enzyme-linked immunosorbent assay (ELISA) were used to characterize the *in vitro* binding kinetics of the antibodies and their derivatives towards the synthetic peptide, native GV, gvpA fusion protein, and GV's bearing therapeutics.

Results: mAbs were derived that recognize native GV's (K_d ranging from 0.1 to 1 nM) and a gvpA fusion protein (K_d ranging from 0.2 to 3 nM) with high binding affinity. A scFv based on the sequence of the anti-gvpA mAb 2B10 was also found to bind to gvpA with high affinity (K_d = 50 nM) and the GV (K_d = 30 nM). A bispecific scFv is now being developed that will pair this scFv to GV with a scFv that recognizes carcinoembryonic antigen (CEA), an established tumor marker. Characterization of this bispecific construct indicates that both scFvs recognize their respective antigen with high affinities (GV, K_d : 120 nM; CEA, K_d 7nM) as defined by ELISA.

Conclusions: We have developed mAbs and scFv agents which bind GV's and specifically to its main protein component gvpA with high affinity. These mAbs represent versatile tools that can be modified with imaging and cytotoxic agents to generate targeted, long-circulating GV's. As such, my future work will focus on using mAbs as well as bispecific scFvs to develop tumor-targeted GV's as theranostic agents.

References:

Balakrishnan A, DasSarma P, Bhattacharjee O, Kim JM, DasSarma S, et al (2016). Halobacterial nano vesicles displaying murine bactericidal permeability-increasing protein rescue mice from lethal endotoxic shock. *Sci Rep*, 6: 33679.

Fernando A and Gariépy, J (2020) Coupling Chlorin e6 to the surface of Nanoscale Gas Vesicles strongly enhances their intracellular delivery and photodynamic killing of cancer cells. *Sci Rep*, 10: 2802.

Shapiro MG, Goodwill PW, Neogy A, Yin M, Foster FS, et al. (2014) Biogenic gas nanostructures as ultrasonic molecular reporters. *Nat. Nanotechnol.* 9:311–316.

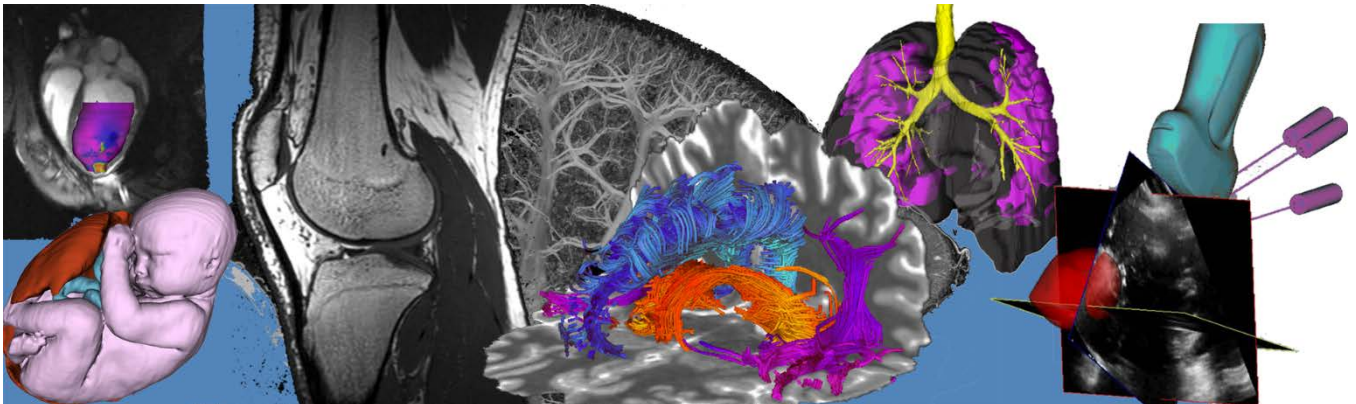
Sremac M and Stuart ES. (2008) Recombinant gas vesicles from *Halobacterium* sp. displaying SIV peptides demonstrate biotechnology potential as a pathogen peptide delivery vehicle. *BMC Biotechnol* 8: 9

Strunk T, Hamacher K, Hoffgaard F, Engelhardt H, Zillig MD et al. (2011) Structural model of the gas vesicle protein GvpA and analysis of GvpA mutants in vivo. *Mol Micro* 81:56-68.

Walsby A (1994) Gas vesicles. *Microbiol. Rev.* 58:94–

Oral Presentation Abstract

Session 25: Machine Learning IV



Prediction of stroke thrombus RBC content from multiparametric MRI using machine learning

Emily Qin,¹ Spencer Christiansen,^{1,2} and Maria Drangova^{1,2}

¹Dept. of Medical Biophysics Western University, ²Robarts Research Institute

Introduction: Acute ischemic stroke (AIS) is a prevalent disease with multiple causes, known as etiologies. AIS thrombus red blood cell (RBC) content has been shown to vary between etiologies and is predictive of response to endovascular thrombectomy (EVT) and tissue plasminogen activator (tPA) therapies.¹ However, RBC content can currently only be assessed through histological analysis on thrombi successfully retrieved by EVT. Non-invasive methods for predicting thrombus RBC content in patients *in vivo* before treatment would improve assessment of treatment candidacy and stroke etiology.¹ Quantitative MR R2* and quantitative susceptibility mapping (QSM) values have shown to be sensitive to blood clot RBC content *in vitro*.² In this study, we evaluate the ability of machine learning (ML) algorithms to predict histological RBC content of AIS thrombi using texture features extracted from *ex vivo* thrombus MR R2*, QSM and gradient echo (GRE) images.

Methods: Thrombus collection - 48 thrombi retrieved by EVT at University Hospital between February 2016 and November 2017 were included in this study. Retrieved thrombi were kept at room temperature inside a plastic jar and scanned within 6 hours of retrieval.

Imaging - Thrombi were scanned *ex vivo* at 3T using a dual echo train multi-echo GRE sequence (TE₁: 3.2 ms, TE₁₀: 46 ms, TR: 47.6 ms, bandwidth: 142.86 kHz, flip angle: 10°, field of view: 18 cm, resolution: 0.94 × 0.94 × 1.0 mm³, scan time: 5 min 33 sec).³ A co-registered FIESTA-C sequence with identical resolution was also acquired.

Image post-processing - Channel-combined complex data were processed using the non-iterative B0-NICE⁶ and MEDI QSM⁷ algorithms to calculate R2* and QSM maps, respectively.^{5, 6, 7} Late-echo GRE magnitude images (TE = 31 ms) were derived using sum-of-squares channel combination. Thrombi were segmented in Matlab using the FIESTA-C images. 1032 thrombus texture features were calculated from binned, segmented 3D thrombus R2*, QSM and GRE images using a previously developed Matlab code (Figure 1).⁴

Histology - Following imaging, thrombi were formalin fixed, sliced at 5 µm and stained with hematoxylin & eosin (H&E). Histological RBC content was determined using ImageJ colour segmentation.

Machine Learning - Texture feature selection was performed in WEKA using the Correlation-based Feature Subset Selection method. Linear regression, multilayer perceptron and Gaussian processes classifier models were developed in WEKA to predict histological RBC content, and evaluated using 8-fold cross validation. Average correlation coefficient, mean absolute error and root mean squared error (RMSE) across all folds were recorded. Classifier RBC content predictions were also plotted against histological values to calculate regression slopes.

Results: The performance of each ML algorithm for predicting thrombus RBC content is shown in Table 1. Of the tested algorithms, linear regression produced the highest correlation coefficient and slope (0.60 and 0.74, respectively), with similar error values to the Gaussian processes algorithm.

Conclusion: AIS thrombus R2*, QSM, and GRE texture features were able to accurately predict histological RBC content using all ML algorithms, with linear regression providing the best performance. These findings show promise for MR texture analysis to predict thrombus RBC content in AIS patients *in vivo*.

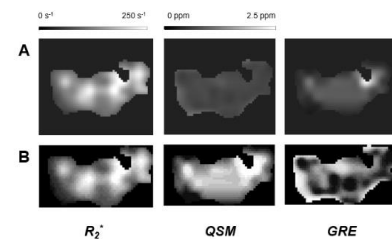


Fig. 1: Representative segmented thrombus R2*, QSM and GRE images shown with original values (A), and after pixel binning for texture feature extraction (B).

Algorithm Type	Correlation Coefficient	Mean Absolute Error	Root Mean Squared Error
Linear Regression	0.60	0.09	0.13
Multilayer Perceptron	0.52	0.13	0.17
Gaussian Processes	0.57	0.08	0.10

Table 1: ML algorithm results for correlation coefficient, mean absolute error, and RSME.

References: [1] Velasco Gonzalez A et al. Transl Stroke Res 2020. [2] Christiansen SD et al. J NeuroIntervent Surg 2019. [3] Liu J et al. NeuroImage 2018. [4] Vallières M et al. Phys Med Biol 2015. [5] Liu J et al. Magn Reson Med 2015. [6] Liu J et al. NeuroImage 2012. [7] Li J et al. Magn Reson Med 2012.

A Multiple Instance Learning Framework for MRI-based Multifocal Cancer Outcome Prediction

Jianan Chen^{1,2}, Helen Cheung^{2,3}, Laurent Milot⁴, Anne Martel^{1,2}

¹Department of Medical Biophysics, University of Toronto; ²Sunnybrook Research Institute, Toronto, ON, CA; ³Department of Medical Imaging, University of Toronto; ⁴Edouard Herriot Hospital, Lyon, FR

Introduction: Multifocal cancer is present when two or more invasive tumors occur in a single organ. It frequently occurs in the prostate, brain, liver and lungs and is more prevalent in metastatic disease. Previous studies suggest that multifocal cancers tend to be more aggressive and less successfully treated than unifocal ones. Most existing imaging biomarkers make prognosis predictions based on the largest lesion in multifocal disease while truly multifocal cancer outcome prediction is relatively unexplored. We hypothesize that using features from all lesions of multifocal cancer will improve outcome prediction. Here, we propose a multiple instance learning framework that was trained and evaluated on a colorectal cancer liver metastases (CRLM) MR cohort.

Methods: We used a retrospective cohort of 50 patients with multifocal CRLM who were treated with hepatic resection at our institute [1]. Informed consent was waived by the institutional review board. 10-min delayed Gadobutrol-enhanced magnetic resonance imaging was acquired for all patients prior to surgery. We first extracted radiomic features of each individual lesion (using pyradiomics [2]) from 3D MRI scans based on tumor segmentations generated by radiologists. Then we built a multi-task deep neural network to predict 3-year survival of our patients (**Figure 1**). The autoencoder branch performs feature reduction by reconstructing the 100 radiomic features inputted. The multiple instance branch of the network transforms the latent features from the bottleneck layer of the autoencoder to instance-level (lesion-level) representations, aggregates them into a bag-level (patient-level) representation, and makes survival predictions. The two branches are jointly optimized so the autoencoder learns prognosis-relevant features.

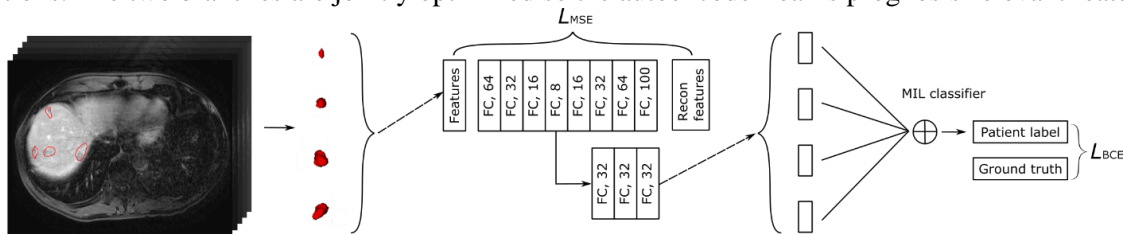


Figure 1. Overview of the proposed end-to-end multiple instance learning pipeline. The network structure between the curly brackets is shared for each tumor lesion of the same patient.

Results: In 10 runs of 3-fold cross validation, our framework achieved an averaged Area under the ROC curve (AUC) of 0.698 ± 0.080 and an accuracy of 0.677 ± 0.087 for the prediction of 3-year survival. It greatly outperformed commonly-used baseline methods – composed of LASSO [3] for feature selection and traditional machine learning methods e.g. random forest or logistic regression for prediction – by a 19.5% increase in AUC. We also built a signature from the output of our network and compared it to three CRLM-specific clinical and imaging biomarkers, including Fong clinical risk score, Tumor burden score and Target tumor enhancement. Our signature is the only one that achieved statistical significance in univariate and multivariate cox proportional hazard modeling in our cohort of multifocal CRLM patients.

Conclusions: We propose a multiple instance learning framework that has achieved state-of-the-art performance in multifocal CRLM outcome prediction. We empirically validated our hypothesis that incorporating imaging features of all lesions improves outcome prediction for multifocal cancer.

References:

- [1] Chen et al., *MICCAI*, 2019.
- [2] van Griethuysen, *Cancer research*, 2017.
- [3] R Tibshirani, *Journal of the Royal Statistical Society: Series B*, 1996

A multi-modality radiomics-based model for predicting recurrence in non-small cell lung cancerJaryd R. Christie^{1,2}, Mohamed Abdelrazek³, Pencilla Lang^{2,4}, and Sarah A. Matttonen^{1,2,4}¹Department of Medical Biophysics, Western University, London, Ontario, Canada²Baines Imaging Research Laboratory, London Regional Cancer Program, London, Ontario, Canada³Department of Medical Imaging, ⁴Department of Oncology, Western University, London, Ontario, Canada

Introduction: Lung cancer remains the most common cause of cancer death worldwide and despite early diagnoses, up to half of these patients will develop a recurrence 5 years post-surgery [1]. Imaging methods such as computed tomography (CT) and positron emission tomography (PET) are widely used for staging, the current gold standard for predicting the likelihood of recurrence. However, there is a plethora of other information in medical images that can be used to aid clinicians in decision-making. Radiomics is a field of study in which large amounts of advanced quantitative imaging features are extracted from medical images for applications in diagnosis, treatment selection and response assessment [2]. A multi-modality radiomics approach incorporating quantitative and qualitative features from the tumor and its surrounding regions, along with clinical features, has yet to be explored. Therefore, the aim of this study was to develop an integrated model to improve risk-stratification of non-small cell lung cancer (NSCLC) patients compared to cancer stage alone.

Methods: We used the pre-treatment CT and PET images of 135 patients with early-stage NSCLC who underwent surgical resection. A threshold-based semi-automated segmentation algorithm was developed in MATLAB to define the tumour volume of interest (VOI) on CT (Figure 1). The PET images were segmented using a semi-automatic gradient-based algorithm in MIM Software. The Quantitative Image Feature Engine (QIFE) was used to compute radiomic features from the CT and PET VOIs [3]. These features included shape, size, first-order, and second-order gray level co-occurrence matrix (GLCM) texture features. Clinical and qualitative image features were also assessed, resulting in a total of 1030 features. Variable selection was performed on the training cohort (n=94) using the least absolute shrinkage and selection operator (LASSO) to select the top performing features for recurrence prediction. A multivariate Cox proportional hazards model was built using the most predictive features and the coefficients of the variables were then locked and evaluated on the testing cohort (n=41). This model was compared to a baseline clinical model with cancer stage to determine its incremental value in predicting recurrence.

Results: Nine features were selected as the top performing features in predicting recurrence using the LASSO regression. Seven of the top nine features were texture features with the remaining two features being stage and smoking status. The locked multivariate model achieved a concordance of 0.81 in the training cohort and was also able to predict time to recurrence in the testing cohort with a concordance of 0.78. Patients were separated into high- and low- risk groups using the median risk score in the training cohort. Kaplan-Meier curves for both cohorts using the multivariate model are shown in Figure 2. The locked model outperformed the clinical model consisting of cancer stage only, with concordances of 0.69 and 0.68 for the training and testing cohorts, respectively.

Conclusions: Our multi-modal radiomics model outperformed the clinical model for NSCLC recurrence prediction and risk stratification. These results demonstrate that radiomics has the potential to augment staging information in a clinical setting. These non-invasive software tools can be implemented into the clinic and could allow physicians to more accurately identify patients who are at higher risk of treatment failure.

References: [1] Brenner, D. R., et al. 2020 [2] Rizzo, S., et al. 2018 [3] Echegaray, S., et al. 2018

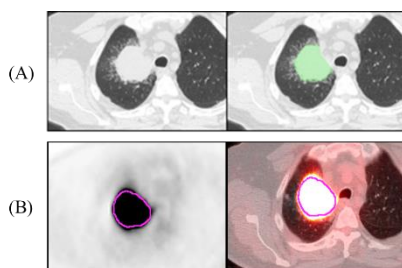


Figure 1. Pre-treatment diagnostic (A) CT and (B) PET. The semi-automatic segmentation result is shown on CT in green and on PET in pink.

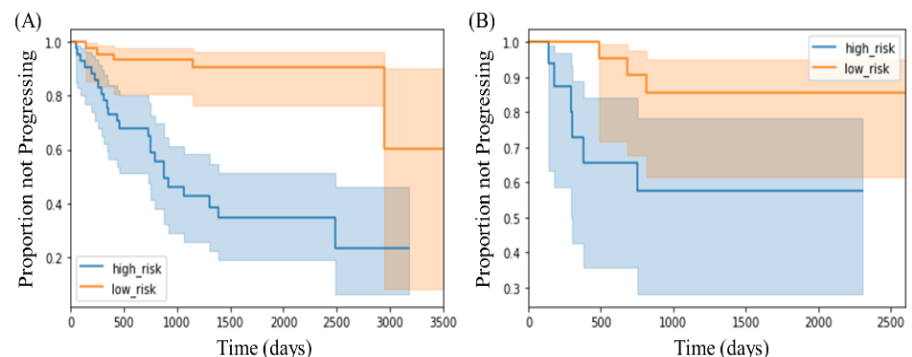


Figure 2. Kaplan-Meier curves for the multivariate model in the (A) training cohort (n=94, p<0.001) and (B) testing cohort (n=41, p=0.03). Shaded region is the 95% confidence interval.

Radiomics for head and neck cancer prognostication: results from the RADCURE machine learning challenge

Michal Kazmierski^{1,2}, Mattea Welch^{1,2,4}, Sejin Kim^{1,2}, Chris McIntosh^{1,2,4}, Andrew Hope^{2,3}, Tirth Patel^{2,4}, Tony Tadic^{2,3,4}, Scott Bratman^{1,2,3}, Benjamin Haibe-Kains^{1,2}

¹Department of Medical Biophysics, University of Toronto, ²Princess Margaret Cancer Centre, ³Department of Radiation Oncology, University of Toronto, ⁴TECHNA Institute, Toronto, ON

Introduction

Recently, there has been significant interest in using rich, multi-modal data routinely collected in the clinic, including imaging and information from electronic medical records (EMR) for prognostic factor discovery in cancer. In particular, the emerging field of radiomics makes use of computational tools to extract quantitative features from radiological images, with the aim of capturing the morphological and biological characteristics of tumors. Previous studies have demonstrated the potential of computed tomography (CT) imaging features as independent prognostic factors for overall survival in multiple types of cancer, including head and neck (HNC). However, poor reproducibility and lack of large, rigorous validation studies have hindered widespread clinical use of radiomics so far. We conducted a survival prediction challenge with the aim of 1) developing an accurate prognostic model for survival using EMR and routinely collected CT imaging data and 2) evaluating the true added value of CT radiomics compared to other prognostic factors.

Methods

Using a large, retrospective cohort of 2552 HNC patients from across all HNC disease subsites (including oropharynx, larynx and others), we assessed prognostic performance of 12 different approaches developed by several research groups (including some of the authors) at University Health Network in Toronto, making use of engineered radiomics, deep learning, EMR data and combinations of those. To allow for unbiased comparison between different approaches, all participants had access to a public training dataset of 1802 patients, while 750 were held out for evaluation. EMR variables exposed for modeling included: age, sex, disease site, stage and stage group, human papillomavirus (HPV) status, performance status and treatment.

Results

The best challenge submission used a deep multi-task logistic regression approach [1] with 1 hidden layer on EMR data and tumour volume, outperforming (in terms of AUROC) the best EMR-only model ($p < .05$), best radiomics-only model ($p < .05$), as well as the best model combining deep learning on images with EMR features ($p < .05$) (table 1). We also used an ensemble approach to combine the predictions of all challenge submissions to determine whether the ensemble achieved stronger performance than any individual model, indicating that there might be complementary information between the different data modalities.

kind	AUROC	C-index
ensemble	0.825 [0.781–0.866]	0.808 [0.770–0.843]
combined	0.823 [0.777–0.866]	0.801 [0.757–0.842]
EMR	0.798 [0.748–0.845]	0.785 [0.740–0.827]
radiomics	0.766 [0.718–0.811]	0.748 [0.703–0.790]

Table 1. Performance of the best submission in each category and the ensemble of all submissions.

Conclusions

Our rigorous challenge framework allowed us to evaluate a diverse collection of prognostic models in a large multi-modal dataset, demonstrating the value of machine learning in HNC prognostication, as well as the advantages of simple imaging features over several hand-engineered and deep radiomics approaches. Furthermore, our ensemble approach achieves excellent performance for both 2-year and lifetime risk prediction, establishing new state-of-the-art in HNC prognostic modelling.

References

[1] C.-N. Yu et al., ‘Learning patient-specific cancer survival distributions as a sequence of dependent regressors’, in *NIPS 24*, 2011.

Radiomics Analysis to Predict Chronic Obstructive Pulmonary Disease Presence in Computed Tomography Imaging using Machine Learning

Ryan Au¹, Wan C Tan², Jean Bourbeau³, James C Hogg², Miranda Kirby¹

¹Department of Physics, Ryerson University, Toronto Canada; ²Centre for Heart Lung Innovation, University of British Columbia, Vancouver Canada; ³McGill University Health Centre, McGill University, Montreal Canada

INTRODUCTION: Chronic obstructive pulmonary disease (COPD) is a progressive lung disease that is characterized by emphysematous tissue destruction and airway wall thickening. Computed tomography (CT) imaging can be used to identify the presence and quantify the extent of disease.^[1] However, existing quantitative CT (QCT) features only assess structural features (e.g. airway wall thickness). Radiomics analysis is an emerging quantitative technique that assesses spatial relationships between image voxels. The purpose of this work was to evaluate COPD prediction using radiomics and QCT features. We hypothesized that CT radiomics features can be developed and used alongside existing QCT measurements to predict the presence of COPD in CT lung images.

METHODS: Spirometry and full inspiratory lung CT images were acquired prospectively in the Canadian Cohort of Obstructive Lung Disease population-based study.^[2] Participants were classified as COPD or no COPD. COPD was defined using spirometry when the forced expiratory volume in 1 second to forced vital capacity (FEV₁/FVC) ratio was less than 0.70. Well-established QCT features were extracted and included: the percentage of low attenuation areas below -950HU, 15th percentile of the CT density histogram, low attenuation cluster slope, CT tissue volume, total airway count, and estimated wall thickness for an idealized airway of 10mm lumen perimeter (VIDA Diagnostics, Inc.; Coralville, IA, USA). Whole lung segmentation, airway segmentation, voxel resampling to 1x1x1mm³, and edgmentation were used to process CT images prior to extraction of grey level co-occurrence, grey level run length, grey level size zone, neighbourhood grey tone difference, and neighbouring grey level dependence texture-based radiomics features.^[3] The edgmentation image processing technique was a modified split-merge algorithm designed to highlight regional and edge textures. QCT and radiomics features were normalized as z-scores and highly correlated features were removed. A 10-fold cross validation least absolute shrinkage and selection operator (LASSO) was used for feature selection. All nonzero coefficients were linearly combined with the corresponding normalized feature value to create the feature-score. A machine learning logistic regression model with LASSO regularization was trained using 70% of the cohort, while the remaining 30% were used for model testing. CT scanner model and relative lung volume (CT lung volume to total lung capacity ratio) were used as model covariates. Model prediction performance was assessed by calculating the area under the receiver operating characteristic curve (AUC), sensitivity, specificity, and accuracy.

RESULTS: A total of 1174 participants were evaluated: n=582 without COPD and n=592 with COPD. AUC values were 0.82 (95% confidence interval [CI]: 0.81, 0.82), 0.77 (95% CI: 0.76, 0.77), and 0.80 (95% CI: 0.80, 0.80) for the models trained with QCT and radiomics features, only radiomics features, and only QCT features, respectively. As shown in Figure 1, the prediction accuracies were 73.7% (95% CI: 73.2%, 74.1%), 68.9% (95% CI: 68.5%, 69.3%), and 71.9% (95% CI: 71.5%, 72.3%) for the models trained with QCT and radiomics features, only radiomics features, and only QCT features, respectively. Furthermore, sensitivity/specificity for COPD prediction was highest using the QCT and radiomics feature trained model (74.4%/72.9%) compared to the model trained with only radiomics features (69.9%/68.0%) or only QCT features (72.0%/71.8%).

CONCLUSION: CT radiomics features may provide complimentary information and aid in COPD prediction using CT images. These findings will motivate future longitudinal studies assessing COPD progression to investigate CT radiomics features as a potential imaging biomarker.

REFERENCES:

^[1]Matsuoka, Shin *et al. Radiographics*. 2010.

^[2]Bourbeau, Jean, *et al. COPD*. 2014.

^[3]Zwanenburg, Alex, *et al. Radiology*. 2020.

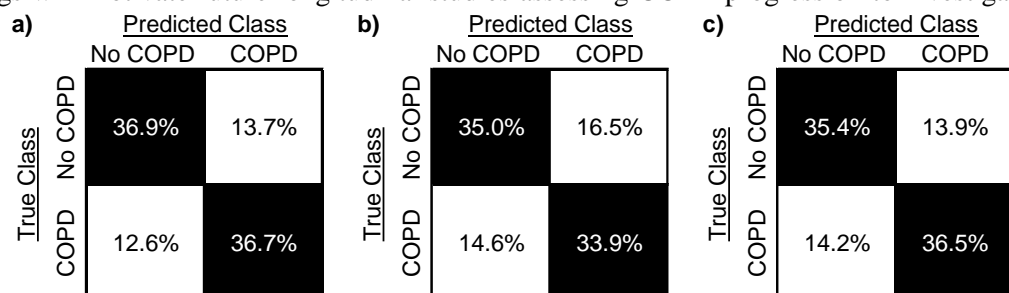
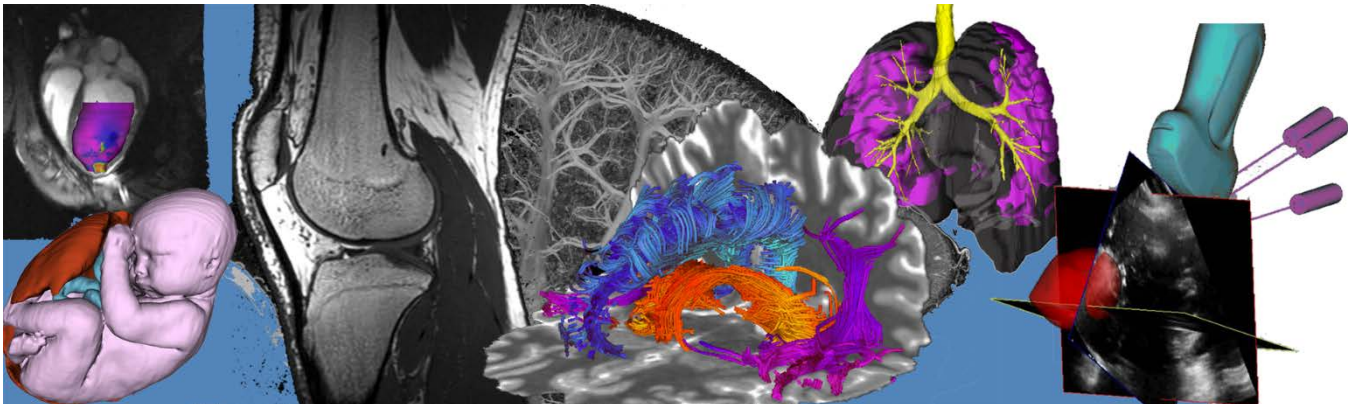


Figure 1: Confusion matrices from the testing cohort using: **a)** the model trained with both QCT and radiomics features; **b)** the model trained with only radiomics features; and **c)** the model trained with only QCT features.

Oral Presentation Abstract

Session 26: MRI Contrast & Devices



Validation of a mechatronics-assisted needle delivery system for MRI-guided prostate focal laser ablation

Eric Knull^{1,2*}, Claire K. Park^{2,3}, Jeffrey Bax², David Tessier², Aaron Fenster^{1,2,3}

¹Biomedical Engineering Graduate Program, Faculty of Engineering, ²Imaging Research Laboratories, Robarts Research Institute, ³Department of Medical Biophysics, Western University, London, Ontario, Canada

Introduction: Prostate cancer is the most frequently diagnosed non-skin cancer and second leading cause of cancer related deaths in Canadian men. Whole gland surgery and radiation therapy for prostate cancer are highly effective treatments for long-term cancer control but are often associated with overtreatment and adverse side effects, which impact quality of life.¹ Magnetic resonance imaging (MRI)-guided focal laser ablation (FLA) is an emerging, minimally invasive treatment for localized prostate cancer.² FLA involves the therapy of small regions of the prostate, while preserving surrounding healthy tissues and critical structures. Accurate needle delivery is crucial for the therapeutic success of FLA. We propose an in-bore MRI-compatible remotely actuated needle delivery system for MRI-guided FLA to localized prostate lesions. This work presents the mechatronic system design, evaluation of MRI-compatibility, and open-air and in-bore needle positioning testing.

Methods: The mechatronic needle delivery system was constructed from entirely non-ferromagnetic components with actuation controlled by MRI-compatible piezoelectric motors and optical encoders. It contains a remotely actuated, four degrees-of-freedom transperineal positioning needle delivery mechanism, and an adaptable needle-guide, which is a unique design component to accommodate for any focal therapy energy modality or needle intervention. When a FLA region (target) is detected on MRI, the needle-guide is remotely actuated and its mechatronic components are locked, and then needles are manually inserted through the intended needle-guide for FLA, illustrated in Figure 1.

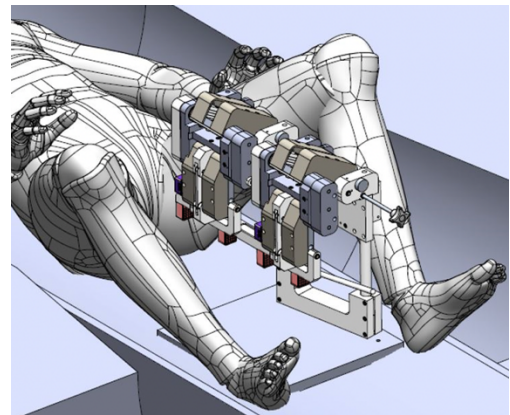


Figure 1: Computer-aided design (CAD) of the mechatronic needle delivery system for in-bore MRI-guided FLA in localized prostate lesions. Remotely actuated needle-guides (illustrated in dark red) are positioned for manual needle insertion.

Validation of the mechatronic needle delivery system for MRI-compatibility was performed to ensure compliance with the American Society for Testing and Materials (ASTM) standards for image quality, including image distortions, signal-to-noise ratio (SNR), safety testing and interference.³ Gradient recalled echo (GRE) T2-weighted images of a grid phantom were acquired on a Discovery MR750 3T MRI Scanner (GE Healthcare, Chicago, Illinois, United States) to measure image distortion and SNR. Needle positioning testing was performed over the mechatronic range-of-motion to selected three-dimensional virtual target positions with an insertion depth of 10.0 cm. In open-air testing, the position of the needle guide calculated using the system's encoders was compared with the position measured using an external Polaris optical tracking system (Northern Digital Inc., Waterloo, Ontario, Canada). In-bore testing was performed using a fiducial arrangement mounted at a 10.0 cm insertion depth for registration with the MRI coordinates and measurement of the needle tip position. The root-mean-square needle tip error and standard deviation (SD) were quantified.

Results: In-bore MRI-compatibility testing resulted in an 'MR-conditional' system in compliance with ASTM image quality and safety standards,³ under all intended acquisition sequences. Open-air and in-bore needle positioning testing over the mechatronic range-of-motion resulted in a mean needle tip error (SD) of 0.71 ± 0.30 mm and 1.80 ± 0.56 mm (N=10), respectively. A one-sided upper 95% confidence interval on the mean in-bore needle tip error was 2.16 mm.

Conclusions: We developed an MRI-compatible mechatronics-assisted needle delivery system for MRI-guided FLA of prostate lesions. In-bore needle positioning allows regions 2.16 mm to be targeted with 95% confidence. This error is clinically acceptable, but an extended in-bore analysis with tissue-mimicking prostate phantoms is required to fully determine its accuracy for MRI-guided FLA. Our proposed mechatronics-assisted needle delivery system may allow for accurate in-bore needle positioning, while maintaining manual clinician needle insertion to improve safety with haptic feedback and optimizing MRI-guided FLA intervention workflow.

[1] JJ Van Tol-Geerdink, et al. (2013) Br. J. Cancer. 108(9) [2] T Lee, et al. (2014) Rev. Urol. 16(2) [3] ASTM. An. B. Stand. (2017)

An Exploration of Myocardial Blood Flow, Blood Volume, and Oxygen Consumption at Varying Levels of Hyperemic Stress Reveals Blood Flow as the Dominant Influence on T2 Relaxation Time.

Jill J. Weyers¹, Venkat Ramanan¹, Jennifer Barry¹, Melissa Larsen¹,
Krishna Nayak², Graham A. Wright^{1,3,4}, Nilesh R. Ghugre^{1,3,4}

¹ Physical Sciences Platform, Sunnybrook Research Institute, Toronto, ON; ² Ming Hsieh Department of Electrical Engineering, University of Southern California, Los Angeles, CA; ³ Schulich Heart Research Program, Sunnybrook Health Sciences Centre, Toronto, ON; ⁴ Department of Medical Biophysics, University of Toronto, Toronto, ON.

Introduction: Many forms of diseased myocardium can be identified by comparing hemodynamics during rest and hyperemic stress. Hyperemia induces changes in multiple hemodynamic factors, including blood flow, blood volume and venous blood oxygen levels (PvO₂). MRI-based T2 mapping is sensitive to all of these changes and therefore is a promising non-contrast option for rest-stress comparisons; however, the impact each individual hemodynamic factor has on T2 is poorly understood, making the connection between changes within the tissue and altered T2 difficult.

Methods: To better understand this interplay, we performed T2 mapping (T2-prepared spiral sequence on a 3T scanner) and measured each hemodynamic factor independently in healthy pigs (n=12) at multiple levels of hyperemic stress, induced by different doses of adenosine (0.14 mg/kg/min, and 2x, 3x and 4x of the starting dose). T1 mapping (MOLLI sequence on a 3T scanner) determined changes in myocardial blood volume. Myocardial blood flow was quantified by microsphere injection, and oxygen consumption was determined by the rate pressure product. T2 simulations were also run using a two-compartment model (intra- and extravascular) to better isolate the effects of PvO₂ and blood volume.

Results: T2, blood flow, oxygen consumption, and blood volume all changed to varying extents between each level of hyperemia (Figure 1). Trend comparisons and multivariable analyses revealed blood flow as the dominant influence on T2 relaxation time, with greater effect at low hyperemia. Oxygen consumption had minimal effect on T2; therefore, PvO₂ changes detected by T2 can be attributed solely to blood flow. T2 simulations confirmed PvO₂ has the strongest influence on T2, but blood volume becomes important at high PvO₂.

Conclusions: T2 is most sensitive to changes in blood flow, but it also detects blood volume at high hyperemia. Myocardial oxygen consumption has almost no effect on T2. With this improved understanding of how to interpret T2 signal changes, T2 mapping becomes a viable non-contrast option to detect several forms of damaged myocardial tissue.

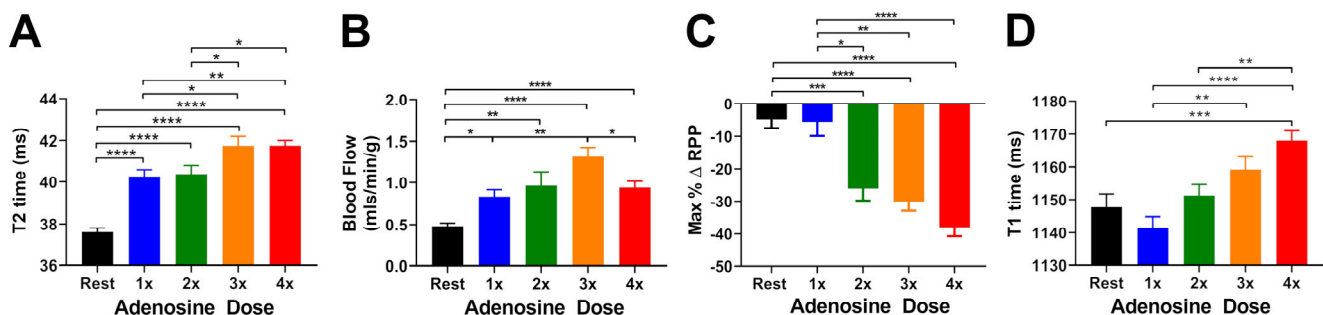


Figure 1: Summary of experimental results measuring T2 (A), blood flow (B), rate pressure product (C), and blood volume (D) at varying levels of hyperemia. Error bars are SEM.

Development of a Human-Based Dual PET/MR Reporter Gene System for In Vivo Cell Tracking

Authors: Shalaby, N.¹, Kelly, J.¹, Martinez, F.¹, Hicks, J.^{1,2,3,4}, Fox, M.^{2,4}, Scholl, T.^{1,5}, Ronald, J.^{1,2}

¹Department of Medical Biophysics, Western University, ²Lawson Health Research Institute, ³Lawson Cyclotron and Radiochemistry Facility, ⁴Saint Joseph's Health Care, ⁵Ontario Institute for Cancer Research

Introduction: While cell-based therapies, particularly cancer immunotherapies, have shown remarkable clinical success, there has been significant differences among patients in terms of treatment response and side effects. Non-invasive methods for monitoring the distribution, migration, viability and persistence of cellular therapies are in need. A multi-modal imaging approach would combine the benefits of more than one imaging tool to provide more comprehensive information on the fate of therapeutic cells. For this work, we are investigating a dual PET and MRI reporter gene system for safe and sensitive longitudinal tracking of cell fate. This system would combine the quantification and sensitivity benefits of PET with the non-irradiative longitudinal tracking benefits of MRI. **Methods:** Human MDA-MB-231 (231) triple negative breast cancer cells were engineered with lentivirus to co-express zsGreen (zsG), a human organic anion transporter polypeptide 1B3 (OATP1B3), which promotes intracellular accumulation of the paramagnetic MRI contrast agent Gd-EOB-DTPA (Primovist). Cells were also co-engineered to express the human sodium iodide symporter (NIS), which promotes the intracellular uptake of the PET tracer, ¹⁸F-tetrafluoroborate (¹⁸F-TFB). *In-vitro* characterization was performed to confirm the transduction efficiency, protein expression, and functionality of both reporter proteins. Mice implanted with naïve and engineered 231 cells into contralateral mammary fat pads were imaged with PET and MRI, after administration of their respective imaging probes. **Results:** Flow cytometry revealed no fluorescence in naïve control cells (Fig.1A), while 93% of the transduced cells were zsG-positive (B). ZsG presence was confirmed by fluorescence microscopy (C). Protein expression of NIS and OATP1B3 was confirmed with Western blots (D). Reporter gene function was tested with MRI of cell pellets and showed a 30% increase in spin lattice relaxation rate in NIS-OATP1B3 and OATP1B3 cells incubated with Gd-EOB-DTPA compared to all other controls (E). Next, we measured a 45-fold significant increase in ¹⁸F-TFB tracer uptake in NIS-OATP1B3 cells compared to naïve control cells (F). *In-vivo* uptake showed significantly higher ¹⁸F-TFB uptake in NIS-expressing tissue as well as the NIS-OATP1B3 tumour (G). *T*₁-weighted MRI imaged showed contrast enhancement in NIS-OATP1B3 tumour post primovist administration compared to naïve tumour (H). **Conclusion:** We have developed the first dual PET and MRI reporter gene system for *in-vivo* cell tracking. Our system uses human-derived reporter genes in combination with clinically approved imaging contrast agents, highlighting the high translation potential of our system.

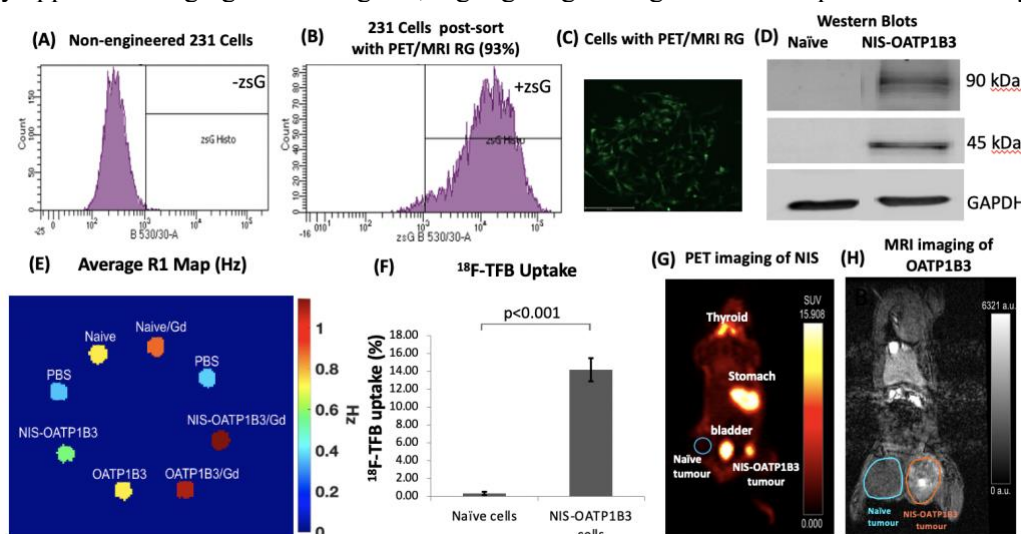


Figure 1: No zsG in naïve cells (A) and 93% transduction efficiency in NIS-OATP1B3-zsG cells (B). Western blots confirmed the presence of OATP1B3 at 90kDa and NIS at 45kDa in NIS-OATP1B3 cells (C). Functional tests with MRI showed over a 30% increase in average R1 of NIS-OATP1B3 cells than in naïve cells (E). Significantly higher ($p < 0.001$) ¹⁸F-TFB tracer uptake in NIS-expressing cells as opposed to naïve cells (F). A PET MAP showing uptake of ¹⁸F-TFB uptake in NIS expressing tissues as well as our NIS-OATP1B3 tumour (G). A *T*₁-weighted MRI image showing contrast enhancement in the NIS-OATP1B3 tumour (H).

Magnetic Field Mapping in High Susceptibility Region Using Pure Phase Encoding MRI

Layale Bazzi, Dan Xiao

Department of Physics, University of Windsor, ON, Canada

Introduction: It is highly challenging to perform MRI experiments in regions of high magnetic susceptibility, such as around metal implants. The drastic magnetic field distortion leads to severe MRI image artifacts. Some methods have been developed for MRI around metal, such as SEMAC [1] and MAVRIC [2]. Mapping the magnetic field B_0 distribution in these high susceptibility regions could enable more advanced novel spatial encoding schemes, exploiting the distorted magnetic field from metal objects for non-linear spatial encoding [3]. The conventional B_0 mapping methods, which employ two gradient echo images acquired at different echo times, are not applicable since the MR signal lifetimes are significantly shorter than the achievable echo times. Rapid intravoxel dephasing leads to signal voids. We propose to employ a pure phase encoding method to measure the magnetic field distribution around metal. This will enable the development of novel MRI techniques for the challenging problem of imaging around metal.

Methods: The pure phase encoding SPRITE method [4] has the advantage of acquiring signals after a very short evolution time t_p following the RF excitation. The echo time can be as short as the probe ringdown time, which ensures capturing the short lifetime signals in high magnetic susceptibility region. The SPRITE signal equation is

$$S(\vec{k}) = \int d^3r \rho(\vec{r}) e^{-i\gamma\Delta B_0 t_p} e^{-i2\pi\vec{k}\cdot\vec{r}},$$

where t_p is a constant for a certain image. Multiple images with different t_p values can be acquired with no extra cost, and the B_0 map can be extracted from the phase of these images.

Results and Discussion: MRI experiments were performed on a phantom consisting of one titanium nut suspended in agar gel, at 1T. 3D SPRITE and GRE images were acquired, as shown in Fig. 1. With t_p values up to 100 μ s, the SPRITE images were artifact-free. The nut hexagon shape is discernible. A large signal void is observed in GRE, Fig. 1b, confirming that conventional GRE based B_0 mapping methods are not feasible in this system. The acquisition time for SPRITE was 15 mins (matrix size 64^3). 16 GRE signal averages were employed for the same data acquisition time.

The B_0 map derived from SPRITE images is shown in Fig. 2a. Excellent agreement has been achieved compared with the theoretical magnetic field distribution, in Fig. 2b, calculated with the analytical solution for a coaxial cylinder model [5]. The metal is indicated by the void in the center. The slight asymmetry in Fig. 2a was due to a small tilt of the nut in the gel. The method can also be applied to evaluate signal amplitude changes between images of different echo times and acquire a T_2^* map.

More severe magnetic susceptibility induced field distortion is expected in high B_0 , leading to a more rapid intravoxel dephasing. At 3T, the t_p upper limit is estimated to be 75 μ s for a 1 mm³ voxel size, where the B_0 mapping would require a gradient amplitude of approximately 300 mT/m.

Conclusions: We have presented a technique to map the magnetic field in regions with high magnetic susceptibility and severe magnetic field distortion. The magnetic field maps will enable the development of advanced spatial encoding schemes around metal object.

References: [1] Lu et al, *MRM* 62, 66-76, 2009. [2] Hayter et al, *AJR* 197, 405-411, 2011. [3] Hennig et al, *Magn Reson Mater Phy* 21, 5-14, 2008. [4] Balcom et al, *JMR* 123, 131-134, 1996. [5] Bhagwandien et al, *MRI* 10, 299-313, 1992.

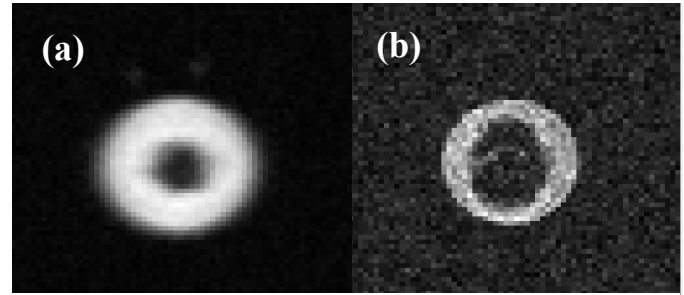


Figure 1. A slice from 3D (a) SPRITE and (b) GRE images of a gel phantom with a titanium nut.

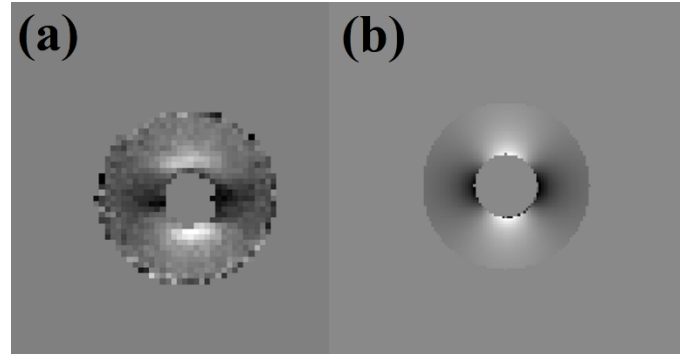


Figure 2. B_0 field distribution around metal (a) measured with SPRITE and (b) simulated.

An activatable reporter gene system to visualize cell-cell communication in cancer immunotherapies

TianDuo Wang^{1,2}, Yuanxin Chen¹, Nivin Nystrom^{1,2}, Shirley Liu^{1,2}, Rangana Guruge², John. A. Ronald^{1,2,3}

1. Robarts Research Institute – Imaging; 2. Department of Medical Biophysics, University of Western Ontario;

3. Lawson Health Research Institute, London, ON, Canada.

INTRODUCTION: Immunotherapy aims to boost a patient's immune system to combat cancer. Cell-based immunotherapies are one of the most promising approaches by harnessing the innate tumour-homing ability of immune cells to better accumulate within malignant lesions. Additionally, immune cells can be engineered with receptors, such as chimeric antigen receptors (CAR)¹, to recognize cancer surface antigens and better kill cancer cells. CAR-T cells have already shown remarkable success in treating B-cell cancers, with potential for many other cancer types on the horizon. Despite clinical success, however, many patients still suffer from inadequate efficacy and/or adverse side effects, thought to be due to sub-optimal tumour homing and off targeting of normal tissues. This study aims to develop a reliable and non-invasive imaging tool to visualize when immune cells interact with its targeted antigen – the prerequisite for inducing cancer cell killing. The synthetic notch (SynNotch) receptor is a uniquely versatile system that signals cell-cell contact via transcriptional modulation of desired genes in response to SynNotch receptor-antigen binding² (Fig. 1A). Our approach is to engineer immune cells with SynNotch receptors which will activate the expression of imaging reporter genes in response to cancer antigen binding. We hypothesize this system will allow for activatable imaging of immune-cancer cell communication.

METHODS: We engineered Jurkat cells, a human T cell line, via sequential lentiviral transduction of two components: (1) a SynNotch receptor directed against CD19, and (2) a trimodal reporter response element containing tdTomato for fluorescence, firefly luciferase (Fluc) for bioluminescence, and organic anion transporting polypeptide 1B3 (OATP1B3) for MRI³ (Fig. 1B). The B-cell surface antigen CD19 was chosen as it is the most successful target of CAR-T immunotherapy in humans⁴. Successfully dual-engineered Jurkat cells were isolated using fluorescence activated cell sorting and expanded. To validate this activatable system *in vitro*, 10⁵ Jurkat cells were co-cultured in well plates with CD19+ Nalm6 B-cell leukemia cells at a 1:1 ratio. As a negative control, we used CRISPR-knockout to generate CD19- Nalm6 cells. Twenty-four hours after co-culturing, tdTomato and Fluc expression in Jurkat cells were assessed using fluorescence microscopy and bioluminescence imaging respectively.

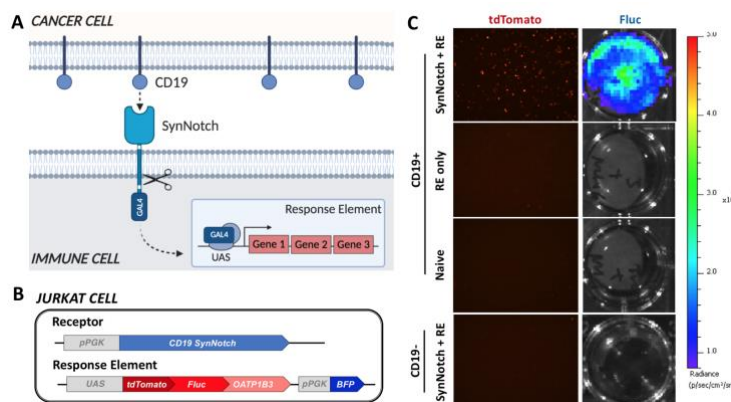


Figure 1. (A) Schematic of SynNotch system. CD19 binding by the CD19-targeted SynNotch receptor induces intracellular cleavage of a GAL4-VP64 transactivator, which binds to an upstream activating sequence (UAS) to initiate transcription of genes of interest encoded in the response element. (B) Jurkat cells were engineered with CD19-targeted SynNotch driven by the phosphoglycerate kinase 1 promoter (pPGK), and a response element containing reporter genes as well as a pPGK-driven blue fluorescence protein (BFP) for sorting. (C) TdTomato fluorescence and Fluc bioluminescence images of Jurkat cells 24 hours after co-culturing with CD19+/- NALM6 cells.

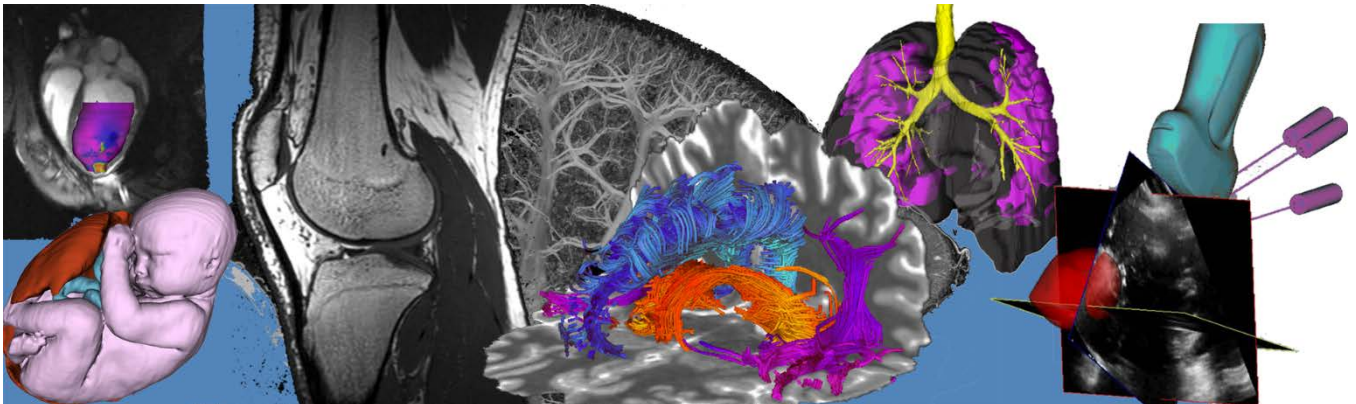
RESULTS: Co-culturing of dual-engineered Jurkat cells with CD19+ Nalm6 cells resulted in higher tdTomato expression and significantly higher Fluc signal ($p < 0.001$, Fig. 1C). In contrast, reporter expression was not observed when Jurkat cells engineered with the response element only or naïve Jurkat cells were co-cultured with CD19+ cells, nor when the dual-engineered Jurkat cells were co-cultured with CD19- Nalm6 cells.

DISCUSSION: We have demonstrated the ability to activate reporter genes in immune cells interacting with cancer cells in a CD19-specific manner. For our future work, we will transfer this system into primary T-cells, imaging our engineered T-cells in a CD19 Nalm6 leukemia mouse model via BLI and MRI, and expanding the potential antigens we can target with SynNotch. Development of this system would provide a non-invasive and specific monitoring tool for cell-based cancer immunotherapies, ultimately improving our ability to understand response/non-response and side effects in individual patients.

REFERENCES: [1] Maude et al., *NEJM*, 2014, 371: 1507-1517. [2] Morsut et al., *Cell*, 2016, 164: 780-791. [3] Nystrom et al., *Invest Radiol*, 2019, 54(5): 302-311. [4] Sadelain et al., *J Clin Invest*, 2015, 125(9): 3392-3400.

Oral Presentation Abstract

Session 27: Neuro Imaging II



Characterization of the Cold Head Artifact Present in Simultaneous Studies of Functional Magnetic Resonance Imaging and Electroencephalography

A. Amador^{1,2}, A. Harrison^{2,3}, and M.D. Noseworthy^{1,2,4,5,6}

¹McMaster School of Biomedical Engineering. ²Imaging Research Centre, St. Joseph's Healthcare, Hamilton.

³Hamilton Health Sciences, Neuroscience Program. ⁴Diagnostic Imaging, St. Joseph's Healthcare, Hamilton.

⁵Department of Radiology, McMaster University, Hamilton, ON.

⁶Electrical and Computer Engineering, McMaster University, Hamilton, ON, Canada.

Introduction: Simultaneous studies of fMRI/EEG provide hemodynamic and electrophysiological information about brain function [1] with high spatial and temporal resolution. However, EEG recordings have always been thought to be contaminated by the cold head artifact generated by the helium pump of the MRI cooling system. The pump is commonly turned off when acquiring concurrent fMRI/EEG data [2] in order to avoid the artifact, at the cost of reducing the pump lifespan. The research objective was to characterize the cold head artifact present in EEG recordings, during simultaneous fMRI/EEG, and to design a filter to allow for its removal without requiring cold head shut-down.

Methods: EEG data were acquired inside a GE Discovery MR750 3T MRI scanner and 32-channel RF receiver coil, using an MRI-compatible EEG amplifier and 64-channel cap with scalp electrodes following the International 10-20 system (Brain Products, Germany). Data were sampled at 5 kHz with 0.5 μ V resolution, and referenced to position FCz. Electrode impedances were kept below 5 k Ω . EEG recordings were collected for 5 minutes from a spherical MRI phantom covered by a layer of EEG gel, with the MRI helium pump (model RDK-408A3, Sumitomo) turned on and off, and from 3 healthy volunteers with and without a gradient-echo EPI sequence (TE/TR=35/2000 ms, 64x64 matrix, 4 mm thickness). Equipment that could be sources of other EMF electrical noise (e.g. MRI scanner lighting and ventilation, MRI compatible projector) was turned off. EEG recordings were downsampled to 1024 Hz, band-pass filtered at 1-200 Hz and corrected for gradient, pulse and blink artifact using EEGLab [3]. Spectral analysis (Kaiser window, $\beta=6$, overlap=25%) was performed on the EEG phantom and volunteer data using Matlab (The MathWorks Inc., Natick, USA).

Results: Phantom power spectrum showed cold head artifact peaks from 11 to 150 Hz (Fig. 1) with the highest peak at 12 Hz and a peak group at \sim 115 Hz. With phantom EEG data as reference, volunteer recordings only showed the peak group at \sim 115 Hz. Commonly studied EEG frequency bands include delta to gamma waves within 0.1-40 Hz, and this range is not affected by the cold head artifact in EEG volunteer recordings (Fig. 2). Moreover, artifact peaks above 40 Hz can be filtered with a low-pass filter which would attenuate the peak group at \sim 115 Hz.

Conclusions: Data shows that newer liquid helium recycling systems have minimal cold head artifact in EEG recordings, and could be filtered out, as compared to previously published studies. We suggest turning the cold head off for simultaneous fMRI/EEG is not necessary. Nonetheless, characterization of this artifact should be carried out for each MRI system to conclude whether turning the helium pump off is necessary.

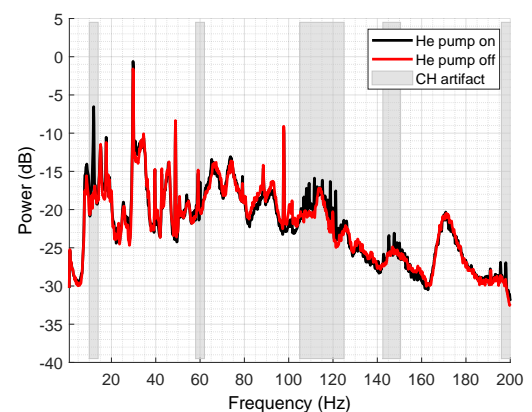


Figure 1: Average power spectra of EEG phantom recordings with the He pump on (black) and off (red). Peaks associated with the cold head artifact are shown in shaded gray areas.

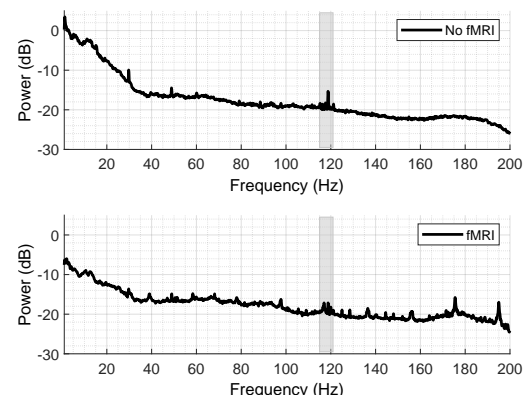


Figure 2: Average power spectra of EEG volunteer recordings with no fMRI sequence (top) and with fMRI sequence (bottom) at rest. Peaks associated with the cold head are at \sim 115 Hz (shaded gray).

1. Mulert, C. *et al.* (eds Mulert, C. *et al.*) (Springer Berlin Heidelberg, Berlin, Heidelberg, 2010).
2. Nierhaus, T. *et al. NeuroImage* **74**, 70–76 (July 2013).
3. Delorme, A. *et al. J. neuroscience methods* **134**, 9–21 (2004).

Two multi-echo SPGR acquisitions for the simultaneous generation of SWI, qT1 and other parametric maps: preliminary data

Vishaal Sumra^{1,3} and Sofia Chavez^{1,2,3}

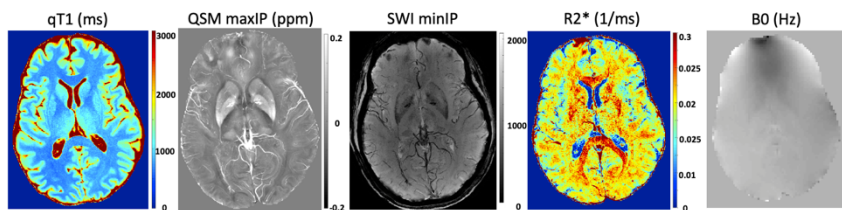
¹Brain Health Imaging Centre – MRI, Centre for Addiction and Mental Health, Toronto, ON, Canada

²Department of Psychiatry, University of Toronto, Toronto, ON, Canada

³Institute of Medical Science, University of Toronto, Toronto, ON, Canada

Introduction: Quantitative T1 (qT1) maps provide information relating to tissue microstructure¹, whereas susceptibility weighted image (SWI) contrast is dependent on local changes in magnetic susceptibility². Both qT1 and SWI are typically generated using the spoiled-gradient-echo (SPGR) sequence, with qT1 maps using magnitude data³, and SWI using complex data². Multi-echo (ME) complex data from SPGR scans can be used to generate quantitative susceptibility maps (QSM), B0 maps and R2* (1/T2*) maps. Quantitative maps are computed from separate acquisitions, increasing scan time and mis-registrations. Recently, two acquisitions have been designed where qT1 and SWI data can be acquired using complex data from the same set of scans^{4,5}. We propose a new implementation which uses complex data from two ME-SPGR scans (and a B1 map) to generate qT1, SWI, QSM, R2* and B0 maps at high resolution, in the same space.

Methods: Four healthy volunteers were scanned using a 32-channel head coil (Nova Medical), in a 3T MRI scanner (MR750, GE Healthcare) according to institutional REB. A modified SPGR sequence was used to enable ME acquisitions (ME-SPGR). Axial ME-SPGR (0.5×0.75×2 mm³) phase and magnitude data were acquired at two flip angles ($\alpha = 3^\circ$ & 24°), for 6 echoes (TE₁ = 3.57 ms, echo spacing = 4.42 ms), TR=31ms, total scan time= 5.5 min×2=11 min. For validation, our standard 1 mm³ 3D-qT1 mapping protocol⁶ (8 min, including B1 mapping with an efficient FSE-based calibrated DAM⁷) was acquired as well as two EPI-T2w images collected in opposing phase encode directions for B0 mapping using an independent method⁸. Images were processed using FSL (FMRIB Software Library). Phase processing was done with MATLAB (The MathWorks, Inc., MA), and STI Suite⁹ for QSM. For SWI and QSM, complex data from echoes 2-6 were individually phase rotated relative to TE₁ (their phase was replaced by the phase difference, relative to TE₁), to remove background phase effects and ensure phase alignment across both flip-angles. Data was then complex-averaged to create a dataset consisting of 5-echoes (TE₂– TE₆). Phase from the rotated, averaged TE₆ was unwrapped (using PRELUDE), filtered and processed to create SWIs². Phase from the five averaged echoes (TE₂ to TE₆) were processed with STI Suite⁹ using the STAR-QSM algorithm. B0 maps were generated from a resampled complex dataset for both flip angles (resampled to 2×2×2 mm³) that were complex-averaged and phase-unwrapped and fit to a linear function ($\Delta\theta$ vs ΔTE) to generate B0 maps. R2* maps were obtained by fitting the magnitude-averaged signal across flip angles at all 6 echoes to an exponential decay function.



Results: High-resolution multi-parametric maps (see figure) were generated in the same space through processing of complex data from our protocol. ME-qT1 maps and B0 maps were validated by comparing with separately acquired qT1 and

B0 maps for all subjects. Averaging of magnitude data from both flip-angle datasets prior to R2* mapping increased image quality. Phase-rotating TE₂ to TE₆ relative to TE₁ aided in phase unwrapping while allowing for complex-averaging across flip angles prior to SWI and QSM phase-processing. SWIs & QSM showed robust depictions of vasculature over min/Max intensity projections (IP), respectively with QSM being less affected by distortions and phase artifacts.

Conclusions: Six-echo SPGR complex datasets at two flip-angles allows for multi-parametric mapping while also limiting errors related to misregistrations and phase unwrapping. Compared to STAGE⁵, more than 2 echoes at each flip-angle is beneficial because it allows for phase-rotating relative to TE₁. By having qT1 and QSM in the same space, the T1 of blood can be estimated in vasculature¹⁰. Future work includes using complex data for all computations, including T1 and R2*, and decreasing the number of echoes to decrease scan time.

References: 1. Lorio S, et al. Hum Brain Mapp; 37, 2016
2. Haacke EM, et al. Am J Neuroradiol; 30, 2009
3. Chavez S, Stanisiz GJ. NMR in Biomed; 25, 2012
4. Cao T, et al. Abstract #881, ISMRM, 2020
5. Chen Y, et al. Magn Reson Imaging; 46, 2018

6. Chavez S, abstract #537, ISMRM, 2018
7. Desmond K, Chavez S. MRI ;77, 2021
8. Andersson JLS et al. Neuroimage. 20(2), 2003
9. Li W, et al. Abstract #3265, ISMRM, 2014
10. Sumra V, Chavez S, abstract #76, ImNO, 2020.

Cross validation of 3AM Diffusion MRI phantoms using microscopy, synchrotron micro computed-tomography, and simulation.

Farah N. Mushtaha, Tristan K. Kuehn¹, Omar El-Deeb, Seyed A. Rohani, Luke W. Helpard, Hanif Ladak, Amanda Moehring, Corey A. Baron, Ali R. Khan

Robarts Research Institute, Western University, London, Canada

Introduction: Diffusion MRI (dMRI) is a promising imaging method to quantify histological features of the brain at a micrometre scale¹. However, there is no “ground truth” to validate it. 3D printed axon-mimetic phantoms (3AM) possess that can mimic diffusion characteristics of axons². In this study, we construct an analytic model of diffusion in 3AM phantoms based on confocal microscopy and synchrotron micro computed tomography (micro-CT) imaging and compare simulated diffusion signal from the analytic model to reported measured diffusion signals².

Methods: phantom blocks were produced and sliced into 50 μm slices, then dyed with Rhodamine Beta, and mounted on positive microscope slides. Confocal microscopy was performed using a Leica SP5 laser system microscope with a 40X oil-immersion objective lens. Using MATLAB's image processing toolbox, averaged z-stack confocal microscopy images were segmented using an adaptive thresholding technique³. A cylindrical 3AM phantom was prepared for propagation-based phase-contrast micro-CT scan using the Biomedical Imaging and Therapy beamline(05ID-2) at the Canadian Light Source Inc. (Saskatoon, Canada). The micro-CT volume was segmented to calculate the pore diameter and distribution. Camino⁴ was used to construct an analytic diffusion model composed of a free water compartment with a volume fraction estimated from the micro-CT volume, and a second compartment composed of spins within parallel cylinders with radii distributed according to a gamma distribution. The simulation used a diffusivity of $2.1 \times 10^{-3} \text{ mm}^2/\text{s}$. We simulated a diffusion MRI scan of our analytic model using experimental scan parameters², and fit Diffusion Kurtosis Imaging (DKI) to the simulated signal using DiPy.

Results: The segmented pores confocal microscopy images had a mean equivalent diameter of 7.57 μm , a median equivalent diameter of 3.51 μm , and a standard deviation of 12.13 μm (Figure 1). The segmented pores from one x-z slice of the micro-CT volume had a mean equivalent diameter of 8.69 μm , a median equivalent diameter of 5.71 μm , and standard deviation of 20.40 μm (Figure 1).

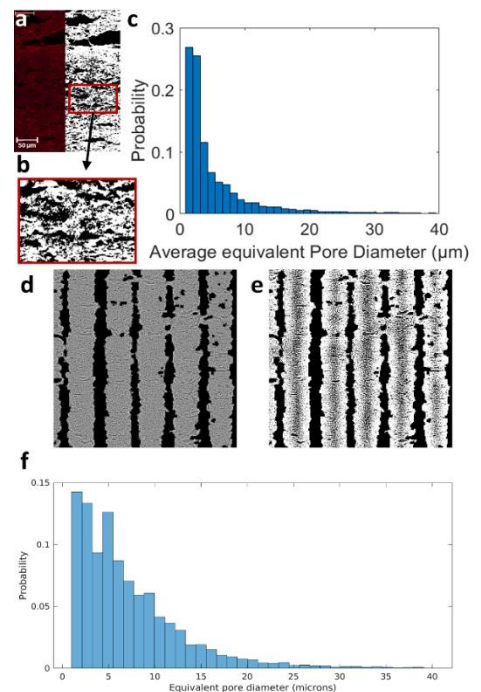
Fitting DKI to the simulated signal yielded a radial diffusivity of $0.944 \times 10^{-3} \text{ mm}^2/\text{s}$ and radial kurtosis of 1.19, which is nearly identical to the experimentally observed values of $1.01 \times 10^{-3} \text{ mm}^2/\text{s}$, and 1.13 for radial diffusivity, and radial kurtosis, respectively².

Conclusion: The close correspondence between simulated and reported² diffusion behaviour suggests that the microscopy images resolve most of the phantoms' pores, and that the pores are approximated well as straight cylinders.

Acknowledgements. This work was supported by the Canada First Research Excellence Fund, Brain Canada, and Discovery Grants from the Natural Sciences and Engineering Research Council (NSERC).

References. [1] Alexander D.C, *et al.* *NMR in Biomedicine*. 2017;e3841. doi:10.1002/nbm.3841. [2] Mushtaha F.N *et al.* *OHBM Annual Meeting*. 2020, 3516.[3] *Journal of Graphics Tools*. 2007;12:13–21. [4] Cook P.A *et al.* *ISMRM Annual Meeting*. 2006. Vol. 2759. p. 2759.

Figure1. a) Confocal microscopy image before (left) and after (right) segmentation. Pores are shown in black. c) Normalized histogram of pore equivalent diameters from total segmentations (N = 10762). d) Preprocessed micro-CT slice with air-filled regions masked out. e) Segmentation results with pores shown in black. f) Histogram of pore equivalent diameters from micro-CT.



Optimized oscillating gradients for frequency dependent *in vivo* diffusion kurtosis measurement

KB Borsos^{1,2}, DHY Tse^{2,3}, PI Dubovan^{1,2}, CA Baron^{1,2,3}

¹ Department of Medical Biophysics, Western University, London Ontario, ² Centre for Functional and Metabolic Mapping, Western University, London Ontario, ³ Robarts Research Institute, London Ontario

Introduction: Oscillating gradient spin-echo (OGSE) sequences have gained significant traction in recent years as a technique to investigate the spectral and temporal dependence of diffusion in the human brain. Shorter diffusion times are realized with increasing oscillation frequency and thus enable the probing of restricted diffusion. Observation and modeling of the frequency dependence of diffusion metrics can thereby provide key insight into the microstructural properties of diseased and healthy tissue [1]. While the frequency dependence of *in vivo* diffusivity has been thoroughly investigated [2], the dependence of diffusion kurtosis remains to be fully realized. The rapid reduction in b-value with increasing frequency has historically made kurtosis difficult to measure with oscillating gradients. Recent work has shown a decrease in mean kurtosis with increasing oscillation frequency however this work relies on a high-performance gradient insert coil, which achieves max gradient amplitudes of 200 mT/m and slew rates in excess of 500 T/m/s [3]. Therefore, in this work we demonstrate, for the first time with a conventional gradient system, the frequency dependence of *in vivo* kurtosis using an optimized OGSE sequence.

Methods: A dual-loop oscillating gradient waveform was designed to minimize the echo time of the acquisitions by reducing the number of periods of the pulse (see Figure 1A). An equation for the signal-to-noise ratio (SNR) of the kurtosis difference between conventional pulsed gradient spin-echo, PGSE ($f = 0$ Hz) and OGSE ($f > 0$ Hz) acquisitions was derived from noise variance propagation and maximized for possible scan parameters including frequency, echo time and b-value. Based on the optimization results (see Figure 1C), 25 Hz OGSE and PGSE data was acquired in two healthy male volunteers using single shot EPI readout on a 7T system (max gradient amplitude 80 mT/m, slew rate 333 T/m/s). The optimized scan parameters were as follows: 4-direction tetrahedral diffusion scheme, TE/TR = 86/5000 ms, b-value = 0, 1000, 2000 s/mm² and 8 averages with 2 mm isotropic resolution. Images were corrected for eddy currents using a clip-on field monitoring system (Skopec, Switzerland), and corrected for Gibbs ringing using MRtrix. Diffusion data was directionally averaged and fitted with a nonnegative least-squares algorithm on a voxel-wise basis to produce kurtosis maps.

Results: Calculated kurtosis maps for the PGSE and OGSE acquisitions are shown in Figures 2A & 2B respectively. The average kurtosis within a selected ROI for the images are presented in Figure 2C. We demonstrate ~12% difference in kurtosis values between 25 Hz OGSE and PGSE acquisitions in the same selected white matter region.

Conclusions: We've demonstrated the frequency dependence of kurtosis for the first time using oscillating gradients without the aid of a gradient insert. We anticipate this development to enable widespread integration with kurtosis imaging in future works to investigate and model changes in healthy and diseased tissue.

References: [1] Novikov *et al.* *NMR in Biomed*, 2019; 32(4) [2] Arbabi *et al.* *MRM*, 2020; 83(6) [3] Yang *et al.* *Proc. Intl. Soc. Mag. Reson. Med.* (2020) 0962

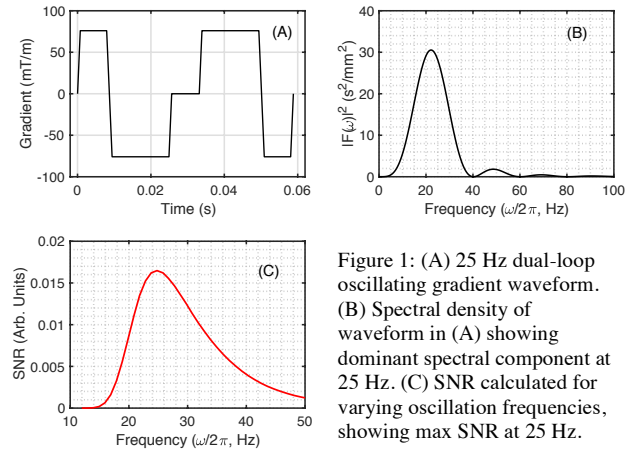


Figure 1: (A) 25 Hz dual-loop oscillating gradient waveform. (B) Spectral density of waveform in (A) showing dominant spectral component at 25 Hz. (C) SNR calculated for varying oscillation frequencies, showing max SNR at 25 Hz.

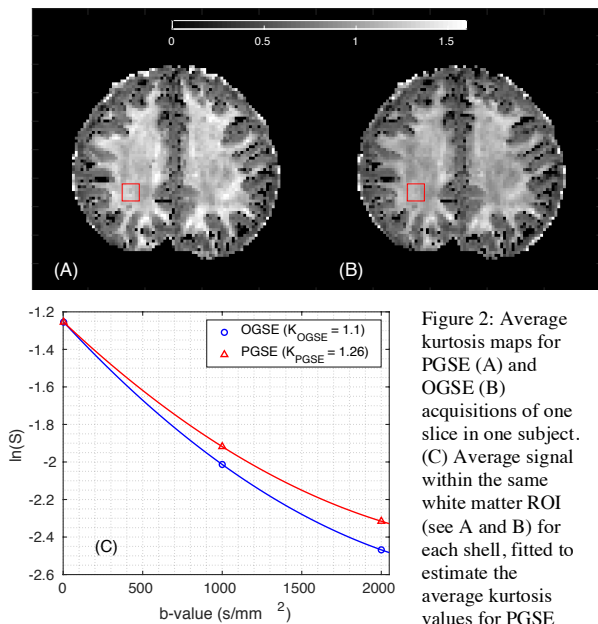


Figure 2: Average kurtosis maps for PGSE (A) and OGSE (B) acquisitions of one slice in one subject. (C) Average signal within the same white matter ROI (see A and B) for each shell, fitted to estimate the average kurtosis values for PGSE and OGSE.

Measuring Ischemic Volumes using Quantitative Multiphase CT Angiography Perfusion Maps

Kevin J. Chung,^{a,d} Donald H. Lee,^b Sachin Pandey,^b Mayank Goyal,^c Bijoy K. Menon,^c Andrew M. Demchuk,^c Alexander V. Khaw,^c Jennifer Mandzia,^c Ting-Yim Lee^{a,d}

^aDepartments of Medical Biophysics, ^bMedical Imaging, ^cClinical Neurological Sciences, University of Western Ontario, London, Ontario; ^dRobarts Research Institute and Lawson Health Research Institute, London, Ontario;

^eDepartments of Radiology and Clinical Neurosciences, University of Calgary, Calgary, Alberta

Introduction: CT perfusion allows the measurement of cerebral blood flow (CBF) and other hemodynamic parameters by analyzing the passage of contrast through the brain from dynamic CT scans. These perfusion parameters are physiological indicators for ischemia in acute ischemic stroke and may help triage patients for treatment. The technical proficiency required for a reliable CT perfusion study inhibits its use in smaller community hospitals where trained technicians may not be readily available. In these settings, using routine scans such as non-contrast CT (NCCT) and contrast-enhanced CT angiography (CTA) may simplify perfusion imaging at the expense of dynamic information. In this study, we mitigate the challenge of limited dynamic information by using a model-based algorithm to calculate for perfusion parameters, which reduces the degrees of freedom of the solution. We hypothesize that a dynamic imaging sequence comprising NCCT and time-resolved multiphase CTA (mCTA) can be used to calculate CT perfusion-like maps from which ischemic volumes can be measured.

Methods: Twenty-five patients presenting with acute ischemic stroke who received NCCT, mCTA, and CT perfusion imaging were included in this study. Our proposed dynamic sequence (mCTA-perfusion, mCTA-P) consisted of four images: the NCCT and three phases of mCTA. The first phase of mCTA was scanned at the peak contrast enhancement of a major cerebral artery in the healthy brain followed by two additional phases after an 8 s and 16 s delay. For CT perfusion, 22 dynamic images were serially acquired over 60 s after contrast injection to monitor the passage of contrast through the brain at high temporal resolution. A prototype model-based deconvolution algorithm (CT Perfusion 4D, GE Healthcare) was used to calculate CBF and Tmax maps using each mCTA-P and CT perfusion series. Tmax is a measure of the delay time in contrast arriving at and time required to pass through a voxel of tissue. Relative CBF (rCBF) maps were calculated by normalizing CBF maps by the mean CBF in the contralateral hemisphere. The ischemic brain region was identified by voxels with Tmax > 8 s. Ischemic voxels with rCBF less than a validated time-dependent threshold was considered infarct (irreversibly dead brain) while those greater than the rCBF threshold were considered penumbra (potentially salvageable ischemic tissue). Volume agreement and reliability between mCTA-P and CT perfusion ischemic volumes were assessed by Bland-Altman analysis and the intraclass correlation coefficient, respectively.

Results: Ischemic regions appeared similar between mCTA-P and CT perfusion maps by qualitative inspection. Bland-Altman analysis revealed good agreement between CT perfusion and mCTA-P volume measurements as mean differences (limits of agreement) were -1.0 (-14.9 to 12.9) ml for infarct and 8.4 (-42.4 to 59.1) ml for penumbra. Intraclass correlation (95% confidence interval, $p < 0.05$) between CT perfusion and mCTA-P volumes were 0.72 (0.46 to 0.87) for infarct and 0.68 (0.41 to 0.85) for penumbra, indicating good to moderate reliability.

Conclusions: Quantitative perfusion can be estimated from routine NCCT and mCTA without introducing additional scan time, radiation dose, and contrast injections associated with CTP. Further studies are required to compare treatment decisions made with mCTA-P versus CT perfusion.

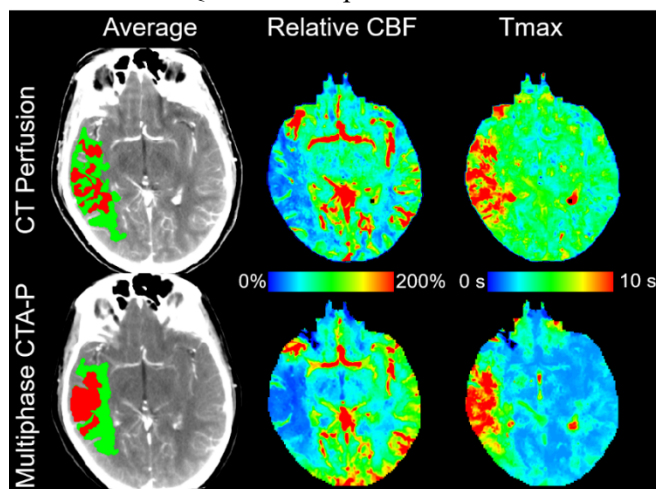


Figure. Perfusion maps derived from CT perfusion (top row) and mCTA-P (bottom row). Infarct (red) and penumbra (green) overlaid on dynamic CT average maps (left column). Relative CBF (middle column) and Tmax maps (right column) show similar ischemic regions.

Name	Presentation	Page	Name	Presentation	Page
Abbas-Aghababazadeh, Farnoosh	P6-1	63	Bartlett, Jason	O15-4	137
Abdelrazek, Mohamed	O25-3	205	Bastian-Jordan, Matthew	O1-4	28
Adam, Ramina	P17-7	152	Bataghva, Mahsa	O15-5	138
Adams, John	P18-5	158	Bauman, Glenn	O1-4	28
Agarwal, Anush	O14-4	131	Bax, Jeffrey	O1-2	26
Akbarifar, Faranak	P11-5	111		P5-3	55
Allam, Nader	P24-3	197		O26-1	209
Allen, Christine	P4-5	47	Bazzi, Layale	O26-4	212
Allen, Daniel	P4-4	46	Beauchet, Olivier	P10-7	105
Amador, Alejandro	O27-1	215	Belanger, Nicholas	O19-1	163
Anazodo, Udunna	P12-4	118	Belli, Michael	P5-5	57
Anderson, William	P18-4	157		P8-1	82
Annweiler, Cedric	P10-7	105	Bellyou, Miranda	P10-7	105
Appleton, Tom	O3-3	39		O15-2	135
Aragaki, Masato	P12-1	115	Beneteau, Jean-Marc	P8-6	87
Arezza, Nico	P7-1	73	Berih, Maryam	O2-5	35
	P7-3	75	Berman, David	P6-8	70
	O15-1	134	Bernards, Nicholas	P12-1	115
Armstrong, Mark	O2-1	31		O13-3	124
Arrowsmith, Collin	P6-1	63	Biernaski, Heather	P24-6	200
Asghar, Huma	O2-2	32	Black, Sandra	O19-4	166
Athwal, George	P10-4	102	Bock, Nicholas	O19-3	165
Au, Jason	P11-2	108	Boni, Enrico	P8-2	83
Au, Ryan	O25-5	207	Borsos, Kevin	O15-1	134
Aubert, Sarah	P8-1	82		O27-4	218
Azma, Roxana	O14-1	128	Bourbeau, Jean	O2-3	33
Babichev, Yael	P4-5	47		O15-3	136
Bainbridge, Daniel	O14-2	129		O15-4	137
Barker, Kevin	P24-2	196		P22-3	183
Baron, Corey	P5-1	53		O25-5	207
	P7-1	73	Boyle, Amanda	O13-2	123
	P7-3	75	Brackstone, Muriel	O13-3	124
	P7-5	77		P24-6	200
	O15-1	134	Branco, Cassandra	P17-2	147
	O19-5	167	Bratman, Scott	P6-1	63
	O27-3	217		O25-4	206
	O27-4	218	Broberg, Dana	P10-7	105
Barr, Colton	O21-2	176	Broberg, Jordan	O3-2	38
Barry, Jennifer	P9-5	95	Brown, Arthur	O15-1	134
	O26-2	210	Brun, Emilie	P12-3	117
Bartha, Robert	P10-7	105	Buchler, Ariel	P23-2	188
	O15-2	135	Bulnar, Sharshi	O20-5	173
	O19-2	164	Burgers, Kyle	P24-1	195
	O19-5	167	Burns, David	P4-3	45
	P23-4	190	Butler, John	P9-7	97

Name	Presentation	Page	Name	Presentation	Page
Calvert, Nicholas	P12-3	117	Chugh, Brige	P24-5	199
Camire, Daenis	P16-3	142	Chung, Kevin	P17-4	149
	O21-1	175		O27-5	219
Campbell, Mikki	P24-5	199	Clarke, Collin	P4-4	46
Cao, Daniel	P17-3	148	Cobos, Santiago	P7-7	79
Cardinell, Jillian	O14-1	128		P23-3	189
Carnahan, Patrick	O14-2	129	Cojocari, Veronica	P22-5	185
Carreno, Isaac	O21-5	179	Coleman, Kristy	O19-5	167
Carter, Anthony	P9-2	92	Connolly, John	O19-3	165
Chad, Jordan	O19-4	166	Connolly, Laura	P4-7	49
Chan, Rachel	P24-5	199		P11-5	111
Chang, Patrick Dong Min	O20-5	173	Cook, Moses	P23-6	192
Chau, Oi Wai	P24-1	195	Cool, Derek	O1-4	28
Chavez, Sofia	P5-9	61	Cotechini, Tiziana	P5-8	60
	P7-4	76	Cron, Greg	P9-2	92
	O27-2	216	Cronin, Alicia	O19-2	164
Chee, Adrian	P8-2	83		P23-4	190
	P9-6	96	Cunningham, Ian	P8-8	89
	P11-2	108	Curpen, Belind	P16-1	140
	O21-4	178	Czarnota, Gregory	O13-4	125
Chen, Elvis	P4-4	46		P24-5	199
	P4-9	51	Daher, Baraa	P10-4	102
	P5-2	54	Daly, Michael	P4-6	48
	O14-2	129	Danielli, Ethan	O19-3	165
Chen, Jean	O19-4	166	Davieau, Kieffer	P12-4	118
Chen, Matthew	P12-1	115	Davies, Joel	P4-2	44
Chen, Yuanxin	O26-5	213		P16-4	143
Chen, Jianan	O25-2	204	Day, James	P18-1	154
Cheng, Ivy	O19-4	166	de Ribaupuerre, Sandrine	P11-3	109
Cheung, Alison	O14-3	130		P17-7	152
Cheung, Helen	O25-2	204		O19-1	163
Chin, Joseph	O1-4	28	Deguet, Anton	P4-7	49
Chinnery, Tricia	P6-6	68	DeKraker, Jordan	P17-6	151
	P6-7	69		P18-8	161
Cho, Sherwin	O14-1	128	Delhaes, Flavien	P23-7	193
Cho, Eunyoung	P9-4	94	DeMatteo, Carol	O19-3	165
Christiansen, Spencer	P23-3	189	Demchuk, Andrew	P17-4	149
	O25-1	203		O27-5	219
Christidis, Nickolas	P17-6	151	Demidov, Valentin	P24-3	197
Christie, Jaryd	O25-3	205	Dempsey, Sergio	P18-3	156
Chronik, Blaine	P5-4	56	Dempster, Kara	O2-4	34
	P8-3	84	den Otter Moore, Imogen	O3-4	40
	P8-5	86		O3-5	41
	P18-5	158	Detombe, Sarah	O19-2	164
Chu Kwan, William	O3-4	40		P23-4	190
	O3-5	41	Detsky, Jay	P24-5	199

Name	Presentation	Page	Name	Presentation	Page
Devlin, Megan	O19-5	167	Fauerbach, Paola Nasute	P6-9	71
DeVries, David	P6-2	64	Fenster, Aaron	O1-2	26
Dhahri, Wahiba	P23-6	192		O1-5	29
Diao, Babacar	O1-3	27		O3-3	39
Dima, Robert	O3-3	39		P5-3	55
Ding, Xiao Fan	P7-2	74		P10-5	103
Diop, Mamadou	O3-1	37		P11-3	109
Doad, Jagroop	P10-7	105		O19-1	163
Doyle, Thomas	P11-1	107		O21-3	177
	P22-2	182		P24-2	196
Drake, James	O3-4	40		O26-1	209
	O3-5	41	Fernando, Ann	P24-7	201
	P4-5	47	Fialkov, Jeff	P4-1	43
Drangova, Maria	P11-6	112	Fichtinger, Gabor	O1-1	25
	P11-7	113		O1-3	27
	P23-3	189		P4-7	49
	O25-1	203		P6-9	71
D'Souza, David	O1-2	26		P11-5	111
	O1-4	28		P16-3	142
	O21-3	177		O21-1	175
du Toit, Carla	P10-5	103		O21-2	176
Dubovan, Paul	P5-1	53		P22-1	181
	O27-4	218	Finger, Elizabeth	O19-5	167
Duerden, Emma	P17-3	148	Finkelstein, Joel	P6-4	66
Duggal, Camille	O19-2	164		O21-5	179
Duggal, Neil	O19-2	164	Fishman, Zachary	P4-1	43
	P23-4	190	Fleisig, Jacqueline	P4-6	48
Eagleson, Roy	P17-7	152	Flynn, Lauren	O15-5	138
Ehrlich, Josh	P6-9	71	Foltz, Warren	P4-5	47
El-Deeb, Omar	O27-3	217	Ford, Sabrina	O2-4	34
Eles, Christopher	P6-1	63		P17-2	147
Elfaal, Mohamed	O14-4	131	Forte, Vito	P4-2	44
Elsaid, Sonja	P5-9	61		P16-4	143
Emmenegger, Urban	P6-4	66	Foster, Paula	O2-5	35
Empey, Mary-Ellen	P23-7	193		O13-1	122
Engel, Jay	P6-9	71		O20-4	172
	P22-1	181	Fowler, Robert	O19-4	166
Ensminger, Yara	O20-5	173	Fox, Matthew	P7-8	80
Erb, Jason	P16-3	142		P9-1	91
	O21-1	175		P12-4	118
Ertl-Wagner, Brigit	O14-1	128		P12-6	120
Escartin, Terenz	P9-5	95		O26-3	211
Faber, Cornelius	O2-1	31	Fradin, Cecile	O20-2	170
Farag, Adam	P12-4	118	Fraser, Douglas	O19-5	167
Farber, Gedaliah	P23-2	188	Friesen-Waldner, Lanette	P23-7	193
Farrag, Nadia	O14-5	132	Fu, Yanghao	O13-5	126

Name	Presentation	Page	Name	Presentation	Page
Fullerton, Kelly	P6-4	66	Hajdok, George	P6-2	64
Gaede, Stewart	P5-7	59	Halder, Arjama	P5-4	56
	O13-3	124		P8-5	86
	P24-1	195	Hall, Geoffrey	O19-3	165
	P24-6	200	Hamilton, Amanda	O13-5	126
Gaikar, Rohini	P16-2	141	Hamilton-Wright, Andrew	P11-4	110
Gao, Fuqiang	O19-4	166	Han, Wenchao	O14-3	130
Gardi, Lori	P5-3	55	Handler, William	P5-4	56
	P24-2	196		P8-3	84
Gariepy, Jean	P24-7	201		P8-5	86
Gelman, Neil	O13-3	12		P18-5	158
	P24-6	200	Handsor, Stephanie	O19-5	167
Gerolami, Justin	P6-9	71	Hardisty, Michael	P4-3	45
Gevaert, Julia	O20-4	172		P6-4	66
Ghahari, Daamoon	P17-7	152		P10-2	100
Ghugre, Nilesh	P23-6	192		O21-5	179
	O26-2	210	Harrison, Amabilis	O27-1	215
Gilbank, Ashley	P4-6	48	Heidari, Helma	O19-5	167
Gilboa, Asaf	O19-4	166	Helpard, Luke	O27-3	217
Gillies, Derek	O3-3	39	Hess, David	O15-5	138
	O21-3	177	Hewlett, Miriam	P11-6	112
Gladdy, Rebecca	P4-5	47		P11-7	113
Glikstein, Rafael	P9-2	92	Heyn, Chinthaka (Chris)	O19-4	166
Goertz, David	O20-5	173	Hicks, Justin	P7-8	80
Goldhawk, Donna	O20-1	169		P12-4	118
	O20-2	170		O26-3	211
	P23-5	191	Hindmarch, Charles	P5-8	60
Gomez-Lemus, Jose	O1-4	28	Hisey, Rebecca	P16-3	142
Goubran, Maged	O19-4	166		O21-1	175
Goyal, Mayank	O27-5	219		O21-2	176
Graham, Charles	P5-8	60	Ho, Rachelle	O19-3	165
Graham, Simon	O19-4	166	Hogg, James	O2-2	32
Gregor, Alexander	P12-1	115		O2-3	33
Groves, Leah	P4-9	51		O15-3	136
Gualtieri, Tommaso	P4-6	48		O15-4	137
Guevorguian, Philipp	P6-6	68		P22-3	183
Guo, Wenzhangzhi	P4-2	44		O25-5	207
	P16-4	143	Holdsworth, David	P7-7	79
Gupta, Maya	P17-2	147		P10-6	104
Guruge, Rangana	O26-5	213		P10-7	105
Gutsol, Alexey	P9-2	92		P18-2	155
Gyackov, Igor	O21-3	177		P18-4	157
Haast, Roy	P17-6	151		P23-3	189
Hague, Cameron	O15-3	136	Holterman, Chet	P9-2	92
Haibe-Kains, Benjamin	P6-1	63	Hong, Gregory	P23-3	189
	O25-4	206			

Name	Presentation	Page	Name	Presentation	Page
Hoover, Douglas	O1-2	26	Kassam, Zahra	O1-4	28
	O1-4	28	Kaufmann, Martin	P6-8	70
	O21-3	177		P11-5	111
Hope, Andrew	P6-1	63		P22-1	181
	O25-4	206	Kazmierski, Michal	O25-4	206
Hopfgartner, Adam	P4-3	45	Keller, Brian	P24-5	199
Howard, James	O3-2	38	Kelly, John	O13-5	126
Howes, Daniel	P16-3	142		O26-3	211
	O21-1	175	Kennedy, Chris	P9-2	92
Hu, Zoe	P6-9	71	Kerhoulas, Zoe	P24-6	200
Huang, Bao Yi (Emily)	P4-2	44	Keunen, Ben	P4-5	47
	P16-4	143	Khan, Ali	P17-3	148
Hussain, Uzair	P18-8	161		P17-6	151
Idriss, Ahmedou Moulaye	O1-1	25		P18-8	161
Innis, Robert	O13-2	123		O27.3	217
Ioussoufovitch, Seva	O3-1	37	Khaw, Alexander	O27-5	219
Irish, Jonathan	P4-6	48	Khazae, Tina	P23-3	189
Isaac, Methvin	P12-2	116	Kheirkhah, Niusha	O13-4	125
Iseman, Rachael	P6-8	70	Kholer, Stefan	P17-6	151
Isen, Jonah	P16-5	144	Kikinis, Ron	O1-1	25
Ishii, Takuro	P11-2	108		O1-3	27
Ismailani, Uzair	P23-2	188	Kim, Sejin	O25-4	206
Ivanov, Todor	P18-4	157	Kim, Janny	P23-1	187
Jabs, D.	P6-9	71	Kirby, Alexia	P12-3	117
Jafari, Parya	P18-3	156	Kirby, Miranda	O2-2	32
Jamaspishvili, Tamara	P6-8	70		O2-3	33
Jamzad, Amoon	P5-8	60		O15-3	136
	P6-8	70		O15-4	137
	P11-5	111		P22-3	183
	P22-1	181		P22-4	184
Janssen, Natasja	P11-5	111		O25-5	207
	P22-1	181	Klein, Geoff	P6-4	66
Jegatheesan, Aravinthan	O19-4	166		O21-5	179
Jeon, Peter	O2-4	34	Knier, Natasha	O13-1	122
	P17-1	146	Knight, Ashley	P17-5	150
	P17-2	147	Knull, Eric	P5-3	55
Ji, Xiang	O19-4	166		O26-1	209
Jones, Blake	P24-3	197	Koff, Matt	O3-2	38
Joschko, Abigayel	P4-4	46	Konyer, Norman	P5-6	58
Jurkiewicz, Michael	O19-5	167		P8-4	85
Kadhim, Sarah	O2-3	33	Kornecki, Anat	O13-3	124
Kahrs, Lueder	P4-2	44	Kosik, Ivan	P4-8	50
	P16-4	143	Kovacs, Michael	P9-7	97
Kamegawa, Rimpei	P12-1	115	Krahn, Philippa	P9-5	95
Kanagasabai, Kesavi	P7-6	78	Kuehn, Tristan	O27-3	217
Karat, Bradley	P18-8	161	Kuling, Grey	P16-1	140

Name	Presentation	Page	Name	Presentation	Page
Lacefield, James	O15-5	138	Logan, Kathryn	P22-1	181
Lacoste, Baptiste	P9-2	92	Lynn, Kalan	O13-3	124
Ladak, Hanif	O27-3	217	Lyons, Frank	P6-4	66
Laflamme, Michael	P23-6	192	MacIntosh, Bradley	O19-4	166
Lagerwaard, Frank	P6-2	64	MacKenzie, Scott	P24-5	199
Lalone, Emily	P10-1	99	MacKinley, Michael	O2-4	34
	P10-3	101		P17-1	146
	P10-4	102		P17-2	147
	P10-5	103	Maffett, Rebekah	P8-2	83
Lam, Ben	O19-4	166	Mair, Braeden	P23-2	188
Lang, Pencilla	P6-6	68	Mak, Helium	P10-6	104
	P6-7	69	Mandzia, Jennifer	O27-5	219
	O25-3	205	Maneas, Efthymios	P5-2	54
Lanting, Brent	O3-2	38	Manokaran, Jenita	P11-4	110
Larsen, Melissa	P9-5	95	Maralani, Pejman	P24-5	199
	O26-2	210	Marcus, T.	O1-4	28
Lasso, Andras	P4-7	49	Martel, Anne	O14-3	130
Lau, Angus	P24-5	199		P16-1	140
Lawrence, Liam	P24-5	199		O21-5	179
Le Foll, Bernard	P5-9	61		O25-2	204
Leclerc, Christopher	O15-5	138	Martin, Allan	P4-3	45
Lee, Donald	O27-5	219	Martinez, Paco	O26-3	211
Lee, Mitchell	P9-4	94	Martinez, Diego	P8-5	86
Lee, Ting-Yim	P5-7	59	Masellis, Mario	O19-4	166
	P17-4	149	Mason, N. Scott	P17-5	150
	P24-1	195	Mathis, Chester	P17-5	150
	O27-5	219	Matsuura, Naomi	P12-1	115
Lee, Young	O21-5	179		O20-5	173
Leipsic, Jonathon	O15-3	136	Matthews, Jordyn	P8-6	87
Li, Alex	O15-2	135	Mattonen, Sarah	P6-3	65
Li, Chen	P7-2	74		P6-6	68
Li, Daniel	P23-1	187		P6-7	69
Li, Natalie	P4-9	51		O25-3	205
Liebig, Patrick	P23-4	190	McCormack, David	P9-1	91
Limongi, Roberto	O2-4	34		P12-5	119
	P17-2	147	McCready, Matthew	P8-3	84
Lindberg, Anton	P17-5	150	McCrindle, Brian	P11-1	107
Litvack, Michael	P23-1	187	McGrath, Sean	P12-1	115
Liu, Jerry	P4-1	43	McIntosh, Chris	O25-4	206
Liu, Junmin	P23-3	189	McKay, Doug	P11-5	111
Liu, Hanlin	O20-3	171		P22-1	181
Liu, Shirley	O13-5	126	McKee, Trevor	P22-5	185
	O26-5	213	McKenzie, Charles	P23-7	193
Lo, Justin	O14-1	128	Mendez, Adrian	O1-5	29
Lock, Michael	O13-3	124	Mendez, Lucas	O1-2	26
	P24-6	200			

Name	Presentation	Page	Name	Presentation	Page
Menon, Bijoy	P17-4	149	Nithiyanantham, Saiee	O14-1	128
	O27-5	219	Norley, Chris	P10-7	105
Menon, Ravi	P7-5	77	Norman, Elizabeth	P10-1	99
	O19-5	167		P10-3	101
Merchant, Shaila	P6-9	71	Noseworthy, Michael	P5-6	58
	P22-1	181		P8-4	85
Miller, Steven	O14-1	128		P11-1	107
Milot, Laurent	O25-2	204		O19-3	165
Miranda, Dayton	P18-3	156		P22-2	182
Moehring, Amanda	O27-3	217		O27-1	215
Montero-Odasso, Manuel	P10-7	105	Nowikow, Cameron	P5-6	58
Moore, John	P4-4	46		P8-4	85
	P5-2	54	Nyström, Nivin	O13-5	126
	O14-2	129		O15-2	135
Morris, Lindsay	P23-7	193		O26-5	213
Moslemi, Amir	P22-3	183	O'Driscoll, Olivia	P16-3	142
	P22-4	184	Omer, Mohammad	P7-3	75
Motooka, Yamato	P12-1	115	Onuska, Kate	P7-8	80
Mouawad, Matthew	O13-3	124	Orlando, Nathan	O21-3	177
	P24-6	200	Ouriadov, Alexei	P9-1	91
Mousavi, Parvin	O1-1	25		P12-4	118
	O1-3	27		P12-5	119
	P4-7	49		P12-6	120
	P5-8	60	Pac, Sara	P17-3	148
	P6-8	70	Palaniyappan, Lena	O2-4	34
	P6-9	71		P7-6	78
	P11-5	111		P17-1	146
	P16-5	144		P17-2	147
	P22-1	181	Pantazopoulos, Koula	O19-5	167
Moussa, Madeleine	O1-4	28	Papernick, Sam	O3-3	39
Mozaffari, Maryam	O15-2	135		P24-2	196
Mrkobrada, Marko	O19-5	167	Parasram, Tristhal	P18-6	159
Munch, Maxime	P23-2	188		P18-7	160
Murrell, Emily	P12-2	116	Park, Claire	O1-5	29
Muscedere, Giulio	O13-3	124		P5-3	55
Mushtaha, Farah	O27-3	217		P24-2	196
Myrehaug, Sten	P24-5	199		O26-1	209
Nachum, Ilanit	O13-3	124	Parraga, Grace	P9-1,	91
Nahas, Hassan	P11-2	108		P12-5	119
Nayak, Krishna	O26-2	210	Pasternak, Stephen	O19-5	167
Nichols, Anthony	P6-6	68	Patel, Tirth	O25-4	206
	P6-7	69	Paula, Demetrius	P5-4	56
Nikolov, Hristo	P18-2	155	Pautler, Stephen	O1-4	28
Nikolova, Natalia	P5-6	58	Penner, Samuel	P12-1	115
	P8-4	85	Perera-Ortega, Andrea	P16-5	144
Nisar, Hareem	P5-2	54	Perron, Samuel	P12-6	120

Name	Presentation	Page	Name	Presentation	Page
Peters, Terence	P4-4	46	Rezaiee, Aria	P6-1	63
	P4-9	51	Richardson, Lauryn	O19-5	167
	P5-2	54	Robert, Normand	P10-2	100
	O14-2	129	Robinson, Sydney	P10-1	99
Petrov, Ivailo	P11-6	112		P10-3	101
	P11-7	113	Rodgers, Jessica	O1-2	26
Piazza, Roberta	P5-2	54	Rodrigues, George	P6-2	64
Pichardo, Samuel	P4-5	47	Rohani, Seyed Alireza	O27-3	217
Picot, Paul	P8-8	89	Romagnoli, Cesare	O21-3	177
Pike, Victor	O13-2	123	Ronald, John	O13-5	126
Pinault-Masson, Emile	P12-3	117		O26-3	211
Piorkowska, Karolina	O3-4	40		O26-5	213
	O3-5	41	Rotstein, Benjamin	P23-2	188
	P4-5	47	Roudaia, Eugenie	O19-4	166
Polak, Paul	P5-6	58	Rudan, John	P4-7	49
Pollmann, Steven	P7-7	79		P6-9	71
	P18-2	155		P11-5	111
Pope, Josh	P4-1	43		P22-1	181
Post, Martin	P23-1	187	Ruschin, Mark	P24-5	199
Potter, Hollis	O3-2	38	Rusu, Doris	P8-6	87
Powe, Laura	P17-2	147	Sachin, Pandey	O27-5	219
Prado, Marco	P7-8	80	Sadanand, Siddharth	P8-7	88
Prado, Vania	P7-8	80	Sadeghi, Saman	P24-4	198
Prajapati, Rahil	P23-5	191	Sadeghi-Naini, Ali	O13-4	125
Prato, Frank	P9-7	97	Sahgal, Arjun	O21-5	179
	O13-3	124		P24-5	199
	O20-1	169	Sahovaler, Axel	P4-6	48
	O20-2	170	Sailasuta, Napapon	P5-9	61
	P23-5	191	Sainani, Viveka	P24-2	196
	P24-1	195	Salsali, Alex	P8-8	89
	P24-6	200	Samani, Abbas	O13-4	125
Qin, Emily	O25-1	203		P18-3	156
Rabin, Jennifer	O19-4	166	Santilli, Alice	P11-5	111
Radelet, April	P17-5	150		P22-1	181
Rahman, Naila	P7-3	75	Santyr, Giles	P23-1	187
	O15-1	134	Savoia, Alessandro	P8-2	83
Rainbow, Michael	P10-1	99	Schieda, Nicola	P6-5,	67
Rajkotwala, Murtuza	P4-6	48		O14-4	131
Ramalli, Alessandro	P8-2	83		P16-2	141
Ramanan, Venkat	O26-2	210	Schmitz, Taylor	P7-8	80
Ranota, Tuneesh	P12-5	119	Scholl, Tim	O15-2	135
Regenold, Max	P4-5	47		O26-3	211
Regnault, Timothy	P23-7	193	Sedghi, Alireza	O1-3	27
ReiaziReza	P6-1	63		P16-5	144
Ren, Kevin Yi Mi	P11-5	111		P22-1	181
	P22-1	181	Seed, Michael	O14-1	128

Name	Presentation	Page	Name	Presentation	Page
Sehl, Olivia	O2-5	35	Surry, Kathleen	O1-4	28
	O20-4	172	Sussman, Dafna	P8-7	88
Sekuler, Allison	O19-4	166		P9-4	94
Sembhi, Ramanpreet	P12-4	118		O14-1	128
Serack, Fiona	O15-5	138	Svensson, Samuel	P17-5	150
Serrai, Hacene	P12-4	118	Sykes, J.	P9-7	97
	P12-5	119	Szentimrey, Zachary	P11-3	109
	P12-6	120		O19-1	163
Sethi, Simran	P23-7	193	Tadic, Tony	O25-4	206
Shalaby, Nourhan	O26-3	211	Tan, Wan-Cheng	O2-2	32
Shangguan, Hanyue	P9-6	96		O2-3	33
Shanks, Hayley	P7-8	80		O15-3	136
Shen, Yu-Jack	P12-1	115		O15-4	137
Shmuilovich, Ogla	O13-3	124		P22-3	183
Shuhendler, Adam	P12-3	117		O25-5	207
Siddiqui, Maryam	P4-5	47	Tang, Anthony	O19-5	167
Siemens, Robert	P5-8	60	Tang, Keith	P9-3	93
Silverman, Michael	O19-5	167	Tanguay, Jesse	P5-5	57
Simard, Nicholas	P11-1	107		P8-1	82
Singh, Sheila	P24-4	198		P8-8	89
Singh, Sheldon	P9-5	95		P18-1	154
Smailovic, Haris	P9-7	97	Taylor, Edward	P24-3	197
Smil, David	P12-2	116	Taylor, Russ	P4-7	49
Smith, Lauren	P23-7	193	Teeter, Matthew	O3-2	38
Smith, Christopher	O1-4	28	Tessier, David	P10-5	103
Soddu, Andrea	P5-4	56		P24-2	196
Sohn, Daniel	P17-5	150		O26-1	209
Spicer, Erin	O19-5	167	Tfeil, Yahya	O1-1	25
Sposato, Luciano	O19-5	167	Théberge, Jean	O2-4	34
Stanisz, Greg	P8-7	88		P7-6	78
	P24-5	199		P17-1	146
Steven, David	P17-6	151		P17-2	147
Stewart, James	P24-5	199	Thibodeau, Jean Francois	P9-2	92
Stillo, David	O19-3	165	Thiessen, Jonathan	P7-8	80
Stodilka, Rob	P18-2	155		P9-7	97
Suchý, Mojmír	P12-3	117		P12-4	118
Suh, Nina	P10-1	99	Thirumal, Sindhura	P5-8	60
	P10-3	101	Thompson, R. Terry	O13-3	124
Sullivan, Rebecca	P9-7	97		O20-1	169
Sumra, Vishaal	O27-2	216		O20-2	170
Sun, Allen	O13-3	124		P24-6	200
Sun, Qin	O20-1	169	Tolgyesi, Allison	P10-2	100
	O20-2	170	Tong, Junchao	P12-2	116
	P23-5	191		O13-2	123
Sunderland, Kyle	P4-7	49		P17-5	150
Suppiah, Suganth	P4-3	45	Tortoli, Piero	P8-2	83

Name	Presentation	Page	Name	Presentation	Page
Truong, Yen	P12-3	117	Ward, Aaron	O1-4	28
Truong, Peter	P5-9	61		P6-2	64
	P7-4	76	Waspe, Adam	O3-4	40
Tse, Desmond	P7-1	73		O3-5	41
	O27-4	218		P4-5	47
Tseng, Chia-Lin	P24-5	199	Watson, Iain	P12-2	116
Ukwatta, Eranga	P6-5	67	Weersink, Robert	P4-8	50
	P11-3	109	Welch, Mattea	P6-1	63
	P11-4	110		O25-4	206
	O14-4	131	Weyers, Jill	O26-2	210
	O14-5	132	White, James	O14-5	132
	P16-2	141	Whitehead, Shawn	P12-4	118
	O19-1	163	Whyne, Cari	P4-1	43
Umoh, Joseph	P10-6	104		P4-3	45
	P10-7	105		P6-4	66
Ungi, Tamas	O1-1	25		P10-2	100
	O1-3	27		O21-5	179
	P4-7	49	Wiercigroch, Julia	O1-1	25
	P6-9	71	Wihlidal, Jacob	O1-5	29
	P16-3	142	Wilk, Benjamin	P9-7	97
	O21-1	175	Wilson, Brian	P4-6	48
	O21-2	176		P4-8	50
Valliant, John	P24-4	198	Wilson, Sydney	P18-2	155
Valsamis, Jake	P5-1	53	Winston, Gavin	P16-5	144
Vanberlo, Blake	P4-9	51	Wisenberg, Gerald	P9-7	97
Vanderbeck, Kaitlin	P11-5	111		P24-1	195
Varela-Mattatall, Gabriel	P7-5	77	Wong, Dickson	P10-7	105
Varma, Sonal	P22-1	181	Wong, Suzanne	P4-5	47
Vasdev, Neil	P12-2	116	Wong, Timothy	P6-5	67
	O13-2	123	Woodward, Elise	P9-1	91
	P17-5	150	Wright, Alex	O20-5	173
Veinberg, Natan	P4-9	51	Wright, Graham	P9-5	95
Virdee, Sukhraj	O15-3	136		P23-6	192
Vitkin, I. Alex	P24-3	197		O26-2	210
Vivekanantha, Prushoth	O20-1	169	Wu, Tingting	P9-1	91
Vos, Sjoerd	P16-5	144	Wu, Victoria	P6-9	71
Waddell, Nicole	P8-7	88	Wu, Catherine	O1-3	27
Wade, Trevor	P23-7	193	Wunker, Claire	P4-5	47
Wagner, Matt	O14-1	128	Wyszatko, Kevin	P24-4	198
Walker, Ross	P6-9	71	Xiang, Yun	P12-1	115
Wallis, Julie	P22-1	181		O20-5	173
Wan, Wankei	P10-6	104	Xiao, Dan	O2-1	31
Wang, Ami	P11-5	111		P8-6	87
	P22-1	181		P18-6	159
Wang, TianDuo	O26-5	213		P18-7	160
				O26-4	212

Name	Presentation	Page
Xiao, Yiming	P17-6	151
Xiao, Di	O21-4	178
Xu, Kathy	O15-1	134
Yaffe, Martin	O14-3	130
Yaremko, Brian	O13-3	124
Yasufuku, Kazuhiro	P12-1	115
Yeung, Timothy	P6-2	64
Yiu, Billy	P9-6	96
	P11-2	108
	O21-4	178
Young, Dylan	O14-1	128
Young, Heather	P5-7	59
	P24-1	195
Yu, Alfred	P8-2	83
	P9-6	96
	P11-2	108
	O21-4	178
Zabel, William	P24-3	197
Zabihollahy, Fatemeh	P11-4	110
	P16-2	141
Zaidi, Mark	P22-5	185
Zanette, Brandon	P23-1	187
Zelko, Lauren	P6-3	65
Zhang, Lifeng	P7-2	74
Zhang, Xiao-An	P9-3	93
	O20-3	171
Zhu, Lihua	P9-2	92
Zhu, Ning	P7-2	74
Zhu, Calvin	P22-2	182
Zindler, Jaap	P6-2	64
Zoghbi, Sami	O13-2	123
Zou, Yiran	P12-1	115
	O20-5	173

Name	Presentation	Page
------	--------------	------

The Scientific and Organizing Committee for the ImNO 2021 Annual Symposium would like to thank you for attending and acknowledge our supporting consortia and sponsors.

We invite you to attend the 20th ImNO Annual Symposium in March 2022 in Toronto, Ontario.

